Sequence-defined DNA Polymers: Applications in Drug Delivery and Supramolecular Assembly

by

Danny Bousmail

A thesis submitted to McGill University in partial fulfillment of the requirements of the degree of

Doctor of Philosophy

Department of Chemistry
McGill University
Montreal, Quebec, Canada

August 2018

To my parents, Rima and Kamil, and my brother Ryan
for your unconditional love and support.
You are my whole world!

Abstract

DNA has gained great attention both as a biological molecule and structural building block due to its well-defined structure, molecular recognition properties and programmability. The marriage of DNA with synthetic polymers, creating DNA-polymer hybrids, has allowed the realization of novel materials with added functionalities, that could not be achieved otherwise. To date, different synthetic routes have been proposed for the generation of DNA block copolymers. However, the generation of monodisperse DNA-polymer conjugates with control over the sequence of monomer and length of strand has been a challenge. These limitations have impacted the potential applications of DNA-polymer conjugates, where structural polydispersity has limited their use in drug delivery and materials science. Recently, a new class of monodisperse sequence-defined DNA-polymers has been reported. This thesis examines this new class of DNA-polymer hybrids in the context of drug delivery and supramolecular assembly. Using this DNA-polymer platform, different strategies that address key challenges of self-assembled materials in drug delivery are investigated. Firstly, the examination of DNA nanoparticles as a structurally monodisperse drug delivery platform is described. Detailed investigation of the stability of structures, cellular uptake, and *in vitro* activity demonstrates the high efficacy of drug-loaded structures. Additionally, *in vivo* studies of this system show full-body biodistribution, long circulation times and tumor accumulation in mouse models. The great potential of these DNA-polymer vehicles as a general platform for chemotherapeutic drug delivery is highlighted. Secondly, different approaches to tackle limitations of nanocarrier-based delivery systems are investigated. Through a range of optimization studies to our first-generation DNA nanoparticle system, we show progress towards creating a highly functional "smart" delivery platform for biomedical applications. Thirdly, an application of sequence-defined DNA polymers in supramolecular assembly in described. A discovery is reported where the site-specific introduction of a single cyanine dye into DNA-polymer conjugates causes a complete morphological shift from spheres to 1D nanofibers with controlled length and dimensionality. DNA fibers are formed through a seeded growth mechanism and can also be used as bioanalytical tools due to changes in their optical properties upon assembly. These structures also form complex hierarchical hybrid structures when combined with other nanomaterials. Overall, this thesis provides a critical evaluation of the exciting applications of this new class of DNA-polymers, highlighting approaches to tackle the challenges of nanomaterials at the interface of biomedicine and materials science.

Résumé

L'ADN éveille la curiosité des scientifiques au-delà de ses propriétés biologiques : des groupes de recherches utilisent la molécule d'ADN comme un matériau de construction moléculaire. En effet, l'information contenue dans sa structure lui confère des propriétés de reconnaissance moléculaire et une très grande programmabilité. L'ajout de polymères synthétiques sur des brins d'ADN a permis la création de nouveaux matériaux et de structures auto-assemblées aux propriétés uniques. Jusqu'à aujourd'hui, différentes voies ont été développées pour la synthèses de ces matériaux hybrides. Cependant, il reste encore difficile de contrôler précisément, lors de la synthèse, la séquence et la longueur du copolymère. La polydispersité du produit obtenu a ainsi limité l'utilisation de ces conjugués en chimie des matériaux ou pour des applications thérapeutiques. Récemment, nous avons développé une méthode de synthèse de polymères hybrides qui permet de contrôler précisément la séquence à l'échelle moléculaire. Ces polymères forment des structures monodisperses. Dans cette thèse, nous proposons d'examiner les propriétés d'auto-assemblage de ces matériaux hybrides à la séquence connue et définie, ainsi que leur utilisation comme système d'administration de médicaments. Dans le premier chapitre, nous présentons une méthode pour encapsuler un agent anti-cancéreux dans des structures micellaires. Nous avons étudié la stabilité de ces nanoparticules en milieu biologique ainsi que leur internalisation dans les cellules. Les résultats *in vitro* ont montré que les particules pouvaient détruire les cellules cancéreuses en libérant le principe actif. Enfin, des expériences sur des modèles de souris ont révélées que la particule circulait à travers tout le corps, possédait une grande stabilité et s'accumulait dans les tissus cancéreux. Dans une deuxième partie, nous avons cherché à améliorer les propriétés du système d'encapsulation développé précédemment, afin de créer une particule intelligente. Les expériences ont révélé le potentiel de ces véhicules de seconde-génération dans l'administration de médicaments. Enfin, nous avons étudié les propriétés d'assemblage de polymères à séquence contrôlée. Nous avons introduit une molécule de cyanine dans le conjugué ADN-polymère causant un changement de morphologie. L'insertion de la molécule dans la séquence conduit à la formation de nanofibres, au lieu de sphères, dont on peut

contrôler la longueur et la dimension. Une étude mécanistique a révélé que ces fibres d'ADN se formaient à partir d'un noyau moléculaire (mécanisme par nucléation). Lors de l'assemblage, les propriétés optiques de la structure changent, ce qui rend ces matériaux intéressants pour des applications bio-analytiques. Finalement, nous avons utilisé ces structures en combinaison avec d'autres nanomatériaux afin de créer des structures hybrides d'une très grande complexité. En conclusion, cette thèse propose d'étudier différentes applications des conjugués ADN-polymères, en apportant de nouvelles solutions aux défis actuels dans le développement de nanomatériaux utilisés en biomédecine et en chimie des matériaux.

- *Translation by Aurelie Lacroix*

A prayer to start off…

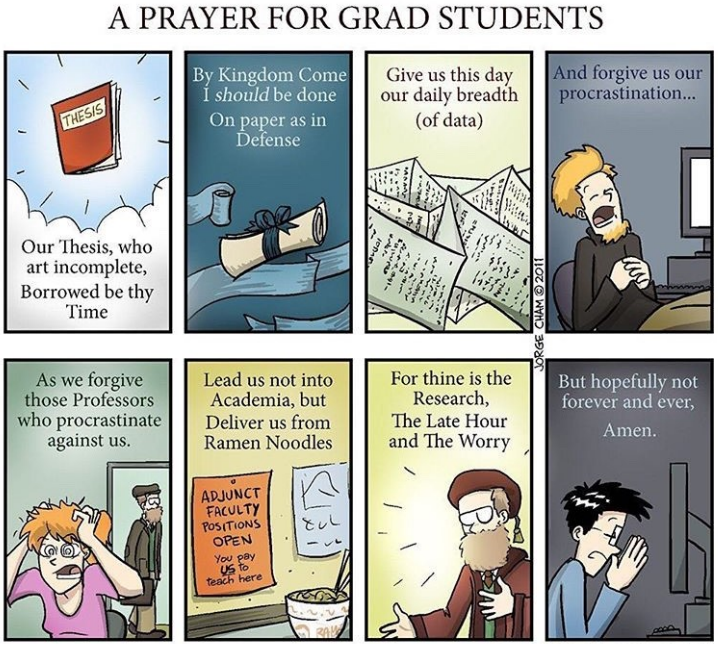

Acknowledgements

What a journey it has been! To all the people who have been part of it, in Montreal and elsewhere, I am deeply grateful. Firstly, I would like to thank my research supervisor, Professor Hanadi Sleiman for her mentorship and guidance over the past 5 years. Her creativity and enthusiasm have greatly inspired me, whether it be in scheduled meetings, or sudden "eureka-moment-come-to-my-office" sessions. I have been very lucky to be part of it! I am evermore grateful for her fine balance of hands-off support, constructive criticism and creative encouragement which has fostered my development both as a scientist and as a person. Thank you!

I would also like to thank all the faculty and professors in the McGill Chemistry Department who have helped me along the way. Professor Auclair, for her support as a review committee member and an academic reference. Professor Cosa, for all the feedback as a review committee member and for granting me unlimited access to his lab's instrumentation.

Next, I would like to thank the Sleiman lab crew (Sleimanellas/Sleimanellos) who has undergone a rapid turnover of graduate students during my stay. It has been amazing since day one, I think of us not as a group but as a family (Pretty Big Family if you will). To the first generation of people (my four bench neighbours), I am grateful for my first mentor and friend, Tom (Tombo), and for all your "cool stories, bro" about the art of brewing, heavy metal and for introducing me to "UnTappd" – an app equivalent to Tinder but for beer (not weird at all)! To Johans, besides being a great work collaborator and like a brother to me, you're "a gentleman and a scholar" and I'm not "angry with you, I'm just disappointed in you" for not appreciating Apple products. Also, thanks for always welcoming me at your place, our awesome lunch discussions and for bringing joy and laughter into my days in the lab. Justin, the ultimate lab DJ, introducing us to the hottest radio hits, check out his PhD playlist in his thesis for more info (always advertising your work). I've learned a great deal about IPA and hops from you. Kai, my gym "bro", you've added a new dimension to scientists who powerlift, great gym discussions we had, keep it Blasian.

To the members who joined after my time: Hassan, who will never agree that Lebron is the G.O.A.T. Great memories when you first arrived "Terrasses Bonsecours waddap!", gym push-season, NBA nights. We'll definitely connect down the line. Aurelie, a walking laughing machine haha, introducing me to the world of Belugas. Composer of the "We gonna $$ tonight, $$, $S, tonight." musical. Stay awesome, Oreo! Emparo, the Queen of Paella and originator of "Wa ra faa" phrase, who could handle more liquor than most of the guys in lab. I'll see you soon in Valencia (or was it Balencia?). Alex Rousina, keep pumping! By now you've probably landed on a new weird gym supplement that you found on some sketchy website. Tuan, "crosslink?" Our Neflix parent, and most trusted provider of Tuna streaks for "turning points". Carla, a certified undercover C.I.A. agent, and our go-to background check specialist. Thanks for the daily funny Memes that made my PhD writing experience more bearable and inspired me for PhD comics. Michael, how you going, mate?! Always watch for "the Shaaks in the Wotaa". A big thanks to Nicole the Choir Angel and Tadoussac boat crew member, Pongphak the lab member I spent the longest time with (5 solid years) thanks for a great collaboration. I hope the Meijer lab don't take as many pictures of you while napping. Donatien, our French connection and the early host of the most epic house parties (one of which is still remembered to this day). Katherine, the "Awesome" Strawberry lover, thanks for putting Magog on the map and for all the apples. Amani (Amauuuni) you're not Lebanese you're Canadian. Alex Prinzen my Ontario fellow and most consistent Benelux member. Daniel Saliba the founder of "Calexo (killak zo2)" term, thanks for teasing Johans and Hassan. Xin my office neighbour and specialist in Dragon-themed wall graffiti/chalk art. Thanks for introducing me to my first ever (maybe last?) chicken feet food experience. Casey, I want to see your little Bakery open by 2025. Chris, always there to enhance our moods. Violeta, my first ever Secret Santa in the lab (who I had so much trouble guessing), thanks for all the help with synthesis. Janane "Great, ya 3youne" thanks for the help in my early PhD stages. To Graham, Katie, Karina, Macieg, Kim, Mohammad, Kamila, Adrienne, John, Hammond, Sally, Sonia, Albert, Farhad, Maya, Tolulupe, Klaudia, and all the other Sleiman lab members, it has been a pleasure working with you!

I would also like to express my gratitude to Chantal Marotte who has been very helpful and provided great assistance from before I even arrived at the department right to the end.

To my main crew, I'll keep it brief since I will be thanking you in person very soon. My Toronto fam jam: Mahoura, my best friend and our famed dentist. Toronto V2.0 coming soon! JeeJee, my bestie, my undergrad study partner, and our go-to corporate lawyer and MBA, cheers to over a decade of an awesome friendship and many more. Roni, my Toronto partner-in-crime, and NYC's/LA's renowned fashion photographer. Thanks for giving me a taste of how to live like a celebrity, get into VIP fashion parties and meet all these important people. Mandy, the original member of the TO crew and the one who finds me very entertaining, “Cuttles ya Cuttle”. Titi, (Oh My God!), countless great memories in Montreal, and many more soon in TO. Thanks for bearing with me throughout my swings in last few hysterical years of my degree. MK, the female version of me with an alarmingly scary character similarity, you were always there to listen to my WhatsApp dwelling about life/school. Simi, the Cheetos monster, stay “litty” always. It’s funny how as we were finishing undergrad in Toronto, the whole crew would sit down and talk about what will happen years down the line. I’m blessed to still have you all in my life, and I’m so proud of all your amazing achievements.

To my childhood friends: Salo, Hazo, Juju, Ago, Khalife, Hassoun, Peter, Raoum, l 3emer, Nimri. We’ve been brothers since we were kids. From our August reunions, to the active chat group with 500+ unread messages to go over everyday after work (most of them useless with Salo picking on Peter or Khalife) – it’s been grand!

Finally, to my loving family, you all know your importance in my life. This journey wouldn’t have been possible without your unwavering love and support. Thanks for always believing in me and encouraging me along the way. My mom and brother, you were always there for me no matter what. My uncles, and aunts, cousins and all the extended family, thanks for all the support. Lastly, to my dad watching over me from the heavens above, I know you’ve always been guiding me through this degree. I hope I made you proud. *This one’s for you, pops!*

Table of Contents

3 Optimization of DNA Nanostructures for Targeted Drug Delivery Applications

Table of Figures

List of Tables

List of Abbreviations

1D	One dimensional
2D	Two dimensional
3D	Three dimensional
A	Adenine
AGE	Agarose gel electrophoresis
AFM	Atomic force microscopy
AuNP	Gold nanoparticle
bp	Base pair
C	Cytosine
CLL	Chronic lymphocytic leukemia
CLSM	Confocal laser scanning microscopy
CMC	Critical micelle concentration
CPG	Controlled pore glass
Cy3	Cyanine 3
Cy5	Cyanine 5
Cy5.5	Cyanine 5.5
D-DNA	Dendritic DNA amphiphile
DLS	Dynamic light scattering
DMEM	Dulbecco's modified eagle's medium
DMT	Dimethoxytrityl
DNA	Deoxyribonucleic acid
ds	Double-stranded
DS	Disulfide
DTT	Dithiothreitol
EDTA	Ethylenediaminetetraacetic acid
ESI	Electrospray ionization
FACS	Fluorescence-activated cell sorting
FBS	Fetal bovine serum
FRET	Förster resonance energy transfer
G	Guanine
HEG	Hexaethylene glycol
$\mathbf{HE_{12}}$	Dodecane
HPLC	High performance liquid chromatography
HSA	Human serum albumin
$\mathbf{L_n}$	Number-average contour length
$\mathbf{L_w}$	Weight-average contour length
LC-MS	Liquid chromatography-mass spectrometry
LNA	Locked nucleic acid
miRNA	Micro RNA
MW	Molecular weight
OD	Optical density

PAGE	Polyacrylamide gel electrophoresis
PBS	Phosphate-buffered saline
PPO	Polypropylene oxide
PCR	Polymerase chain reaction
PEG	Polyethylene glycol
R_H	Hydrodynamic radius
ROMP	Ring opening metathesis polymerization
RNA	Ribonucleic acid
RT	Room temperature
SDS	Sodium dodecyl sulfate
siRNA	Small interfering RNA
ss	Single-stranded
T	Thymine
TAMg	Tris-acetate-magnesium buffer
TBE	Tris-boric acid-EDTA buffer
TEM	Transmission electron microscopy
TEMED	Tetramethylethylenediamine
Tris	Tris(hydroxymethyl)aminomethane
UV-Vis	Ultraviolet-visible

1

Introduction

1.1 Historical perspective

The autonomous organization of molecules and macromolecules into structures and patterns is a fundamental theme spanning all forms of life. This type of self-organization occurs without human intervention and is particularly fascinating to us - we are strongly attracted to the appearance of order from disorder. From a philosophical perspective, cells, the smallest living forms of life are created by self-assembly and understanding the origins of life will hence require understanding the rules of self-assembly. From an architectural perspective, self-assembly is an efficient way for constructing larger complex materials. Historically, chemists have sought to control, transform and even create new forms of matter – chemists build things. As our capabilities have advanced, we are now thriving to find more sophisticated ways to create complexity. For the past century, scientists have relied on a central theme in most discoveries - the formation or breaking of covalent bonds. This strategy has allowed the creation of a plethora of molecular configurations from as many as 1000 atoms in some cases. As impressive as these discoveries have been, the level of complexity achieved in covalently linked structures is still exiguous in comparison to the natural world; the size range of molecules synthesized is limited to several nanometers. This has motivated chemists to start looking "to increase complexity beyond the molecule" and engineer interactions between molecules and macromolecules as construction strategies – the theme of supramolecular chemistry.[1]

1.2 Supramolecular Chemistry

The term "supramolecular chemistry" was coined by Jean Marie Lehn in 1978. It was used to describe the construction of species with higher complexity using intermolecular non-covalent interactions. The assembly of supramolecular species is usually characterized by the nature of interactions that hold the structure together, and the spatial arrangement and architecture of the components that make up the so-called superstructure. Some of the early examples of supramolecular systems include crown ethers (Figure 1.1a) discovered by Pedersen,[2] cryptands (Figure 1.1b) developed by Jean-Marie Lehn[3] and spherands (Figure 1.1c) developed by Cram.[4] These early examples showed cation-binding specificity based on their varying degrees of host pre-organization. Based on these seminal works, the 1987 Nobel Prize in Chemistry was awarded to Donald J. Cram, Jean-Marie Lehn and Charles J. Pederson for their discoveries of molecules with highly-selective structure specific interactions, which laid a strong foundation in the field of supramolecular chemistry. As the field expanded, more complex systems were discovered which include cavitands (such as curcurbiturils)[5] (Figure 1.1d) and supramolecular capsules (Figure 1.1e).[6] Since then, the field has undergone great expansion, which led to many developments in host-guest and molecular recognition chemistries, and the examples of systems that rely on the host-preorganization for high binding selectivity and the use of predictable non-covalent interactions are only ever increasing.[7-8]

Nowadays, scientists take advantage of these early rules in supramolecular chemistry and design complex nanoscale architectures in high yields. The quest for structures that rely on weak non-covalent interactions such as hydrogen bonding (H-bonding), electrostatic, hydrophobic, π-π stacking, metal coordination and Van der Waals interactions has resulted in a plethora of elegant systems, each displaying different architecture and functionality. Unlike covalent systems, the use of weak interactions allows for error correction, reversibility, and structural manipulation. Assembly conditions such as ionic strength, concentration of molecules, temperature can be controlled and varied to force different types of assemblies. Additionally, the shape, size, flexibility, and charge of the components play a major role in the overall structure. With that thorough understanding of such factors, scientists are now creating highly complex systems. However, it is noteworthy to say that this process is in no way straightforward and trivial. The design of complex assemblies requires multiple exhaustive efforts for reproducible synthetic routes, detailed characterization methods to yield stable structures. However, the level of structural complexity achieved by scientists is moving at an extraordinary pace, and self-assembly as means of material fabrication is drawing a considerable amount of both economical and scientific attention.

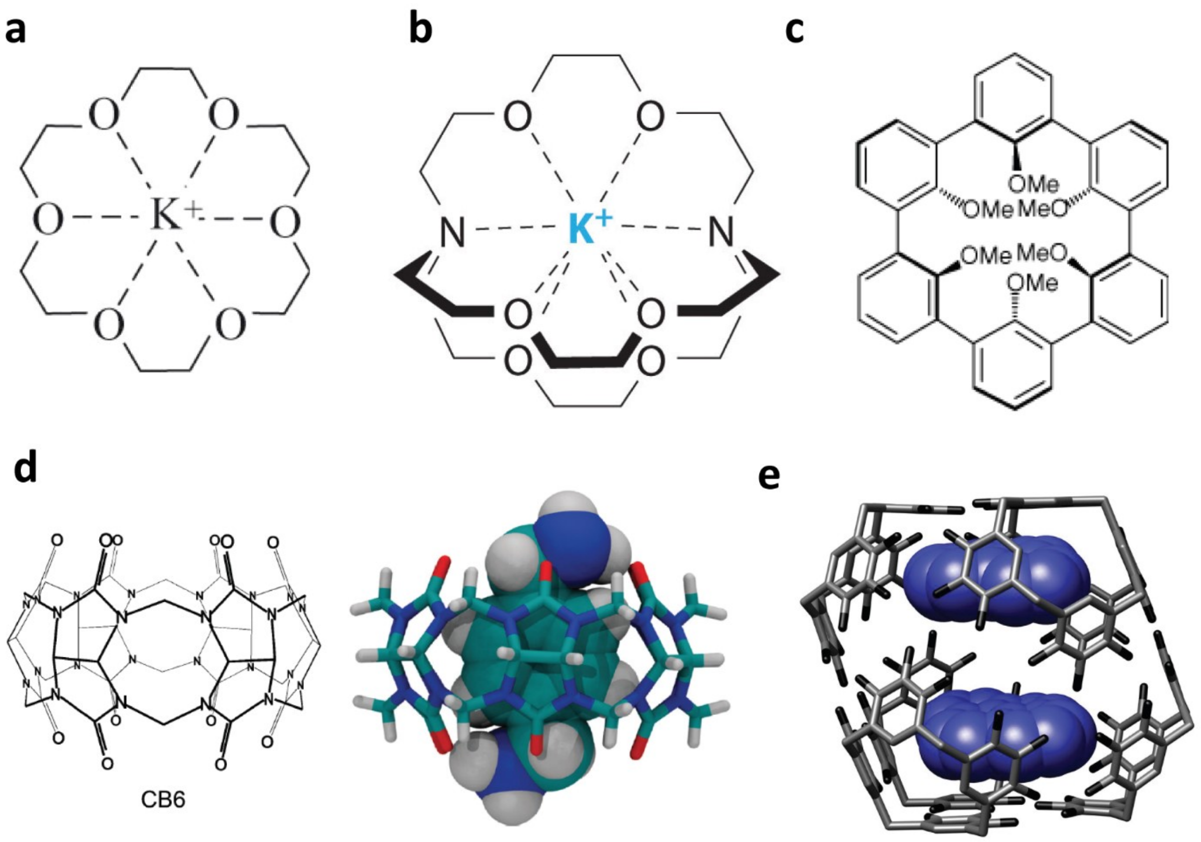

Figure 1.1 – Examples of supramolecular systems displaying molecular recognition and specific host-guest non-covalent interactions. a) metal-coordinating crown ether,[2] b) metal-coordinating cryptand,[3] c) spherand,[4] (Adapted from Wikipedia). d) left: molecular structure of a cavitand (Curcurbituril CB6) and right: X-ray structure of CB6 encapsulating a host molecule.[5] Adapted with permission (Royal Society of Chemistry, 2015). e) hexameric nanocapsule binding two guest molecules.[6] Reproduced with permission (American Association for the Advancement of Science (AAAS), 2005).

Impressive as it is, the level of complexity that researchers have achieved in self-assembled systems still pales when compared to what nature offers.[9] From the communication between cells, to protein folding, to the H-bonded double-helix of DNA and hydrogen bonding of liquid water molecules, to the organization of lipids to make up cell membranes, cells to form tissues, the combination of tissues to create organisms – all examples that nature makes look easy and routine. As much as we would like to match the level of structural and functional complexity, we are still limited by our understanding of the rules governing the interplay of interactions when many components are involved. *Will we ever get there?* Well, we have made a start. We have made great leaps in learning some rules of nature and at emulating some of its construction principles. One important organizing principle is amphiphilicity, which nature uses to create compartments such as cells and organelles. This type of self-organization is largely driven by the hydrophobic effect wherein lipid groups of nature's amphiphilic molecules self-assemble into bulk-like nonpolar phases minimizing water contact, while hydrophilic regions exposed to the surrounding form H-bonds with water molecules. Towards mimicking nature's complexity, we will be using these assembly rules and building blocks that self-organize in well-understood regimes similar to nature's amphiphilic molecules. Amphiphilic block copolymers have emerged as great candidates in that respect. Particularly, DNA block copolymers have recently emerged as a new promising class of amphiphilic block copolymers. The concepts, synthesis, self-assembly, and applications of amphiphilic block copolymers with emphasis on DNA amphiphiles will be discussed in view of this.

1.3 Amphiphilic Block Copolymers

Amphiphilic as a term in Greek means "loving both". In molecules, this attribute is frequently given to oil and water, but in general, amphiphilicity can be described towards any two solvents incompatible with each other. Two general types of amphiphiles are often described: small and large molecules. The former represents a class of molecules with molecular weights on the order of 500. The latter describes molecules that are up to 1000 times larger than "small" molecules.[10] Surfactants and polar lipids are representative examples of small amphiphiles. These examples display characteristic molecular self-assembly behaviour in solutions and in bulk generating nanomaterials of different geometries.[11] An early question in this field was to understand how the molecular structure of surfactants controls the size and shape of the resulting aggregate. Israelachvili pioneered one of the most important studies to address this question and his concepts currently dominate our understanding of self-assembling systems.[12] Israelachvili and co-workers introduced the concept of molecular packing to relate the calculated equilibrium area per molecule to the shape of the equilibrium aggregate.[12] The molecular packing parameter (or critical packing parameter CPP) is defined as $v_0/a_e l_0$, where v_0 and l_0 are the volume and extended length of the surfactant tail and a_e is the surface area of the hydrophobic core in the equilibrium aggregate (Figure 1.2).[13] Considering a spherical micelle of core radius R and composed of g number of molecules, the volume of its core is then $V = g\ v_0 = 4\pi R^3/3$. The surface area of the core is $A = g\ a_e = 4\pi R^2$, hence $R = 3\ v_o/a_e$ (Figure 1.2). Assuming the micelle core is packed with no empty space, then radius R can not exceed the extended length l_0 of the tail. Applying this constraint in the expression for R gives $0 \leq v_0/a_e l_0 \leq 1/3$ for spherical micelles. Using this constraint, these geometric relations have led to the well-known connection between critical packing parameter and aggregate shape: $0 \leq v_0/a_e l_0 \leq 1/3$ for a sphere, $1/3 \leq v_0/a_e l_0 \leq 1/2$ for a cylinder, and $1/2 \leq v_0/a_e l_0 \leq 1$ for a bilayer.

Variable	*Sphere*	*Cylinder*	*Bilayer*
Volume of core $V= g\ v_o$	$4\pi R^3/3$	πR^2	$2R$
Surface area of core $A = g\ a$	$4\pi R^2$	$2\pi R$	2
Area per molecule a	$3v_o/R$	$2v_o/R$	v_o/R
Shape parameter v_o/aR	$1/3$	$1/2$	1
Largest aggregation number g_{max}	$4\pi\ell_o^3/3v_o$	$\pi\ell_o^2/v_o$	$2\ell_o/v_o$
Aggregation number g	$g_{max}\ (3v_o/a\ell_o)^3$	$g_{max}\ (2v_o/a\ell_o)^2$	$g_{max}\ (v_o/a\ell_o)$

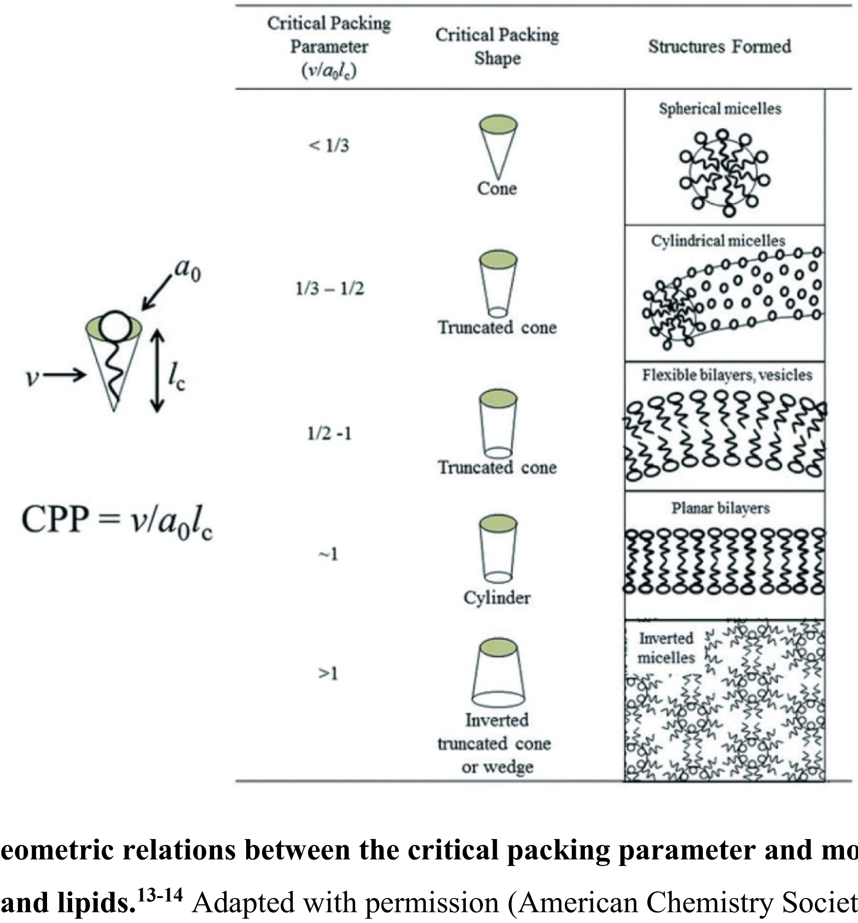

Figure 1.2 – Geometric relations between the critical packing parameter and molecular shapes of surfactants and lipids.[13-14] Adapted with permission (American Chemistry Society, 2011 & Royal Society of Chemistry, 2014)

Block copolymers are considered large amphiphiles, where one block of a certain type of homopolymer is covalently linked to another block of a different type (Figure 1.3a).[15] Amphiphilic block copolymers are synthesized through a wide range of living or controlled polymerization protocols, such as, anionic, living free radical and metal-catalyzed polymerization.[16-18] Such methods have produced polymers with various architectures and compositions. Analogous to the self-assembly behaviour of small molecules, block copolymers organize into different morphologies both in bulk and in solution.[19] This property is due to microphase separation of the two blocks with different solubilities. However, compared to molecular assemblies, block copolymer-based structures exhibit higher durability and stability due to their physical properties. Based on these favourable characteristics, block copolymer self-assembly has not only received scientific interest, but has also seen various applications in drug delivery, biomaterials, catalysis, electronics, photonics, etc.[10, 20-23]

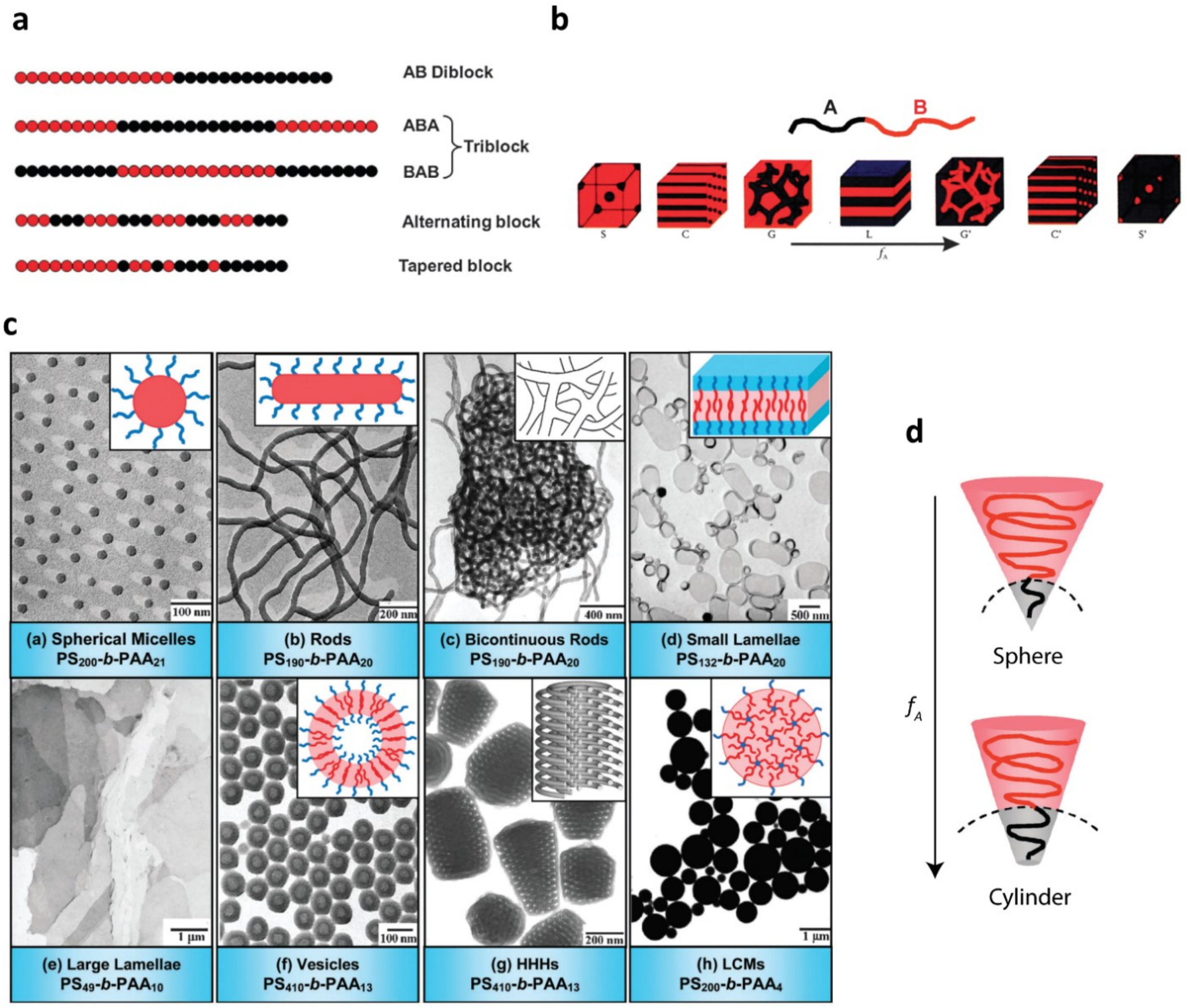

Figure 1.3 – Self-assembly of amphiphilic block copolymers.[15] a) Common structures of block copolymers containing two different types of blocks, A and B. b) Equilibrium morphologies of block copolymers in bulk. S and S' = body-centered-cubic spheres, C and C' = hexagonally packed cylinders, G and G' = bicontinuous gyroids, and L = lamellae. c) Transmission electron microscopy (TEM) images and relative schematic diagrams of various morphologies formed from amphiphilic polystyrene-*b*-poly(acrylic acid) (PS_m-*b*-PAA_n) copolymers in solution. HHH: hexagonally packed hollow hoop (or inverse rod). LCMs: large compound micelles. d) Schematic of possible morphologies and polymer arrangement in AB block copolymers varying from spheres to cylinders. Figures adapted with permission (Royal Society of Chemistry, 2012)

1.3.1 Self-assembly of amphiphilic block copolymers

Self-assembly of amphiphilic block copolymers is a very wide and active area of study. In bulk, block copolymer self-assembly has been studied since the 1960's and is generally well-understood.[10, 22] In such cases, block copolymers containing immiscible units can microphase separate into various morphologies which include spheres (S), cylinders (C), gyroids (G), lamaella (L) and other structures (Figure 1.3b).[24] The assembly is driven by thermodynamics; the competition between unfavourable mixing enthalpy and entropy. Different morphologies are obtained as a result of two competing factors: the interfacial energy between the blocks (enthalpic) and chain stretching (entropic). The microphase separation of block copolymers relies on a few parameters, which include (1) the volume fraction f of the A and B blocks (with $f_A + f_B = 1$), (2) the degree of polymerization ($N = N_A + N_B$) and (3) the Flory-Huggins parameter χ_{AB} which describes the strength of the separation power (or incompatibility) between the two blocks.

Multiple theoretical and experimental studies have characterized the phase behaviour of block copolymers in bulk. Between 1970's–1990's, a number of theoretical studies appeared by Wasserman, Leibler and Bates, which showed the transition of block copolymer assembly into different morphologies with increasing volume fraction f_A at a fixed χN (Figure 1.3b).[25-27] The structure which forms at a given scale is determined by the competition of the two blocks A and B as to which will pay the entropic cost of stretching. Both blocks would prefer to be on a curved interface which affords them more volume. If the two blocks have equal volume fractions $f_A = f_B$, then the balanced competition results in flat interfaces, seen as lamellae. If the blocks are not comparable, then it is more entropically favourable to form a curved interface where the larger block relaxes on the convex side, and the small block stretches (Figure 1.3d).[28] As the block asymmetry is further increased, it becomes more favourable to induce larger mean curvature in structures, which leads to the transition from the lamellar (L) phase to hexagonal packed cylinders (H) to cubic packed spheres (S'). Experimental studies performed in the 1990's by Bates and Mortensen also validated the theoretical predictions.[29] A range of different thermodynamically stable and kinetically frozen morphologies was obtained by heating polymer samples to temperatures above their glass transition T_g temperature followed by quenching to a temperature below T_g.

In solution, block copolymer self-assembly has been a very active area of study. Thermodynamically, this process involves the interplay between enthalpy and entropy. Self-assembly pays an entropic cost of organizing single chains but prevents a larger enthalpic penalty resulting from energetically unfavourable hydrophobe-water interactions. Grouping of chains also leads to an increase of entropy in disordered solvent molecules, therefore lowering the total energy of the system ($\Delta G < 0$). Early studies led by Eisenberg and co-workers showed the observation of different stable aggregated morphologies of a highly asymmetric family of polystyrene (PS)-polyacrylic acid (PAA) block copolymers in aqueous solutions.[30] These structures consisted of spheres, rods, lamellae and vesicles (Figure 1.3c). Eisenberg's work on PS-PAA block copolymers showed that depending on the fraction of hydrophobic to hydrophilic blocks in the polymers, a range of thermodynamically stable morphologies can be obtained. For instance, spherical micelles are formed at a low fraction of hydrophobic to hydrophilic block. As the fraction of hydrophobic block f_A increases, it drives the formation of different morphologies (Figure 1.3d). This is explained through core-chain stretching influencing the free energy of aggregation.[31] At a relatively long hydrophilic block, spherical micelles are observed. As the fraction of hydrophilic block decreases (higher f_A), repulsive forces in the coronal block chains decrease, more chains can aggregate leading to bigger spheres. Bigger spheres cause the polystyrene chains to stretch from the core to the corona-core interface. When the spheres become large enough, the entropic penalty of stretching the core-block renders spheres unfavourable energetically, rods are then formed with a decreased core diameter. As f_A is further increased, it drives the formation of lamellae and so forth. Morphological changes also depend on the water content and copolymer concentration. For example, PS_{190}-PAA_{20} monomers (numbers denote the degrees of polymerization) in DMF-water mixtures change from spheres to rods as the concentration is increased. The architecture of rods provides an ideal surface for the linear templation of nanomaterials, and many examples have been reported for the organization of semiconductor, magnetic and metallic nanoparticles.[32-33] Additionally, control of rod dimensionality and length is an area of high interest. As for spherical micelles, these structures are characterized by a hydrophilic corona that affords water solubility and a hydrophobic core. The core provides an ideal environment for the encapsulation of fluorescent molecules, proteins, genes, and hydrophobic drugs.[34-37] Hence, spherical micelles are under extensive investigation for applications in drug delivery and bioimaging.

Despite the recent advances in block copolymer self-assembly, conventional amphiphilic block-copolymers consisting of synthetic polymer segments still display molecular weight polydispersity hampering control over their assembly behaviour. This is particularly important for drug delivery applications, where precise control over the structure and shape is necessary to ensure reproducibility in the predicted therapeutic effect.[38] To construct more useful block copolymers, integrating a well-defined information-rich biomacromolecule as one of the blocks is a feasible way to synthesize novel structures with a set of functionalities that couldn't be realized otherwise. As one of the most fascinating biomacromolecules, DNA can be precisely tailored and conjugated with synthetic polymers. Besides its biological roles, DNA can be used as a building block based on its excellent molecular recognition and programmability.[39] The introduction of DNA into block copolymers will bring many unique properties that never existed in conventional block copolymers which include a precise chemical structure and sequence, compatibility with different orthogonal modifications, well-defined self-assembly behaviour and high molecular recognition properties. As such, DNA block copolymers (or DNA amphiphiles) are receiving increased attention and application in novel nanostructure design, drug delivery and materials science.[40]

1.4 DNA Amphiphiles

Since the discovery of its structure in 1953, the fascinating DNA double-helix and its well-known Watson-Crick base pairing has captivated scientists in various fields of science.[41] Originally, solely deemed as the "molecule of life", the carrier of genetic information, researchers soon realized that DNA could be an excellent candidate for building new materials due to its highly programmable properties and self-recognition.[42] Aided by the invention of different chemical synthetic methods of DNA starting in the 1960s,[43] the properties of DNA have been well-exploited to construct well-defined architectures, as witnessed by the rapid development of the field of structural DNA nanotechnology.[44]

1.4.1 DNA and Structural Features

Double-stranded DNA (dsDNA) bears a very well-defined structure which makes it ideal as a material of construction. It exists in a number of conformations; however, the B-form conformation is the most common. This form of DNA helix is characterized by a diameter of 2.0 nm, and a pitch height of 3.4 nm made from 10.5 bases (Figure 1.4b).[45] In a double-stranded DNA helix, each strand is composed of a backbone of repeating deoxyribose sugar units linked through phosphodiester bonds between the 5' and 3' hydroxyl groups on the sugars (Figure 1.4a). The DNA sequence is determined by the order and identity of four nucleobases; the purines: adenine (A) and guanine (G), and the pyrimidines: thymine (T) and cytosine (C). The molecular specificity of DNA lies in the hydrogen bonding (H-bonding) interactions between base pairs. Adenine forms two hydrogen bonds with thymine, while guanine forms 3 hydrogen bonds with cytosine (Figure 1.4c,d). The stability of a DNA duplex also relies on the AT to GC content.[46] A higher GC content results in a higher number of H-bond interactions and fewer repulsive secondary interactions between bases, making the DNA duplex more stable. In addition to base complementarity, π-stacking interactions between the aromatic bases add further stability and contribute to the cooperative behaviour (formation of one DNA base pair increases the affinity of formation of an adjacent one) in double-stranded DNA.[47]

Perhaps one of the most important properties of dsDNA, from a structural standpoint, is its persistent length of 50 nm, which allows it to act as a rigid polymer ideal for construction of scaffolds in nanostructures.[48] From 2D tiles and arrays, to 3D nanostructures and DNA origami, the well-defined self-assembly properties of DNA have opened the door to sophisticated geometries and systems with different functionalities.[39, 49-51] Along this direction, DNA has been widely applied in oligonucleotide therapeutics and gene delivery, which has resulted in many DNA-based nanostructures currently investigated for biomedical applications.

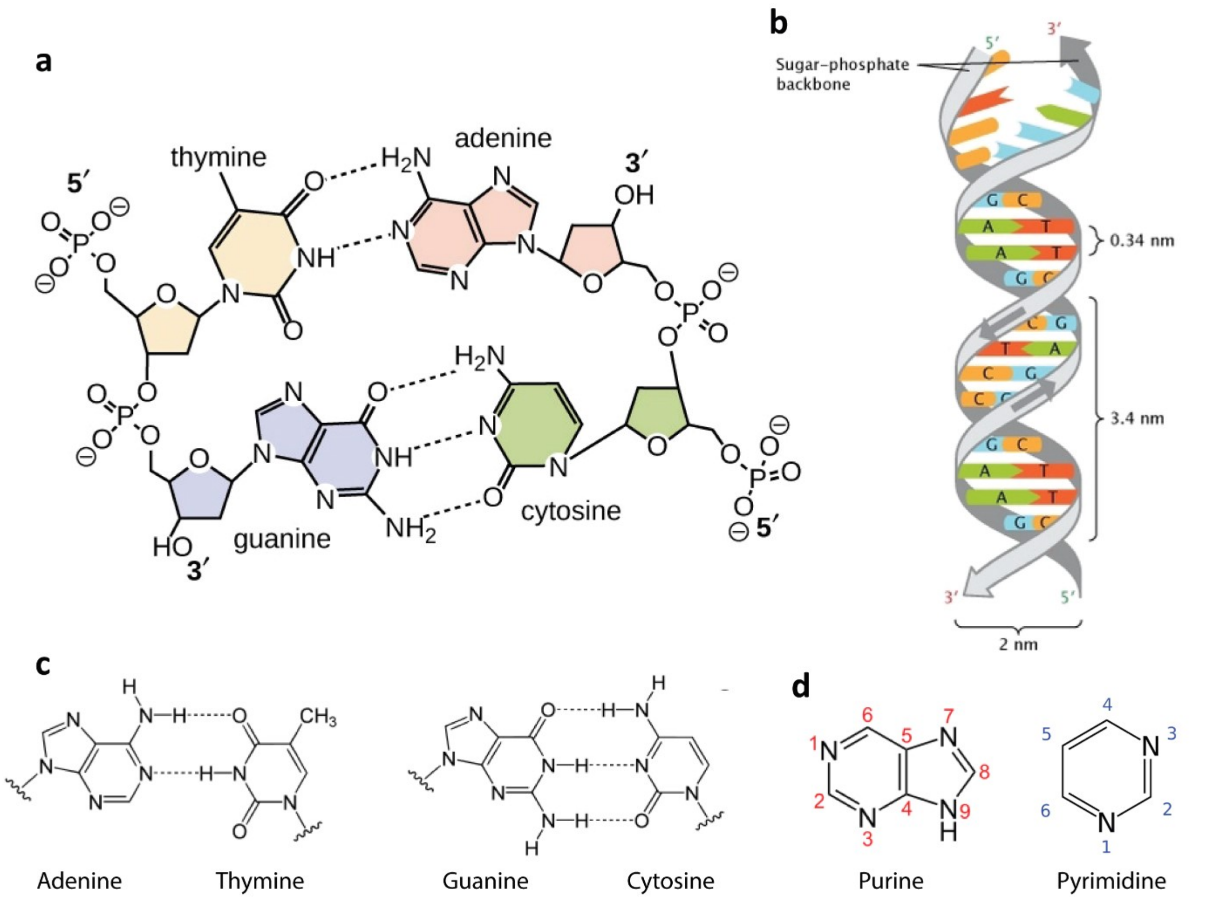

Figure 1.4 – Structural features of DNA. a) Chemical structure of DNA nucleotides showing the H-bonding interactions between nucleobases. b) B-form helix of DNA with its structural dimensions. c) Watson-Crick base pairing between DNA bases and their chemical structures. d) The two types of core composition of DNA bases (Adapted from Wikipedia).

The information-richness of DNA has also attracted many efforts to use it in applications by incorporating different functionalities into its sequence. Perhaps one of the most common early examples of functional groups are fluorescent molecules which in conjunction with DNA have been used as analytical tools and in bioimaging.[52-53] While these approaches expand the breadth of DNA-based functionality, a main focus has been to chemically couple synthetic moieties to DNA that would change the molecule's structure and introduce novel self-assembly properties.[54] Such combinations would afford practical advantages by allowing simultaneous access to the languages of DNA (Watson-Crick base pairing) and synthetic polymers (electrostatic, hydrophobic, H-bonding, π-π stacking, Van der Waals interactions). This class of material is called DNA-polymer conjugates (or DNA hybrids). Currently, DNA hybrid materials find many applications in a wide range of fields, ranging from drug delivery to electronics to diagnostics, and others.[55-56] It is important to mention, however, that the present burst in DNA-polymer synthesis and applications would not be possible without the great advances in solid-phase synthetic methods of DNA. What is now taken for granted, is the result of tremendous accumulated efforts spanning over more than half a century since the invention of chemical synthesis of DNA in the 1960's. While the in-depth historical review is beyond the scope of this thesis, the section below will briefly provide an overview of the key advancements in solid-phase DNA synthesis that have led to the current methods for synthesis of DNA-polymer conjugates.

1.4.2 Automated DNA synthesis

An early challenge in DNA synthesis was to achieve sequence fidelity, i.e. to ensure a given backbone contains all the right identity and order of the desired nucleobases. This early challenge was first tackled by Khorana in 1956, who showed a method for DNA synthesis using solution-phase phosphodiester chemistry (Figure 1.5a).[57] The method by Khorana allowed the synthesis of the first 72-mer DNA gene encoding a transfer RNA (t-RNA).[58] Later in the 1960s, building on Khorana's earlier work, Letsinger developed a DNA synthesis method using solid-phase chemistry.[59] This approach greatly enhanced the removal of side-products and excess used reagents. As part of his strategy, Letsinger adopted phosphotriester chemistry in hopes of increasing yield and decreasing reactivity times (Figure 1.5b).[60] However, it was quickly realized that phosphotriesters were unstable for long-term storage. Nevertheless, Letsinger's work set the stone for Caruthers and Beaucage's phosphoramidite chemistry developed in 1981, which is still mainly used in present day (Figure 1.5c).[61] In phosphoramidites, the stability of the phosphorous III groups was greatly enhanced by replacing the chloride groups with an amine, which allowed higher efficiency of coupling reactions. In the same year, Ogilvie realized the potential in automating the phosphoramidite method, and developed the first automated DNA synthesizer.[62]

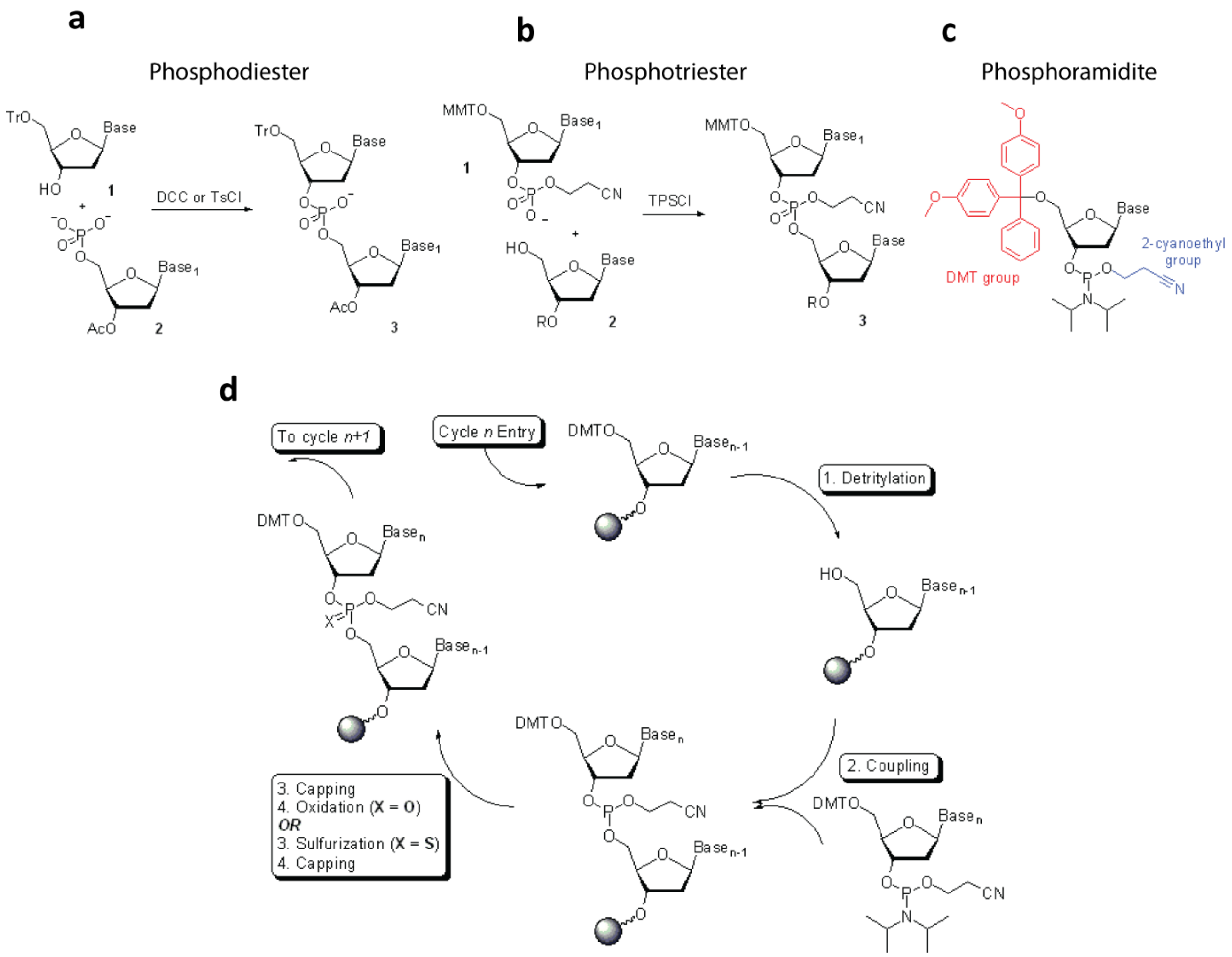

Figure 1.5 – The evolution of automated DNA synthesis. a) Scheme showing the synthetic methodology by Khorana for solution phase synthesis of phosphodiesters.[58] b) Scheme illustrating the synthetic pathway by Letsinger for solid-phase synthesis of phosphotriesters.[60] c) General structure of a phosphoramidite as developed by Caruthers and Beaucage.[61] d) The automated solid-phase synthesis cycle of DNA. The cycle consists of 4 main steps: 1) Detrilylation to free the 5’ OH group, 2) coupling of the next base 3) capping of the unreacted bases 4) oxidation of the phosphorus III to phosphorus V. DCC: N,N’-dicyclohexylcarboiimide. TsCl: p-toluenesulfonyl chloride. Tr: Trityl protecting group. TPSCl: 2,4,6-triisopropylbenzenesulfonylchloride. MMT: 4-methoxytrityl. DMT: 4,4’-dimethoxyltrityl. (The figures were adapted from Wikipedia)

Automated solid-phase synthesis of DNA proceeds through 4 main steps: 1) Deblocking (or detritylation), 2) Coupling, 3) Capping and 4) Oxidation (Figure 1.5d). Deblocking removes the protecting group on the 5' hydroxyl. The most common protecting group is dimethoxytrityl (DMT), which is cleaved under mild acidic conditions. This is usually the first step in the synthesis. Next comes coupling of the incoming base in the form of a 3' phosphoramidite derivative, which favourably reacts with the 5' OH of the previous base in the presence of an acidic activator, usually a tetrazole derivative. The capping step follows next to reduce side products caused by unreacted 5' hydroxyl groups of the growing strands. The 5' hydroxyls are usually capped with an acetyl group and cannot react any further. Next, the oxidation step converts the phosphorous group from an oxidation state of (III) to (V), which makes it more stable in acidic conditions. The cycle then repeats, with the next base added to the growing chain. Finally, the oligonucleotide is cleaved from the solid support with aqueous ammonia. This step also removes the labile nucleobase protecting groups and cyanoethyl protecting groups, and the crude oligonucleotide is now ready for further purification.

The methods used in solid-phase DNA synthesis have quickly been extended to other building blocks, besides DNA.[63-65] Scientists today can incorporate a wide variety of molecules in the form of a phosphoramidite derivatives into any given DNA sequence.[55, 66-67] This progress in DNA synthesis has laid the foundation for the synthesis of DNA-polymer hybrids. In the next section, synthesis of DNA-polymer hybrids will be discussed, highlighting both solid-phase and solution-based synthetic methodologies.

1.4.3 Synthesis of DNA Amphiphiles

1.4.3.1 Solution-based synthesis of DNA amphiphiles

Solution-based coupling often involves the addition of different functional groups to already made DNA strands that contain a reactive moiety (e.g. thiols, amines, azides, hydroxyl) (Figure 1.6). Many approaches have been developed for solution-based coupling of first generation DNA amphiphiles.

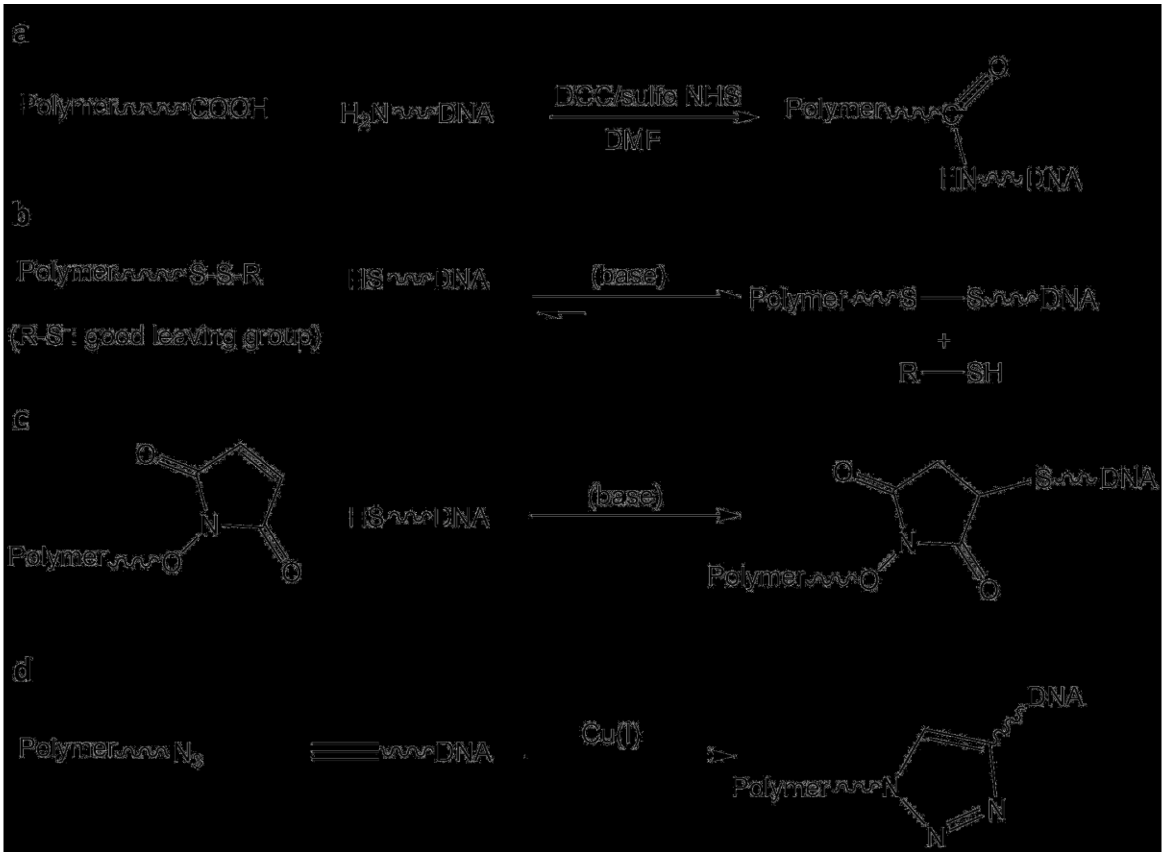

Figure 1.6 – Coupling strategies for solution-based synthesis of DNA amphiphiles. a) Polymer functionalized with carboxylic acid is conjugated to amine-modified DNA. b) Disulfide bond formation between a polymer and DNA through thiol-disulfide exchange. c) Michael addition of a polymer carrying a terminal maleimide with thiol-modified DNA. d) Click chemistry between an azide-functionalized polymer and alkyne-DNA.

For example, Jeong and Park, utilized amide bond formation to generate biodegradable poly(lactic-co-glycolic acid)-DNA hybrids that self-assemble into micellar structures in aqueous media.[68] Later, Kataoka and co-workers used disulfide chemistry to conjugate a disulfide-PEG to a thiol-modified antisense oligonucleotide, which was incorporated into polyion complex micelles for cytoplasmic delivery (Figure 1.7a).[69] This reaction proceeds through a thiol-disulfide exchange click mechanism which reduces the number of side products in disulfide bond formation.[70] Liu and co-workers synthesized polypeptide-DNA conjugates via Cu^+ catalyzed click chemistry between poly (L-glutamic acid-co-propargyl-L-glutamate) and azide-modified DNA (Figure

1.7b). These polypeptide-DNA conjugates were used for multifunctional hydrogel formation.[71] Copper-free click chemistry has also been used for DNA functionalization.[72] Michael additions were used by Maeda and co-workers for the attachment of acrylate-modified polymers to thiol-functionalized DNA for formation of temperature responsive micelles.[73]

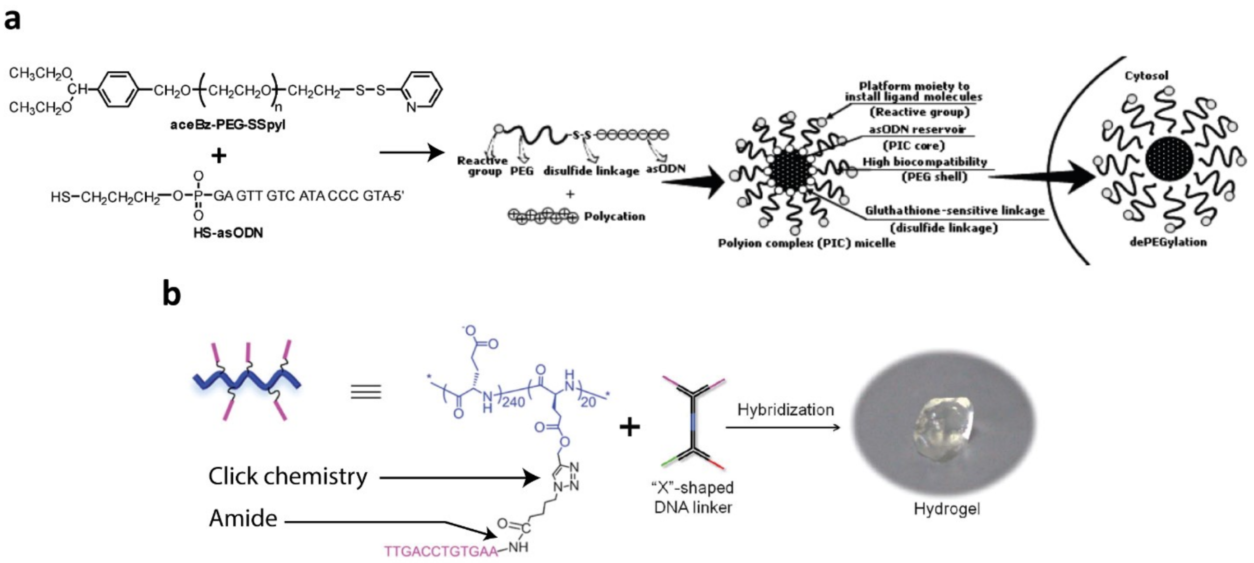

Figure 1.7 – Examples of solution-based synthetic methods of DNA amphiphiles. a) Disulfide bond formation between therapeutic antisense DNA and modified PEG chains for the formation of polyion complex micelles for intracellular oligonucleotide delivery.[69] Reproduced with permission (American Chemical Society, 2005). b) Polypeptide-DNA conjugates using click chemistry for hydrogel formation.[71] Adapted with permission (Wiley-VCH, 2014).

As useful as solution-based methods have been for DNA functionalization, the limited organic solubility of DNA presents a limitation. This usually results in low yields of coupling due to the incompatibility of the DNA and hydrophobic components. For that reason, the strategies mentioned earlier have mainly focused on conjugation of hydrophilic molecules to DNA, and the incorporation of hydrophobic polymers has remained a challenge. To tackle this problem, Hermann and co-workers developed a method in which a DNA-surfactant complex was introduced to increase the solubility of DNA in organic solvents, thus, enhancing coupling efficiency of DNA in organic solutions (Figure 1.8a).[74] Using this approach, a range of organic polymers have been conjugated including polystyrene (PS), propylene oxide (PPO) and others. In aqueous solutions, another strategy has also been devised to enhance coupling efficiency of hydrophobic molecules. Here, the incorporation of oligo(ethylene glycol) between the DNA and hydrophobic moiety has shown to give modest coupling yields in aqueous media.[75] Later, Herrmann et al. reported a method for using DNA micelles to template organic reactions by using organic molecules as cross-linkers of two DNA strands (Figure 1.8b).[76] More recently, Sleiman and co-workers reported a different micelle-templated method to enhance the reactivity of DNA with hydrophobic molecules in aqueous solutions (Figure1.8c).[77] In their approach, hydrophobic micelle cores were used as reaction centers, and showed significantly increased coupling yields of a range of hydrophobic organic molecules to DNA.

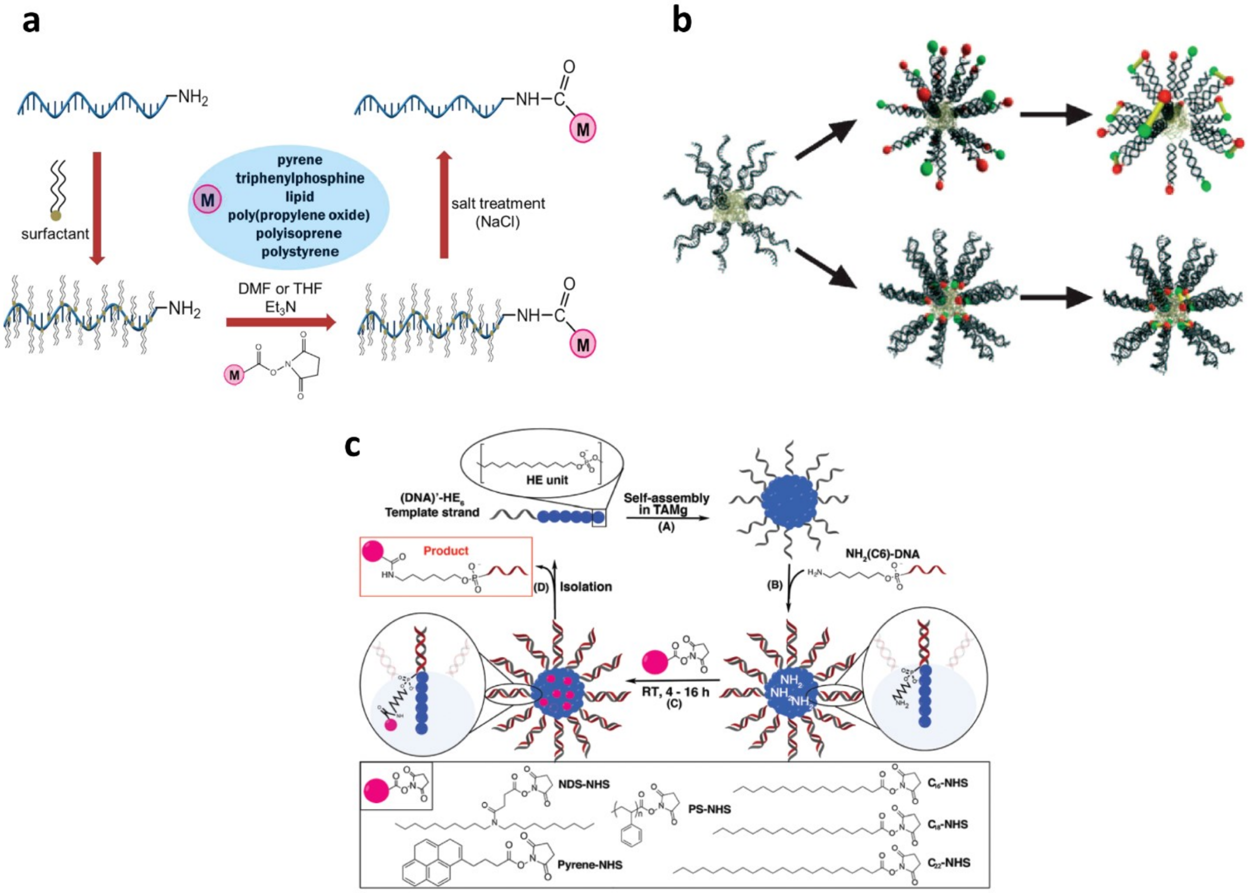

Figure 1.8 – Optimization of solution-based synthetic methods of DNA amphiphiles. a) Schematic illustration of organic-phase synthesis of DNA amphiphiles with the addition of surfactants.[74] Reproduced with permission (American Chemical Society, 2014). b) Micelle-templated organic reactions for the formation of cross-linked DNA strands through conjugation to hydrophobic

molecules.[76] Adapted with permission (Wiley-VCH, 2006). c) Synthetic methodology of DNA micelle-templated conjugation of various hydrophobic molecules to DNA in high yields in aqueous media.[77] Reproduced with permission (Royal Society of Chemistry, 2016).

1.4.3.2 Solid-phase synthesis of DNA amphiphiles

Although surfactant-assisted coupling and micelle-templated reactions have enabled the addition of a wide range of hydrophobic moieties to DNA, both methods present their own set of limitations. To achieve DNA-polymer hybrids with high purity, it would require the complete removal of excess surfactant in the first approach, and separation of newly formed DNA amphiphiles from the ones used for the micellar host in the second. In this regard, solid-phase synthesis of DNA amphiphiles has proved far superior than solution-based methods. Unlike solution-based synthesis, the addition of hydrophobic moieties to DNA does not drastically lower the reaction yield. Additionally, this method is compatible with a wider range of organic solvents as the coupling process occurs completely on the solid-support.

In solid-phase synthesis, hydrophobic molecules can be conjugated to DNA through several methods. In the first approach, hydrophobic units can be covalently attached to the 5' end of a growing DNA chain in the form of a phosphoramidite (Figure 1.9a). This requires DNA synthesis, followed by detritylation of the 5' end OH of the grown DNA chain and subsequent addition of the hydrophobic moiety. Conjugating hydrophobic units at the 3' end requires a different approach. In one method, a custom solid-support containing the desired hydrophobic chain can be used (Figure 1.9b). This requires a labile linker between the chain and support which can be cleaved following synthesis (e.g., carboxylic ester).[78] It is also possible to use a different approach where hydrophobic units are added first, followed by the conjugation of DNA. However, this necessitates functionalization of hydrophobic molecules with both a DMT-protected hydroxyl and phosphoramidite, which could be synthetically challenging and limited to a small number of hydrophobic units compatible with these chemical transformations. Conversely, reverse amidites can be used in which the DNA is elongated in the opposite direction (5' – 3') followed by a final addition of the hydrophobic block.[79]

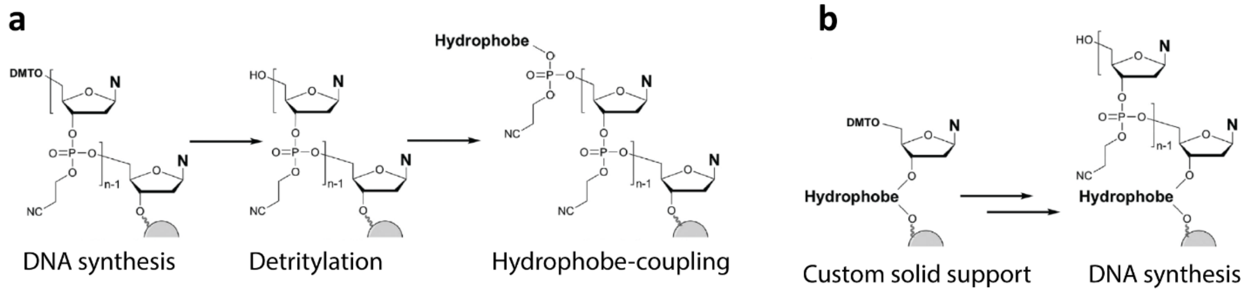

Figure 1.9 – Solid-phase synthesis of DNA block copolymers.[55] a) Addition of the hydrophobic block at the 5' end post synthesis of the DNA strand. b) Solid-support functionalized with a hydrophobic block for its addition at the 3' end of the DNA amphiphile. Reproduced with permission (Royal Society of Chemistry, 2011).

In 2004, Mirkin and co-workers reported a strategy for the preparation of novel DNA-polystyrene conjugates using solid-phase synthesis.[80] In their approach, a pre-designed DNA strand on a controlled pore glass (CPG) was synthesized and attached to a polystyrene phosphoramidite *via* syringe method (where the CPG is removed from the synthesizer and attached to a syringe that is used to mix the coupling reagents) (Figure 1.10a). Later in 2006, Tan and co-workers developed a similar method for coupling DNA to conjugated polyelectrolytes.[81] Around the same time, Hermann and co-workers also synthesized DNA-poly(propylene oxide) block copolymers using solid-phase synthesis.[55] More recently, Liu and co-workers reported the solid-phase synthesis of DNA-dendron hybrids (Figure 1.10b).[82] Solid-phase "click" synthesis has also been reported by Zhang and co-workers to conjugate alkyne-functionalized DNA with azide-polystyrene polymers (Figure 1.10c).[83] Conjunctly, nucleic acid-lipid conjugates have also been achieved using solid-phase synthesis. For example, Boxer and co-workers showed a solid-phase synthetic method for lipid-oligonucleotide conjugates that insert into lipid vesicles.[84] Additionally, the Barthelemy group generated DNA-DOPC lipid conjugates that self-assemble into liposomes for biosensing applications (Figure 1.10d).[85] Tan and co-workers also showed the synthesis of DNA-pyrene-lipid and DNA-PEG-lipid conjugates that self-assemble into spherical micelles (Figure 1.10e). These structures have been used as vehicles for bio-imaging and targeted delivery.[86]

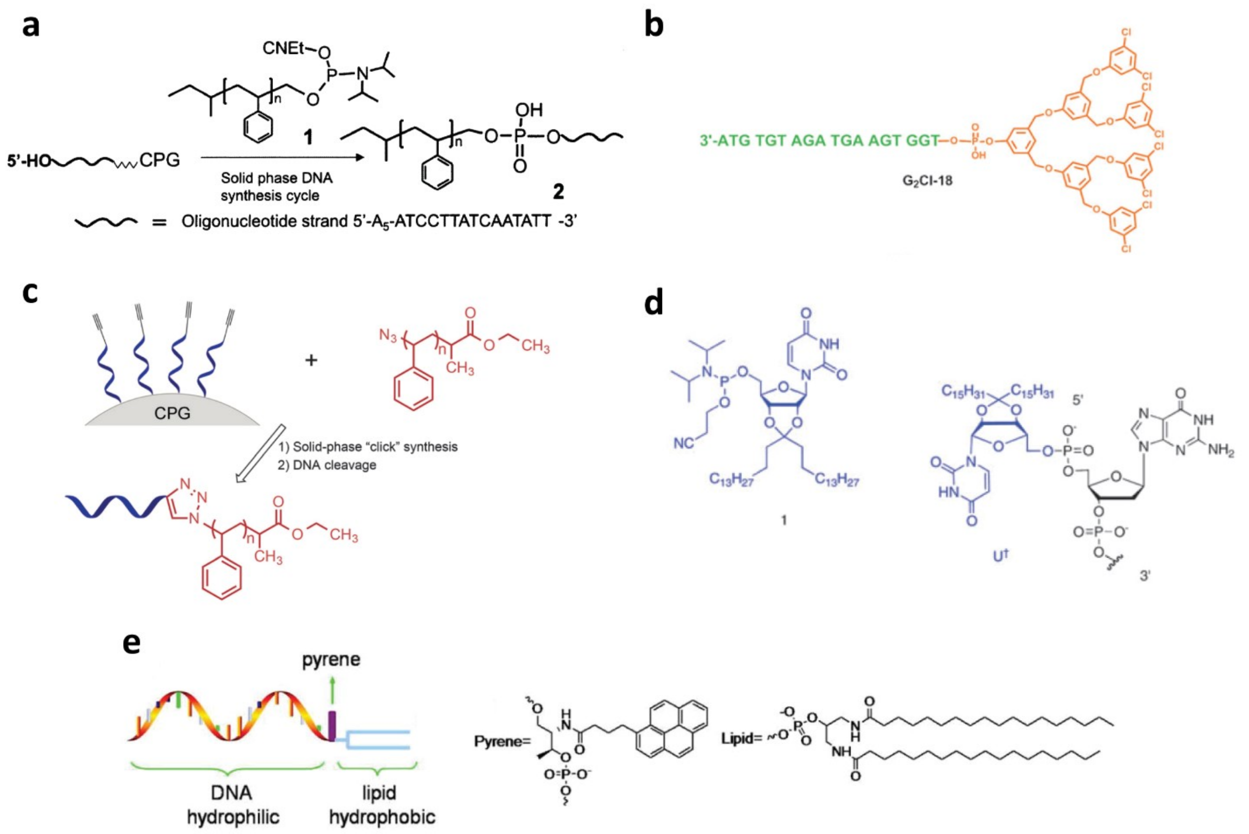

Figure 1.10 – DNA amphiphiles generated by solid-phase synthesis. a) DNA-polystyrene block copolymers reported by Mirkin et al.[80] Adapted with permission (American Chemical Society, 2004). b) DNA-dendron hybrids generated by Liu and co-workers.[82] Adapted with permission (Royal Society of Chemistry, 2012). c) Solid phase "click" synthesis of DNA-polystyrene amphiphiles reported by Zhang and co-workers.[83] Reproduced with permission (Royal Society of Chemistry, 2015). d) DNA-DOPC lipid conjugates synthesized by Barthelemy et. al.[85] Reproduced with permission (Royal Society of Chemistry, 2008). e) DNA-pyrene-lipid amphiphiles generated by Tan and co-workers.[87] Adapted with permission (Wiley-VCH, 2010).

While the approaches described above have allowed access to a wide variety of linear and branched DNA amphiphiles, the synthesis of DNA amphiphiles is still fundamentally challenging. The conjugation reaction requires end-to-end coupling of a highly hydrophilic and charged DNA strand with a hydrophobic polymer chain, resulting in sub-optimal yields. Additionally, in such methods, the polymer block is usually synthetized first through traditional polymerization methods, prior to its transformation into a phosphoramidite and conjugation to the DNA. This results in DNA amphiphiles that display molecular weight variation and structural dispersity which often translate to the overall assembly. To tackle these limitations, Sleiman and co-workers reported a solid-phase approach for synthesizing monodisperse dendritic alkyl-DNA conjugates in high yields using commercially available starting materials.[88] Later, the same group reported a step-wise solid-phase approach for the generation of completely monodisperse and sequence-defined DNA amphiphiles (Figure 1.11a).[66] In their approach, hydrophobic monomers are added sequentially as phosphoramidite derivatives to DNA on a solid-support. This method offers full control over the length and sequence of the hydrophobic units in the final structure. This method has been extended to the sequence-controlled addition of hydrophilic units, as well as perfluorinated monomers to generate DNA-Teflon conjugates (Figure 1.11b).[89]

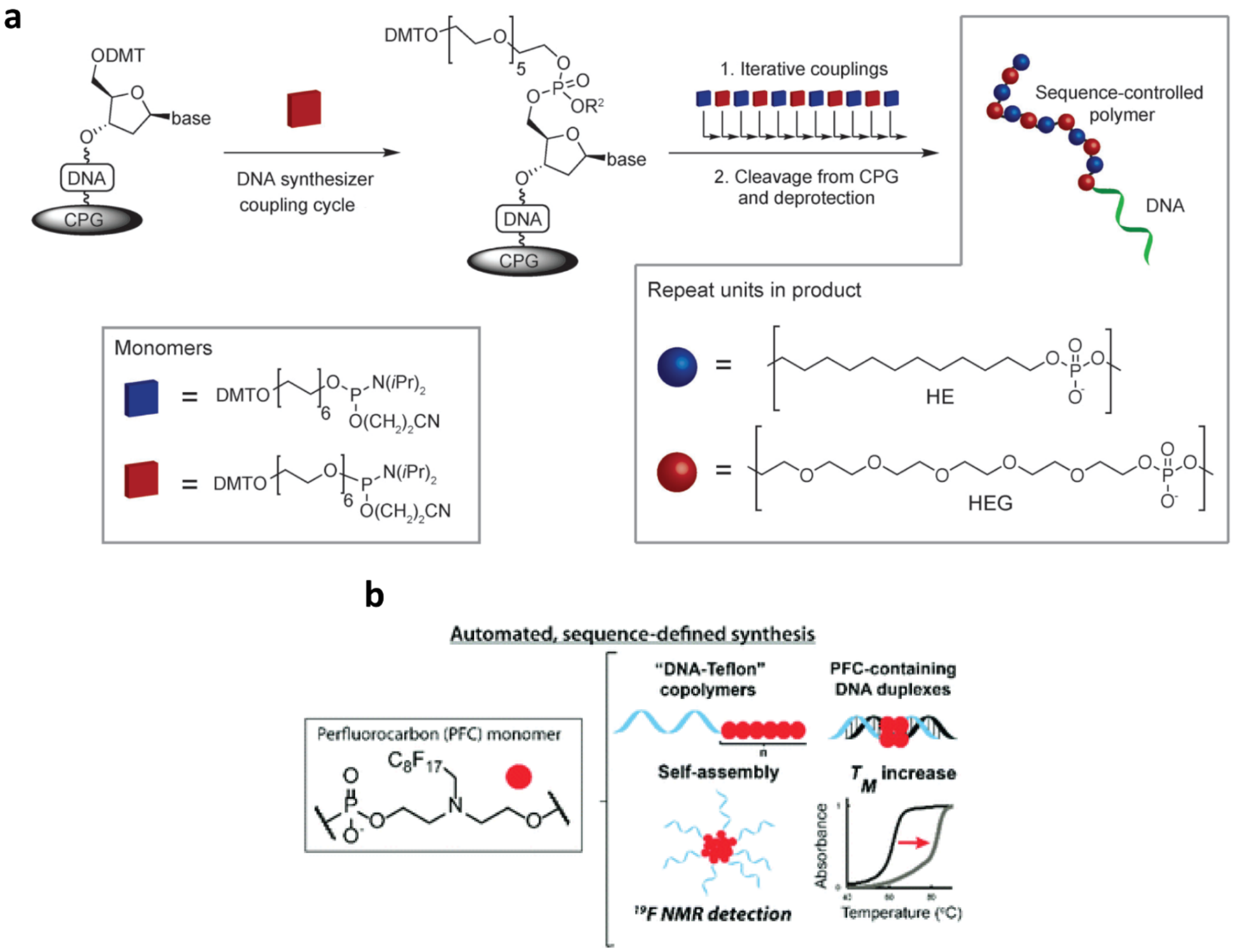

Figure 1.11 – Solid-phase synthetic route to generate sequence-defined DNA-polymer conjugates described by Sleiman and co-workers.[66, 89] a) Preparation of sequence-defined DNA-polymer conjugates by the sequential addition of either hydrophobic or hydrophilic monomers to DNA.[66]

Adapted with permission (Wiley-VCH, 2014). b) Sequence-defined DNA-Teflon conjugates containing perfluorocarbons (PFCs).[89] Reproduced with permission (Royal Society of Chemistry, 2016).

1.4.3.3 Molecular Biology techniques

Although most DNA-block copolymers have been generated by solution-based or solid-phase synthesis, it is worth noting that advanced molecular biology techniques have also been used to synthesize DNA amphiphiles.

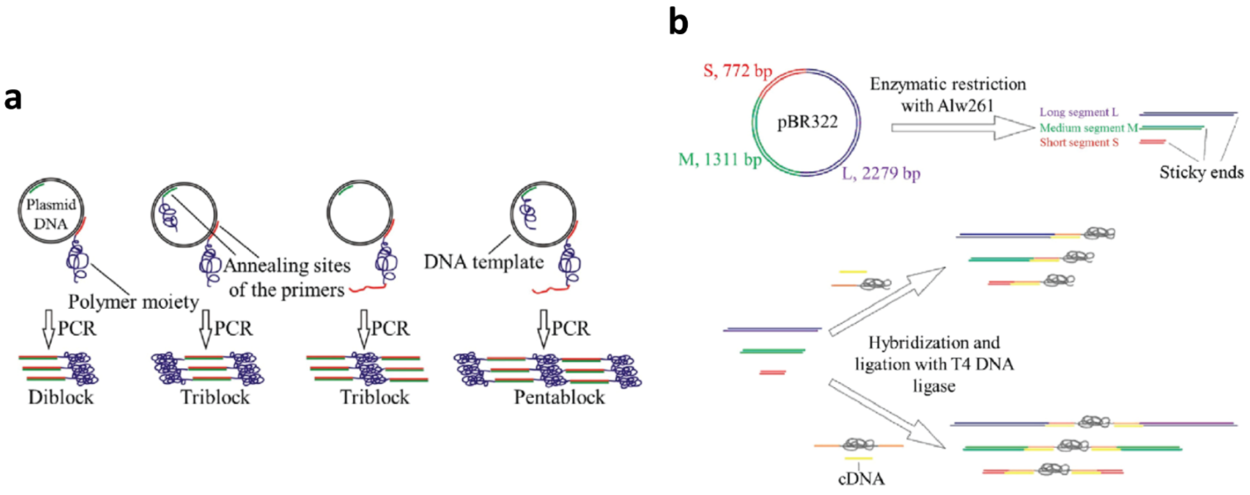

Figure 1.12 – DNA amphiphiles generated by molecular biology methods. a) Schematic representation of DNA block copolymer synthesis using PCR.[40, 90] Adapted with permission (American Chemical Society, 2009). b) Scheme of DNA block polymer synthesis using restriction enzymes and ligation technique.[40, 91] Reproduced with permission (Royal Society of Chemistry, 2011).

For example, polymerase chain reaction (PCR) was used to synthesize well-defined DNA block copolymers.[90] Di-block, tri-block and pentablock copolymers could be obtained by this approach by varying the number of ssDNA block copolymers and primers complementary to plasmid DNA (Figure 1.12a).[40] With PCR, complex DNA block copolymers with high molecular weight and well-defined multiblock copolymers could be achieved. In addition to PCR, enzymatic restriction and ligation has also been reported as a method to achieve ultrahigh molecular weight DNA block copolymers.[91] The method utilizes restriction enzymes to generate 3 dsDNA strands with sticky ends, then DNA block copolymers are synthesized in one-pot by mixing with T4 DNA ligase and incubation (Figure 1.12b).[40] These strategies have opened a new avenue of synthetic approaches to construct DNA block copolymers with very long, yet, length-controlled DNA segments that are highly information-rich toward developing functional materials.

1.4.4 Self-assembly of DNA Amphiphiles

DNA amphiphiles self-assemble into several morphologies owing to their hydrophilic and hydrophobic components. The range of accessible morphologies can also be tailored by varying the ratio of hydrophilic to hydrophobic blocks. Self-assembly can either occur based on the hydrophobic interactions of the polymer segment or specific molecular recognition events of the DNA segment. One advantage of using DNA as the hydrophilic block is the precise control over its sequence and structure which results in great spatial addressability. The addition of a programmable component to the structure also allows for dynamic structural manipulation in response to stimuli. As such, a wide range of self-assembled DNA amphiphilic structures have been reported in the past two decades, and which will be highlighted.

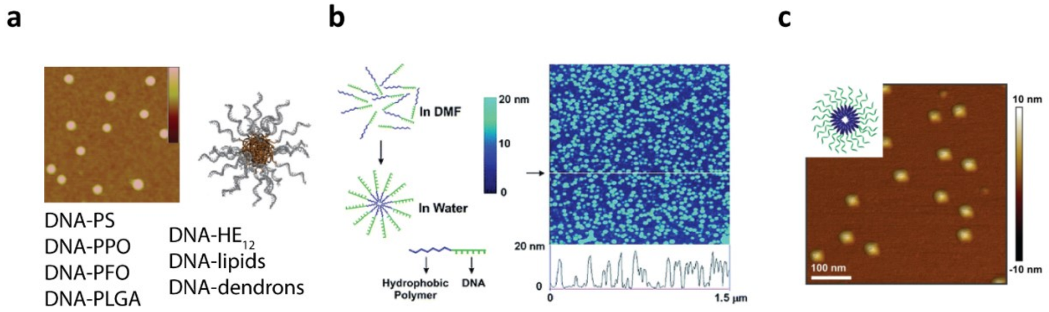

Figure 1.13 – Self-assembly of DNA amphiphiles into spherical micelles. a) Schematic illustration and AFM image of DNA-polystyrene micelles. Micellar aggregates have also been observed for DNA-poly(propylene oxide) (DNA-PPO), DNA-poly(9,9-di-n-octylfluorene) (DNA-PFO), DNA-poly(styrene) (DNA-PS), DNA-poly(lactic-co-glycolic acid) (DNA-PLGA), DNA-(hexaethylene)$_{12}$ (DNA-HE$_{12}$), DNA-lipids and DNA-dendrons.[40] Reproduced with permission (American Chemical Society, 2012). b) Early reports of spherical micelles by Mirkin and co-workers.[80] Adapted with permission (American Chemical Society, 2004). c) Monodisperse spherical micelles generated from sequence-defined DNA-polymers.[66] Reproduced with permission (Wiley-VCH, 2014).

Spherical particles are the most common geometry obtained for self-assembled DNA amphiphiles. Many DNA amphiphiles have been observed to form spherical micelles with diameters ranging from 5 – 50 nm as measured by dynamic light scattering and atomic force microscopy (Figure 1.13a-c).[40, 66, 80, 87, 92] The presence of DNA as a building block allows for programmable structural manipulation of micelles. This was highlighted by the Tan group, who showed that micelle diameter can be tuned by precise control over the length of the DNA, and demonstrated size-dependent cellular permeability of DNA micelles (Figure 1.14a).[87] Size control of DNA micelles was also reported with enzymatic manipulation of the DNA. Hermann and co-workers showed that when micelles consisting of DNA-PPO blocks were treated with an enzyme that catalyzed nucleotide addition at the 3’ end of single-stranded DNA, the DNA polymerase added 60 nucleotides to the termini of the DNA in the corona (Figure 1.14b).[93] This resulted in micellar height increase from 5 to 11 nm.

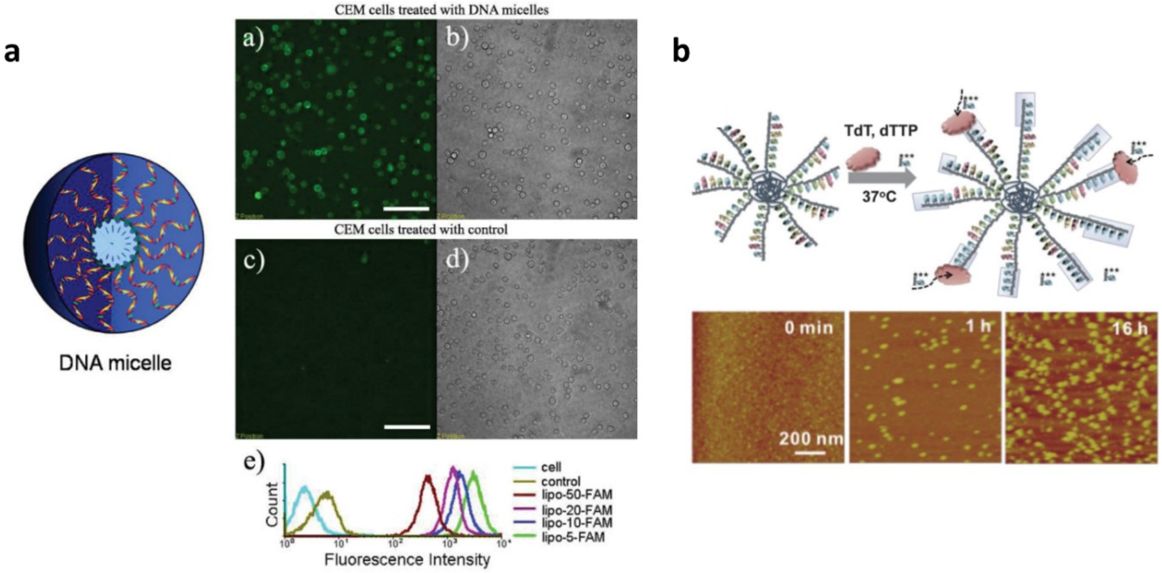

Figure 1.14 – DNA sequence manipulation in spherical micelles. a) Tuning micelle diameter by changing the length of the DNA strand for size-dependent cellular penetration.[87] The numbers in samples lipo-50-FAM, lipo-20-FAM, lipo-10-FAM, lipo-50-FAM indicate the number of bases in the DNA strand. Reproduced with permission (Wiley-VCH, 2010). b) DNA polymerase-catalyzed addition of nucleotides to ssDNA ends of spherical micelles results in increase of micelle height on surface.[93] Adapted with permission (Wiley-VCH, 2008).

In addition to spherical geometries, one-dimensional rod-shaped assemblies (3D structures extended in one dimension) have also been obtained from DNA amphiphiles. One method relies on DNA sequence manipulation for the generation of DNA rods from spherical micelles. As such, the Hermann group showed that the addition of a long DNA template consisting of 5 repeats complementary to the DNA sequence in the micelle corona resulted in the dis-integration of micelles and generation of rod-like aggregates (Figure 1.15a).[94] The Gianneschi group also reported shape-shifting of DNA micelles into rods upon external stimuli – enzymatic digestion in this case (Figure 1.15b).[95] In their approach, brush type DNA amphiphiles were prepared through ring-opening metathesis polymerization (ROMP) and showed reversible switching from spherical micelles to rods and back to spheres. Additionally, the Liu group reported reversible switching between spherical micelles and rods for DNA-dendron hybrids under different buffer and temperature conditions (Figure 1.15c).[82] Zhang and co-workers showed the isolation of rods as a kinetic product of nucleic-acid amphiphilic assembly (Figure 1.15d).[83] Subsequent heating of the rod-like structure resulted in the formation of spherical thermodynamically stable structures.

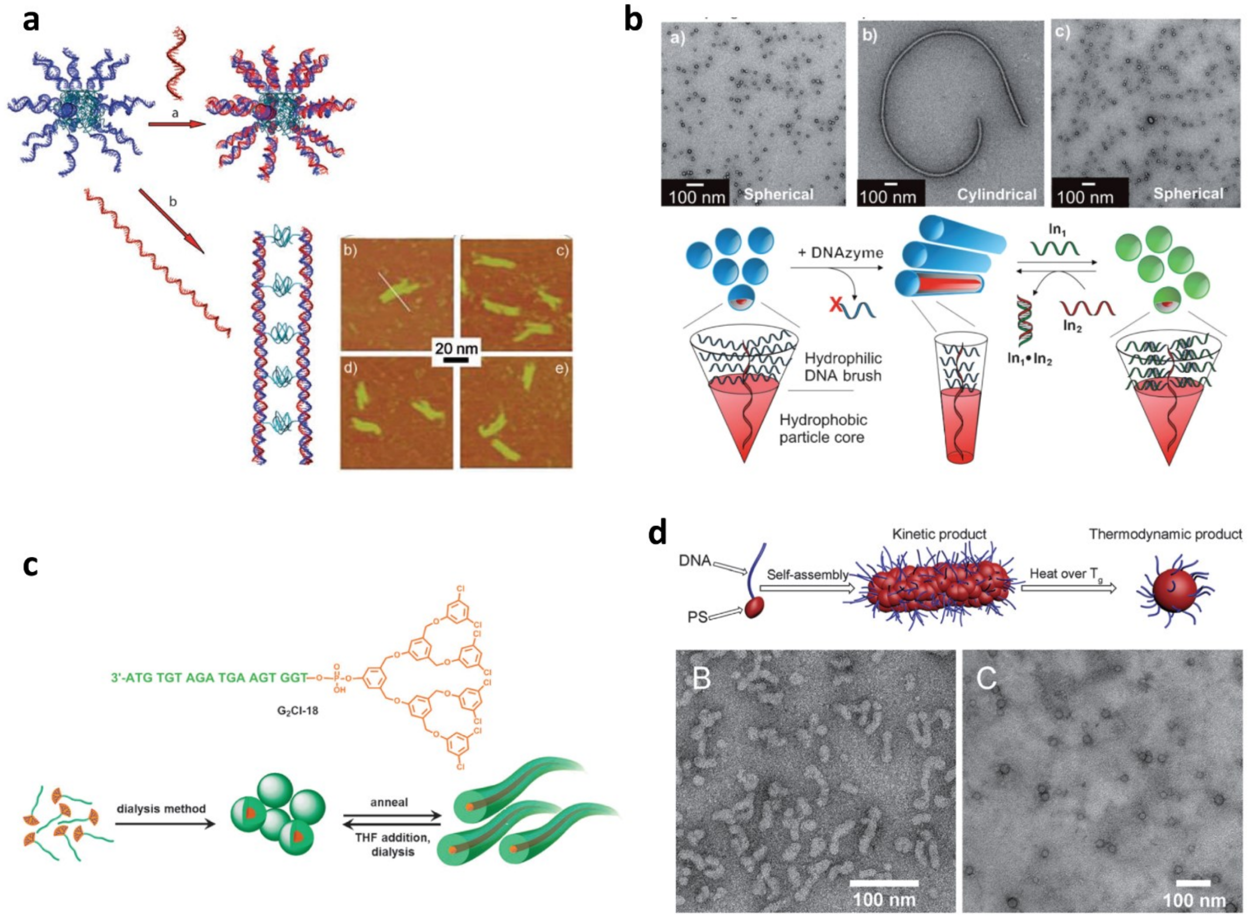

Figure 1.15 – Self-assembly of DNA amphiphiles into one-dimensional rods. a) Shifting of DNA spheres to rods upon addition of a long DNA template complementary to the micelle DNA strands.[94] Adapted with permission (Wiley-VCH, 2007). b) Stimuli-responsive shape-shifting of DNA micelles to rods after addition of enzymes.[95] Reproduced with permission (Wiley-VCH, 2010). c) Reversible switching between spheres and rods of DNA-dendron hybrids under different buffer and thermal conditions.[82] Reproduced with permission (Royal Society of Chemistry, 2012). d) Kinetic micellization of DNA-PS conjugates into nanorods.[83] Adapted with permission (Royal Society of Chemistry, 2015).

Growth of rod-like structures could also be achieved under thermal treatment. Häner and co-workers explored this concept with the self-assembly of oligo(pyrene)-DNA conjugates (Figure 1.16). The group observed the formation of 1D helical nanoribbons driven by stacking interactions among pyrene units in aqueous media, whose length was dependent on the ionic strength. Through a cooperative nucleation-elongation growth, the degree of order of pyrene can be increased resulting in 1D helical nanoribbons under different thermal treatment.[96] At elevated temperatures, oligomeric molecules exist as molecularly dissolved chains. Upon cooling, assembly of strands leads to the formation of nuclei that serve as templates for the elongation of the polymers as the temperature is further decreased (Figure 1.16c). Despite the elegant examples, controlling the length and dimensionality of DNA rods is still limited. The access of amphiphilic DNA structures with controlled length and narrow size dispersity is desirable as it allows for applications in biomedicine and materials science.

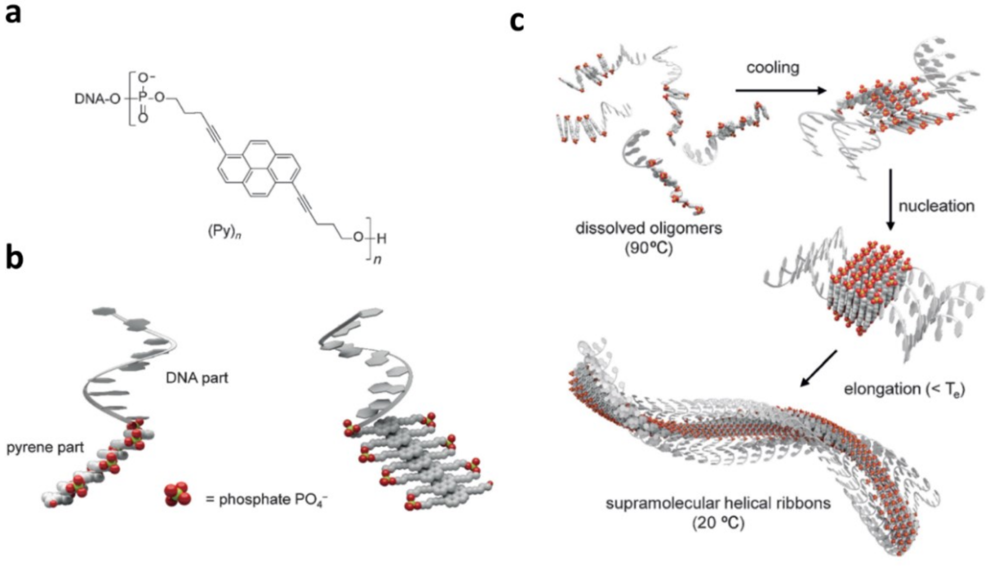

Figure 1.16 – Formation of DNA-grafted supramolecular polymers from DNA-oligo(pyrene) conjugates.[96] a) Chemical structure of the oligo(pyrene)-DNA hybrids. b) Model for the pyrene-DNA chimeric oligomers. The DNA is illustrated as a right-handed helix, and pyrene units arrange in a star-like fashion. c) Formation of DNA-grafted supramolecular polymers through a nucleation-elongation mechanism. Reproduced with permission (Wiley-VCH, 2015).

Most recently, DNA amphiphiles have been decorated for constructing more complex architectures, such as hollowed vesicles. For example, conjugates of DNA with poly[3-(2,5,8,11-tetraoxatridecanyl)thiophene] (PTTOT) were shown to assemble into vesicles in aqueous solutions, where DNA acts as the hydrophilic shell and the polymer aggregates tightly through π-π interactions (Figure 1.17a).[97] These structures retained the optoelectronic properties of π-conjugated polythiophenes and their size could be altered by changing the concentration of DNA-PTTOT in the assembly. Linear DNA-poly(butadiene) conjugates have been reported to form vesicles of 80 nm diameter upon self-assembly (Figure 1.17b).[98] The isolation of the vesicular interior from the surrounding was demonstrated by using fluorescent probes. Bodipy, a fluorescent hydrophobic dye and another DNA-specific dye Syto9, were incubated with the vesicles. Fluorescence microscopy showed that the hydrophobic dye, Bodipy, was entrapped in the poly(butadiene) environment, while the DNA dye interacted with the DNA corona. Vesicles have also been reported from DNA-dendrons by Liu and co-workers.[99] Inspired by how cytoskeletal proteins provide an internal frame for cell structures, the group introduced the concept of "frame-guided assembly" in which customized frames can be used to guide amphiphiles into tailored assemblies (Figure 1.17c). Using a DNA-functionalized gold nanoparticle (DNA-AuNP) scaffold and complementary DNA-dendron conjugates, the group showed the formation of well-defined vesicles whose size can be specifically tailored by varying the length of the DNA chains. This concept has been expanded to the formation of a range of other exciting structures including cuboids and 2D nanosheets.[100-102] Vesicle (or liposomes) have also been achieved from DNA-lipid conjugates. Gianneschi and co-workers reported stimuli-responsive liposomes made from DNA-lipids consisting of a 9-mer DNA bound to two 18-carbon lipid tails (Figure 1.17d). These structures undergo reversible morphological switch from liposomes to spherical micelles and back to liposomes upon DNA sequence manipulation.[103] More examples from the Boxer and Barthelemy groups have demonstrated functional DNA-lipid vesicles used as fluorescent on/off switches and to study vesicle fusion (Figure 1.17e).[84-85] Fluorescently labeled vesicles were prepared, and upon fusion of their membranes, their fluorescent probes mix and diffuse within the bilayer leading to quantitative change of intensity. The wide range of accessible structures of DNA amphiphiles highlights their importance as structural building blocks. Looking at recent examples, it is obvious that the incorporation of a programmable DNA component is advantageous, especially for applications in biomedicine and materials science. Another thrilling avenue is the integration of DNA amphiphiles with DNA nanostructures, creating hierarchical hybrid assemblies with new orthogonal functions.

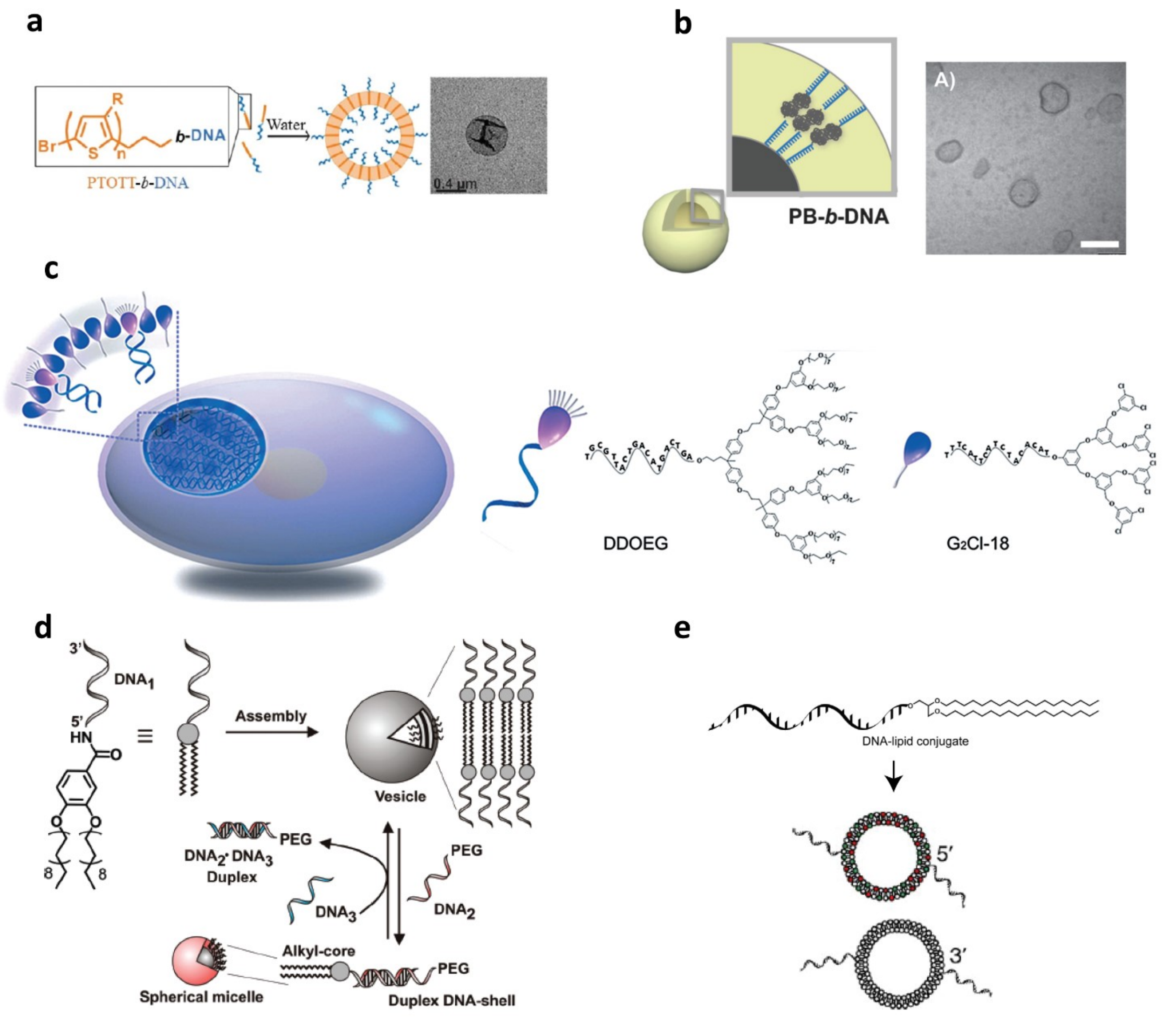

Figure 1.17 – Self-assembly of DNA amphiphiles into vesicles. a) Self-assembly of DNA-PTOTT conjugates into hollow vesicles in water.[97] Adapted with permission (American Chemical Society,

2014). b) Self-assembly of DNA-poly(butadiene) amphiphiles into vesicles.[98] Reproduced with permission (Royal Society of Chemistry, 2007). c) Frame-guided assembly of vesicles in a dendron-DNA system with AuNPs as the scaffold.[99] Adapted with permission (Wiley-VCH, 2014). d) Reversible switching between vesicles and micelles of DNA-lipid conjugates.[103] Reproduced with permission (American Chemistry Society, 2010). e) DNA-decorated vesicles used in membrane fusion studies.[85] Reproduced with permission (Royal Chemistry Society, 2008)

1.4.5 Interfacing DNA amphiphiles with DNA nanostructures

The unique molecular recognition properties of DNA allow DNA amphiphiles to form hierarchical assemblies when combined with DNA nanostructures. This hybrid material can display complex architectures and sophisticated functions, which are not easily realized by other means. In this context, Sleiman and co-workers initially developed a group of DNA polymers by using ring-opening metathesis polymerization (ROMP) to generate a short polymer containing PEG chains as repeat units, and then covalently attached it to DNA (Figure 1.18a). A cubic scaffold with addressable single-stranded regions was used to position these amphiphiles in 3D.[104] This selective positioning resulted in a significant increase in nuclease resistance of the cubic scaffold. The group further extended this method to other 1D structures. DNA nanotubes displaying periodic single-stranded regions were decorated by DNA-PEG and DNA-polystyrene amphiphiles in a similar fashion.[105] The result was stimuli-responsive hybrid structures that could selectively shed DNA conjugates upon the addition of DNA strands fully complementary to the scaffold. The cubic scaffold has also been used to decorate DNA-polymer conjugates containing hydrophobic dendritic alkyl chains (Figure 1.18b).[88] Depending on the number and orientation of DNA-polymer conjugates on the scaffold, different assembly modes were achieved. When four strands were positioned on one face of the cube, dimeric structures were observed. However, when the other cube face was also decorated with four DNA-polymer strands, the polymer units oriented and aggregated inside the cube core, forming a micellar microenvironment, which could be loaded with hydrophobic dyes or small molecule drugs. The addition of a specific DNA strand led to conditional release of the drug cargo.

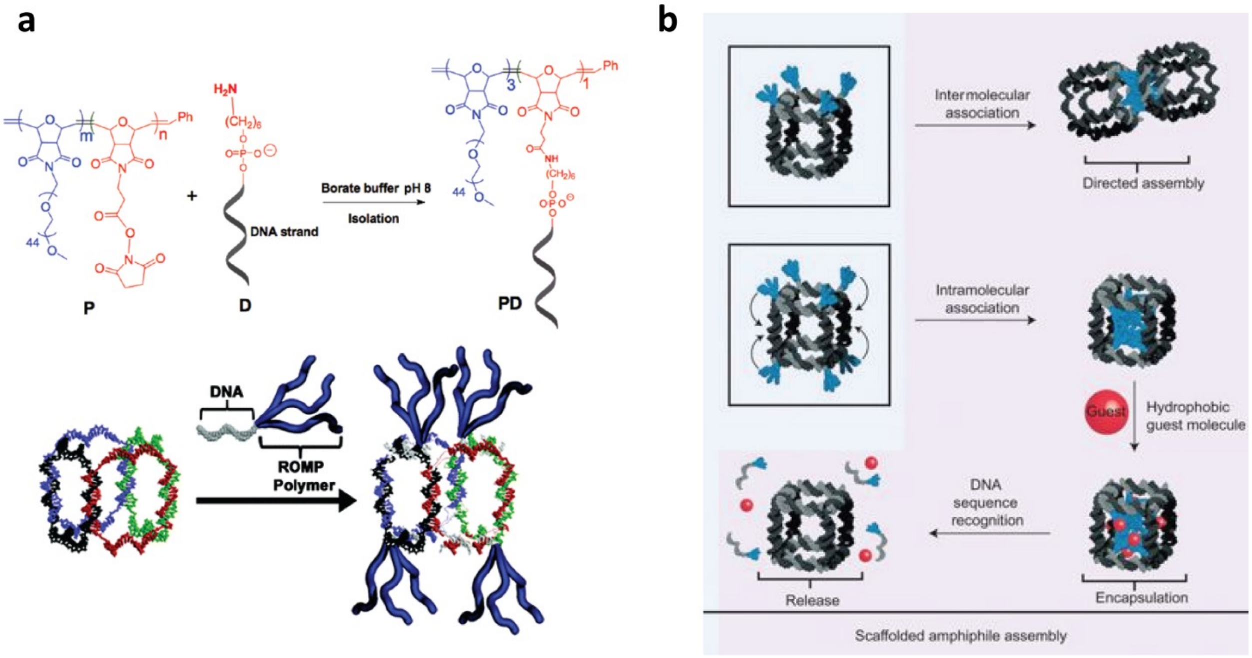

Figure 1.18 – Interfacing DNA amphiphiles with 3D DNA nanostructures. a) Positioning DNA amphiphiles on a 3D cubic scaffold results in its increased nuclease resistance.[104] Reproduced with permission (American Chemical Society, 2012). b) Site-specific positioning of dendritic DNA-polymer conjugates shows different modes of self-assembly.[88] Adapted with permission (Nature Publishing Group, 2013).

While many examples have showed 3D DNA structures templating DNA amphiphiles,[39, 88, 105] the converse has also been reported. DNA-polymer conjugates developed by Sleiman and co-workers have been used as scaffolds for templating 3D cubes to form monodisperse hybrid superstructures externally decorated by cubic structures (Figure1.19a). The group showed that by varying the position and number of hydrophobic units on the DNA-polymer conjugate different highly ordered hierarchical structures were achievable with control over the aggregation number.[106-107] Turberfield and co-workers showed that temperature-responsive DNA-poly(N-isoproylacrylamide) poly((NIPAM)) can regulate the formation of hierarchical structures when attached to DNA tetrahedra under different thermal conditions (Figure 1.19b). At room temperature, poly(NIPAM) segments dissolve in solution resulting in DNA tetrahedra with protruding polymeric tails. However, when the temperature is increased to 40 °C, aggregation of the polymer drives the formation of micelle-like structures with a hydrophobic poly(NIPAM) core and a hydrophilic corona composed of DNA tetrahedra. DNA amphiphiles have also been used with DNA origami. For example, the Simmel group used cholesterol-modified DNA strands with DNA origami structures to guide the folding of hinged DNA origami, forming sandwich-like bilayer structures (Figure 1.19c).[108]

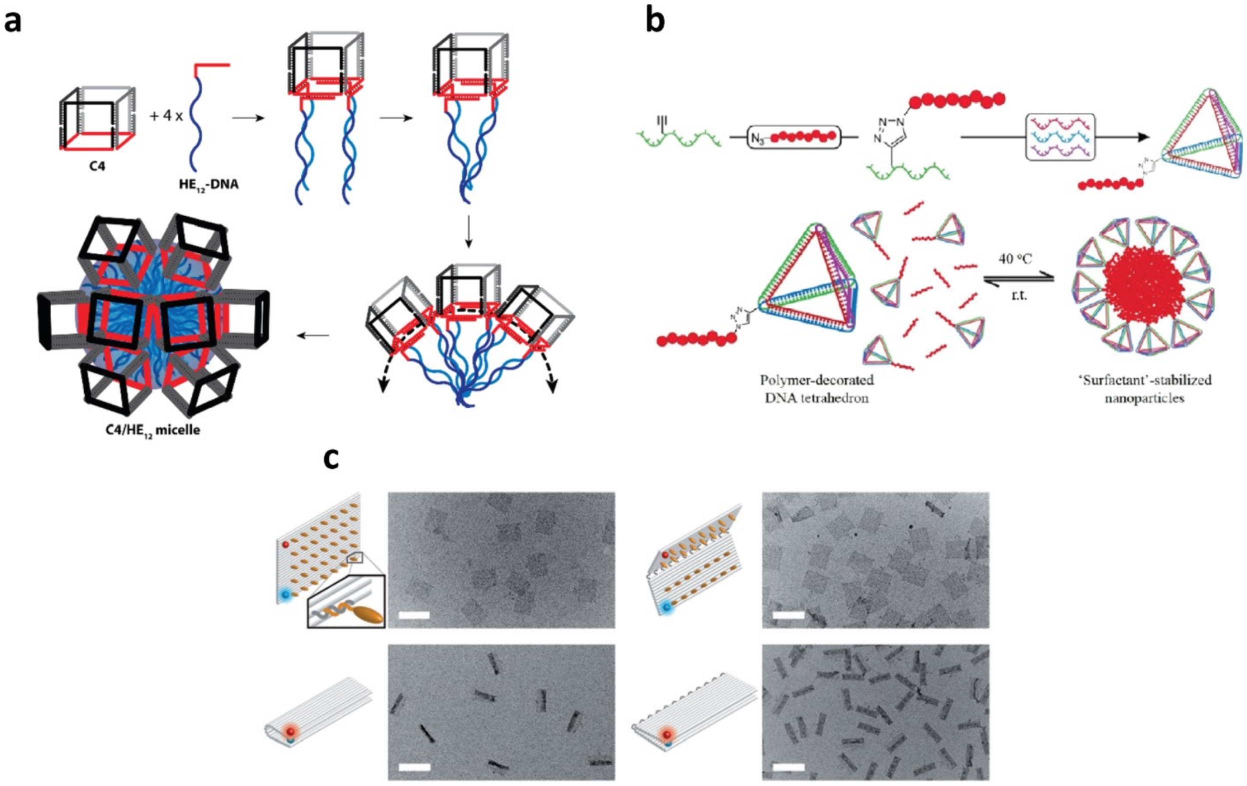

Figure 1.19 – DNA amphiphile-mediated hierarchical assembly of hybrid DNA structures. a) Formation of highly ordered DNA micelle superstructures decorated with a corona of 3D DNA cubes.[106] Reproduced with permission (American Chemical Society, 2014) b) Thermo-responsive DNA amphiphiles allow switching between polymer-decorated DNA tetrahedra and micellar structures surrounded by tetrahedra, under different thermal conditions.[109] Adapted with permission (American Chemical Society, 2013). c) Hinged DNA origami folded by cholesterol interactions of cholesterol-DNA bound on the origami surface.[108] Adapted with permission (Wiley-VCH, 2014).

The application of DNA amphiphiles for templating assembly is not limited to 3D DNA nanostructures. They have also been studied in relevance to deposition on lipid bilayers. The hydrophobic portions of amphiphiles serve as anchors which insert into the bilayer and position negatively charged DNA structures on the surface or within the lipid bilayer. Taking advantage of the fluid nature of lipid membranes, studies on the dynamics of assembly/disassembly of nanostructures on bilayers have been explored. For example, Sleiman and co-workers reported the anchoring of cholesterol-modified 3D DNA cages on spherically supported lipid bilayers and showed their dynamic behaviour on the bilayer surface (Figure 1.20a).[110] Sugiyama and co-workers reported real-time AFM tracking of the dynamic assembly of cholesterol-modified hexagonal origami structures (Figure 1.20b).[111] The structures were also functionalized with an azobenzene unit and showed reversible photo-responsive assembly and disassembly on the bilayer. Walter, Yan and co-workers showed the assembly of cholesterol-modified DNA origami "barges" (Figure 1.20c).[112] Through DNA-PAINT, a super-resolution imaging technique that relies on transient programmable hybridization between short dye-labeled oligonucleotide strands to allow single-molecule visualization, these structures showed reversible association and lateral diffusion on supported bilayers, allowing them to be used as probes of membrane structure and map out regions of the membrane with high spatial accuracy. The creation of artificial membrane channels has also been explored using both cholesterol-modified and porphyrin-functionalized DNA structures (Figure 1.20d).[113-114] In this example, DNA origami was used to generate a DNA nanopore through a barrel-like structure with a bilayer spanning hollow stem (42 nm in length, 2 nm diameter). Membrane anchoring was mediated through 26 DNA-cholesterol modifications in the structure. TEM analysis showed that the pore was directed into the bilayer with the correct orientation.

DNA amphiphiles have also been utilized to study biological processes such as vesicle fusion. Boxer and co-workers used synthetic DNA-lipid conjugates to develop fluorescently labeled vesicles and observe their membrane fusion events through fluorescence microscopy (Figure 1.20e).[115] Upon fusion of the membrane, their fluorescent molecules mix and diffuse within the bilayer leading to a direct quantification of fluorescence decrease. In other studies, DNA-lipid conjugates with varying DNA lengths were used to study the effect of linker DNA on vesicle fusion.[116] Using FRET, it was found that longer complementary DNA strands induced higher vesicle docking rates, but reduced rates and extent of lipid mixing. Similarly, other FRET-based studies on DNA-cholesterol conjugates were also used to study fusion of vesicles with varying cholesterol composition. It was found that DNA hybridization forcing vesicles in close proximity resulted in efficient fusion and lipid mixing of inner and outer lipid bilayer leaflets.[117] Vesicle fusion mediated by DNA-lipid conjugates has also been reported by Rothman and co-workers.[118] The group developed DNA-lipid tethers capable of mimicking SNARE function, the core machinery to drive vesicle fusion and docking in biological systems. The group showed that using these artificial tethers, SNARE-mediated lipid mixing was significantly accelerated, and the fusion rate was highest when the length of the linker was less than 40 nucleotides. Anchoring of nascent DNA amphiphiles has also been studied by Albinson and co-workers. In their work, zinc-porphyrin linear DNA constructs were designed to position parallel to the membrane surface when bound, creating 2D DNA patterns.[119] The effect of number of anchors, linker length between the DNA and porphyrin, and ssDNA vs dsDNA was studied. In other studies, the group showed porphyrin-mediated attachment of a 2D DNA hexagonal assembly to a soft-lipid membrane (Figure 1.20f).[120] Their studies showed that at least 3 attachment points (porphyrin molecules) were required to align the DNA construct onto the surface.

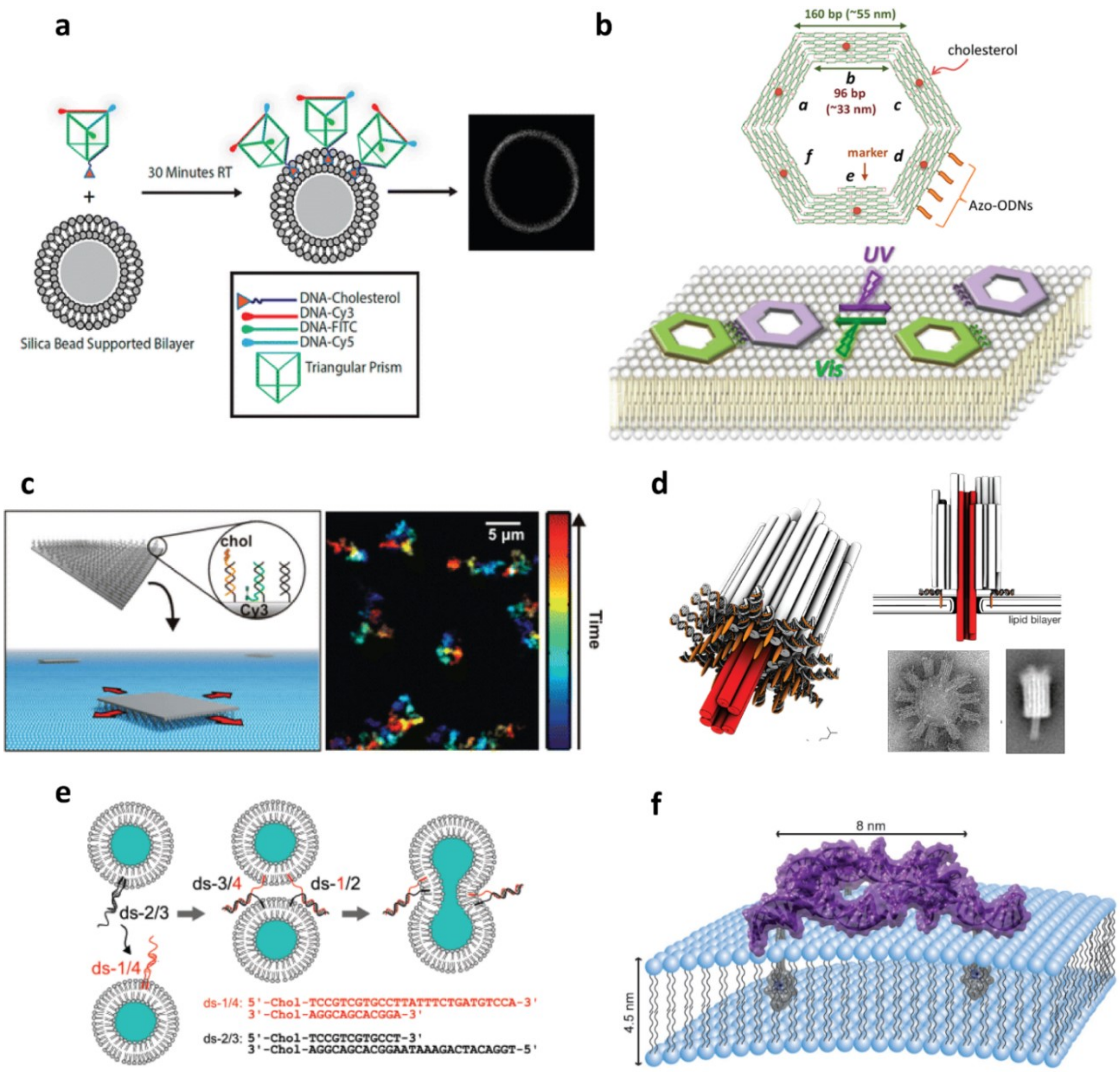

Figure 1.20 – Interaction of DNA amphiphiles with lipid bilayers. a) Cholesterol-functionalized DNA prism binding and dynamics on supported lipid bilayers.[110] Adapted with permission (American Chemical Society, 2014). b) Photoinduced reversible dimerization of cholesterol-modified DNA origami structure containing azobenzene units on bilayers.[111] Reproduced with permission (American Chemical Society, 2014). c) Cholesterol-DNA barges used for DNA-PAINT to study lateral diffusion and surface mapping of lipid bilayers.[112] Adapted with permission (American Chemical Society, 2014). d) DNA origami nanopore functionalized with 26 cholesterol units to span lipid bilayers.[113] Reproduced with permission (AAAS, 2012). e) Studying vesicle fusion through vesicle-forming complementary DNA-lipid conjugates.[116] Adapted with permission (AVS, 2008). f) A 2D DNA hexagon aligned on a lipid bilayer using 3 porphyrin anchors.[120] Reproduced with permission (Wiley-VCH, 2011).

1.4.6 Applications of DNA Amphiphiles

1.4.6.1 Gene Regulation

DNA amphiphiles have shown great promise as drug delivery vehicles, either by incorporating small molecule drug agents or using the oligonucleotide portion as the therapeutic itself. In their natural form, however, nucleic acids are quite susceptible to hydrolysis by enzymatic degradation, limiting their applications for *in vivo* therapy and detection. Many groups have directed their efforts towards increasing the stability of amphiphilic DNA structures to enhance their potential biomedical applications. Early studies by Mirkin and co-workers found that spherical nucleic acids containing gold nanoparticle (AuNP) cores showed slower enzymatic degradation rates and increased structural stability in biological media.[121] The group then extended this system to spherical particles with both lipid or cross-linked polymeric cores which also showed enhanced serum stability.[122-123] Later, the Gianneschi group found that polymeric micellar DNA nanoparticles showed increased resistance to nuclease digestion (Figure 1.21a).[124] The dense packing of DNA in the corona of spherical structures creates a protected environment inaccessible for nucleases. It appeared that the same extent of nuclease resistance in structures with AuNP cores could be achieved using polymeric cores. The group further built on these findings by using antisense locked-nucleic acids (LNA)-polymer conjugates (where the ribose sugar moiety is modified with an bridge connecting the 2’ oxygen with the 4’ carbon) that self-assemble into spherical nanoparticles.[125] These structures showed high cellular uptake and gene regulation by binding to survivin messenger RNA (mRNA) causing gene knockdown (Figure 1.21b).

In another example, Mirkin and co-wokers showed that gold nanoparticle-oligonucleotide complexes exhibited efficient cellular uptake and gene knockdown without the use of transfection agents.[126] The same group then reported lipid-based spherical nucleic acids consisting of an FDA-approved lipid which showed high cellular internalization and gene regulation in ovarian carcinoma cells.[123] Tan et al. reported molecular beacon micelle flares (MBMFs) that showed combined mRNA detection and gene therapy without transfection (Figure 1.21c).[127] Initially in an off-state due to fluorescence quenching, cellular internalization and binding to mRNA caused a structural change of the flare’s DNA corona, resulting in simultaneous fluorescence enhancement and gene knockdown. Zhang and co-workers developed a DNA-brush copolymer micelle that showed high cellular internalization and effective EGFP gene knockdown *in vitro* (Figure 1.21d).[128] To date, there are only very few examples of systems inducing gene knockdown without the aid of transfection agents or charge-stabilizing molecules. More recently, Sleiman and co-workers reported the synthesis of sequence-controlled antisense oligonucleotides.[129] The self-assembled precision spherical micelles showed enhanced cellular uptake and gene silencing at much lower concentrations of polyethyleneimine (PEI) transfection agent than previously reported (Figure 1.21e). Their studies also demonstrated that in the presence of PEI, 3D nanostructures show increased activity compared to the antisense-polymer conjugates, indicating that the 3D geometry plays an important role in cellular uptake.

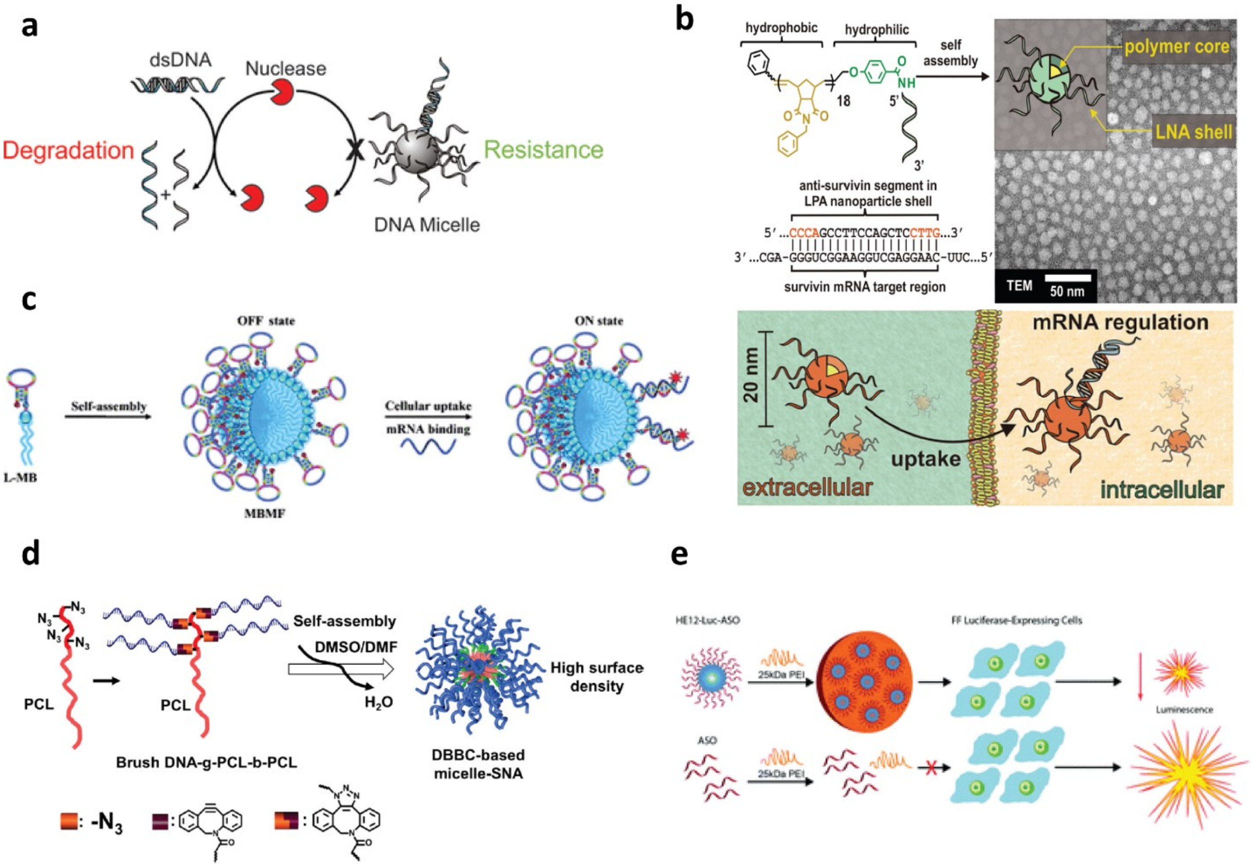

Figure 1.21 – DNA amphiphile-based systems for gene regulation. a) The organization of DNA in a dense 3D structure increases resistance to nuclease degradation.[124] Adapted with permission (American Chemical Society, 2013). b-d) DNA-amphiphile systems for gene regulation without transfection. b) Antisense LNA-polymer conjugates showing high cellular uptake and knockdown of survivin gene.[125] Reproduced with permission (American Chemical Society, 2014). c) Molecular beacon micelle flare (MBMF) showing combined mRNA detection and knockdown.[127] Adapted with permission (Wiley-VHC, 2013). d) DNA-brush type micelle with high cellular internalization and EGFP gene knockdown *in vitro*.[128] PCL: polycaprolactone, a biodegradable polyester. Reproduced with permission (Wiley-VCH, 2015). e) Precision antisense DNA nanoparticles showing the importance of the 3D nanostructure for efficient gene knockdown.[129] Adapted with permission (Royal Society of Chemistry, 2015).

1.4.6.2 Drug delivery

Apart from gene regulation, DNA amphiphiles have seen many applications in delivery of small molecular drugs, particularly for cancer therapy. The hydrophobic core of micelles formed upon self-assembly presents an ideal environment for the encapsulation of hydrophobic drugs. For cancer therapy, poly(propylene oxide)-DNA (PPO-DNA) micelles developed by the Hermann group were equipped with both a hydrophobic anticancer drug, doxorubicin, in the micelle core, and folic acid (FA), a targeting ligand conjugated to a DNA that is hybridized to the corona (Figure 1.22a).[130] These structures showed high uptake in CaCo-2 cell lines and efficient cytotoxicity *in vitro*. In a different approach, Tan and co-workers showed that the nucleic acid portion of the micelle can itself be used for targeting. The group developed DNA aptamer-lipid conjugates (TD05 aptamer specific for Ramos receptors) that self-assemble into micelles and showed enhanced targeting toward Ramos cells (Figure 1.22b).[86, 131] Their studies also showed that multi-valency of the DNA aptamers on the micelle surface play an important role in enhanced targeting, compared to the aptamer itself. Recently, Hermann and co-workers reported a DNA micelle system for ophthalmic drug delivery.[132] DNA micelles were loaded with two antibiotics, kanamycin and neomycin, in addition to two targeting aptamers. The structures showed long adherence to the corneal surface and decreased bacterial growth on *ex-vivo* treated porcine corneas.

Although these examples are promising as carriers for anticancer drugs, there is an inherent limitation of their use *in viv*o. Structures based on DNA amphiphile self-assembly suffer from nuclease degradation as well as premature drug leakage and disassembly upon dilution below their critical micellar concentration, hindering their success for *in vivo* applications. In one strategy to overcome this challenge, Zhang and co-workers developed stimuli-responsive DNA-drug conjugates where the drug is covalently attached to the DNA through a cleavable bond.[133] DNA-camptothecin conjugates were synthesized and upon self-assembly produced a DNA-shelled camptothecin core structure, burying the hydrophobic anticancer drug in the interior (Figure 1.22c). Upon irradiation with UV light, the DNA segment gets cleaved, releasing the prodrug, which through an irreversible self-immolative process releases free camptothecin drug molecules. The strategy provides a system for stimuli-responsive controlled drug release. The challenge of particle dissociation upon dilution has also been addressed by Hermann and co-workers. Here, they relied on the use of additional nanocarriers – viral capsids.[134] The group showed that DNA amphiphiles can act as templates for the self-assembly of Cowpea Chrlorotic Mottle Virus capsids (Figure 1.22d). In their strategy, a hydrophobic drug was first encapsulated in the micelle core, the product was then mixed with viral capsids which coated the micellar structures at neutral pH. The resulting structures showed increased stability against dilution and an example of loading drug-containing structures into protein nanocarriers. More recently, Mirkin and co-workers reported a cross-linking strategy to increase micelle stability through amide bond formation.[122]

Despite the promise that many DNA amphiphilic nanocarriers show for drug delivery, the breadth of studies is still limited to *in vitro* experiments. The potential behaviour and activity of these structures *in vivo* have not been visited and are still far from being understood. Studying the biodistribution and therapeutic activity of these constructs *in vivo* will bring many advances in their biomedical applications especially regarding their stability, pharmacokinetics of their payloads and their efficacy in model systems. This will require combined efforts of many disciplines, both scientific and medical. Nevertheless, the future of this field is both exciting and promising.

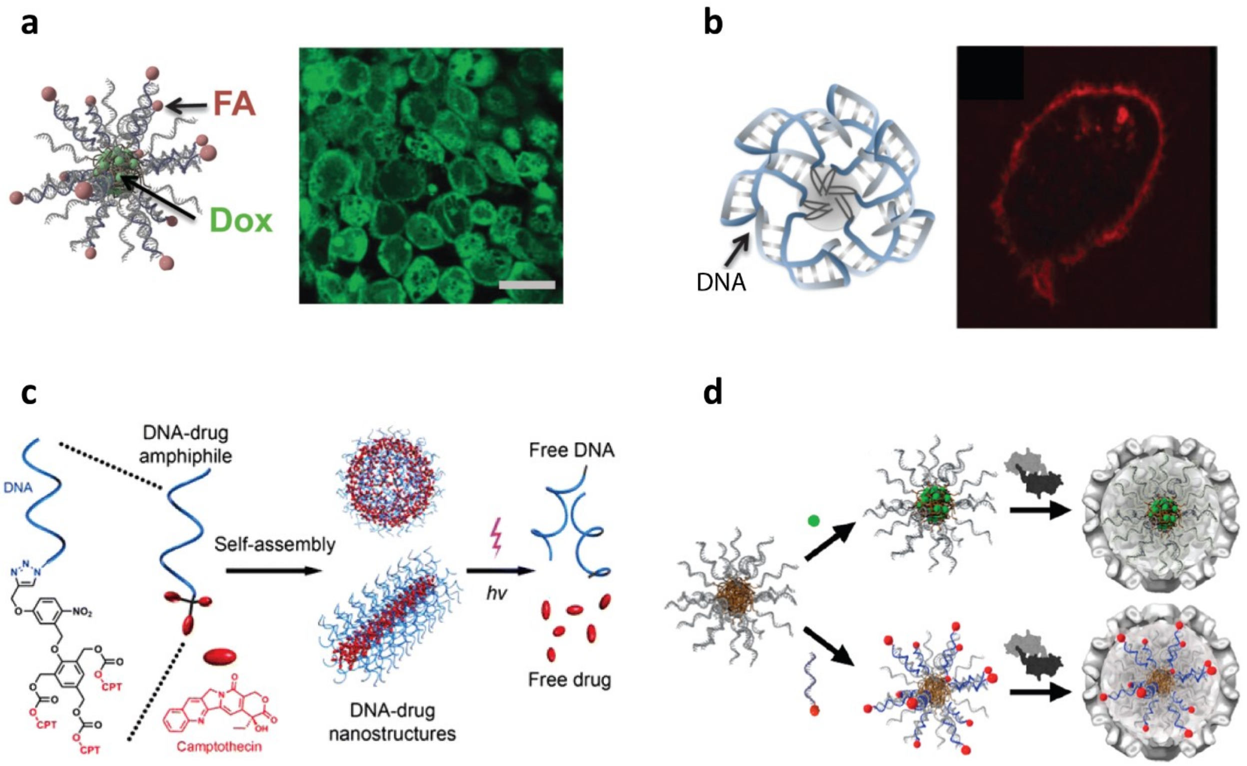

Figure 1.22 – DNA amphiphile-based systems for drug delivery. a) PPO-DNA micelles encapsulating doxorubicin and displaying folate targeting ligands.[130] Adapted with permission (Wiley-

VCH, 2008). b) TD05 aptamer micelles for specific targeting of Ramos cells.[86] Adapted with permission (PNAS, 2010). c) DNA-camptothecin nanostructures for light-triggered self-immolative drug delivery.[133] Adapted with permission (American Chemical Society, 2015) d) Virus-coated drug-loaded (top) and folate-decorated (bottom) DNA micelles for enhanced stability.[134] Adapted with permission (American Chemical Society, 2010).

1.4.6.3 3D printing and tissue engineering

In recent years, there has been an explosive growth of the field of 3D printing in application to tissue engineering. An ideal biodegradable 3D printed scaffold should include features such as high porosity, well-interconnected porous networks and have consistent pore sizes.[135] In that respect, hydrogels have emerged as the most promising scaffolds for artificial tissue engineering.[136] The most commonly investigated systems are hydrogels composed of covalently cross-linked polymer chains which bring them high stability, mechanical strength and shape-memory properties.[137] Strong cross-linking, however, limits cell migration and proliferation limiting their applications in 3D tissue printing.[138] Conversely, hydrogels based on amphiphilic molecules rely on weak non-covalent interactions such as H-bonding, electrostatic and host-guest binding to cross-link. These interactions invoke a dynamic nature in hydrogels providing self-healing properties and the possibility of cell migration.[139] An important requirement in hydrogel design for 3D printing is the ability to precisely control the cross-linked framework and pore size. Most polymers tend to have a very short persistence length and undergo folding and chain curling introducing variation in the backbone between cross-linked points. One solution to this problem, is to use a water-soluble long and rigid polymer in the backbone. In this regard, DNA is a promising candidate as a cross-linker due to its specific base-pairing and predicted secondary structure which allow the preparation of given-sized structures with precise control over length and dimensionality.[140] Thus, DNA hydrogels have received great attention as bio-inks in bioprinting due to the molecular-recognition properties of DNA and their biocompatibility, permeability, and biodegradability.[141] Toward that, Liu and co-workers have developed supramolecular polypeptide-DNA hydrogels and showed *in situ* multi-layer 3-dimensional bioprinting (Figure 1.23).[142] In their approach, two complementary bio-inks were deposited on a substrate and showed high self-healing properties and mechanical strength to develop geometrically uniform shapes (Figure 1.23a). The group further demonstrated 3D cell printing to fabricate hydrogels with live cells and organelles (Figure 1.23b). This approach generates dynamic, mechanically strong and biocompatible hydrogels with excellent molecular permeability and is promising for the fabrication complex predefined 3D biomaterials for applications in tissue engineering.

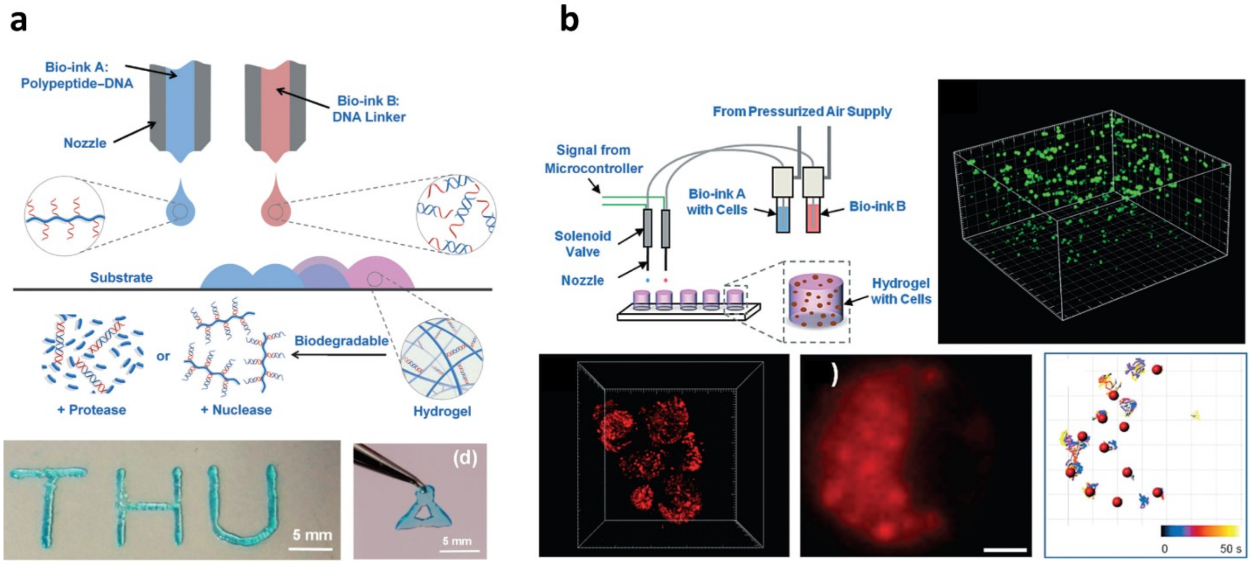

Figure 1.23 – 3D printing using DNA amphiphiles.[71, 142] a) Polypeptide-DNA hydrogels for 3D bioprinting of arbitrary designs b) Cell-printing process for 3D bioprinting of polypeptide-DNA hydrogels with AtT-20 cells. Adapted with permission (Wiley-VCH, 2015).

1.4.6.4 Nanoelectronics

The isolation and purification of individual carbon nanotubes has long been a challenge to take full advantage of their exceptional electronic, mechanical, thermal and optical properties.[143] Particularly, sorting of single-walled nanotubes (SWNTs) with minimal amount of defects and narrow diameter distribution has been a key objective and of high technological interest.[144] The selective dispersion of carbon nanotubes by pristine DNA has been realized through wrapping of complementary DNA (cDNA) around carbon nanotubes or covalent bond formation between the two moieties.[145-149] However, the translation of such methods to scalable device applications has been limited by sub-optimal yields and abundance of metallic nanotubes in the samples. Toward that end, Hermann and co-workers reported the use of a 22-mer DNA-poly(9,9-di-*n*-octylfluoenyl-

2,7-diyl) (PFO) conjugate to allow diameter-selective dispersion of semi-conductive SWNTs (Figure 1.24).[150] The interaction between the amphiphile and nanotube was mediated by strong π-π interactions of the PFO block with the nanotube sidewalls. The DNA part provided aqueous solubility and allowed hybridization with DNA-modified gold nanoparticles and selective SWNT immobilization on substrates such as field-effect transistors. This device fabrication process afforded high yields of 98% for SWNT field-effect transistors (Figure 1.24d). The group later showed that the hybridization of complementary DNA strands could be detected with high sensitivity, through signal transduction of the chemical recognition event into electrical doping, with an analyte sensitivity of 10 fM.[151] Electrical-based detection methods with such high sensitivity open the door for nucleic acid diagnostics without the need of DNA amplification.

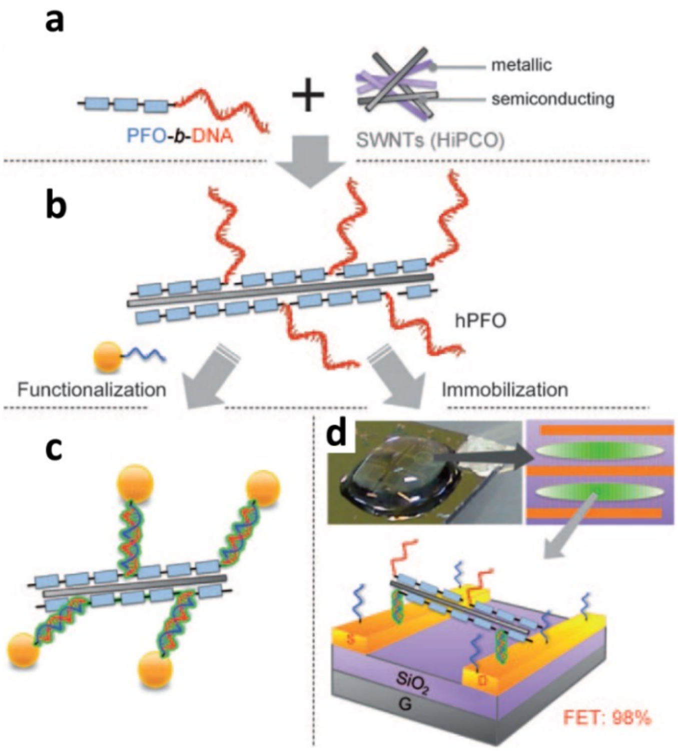

Figure 1.24 – DNA amphiphiles for sorting of SWNTs and applications in nanoelectronics.[150] a-b) PFO-DNA amphiphiles used for solubilization and selective functionalization of SWNTs in aqueous media. c) Functionalization of SWNT with gold nanoparticles using a target complementary DNA-AuNP. d) Selective assembly of SWNTs on the surface of substrates for nanoelectronics. Reproduced with permission (Wiley-VCH, 2011).

1.5 Context and Scope of this Thesis

DNA block copolymers have seen a wide range of applications due to the molecular recognition properties of DNA and the interesting self-assembly modes of hydrophobic polymers. From a synthetic point of view, one of the challenges with respect to DNA block copolymers, is the generation of highly monodisperse conjugates with monomeric control over the sequence and length of the chain. In that sense, solid-phase methods for the generation of sequence-defined DNA conjugates can offer many solutions to such limitations.[66] From a self-assembly point of view, the ability to generate supramolecular one-dimensional (1D) structures with high aspect ratio is desirable for applications of nanomaterial templation and drug delivery. Elongated 1D structures display improved *in vitro* and *in vivo* cellular uptake profiles, circulation lifetimes and pharmacokinetics compared to other architectures.[152-153] However, control over the length of one-dimensional DNA architectures is often limited. In fact, even for spherical particles, particle polydispersity presents a main challenge for their use as drug delivery vehicles hampering their translation into clinical studies. In this vein, most drug delivery applications of the DNA block copolymer systems have been limited to *in vitro* studies.

The research covered in this thesis is focused on sequence-defined DNA block copolymers and investigates their design, self-assembly and application in materials science and drug delivery, highlighting their behavior *in vitro* and *in vivo*. This work also explores strategies to tackle some of the inherent limitations of nanocarrier-based systems to increase their efficacy as drug delivery vehicles. Moreover, a strategy for achieving different modes of supramolecular self-assembly of DNA block copolymers is presented, demonstrating an unprecedented growth mechanism of one dimensional DNA fibers with controlled length and dimensionality.

Chapter 2 describes the examination of sequence-defined DNA block copolymers as drug delivery vehicles of anticancer drugs, specially BKM120, a small molecule drug for the treatment of chronic lymphocytic leukemia (CLL). The design, synthesis, drug encapsulation and characterization of drug-loaded structures are investigated. The structural stability of these structures and their resistance to nuclease is examined. Following that, the cellular uptake of these structures is characterized in cancer cell lines. The activity of drug-loaded nanoparticles is then investigated *in vitro* in cancer cell lines and primary patient CLL cells. Finally, the *in vivo* biodistribution, circulation, organ and tumor-specific accumulation of these particles is examined using intravenous and intraperitoneal routes of administration. The result is a robust DNA-based platform for the delivery of chemotherapeutic drugs.

Building on the findings from Chapter 2, Chapter 3 investigates strategies to increase the targeting capability and efficacy of the first-generation drug delivery platform. Increased targeting capabilities of these structures are realized upon the incorporation of DNA aptamers as targeting ligands. Stimuli-responsive DNA nanoparticles are also described, where a nucleic acid-dye cargo is released upon binding to a target microRNA. The potential application of DNA amphiphile-based particles for targeting normal skin epidermal cells and their intracellular structural integrity is investigated. Additionally, using DNA analogs, a simple strategy to significantly increase nuclease resistance of nanoparticles is demonstrated. Detailed studies are conducted on the interaction of DNA nanoparticles with human serum albumin, the most abundant protein in human blood serum. Attachment of labile PEG moieties to further shield nanoparticles from serum proteins and increase circulation half-life is described. Finally, different cross-linking strategies, mediated through disulfide bond formation are investigated to increase the overall stability of DNA nanoparticles. These strategies pave the way toward a more customized drug delivery system for increased selectivity and therapeutic effect.

Chapters 2 and 3 were focused on drug delivery applications of DNA amphiphiles. Chapter 4 expands on the range of applications and describes their importance in giving rise to new supramolecular self-assembled structures with interesting properties and function. In this case, the site-specific introduction of a single Cyanine dye (Cy3) molecule to DNA-polymer conjugates causes a drastic morphological shift in their self-assembly from spheres to one-dimensional rods. A strategy to generate rods with controlled dimensionality and length is presented. Additionally, an unprecedented supramolecular growth mechanism of one dimensional DNA fibers is discovered. Due to their change in optical properties upon assembly/disassembly, these structures could be used as fluorescent bioanalytical tools. Finally, examples are described for the templation of nanomaterials on DNA fibers and the site-specific alignment of fibers along DNA origami en route toward complex hybrid architectures with sophisticated function.

Taken together, these studies provide a critical evaluation of sequence-defined DNA-polymers in the context of biomedical applications and materials science.

1.6 References

1. M Lehn, J., *Supramolecular Chemistry. Concepts and Perspectives*. **1995**; Vol. 9.
2. Pedersen, C. J., *J. Am. Chem. Soc.* **1967,** *89* (26), 7017-7036.
3. Lehn, J. M., *Acc. Chem. Res.* **1978,** *11* (2), 49-57.
4. Cram, D. J.; Kaneda, T.; Helgeson, R. C.; Lein, G. M., *J. Am. Chem. Soc.* **1979,** *101* (22), 6752-6754.
5. Assaf, K. I.; Nau, W. M., *Chem. Soc. Rev.* **2015,** *44* (2), 394-418.
6. Dalgarno, S. J.; Tucker, S. A.; Bassil, D. B.; Atwood, J. L., *Science* **2005,** *309* (5743), 2037.
7. Lehn, J.-M., *Chem. Soc. Rev.* **2017,** *46* (9), 2378-2379.
8. Diederich, F., *Angew. Chem. Int. Ed.* **2006,** *46* (1-2), 68-69.
9. Mendes, A. C.; Baran, E. T.; Reis, R. L.; Azevedo, H. S., *Wiley Interdiscip Rev Nanomed Nanobiotechnol* **2013,** *5* (6), 582-612.
10. Alexandridis, P.; Lindman, B., *Amphiphilic Block Copolymers: Self-Assembly and Applications*. Elsevier Science: 2000.
11. Lombardo, D.; Kiselev, M. A.; Magaz; #xf9; , S.; Calandra, P., *Advances in Condensed Matter Physics* **2015,** *2015*, 22.
12. Israelachvili, J. N.; Mitchell, D. J.; Ninham, B. W., *Journal of the Chemical Society, Faraday Transactions 2: Molecular and Chemical Physics* **1976,** *72* (0), 1525-1568.
13. Nagarajan, R., *Amphiphiles: Molecular Assembly and Applications*. American Chemical Society: 2011; Vol. 1070, p 0.
14. Salim, M.; Minamikawa, H.; Sugimura, A.; Hashim, R., *MedChemComm* **2014,** *5* (11), 1602-1618.
15. Mai, Y.; Eisenberg, A., *Chem. Soc. Rev.* **2012,** *41* (18), 5969-85.
16. Hsieh, H. L.; Quirk, R. P., *Anionic polymerization: principles and practical applications*. Marcek Dekker: New York, **1996**.
17. Georges, M. K.; Veregin, R. P. N.; Kazmaier, P. M.; Hamer, G. K., *Macromolecules* **1993,** *26* (11), 2987-2988.
18. Gilliom, L. R.; Grubbs, R. H., *J. Am. Chem. Soc.* **1986,** *108* (4), 733-742.
19. Otsuka, H.; Nagasaki, Y.; Kataoka, K., *Mater. Today* **2001,** *4* (3), 30-36.
20. Adams, M. L.; Lavasanifar, A.; Kwon, G. S., *J. Pharm. Sci.* **2003,** *92* (7), 1343-1355.
21. Kutikov, A. B.; Song, J., *ACS Biomaterials Science & Engineering* **2015,** *1* (7), 463-480.
22. Förster, S.; Antonietti, M., *Adv. Mater.* **1999,** *10* (3), 195-217.
23. Fink, Y.; Urbas, A. M.; Bawendi, M. G.; Joannopoulos, J. D.; Thomas, E. L., *Journal of Lightwave Technology* **1999,** *17* (11), 1963-1969.
24. Bates, F. S.; Fredrickson, G. H., *Annu. Rev. Phys. Chem.* **1990,** *41* (1), 525-557.
25. Helfand, E.; Wasserman, Z. R., *Macromolecules* **1978,** *11* (5), 960-966.
26. Leibler, L., *Macromolecules* **1980,** *13* (6), 1602-1617.
27. Matsen, M. W.; Bates, F. S., *Macromolecules* **1996,** *29* (4), 1091-1098.

28. Matsen, M. W.; Schick, M., *Macromolecules* **1994,** *27* (23), 6761-6767.

29. Khandpur, A. K.; Foerster, S.; Bates, F. S.; Hamley, I. W.; Ryan, A. J.; Bras, W.; Almdal, K.; Mortensen, K., *Macromolecules* **1995,** *28* (26), 8796-8806.

30. Zhang, L.; Eisenberg, A., *Science* **1995,** *268* (5218), 1728-31.

31. Cameron, N. S.; Corbierre, M. K.; Eisenberg, A., *Can. J. Chem.* **1999,** *77* (8), 1311-1326.

32. Yuan, J.; Müller, A. H. E., *Polymer* **2010,** *51* (18), 4015-4036.

33. Mai, Y.; Eisenberg, A., *Macromolecules* **2011,** *44* (8), 3179-3183.

34. Kwon, G. S.; Naito, M.; Kataoka, K.; Yokoyama, M.; Sakurai, Y.; Okano, T., *Colloids Surf., B* **1994,** *2* (4), 429-434.

35. Kataoka, K.; Harada, A.; Nagasaki, Y., *Advanced Drug Delivery Reviews* **2001,** *47* (1), 113-131.

36. Dubertret, B.; Skourides, P.; Norris, D. J.; Noireaux, V.; Brivanlou, A. H.; Libchaber, A., *Science* **2002,** *298* (5599), 1759.

37. Valentine, K. G.; Peterson, R.; Saad, J. S.; Summers, M. F.; Xu, X.; Ames, J. B.; Wand, A. J., *Structure (London, England : 1993)* **2010,** *18* (1), 9-16.

38. Danaei, M.; Dehghankhold, M.; Ataei, S.; Hasanzadeh Davarani, F.; Javanmard, R.; Dokhani, A.; Khorasani, S.; Mozafari, M. R., *Pharmaceutics* **2018,** *10* (2).

39. Seeman, N. C.; Sleiman, H. F., *Nat. Rev. Mater.* **2017,** *3*, 17068.

40. Schnitzler, T.; Herrmann, A., *Acc. Chem. Res.* **2012,** *45* (9), 1419-1430.

41. Watson, J. D.; Crick, F. H. C., *Nature* **1953,** *171*, 737.

42. Marks, A. R., *J. Clin. Invest.* **2003,** *112* (7), 972-972.

43. Ma, S.; Tang, N.; Tian, J., *Curr. Opin. Chem. Biol.* **2012,** *16* (3-4), 260-267.

44. Seeman, N. C., *Nature* **2003,** *421*, 427.

45. Sinden, R., *DNA Structure and Function*. Academic Press: 2012.

46. Marmur, J.; Doty, P., *Nature* **1959,** *183*, 1427.

47. Yakovchuk, P.; Protozanova, E.; Frank-Kamenetskii, M. D., *Nucleic Acids Res.* **2006,** *34* (2), 564-74.

48. Frontali, C.; Dore, E.; Ferrauto, A.; Gratton, E.; Bettini, A.; Pozzan, M. R.; Valdevit, E., *Biopolymers* **1979,** *18* (6), 1353-73.

49. Rothemund, P. W. K., *Nature* **2006,** *440* (7082), 297-302.

50. Kallenbach, N. R.; Ma, R.-I.; Seeman, N. C., *Nature* **1983,** *305*, 829.

51. Chen, J. H.; Seeman, N. C., *Nature* **1991,** *350* (6319), 631-3.

52. Rye, H. S.; Yue, S.; Wemmer, D. E.; Quesada, M. A.; Haugland, R. P.; Mathies, R. A.; Glazer, A. N., *Nucleic Acids Res.* **1992,** *20* (11), 2803-2812.

53. Dorak, M. T., *Real-time PCR*. Taylor & Francis Group: New York, 2006.

54. Alemdaroglu, F. E.; Herrmann, A., *Org. Biomol. Chem.* **2007,** *5* (9), 1311-20.

55. Kwak, M.; Herrmann, A., *Chem. Soc. Rev.* **2011,** *40* (12), 5745-5755.

56. Pan, G.; Jin, X.; Mou, Q.; Zhang, C., *Chin. Chem. Lett.* **2017,** *28* (9), 1822-1828.

57. Khorana, H. G.; Tener, G. M.; Moffatt, J. G.; Pol, E. H., *Chemistry and Industry (London)* **1956**, 1523.

58. Khorana, H. G.; Agarwal, K. L.; Büchi, H.; Caruthers, M. H.; Gupta, N. K.; Klbppe, K.; Kumar, A.; Ohtsuka, E.; RajBhandary, U. L.; van de Sande, J. H.; Sgaramella, V.; Tebao, T.; Weber, H.; Yamada, T., *J. Mol. Biol.* **1972,** *72* (2), 209-217.

59. Letsinger, R. L.; Mahadevan, V., *J. Am. Chem. Soc.* **1965,** *87* (15), 3526-3527.

60. Letsinger, R. L.; Lunsford, W. B., *J. Am. Chem. Soc.* **1976,** *98* (12), 3655-3661.

61. Beaucage, S. L.; Caruthers, M. H., *Tetrahedron Lett.* **1981,** *22* (20), 1859-1862.

62. Alvarado-Urbina, G.; Sathe, G. M.; Liu, W. C.; Gillen, M. F.; Duck, P. D.; Bender, R.; Ogilvie, K. K., *Science* **1981,** *214* (4518), 270-4.

63. Merrifield, R. B., Solid-Phase Peptide Synthesis. In *The Chemistry of Polypeptides: Essays in Honor of Dr. Leonidas Zervas*, Katsoyannis, P. G., Ed. Springer US: Boston, MA, **1973**; pp 335-361.

64. Usman, N.; Ogilvie, K. K.; Jiang, M. Y.; Cedergren, R. J., *J. Am. Chem. Soc.* **1987,** *109* (25), 7845-7854.

65. Wojcik, F.; Ponader, D.; Mosca, S.; Hartmann, L., Recent Advances in Solid Phase Polymer Synthesis: Polyamides from Tailor-Made Building Blocks. In *Sequence-Controlled Polymers: Synthesis, Self-Assembly, and Properties*, American Chemical Society: **2014**; Vol. 1170, pp 85-101.

66. Edwardson, T. G.; Carneiro, K. M.; Serpell, C. J.; Sleiman, H. F., *Angew. Chem. Int. Ed. Engl.* **2014,** *53* (18), 4567-71.

67. Wang, L.; Feng, Y.; Sun, Y.; Li, Z.; Yang, Z.; He, Y.-M.; Fan, Q.-H.; Liu, D., *Soft Matter* **2011,** *7* (16), 7187-7190.

68. Jeong, J. H.; Park, T. G., *Bioconjugate Chem.* **2001,** *12* (6), 917-923.

69. Oishi, M.; Hayama, T.; Akiyama, Y.; Takae, S.; Harada, A.; Yamasaki, Y.; Nagatsugi, F.; Sasaki, S.; Nagasaki, Y.; Kataoka, K., *Biomacromolecules* **2005,** *6* (5), 2449-2454.

70. Singh, R.; Whitesides, G. M., Thiol-disulfide interchange. In *PATAI's Chemistry of Functional Groups*, 2010.

71. Li, C.; Chen, P.; Shao, Y.; Zhou, X.; Wu, Y.; Yang, Z.; Li, Z.; Weil, T.; Liu, D., *Small* **2014,** *11* (9-10), 1138-1143.

72. Baskin, J. M.; Prescher, J. A.; Laughlin, S. T.; Agard, N. J.; Chang, P. V.; Miller, I. A.; Lo, A.; Codelli, J. A.; Bertozzi, C. R., *Proceedings of the National Academy of Sciences* **2007,** *104* (43), 16793.

73. Isoda, K.; Kanayama, N.; Miyamoto, D.; Takarada, T.; Maeda, M., *React. Funct. Polym.* **2011,** *71* (3), 367-371.

74. Liu, K.; Zheng, L.; Liu, Q.; de Vries, J. W.; Gerasimov, J. Y.; Herrmann, A., *J. Am. Chem. Soc.* **2014,** *136* (40), 14255-14262.

75. Defrancq, E.; Singh, Y.; Spinelli, N., *Curr. Org. Chem.* **2008,** *12* (4), 263-290.

76. Alemdaroglu, F. E.; Ding, K.; Berger, R.; Herrmann, A., *Angew. Chem. Int. Ed. Engl.* **2006,** *45* (25), 4206-10.

77. Trinh, T.; Chidchob, P.; Bazzi, H. S.; Sleiman, H. F., *Chem. Commun.* **2016,** *52* (72), 10914-10917.

78. Guzaev Andrei, P.; Pon Richard, T., *Curr. Protoc. Nucleic Acid Chem.* **2013,** *52* (1), 3.2.1-3.2.23.

79. Lyttle, M. H.; Hudson, D.; Cook, R. M., *Nucleic Acids Res.* **1996,** *24* (14), 2793-2798.

80. Li, Z.; Zhang, Y.; Fullhart, P.; Mirkin, C. A., *Nano Lett.* **2004,** *4* (6), 1055-1058.

81. Yang, C. J.; Pinto, M.; Schanze, K.; Tan, W., *Angewandte Chemie (International ed. in English)* **2005,** *44* (17), 2572-2576.

82. Wang, L.; Feng, Y.; Yang, Z.; He, Y.-M.; Fan, Q.-H.; Liu, D., *Chem. Commun.* **2012,** *48* (31), 3715-3717.

83. Jia, F.; Lu, X.; Tan, X.; Zhang, K., *Chem. Commun.* **2015,** *51* (37), 7843-7846.

84. Chan, Y.-H. M.; van Lengerich, B.; Boxer, S. G., *Proceedings of the National Academy of Sciences* **2009,** *106* (4), 979.

85. Gissot, A.; Di Primo, C.; Bestel, I.; Giannone, G.; Chapuis, H.; Barthélémy, P., *Chem. Commun.* **2008,** (43), 5550-5552.

86. Wu, Y.; Sefah, K.; Liu, H.; Wang, R.; Tan, W., *Proc. Natl. Acad. Sci. U. S. A.* **2010,** *107* (1), 5-10.

87. Liu, H.; Zhu, Z.; Kang, H.; Wu, Y.; Sefan, K.; Tan, W., *Chem. Eur. J.* **2010,** *16* (12), 3791-7.

88. Edwardson, T. G. W.; Carneiro, K. M. M.; McLaughlin, C. K.; Serpell, C. J.; Sleiman, H. F., *Nat. Chem.* **2013,** *5*, 868.

89. de Rochambeau, D.; Barłóg, M.; Edwardson, T. G. W.; Fakhoury, J. J.; Stein, R. S.; Bazzi, H. S.; Sleiman, H. F., *Polymer Chemistry* **2016,** *7* (31), 4998-5003.

90. Alemdaroglu, F. E.; Zhuang, W.; Zophel, L.; Wang, J.; Berger, R.; Rabe, J. P.; Herrmann, A., *Nano Lett.* **2009,** *9* (10), 3658-62.

91. Ayaz, M. S.; Kwak, M.; Alemdaroglu, F. E.; Wang, J.; Berger, R.; Herrmann, A., *Chem. Commun.* **2011,** *47* (8), 2243-2245.

92. Anaya, M.; Kwak, M.; Musser, A. J.; Mullen, K.; Herrmann, A., *Chem. Eur. J.* **2010,** *16* (43), 12852-9.

93. Alemdaroglu Fikri , E.; Wang, J.; Börsch, M.; Berger, R.; Herrmann, A., *Angew. Chem. Int. Ed.* **2008,** *47* (5), 974-976.

94. Ding, K.; Alemdaroglu, F. E.; Börsch, M.; Berger, R.; Herrmann, A., *Angew. Chem. Int. Ed.* **2007,** *46* (7), 1172-1175.

95. Chien, M.-P.; Rush, A. M.; Thompson, M. P.; Gianneschi, N. C., *Angew. Chem. Int. Ed.* **2010,** *49* (30), 5076-5080.

96. Vyborna, Y.; Vybornyi, M.; Rudnev, A. V.; Häner, R., *Angew. Chem. Int. Ed.* **2015,** *54* (27), 7934-7938.

97. Kamps, A. C.; Cativo, M. H. M.; Chen, X.-J.; Park, S.-J., *Macromolecules* **2014,** *47* (11), 3720-3726.

98. Teixeira Jr, F.; Rigler, P.; Vebert-Nardin, C., *Chem. Commun.* **2007,** (11), 1130-1132.

99. Dong, Y.; Sun, Y.; Wang, L.; Wang, D.; Zhou, T.; Yang, Z.; Chen, Z.; Wang, Q.; Fan, Q.; Liu, D., *Angew. Chem. Int. Ed.* **2014,** *53* (10), 2607-2610.

100. Dong, Y.; Yang, Y. R.; Zhang, Y.; Wang, D.; Wei, X.; Banerjee, S.; Liu, Y.; Yang, Z.; Yan, H.; Liu, D., *Angew. Chem. Int. Ed. Engl.* **2017,** *56* (6), 1586-1589.

101. Zhiyong, Z.; Chun, C.; Yuanchen, D.; Zhongqiang, Y.; Qing-Hua, F.; Dongsheng, L., *Angew. Chem. Int. Ed.* **2014,** *53* (49), 13468-13470.

102. Chao, Z.; Yiyang, Z.; Yuanchen, D.; Fen, W.; Dianming, W.; Ling, X.; Dongsheng, L., *Adv. Mater.* **2016,** *28* (44), 9819-9823.

103. Thompson, M. P.; Chien, M.-P.; Ku, T.-H.; Rush, A. M.; Gianneschi, N. C., *Nano Lett.* **2010,** *10* (7), 2690-2693.

104. McLaughlin, C. K.; Hamblin, G. D.; Hänni, K. D.; Conway, J. W.; Nayak, M. K.; Carneiro, K. M. M.; Bazzi, H. S.; Sleiman, H. F., *J. Am. Chem. Soc.* **2012,** *134* (9), 4280-4286.

105. Carneiro, K. M. M.; Hamblin, G. D.; Hänni, K. D.; Fakhoury, J.; Nayak, M. K.; Rizis, G.; McLaughlin, C. K.; Bazzi, H. S.; Sleiman, H. F., *Chemical Science* **2012,** *3* (6), 1980-1986.

106. Serpell, C. J.; Edwardson, T. G. W.; Chidchob, P.; Carneiro, K. M. M.; Sleiman, H. F., *J. Am. Chem. Soc.* **2014,** *136* (44), 15767-15774.

107. Chidchob, P.; Edwardson, T. G. W.; Serpell, C. J.; Sleiman, H. F., *J. Am. Chem. Soc.* **2016,** *138* (13), 4416-4425.

108. List, J.; Weber, M.; Simmel, F. C., *Angew. Chem. Int. Ed. Engl.* **2014,** *53* (16), 4236-9.

109. Wilks, T. R.; Bath, J.; de Vries, J. W.; Raymond, J. E.; Herrmann, A.; Turberfield, A. J.; O'Reilly, R. K., *ACS Nano* **2013,** *7* (10), 8561-8572.

110. Conway, J. W.; Madwar, C.; Edwardson, T. G.; McLaughlin, C. K.; Fahkoury, J.; Lennox, R. B.; Sleiman, H. F., *J. Am. Chem. Soc.* **2014,** *136* (37), 12987-12997.

111. Suzuki, Y.; Endo, M.; Yang, Y.; Sugiyama, H., *J. Am. Chem. Soc.* **2014,** *136* (5), 1714-1717.

112. Johnson-Buck, A.; Jiang, S.; Yan, H.; Walter, N. G., *ACS Nano* **2014,** *8* (6), 5641-5649.

113. Langecker, M.; Arnaut, V.; Martin, T. G.; List, J.; Renner, S.; Mayer, M.; Dietz, H.; Simmel, F. C., *Science* **2012,** *338* (6109), 932-6.

114. Burns, J. R.; Göpfrich, K.; Wood, J. W.; Thacker, V. V.; Stulz, E.; Keyser, U. F.; Howorka, S., *Angew. Chem. Int. Ed.* **2013,** *52* (46), 12069-12072.

115. van Lengerich, B.; Rawle, Robert J.; Bendix, Poul M.; Boxer, Steven G., *Biophys. J.* **2013,** *105* (2), 409-419.

116. Chan, Y.-H. M.; van Lengerich, B.; Boxer, S. G., *Biointerphases* **2008,** *3* (2), FA17-FA21.

117. Stengel, G.; Zahn, R.; Höök, F., *J. Am. Chem. Soc.* **2007,** *129* (31), 9584-9585.

118. Xu, W.; Wang, J.; Rothman, J. E.; Pincet, F., *Angewandte Chemie (International ed. in English)* **2015,** *54* (48), 14388-14392.

119. Woller, J. G.; Börjesson, K.; Svedhem, S.; Albinsson, B., *Langmuir* **2012,** *28* (4), 1944-1953.

120. Börjesson, K.; Lundberg Erik, P.; Woller Jakob, G.; Nordén, B.; Albinsson, B., *Angew. Chem. Int. Ed.* **2011,** *50* (36), 8312-8315.

121. Seferos, D. S.; Prigodich, A. E.; Giljohann, D. A.; Patel, P. C.; Mirkin, C. A., *Nano Lett.* **2009,** *9* (1), 308-311.

122. Banga, R. J.; Meckes, B.; Narayan, S. P.; Sprangers, A. J.; Nguyen, S. T.; Mirkin, C. A., *J. Am. Chem. Soc.* **2017,** *139* (12), 4278-4281.

123. Banga, R. J.; Chernyak, N.; Narayan, S. P.; Nguyen, S. T.; Mirkin, C. A., *J. Am. Chem. Soc.* **2014,** *136* (28), 9866-9869.

124. Rush, A. M.; Thompson, M. P.; Tatro, E. T.; Gianneschi, N. C., *ACS Nano* **2013,** *7* (2), 1379-1387.

125. Rush, A. M.; Nelles, D. A.; Blum, A. P.; Barnhill, S. A.; Tatro, E. T.; Yeo, G. W.; Gianneschi, N. C., *J. Am. Chem. Soc.* **2014,** *136* (21), 7615-7618.

126. Rosi, N. L.; Giljohann, D. A.; Thaxton, C. S.; Lytton-Jean, A. K.; Han, M. S.; Mirkin, C. A., *Science* **2006,** *312* (5776), 1027-30.

127. Chen, T.; Wu Cuichen, S.; Jimenez, E.; Zhu, Z.; Dajac Joshua, G.; You, M.; Han, D.; Zhang, X.; Tan, W., *Angew. Chem. Int. Ed.* **2013,** *52* (7), 2012-2016.

128. Zhang, C.; Hao, L.; Calabrese Colin, M.; Zhou, Y.; Choi Chung Hang, J.; Xing, H.; Mirkin Chad, A., *Small* **2015,** *11* (40), 5360-5368.

129. Fakhoury, J. J.; Edwardson, T. G.; Conway, J. W.; Trinh, T.; Khan, F.; Barlog, M.; Bazzi, H. S.; Sleiman, H. F., *Nanoscale* **2015,** *7* (48), 20625-34.

130. Alemdaroglu, F. E.; Alemdaroglu, N. C.; Langguth, P.; Herrmann, A., *Adv. Mater.* **2008,** *20* (5), 899-902.

131. Mallikaratchy, P. R.; Ruggiero, A.; Gardner, J. R.; Kuryavyi, V.; Maguire, W. F.; Heaney, M. L.; McDevitt, M. R.; Patel, D. J.; Scheinberg, D. A., *Nucleic Acids Res.* **2011,** *39* (6), 2458-2469.

132. Willem de Vries, J.; Schnichels, S.; Hurst, J.; Strudel, L.; Gruszka, A.; Kwak, M.; Bartz-Schmidt, K.-U.; Spitzer, M. S.; Herrmann, A., *Biomaterials* **2018,** *157*, 98-106.

133. Tan, X.; Li, B. B.; Lu, X.; Jia, F.; Santori, C.; Menon, P.; Li, H.; Zhang, B.; Zhao, J. J.; Zhang, K., *J. Am. Chem. Soc.* **2015,** *137* (19), 6112-6115.

134. Kwak, M.; Minten, I. J.; Anaya, D.-M.; Musser, A. J.; Brasch, M.; Nolte, R. J. M.; Müllen, K.; Cornelissen, J. J. L. M.; Herrmann, A., *J. Am. Chem. Soc.* **2010,** *132* (23), 7834-7835.

135. An, J.; Teoh, J. E. M.; Suntornnond, R.; Chua, C. K., *Engineering* **2015,** *1* (2), 261-268.

136. Drury, J. L.; Mooney, D. J., *Biomaterials* **2003,** *24* (24), 4337-4351.

137. El-Sherbiny, I. M.; Yacoub, M. H., *Global Cardiology Science & Practice* **2013,** *2013* (3), 316-342.

138. Annabi, N.; Tamayol, A.; Uquillas, J. A.; Akbari, M.; Bertassoni, L. E.; Cha, C.; Camci-Unal, G.; Dokmeci, M. R.; Peppas, N. A.; Khademhosseini, A., *Adv. Mater.* **2014,** *26* (1), 85-123.

139. Appel, E. A.; del Barrio, J.; Loh, X. J.; Scherman, O. A., *Chem. Soc. Rev.* **2012,** *41* (18), 6195-6214.

140. Pinheiro, A. V.; Han, D.; Shih, W. M.; Yan, H., *Nature Nanotechnology* **2011,** *6*, 763.

141. Shao, Y.; Jia, H.; Cao, T.; Liu, D., *Acc. Chem. Res.* **2017,** *50* (4), 659-668.

142. Li, C.; Faulkner-Jones, A.; Dun Alison, R.; Jin, J.; Chen, P.; Xing, Y.; Yang, Z.; Li, Z.; Shu, W.; Liu, D.; Duncan Rory, R., *Angew. Chem. Int. Ed.* **2015,** *54* (13), 3957-3961.

143. Hersam, M. C., *Nature Nanotechnology* **2008,** *3*, 387.

144. Nish, A.; Hwang, J.-Y.; Doig, J.; Nicholas, R. J., *Nature Nanotechnology* **2007,** *2*, 640.

145. Zheng, M.; Jagota, A.; Semke, E. D.; Diner, B. A.; McLean, R. S.; Lustig, S. R.; Richardson, R. E.; Tassi, N. G., *Nature Materials* **2003,** *2*, 338.

146. Tu, X.; Manohar, S.; Jagota, A.; Zheng, M., *Nature* **2009,** *460*, 250.

147. Jung, S.; Cha, M.; Park, J.; Jeong, N.; Kim, G.; Park, C.; Ihm, J.; Lee, J., *J. Am. Chem. Soc.* **2010,** *132* (32), 10964-10966.

148. Yang, W.; Moghaddam, M. J.; Taylor, S.; Bojarski, B.; Wieczorek, L.; Herrmann, J.; McCall, M. J., *Chem. Phys. Lett.* **2007,** *443* (4), 169-172.

149. Keren, K.; Berman, R. S.; Buchstab, E.; Sivan, U.; Braun, E., *Science* **2003,** *302* (5649), 1380.

150. Kwak, M.; Gao, J.; Prusty Deepak, K.; Musser Andrew, J.; Markov Vladimir, A.; Tombros, N.; Stuart Marc, C. A.; Browne Wesley, R.; Boekema Egbert, J.; ten Brinke, G.; Jonkman Harry, T.; van Wees Bart, J.; Loi Maria, A.; Herrmann, A., *Angew. Chem. Int. Ed.* **2011,** *50* (14), 3206-3210.

151. Kim, J. H.; Smit, J.; K Prusty, D.; Musser, A.; Tombros, N.; Lee, P.; Herrmann, A.; Kwak, M., *Ultrasensitive Detection of Oligonucleotides: Single-Walled Carbon Nanotube Transistor Assembled by DNA Block Copolymer*. **2017**; Vol. 17, p 5175-5180.

152. Zhao, Y.; Wang, Y.; Ran, F.; Cui, Y.; Liu, C.; Zhao, Q.; Gao, Y.; Wang, D.; Wang, S., *Sci. Rep.* **2017,** *7* (1), 4131.

153. Huang, X.; Teng, X.; Chen, D.; Tang, F.; He, J., *Biomaterials* **2010,** *31* (3), 438-448.

Preface

In chapter 2, sequence-defined DNA polymers are examined as a drug delivery platform for small molecule chemotherapeutics. The encapsulation of BKM120, a small molecule drug for the treatment of chronic lymphocytic leukemia (CLL) is evaluated. The design, characterization and stability of drug-loaded particles is investigated. The cellular uptake of structures in cancer cell lines, delivery of cargo and *in vitro* activity of drug-loaded structures in primary patient cancer CLL cells highlight their high internalization and cytotoxicity in cancer cells. Finally, we present the first *in vivo* study of DNA-polymer nanoparticles that shows long circulation, full body biodistribution and tumor accumulation. The structures do not penetrate the blood-brain barrier and thus could bypass the side-effects of BKM120. These studies describe a robust DNA-based platform for the delivery of chemotherapeutic drugs.

Graduate student struggles…

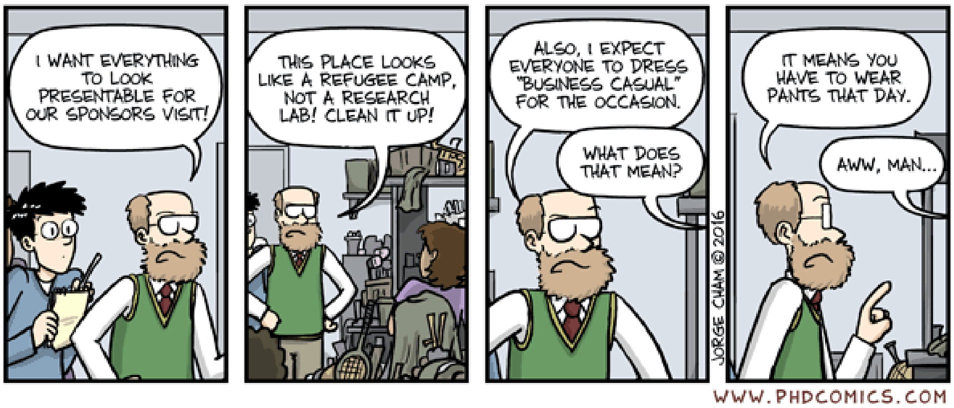

2

Precision Spherical Nucleic Acids for Delivery of Anticancer Drugs

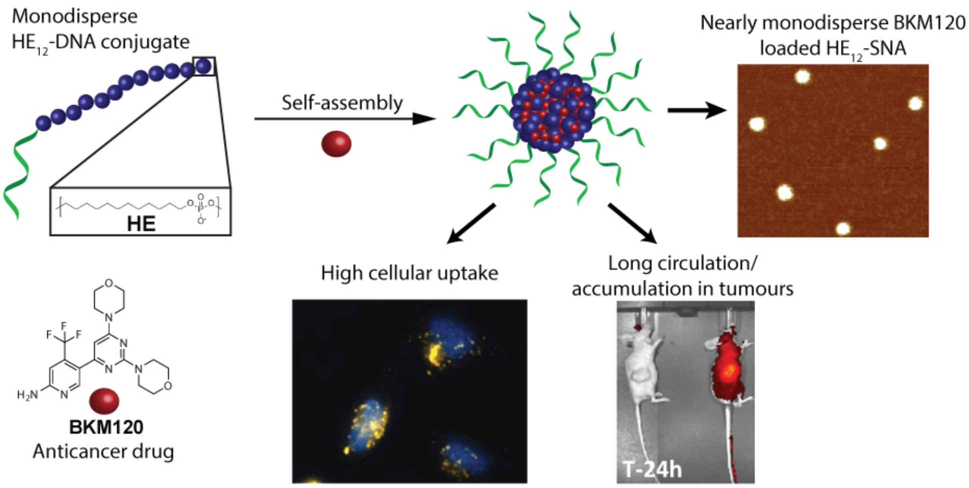

This chapter is composed mainly of work published as “Precision spherical nucleic acids for delivery of anticancer drugs” by Danny Bousmail, Lilian Amrein, Johans J. Fakhoury, Hassan H. Fakih, John C. C. Hsu, Lawrence Panasci and Hanadi F. Sleiman. *Chemical Science*, 2017, **8**, 6218.

Contribution of authors

Danny Bousmail helped design the project and primarily contributed to the production of experimental data from DNA synthesis, assembly, drug encapsulation, characterization, stability studies, preparation of structures for *in vitro* and *in vivo* experiments and helped with cellular uptake and *in vitro* studies. **Lilian Amrein** conducted the apoptosis studies on primary patient cells and the *in vivo* biodistribution experiments. For the intravenous biodistribution experiments, **Lilian Amrein** was helped by **Hassan Fakih** and **John Hsu**. **Johans Fakhoury** conducted *in vitro* cellular uptake and MTS assay. **Danny Bousmail** and **Johans Fakhoury** both analyzed *in vitro* data and conducted immunogenicity assays. **Hassan Fakih** carried out flow cytometry experiments. **Hanadi F. Sleiman** designed the project, guided interpretation of data and discussion of results. **Danny Bousmail, Lilian Amrein** and **Hanadi F. Sleiman** co-wrote the manuscript.

2.1 Abstract

Targeted delivery of chemotherapeutics to the tumor microenvironment is still a challenge in nanomedicine. The use of nanocarriers can be one strategy to selectively delivery drugs to their target site, however, many drug delivery systems currently suffer from complicated synthesis and particle polydispersity. Since the shape and size of nanoparticles are very important for their biodistribution, circulation and ultimately, their effect, the generation of well-defined structures will be essential for their application as drug delivery vehicles. This chapter reports a spherical nucleic acid (SNA) system composed of DNA amphiphiles for the delivery of BKM120, an anticancer drug for treatment of chronic lymphocytic leukemia (CLL). While promising for cancer treatment, this small molecule drug crosses the blood-brain barrier causing significant side-effects in patients. The DNA nanoparticle encapsulates BKM120 in high efficiency, and is unparalleled in its monodispersity, ease of synthesis and stability in different biological media and in serum. These DNA nanostructures demonstrate efficient uptake in human cervical cancer (HeLa) cells, and increased internalization of cargo. *In vitro* studies show that BKM120-loaded nanoparticles promote apoptosis in primary patient CLL lymphocytes, and act as sensitizers of other antitumor drugs, without causing non-specific inflammation. Evaluation of this drug delivery system *in vivo* shows long circulation times up to 24 hours, full body distribution, accumulation at tumor sites and minimal leakage through the blood-brain barrier. These results demonstrate the great potential of DNA nanoparticles as a general platform for chemotherapeutic drug delivery.

2.2 Introduction

Targeted action of small molecule drugs remains a challenge in medicine. This holds true for antitumor chemotherapeutic drugs, where much of their success has been hampered by off-target side-effects, poor pharmacokinetics and systemic toxicity.[1] One effective approach to tackle this problem is the application of drug delivery systems that would protect the cargo along the administration route and direct it to its target site.[2] Several delivery systems are currently being explored which include dendrimers,[3] liposomes,[4] polymeric nanoparticles,[5] micelles,[6] protein nanoparticles,[7] viral nanoparticles,[8] inorganic nanoparticles[9] and carbon nanotubes.[10] However, many of them suffer from major limitations such as toxicity, rapid clearance, complicated synthesis and particle heterogeneity.[11] In particular, nanostructure size and shape has been demonstrated to play an important role in their biodistribution, circulation half-life, cellular targeting, efficacy and immune response.[12-15] With most current drug delivery platforms suffering from structural polydispersity, the generation of monodisperse nanocarriers with well-defined structures will be essential for their application in drug delivery.

Polymers are some of the most commonly used material for developing nanoparticle-based drug carriers.[16] In particular, amphiphilic block copolymers that contain a water-soluble block, and a hydrophobic block, have been extensively used as building blocks for chemotherapeutic drug delivery. These molecules microphase-separate into micelles that contain a hydrophobic core which can accommodate lipophilic drug molecules and alter their kinetics both *in vitro* and *in vivo*.[17-18] In recent years, a new class of amphiphilic block copolymers has also emerged which contains a hydrophobic synthetic polymer attached to a hydrophilic DNA segment, called DNA-polymer hybrids.[19] These molecules can self-assemble into a wide-range of morphologies,[20] including spherical micellar particles that expose a hydrophilic DNA shell and a hydrophobic core.[21-22] A particularly successful example of such assemblies are spherical nucleic acids (SNAs).[23] These structures are composed of a gold nanoparticle core and a corona of tightly packed DNA strands. SNAs have shown efficient cellular penetration and gene silencing ability both *in vitro* and *in vivo*.[24-26]

Recently, Sleiman and coworkers reported a highly efficient and versatile method to generate DNA-polymer conjugates *via* solid-phase synthesis.[27] Unlike conventional synthetic polymer chemistry, this method yields DNA-polymer conjugates that are fully monodisperse and sequence-defined. This class of material self-assembles spontaneously to generate highly monodisperse spherical micellar DNA nanoparticles in aqueous solution. Several examples in recent years have emerged demonstrating the suitability of DNA nanostructures in mimicking biological systems,[28-29] construction of nanoelectronics[30] and nanophotonics,[31] and delivery of cancer therapeutics.[32] Compared to DNA nanostructures, such as DNA origami,[33] which require a large number of unique DNA strands to generate the designed structure,[32] limiting their use in large-scale applications, micellar DNA nanoparticles are composed of only a single DNA-polymer conjugate strand. This type of hybrid strand also offers advantages over other block copolymers in that the DNA portion can be highly functional and programmable in the final structure.[34] Additionally, the poly-phosphodiester units in both the oligonucleotide and hydrophobic portions of the DNA-polymer strands are biocompatible and biodegradable making them suitable for biological applications.[35-36] Particles of self-assembled DNA-polymer conjugates expose a ssDNA corona, and have been used in ligand targeting,[22, 37-38] delivery of antisense oligonucleotides,[39-41] DNA detection,[42] formation of higher order assemblies,[43-44] and templating organic reactions.[45-46] In particular, these DNA particles have shown great potential in cancer therapy.[22, 37, 47] However, the exploration of these structures for cancer therapy has only been limited to *in vitro* cell studies. Our interest also focuses on cancer therapy, specifically, the development of a DNA nanoparticle delivery system for BKM120, an anticancer drug towards the treatment of Chronic Lymphocytic Leukemia (CLL).

CLL remains the most common type of leukemia with an incidence rate of approx. 4/100,000 people in the United States.[48] Current treatments of CLL include chemotherapeutic agents such as alkylating agents (chlorambucil, cyclophosphamide and bendamustine), purine analogs (fludarabine) and immunotherapeutics (Rituximab, Alemtuzumab).[49-50] The current gold standard for treatment is through chemoimmunotherapy; a combination of fludarabine, cyclophosphamide and rituximab (FCR).[51-54] Unfortunately, none of these treatments results in curative therapy providing strong justification for investigating new therapeutic approaches for CLL. The phosphoinositide 3-kinase (PI3K) pathway has been shown to be a critical component of CLL survival and proliferation.[55-57] The expression of PI3K triggers downstream cellular events that inhibit cell death by inactivating pro-apoptotic proteins.[58-61] Additionally, multidrug resistance (MDR) often accompanies elevated PI3K activity which renders a survival signal to withstand anticancer drugs and irradiation.[62-63] Activated PI3K is also associated with a robust DNA damage repair further protecting CLL against chemotherapeutic agents.[64] This makes the selective inhibition of PI3K a promising approach for the treatment of CLL and a focus of many efforts to develop novel inhibitors targeting this pathway.

Buparlisib (codenamed BKM120) is one such example of a pyrimidine-derived selective pan class I PI3K inhibitor.[65] This molecule has shown high selectivity and potency against class I PI3Ks.[66] BKM120 has demonstrated high cytotoxicity in B-chronic lymphocytic leukemia cells *in* *vitro*, and significant antitumor activity in tumor xenograft models.[66-67] Furthermore, this small molecule selectively inhibits both wild type and mutant PI3K, halting cell proliferation and the DNA repair mechanism. Due to these properties BKM120 has also been used in synergy with anticancer drugs or irradiation for effective treatment of resistant cancer types.[62-63, 68] Currently, this drug is under clinical investigation in advanced solid tumor and CLL patients.[69] However, BKM120 can cross the blood-brain barrier and inhibit PI3K in the central nervous system (CNS), inducing anxiety, low serotonin levels, schizophrenia, and hindering its success for translation into the market.[70] Hence, a strategy to effectively deliver BKM120 to its intended biological target without deleterious side-effects in the CNS would be a major goal for therapy with this small molecule drug.

This chapter reports the development of a DNA nanoparticle platform for the delivery of BKM120. The drug-loaded structures are unique in their monodispersity, can be readily prepared and are stable in different biological media and in serum. These particles show increased cellular uptake of these structures in HeLa cells, and the internalization of their cargo. Moreover, BKM120-loaded DNA particles promote apoptosis in primary patient CLL lymphocytes and induce cell death when co-administered with Doxorubicin in HeLa cells, without eliciting inflammation. Evaluation of this drug delivery system *in vivo* shows long circulation times up to 24 hours, full body distribution, high accumulation at tumor sites and minimal leakage through the blood-brain barrier. These results demonstrate the great potential of these delivery vehicles as a general platform for chemotherapeutic drug delivery. Earlier reports have shown that the DNA component of these structures is able to silence gene expression to a greater extent than DNA antisense structures alone, highlighting the promise of these DNA nanoparticles as combination small molecule and oligonucleotide therapeutics.[39]

2.3 Results and Discussion

2.3.1 Synthesis of DNA nanoparticles

In order to construct a scalable and highly monodisperse drug delivery system, we generated a single type of DNA-polymer conjugates that self-assemble in aqueous buffer to form micellar DNA particles. These conjugates consist of a 19-mer DNA of mixed sequence (14 mixed nucleotides plus 5 thymine nucleotide spacer) attached to 12 dodecane (hexaethylene, HE) units (**HE_{12}-DNA** conjugate) (Figure 2.1). HE_{12} units were appended to DNA by automated solid-phase synthesis using phosphoramidite chemistry.[27] This approach offers monodisperse DNA-polymer conjugates in high yields and provides control over the length and sequence of the monomer units in the final structure. Our group has showed that HE_{12}-DNA conjugates self-assemble into highly monodisperse spherical nucleic acid particles (**HE_{12}-SNAs**) in aqueous media containing divalent cations. These structures consist of an exterior DNA corona, and a hydrophobic HE_{12} core which provides a favourable environment for the entrapment of hydrophobic guest molecules. We also showed the encapsulation of a dye molecule, Nile Red, in the hydrophobic core of DNA nanoparticles.[27] In this current study, we sought to test the encapsulation of a small molecule protein kinase inhibitor, BKM120. We were interested in BKM120 because 1) despite its high potency, it suffers from deleterious side-effects in the CNS of patients. 2) The drug dimensions are compatible with the core size of the DNA nanoparticle system and 3) BKM120 exhibits an aqueous solubility of <1 mg/ml, which makes it a suitable guest for our system.

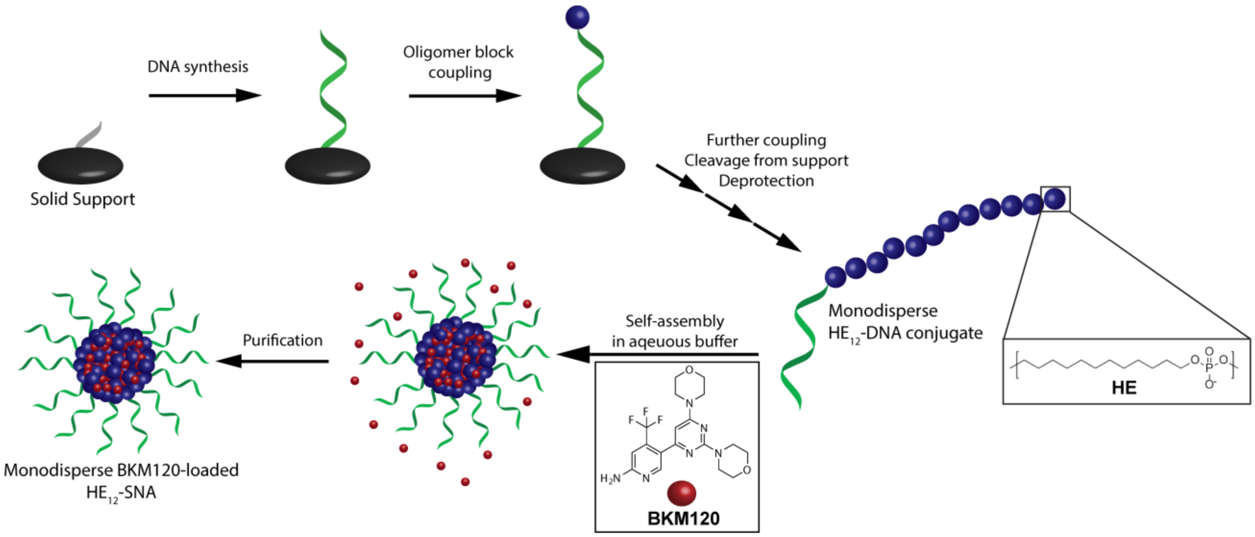

Figure 2.1 – Schematic representation of the synthesis of DNA-polymer conjugates and BKM120 encapsulation method. Phosphoramidite monomers are attached to the 5’ end of the controlled pore glass (CPG) in a step-wise and sequence-controlled fashion. The 19-mer DNA strand is first built from the support, followed by 12 dodecane monomer additions (HE_{12}) yielding monodisperse HE_{12}-DNA

conjugates. Self-assembly of the polymer-DNA conjugates in the presence of BKM120 and subsequent purification results in nearly monodisperse BKM120-loaded HE_{12}-SNAs.

2.3.2 Evaluation of HE_{12}-SNAs as BKM120 delivery vehicles

To prepare BKM120-loaded HE_{12}-SNAs, a solution of BKM120 in ethanol was allowed to evaporate forming a thin-film, which was then re-suspended into a solution of HE_{12}-DNA conjugates in water, followed by the addition of assembly buffer and overnight thermal annealing (95 °C – 4 °C over 4 hours). Thermal annealing was shown to yield less size-variability compared to overnight shaking at room temperature. Following the encapsulation process, the products were purified by size-exclusion chromatography and analyzed by reverse-phase HPLC (RP-HPLC) (Figure 2.2). The success of the purification method was critical to ensure complete removal of free-drug in solution. This was important for accurate determination of the nanoparticle drug-loading capacity and for further biological studies.

Data from RP-HPLC confirmed the encapsulation of BKM120 in HE_{12}-SNAs in comparison to ssDNA and buffer controls. Traces were obtained at two different wavelengths: one selective for DNA at 260 nm, and a BKM120-optimal wavelength at 320 nm. The co-elution of the DNA and BKM120 was only observed in HE_{12}-SNA solutions, indicating the association of the drug with the structure. In the case of ssDNA, only a DNA peak was observed at 260 nm, reflecting the efficiency of the purification method at removing free drug in solution. The drug loading capacity of DNA nanoparticles was calculated from RP-HPLC data and separately confirmed by UV-vis spectroscopy (Figure 2.2b, *Experimental Figure 2.23*). For HE_{12}-SNAs, the loading capacity was approximately 29% w/w, where ~9 molecules of BKM120 were encapsulated per DNA-polymer conjugate. The aqueous solubility of BKM120 in the HE_{12}-SNAs was enhanced to 24.4 μg/ml, compared to <1μg/ml in water. RP-HPLC was also used to calculate the recovered yield following purification. In general, ~65% of the amount of DNA-polymer conjugates was retained following purification (*Experimental Figure 2.23*).

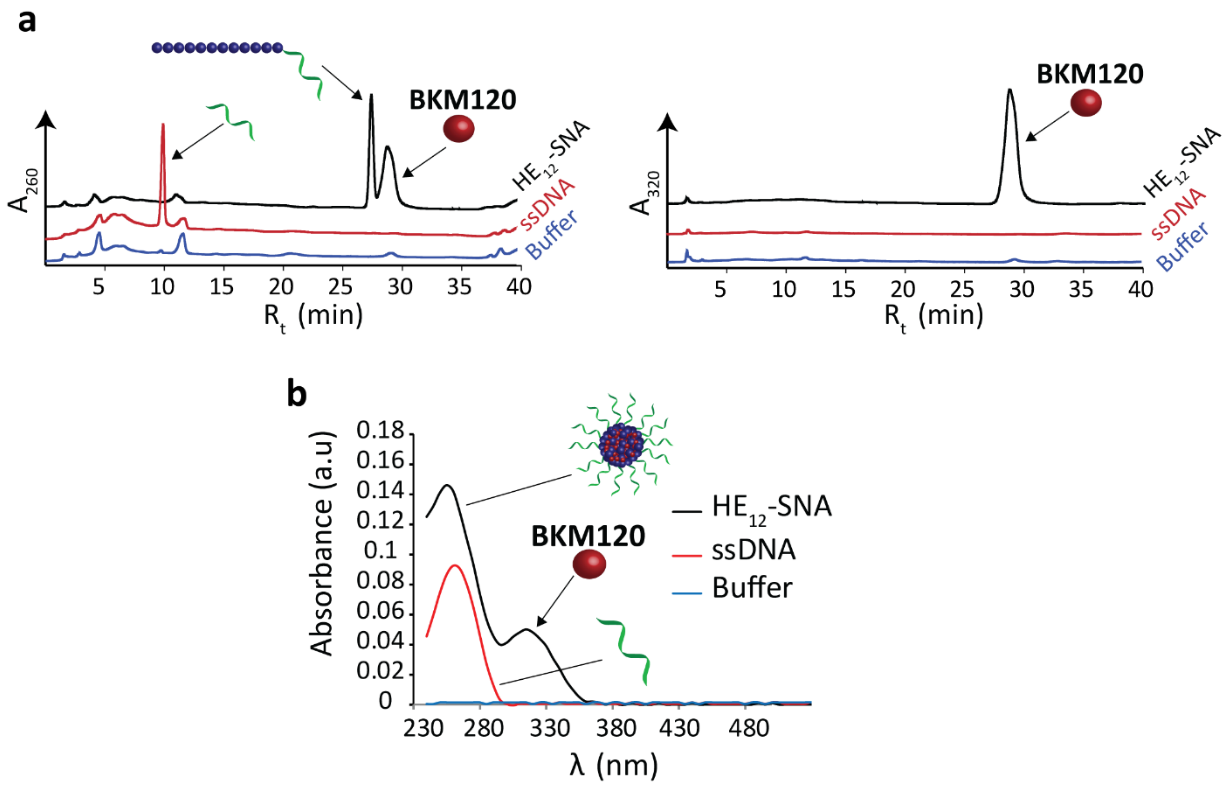

Figure 2.2 - Evaluation of BKM120 encapsulation in HE_{12}-SNAs. a) Reversed phase HPLC analysis of HE_{12}-SNAs (black), ssDNA control (red) and buffer control (blue) following drug purification. Detection at absorbance wavelength 260 nm (left panel) and drug-specific 320 nm (right panel). The presence of a BKM120 peak solely in HE_{12}-SNA samples suggests drug encapsulation. b) UV-Vis measurements of BKM120-incubated HE_{12}-SNAs (black), ssDNA control (red) and buffer control (blue) following purification. Drug encapsulation and loading capacity were determined by RP-HPLC and separately confirmed by UV-Vis measurements. The presence of a diagnostic drug peak at 320 nm in the HE_{12}-DNA nanoparticle sample indicates drug encapsulation.

The storage shelf-life of drug-loaded structures was then characterized when stored at both room temperature and 4 °C (Figure 2.3, *Experimental Section 2.5.6*). Structures were stable for over 4 weeks at both temperature conditions, with no signs of disintegration or degradation. Shelf-life stability is an important characteristic for successful drug formulations to ensure that the structural integrity of the drug is maintained when stored prior to administration – which is usually the case for many pharmaceutical candidates.

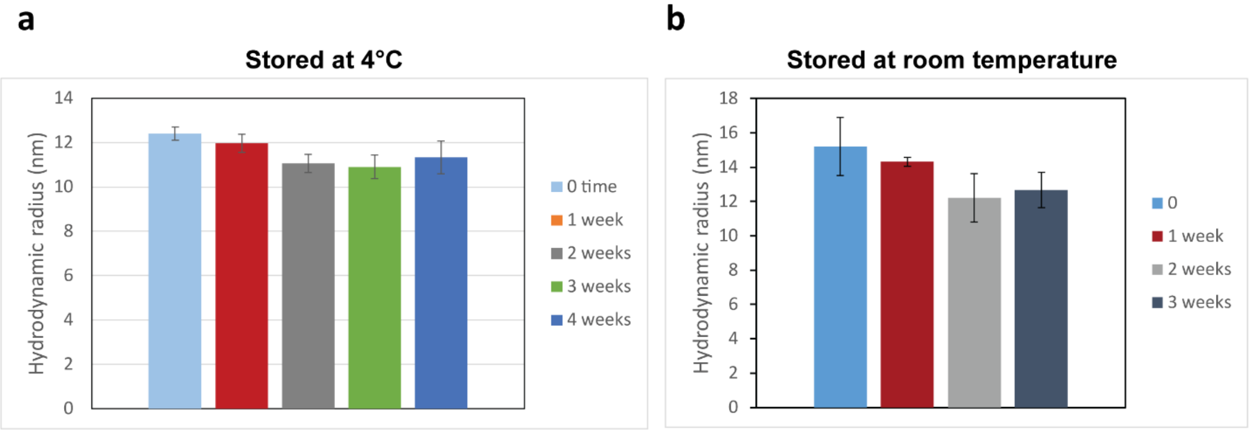

Figure 2.3 - Shelf-life of BKM120-loaded DNA nanoparticles. Dynamic light scattering (DLS) histograms showing the hydrodynamic radius of BKM120-loaded particles over time when stored at a) 4 °C and b) room temperature.

Having confirmed BKM120 encapsulation, we then studied the *in vitro* release kinetics of BKM120 in HE_{12}-SNAs (Figure 2.4a, *Experimental Section 2.5.5.3*). BKM120 release was evaluated by monitoring the decrease in concentration of the drug from a solution of loaded structures dialyzed at room temperature over 24 hours against the assembly buffer 1x TAMg which contains divalent magnesium cations. It was found that HE_{12}-SNAs release BKM120 at a slow and sustained rate with ~40% of the drug retained after 24 hours (Figure 2.4a). The critical micellar concentration (CMC), above which HE_{12}-DNA conjugates aggregate into HE_{12}-SNAs was also studied. It was found that HE_{12}-DNA conjugates aggregate with an associated CMC of 0.5 µM ± 0.2 µM in the presence of 12.5 mM Mg^{2+} (Figure 2.4b, *Experimental Section 2.5.7*). These values are within range of high molecular weight polymeric micelles in clinical trials with CMC values between 0.1-1 µM, and significantly less than lower molecular weight surfactants with CMC values of 10^{-3} to 10^{-4} M.[71-73] The CMC of HE_{12}-DNA could be further reduced through covalent cross-linking.

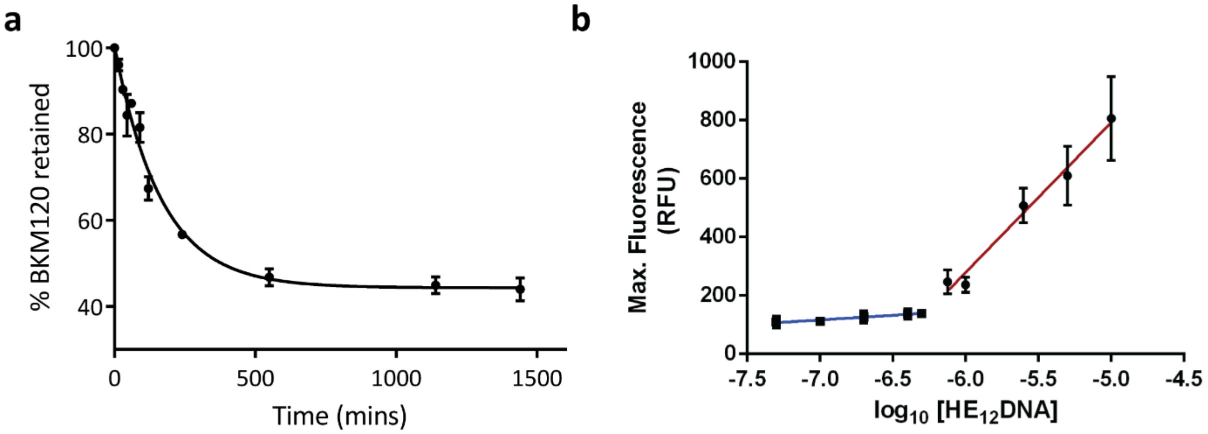

Figure 2.4 – Drug release and self-assembly parameters of SNAs. a) *In vitro* release of BKM120 loaded into HE_{12}-SNAs studied by a dialysis method over 1 day at room temperature in 1x TAMg, measured in triplicate. Error bars represent the standard deviation of measurements. b) Calculation of the critical micelle concentrations of SNAs. Plot of $\log_{10}$ [HE_{12}-DNA] against maximal fluorescence intensity for HE_{12}-DNA in the presence of 100 µM Nile Red (*see Experimental Section 2.5.7)*. The CMC was calculated from the intersection of the two linear fits shown on the graph. The measurements were performed in triplicates.

We then proceeded to characterize the BKM120-loaded products. The sizes of the nanoparticles were studied by agarose gel electrophoresis (AGE), dynamic light scattering (DLS), atomic force microscopy (AFM) and transmission electron microscopy (TEM) (Figure 2.5). Data from AGE revealed the maintained structural integrity of BKM120-loaded particles with no observed side products (Figure 2.5a). DLS analysis revealed a highly monodisperse population of drug-loaded structures in solution with a hydrodynamic radius of 11.8 ± 0.4 nm (Figure 2.5b). AFM and TEM images demonstrated that BKM-120 loaded particles were well-dispersed on surface, with calculated dry-state diameter of 28 ± 4 nm and 21 ± 3 nm, respectively (Figure 2.5c-d, *Experimental Sections 2.5.8.3 & 2.5.8.4*). The structures also appeared to retain high level of monodispersity, despite slightly widened features. The obtained dimensions are in agreement with solution measurements by DLS. The slightly widened morphology could be explained by the deposition of these structures on the surface and drying effects. The drug-loaded nanoparticles seemed to lose their spherical shape upon deposition confirmed by the lower height (8 nm) and slightly widened diameter as calculated by AFM.

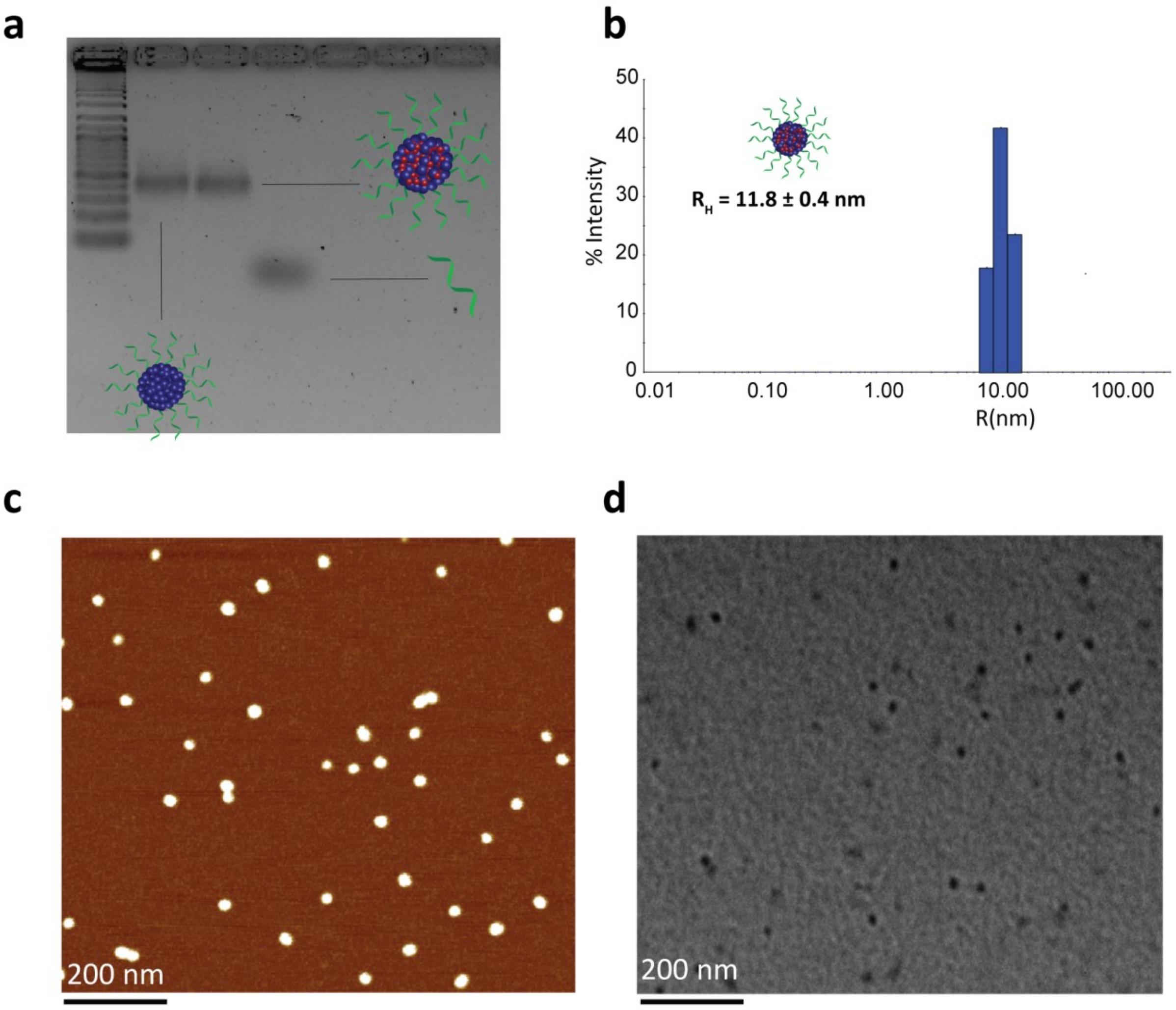

Figure 2.5 - Structural characterization of BKM120-loaded HE$_{12}$-SNAs. a) Agarose gel electrophoresis (AGE) analysis of drug-loaded nanoparticles showing intact structures with no observed side products. b) Dynamic light scattering (DLS) data showing a highly monodisperse population of drug-loaded nanoparticles in solution. c) Atomic force microscopy (AFM) image showing a spherical nearly monodisperse population of drug-loaded products on surface. d) Transmission electron microscopy (TEM) image of drug-loaded products reflecting highly monodisperse structures. Scale bars = 200 nm.

2.3.3 Stability of HE_{12}-SNAs

DNA nanostructures such as DNA origami and 3-dimensional nanoarchitectures purely composed of DNA, are typically assembled in buffers containing moderate concentrations of divalent metal cations (~5-20 mM) in order to mask the electrostatic repulsion between DNA strands.[74-76] Deviations from this window of buffer conditions can have devastating effects on the structures, causing shape distortion, aggregation or total collapse of structure. This limits the use of DNA nanostructures for biological applications. In our case, the assembly of HE_{12}-SNAs was also shown to be dependent on the presence of divalent metal cations, however, the main driving force of assembly is hydrophobic interactions rather than Watson-Crick base-pairing. With this in mind, we sought to test whether our system can withstand variations in ionic concentrations and preserve structural identity in physiologically relevant environments. Evaluation of the nanoparticle stability in different buffer conditions was carried out by DLS measurements (Figure 2.6). We tested concentration variations of two groups of candidates; divalent metal ions (Mg^{2+} and Ca^{2+}) in Tris buffer (Figure 2.6a-b, *Experimental Figures 2.31 & 2.32*) and different titrations of Dulbecco's Phosphate Buffered Saline (DPBS with Mg^{2+} and Ca^{2+}), a buffer used in cell culture (Figure 2.6c, *Experimental Figure 2.33*). Data from DLS showed that HE_{12}-SNAs could withstand large variations in ionic concentrations. At high ionic concentrations (18.75 mM Mg^{2+} and 2x DPBS), no structural aggregation was observed. Additionally, at Mg^{2+} concentrations as low as 0.25 mM (in 0.5x DPBS), the structures maintained their natural morphology with no observed disassembly. The structures were also compatible with a calcium-containing Tris buffer at concentrations similar to physiological plasma concentrations (~1.2-1.5 mM).[77] Only upon total depletion of divalent cations did the structures disassemble into monomeric HE_{12}-DNA units (*Experimental Figure 2.34*). The enhanced stability in different buffer conditions can be partly attributed to hydrophobic interactions providing an additional cohesive force to preserve structural morphology.

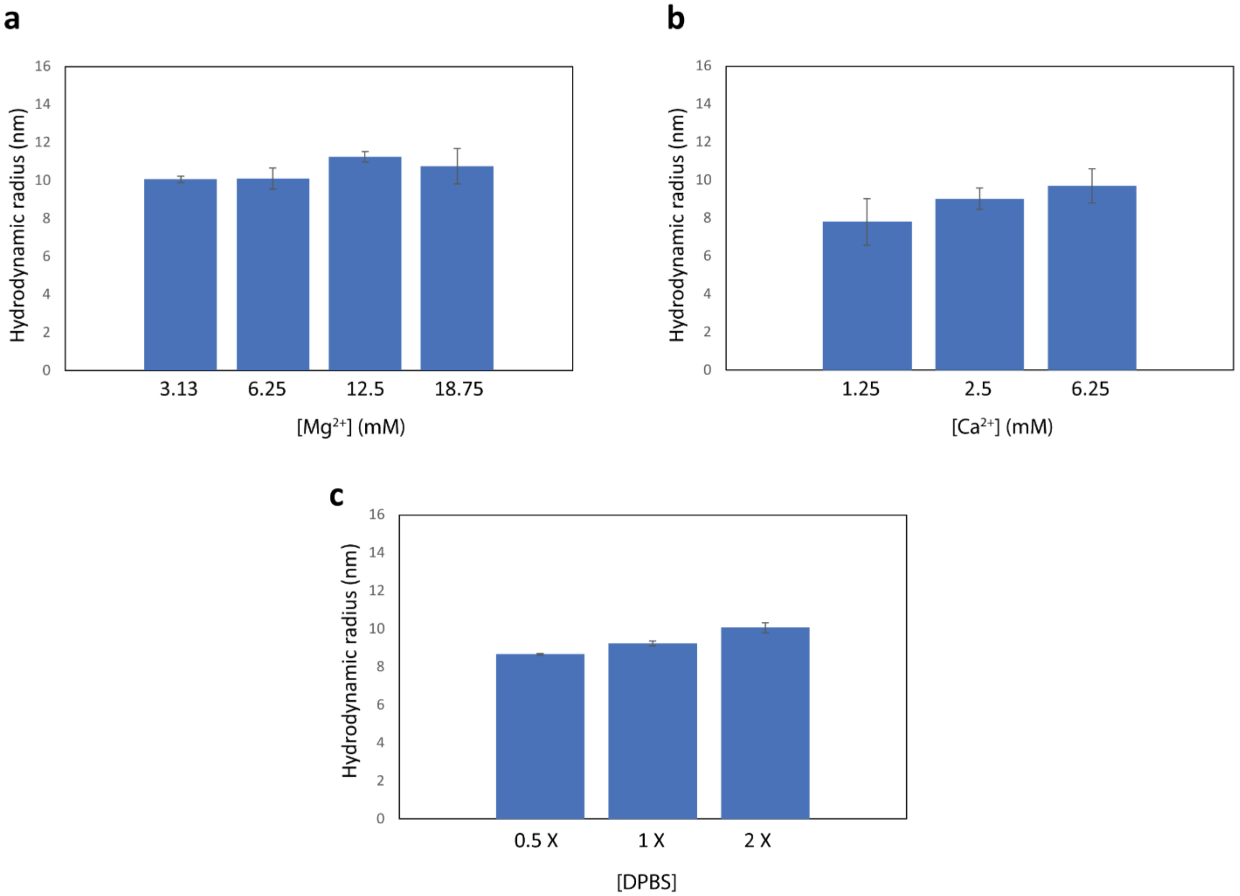

Figure 2.6 – Stability of HE$_{12}$-SNAs in biological relevant conditions. a) DLS histograms displaying the hydrodynamic radius of DNA nanoparticles under variations in a) magnesium concentrations in Tris buffer, b) calcium in Tris buffer and c) with varying amounts of DBPS, a buffer used in cell culture. DLS analysis shows the maintained structural integrity of HE$_{12}$-DNA particles under large variations of ionic conditions. Disassembly of the structure was only observed upon full ionic depletion.

We then proceeded to test the nuclease stability of our structures in 10% fetal bovine serum (FBS) solution at 37°C (Figure 2.7, *Experimental Section 2.5.10*). This was important because rapid nuclease degradation is a major challenge for DNA nanostructures as they are translated to the *in vitro* culture environment.[75] We measured a half-life of 2.2 hrs for HE$_{12}$-SNAs, which was 4.6-fold higher than the results obtained for ssDNA (28 mins). This demonstrated the enhanced stability of our system against nuclease degradation and could be due to the dense packing of DNA creating a steric barrier.

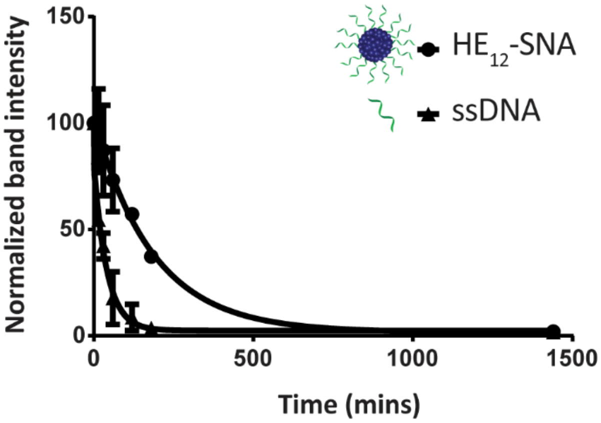

Figure 2.7 – Serum stability of HE$_{12}$-SNAs in biological conditions. HE$_{12}$-SNAs have a measured half-life of 2.2 hrs which is 4.6 times higher than that of ssDNA. Error bars represent the standard deviation of measurements.

2.3.4 Cellular uptake of non-transfected HE$_{12}$-SNAs

The *in vitro* cellular uptake and internalization of HE$_{12}$-SNAs were studied by confocal fluorescence microscopy. As a first step, we generated Cy3-labeled DNA nanoparticles (Figure 2.8a, *Experimental Figure 2.36*). This was achieved by mixing Cy3-HE$_{12}$-DNA (where Cy3 was attached to the HE$_{12}$ polymer at the opposite end of the DNA) and unlabeled HE$_{12}$-DNA conjugates in 25:75 molar ratios, followed by thermal annealing, 95°C – 4°C over 4 hours. (Figure 2.8a). This approach yielded highly monodisperse dye-labeled nanoparticles with the dye molecules likely embedded in the core. This was important as surface projection of a lipophilic dye molecule could alter the uptake profile of the nanoparticles through cell membranes. Following a 24-hour incubation in HeLa cells, fluorescence data indicated the high cellular uptake of Cy3-DNA nanoparticles and localization in the cytoplasm in the perinuclear region (Figure 2.8b). Several intense foci were observed indicating the high efficiency of uptake.

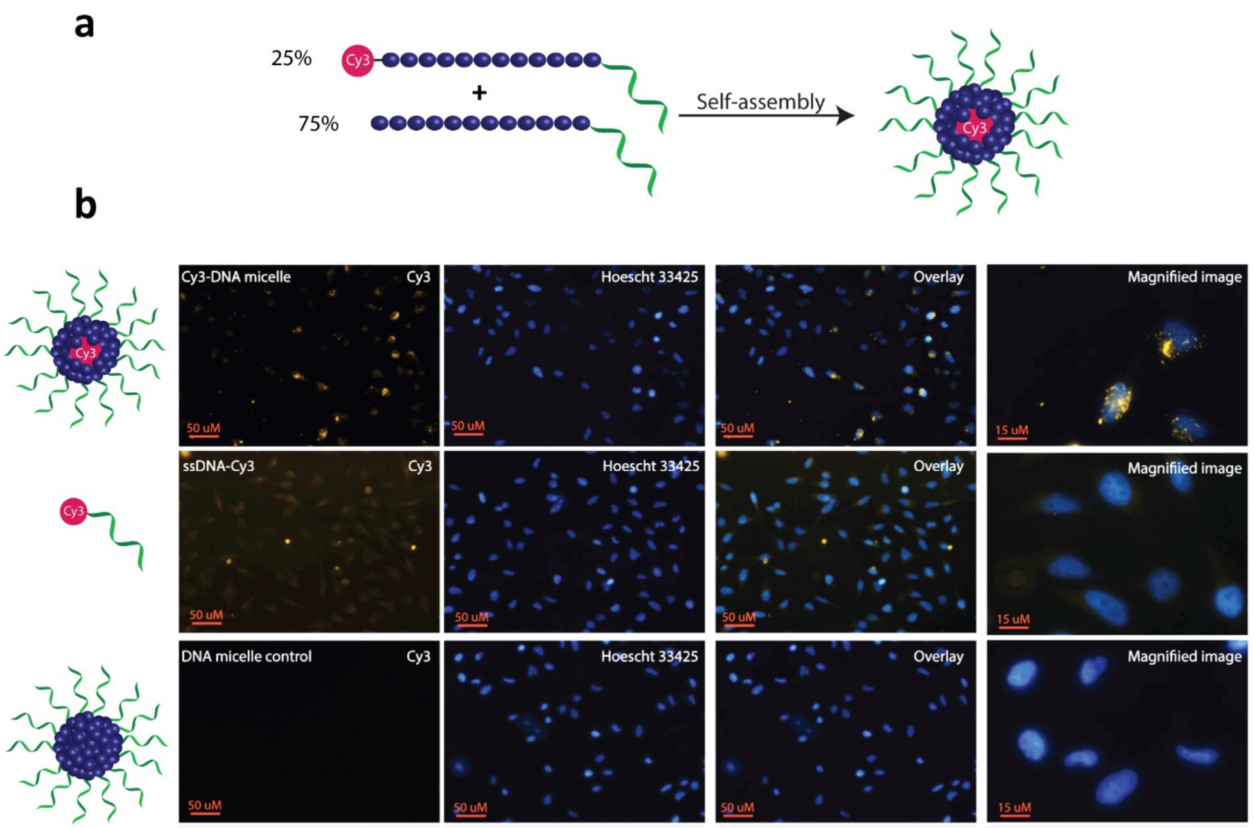

Figure 2.8 – Cellular uptake and localization of HE$_{12}$-SNAs. a) Preparation of Cy3-labeled nanoparticles. Cy3-HE$_{12}$-DNA and HE$_{12}$-DNA were mixed in 25:75 molar ratios to generate nearly monodisperse Cy3-labeled HE$_{12}$-DNA nanoparticles. b) Confocal microscopy images demonstrating the cellular uptake of Cy3-labeled particles in HeLa cells after a 24-hour incubation.

We were then interested in studying the internalization of encapsulated cargo. Knowing that BKM120 has poor fluorescence properties, we decided to monitor the uptake of a fluorescent dye, Nile Red, encapsulated in our DNA nanostructures (Figure 2.9a, *Experimental section 2.5.12.1*). The encapsulation of Nile Red further demonstrates the versatility of this delivery system for accommodating different guest molecules, highlighting its potential application as a general drug delivery platform. HeLa (adenocarcinoma) cells were incubated with Nile Red loaded-nanoparticles (unloaded Nile Red was purified), Nile Red alone or DNA nanoparticle control at 37 °C. Flow cytometry was used to quantify the amount of Nile Red uptake by HeLa cells (Figure 2.9b). After 12 hours of incubation and several washing steps, analysis of the flow cytometry data revealed significantly higher intracellular fluorescence of Nile Red when delivered by HE$_{12}$-DNA nanoparticles compared to low non-specific internalization of Nile Red control (Figure 2.9b-c, *Experimental Figure 2.38*). The higher uptake of Nile Red was also confirmed by confocal fluorescence microscopy, where the dye was mostly observed in the cytoplasm in the perinuclear region, confirming high uptake efficiency (*Experimental section 2.5.12.3*). Taken together, these experiments suggest that the increase in Nile Red uptake is due to its encapsulation and internalization by HE$_{12}$-DNA nanoparticles.

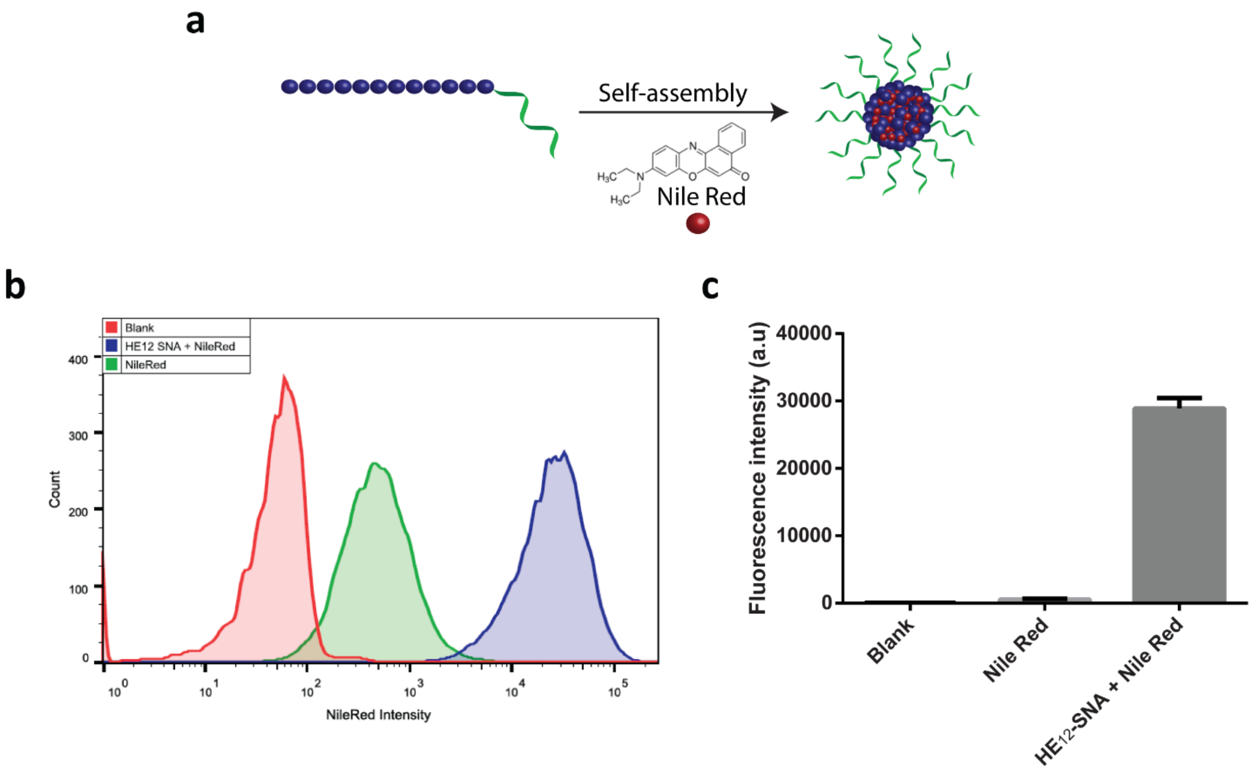

Figure 2.9 – Cellular uptake of encapsulated cargo. a) Preparation of Nile Red-loaded DNA nanoparticles. d) Flow cytometry measurements showing the increased uptake of Nile Red when delivered by HE$_{12}$-SNAs. All samples were incubated for 12 hours. [Nile Red] = 375 nM in cell culture media. Nile Red images were acquired using exc. 516 nm and YellowG_670/30 filter. e) Quantification of Nile Red intensity measured by flow cytometry. All measurements were performed in triplicates, and the error bars represent the standard deviation of measurements.

2.3.5 *In vitro* efficacy of BKM120-loaded HE_{12}-SNAs

Based on the cellular uptake and dye internalization studies in HeLa cells, we were interested if the higher uptake of our nanostructures would correlate to increased therapeutic activity of the drug-loaded constructs. The *in vitro* efficacy of BKM120-loaded HE_{12}-SNAs was measured against human cervical cancer (HeLa) cells. Efficacy was evaluated by comparing a dose-dependent administration of BKM120 in DNA nanoparticles with naked BKM120 and DNA particles as controls (Figure 2.10). In the tested concentration range, HE_{12}-DNA particles loaded with BKM120 showed low cellular death in HeLa cells.

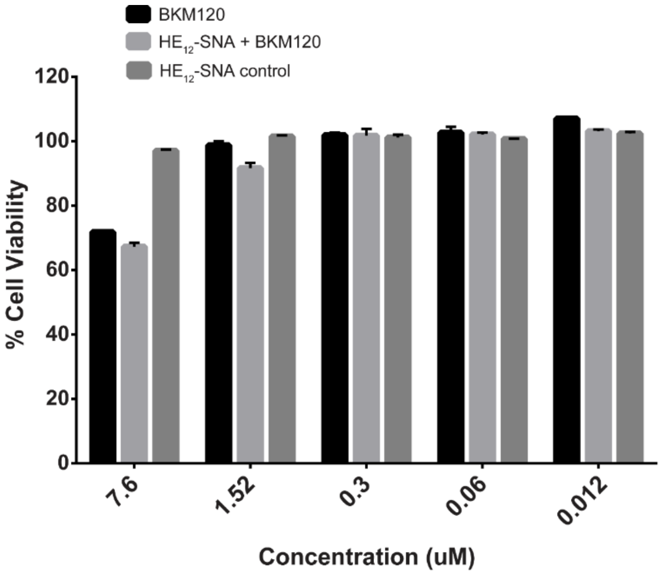

Figure 2.10 – *In vitro* efficacy of BKM120-loaded SNAs in Hela cells. Dose-dependent administration of BKM120 or BKM120-loaded particles showed low cellular death in HeLa cells.

Based on these results, we then tested the synergistic effect of loaded BKM120 in combination with doxorubicin (Dox). In clinical studies, BKM120 has been used in synergy with both anticancer drugs and irradiation for the treatment of drug/radiation resistant cancer types.[62-63] Our platform acting as a sensitizer in HeLa cells also highlights the versatility of our system as a general drug delivery system for anticancer drugs. For this study, HeLa cells were initially sensitized with three different concentrations of BKM120-loaded particles prior to incubation with various Dox dosages (Figure 2.11a-c). Interestingly, as illustrated in Figure 2.11, the efficacy of

Dox was enhanced upon co-administration with BKM120-loaded particles in a dose-dependent manner. The effect was most pronounced at higher Dox concentrations (Figure 2.11c). The reduced differences in efficacy between loaded BKM120 versus its un-encapsulated form, is in part due to the lipophilic nature of the drug which can diffuse passively through cell membranes and cause cell death. However, we anticipate that this nanocarrier platform could provide advantages in the delivery of BKM120 and other chemotherapeutic drugs by altering their *in vivo* delivery profile. Additionally, the capability of functionalizing HE$_{12}$-SNAs with targeting ligands could also limit some of the drug's manifested side-effects and provide a targeted delivery regimen in tumors.

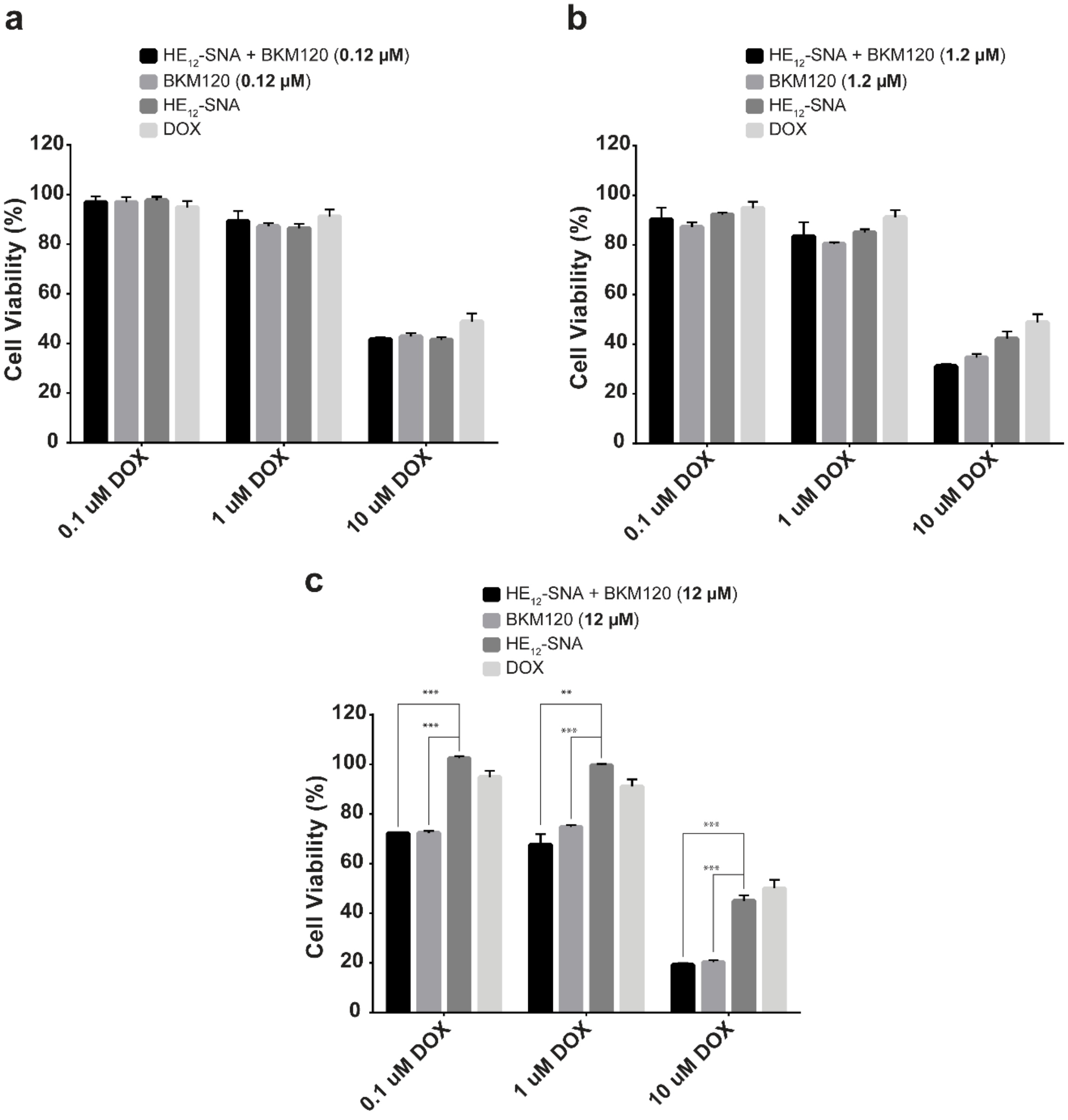

Figure 2.11 – *In vitro* efficacy of BKM120-loaded SNAs in synergy with doxorubicin in Hela cells. Efficacy of BKM120-loaded nanoparticles when administered at concentrations a) 0.12 μM b) 1.2 μM c) 12 μM prior to doxorubicin treatment, measured over 24 hours. *** corresponds to $p<0.0001$ and ** to $p<0.001$. Error bars represent the standard deviation of measurements.

In vitro studies on BKM120 have shown this drug to induce cell death in B-cell Chronic Lymphocytic Leukemia (B-CLL) cells and promote apoptosis.[63] Thus, we asked whether BKM120-loaded particles can promote cell apoptosis. To address this question, we investigated the induction of apoptosis through Annexin V/propidium iodide (PI) staining assay in primary patient CLL lymphocytes (Figure 2.12a). Earlier studies have shown that stromal cells induce drug resistance and promote cell survival through secretion of chemokines and cell-cell interaction.[78] Additionally, the bone marrow microenvironment has shown to prevent apoptosis in primary CLL lymphocytes by modulating the PI3K/Akt pathway.[79] As expected, the stromal microenvironment model (BSM2 stromal cells) protected CLL lymphocytes from spontaneous apoptosis as seen with the untreated controls (Figure 2.12a). We found that BKM120-loaded structures promoted apoptosis in primary BMS2 cocultured CLL lymphocytes from 3 different patients, 24 hours after treatment. To further confirm these findings, we monitored the cleavage of caspase-3, a catalytic step in the apoptotic pathway. In accordance with the Annexin V/PI analysis, BKM120-loaded particles induced caspase-3 activity in CLL lymphocytes; both in the presence and absence of BMS2, confirming their enhanced activity in complex patient cellular environments (Figure 2.12b, *Experimental Figure 2.40*).

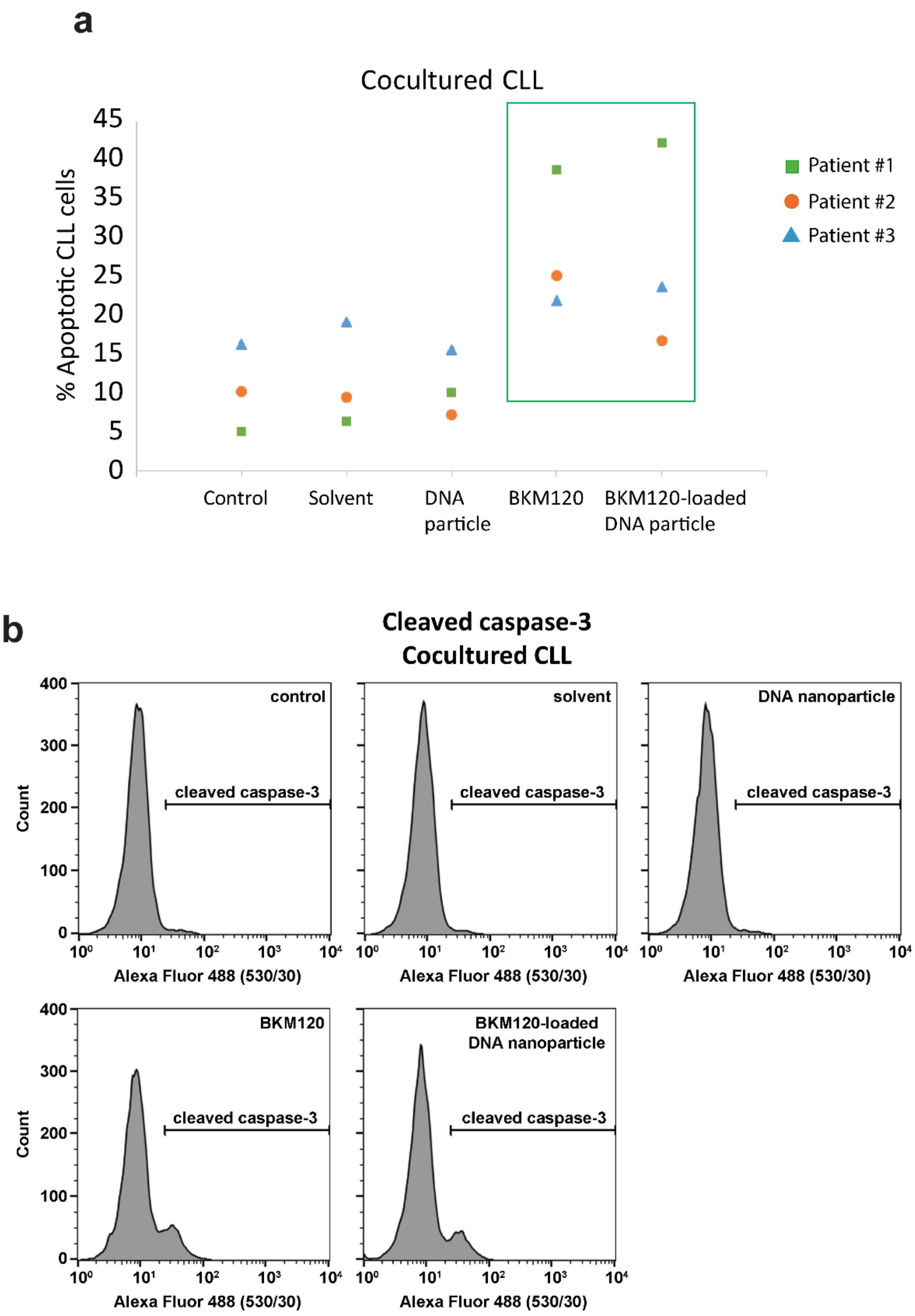

Figure 2.12 – Apoptosis studies of BKM120-loaded SNAs in CLL primary patient cells. a) Annexin/PI staining and b) cleaved caspase-3 assay showing the potency of BKM120-loaded particles at inducing apoptosis in primary patient B-CLL lymphocytes in the presence of the BMS2 stromal cells support (cocultured CLL), analyzed by flow cytometry.

To evaluate the potential immunogenicity of this delivery system, we investigated the effect of HE_{12}-SNAs on TNF-alpha induction (Figure 2.13). TNF-alpha is a signalling protein involved in systemic inflammation.[80] Higher levels of this protein indicate an elicited immune response. We tested our system in comparison to lipopolysaccharide (LPS) and a synthetic dsRNA (Poly IC) which have been reported to induce the expression TNF-alpha.[81-82] It has also been reported that the time course of TNF-alpha induction shows a rise and decline profile with peak elevation at 2-6 hours post exposure.[83-84] As illustrated in Figure 2.13, after 5 hours of incubation HE_{12}-SNAs exhibited no systemic inflammation with very low levels of TNF-alpha induction compared to LPS and PolyIC. As expected, the effect becomes less pronounced at the 12 and 24-hour mark. This result supports the non-immunogenic nature of HE_{12}-SNAs.

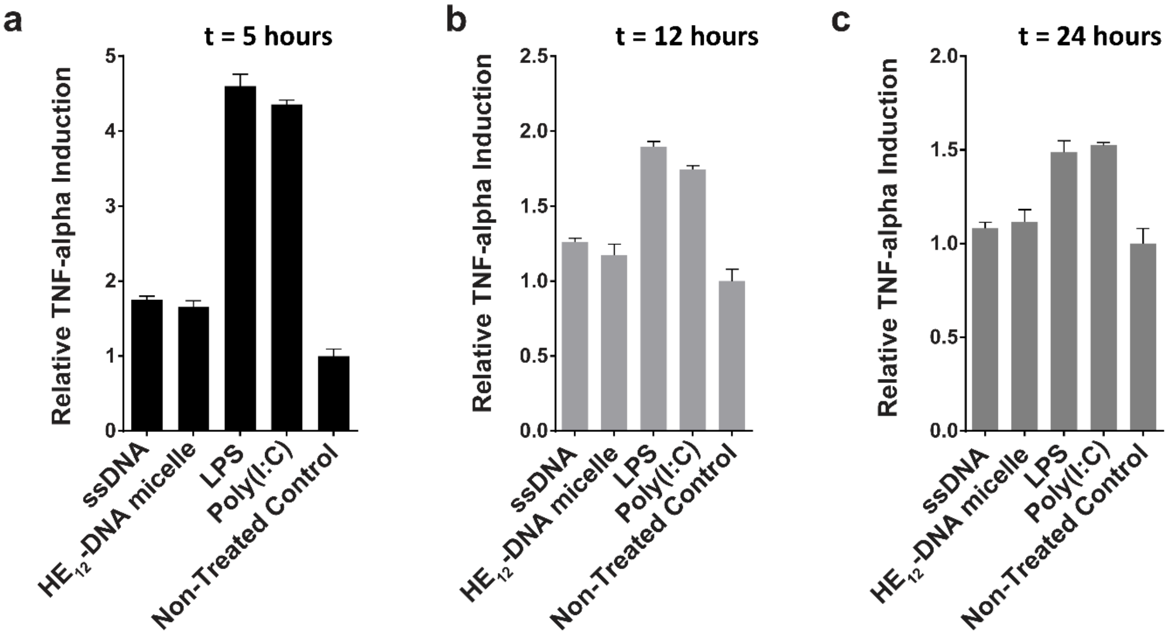

Figure 2.13 – Evaluating the immunogenicity of HE_{12}-SNAs. Time-dependent effect of HE_{12}-SNAs on TNF-alpha induction in RAW264.7 mouse monocytes, measured at a) 5 hours, b) 12 hours and c) 24 hours after treatment.

2.3.6 *In vivo* fluorescence imaging of HE_{12}-SNAs

To our knowledge, the *in vivo* behaviour of polymeric DNA nanoparticles has not been previously studied. With that in mind, we proceeded with an *in vivo* screening via optical imaging which would allow for real-time tracking and overall biodistribution profiles. For this purpose, highly monodisperse Cy5.5-HE_{12}-DNA nanoparticles were prepared which contained the dye molecule in their core. This was achieved by mixing Cy5.5-HE_{12}-DNA (where Cy5.5 was attached to the HE_{12} polymer at the opposite end of the DNA) and unlabeled HE_{12}-DNA conjugates in 25:75 molar ratios, followed by thermal annealing (95 °C – 4 °C over 4 hours) (Figure 2.14, *Experimental Figure 2.41*).

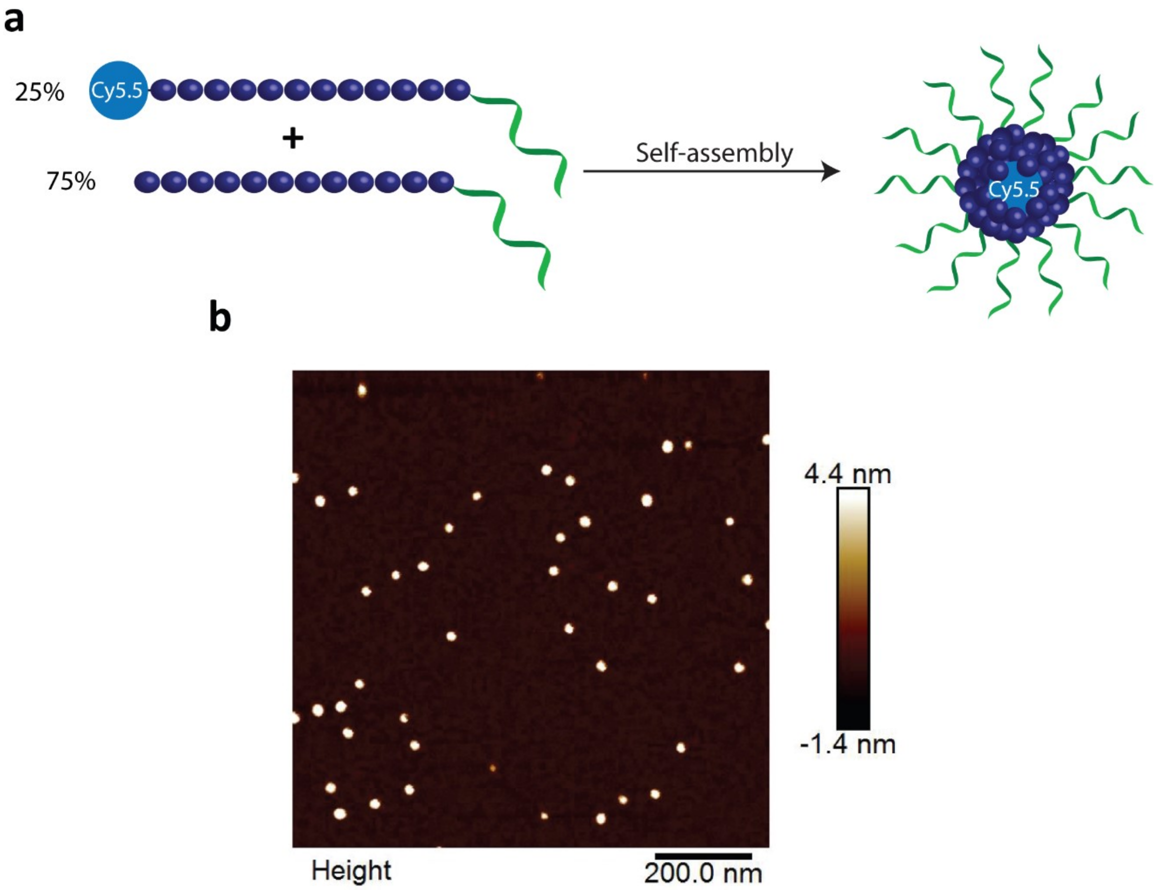

Figure 2.14 – Cy5.5-DNA nanoparticles for *in vivo* fluorescence imaging studies. a) General methodology for preparing Cy5.5-labeled DNA nanoparticles. b) Atomic force microscopy (AFM) images of Cy5.5-labeled nanoparticles showing monodisperse structures with average diameter of 26.8 ± 2.7 nm.

Nanoparticle biodistribution was evaluated by fluorescence imaging, following intraperitoneal injection (Figure 2.15) and intravenous administration of Cy5.5-labeled structures measured over 24 hours (Figure 2.16). Remarkably, Cy5.5-labeled DNA particles showed full-body distribution with long circulation times up to 24 hours (Figures 2.15 & 2.16). Control experiments using Cy5.5-labeled single stranded DNA, showed loss of fluorescence, most likely due to DNA degradation. Similarly, the dye only Cy5.5 sample showed immediate loss of fluorescence, likely because of its insolubility. In contrast, the prolonged fluorescence biodistribution of Cy5.5-HE$_{12}$-DNA nanoparticles could indicate very slow structural degradation in the blood stream.

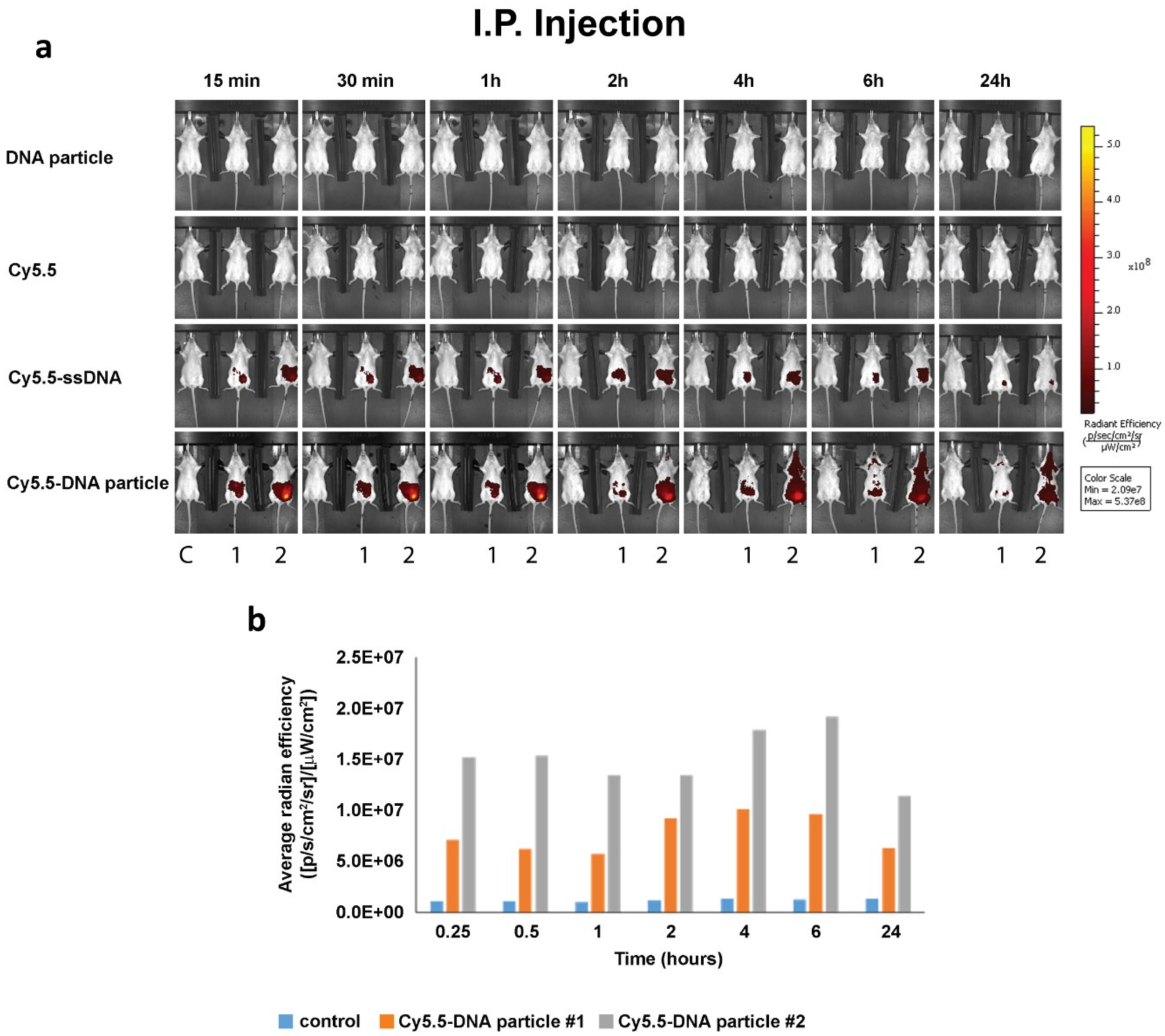

Figure 2.15 – *In vivo* fluorescence imaging of Cy5.5-labeled HE$_{12}$-DNA nanoparticles. a) Fluorescence data overlaid on X-ray images measured over time after intraperitoneal injection. Top: unlabeled HE$_{12}$-DNA nanoparticle. 2nd top: Cy5.5 dye molecule, 2nd bottom: Cy5.5-ssDNA, bottom:

Cy5.5-ssDNA, bottom: Cy5.5-HE$_{12}$-DNA nanoparticle. b) Quantified fluorescence data of Cy5.5 intensity measured as a function of time for Cy5.5-HE$_{12}$-DNA nanoparticles. Particles #1 and #2 measurements were taken for mice 1 and 2 in panel (a).

This behavior was further observed with intravenous injection of Cy5.5-HE$_{12}$-SNAs (Figure 2.16). Compared to Cy5.5-ssDNA which showed rapid decrease in signal after 30 minutes, Cy5.5-HE$_{12}$-SNA exhibited a delayed decrease starting at 6 hours. These results also corroborate our *in vitro* experiments that demonstrate enhanced stability of these DNA structures under physiological conditions (Figures 2.6, 2.7 & 2.8), and could also indicate that the DNA portion of Cy5.5-HE$_{12}$-SNA is more shielded as the nanostructure circulates in the body. Interestingly, at the 6 hour mark, the rate of signal decrease in both Cy5.5-ssDNA and Cy5.5-HE$_{12}$-SNAs appear to be similar which could indicate that at this point, the DNA portion of Cy5.5-HE$_{12}$-SNAs may be degraded, and the remaining Cy5.5-HE$_{12}$ portion behaves similarly to the remaining Cy5.5 dye in the Cy5.5-ssDNA sample (Figure 2.16).

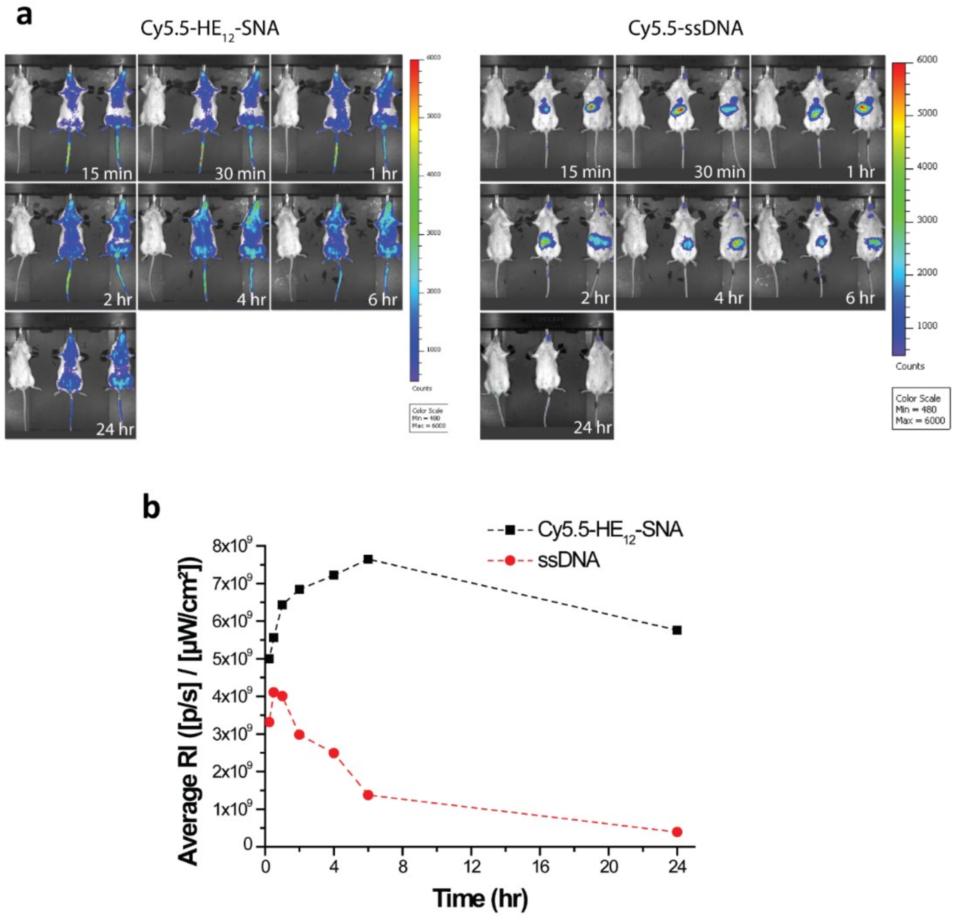

Figure 2.16 – *In vivo* imaging of Cy5.5-labeled HE_{12}-DNA nanoparticles after intravenous administration. a) Cy5.5 fluorescence data overlaid on X-ray images measured over time. b) Quantified fluorescence data of Cy5.5 intensity measured as a function of time for Cy5.5-HE_{12}-DNA nanoparticles.

Further 3D fluorescence imaging, which highlights organ-specific distribution, indicated low levels of excretion (liver and kidney) (Figure 2.17). Notably, low levels of fluorescence were also observed in the brain after 2 and 24 hours (Figure 2.71, *Experimental Figure 2.43*). The biodistribution within the blood stream without accumulation in non-specific organs, particularly in the brain where BKM120 manifests side-effects, is important to decrease adverse effects observed during systemic drug treatments.

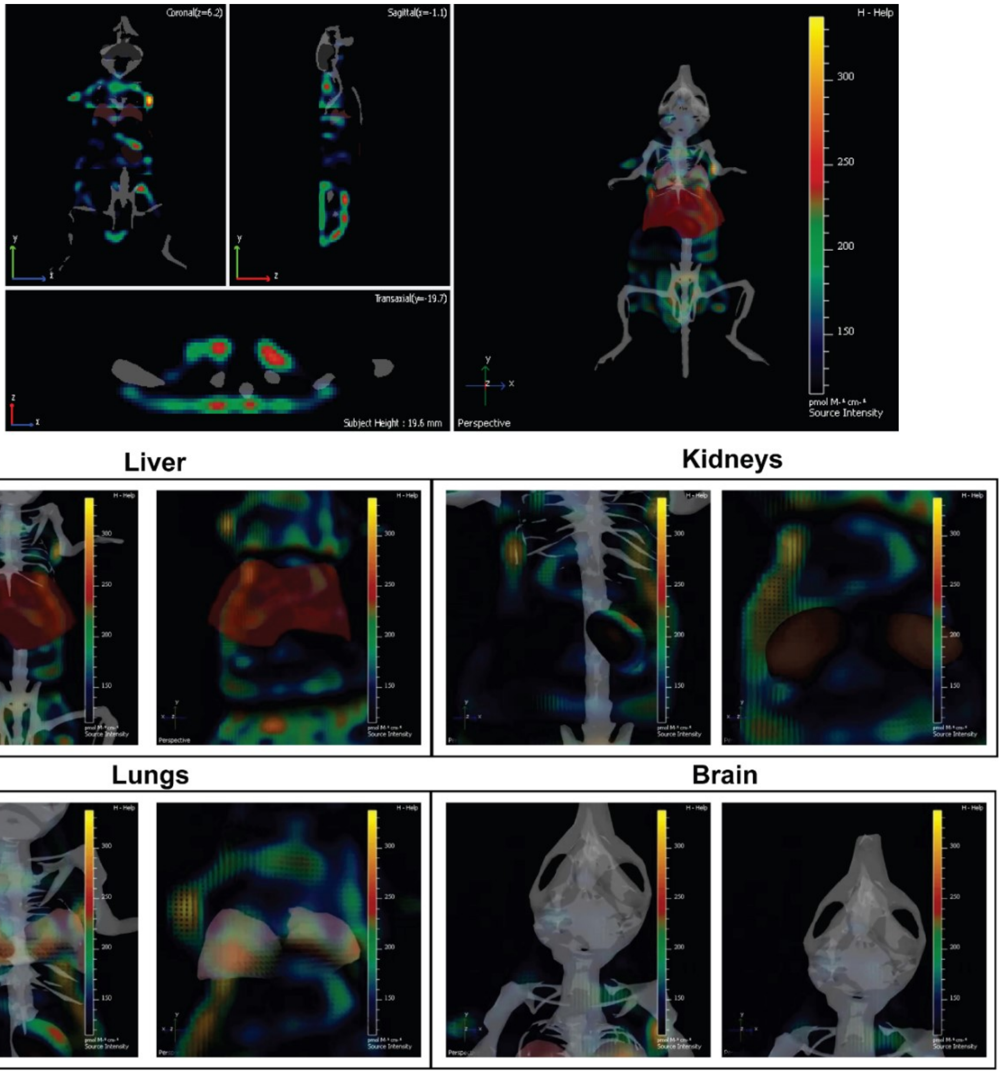

Figure 2.17 – Organ-specific biodistribution of Cy5.5-SNAs at 24 hours. 3D full body fluorescence scan at 24 hrs, overlaid with body organs (liver highlighted in red). Organ-specific distribution showing low nanoparticle accumulation in the liver, kidneys and brain.

The next question was to test whether our DNA nanostructures could reach and accumulate in solid tumors. To address that, the biodistribution of Cy5.5-labeled structures was evaluated in a cancer xenograft model. In our hands, the success of forming CLL xenografts was hampered by the inefficient engraftment of MEC-1 (CLL cell line) into rag2-/-γc-/-mice. Compared to CLL, colon cancer xenografts formed solid tumors much more efficiently in our mouse model. Therefore, HCT116 colon cancer xenografts were used as a model system to test the biodistribution of our DNA nanostructures. Previous reports have demonstrated that nanoparticles tend to accumulate in higher levels in tumor tissue, a phenomenon known as the enhanced permeation and retention (EPR) effect.[77-78] In our case, we measured the accumulation of nanoparticles at the tumor site over time following intraperitoneal injection (Figure 2.18a). Cy5.5-labeled DNA particles showed a steady increase in accumulation at tumor sites for up to 24 hours (Figure 2.18b).

High accumulation in tumors was also observed under intravenous administration. As expected, Cy5.5-labeled structures exhibited higher diffusion rates compared to intraperitoneal delivery with accumulation peaking at 6 hrs (*Experimental Figure 2.44*). The steady increase in accumulation of Cy5.5-labeled particles at the tumor site is predicted to translate into the same pattern of anticancer drug delivery by HE_{12}-DNA structures, which will provide an important mechanism to minimize potential complications of this drug. Overall, the *in vivo* stability and biodistribution profiles of HE_{12}-DNA nanoparticles highlight their great potential as a robust drug delivery system.

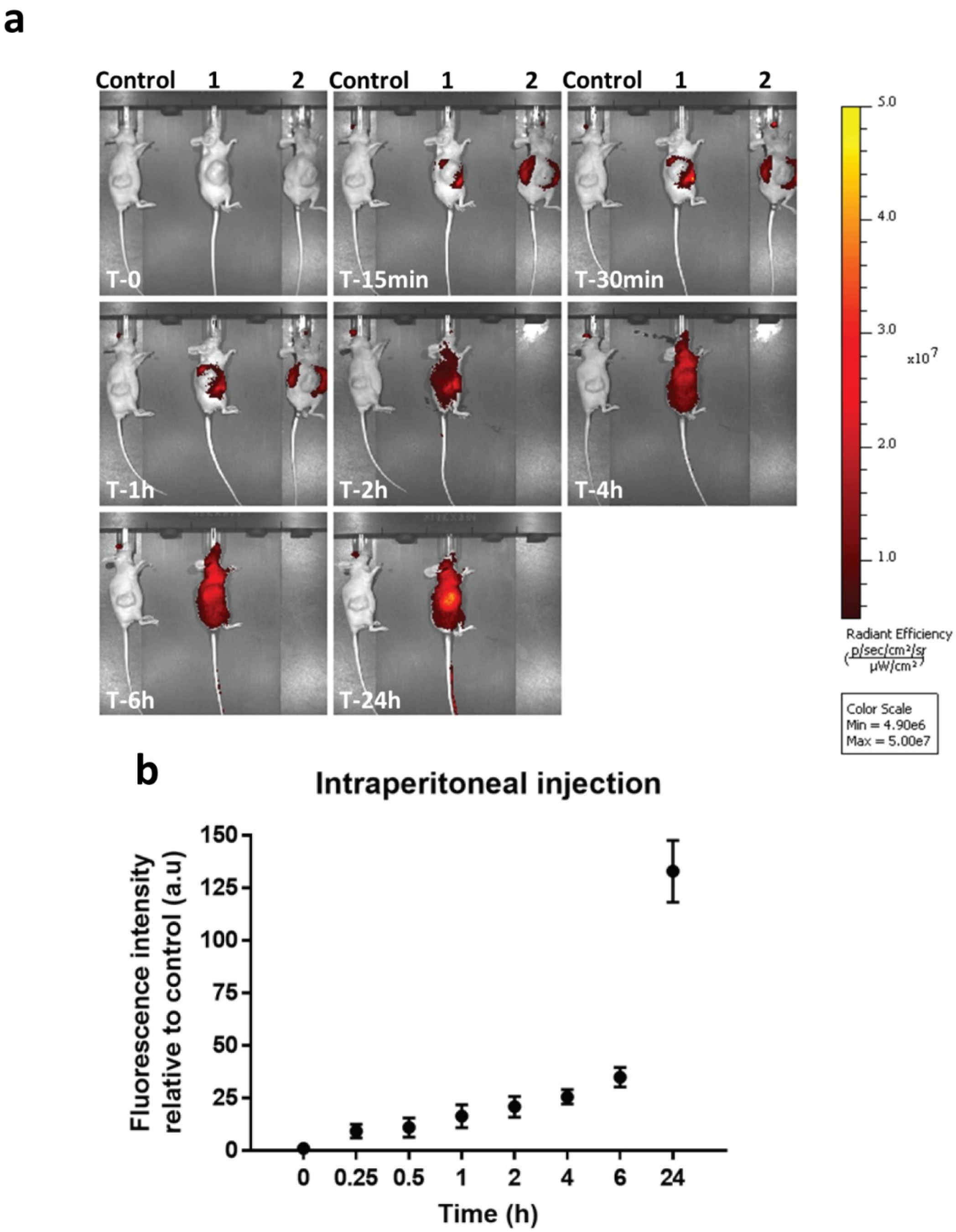

Figure 2.18 – Fluorescence imaging of Cy5.5-labeled DNA nanoparticles in HCT116 colon cancer xenograft. a) Cy5.5 fluorescence data overlaid on X-ray images measured over time following intraperitoneal injection. Control: treated with unlabeled particle, 1&2: treated with Cy5.5-DNA particles. b) Quantified fluorescence intensity of Cy5.5-HE$_{12}$-DNA particles at the tumor site measured over time. Error bars represent the standard deviation of measurements.

2.4 Conclusion

We have developed a highly monodisperse DNA nanoparticle delivery platform for small molecule chemotherapeutics. Our structures show effective loading and slow release of BKM120, a PI3K inhibitor, and have a long shelf-life. The DNA nanoparticles are made of monodisperse, sequence-defined polymers units, they are stable under physiological ionic concentrations, and exhibit increased resistance to nucleases in biological environments. Furthermore, these structures demonstrate efficient uptake in cancer cells, and increased internalization of cargo. *In vitro* studies show the ability of BKM120-loaded particles to induce cellular death and apoptosis, including synergistic effects between BKM120 and antitumor drugs, without causing non-specific inflammation. Further *in vivo* fluorescence imaging of DNA nanoparticles demonstrates full-body distribution and long circulation times of these structures. Furthermore, the particles are not observed to cross the blood-brain barrier an important feature towards limiting the side-effects of BKM120 or any drug molecule with CNS off-target activity. The structures also show high tumor accumulation in xenograft models highlighting their potential for targeted cancer therapy.

Given our findings, HE_{12}-DNA nanoparticles show great promise as delivery vehicles for chemotherapeutics. This initial work has demonstrated the ability to load drugs and protect them in different biological conditions, achieve *in vitro* activity in primary patient cell lines, and monitor the *in vivo* biodistribution of these structures in mice to understand their real-time trafficking and stability. Future studies on this platform will focus on adapting cross-linking strategies to enhance drug loading capacity, retention and structural stability *in vivo*. Additionally, taking advantage of the DNA shell, surface modifications such as targeting ligands and oligonucleotide therapeutics will be implemented. We envisage this system to see applications in targeted cancer therapy and delivery of combinational small-molecule and oligonucleotide therapeutics.

2.5 Experimental Section

2.5.1 General information

Tris(hydroxymethyl)aminomethane (Tris), ethylenediaminetetraacetate (EDTA), urea, 40% acrylamide/bis-acrylamide (19:1), ammonium persulfate (APS), N,N,N',N'-tetramethylethane-1,2-diamine (TEMED) and agarose were purchased from BioShop Canada Inc and used without further purification. Magnesium acetate and Nile Red were purchased from Sigma-Aldrich. Acetic acid, boric acid, ammonium hydroxide and 10x DPBS (with magnesium, calcium) were purchased from Fischer Scientific and used without further purification. Acetone ACS grade was purchased from Fischer. GelRed^{TM} nucleic acid stain was purchased from Biotium Inc. GeneRuler DNA Ladder Mix and DNA Gel Loading Dye (6X) were obtained from Thermo Scientific. 1 µmole 1000 Å universal synthesis CPG column, standard reagents used for automated DNA synthesis and Sephadex G25 (super fine DNA grade) were purchased from BioAutomation. DMT-1,12-dodecane-diol (HE, cat.# CLP-1114) phosphoramidites was purchased from ChemGenes corporated. 1x TBE buffer is composed of 90 mM Tris, 90 mM boric acid and 2 mM EDTA with a pH ~8.3. 1x TAMg buffer is composed of 45 mM Tris, 20 mM acetic acid and 12.5 mM $Mg(oAc)_2{\cdot}4H2O$, and its pH was adjusted to ~8.0 using glacial acetic acid. 1x DPBS (with magnesium and calcium) is composed of 8 mM sodium phosphate dibasic, 138 mM of sodium chloride, 1.47 mM of potassium phosphate monobasic, 2.6 mM potassium chloride, 0.5 mM magnesium chloride (anhydrous) and 0.9 mM calcium chloride (anhydrous).

2.5.2 Instrumentation

Standard oligonucleotide synthesis was performed on solid supports using a Mermade MM6 synthesizer from Bioautomation. HPLC purification was carried out on an Agilent Infinity 1260. UV absorbance DNA quantification measurements were performed with a NanoDrop Lite spectrophotometer from Thermo Scientific. For structure assembly, Eppendorf Mastercycler 96-well thermocycler and Bio-Rad T100TM thermal cycler were used to anneal all DNA nanoparticles. Polyacrylamide gel electrophoresis (PAGE) was performed using 20x20 cm vertical Hoefer 600 electrophoresis units. Agarose Gel Electrophoresis (AGE) was performed on Owl Mini and Owl EasyCast horizontal gel systems. Gels were imaged by BioRad ChemiDoc MP system. Equilibrium dialysis was performed using single-use DispoEquilibrium Dialyzers (5000 Dalton molecular weight cut-off) from Harvard Apparatus. Fluorescence data were measured by BioTek Synergy H4 Hybrid Multi-Mode Microplate Reader or a Carry Fluorimeter. Multimode 8 scanning probe microscope and Nanoscope V controller (Bruker, Santa Barbara, CA) was used to acquire AFM images. DynaPro (model MS) molecular-sizing instrument was used to measure the particle size distributions. Liquid Chromatography Electrospray Ionization Mass Spectrometry (LC-ESI-MS) was carried out using a Bruker MaXis Impact™. TEM micrographs were acquired on FEI Tecnai 120 kV 12 microscope (FEI electron optics). Fluorescence cell imaging was performed with a Zeiss Axio Imager. Cytotoxicity studies were performed using the CellTiter96 kit from Promega according to the manufacturer’s instructions. Apoptosis studies were analysed using a FACS Calibur flow cytometer. *In vivo* fluorescence measurements were performed using In Vivo Imaging System (IVIS).

2.5.3 Solid-phase synthesis and purification

DNA synthesis was performed on a 1 μmole scale, starting from a universal 1000 Å LCAA-CPG solid-support.[85] Coupling efficiency was monitored after removal of the dimethoxytrityl (DMT) 5′-OH protecting groups. DMT-dodecane-diol phosphoramidite (cat.# CLP-1114) was purchased from ChemGenes. Cyanine 3 Phosphoramidite (cat.# 10-5913-02) and Cy5.5 phosphoramidite (cat# 10-5961-95) were purchased from Glen Research. DMT-dodecane-diol and Cy3 phosphoramidite were dissolved in the acetonitrile under a nitrogen atmosphere in a glove box (<0.04 ppm oxygen and <0.5 ppm trace moisture). For DMT-dodecane-diol (0.1M, anhydrous acetonitrile) and Cy3 (0.1M, anhydrous acetonitrile) amidites, extended coupling times of 10 minutes were used respectively using 0.25M 5-(ethylthio)tetrazole in anhydrous acetonitrile. The Cy3 addition was performed under a nitrogen atmosphere in a glove box. Removal of the DMT protecting group was carried out using 3% dichloroacetic acid in dichloromethane. Completed syntheses were cleaved from the solid support and deprotected in 28% aqueous ammonium hydroxide solution for 16-18 hours at 60 °C. In the case of Cy5.5, the mixture was deprotected in 28% aqueous ammonium hydroxide solution for 24-36 hours at room temperature. Following deprotection, the crude solid was re-suspended in 1 mL Millipore water and passed through a 0.22 μm centrifugal filter prior to HPLC purification. The resulting solution was quantified by absorbance at 260 nm. For HPLC purification, solvents (0.22 μm filtered): 50 mM Triethylammonium acetate (TEAA) buffer (pH 8.0) and HPLC grade acetonitrile. Elution gradient: 3-70% acetonitrile over 30 minutes at 60 ºC. Column: Hamilton PRP-C18 5 μm 100 Å 2.1 x 150 mm. For each analytical separation, approximately 0.5 OD_{260} of crude DNA was injected as a 20-100 μL solution in Millipore water. Detection was carried out using a diode-array detector, monitoring absorbance at 260 nm. Retention times and for the products are summarized in Table ST2. Alternatively, for ssDNA and DNA-polymer conjugates, gel purification could be used. The crude product was isolated, dried, and re-suspended in 1:1 H_2O/8 M urea before loading to 18% polyacrylamide/urea gel. The gel was run at 250 V for 30 minutes followed by 500 V for 60 minutes with 1x TBE as the running buffer. The gel was then imaged and excised on TLC plate under a UV lamp. DNA was extracted from the excised gel slabs by crushing and soaking in 11-12 mL Milli-Q water at 60°C overnight. The solution was dried to approximately 1 mL before loading to Sephadex G-25 column. The purified DNA was quantified by its absorbance at 260 nm.

2.5.4 Sequences of DNA-polymer conjugates and characterization

The sequences of the DNA-polymer conjugates and DNA controls are presented in Table 2.1.

Table 2.1 – Sequences used for DNA amphiphiles and DNA controls. (D = DMT-dodecane-diol), (Cy3= Cyanine 3 phosphoramidite), (Cy5.5= Cyanine 5.5 phosphoramidite).

Strand	**Sequence (5'-xx-3')**
HE$_{12}$-DNA	**DDDDDDDDDDDD**TTTTTCAGTTGACCATATA
Cy3-HE$_{12}$-DNA	**Cy3DDDDDDDDDDDD**TTTTTCAGTTGACCATATA
Cy5.5-HE$_{12}$-DNA	**Cy5.5DDDDDDDDDDDD**TTTTTCAGTTGACCATATA
ssDNA	TTTTTCAGTTGACCATATA
Cy5.5-ssDNA	**Cy5.5**TTTTTCAGTTGACCATATA
Cy3-ssDNA	**Cy3**TTTTTCAGTTGACCATATA

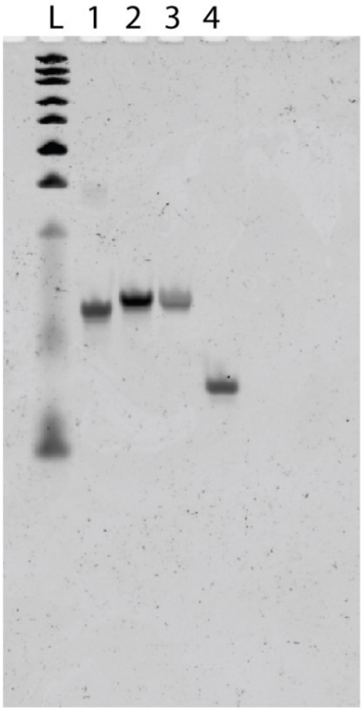

Figure 2.19 – Denaturing gel electrophoresis of the DNA-polymer conjugates. (18% denaturing PAGE). L: ladder, lane 1: HE$_{12}$-DNA, Lane 2: Cy3-HE$_{12}$-DNA, Lane 3: Cy5.5-HE$_{12}$-DNA, Lane 4: ssDNA control.

HE_{12}-DNA conjugate

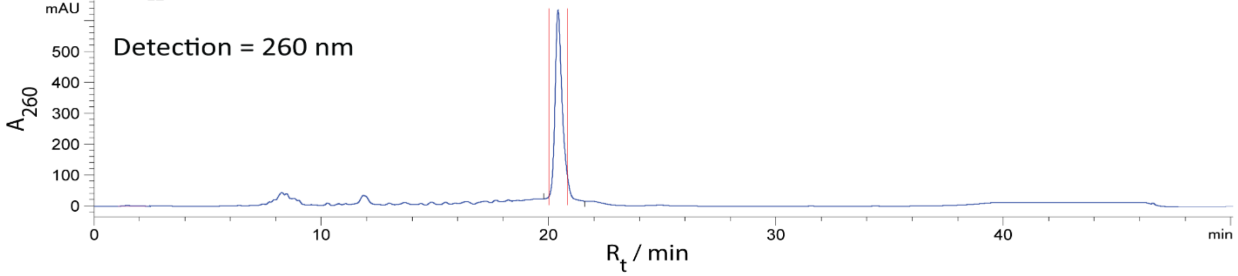

CY3-HE_{12}-DNA conjugate

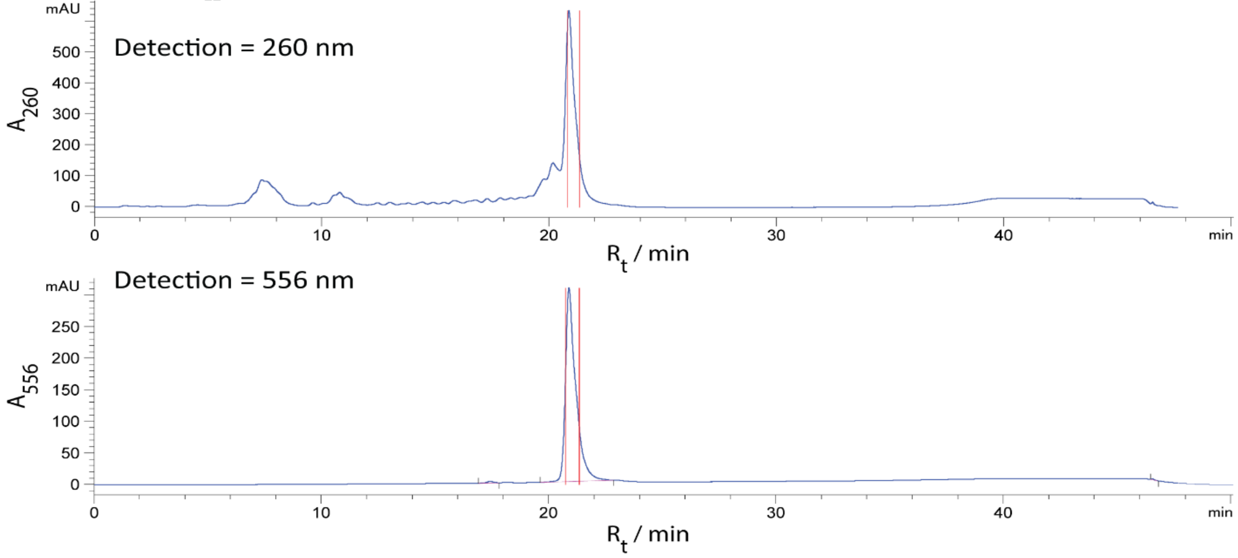

CY5.5-HE_{12}-DNA conjugate

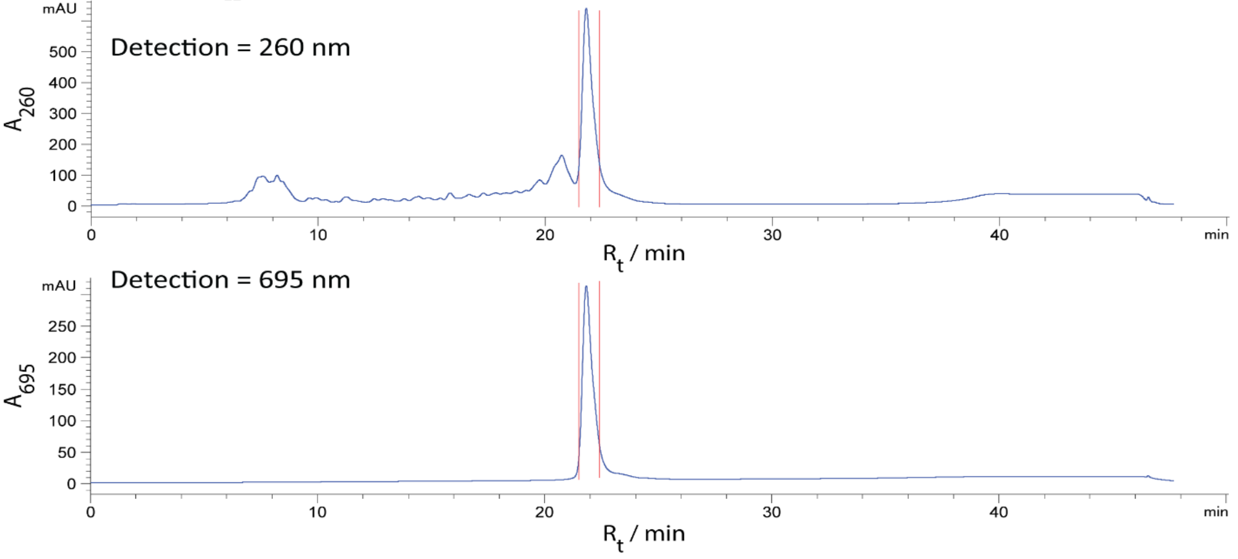

Figure 2.20 – HPLC chromatograms of the crude DNA-polymer products. HPLC signals were measured at 260 nm, 556 nm (Cy3-specific) and 695 nm (Cy5.5-specific). Elution gradient: 3-70% acetonitrile over 30 minutes at 60 °C.

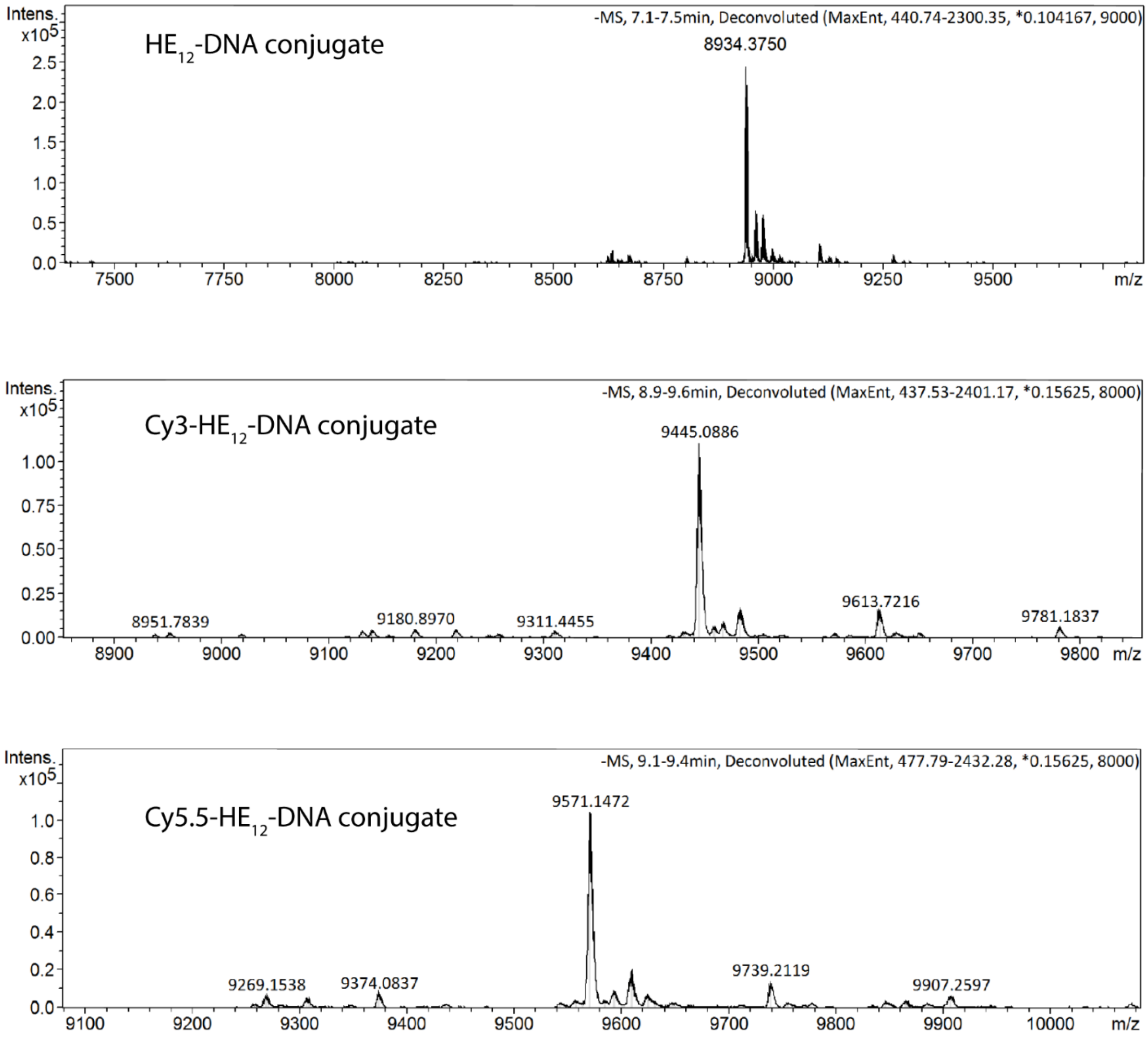

Figure 2.21 – MS characterization of DNA-polymer conjugates.

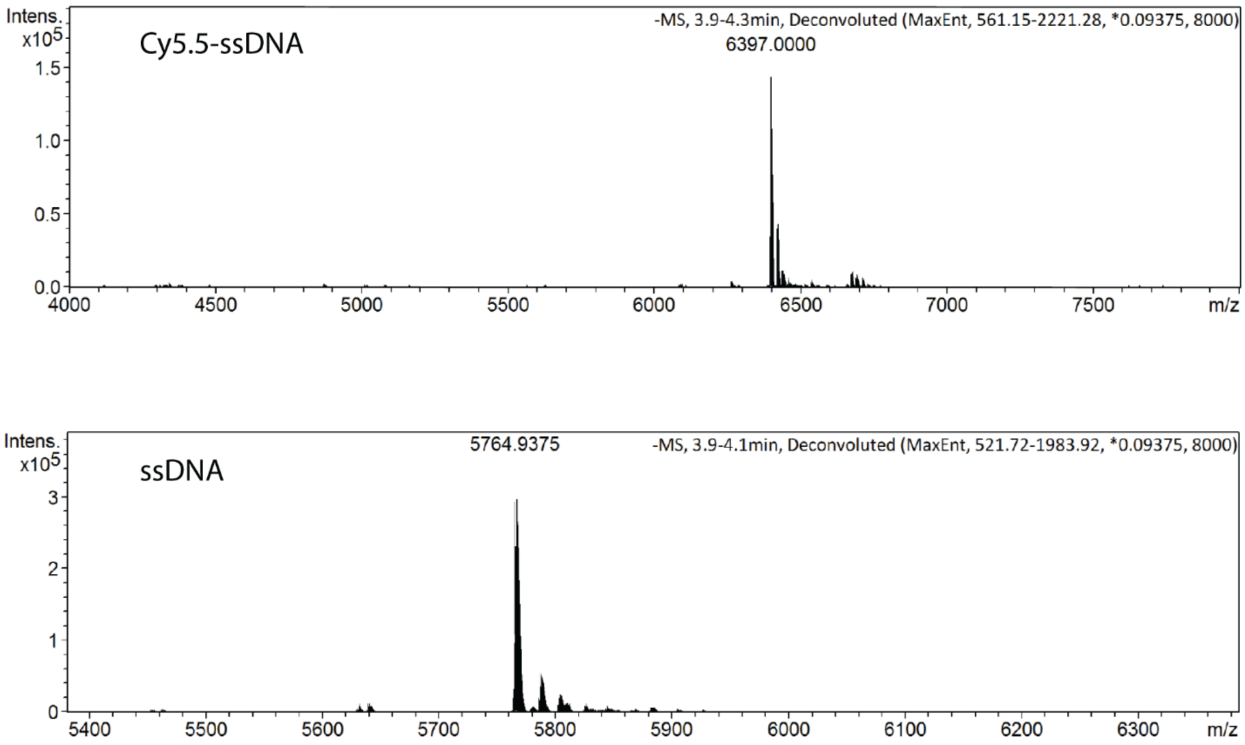

Figure 2.22 – MS characterization of ssDNA controls.

Table 2.2 – LC-ESI-MS. Calculated and experimental m/z values for all DNA amphiphiles synthesized including the unmodified oligonucleotide controls.

Molecule	Calculated m/z	Found m/z
HE_{12}-DNA	8933.77	8934.3750
Cy3-HE_{12}-DNA	9442.02	9445.0886
Cy5.5-HE_{12}-DNA	9568.07	9571.1472
ssDNA	5764.99	5764.9375
Cy5.5-ssDNA	6398.28	6397.000

2.5.5 Evaluation of the encapsulation of BKM120

BKM120 was prepared as a 10 mM working solution in ethanol. Loading of the structures was achieved by adding 10 µL of BKM120 to an eppendorf, followed by solvent evaporation in open air to achieve a thin drug film. HE_{12}-DNA conjugates in water were then added the drug film, mixed and followed by the addition of the assembly buffer (final solution: 100 µL at 10 mM in 1xTAMg buffer). The final solution was 100 µL with 100x excess BKM120 (1 mM). The mixture was vortexed heavily to allow re-suspension of the drug molecules and then annealed at 95 °C to 10 °C over 4 hours. Following the annealing step, removal of free BKM120 was achieved by preparative microcentrifugation (2 cycles of 14,000 rpm for 25 minutes, 4°C) to remove excess drug precipitate. Following microcentrifugation, the mixture was further purified by size-exclusion chromatography using Illustra MicroSpin G-25 Columns (GE Healthcare) using a modified protocol. (The columns were washed twice before resuspension in 1x TAMg. For the elution step, the spinning time was also optimized to ensure higher yield of recovered DNA nanoparticles).

2.5.5.1 BKM120 loading capacity of HE_{12}-SNAs

Reversed phase-HPLC was used to determine the amount of BKM120 loaded in the DNA nanoparticles, For HPLC, 60 µL of the purified supernatant was injected into a Hamilton PRP-1 5µm 100 Å 2.1 x 150mm column. The solvents used are 50 mM triethylammonium acetate (TEAA) buffer (pH 7.8) and HPLC grade acetonitrile. Typical retention times for the products are 27.4 minutes (DNA-polymer conjugate) and 28.733 minutes (BKM120) at 260 nm detection channel. The products were also detected using a drug-only channel at 320 nm (BKM120 maximum absorption peak). BKM120 loading capacity was determined by measuring the DNA peak areas at 260 nm and drug peak area 320 nm (see Figure 2.23). The values were compared with known concentration standards to obtain the number of drug molecules/DNA-conjugate strand. The loading capacity was also calculated based on the equation below:

Loading content (LC) % = mass of BKM120 in nanoparticles / total mass of loaded nanoparticles x 100%. The percent yield was calculated from the peak area of the recovered DNA product using known standards and comparing it to initial starting concentration of 10 µM.

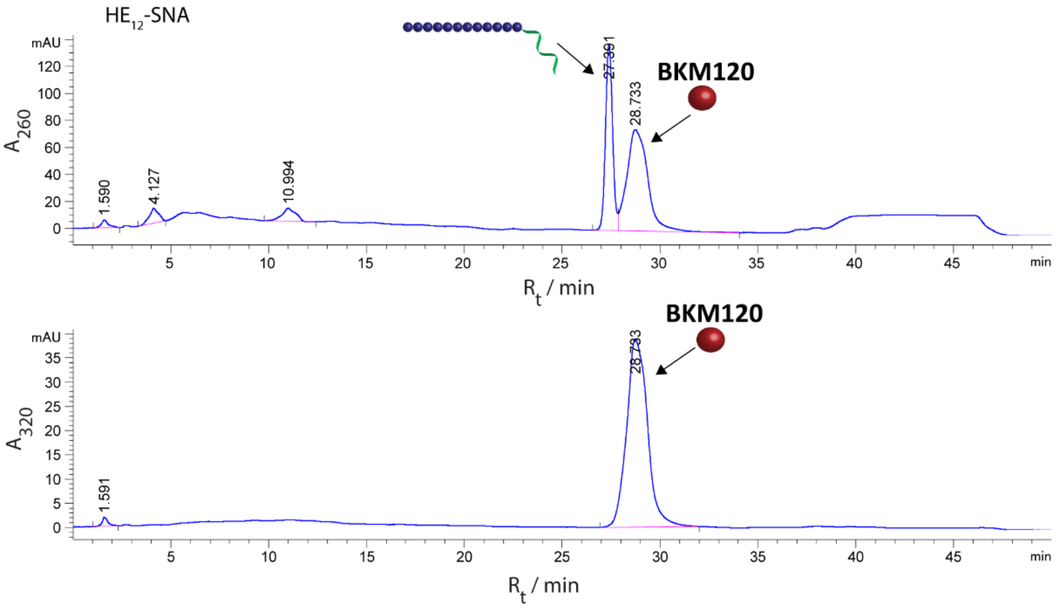

Signal detection: 260 nm		
Peak	**Retention time [min]**	**Average Area (mAU*s)**
HE_{12}-DNA	27.391	3687.33
BKM120	28.733	3168.43

Signal detection: 320 nm		
Peak	**Retention time [min]**	**Average Area (mAU*s)**
BKM120	28.733	2868.46

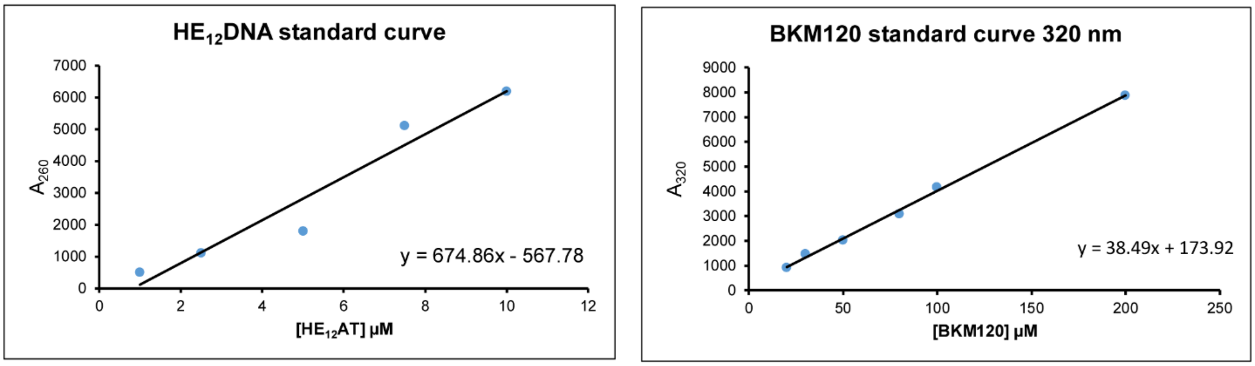

Sample	Calculated [DNA] µM	Yield [%]	Calculated [BKM120] µM	#BKM120 molecules/strand
HE_{12}-SNA	6.3	~ 65	59.5	~ 9

Figure 2.23 – BKM120 loading capacity in HE_{12}-SNAs calculated from RP-HPLC data.

2.5.5.2 UV-vis spectroscopy

UV-vis measurements were used to further evaluate BKM120 encapsulation following the purification method. For each measurement, 100 µL of each of the purified solutions were dropped on a 96-well plate reader and measured through a BioTek Synergy H4 Hybrid Multi-Mode Microplate Reader. Data from UV-vis spectroscopy was used to confirm the calculated drug concentration from RP-HPLC.

2.5.5.3 BKM120 release kinetics

BKM120 release was evaluated by monitoring the decrease in concentration of the drug from a solution of loaded nanoparticles dialyzed against 1x TAMg buffer at room temperature over 24 hours. Immediately following purification, the stock solution was divided into 50 µL aliquots which were dialyzed against 50 µL 1x TAMg buffer using single use DispoEquilibrium Dialyzers (5000 Dalton molecular weight cut-off) from Harvard Apparatus. The samples separated into different tubes and incubated at room temperature, then collected at each timepoint to be analyzed by RP-HPLC. Drug release was assessed by the decrease of drug concentration from the chamber containing the DNA nanoparticles. The amount of DNA remained constant in each measurement indicating no loss of structures throughout the dialysis process. One limitation of the method, however, is the low volume dialyzed from the buffer chamber. This could result in a plateau of drug release from the DNA structures as the buffer solution reaches drug saturation over time.

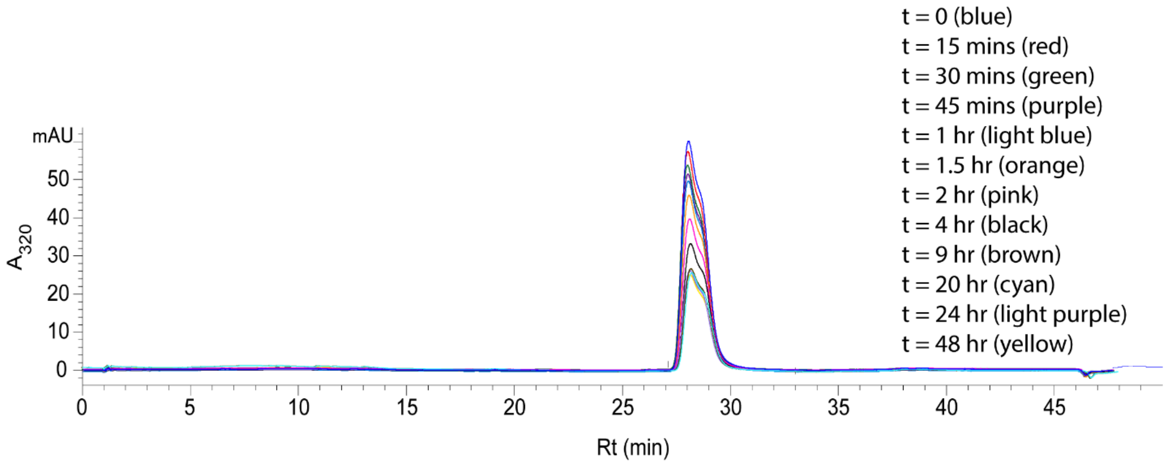

Figure 2.24 – HPLC traces of collected dialysis fractions showing BKM120 release. The samples were detected at a BKM120-specific channel at 320 nm.

2.5.6 Shelf-life of BKM120-loaded nanoparticles

The shelf-life of BKM120-loaded DNA nanoparticles was assessed by dynamic light scattering (DLS). The structures were stored at 4 °C and room temperature, and the hydrodynamic radius was measured over a 4-week period.

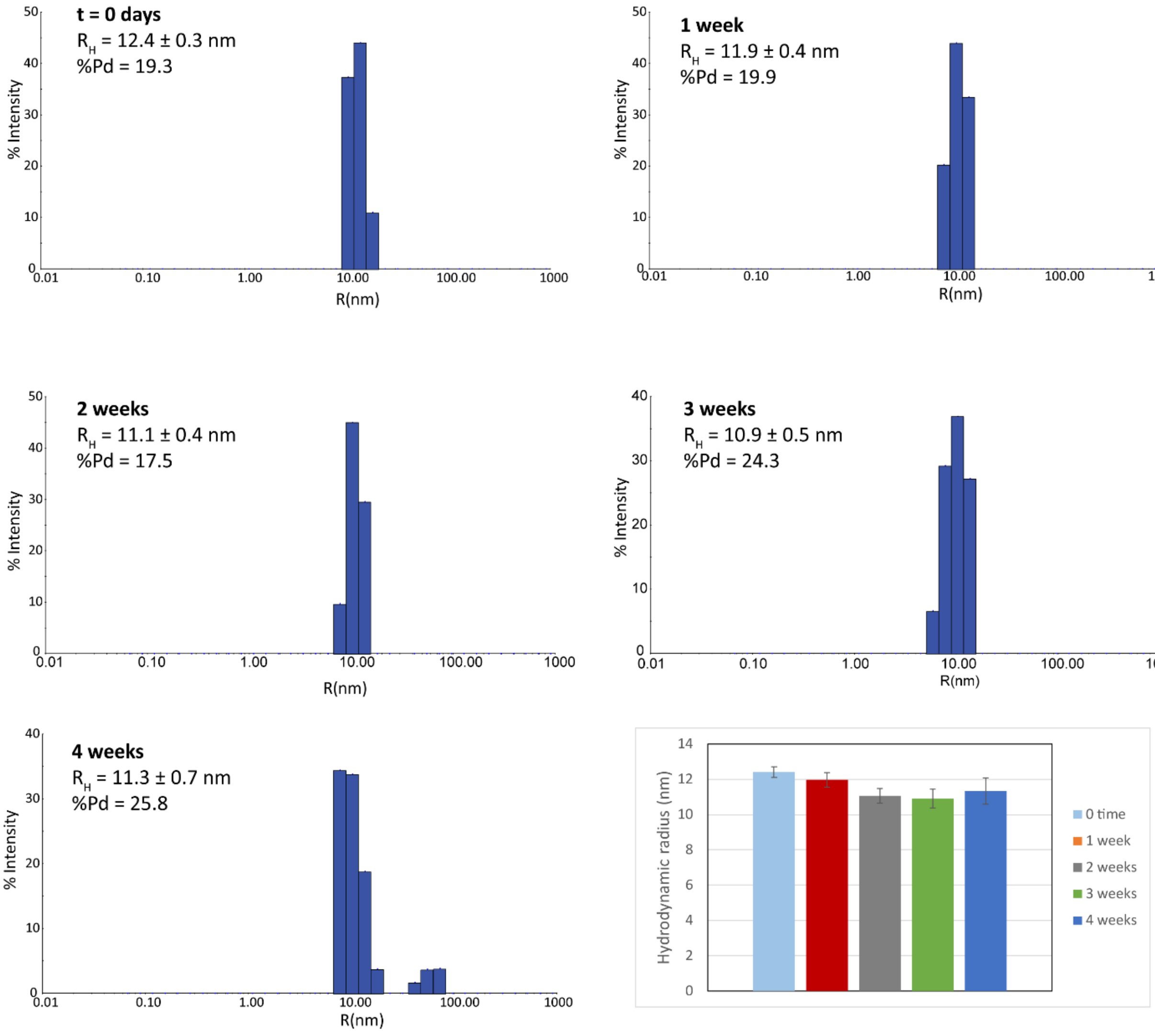

Figure 2.25 – Shelf-life of BKM120-loaded DNA nanoparticles stored at 4 °C. Dynamic light scattering (DLS) histograms showing the hydrodynamic radius of BKM120-loaded nanoparticles over time when stored at 4 °C.

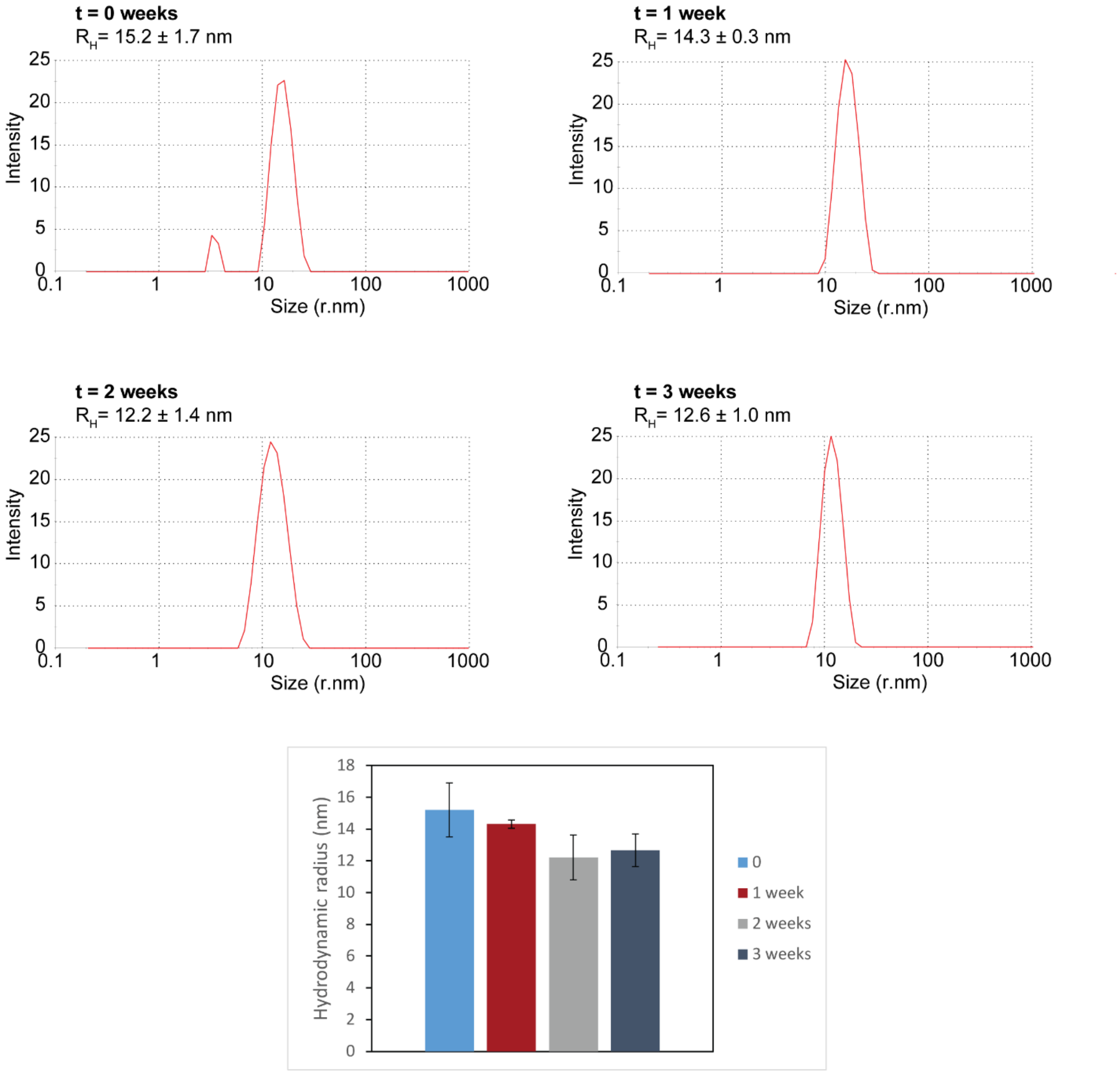

Figure 2.26 – Shelf-life of BKM120-loaded DNA nanoparticles stored at room temperature. Dynamic light scattering (DLS) histograms showing the hydrodynamic radius of BKM120-loaded particles over time when stored at room temperature.

2.5.7 Determination of critical micelle concentration (CMC)

To determine the CMC of HE_{12}-DNA polymer conjugates, fluorescence spectra of 100 µM Nile Red in tris-acetate-magnesium (1 x TAMg) buffer were measured in the presence of increasing concentrations of HE_{12}-DNA polymer conjugates. A stock solution of Nile Red 10 mM in acetone was used for all experiments. 1 µL of Nile Red stock in acetone was added and briefly incubated at room temperature to allow solvent evaporation. Series dilutions of DNA-polymer conjugates (in the range of 50 nM to 10 µM) were made up to a final volume of 100 µL. The mixture was subjected to a heat-cool cycle (95 °C – 4 °C, over 4 hours). The samples were then transferred to a 96-well top-read microplate, and the plate was read using a Bioteck Synergy well-plate fluorimeter. Excitation was at 535 nm with a slit-width of 9 nm and emission was monitored between 560 nm and 750 nm. The CMC of HE_{12}-DNA conjugates was investigated using fluorescence emission of a hydrophobic dye, Nile Red. This molecule is nearly non-emissive in bulk aqueous media, but its inclusive in a nonpolar microenvironment such as the core of HE_{12}-SNAs results in an intense fluorescence signal.[86] A CMC of 0.5 µM ± 0.2 µM was calculated for HE_{12}-DNA conjugates in 12.5 mM Mg^{2+}. We anticipate the CMC to further decrease in the BKM120-loaded structures upon the encapsulation of the drug due to the additional stabilizing π-π interactions between drug molecules and van der walls interactions with the carbon chains of the hydrophobic core.

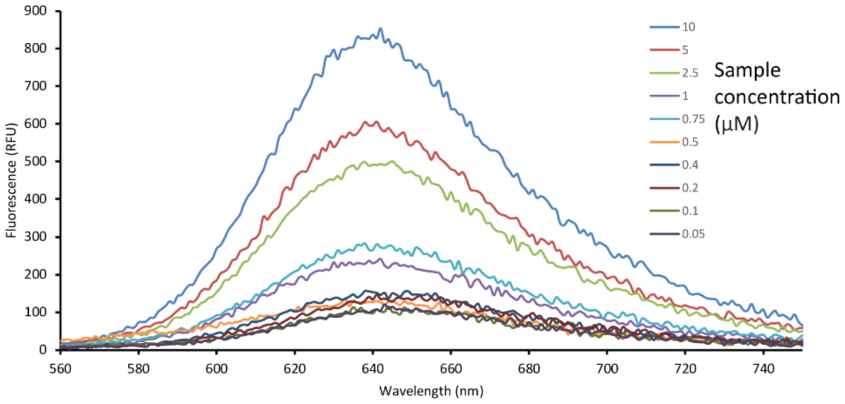

Figure 2.27 – Fluorescence spectra of Nile Red encapsulation for determination of critical micelle concentration (CMC). a) Fluorescence spectra of Nile Red with varying concentration of DNA. 100 µM Nile Red was use for the CMC experiments.

2.5.8 Characterization of BKM120-loaded DNA nanoparticles

2.5.8.1 Gel Mobility Shift Assays

Agarose gel electrophoresis was used to characterize the BKM120-loaded HE_{12}-SNAs. In each case, 2.5% AGE was carried out at 4 °C for 2.5 hours at a constant voltage of 80V. Typical sample loading is 15 picomoles with respect to the DNA, per lane (1.5 µL of 10 µM DNA).

2.5.8.2 Dynamic Light Scattering

Dynamic light scattering (DLS) experiments were carried out using a DynaPro™ Instrument from Wyatt Technology. A cumulants fit model was used to confirm the presence and determine the size the BKM120-loaded HE_{12}-SNAs. Sterile water and 1xTAMg buffer were filtered using a 0.45 µm nylon syringe filter before use in DLS sample preparation. 20 µL of sample (concentration: 10 µM) was used in each measurement. All measurements were carried out in triplicate at 25 °C.

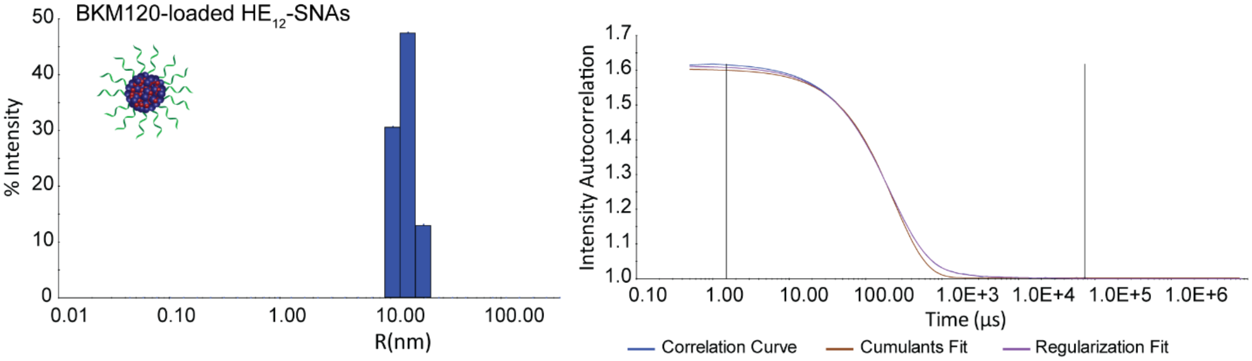

Figure 2.28 – Additional DLS results for BKM120-loaded HE_{12}-DNA nanoparticles. Left: histogram showing the size distribution of the structure; right: the intensity correlation function. The structures show a hydrodynamic radius R_H = 11.8 ± 0.4 nm.

2.5.8.3 Atomic Force Microscopy

Dry AFM was carried out using a MultiMode8™ SPM connected to a Nanoscope™ V controller (Bruker, Santa Barbara, CA). All images were obtained using ScanAsyst mode in air with AC160TS cantilevers (Nominal values: Tip radius – 9 nm, Resonant frequency – 300 kHz, Spring constant – 42 N/m) from Asylum Research. Samples were diluted to 1 µM in TAMg buffer and 4 µL of this solution was deposited on a freshly cleaved mica surface (ca. 7 x 7 mm) and allowed to adsorb for 1-2 seconds. Then 50 µL of 0.22 µm filtered Millipore water was dropped on the surface and instantly removed with filter paper. The surface was then washed with a further 200 µL of water and the excess removed with a strong flow of nitrogen. Samples were dried under vacuum for at least 15-30 minutes prior to imaging.

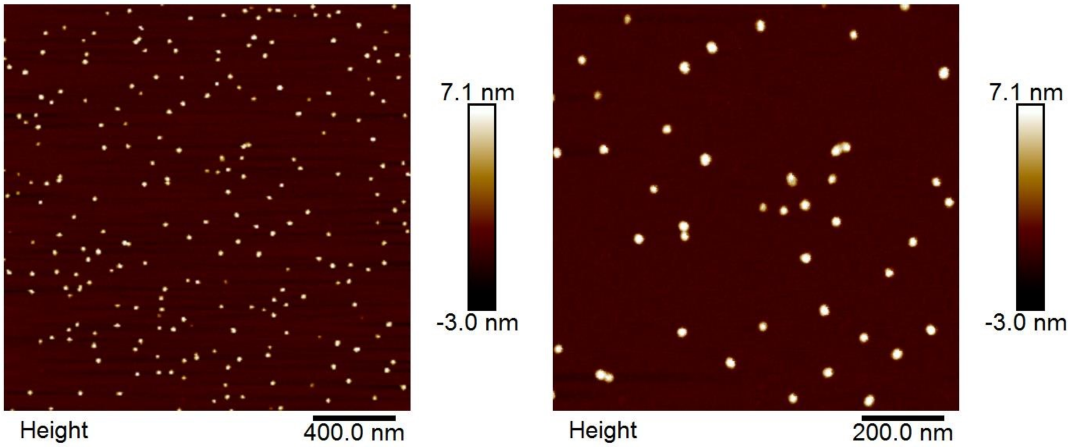

Figure 2.29 – Additional AFM images of BKM120-loaded HE$_{12}$-DNA nanoparticles. Following purification, spherical drug-containing particles are recovered. Average size of the particles was 27.8 ± 4.3 nm, with height of 8.1 ± 0.9 nm (N = 43).

2.5.8.4 Transmission Electron Microscopy

Samples (2 μL at 5 μM w.r.t. total DNA) were deposited on carbon film coated copper EM grids for one minute, followed by blotting off the excess liquid with the edge of a filter paper, and washing three times with 20 μL of water, before drying under vacuum. The samples were imaged using a Tecnai 12 microscope (FEI electron optics) equipped with a Lab6 filament at 120 kV. Images were acquired using a Gatan 792 Bioscan 1k x 1k Wide Angle Multiscan CCD Camera (Gatan Inc.). Contrast was adjusted automatically - note that in the presence of any high-contrast foreign matter, the structures resulted in being almost invisible. Images were analyzed using ImageJ, which required manually setting threshold levels and placing limits on the size and circularity of features to ensure correct particle picking. The area values obtained were converted into radii (for comparison with DLS), making the assumption that the features are circular, which can be readily validated by eye.

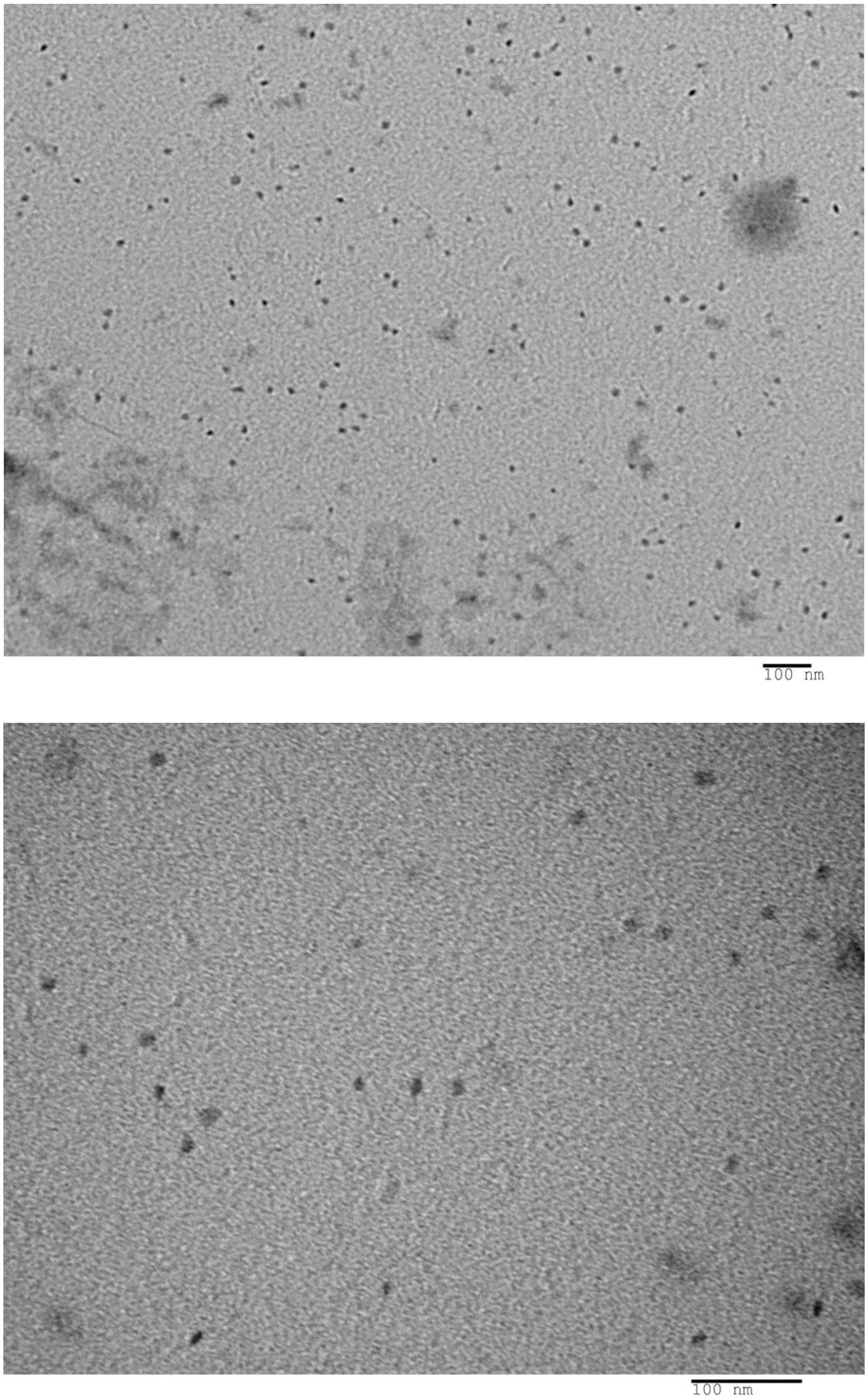

Figure 2.30 – Additional TEM images of BKM120-loaded HE$_{12}$-SNAs. Average diameter was calculated to be 21 ± 3 nm (N = 56).

2.5.9 Buffer stability of HE_{12}-SNAs

The stability of HE_{12}-SNAs in buffer was evaluated by DLS measurements. Tris buffer containing different concentrations of magnesium or calcium was added to HE_{12}-DNA conjugates and the mixture was annealed 95 °C-4 °C over 4 hours. In the case of DPBS buffer, different amounts of DPBS buffer were diluted from an initial 10X stock, mixed with HE_{12}-DNA conjugates in water and annealed 95 °C – 4 °C over 4 hours, prior to DLS analysis.

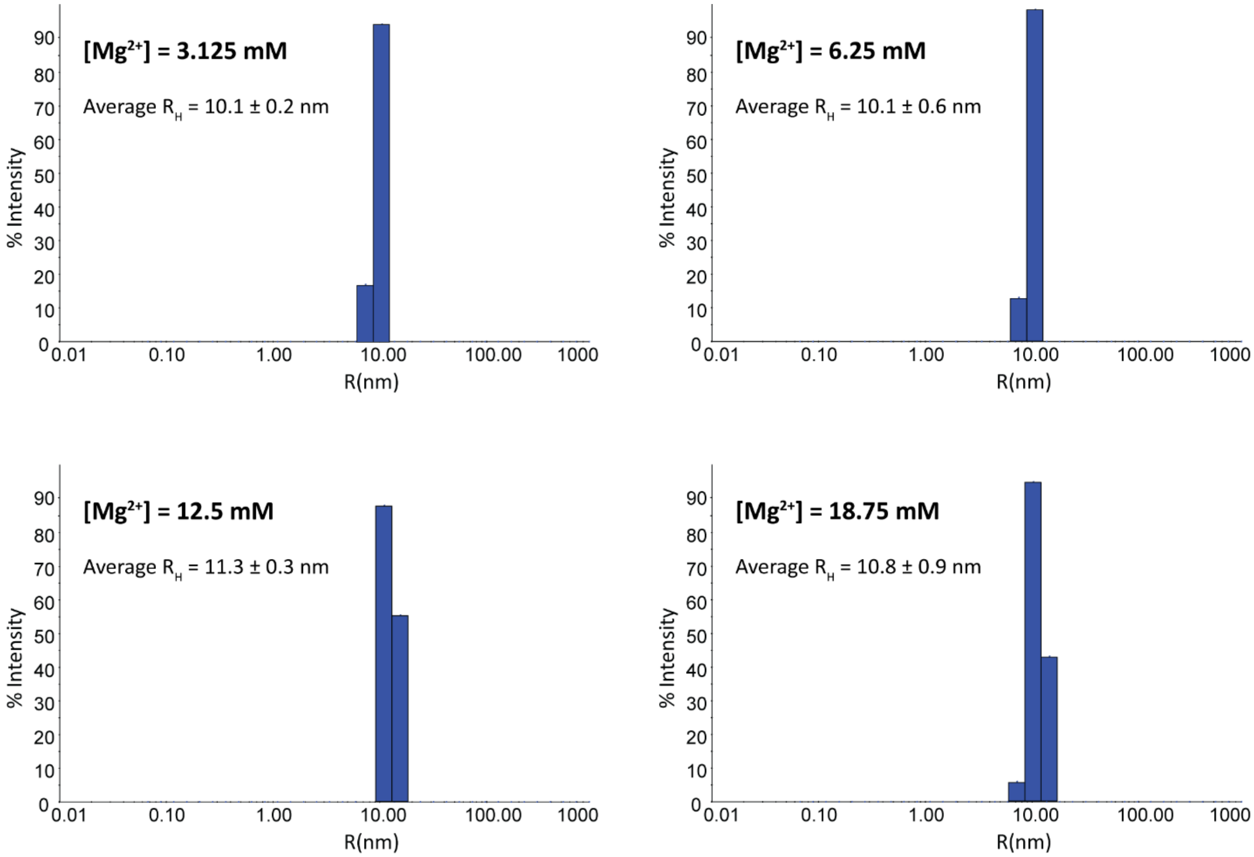

Figure 2.31 – DLS histograms of HE_{12}-SNAs under different magnesium concentrations in Tris buffer.

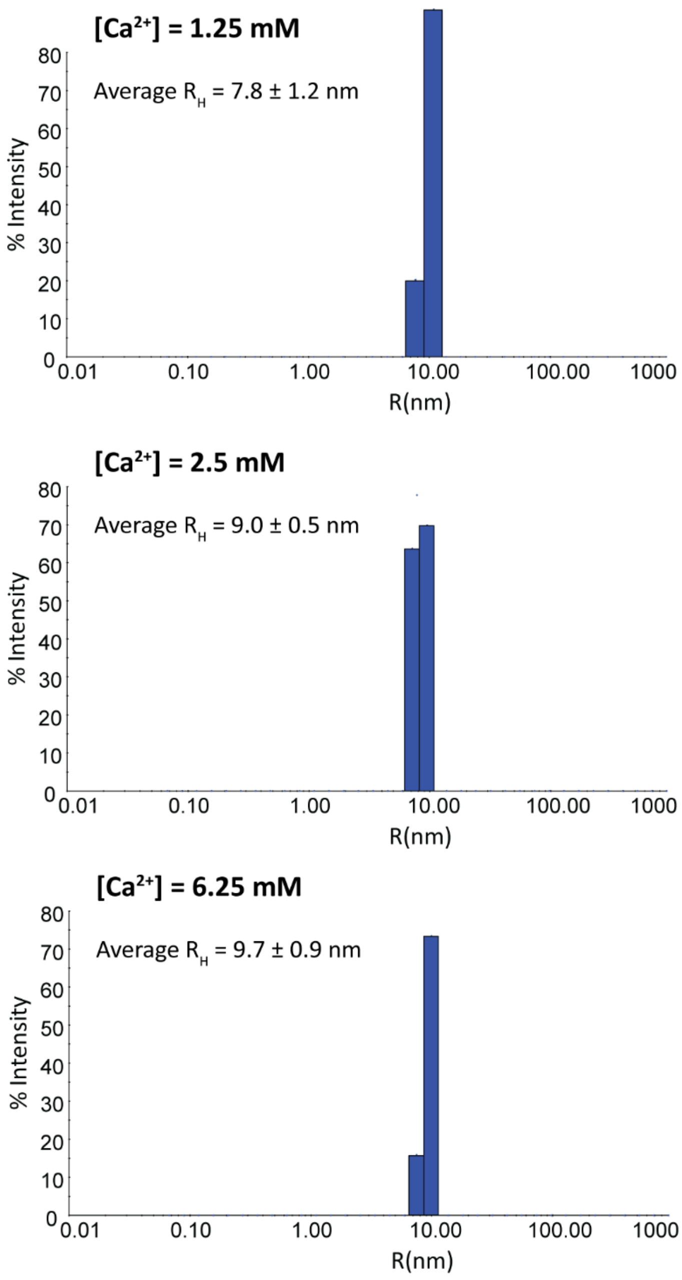

Figure 2.32 – DLS histograms of HE_{12}-SNAs under different calcium concentrations in Tris buffer.

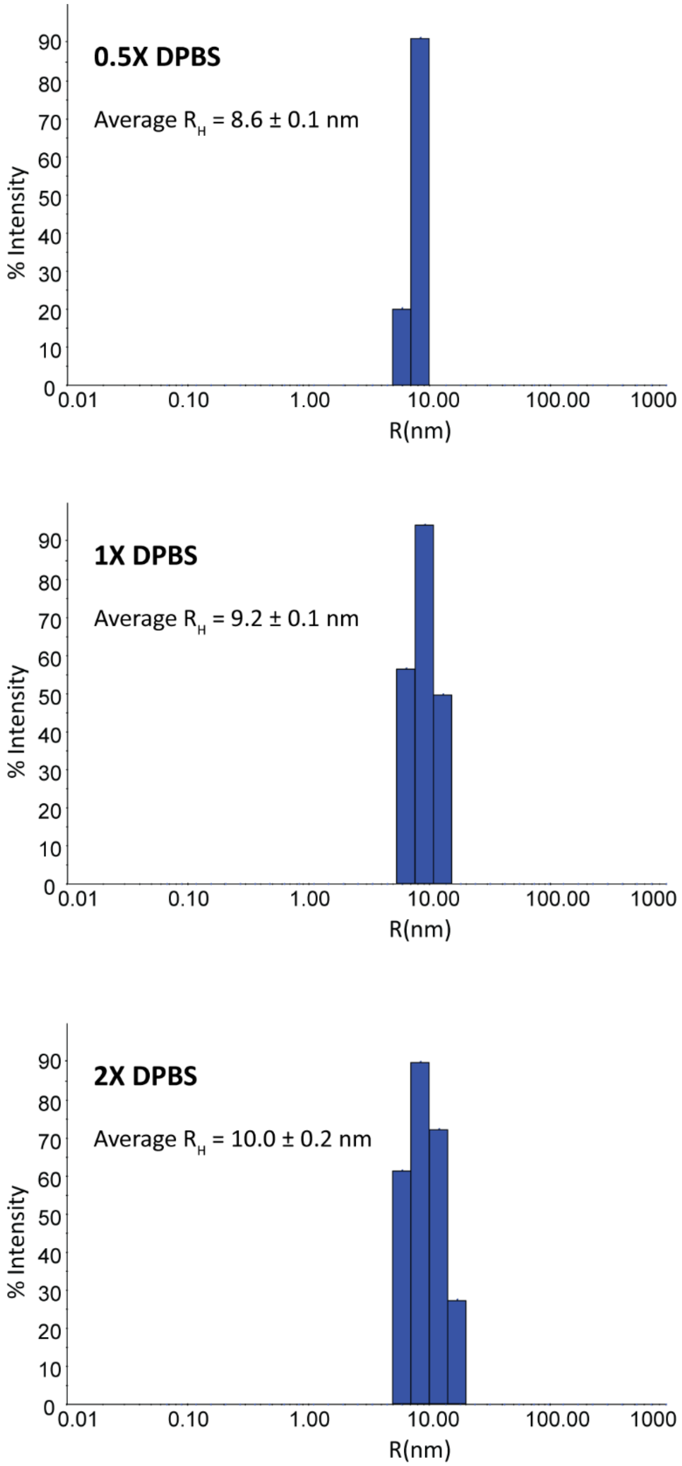

Figure 2.33 – DLS histograms of HE_{12}-SNAs under different amounts of DPBS buffer.

Depletion of divalent cations causes the disassembly of structures into monomeric units. The assembly of HE_{12}-SNAs in a Tris buffer containing no divalent cations, and in water is described below.

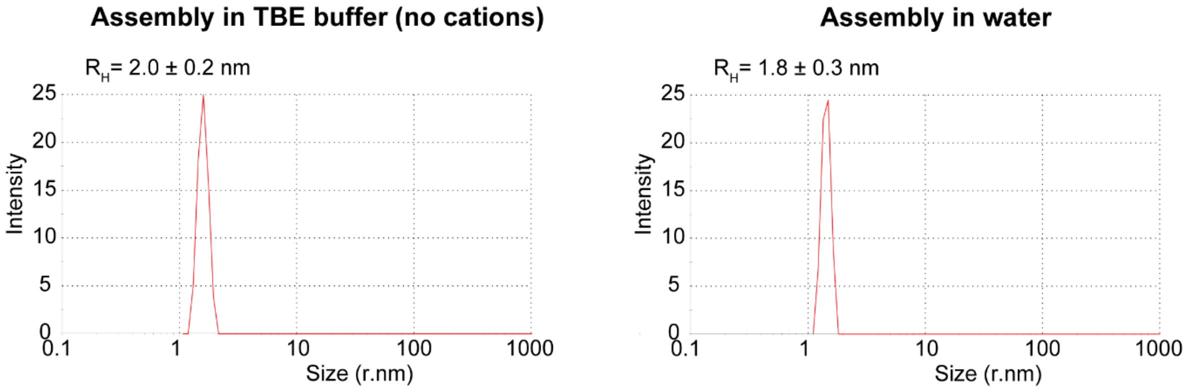

Figure 2.34 – The effect of cation depletion on HE_{12}-SNAs. DLS histograms of HE_{12}-SNAs assembly in TBE buffer (tris buffer containing no divalent cations), and in water. A hydrodynamic radius in the range of 2 nm is indicative of monomeric HE_{12}-DNA conjugate units and the lack of higher order assembly.

2.5.10 Nuclease resistance studies

DNA nanoparticle nuclease resistance compared to single stranded DNA was measured by a nuclease degradation assay published by Conway et. al.[87] Samples (10 µM) were incubated with 10% Fetal Bovine Serum (FBS) for several time points at 37 °C. At each time point an aliquot was removed and immediately added to proteinase K (2 units), then a stop solution (Formamide 50%/SDS 0.01%), and stored at -20°C. Samples were then resolved on 20% PAGE (TBE) denaturing gel (20.7 mL H2O, 1.8 mL of 1x TBE, 7.5 mL 40% acrylamide, 8 M urea). Gels were stained with Gel Red (Biotium, USA) and imaged by a BioRad Imager. Quantification and data analysis were performed using the GraphPad Prism software. The intensity of the lower mobility band (nondegraded structure) was quantified over time. The experiment was performed in triplicate. Half-lives were calculated by fitting a first order decay.

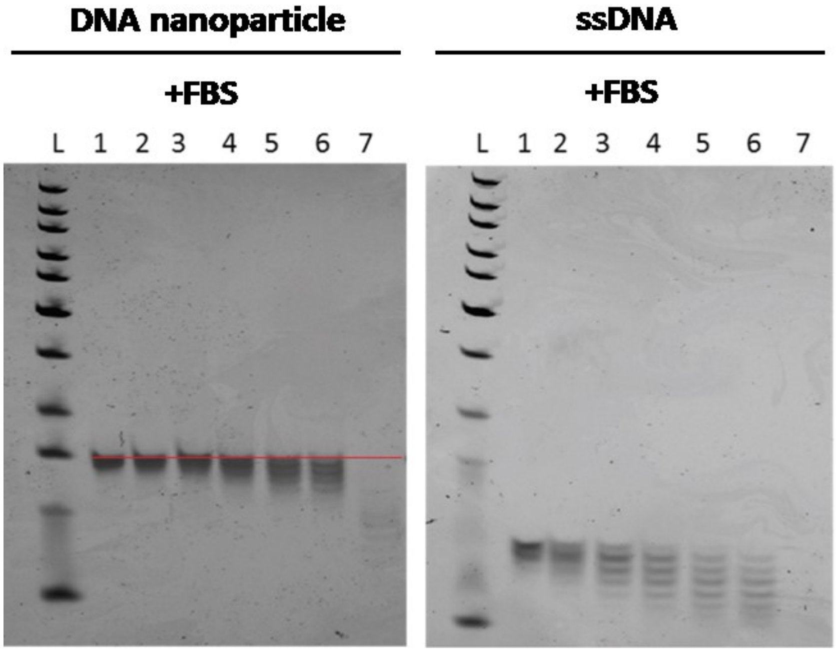

Figure 2.35 – Denaturing PAGE gel of the FBS degradation products. L: ladder, lane 1: time 0, lane 2: 15 mins, lane 3: 30 mins, lane 4: 1 hour, lane 5: 2 hours, lane 6: 3 hours and lane 7: 24 hours. The intensity of the lower mobility band was quantified over time (red line across the gel). The experiment was performed in triplicate.

2.5.11 Cellular uptake studies of DNA nanoparticles

2.5.11.1 Preparation of Cy3-labeled nanoparticles

Cy3-labeled HE_{12}-SNAs were prepared by mixing Cy3-labeled HE_{12}-DNA with unlabelled HE_{12}-DNA strands at a 25:75 percent ratio (DNA concentration 10 μM) followed by an annealing cycle 95 °C – 4 °C over 4 hours. This percentage of labeled/unlabeled strands was observed to give the cleanest assemblies along with high fluorescence intensity for cellular uptake studies.

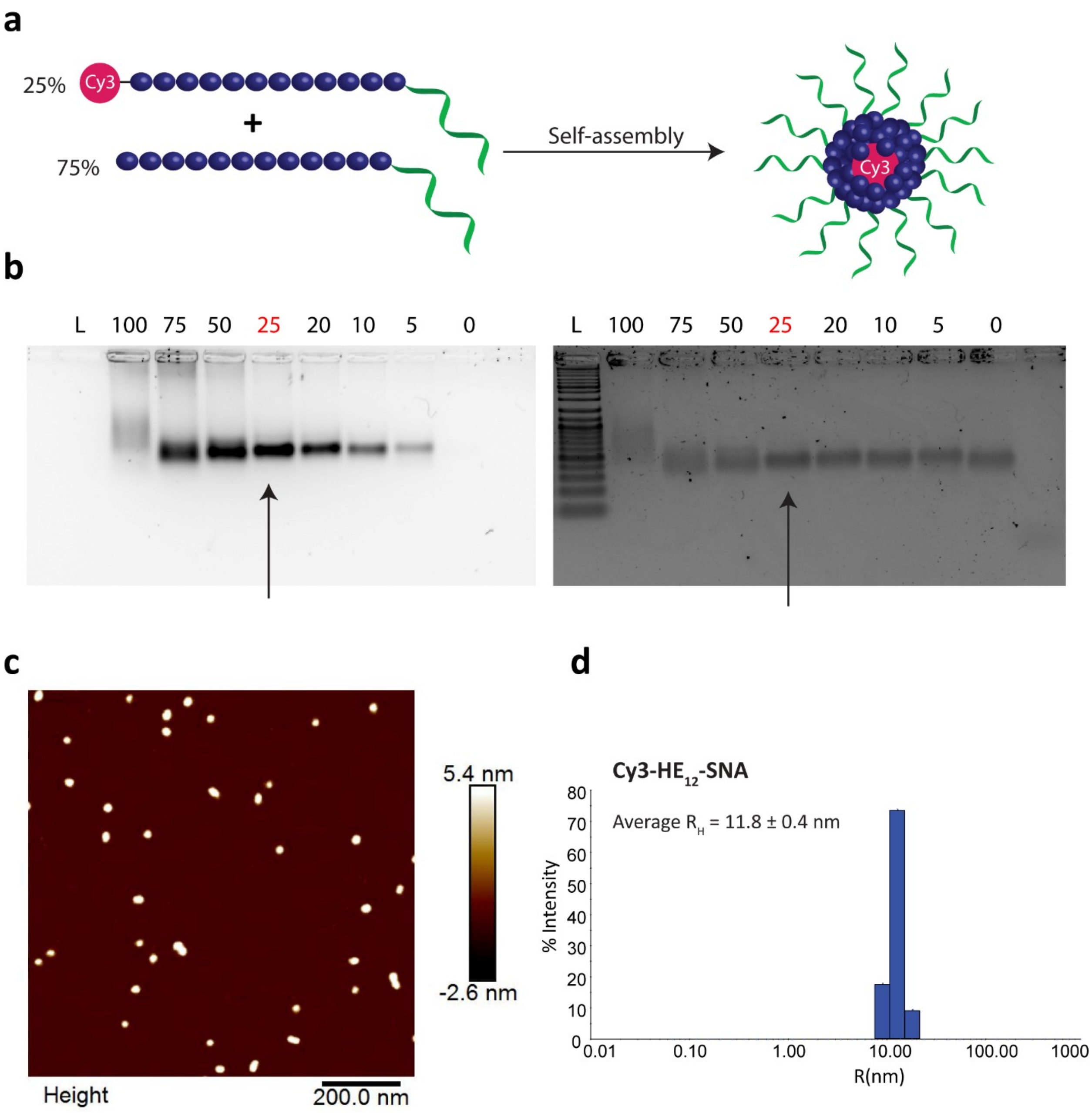

Figure 2.36 – Preparation and characterization of Cy3-labeled HE_{12}-SNAs. a) General methodology for preparing Cy3-labeled DNA nanoparticles. b) Agarose Gel Electrophoresis (AGE) characterization of Cy3-labeled particles imaged under Cy3 channel (left) and Gel Red DNA channel (right). Numbers on lanes indicate the percentage of labeled strands in the final structure. At ratio 25:75 of Cy3-HE_{12}-DNA/unlabeled HE_{12}-DNA strands, the structures show highest fluorescence intensity and morphological integrity c) Atomic force microscopy (AFM) images of Cy3-labeled particles

showing monodisperse structures with average diameter of 28.4 ± 3.6 nm. c) DLS histogram of Cy3-labeled HE_{12}-SNAs showing an in solution hydrodynamic radius of 11.8 ± 0.4 nm.

2.5.11.2 Confocal Microscopy for Cellular Uptake of Cy3-labeled nanoparticles

HeLa (adenocarcinoma) cells were seeded at a density of 5 x 10^5 in 8-well slides. After 24 hours cells were incubated with Cy3-HE_{12}-SNAs, HE_{12}-SNAs, or Cy3-ssDNA (1 μM) at 37 °C for 24 hours. Subsequently, cells were fixed with 2% paraformaldehyde/1X PBS. Cells were then washed with 1X PBS and mounted with Prolong Gold (Invitrogen, USA) and cured overnight at 4°C. Images were recorded using a Leica LS Microscope (Leica, Germany) and images were analyzed using the LASX software (Lecia, Germany).

2.5.12 Cellular uptake of Nile Red-loaded nanoparticles

2.5.12.1 Encapsulation of Nile Red

Nile Red was prepared as a 10 mM working solution in acetone. Loading of the structures was achieved by adding 20 μL of Nile Red to a glass vial, followed by solvent evaporation in open air to achieve a thin drug film. HE_{12}-DNA conjugates in water were then added the drug film, mixed and followed by the addition of the assembly buffer (final solution: 100 μL at 10 μM in 1xTAMg buffer) with excess Nile Red (2 mM). The mixture was vortexed heavily to allow re-suspension of the drug molecules and was annealed overnight (95 °C – 4 °C over 4 hours). The mixture was purified by preparative centrifugation (15,000 x g, 4°C, 1 hour) between 2-4 times) and the concentration of encapsulated Nile Red was determined by fluorescence spectroscopy. Fluorescence emission spectra of each sample were collected in triplicate by mixing a 25 μL aliquot of the purified sample with 75 μL of acetone and recording the emission spectra (Nile Red: exc. 535nm) of the sample in a microplate reader. A standard curve for [dye] versus maximal fluorescence intensity was used to calculate the [dye] present in each sample.

2.5.12.2 Flow cytometry experiments

HeLa cells were seeded at a density of 5 x 10^5 in a 6 well plate. After 24 hours, the cells were incubated with HE_{12}-SNAs + Nile Red or Nile Red alone (125 µL of sample added in a total media volume of 1 mL). The final concentration of Nile Red was 375 nM in both samples. After 12 hours of incubation, cells were detached, washed and resuspended in 1x PBS, followed by fixing with 2% paraformaldehyde. Samples were then processed using FACS FORTESSA. All measurements were performed in triplicates for error analysis.

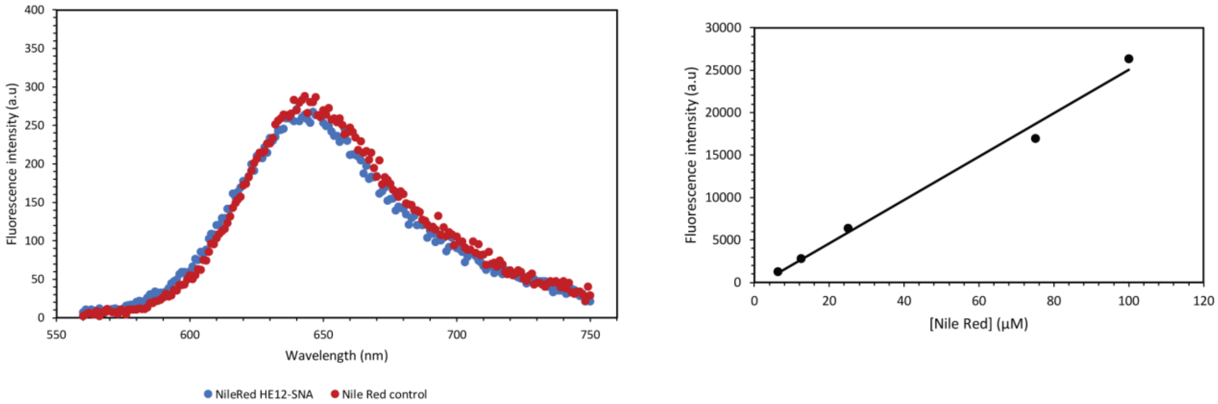

Figure 2.37 – Quantification of encapsulated Nile Red in HE_{12}-SNAs and Nile Red control by fluorescence spectroscopy measurements prior to flow cytometry studies. Following purification of un-encapsulated Nile Red, the initial concentration of dye was prepared at [Nile Red] = 3 µM in both HE_{12}-SNA and Nile Red control, to yield a final dye concentration of 375 nM in cell media.

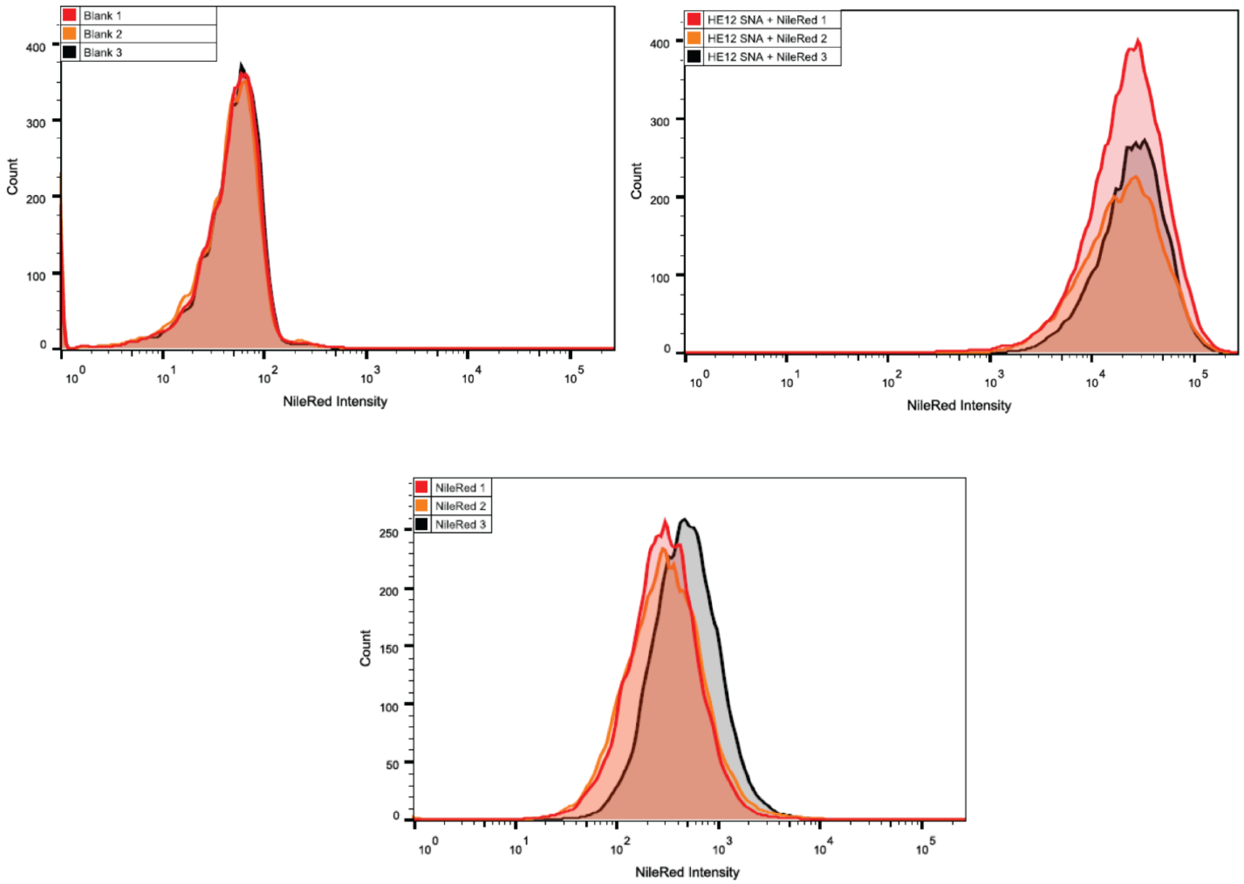

Figure 2.38 – Flow cytometry measurements showing the increased uptake of Nile Red when delivered by HE$_{12}$-SNAs. Final [Nile Red] = 375 nM in cell culture media. Nile Red images were acquired at exc. wavelength 535 nm, emission 670 nm. These images were used for quantification of Nile Red uptake. The studies were performed in triplicates.

2.5.12.3 Fluorescence Microscopy for Nile Red Encapsulation

HeLa (adenocarcinoma) cells were seeded at a density of 5 x 10^5 in 8-well slides. After 24 hours, cells were incubated with HE$_{12}$-SNAs, HE$_{12}$-SNAs + Nile Red, or Nile Red alone (50 µL of sample added in a total media volume of 250 µL, final dye concentration = 400 nM) at 37 °C for 2 hours. Subsequently, cells were fixed with 2% paraformaldehyde/1X PBS. Cells were then washed with 1X PBS and mounted with Prolong Gold (Invitrogen, USA) and cured overnight at 4 °C. Images were recorded using a Zeiss AxioImager and images were analyzed using the Zen software (Zeiss, USA).

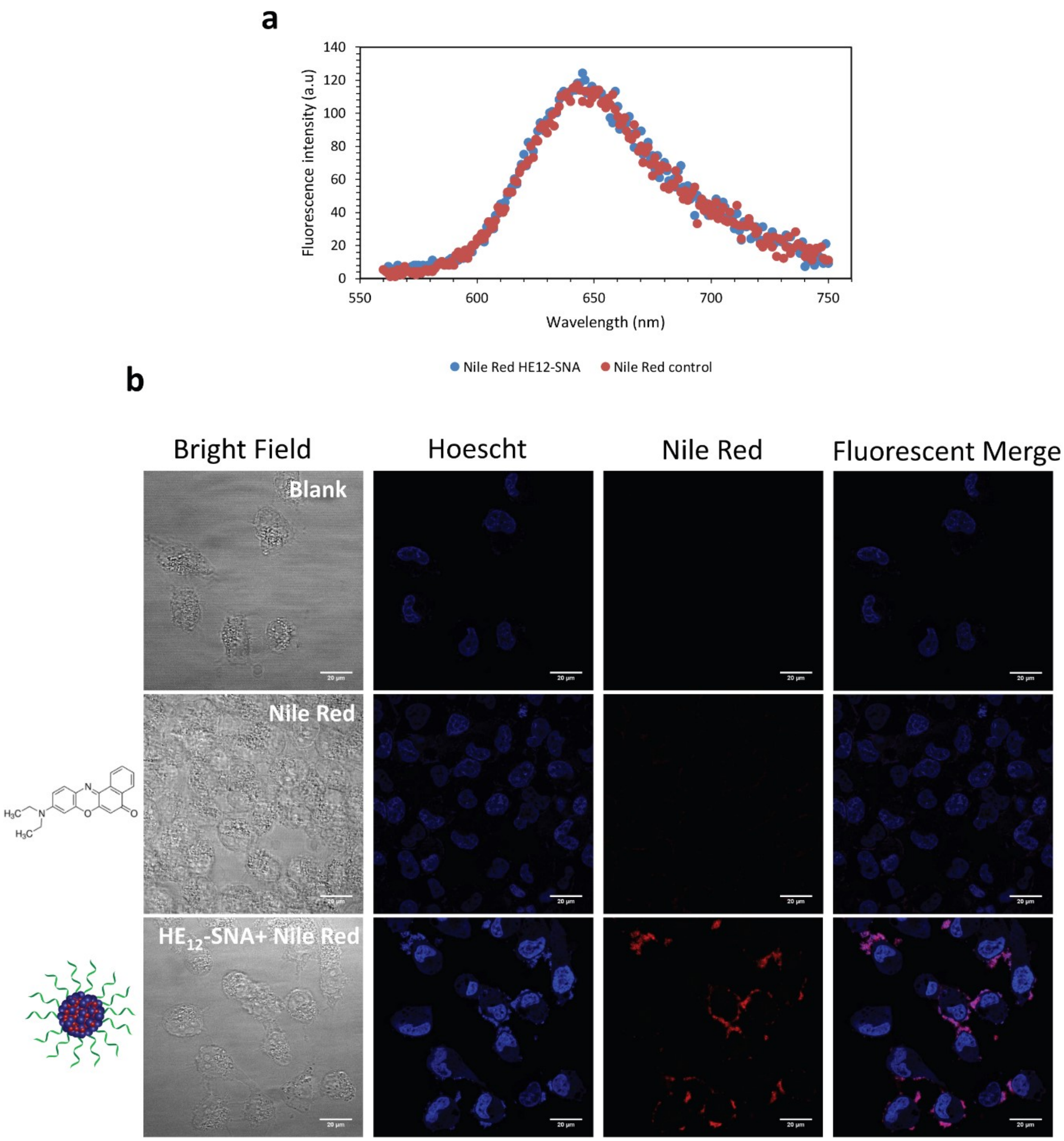

Figure 2.39 – Fluorescence data showing Nile Red internalization in HeLa cells. a) Quantification of encapsulated Nile Red in HE$_{12}$-SNAs and Nile Red control by fluorescence spectroscopy measurements prior to confocal microscopy studies. Following purification of excess un-encapsulated Nile Red, the initial concentration of dye was prepared at [Nile Red] = 2 µM in both HE$_{12}$-SNA and Nile Red control, to yield a final dye concentration of 400 nM in cell media. b) Confocal fluorescence microscopy images demonstrating the cellular uptake of Nile Red when in HeLa cells. All samples were incubated for 12 hours with Nile Red or HE$_{12}$-SNA + Nile Red. Nile Red images were acquired using Ar Ion laser 514 nm and Hoescht 3342 was used as a nuclear stain.

2.5.13 *In vitro* cell studies

2.5.13.1 MTS assay for BKM120 and dox-BKM120 cell viability

Cell viability of HeLa cells after BKM120 treatments or in combination with doxorubicin, was measured using the Cell-Titer Blue assay (Promega, USA). Briefly, cells were seeded in 96-well plates at a density of 1×10^5. After 24 hours, BKM120 was added (final concentrations: 0.06, 0.12, 0.3, 1.52, 7.6 µM) for single treatments. When BKM120 was added in combination with doxorubicin, BKM120 was varied between 0.12, 1.2, and 12 µM, while doxorubicin was maintained at 0.1, 1, and 10 µM for each of those experiments. Subsequently after 24 hours, plates were analyzed at using a Bio Plater Reader using 560 nm Ex/590 nm emission. Data was plotted and analyzed using the GraphPad Prism Software.

2.5.13.2 Apoptosis studies in primary CLL patient cells

Primary B-CLL lymphocytes were maintained in RPMI complemented with 10% fetal bovine serum (FBS). BMS2 stromal cell lines were maintained in Dulbecco's modified eagle medium (DMEM) supplemented with 10% FBS. BMS2 cells were plated at 70×10^4 cells/ml in 24-well plates before being cocultured with primary B-CLL lymphocytes and incubated at 37 ºC, 5% CO_2. For apoptosis assays, 3×10^6 B-CLL lymphocytes were plated in the presence or absence of stromal cell (BMS2) and incubated for 1 hour at 37 ºC, 5% CO_2. Cells were then treated with vehicle, nanoparticle, BKM120, and BKM120-loaded nanoparticles for 24 and 48 hours.

2.5.13.3 AnnexinV /propidium iodide analysis

Cells were harvested, washed with PBS then incubated with 1 µL Annexin V APC conjugated plus 0.5 µg/ml propidium iodide in 100 µL binding buffer for 15 min at room temperature. Cells were then analyzed with a FACSCalibur flow cytometer.

2.5.13.4 Cleaved caspase-3 analysis

Cells were harvested, washed with PBS then fixed for 10 min with 1% paraformaldehyde. After washing, cells were permeabilized and non-specific sites blocked in PBS containing 3% FBS and 0.01% triton X100. Cells were then incubated for 1 hour with an anti-caspase-3 FITC conjugated antibody then analyzed with a FACSCalibur flow cytometer.

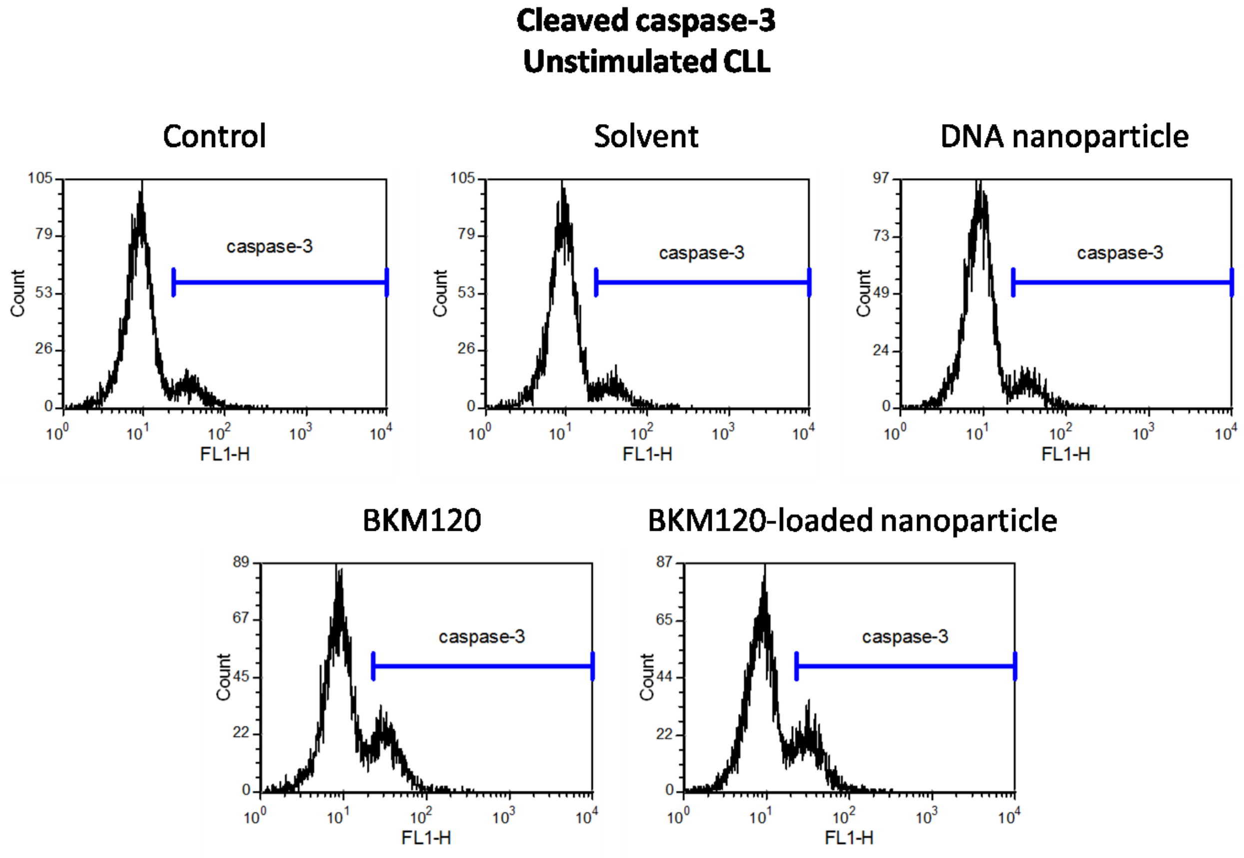

Figure 2.40 – Flow cytometry data showing the level of cleaved-caspase 3 in unstimulated primary CLL lymphocytes.

2.5.13.5 Immunostimulation TNF-α ELISA Assays

Immunostimulation assays were performed using RAW264.7 cells (ATCC), mouse monocytes. Briefly, cells were seeded in a 96-well plate at a density of $1x10^5$. Subsequently, after 24 hours, HE_{12}-SNAs (2 µM), ssDNA (2µM), LPS 500 ng/mL (lipopolysaccharide), poly IC 10 ug/mL+Transfection, were added to the cells and incubated for 5, 24, and 48 hours. At each time-point, supernatants were collected and frozen at -20°C. When all samples were collected, a TNF-α ELISA assay was performed according to the manufacturer's instructions (eBioscience) using the Instant ELISA TNF-α kit. Results were measured using a Bio plate reader at a wavelength of 630 nm and data was analyzed using the Graphpad Prism Software.

2.5.14 *In vivo* studies of HE_{12}-SNAs

2.5.14.1 Preparation of Cy5.5-labeled nanoparticles

Cy5.5 phosphoramidite was appended from the 5' of the HE_{12}-DNA through attachment to one end of the polymer chain (opposite to the DNA) to yield Cy5.5-HE_{12}-DNA conjugates. Cy5.5-labeled DNA nanoparticles were prepared by mixing Cy5.5-labeled HE_{12}-DNA with unlabeled HE_{12}-DNA conjugates in a 25:75 molar ratio (total DNA concentration 17 µM, total Cy5.5-DNA concentration 4.25 µM, total volume 100 µL). This ratio of Cy5.5 labeled/unlabeled strands resulted in high fluorescence intensity of the dye molecules and clean assemblies. For *in vivo* studies, additional UV-Vis measurements were conducted to ensure similar dye absorbance of the Cy5.5-labeled nanoparticles to Cy5.5-ssDNA.

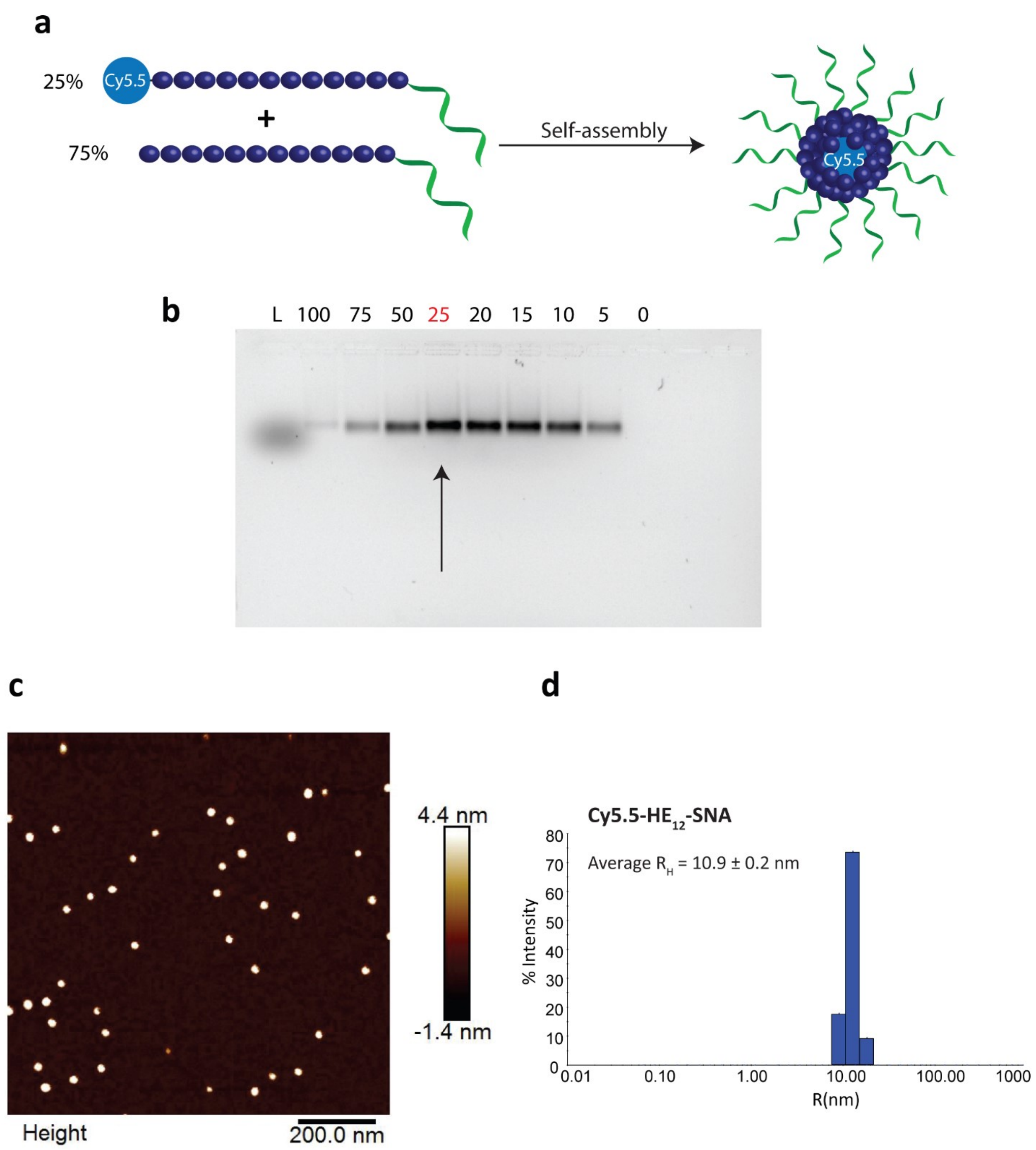

Figure 2.41 – Characterization of Cy5.5-labeled HE$_{12}$-SNAs for *in vivo* imaging studies. a) General methodology for preparing Cy5.5-labeled DNA nanoparticles. b) Agarose gel electrophoresis (AGE) characterization of Cy5.5-labeled particles imaged under Cy5.5 channel. Numbers on lanes indicate the percentage of labeled strands in the final structure. At ratio 25:75 of Cy5.5-HE$_{12}$-DNA/unlabeled HE$_{12}$-DNA strands, the structures show highest fluorescence intensity and morphological integrity. c)

Atomic force microscopy (AFM) images of Cy5.5-labeled nanoparticles showing monodisperse structures with average diameter of 26.8 ± 2.7 nm. c) DLS histogram of Cy5.5-labeled HE_{12}-SNAs showing an in-solution hydrodynamic radius of 11.8 ± 0.4 nm.

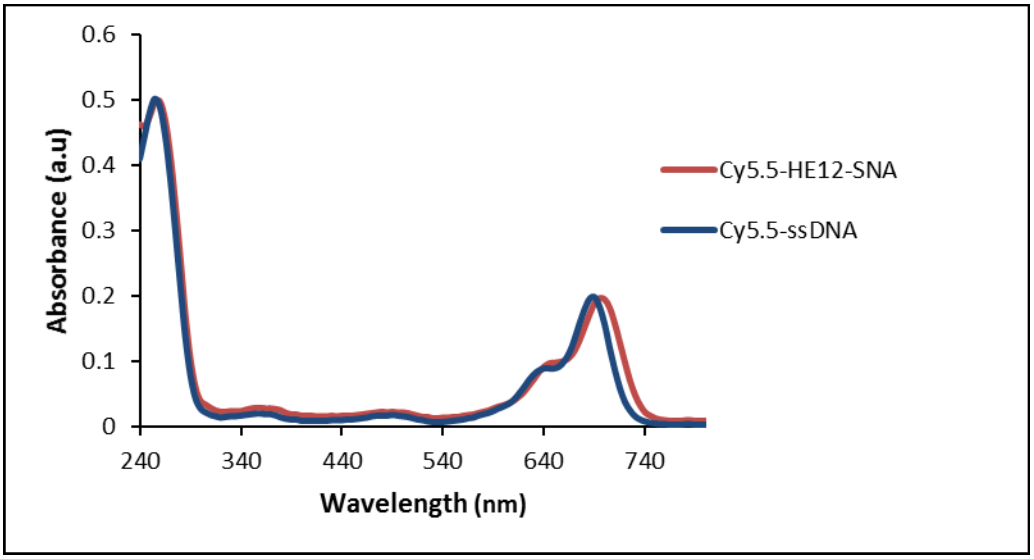

Figure 2.42 – UV-vis spectroscopy of Cy5.5-labeled nanoparticles and Cy5.5-ssDNA used for in vivo studies.

2.5.14.2 In vivo fluorescence imaging in CD1 mice

Experiments for *in vivo* imaging were performed according to a protocol approved by McGill University Animal Care Committee and Lady David Institute for Medical Research Animal Facility (approval # 2013-7350). 12 CD-1 mice were used to determine the biodistribution of Cy5.5-labeled HE_{12}-SNAs by using the IVIS system. Mice were divided in 4 groups: control (4 mice), unlabeled HE_{12}-SNAs (2 mice), Cy5.5 (2 mice), Cy5.5-ssDNA (2 mice) and Cy5.5-labeled HE_{12}-SNAs (2 mice). The biodistribution was evaluated after intraperitoneal or intravenous route of administration. HE_{12}-DNA nanoparticles (100 µL at 17 µM total DNA) were injected in a single dose. The mice were then anesthetized with isoflurane, and then the fluorescence measured using the In Vivo Imaging System (IVIS), 15 mins, 30 mins, 1 hours, 2 hours, 4 hours, 6 hours and 24 hours after treatment. Survival time: 30 hours. Euthanasia: after 30 hours, the mice were euthanized with isoflurane followed by cervical dislocation.

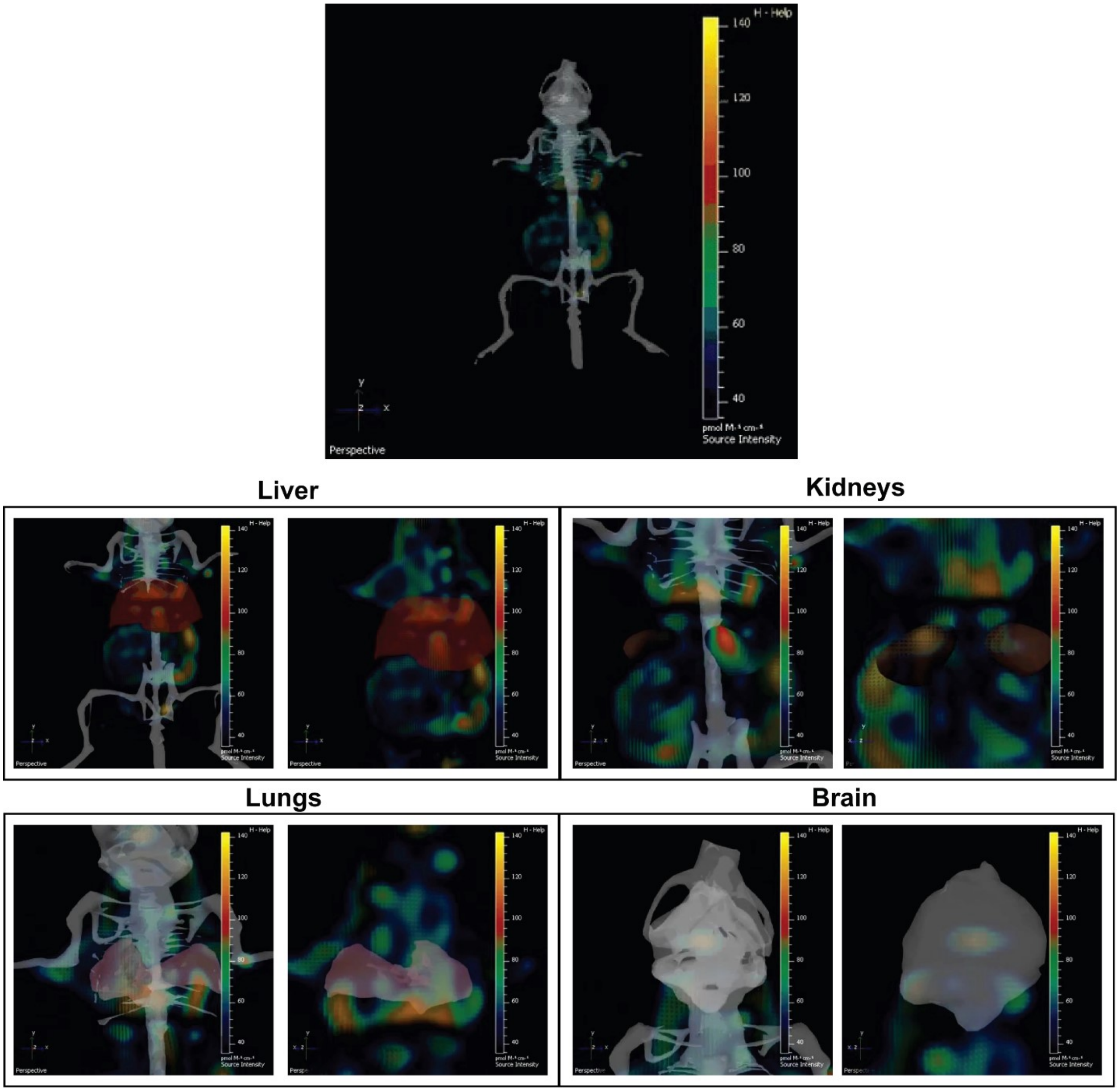

Figure 2.43 – Organ-specific fluorescence of Cy5.5-SNAs after 2 hours. 3D full body fluorescence scan at 2 hrs, overlaid with body organs (liver highlighted in red). Organ-specific distribution showing low nanoparticle accumulation in the liver, kidneys and brain.

2.5.14.3 In vivo fluorescence imaging in HCT116 xenograft models

Intraperitoneal injection

Six female nude mice received subcutaneous injections in the left flank with $3\text{x}10^6$ HCT116 cells in 0.2 mL of saline through a 27-gauge needle. Three weeks later, when the tumor reached a mean tumor volume of 140 mm3, the 5 mice bearing subcutaneous tumors were divided into control (2 mice) or test groups (3 mice). Mice from the test group received intraperitoneal injection of Cy5.5-conjugated DNA nanoparticles in a single dose (100 µL at 17µM total DNA). To assess the biodistribution, mice were anesthetized with isoflurane then fluorescence was measured 0 minutes, 15 minutes, 30 minutes, 1 hour, 2 hours, 4 hours, 6 hours, and 24 hours after injection of Cy5.5-conjugated DNA nanoparticles using the In Vivo Imaging System (IVIS).

Intravenous injection

Six female nude mice received subcutaneous injections in the left flank with $3\text{x}10^6$ HCT116 cells in 0.2 mL of saline through a 27-gauge needle. Three weeks later, when the tumor reached a mean tumor volume of 140 mm^3, the 6 mice bearing subcutaneous tumors were divided into control (2 mice) or test groups (3 mice). Mice from the test group received intravenous injection of Cy5.5-conjugated DNA nanoparticles in a single dose (300 µL at 17µM total DNA). To assess the biodistribution, mice were anesthetized with isoflurane then fluorescence was measured 0 minutes, 15 minutes, 30 minutes, 1 hour, 2 hours, 4 hours, 6 hours, and 24 hours after injection of Cy5.5-conjugated DNA nanoparticles using the In Vivo Imaging System (IVIS).

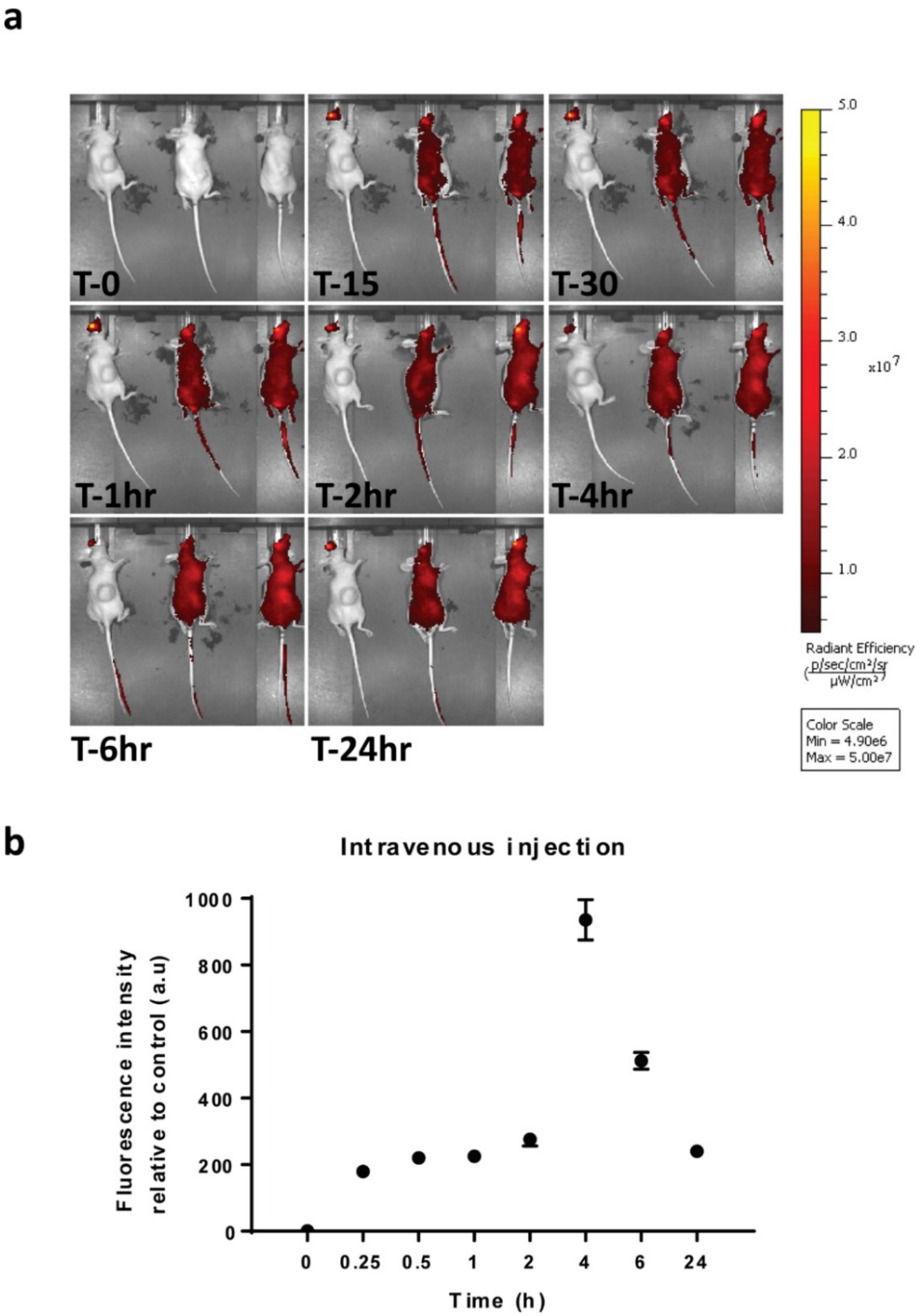

Figure 2.44 – *In vivo* imaging of Cy5.5-labeled HE_{12}-SNAs in HCT116 xenografts following intravenous injection.

2.6 References

1. Hallek, M., *Hematology Am. Soc. Hematol. Educ. Program* **2009**, 440-9.
2. Peer, D.; Karp, J. M.; Hong, S.; Farokhzad, O. C.; Margalit, R.; Langer, R., *Nat. Nano.* **2007,** *2* (12), 751-760.
3. Kukowska-Latallo, J. F.; Candido, K. A.; Cao, Z.; Nigavekar, S. S.; Majoros, I. J.; Thomas, T. P.; Balogh, L. P.; Khan, M. K.; Baker, J. R., *Cancer Res.* **2005,** *65* (12), 5317-5324.
4. Symon, Z.; Peyser, A.; Tzemach, D.; Lyass, O.; Sucher, E.; Shezen, E.; Gabizon, A., *Cancer* **1999,** *86* (1), 72-8.
5. Danson, S.; Ferry, D.; Alakhov, V.; Margison, J.; Kerr, D.; Jowle, D.; Brampton, M.; Halbert, G.; Ranson, M., *Br. J. Cancer* **2004,** *90* (11), 2085-91.
6. Nakanishi, T.; Fukushima, S.; Okamoto, K.; Suzuki, M.; Matsumura, Y.; Yokoyama, M.; Okano, T.; Sakurai, Y.; Kataoka, K., *J. Controlled Release* **2001,** *74* (1–3), 295-302.
7. Flenniken, M. L.; Liepold, L. O.; Crowley, B. E.; Willits, D. A.; Young, M. J.; Douglas, T., *Chem. Commun. (Camb.)* **2005,** (4), 447-9.
8. Ren, Y.; Wong, S. M.; Lim, L. Y., *Bioconjug. Chem.* **2007,** *18* (3), 836-43.
9. Hirsch, L. R.; Stafford, R. J.; Bankson, J. A.; Sershen, S. R.; Rivera, B.; Price, R. E.; Hazle, J. D.; Halas, N. J.; West, J. L., *Proc. Natl. Acad. Sci. U. S. A.* **2003,** *100* (23), 13549-54.
10. Kam, N. W.; O'Connell, M.; Wisdom, J. A.; Dai, H., *Proc. Natl. Acad. Sci. U. S. A.* **2005,** *102* (33), 11600-5.
11. Ediriwickrema, A.; Saltzman, W. M., *ACS Biomater. Sci. Eng.* **2015,** *1* (2), 64-78.
12. Petros, R. A.; DeSimone, J. M., *Nat. Rev. Drug Discov.* **2010,** *9* (8), 615-27.
13. Choi, H. S.; Liu, W.; Liu, F.; Nasr, K.; Misra, P.; Bawendi, M. G.; Frangioni, J. V., *Nat. Nano.* **2010,** *5* (1), 42-47.
14. De Jong, W. H.; Borm, P. J. A., *Int. J. Nanomed.* **2008,** *3* (2), 133-149.
15. Mu, Q.; Jiang, G.; Chen, L.; Zhou, H.; Fourches, D.; Tropsha, A.; Yan, B., *Chem. Rev.* **2014,** *114* (15), 7740-7781.
16. Prabhu, R. H.; Patravale, V. B.; Joshi, M. D., *Int. J. Nanomed.* **2015,** *10*, 1001-1018.
17. Kwon, G. S.; Naito, M.; Kataoka, K.; Yokoyama, M.; Sakurai, Y.; Okano, T., *Colloids Surf., B* **1994,** *2* (4), 429-434.
18. Savic, R.; Eisenberg, A.; Maysinger, D., *J. Drug Target.* **2006,** *14* (6), 343-55.
19. Kwak, M.; Herrmann, A., *Chem. Soc. Rev.* **2011,** *40* (12), 5745-5755.
20. Vyborna, Y.; Vybornyi, M.; Rudnev, A. V.; Häner, R., *Angew. Chem. Int. Ed.* **2015,** *54* (27), 7934-7938.
21. Zhao, Z.; Wang, L.; Liu, Y.; Yang, Z.; He, Y.-M.; Li, Z.; Fan, Q.-H.; Liu, D., *Chem. Commun.* **2012,** *48* (78), 9753-9755.
22. Alemdaroglu, F. E.; Alemdaroglu, N. C.; Langguth, P.; Herrmann, A., *Adv. Mater.* **2008,** *20* (5), 899-902.
23. Mirkin, C. A.; Letsinger, R. L.; Mucic, R. C.; Storhoff, J. J., *Nature* **1996,** *382* (6592), 607-9.
24. Rosi, N. L.; Giljohann, D. A.; Thaxton, C. S.; Lytton-Jean, A. K.; Han, M. S.; Mirkin, C. A., *Science* **2006,** *312* (5776), 1027-30.
25. Jensen, S. A.; Day, E. S.; Ko, C. H.; Hurley, L. A.; Luciano, J. P.; Kouri, F. M.; Merkel, T. J.; Luthi, A. J.; Patel, P. C.; Cutler, J. I.; Daniel, W. L.; Scott, A. W.; Rotz, M. W.; Meade, T. J.; Giljohann, D. A.; Mirkin, C. A.; Stegh, A. H., *Sci. Transl. Med.* **2013,** *5* (209), 209ra152.

26. Wang, X.; Hao, L.; Bu, H. F.; Scott, A. W.; Tian, K.; Liu, F.; De Plaen, I. G.; Liu, Y.; Mirkin, C. A.; Tan, X. D., *Sci. Rep.* **2016,** *6*, 31687.
27. Edwardson, T. G.; Carneiro, K. M.; Serpell, C. J.; Sleiman, H. F., *Angew. Chem. Int. Ed. Engl.* **2014,** *53* (18), 4567-71.
28. Burns, J. R.; Göpfrich, K.; Wood, J. W.; Thacker, V. V.; Stulz, E.; Keyser, U. F.; Howorka, S., *Angew. Chem. Int. Ed.* **2013,** *52* (46), 12069-12072.
29. Krishnan, S.; Ziegler, D.; Arnaut, V.; Martin, T. G.; Kapsner, K.; Henneberg, K.; Bausch, A. R.; Dietz, H.; Simmel, F. C., *Nature Communications* **2016,** *7*, 12787.
30. Fendt, L.-A.; Bouamaied, I.; Thöni, S.; Amiot, N.; Stulz, E., *J. Am. Chem. Soc.* **2007,** *129* (49), 15319-15329.
31. Schreiber, R.; Do, J.; Roller, E.-M.; Zhang, T.; Schuller, V. J.; Nickels, P. C.; Feldmann, J.; Liedl, T., *Nat. Nano.* **2014,** *9* (1), 74-78.
32. Zhang, Q.; Jiang, Q.; Li, N.; Dai, L.; Liu, Q.; Song, L.; Wang, J.; Li, Y.; Tian, J.; Ding, B.; Du, Y., *ACS Nano* **2014,** *8* (7), 6633-43.
33. Rothemund, P. W. K., *Nature* **2006,** *440* (7082), 297-302.
34. Chien, M.-P.; Rush, A. M.; Thompson, M. P.; Gianneschi, N. C., *Angew. Chem. Int. Ed.* **2010,** *49* (30), 5076-5080.
35. Zhang, F.; Zhang, S.; Pollack, S. F.; Li, R.; Gonzalez, A. M.; Fan, J.; Zou, J.; Leininger, S. E.; Pavía-Sanders, A.; Johnson, R.; Nelson, L. D.; Raymond, J. E.; Elsabahy, M.; Hughes, D. M. P.; Lenox, M. W.; Gustafson, T. P.; Wooley, K. L., *J. Am. Chem. Soc.* **2015,** *137* (5), 2056-2066.
36. Appukutti, N.; Serpell, C. J., *Polymer Chemistry* **2018,** *9* (17), 2210-2226.
37. Wu, Y.; Sefah, K.; Liu, H.; Wang, R.; Tan, W., *Proc. Natl. Acad. Sci. U. S. A.* **2010,** *107* (1), 5-10.
38. Kedracki, D.; Maroni, P.; Schlaad, H.; Vebert-Nardin, C., *Adv. Funct. Mater.* **2014,** *24* (8), 1133-1139.
39. Fakhoury, J. J.; Edwardson, T. G.; Conway, J. W.; Trinh, T.; Khan, F.; Barlog, M.; Bazzi, H. S.; Sleiman, H. F., *Nanoscale* **2015,** *7* (48), 20625-34.
40. Jeong, J. H.; Park, T. G., *Bioconjugate Chem.* **2001,** *12* (6), 917-923.
41. Rush, A. M.; Nelles, D. A.; Blum, A. P.; Barnhill, S. A.; Tatro, E. T.; Yeo, G. W.; Gianneschi, N. C., *J. Am. Chem. Soc.* **2014,** *136* (21), 7615-7618.
42. Li, Z.; Zhang, Y.; Fullhart, P.; Mirkin, C. A., *Nano Lett.* **2004,** *4* (6), 1055-1058.
43. Serpell, C. J.; Edwardson, T. G. W.; Chidchob, P.; Carneiro, K. M. M.; Sleiman, H. F., *J. Am. Chem. Soc.* **2014,** *136* (44), 15767-15774.
44. Chidchob, P.; Edwardson, T. G. W.; Serpell, C. J.; Sleiman, H. F., *J. Am. Chem. Soc.* **2016,** *138* (13), 4416-4425.
45. Trinh, T.; Chidchob, P.; Bazzi, H. S.; Sleiman, H. F., *Chem. Commun.* **2016,** *52* (72), 10914-10917.
46. Alemdaroglu, F. E.; Ding, K.; Berger, R.; Herrmann, A., *Angew. Chem. Int. Ed. Engl.* **2006,** *45* (25), 4206-10.
47. Alemdaroglu, F. E.; Alemdaroglu, N. C.; Langguth, P.; Herrmann, A., *Macromol. Rapid Commun.* **2008,** *29* (4), 326-329.
48. Hallek, M., *Am. J. Hematol.* **2015,** *90* (5), 446-460.
49. Rai, K. R.; Peterson, B. L.; Appelbaum, F. R.; Kolitz, J.; Elias, L.; Shepherd, L.; Hines, J.; Threatte, G. A.; Larson, R. A.; Cheson, B. D.; Schiffer, C. A., *N. Engl. J. Med.* **2000,** *343* (24), 1750-7.

50. Hillmen, P.; Skotnicki, A. B.; Robak, T.; Jaksic, B.; Dmoszynska, A.; Wu, J.; Sirard, C.; Mayer, J., *J. Clin. Oncol.* **2007,** *25* (35), 5616-23.

51. O'Brien, S. M.; Kantarjian, H. M.; Cortes, J.; Beran, M.; Koller, C. A.; Giles, F. J.; Lerner, S.; Keating, M., *J. Clin. Oncol.* **2001,** *19* (5), 1414-20.

52. Keating, M. J.; O'Brien, S.; Albitar, M.; Lerner, S.; Plunkett, W.; Giles, F.; Andreeff, M.; Cortes, J.; Faderl, S.; Thomas, D.; Koller, C.; Wierda, W.; Detry, M. A.; Lynn, A.; Kantarjian, H., *J. Clin. Oncol.* **2005,** *23* (18), 4079-88.

53. Wierda, W.; O'Brien, S.; Wen, S.; Faderl, S.; Garcia-Manero, G.; Thomas, D.; Do, K. A.; Cortes, J.; Koller, C.; Beran, M.; Ferrajoli, A.; Giles, F.; Lerner, S.; Albitar, M.; Kantarjian, H.; Keating, M., *J. Clin. Oncol.* **2005,** *23* (18), 4070-8.

54. Tam, C. S.; O'Brien, S.; Wierda, W.; Kantarjian, H.; Wen, S.; Do, K. A.; Thomas, D. A.; Cortes, J.; Lerner, S.; Keating, M. J., *Blood* **2008,** *112* (4), 975-80.

55. Datta, S. R.; Brunet, A.; Greenberg, M. E., *Genes Dev.* **1999,** *13* (22), 2905-2927.

56. Alessi, D. R.; James, S. R.; Downes, C. P.; Holmes, A. B.; Gaffney, P. R.; Reese, C. B.; Cohen, P., *Curr. Biol.* **1997,** *7* (4), 261-9.

57. Cuni, S.; Perez-Aciego, P.; Perez-Chacon, G.; Vargas, J. A.; Sanchez, A.; Martin-Saavedra, F. M.; Ballester, S.; Garcia-Marco, J.; Jorda, J.; Durantez, A., *Leukemia* **2004,** *18* (8), 1391-400.

58. Stokoe, D.; Stephens, L. R.; Copeland, T.; Gaffney, P. R.; Reese, C. B.; Painter, G. F.; Holmes, A. B.; McCormick, F.; Hawkins, P. T., *Science* **1997,** *277* (5325), 567-70.

59. Datta, S. R.; Dudek, H.; Tao, X.; Masters, S.; Fu, H.; Gotoh, Y.; Greenberg, M. E., *Cell* **1997,** *91* (2), 231-41.

60. Cardone, M. H.; Roy, N.; Stennicke, H. R.; Salvesen, G. S.; Franke, T. F.; Stanbridge, E.; Frisch, S.; Reed, J. C., *Science* **1998,** *282* (5392), 1318-21.

61. Kops, G. J. P. L.; Burgering, B. M. T., *J. Anat.* **2000,** *197* (Pt 4), 571-574.

62. Liu, W.-L.; Gao, M.; Tzen, K.-Y.; Tsai, C.-L.; Hsu, F.-M.; Cheng, A.-L.; Cheng, J. C.-H., *Oncotarget* **2014,** *5* (11), 3662-3672.

63. Hu, Y.; Guo, R.; Wei, J.; Zhou, Y.; Ji, W.; Liu, J.; Zhi, X.; Zhang, J., *Cell Death Dis.* **2015,** *6* (12), e2020.

64. Liu, Q.; Turner, K. M.; Alfred Yung, W. K.; Chen, K.; Zhang, W., *Neuro Oncol.* **2014,** *16* (10), 1313-1323.

65. Maira, S. M.; Pecchi, S.; Huang, A.; Burger, M.; Knapp, M.; Sterker, D.; Schnell, C.; Guthy, D.; Nagel, T.; Wiesmann, M.; Brachmann, S.; Fritsch, C.; Dorsch, M.; Chene, P.; Shoemaker, K.; De Pover, A.; Menezes, D.; Martiny-Baron, G.; Fabbro, D.; Wilson, C. J.; Schlegel, R.; Hofmann, F.; Garcia-Echeverria, C.; Sellers, W. R.; Voliva, C. F., *Mol. Cancer Ther.* **2012,** *11* (2), 317-28.

66. Brachmann, S. M.; Kleylein-Sohn, J.; Gaulis, S.; Kauffmann, A.; Blommers, M. J. J.; Kazic-Legueux, M.; Laborde, L.; Hattenberger, M.; Stauffer, F.; Vaxelaire, J.; Romanet, V.; Henry, C.; Murakami, M.; Guthy, D. A.; Sterker, D.; Bergling, S.; Wilson, C.; Brümmendorf, T.; Fritsch, C.; Garcia-Echeverria, C.; Sellers, W. R.; Hofmann, F.; Maira, S.-M., *Mol. Cancer Ther.* **2012,** *11* (8), 1747.

67. Amrein, L.; Shawi, M.; Grenier, J.; Aloyz, R.; Panasci, L., *Int. J. Cancer* **2013,** *133* (1), 247-52.

68. Ren, H.; Chen, M.; Yue, P.; Tao, H.; Owonikoko, T. K.; Ramalingam, S. S.; Khuri, F. R.; Sun, S.-Y., *Cancer Lett.* **2012,** *325* (2), 139-146.

69. Bendell, J. C.; Rodon, J.; Burris, H. A.; de Jonge, M.; Verweij, J.; Birle, D.; Demanse, D.; De Buck, S. S.; Ru, Q. C.; Peters, M.; Goldbrunner, M.; Baselga, J., *J. Clin. Oncol.* **2012,** *30* (3), 282-90.

70. Heudel, P. E.; Fabbro, M.; Roemer-Becuwe, C.; Kaminsky, M. C.; Arnaud, A.; Joly, F.; Roche-Forestier, S.; Meunier, J.; Foa, C.; You, B.; Priou, F.; Tazi, Y.; Floquet, A.; Selle, F.; Berton-Rigaud, D.; Lesoin, A.; Kalbacher, E.; Lortholary, A.; Favier, L.; Treilleux, I.; Ray-Coquard, I., *Br. J. Cancer* **2017,** *116* (3), 303-309.

71. Torchilin, V. P., *J. Control. Release* **2001,** *73* (2-3), 137-72.

72. Gao, Z.; Lukyanov, A. N.; Singhal, A.; Torchilin, V. P., *Nano Lett.* **2002,** *2* (9), 979-982.

73. Adams, M. L.; Lavasanifar, A.; Kwon, G. S., *J. Pharm. Sci.* **2003,** *92* (7), 1343-1355.

74. Woo, S.; Rothemund, P. W., *Nat Commun* **2014,** *5*, 4889.

75. Hahn, J.; Wickham, S. F.; Shih, W. M.; Perrault, S. D., *ACS Nano* **2014,** *8* (9), 8765-75.

76. Gerling, T.; Wagenbauer, K. F.; Neuner, A. M.; Dietz, H., *Science* **2015,** *347* (6229), 1446-52.

77. Fogh-Andersen, N.; Christiansen, T. F.; Komarmy, L.; Siggaard-Andersen, O., *Clin. Chem.* **1978,** *24* (9), 1545-52.

78. Hayden, R. E.; Pratt, G.; Roberts, C.; Drayson, M. T.; Bunce, C. M., *Leuk. Lymphoma* **2012,** *53* (4), 537-49.

79. Shehata, M.; Schnabl, S.; Demirtas, D.; Hilgarth, M.; Hubmann, R.; Ponath, E.; Badrnya, S.; Lehner, C.; Hoelbl, A.; Duechler, M.; Gaiger, A.; Zielinski, C.; Schwarzmeier, J. D.; Jaeger, U., *Blood* **2010,** *116* (14), 2513-21.

80. Locksley, R. M.; Killeen, N.; Lenardo, M. J., *Cell 104* (4), 487-501.

81. van der Bruggen, T.; Nijenhuis, S.; van Raaij, E.; Verhoef, J.; Sweder van Asbeck, B., *Infect. Immun.* **1999,** *67* (8), 3824-3829.

82. North, R. J.; Dunn, P. L.; Havell, E. A., *J. Interferon Res.* **1991,** *11* (6), 333-40.

83. Michishita, M.; Yoshida, Y.; Uchino, H.; Nagata, K., *J. Biol. Chem.* **1990,** *265* (15), 8751-9.

84. Shemi, D.; Azab, A. N.; Kaplanski, J., *J. Endotoxin Res.* **2000,** *6* (5), 377-81.

85. Beaucage, S. L.; Iyer, R. P., *Tetrahedron* **1992,** *48* (12), 2223-2311.

86. Greenspan, P.; Mayer, E. P.; Fowler, S. D., *J. Cell Biol.* **1985,** *100* (3), 965-73.

87. Conway, J. W.; McLaughlin, C. K.; Castor, K. J.; Sleiman, H., *Chem. Commun. (Camb.)* **2013,** *49* (12), 1172-4.

Preface

Building on the findings from Chapter 2, Chapter 3 evaluates strategies to tackle limitations of amphiphilic nanocarriers in drug delivery. Optimization studies of our first-generation DNA-nanoparticle delivery system begin with the introduction of targeting aptamer ligands that show enhanced structural uptake in specific cancer cell types. Then, a stimuli-responsive system is presented that shows selective release of cargo upon binding to a genetic marker. The cellular uptake of DNA nanoparticles and intracellular structural integrity are evaluated in normal human skin cells. Detailed studies are conducted on the interaction of DNA-nanoparticles with serum proteins. Finally, strategies to increase nanoparticle stability are examined. These include modifying the DNA for enhanced nuclease stability, decorating particles with shielding polymers that selectively shed in tumor microenvironments, and cross-linking of particles for enhanced stability. The strategies are expected to provide a fundamental understanding of the challenges facing nanoparticle-based systems in drug delivery and pave the way for a highly customized system for increased selectivity, stability and therapeutic effect.

Lab Coat Rationale…

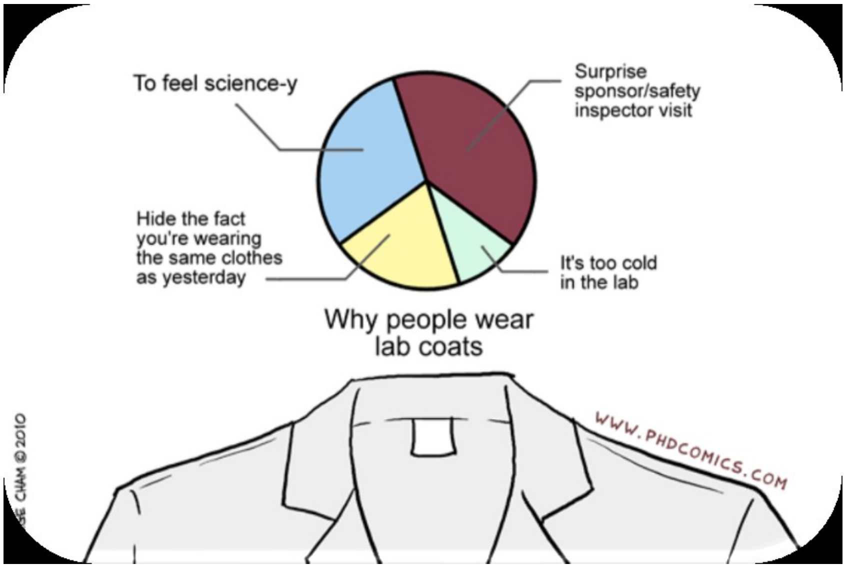

3

Optimization of DNA Nanostructures for Targeted Drug Delivery Applications

A small portion of this chapter is published as "Precision spherical nucleic acids for delivery of anticancer drugs" by Danny Bousmail, Lilian Amrein, Johans J. Fakhoury, Hassan H. Fakih, John C. C. Hsu, Lawrence Panasci and Hanadi F. Sleiman. *Chemical Science*, 2017, **8**, 6218.

Contribution of authors

Danny Bousmail helped design the project and primarily contributed to the production of experimental data for targeted delivery studies, stimuli-responsive nanoparticles, uptake in skin cells, nanoparticle interaction with serum proteins and cross-linking studies. **Hassan Fakih** carried out flow cytometry experiments. **Johans Fakhoury** and **Katherine Bujold** carried out confocal microscopy in skin cells. **Alexander Prinzen** synthesized the PEG-azide and PEG-acetal-azide derivatives and helped with the synthesis of disulfide-modified DNA-polymer conjugates. **Hanadi F. Sleiman** designed the project, guided interpretation of data and discussion of results.

Studies on NHEK skin cells were performed in consultation with ***L'Oreal USA.***

3.1 Abstract

Nanoparticles are faced with many challenges as they are translated into clinical applications. These challenges include non-specific delivery to healthy tissue, off-target release of therapeutics, instability due to high dilution, interaction with serum proteins and nuclease degradation. In this chapter, we describe different strategies that address the above limitations using the DNA nanoparticle platform described in Chapter 2. Using different approaches, we demonstrate the targeted cellular uptake, selective-cargo release upon stimuli, increased blood serum and nuclease stability of DNA nanostructures. We further show the increased uptake and evaluate the intracellular fate of structures in normal skin cells. These various approaches can be implemented within a single DNA nanostructure creating a highly functional "smart" nanodevice for potential applications in biomedicine.

3.2 Introduction

Targeted delivery of therapeutic agents to specific organs or tissue is a challenging task. This is especially true for small molecule drugs which cannot distinguish between normal and diseased states, causing undesirable side effects.[1] To address this problem, one strategy is to use polymeric nanoparticles equipped with targeting ligands for specific cancer cell types.[2] Among polymeric carriers, spherical amphiphilic DNA nanoparticles have emerged as a particularly interesting class due to the unique properties of DNA.[3] These structures are made up of a hydrophobic core composed of polymeric material, and a hydrophilic corona composed of DNA. The hydrophilic DNA shell provides many advantages: it can be used for attaching a number of different targeting ligands for increased accumulation of nanostructures in cancer specific cell-types.[4] Additionally, the molecular recognition properties of DNA can be exploited to generate stimuli-responsive nanoparticles.[5-7] This system is desirable as it allows conditional release of cargo upon recognition of a specific genetic marker, allowing cytoplasmic target-specific delivery of therapeutics. Systems combining targeted and stimuli-responsive delivery could offer "smart" materials with specificity for both cellular and intracellular markers. For structures designed to exhibit intracellular activity, several mechanistic studies on nanostructures in intracellular environments have appeared.[8] However, no universal consensus has been reached thus far. For example, polymeric nanoparticles have been observed to enter multiple intracellular compartments, such as the cytosol, Golgi apparatus and endoplasmic reticulum.[9] Lipid nanoparticles containing siRNA have been shown to get trapped and recycled by the endocytic pathway.[10] Chitosan nanoparticles end up in the lysosome,[11] while peptide-gold nanoparticles get trapped inside endosomes.[12] Hence, it would be of great value to understand the intracellular behaviour of nanostructures, which would provide a better understanding of structure-activity relationships and largely aid in system design.

Over the past two decades, a number of receptor-targeting small molecules have been reported.[13] More recently, a new class of oligonucleotide targeting ligands has emerged, known as aptamers.[14] These are single-stranded oligonucleotides (DNA or RNA) that fold into 3D motifs and bind targets with high affinity and excellent selectivity.[15] Compared to antibodies, aptamers possess a few important advantages, such as lack of immunogenicity, small size and ease of synthesis and modification.[16-17] Additionally, it has been shown that multi-valency, or the presentation of multiple aptamers on nanostructure surfaces, results in greatly improved binding affinity of the aptamers.[18] However, this requires smart design as steric hindrance between neighbouring aptamers can affect receptor binding.[19] These properties have afforded aptamers many applications in delivery chemotherapeutic nanoparticles and nucleic acid therapeutics *in vivo*.[20-21] Most recently, a DNA-based HER2-specific aptamer (HB5) has been shown to selectively bind to HER2 protein and HER2-positive cancer cells.[22-23] HB5 was also shown to selectively deliver doxorubicin to HER2-positive cancer cells *in vitro*.[24] Therefore, the integration of multi-valent HB5 aptamers with DNA nanoparticles would provide a promising strategy for nanocarrier-based targeted delivery to HER2-positive cancer cells.

Micellar DNA nanoparticles with targeting ligands show promise in biomedicine.[4] However, there are more and more reports indicating that micelles are less stable when in contact with biological media.[25] This is mainly due to disintegration upon dilution, the interaction of particles with serum proteins and their susceptibility to nuclease degradation in serum.[26-28] To overcome the burden of nuclease degradation, strategies have been proposed which include modifications to the ribose sugars, phosphate backbone or coating structures with amino acid-poly (ethylene glycol) (PEG) oligomers.[29-31] Additionally, the use of molecules such as PEG that aid prolonged circulation could provide a second layer of protection against serum proteins and nucleases, further improving structural stability.[32] To overcome the premature disintegration of micellar structures, a simple and straightforward strategy is to stabilize them *via* crosslinking, thereby assuring prolonged circulation times and efficient target site accumulation.[33-34]

In this chapter, we demonstrate different strategies for optimizing micellar DNA nanoparticles for drug delivery applications. We show the successful decoration of HB5 aptamers on DNA nanoparticles, and the increased cellular uptake of HER2-functionalized particles in cells overexpressing target receptors. We further show an example of stimuli-responsive DNA nanoparticles that release an oligonucleotide-small molecule cargo upon recognition of miR134 trigger, a microRNA involved in cellular differentiation. The cellular uptake of DNA particles in different cell lines and their intracellular structural integrity are explored in relevance to normal human epidermal keratinocytes (NHEK). Strategies to increase the stability of DNA nanoparticles are then explored. First, we show that phosphorothioated DNA nanoparticles exhibit significantly increased serum stability compared to unmodified DNA nanoparticles. Secondly, we show that the dense oligonucleotide corona protects DNA nanoparticles from interacting with human serum albumin (HSA), a major component of blood serum. We further show the successful attachment of PEG moieties to DNA nanoparticles through cleavable linkers towards increasing the circulation-lifetime of the structures and tumor-selective release of coating. Finally, we report cross-linking approaches to enhance nanoparticle stability. These studies demonstrate different strategies that are now made compatible with DNA nanoparticle assemblies towards optimizing several important parameters for drug delivery systems. Moreover, this work provides a comprehensive understanding of the challenges faced by nanostructures in biomedicine, fundamental to the design of any nanoparticle-based drug delivery platform. Compared to other systems which are less customizable due to exhaustive synthesis, purification or incompatibility of different modifications, the work in this chapter highlights the added advantages of multiple modifications in a single particle towards a tailored drug delivery system exhibiting higher stability, selectivity and therapeutic effect.

3.3 Results and Discussion

3.3.1 Targeted delivery to HER2-positive breast cancer

3.3.1.1 Design, synthesis and activity of aptamer-DNA nanoparticles

Two different design strategies of aptamer-DNA nanoparticles were proposed. The aptamer of choice is a HER2-specific DNA aptamer known as HeA2_3 as reported by Gijs and co-workers (Figure 3.1a).[23] This aptamer is a short optimized version of HB5 that has shown nanomolar range binding affinity to HER2 receptors, and high specificity and internalization in HER2-positive cells. In our first design, the aptamer was synthesized as part of the DNA-polymer conjugate. As such, solid-phase DNA synthesis was used to generated short HB5 aptamer-polymer conjugates (sHB5-HE$_{12}$ conjugates) where the aptamer portion was separated by a 4 thymidine (T) base spacer from 12 hexaethylene units constituting the polymer segment (Figure 3.1b). This spacer would provide some degree of flexibility to allow more efficient self-annealing of the aptamer into its desired 3D structure. Aptamer-nanoparticles were prepared by mixing different ratios of sHB5-HE_{12} conjugates with 19-mer ssDNA-HE_{12} conjugates followed by addition of assembly buffer and thermal annealing (95 °C – 4 °C over 4 hours). This method yields highly monodisperse spherical particles decorated with DNA aptamers on the exterior (Figure 3.1c). ssDNA-HE_{12} was used in the mix to test whether the crowding of aptamers would hinder its ability for proper folding. Increasing the ratio of ssDNA-HE_{12} would decrease the crowding of DNA aptamers in the structure and could reduce inter-strand cross-talk. Two structures were generated: one containing a high-aptamer density (75% of the overall structures), and another with lower aptamer density of 25% aptamer-HE_{12}-conjugate.

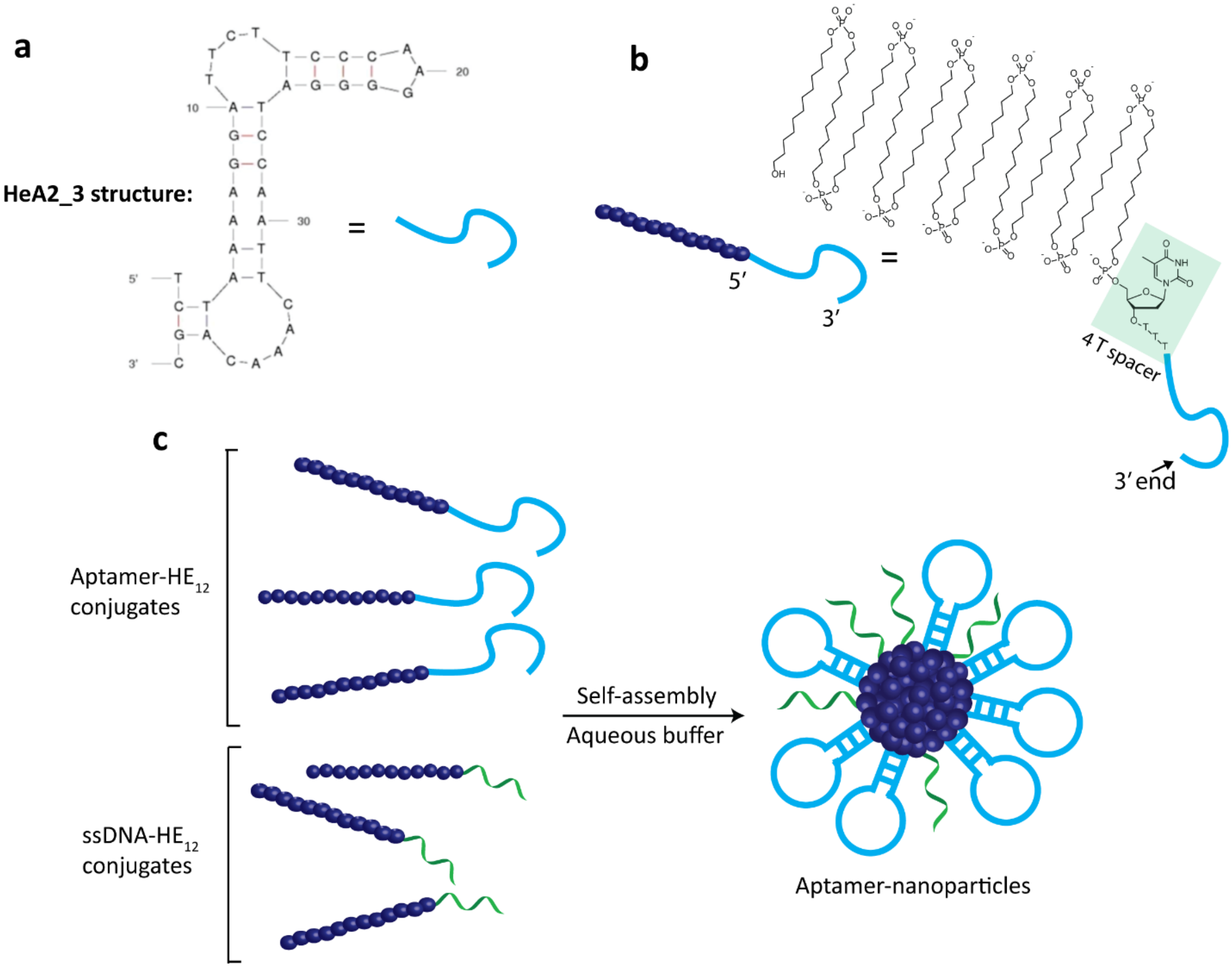

Figure 3.1 – Design and synthesis of aptamer-nanoparticles. a) Structure of HeA2_3 aptamer. b) Structure and schematic representation of the sHB5 aptamer-polymer conjugate. The DNA aptamer was synthesis first by solid-phase synthesis, then 4 thymine (T) nucleotides were added, followed by

the addition of 12 HE units as the polymer segment. c) Schematic representation of the formation of aptamer nanoparticles with different ratios of aptamer from mixtures of aptamer-HE_{12} and ssDNA-HE_{12} conjugates.

Spherical DNA nanoparticles were generated by the self-assembly of aptamer-DNA conjugates in aqueous media. These structures were characterized by agarose gel electrophoresis (AGE) and atomic force microscopy (AFM) (Figure 3.2). Aptamer-nanoparticles were observed by AGE as a tight band with lower mobility as compared to ssDNA-nanoparticles (Figure 3.2a). This indicates the presence of uniform larger structures as compared to spherical ssDNA nanoparticles. Increasing the ratio of aptamer in the mixture from 25% to 75% and 100% resulted in a gel mobility shift, indicating that the overall structure got larger as the ratio of aptamer-containing strands was increased. This result was expected, considering the aptamer folds into a 3D structure that increases the overall size of the nanostructure, compared to bare 19-mer ssDNA. DNA-aptamer structures were further characterized by AFM. As an example, AFM of aptamer nanoparticles containing a ratio of 75% aptamer to 25% ssDNA are illustrated in Figure 3.2b. Spherical structures were observed on surface with a diameter of 50 nm and height of 8 nm.

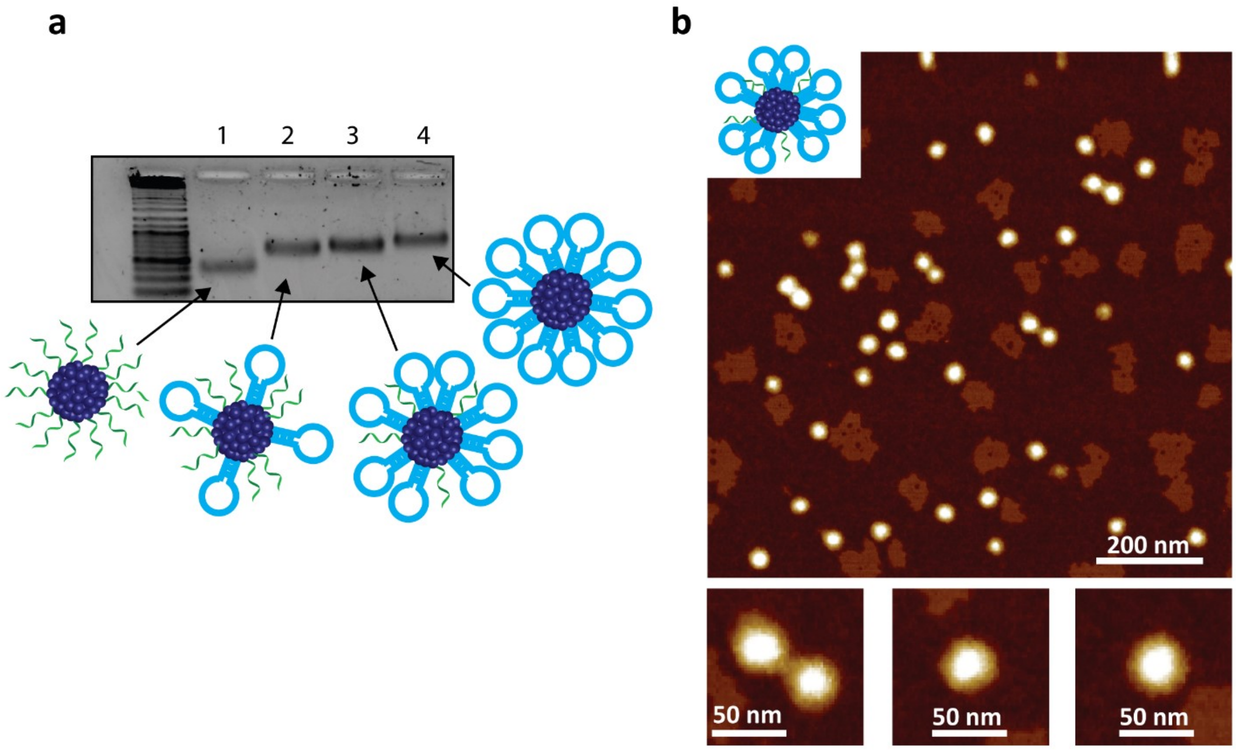

Figure 3.2 – Characterization of aptamer-micelles. a) Agarose gel electrophoresis showing a mobility shift as a result of a higher aptamer ratio in the structure. Lane 1: 100% ssDNA nanoparticle, lane 2: 25% aptamer, 75% ssDNA nanoparticle, lane 3: 75% aptamer, 25% ssDNA nanoparticle, lane 4: 100% aptamer-nanoparticle. b) Representative atomic force microscopy image of aptamer nanoparticles assembled at a ratio of 75% aptamer, 25% ssDNA. The ill-defined structures of lower height are salt deposits from the assembly buffer that could be removed with an additional wash step with de-ionized water.

Following characterization, the cellular uptake of sHB5-nanoparticles was investigated. Flow cytometry was used to compare nanoparticle uptake in a HER2-positive cell line, MB453, and the HER2-negative cervical carcinoma cell line (HeLa). As a first step, Cy5.5-labeled aptamer nanoparticles were generated by a method earlier reported in Chapter 2. sHB5-HE_{12} strands were mixed with ssDNA-HE_{12}-Cy5.5 conjugates followed by thermal annealing (for example a 75% aptamer nanoparticle contains 75% sHB5-HE_{12} and 25% ssDNA-HE_{12}-Cy5.5) (Figure 3.3a). This generates spherical nanoparticles with the dye molecules most likely embedded in the hydrophobic core. After a 2-hour incubation, flow cytometry data indicated that while there was high uptake of both aptamer and ssDNA particles, no enhancement in cellular uptake was observed with sHB5 nanoparticles (Figure 3.3b). Both in the HER2-positive and negative cell lines, similar levels of uptake were observed of structures containing no aptamer, low and high aptamer density.

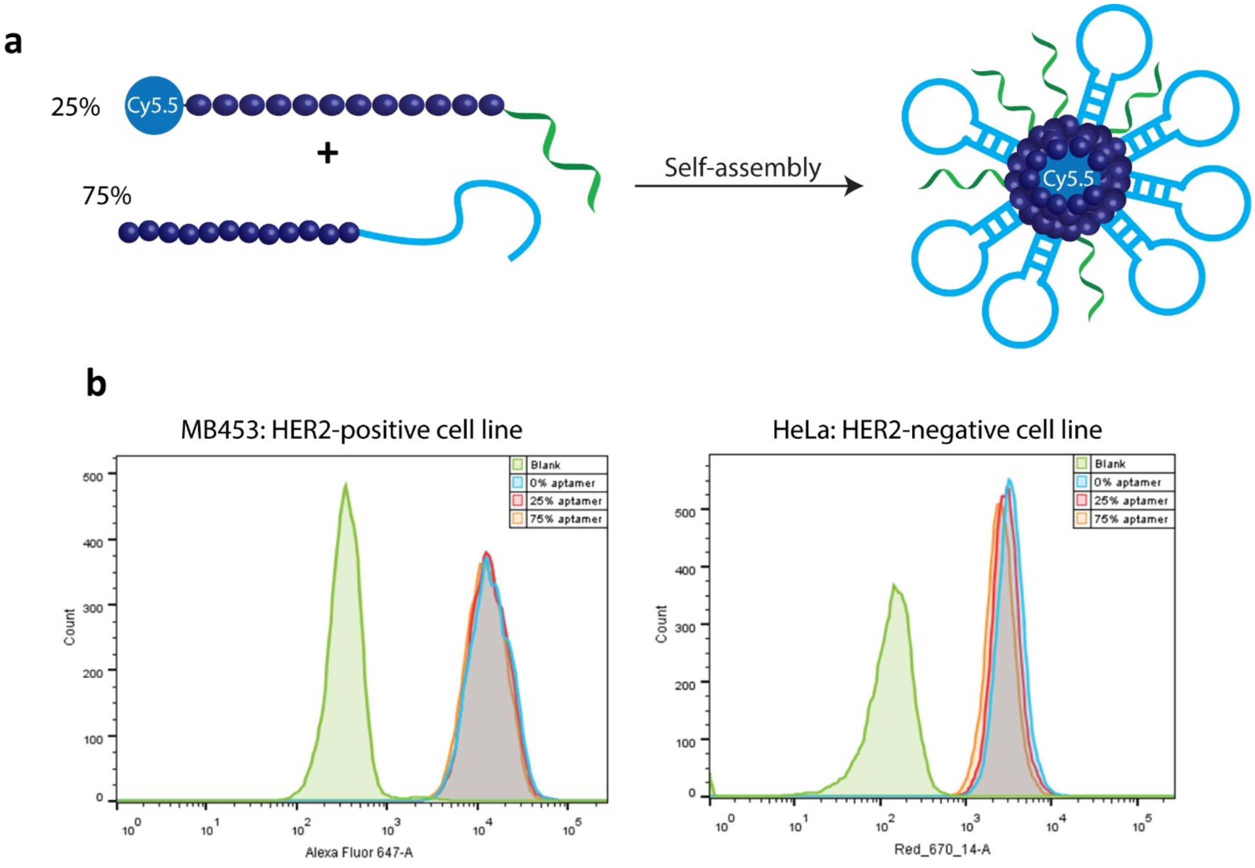

Figure 3.3 – Flow Cytometry measurements of sHB5-nanoparticles in MB453 and HeLa cells. Higher uptake was observed for all nanoparticles, compared to the control, however, aptamer nanoparticles showed no increased uptake in HER2-positive cells compared to DNA structures lacking the aptamer.

In earlier studies, we showed that ssDNA-nanoparticles show high cellular uptake and internalization. Based on the results of the HER2-positive cell lines, we questioned whether the crowding of DNA aptamers influenced their proper folding. Additionally, we asked whether the neighbouring ssDNA could have a masking effect impeding aptamer-receptor recognition. To tackle these questions, a second strategy was proposed wherein sHB5 aptamers were connected to a complementary strand to the ssDNA-nanoparticle (Figure 3.4). In this approach, the aptamer moiety would be projected from the nanoparticle surface. Additionally, a 4-thymine (4 T) spacer was added between the aptamer unit and its extension strand to provide flexibility. In this approach, ssDNA-nanoparticles were first assembled through a thermal annealing cycle (95 °C – 4 °C). Subsequently, aptamers containing complementary extension strands were added at room temperature and incubated for 2 hours to allow binding. Alternatively, structures could be assembled by a one-pot thermal anneal, where ssDNA-HE_{12} conjugates and aptamer strands are mixed prior to a heat/cool cycle. To differentiate these assemblies from the 1^{st} generation particles, these structures will be referred to as "sHB5-particle RT" for room temperature binding and "sHB5-particle 1-pot" for one pot assembly.

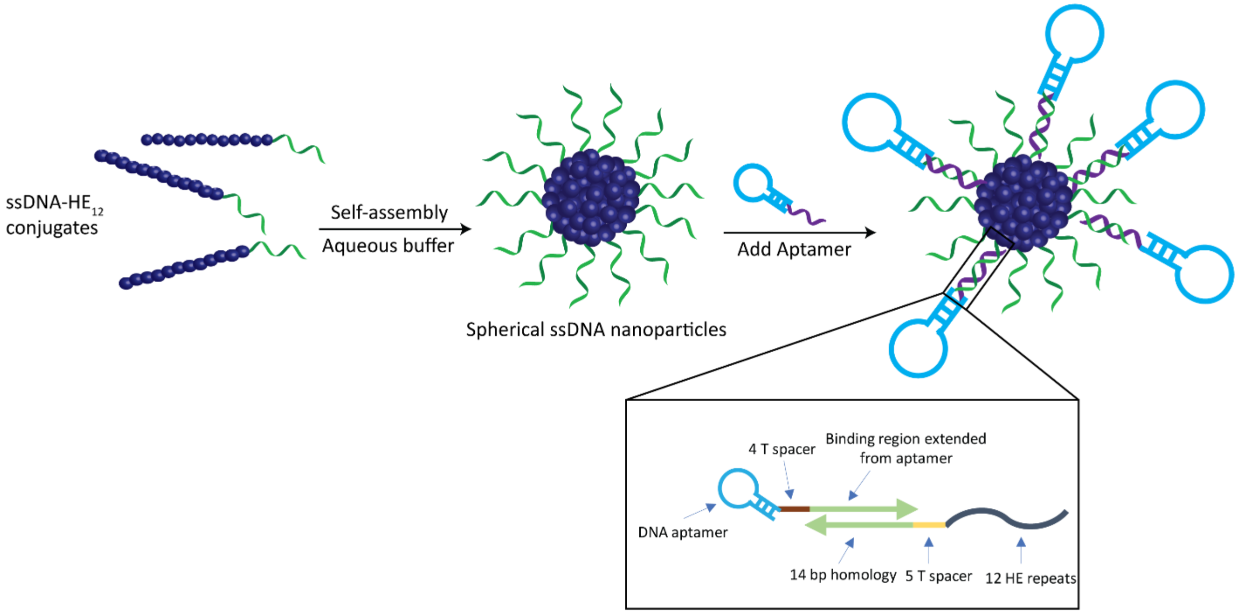

Figure 3.4 – Design of second generation aptamer micelles. In this design, the aptamer is projected from the structure through DNA hybridization.

The next step of this work was to generate dye-labeled aptamer-structures for cellular uptake studies. Cy3-labeled aptamer nanoparticles were generated in a similar protocol as reported earlier. These structures were assembled by mixing 25% ssDNA-HE_{12}-Cy3 with 75% ssDNA-HE_{12} conjugates followed by thermal annealing. To these, 50% aptamer-complementary DNA was added at room temperature (Figure 3.5). For one-pot assembly, the same ratios of strands were mixed then subjected to a heat/cool cycle (95 °C – 4 °C).

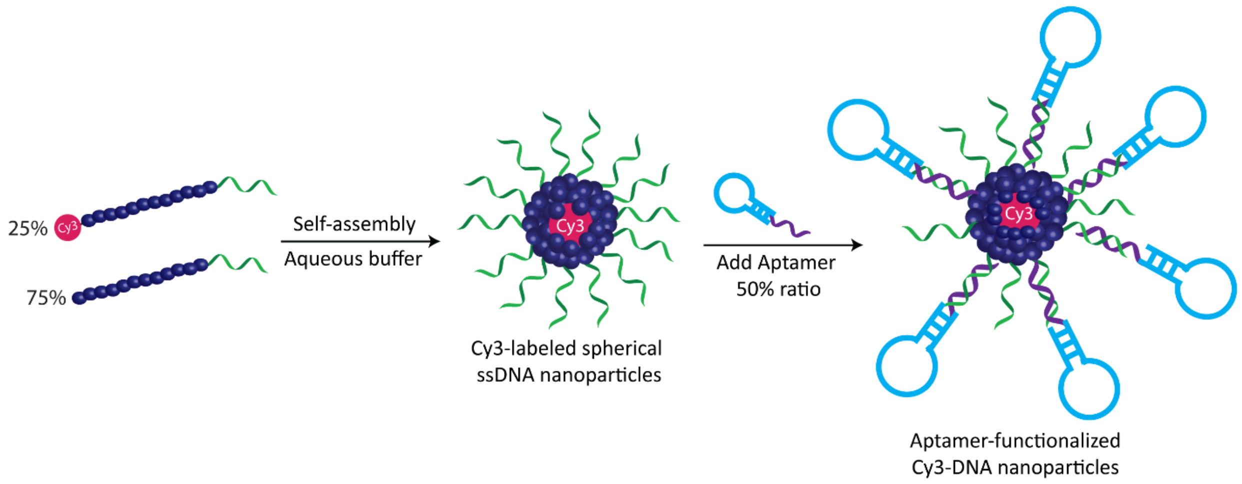

Figure 3.5 – Preparation of sHB5-Cy3-labeled DNA nanoparticles. Spherical Cy3-labeled DNA nanoparticles were prepared as a first step. Then, aptamer strands complementary to the nanoparticle ssDNA were added at a 50% molar ratio relative to the nanoparticle DNA and incubated at room temperature.

Cy3-labeled aptamer structures were then characterized by DLS and AFM (Figure 3.6). Here as an example, we show results on structures formed by room temperature incubation of sHB5 aptamer (Figure 3.5). DLS showed the presence of a population of aptamer-functionalized nanoparticles with an average diameter of 34 nm and a narrow size distribution in solution (Figure 3.6a). AFM analysis showed nearly monodisperse spherical structures with an average diameter of 56 nm and height of 9 nm (Figure 3.6b). As expected, these structures were found to be larger than particles composed of aptamer-HE$_{12}$ conjugates (where the aptamer is part of the strand, average diameter: 50 nm).

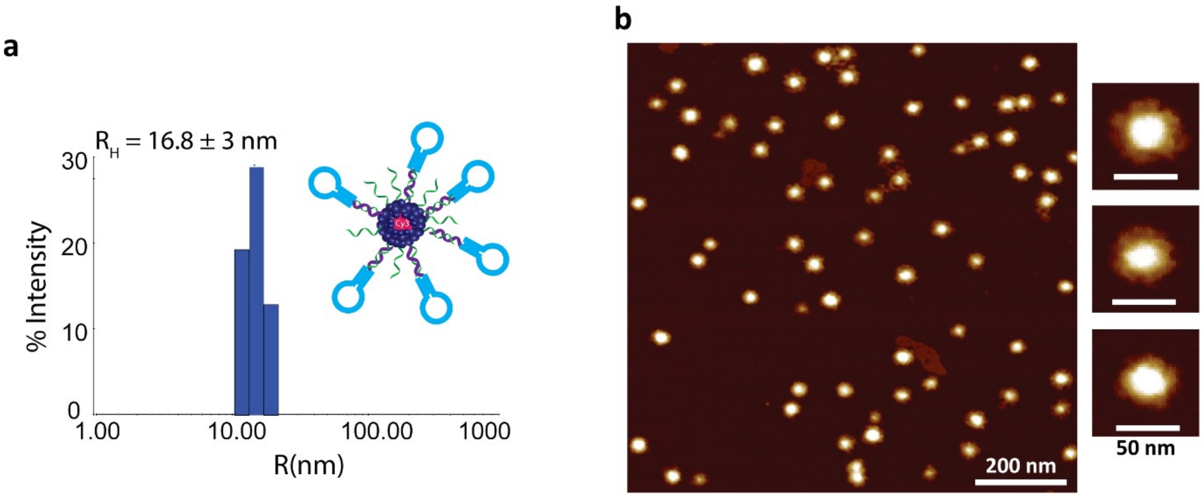

Figure 3.6 – Characterization of sHB5-Cy3-DNA nanoparticles. a) Dynamic light scattering histogram showing the hydrodynamic radius of sHB5-particles in solution. The structures show a narrow size distribution and hydrodynamic diameter of 34 nm. b) Atomic force microscopy image showing the presence of nearly monodisperse spherical particles on surface.

The next step was to investigate the cellular uptake profile of the aptamer-functionalized structures. Flow cytometry was used to quantify the amount of structural uptake in cells. SKBR3 was used as a model HER2-positive cell line and HeLa as a HER2-negative one. Interestingly, after 2 hours of incubation and several washing steps, flow cytometry data revealed higher uptake of 50% aptamer-nanoparticles in HER2-positive cell lines (2-fold increase) compared to structures lacking an aptamer (Figure 3.7). In the negative cell line, all structures showed similar uptake which indicated that the higher uptake of structures in HER2-positive is likely due to aptamer-mediated internalization. Notably, aptamer-structures prepared using both methods (room temperature incubation and one-pot assembly), showed a similar high uptake profile in SKBR3 cell lines, indicating successful aptamer binding, folding and action in both cases.

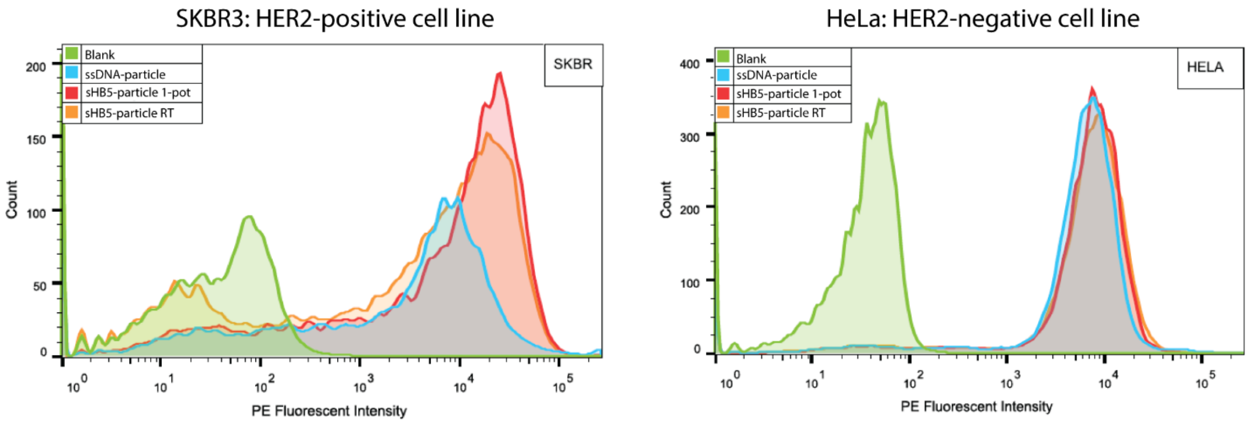

Figure 3.7 – Cellular uptake of second generation sHB5 aptamer nanoparticles in SKBR (HER2-positive) and HeLa (HER2-negative) cell lines. Flow cytometry data showing higher uptake of structures containing sHB5 aptamer in HER2-positive cells.

Based on these findings, we were then interested whether different uptake profiles would be observed in cell lines with different expression levels of HER2-receptors. Toward that end, breast cancer cell lines, SKBR3 and MB453, and cervical carcinoma HeLa cells were used. The expression levels of HER2 and other cancer markers have been characterized in breast cancer cell lines using immunohistochemistry and other methods.[35-36] It has been reported that both SKBR3 and MB453 cell lines are HER2-positive, however SKBR3 exhibits higher expression levels of HER2 compared to MB453.[37-38] Additionally, in our hands, the relative average diameters of the cells lines were 15 µm for HeLa, 15.8 µm for MB453 and 12 µm for SKBR3 cell lines. Based on this data, flow cytometry experiments were preformed with Cy3-labeled sHB5 aptamers in the 3 different cell lines. Interestingly, Cy3-sHB5-aptamers showed higher uptake in both SKBR3 and MB453 compared to HeLa cells (Figure 3.8). Even more remarkable, the aptamers showed higher uptake in SKBR3 cells compared to MB453, indicating a strong correlation between the expression levels of HER2-receptors and aptamer-mediated cellular internalization.

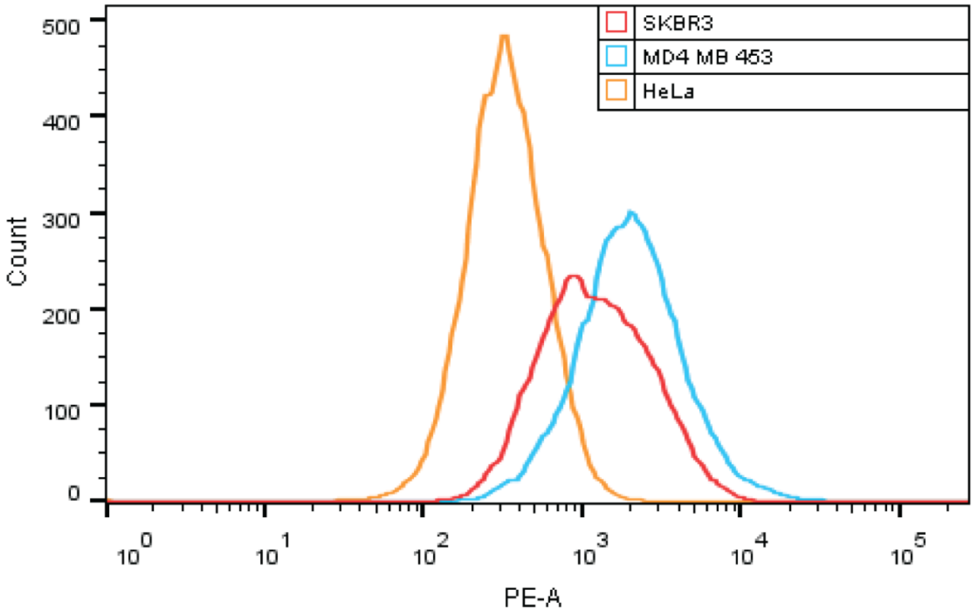

Figure 3.8 – Cellular uptake of Cy3-sHB5-aptamers in cell lines expressing different levels of HER2 receptors. Flow cytometry data of Cy3-labeled sHB5-aptamers showing higher uptake in SKBR3 and MB453 compared to HeLa cells. SKBR3 cells expressing the highest levels of HER2-receptors relative to other cell lines show the highest uptake of sHB5-aptamers.

In summary, we have developed a micellar aptamer-DNA nanoparticle for efficient delivery targeting specific cancer cell lines. These structures show potential for selective delivery of cargo into cells without the use of toxic transfection agents. The ease of synthesis and versatility of our system affords the ability to create hybrid nanostructures displaying both aptamer ligands and oligonucleotides therapeutics on their exterior, and hydrophobic drugs in their core allowing targeted dual therapy. These properties endow this nanoparticle system the potential to function as an efficient targeting drug delivery vehicle in biological systems. Future work will focus on evaluating the effect of targeting ligand density and sterics on cellular uptake. The uptake will also be measured in live cells and the ability to induce a targeted therapeutic activity will be evaluated. Eventually, studies to assess the targeting capability of aptamer-nanoparticles *in vivo* will be underway.

3.3.2 Stimuli-responsive DNA nanoparticles for drug delivery

3.3.2.1 Design of stimuli-responsive particles

Stimuli-responsive nanoparticles undergoing selective signal-transduced unloading of cargo attract great interest as “smart” materials for controlled drug delivery and sensing applications.[39] DNA is particularly interesting as a stimuli-responsive material due to its unique molecular-recognition properties.[40] These properties can be utilized in the context of drug delivery, wherein the selective release of cargo would only occur after intracellular recognition of a genetic marker. With this in mind, we sought to design a stimuli-responsive DNA nanoparticle, capable of releasing a nucleic acid cargo upon binding to a target microRNA. The target microRNA of choice was microRNA134 (mir134), an important marker involved in cellular differentiation.[41] It has also been shown to act as an age-related marker, where it is upregulated in adult keratinocytes.[42] The motivation is to target aged keratinocytes in adults, where mir134 is upregulated. When mir134 is present, binding causes the release of a small molecule anti-aging active in matured skin cells as a cosmetic regimen. Toward this end, solid-phase synthesis was used to generate two different DNA-polymer strands making up the nanostructure. One strand consists of a ssDNA portion fully complementary to mir134, followed by Cy3 dye, and 12 HE units (antiMIR134-Cy3-HE_{12}) (Figure 3.9). The other strand is a 19-mer ssDNA-HE_{12} conjugate that would not bind mir134.

The antiMIR134-Cy3-HE_{12} strand is designed with partial complementarity (14 bp homology) to the cargo strand which bears a Cy5 dye. An important feature of the design of the antiMIR-Cy3-HE_{12} strand necessitates flanking the Cy3 dye at the DNA-polymer interface (Figure 3.9). This ensures that upon binding with the Cy5-cargo strand, Cy3 and Cy5 dyes are positioned in close proximity causing an increase in Forster resonance energy transfer (FRET) signal – which was used as our reporter technique. The partial complementarity between the cargo strand and antiMIR-Cy3-HE_{12} results in an 8-nucleotide ssDNA overhang (or toehold). In the presence of mir134 which is fully complementary to the DNA portion of antiMIR134-HE_{12}, preferential binding to mir134 occurs. This binding generates a more stable duplex and causes unzipping of the Cy5-cargo strand *via* strand-displacement mechanism causing a decrease in the FRET signal.[43]

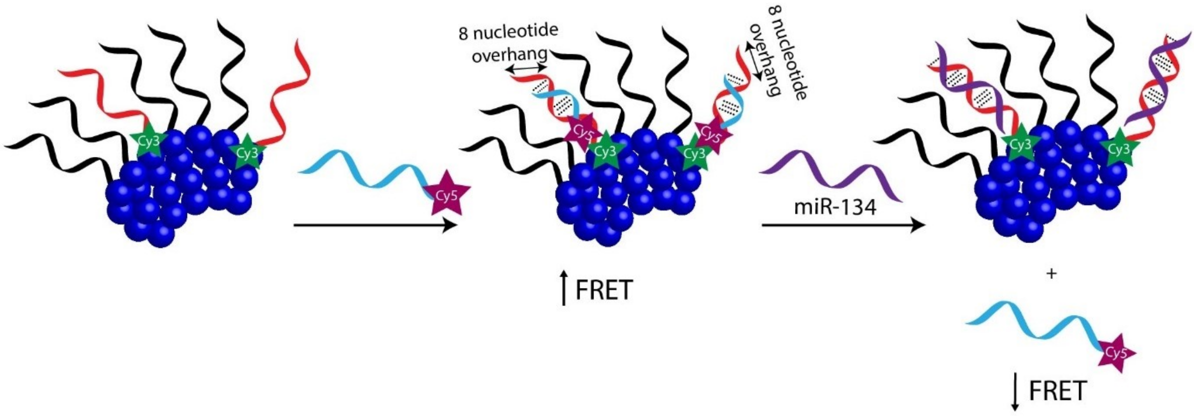

Figure 3.9 – Design of the stimuli-responsive DNA nanoparticle. Spherical nanoparticles were assembled from a mixture of antiMIR134-HE_{12} and ssDNA-HE_{12} conjugates. The cargo strand is labeled with Cy5 dye and displays a 14-bp partial complementarity to antiMIR134-HE_{12}. Upon addition, binding between the two strands leaves an 8-nucleotide overhang but brings the two dyes in close proximity causing an increase in the FRET signal. The addition of mir134, which is fully complementary to antiMIR134-HE_{12} results in preferential binding between those partners, causing the release of the cargo strand and loss of FRET signal.

3.3.2.2 Characterization of the stimuli-responsive particles

Spherical nanoparticles were generated by mixing antiMIR134-HE$_{12}$ with ssDNA-HE$_{12}$ conjugates in an assembly buffer, followed by thermal annealing (95 °C – 4 °C over 4 hours). Initially, higher percentages of antiMIR-Cy3-HE$_{12}$ were used in the assembly mixture. However, we observed that in such cases, Cy3 dye-dye interactions decreased the Cy3 signal (prior to the addition of Cy5-cargo). Hence, the percent of antiMIR-Cy3-HE$_{12}$ conjugates in the final mixture was decreased down to 2.5% to minimize the self-interaction of Cy3 dye molecules upon assembly, which would complicate FRET analysis. Following assembly, and addition of the cargo strand, the structures were characterized by atomic force microscopy (AFM) (Figure 3.10). AFM analysis showed the generation of uniform spherical nanoparticles with an average diameter of 36 nm and height of 7 nm.

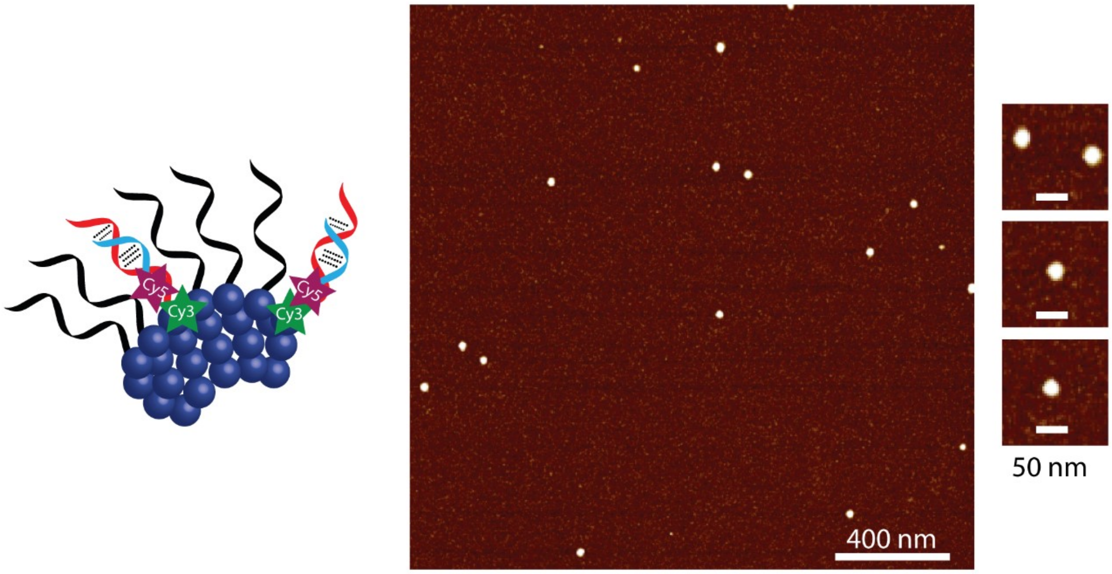

Figure 3.10 – Atomic force microscopy analysis of antiMIR134-nanoparticles. Uniform spherical structures were observed by AFM with an average diameter of 36 nm and height of 7 nm.

Following characterization, we tested whether this platform could release cargo selectively in response to an external stimulus - mir134 in this case. Conditional release of cargo was investigated through fluorescence measurements by monitoring the FRET signal of the Cy3-Cy5 dye pair (Figure 3.11a). Notably, the addition of 2x equivalents of mir134 and overnight incubation resulted in the loss of FRET signal (absence of FRET peak at 665 nm) and the recovery of the Cy3 signal at 556 nm, indicating the binding of mir134 to the target strand and subsequent release of the Cy5-labeled cargo. These results were further confirmed by agarose gel electrophoresis (AGE) analysis. Data from AGE reflects the loss of FRET upon mir134 addition (FRET channel, Lane 2), and the release of Cy5-DNA cargo (Cy5 channel, Lane 2). The Cy3 signal was also enhanced in response to mir134 addition (Cy3 channel, Lane 2), further confirming the success of the strategy. The structures also maintained their structural integrity upon mir134 binding and cargo release as observed through tight bands on gel with no side-products.

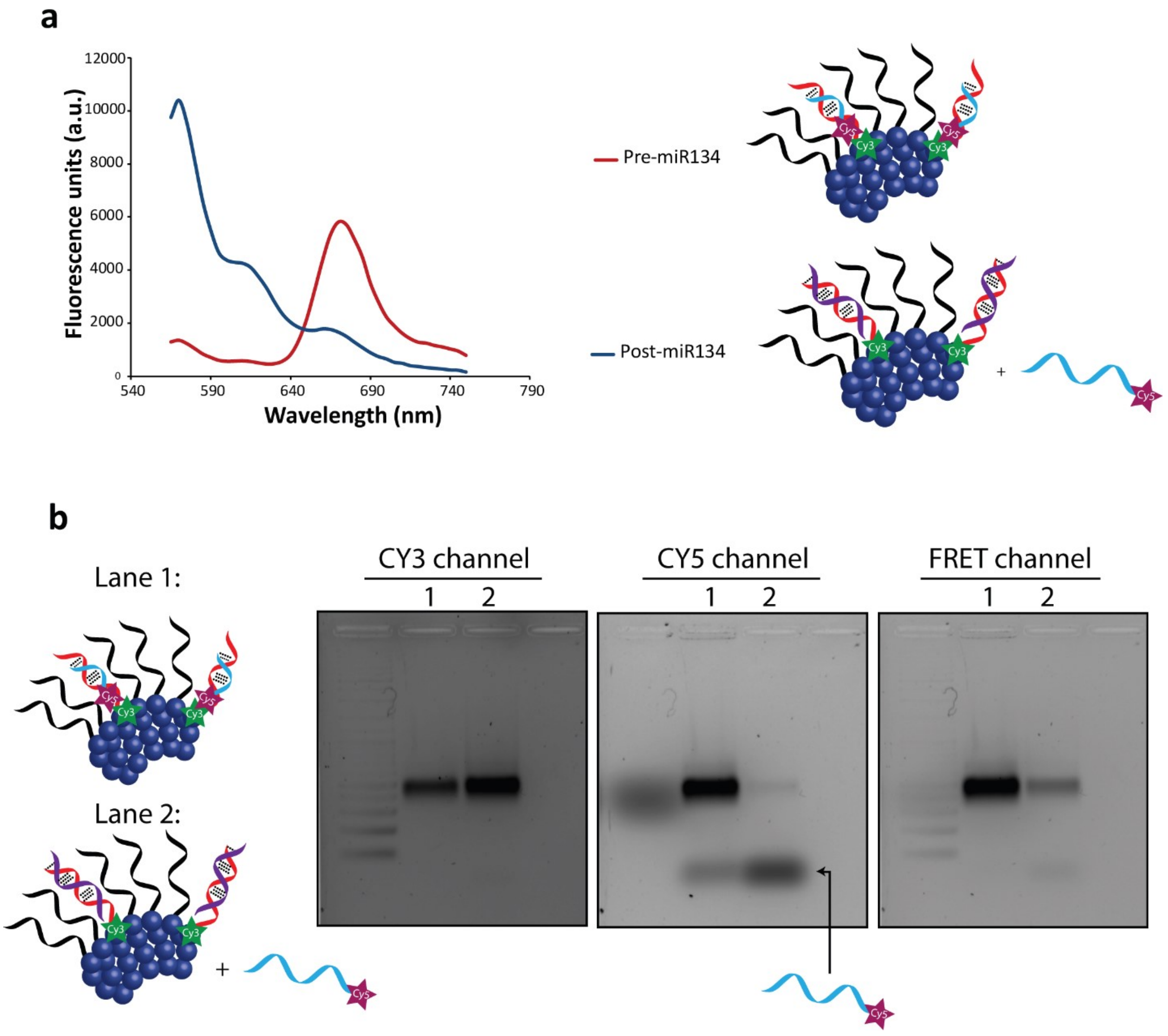

Figure 3.11 – Conditional release of cargo in response to mir134. a) Fluorescence spectroscopy showing the loss of FRET signal upon mir134 addition. b) Agarose gel electrophoresis demonstrating cargo release upon addition of mir134, and the maintained structural integrity of DNA nanoparticles.

This study provides a proof-of-concept system reacting to a specific genetic marker and selectively releasing cargo upon stimulus. The value of DNA is highlighted as an informational tool for cargo release in uniform stimuli-responsive amphiphilic DNA nanoparticles. Due to the versatility and ease of manipulation of nucleic acids, we expect this to be a general platform compatible with various genetic markers. The design and system presented here provide an example of monodisperse adaptable nanostructures for biological applications. However, to realize the full potential of the system, an important next step would be to test this mechanism in live cells. Additionally, studies on the intracellular structural integrity of structures would provide valuable information to predict the system's response in the complicated intracellular environment. One challenge in cells is the endosomal uptake of structures causing degradation or extracellular recycling.[44] Future designs will include the addition of endosomal escape agents which could facilitate that translocation of DNA nanoparticles to the cytoplasm. As for the released cargo, Cy5-DNA was used as a model to highlight the importance of releasing a strand protecting a small molecule. In future designs, an oligomer of small molecules will be attached to a DNA strand in the form of a prodrug through biodegradable linkers. Upon release of the DNA-prodrug conjugate in the intracellular environment, cleavage of the linker would generate the now active drug molecules for action.

3.3.3 Characterizing the uptake and intracellular fate of DNA nanostructures in normal skin cells

Transfection agents have been widely used to aid cellular uptake of DNA nanostructures.[45] However, the commonly used cationic agents exhibit high cellular toxicity hindering their applications in biomedicine.[45] The quest for transfection reagents with low toxicity is ever increasing, with a few examples reported.[45-47] Much more desirable is the development of nanostructures that show high cellular uptake without transfection agents. To date, very few examples have been reported, which include, locked-nucleic acid nanoparticles,[48] gold nanoparticle-cored spherical nucleic acids,[49] molecular beacon micelle flares[50] DNA-brush copolymer micelles,[51] and sequence-defined DNA nanoparticles.[52] These structures have shown high uptake in specific cell types. Highly valuable would be to assess the uptake and activity of structures across different cell lines, particularly, cancerous vs. normal cells, as they present different cellular membrane features and membrane protein makeup.[53-54] Of equal importance is the study of the intracellular fate of nanostructures, which would give great insight into their uptake pathways and trafficking events. Previously, in Chapter 2, we showed the high cellular uptake of DNA nanoparticles in the cervical cancer cell line, HeLa, without transfection. In this section, we expand the scope of our studies to normal skin cells, in particular, NHEK which are primary epidermal keratinocytes as a model human skin cell line. Furthermore, we utilize a dually dye-labeled system and show preliminary results on the intracellular structural integrity of micellar DNA nanoparticles in NHEK cells.

In the first set of studies, spherical Cy5-DNA-HE_{12} nanoparticles were synthesized according to a previously reported protocol (Figure 3.12, also see Chapter 2). In general, Cy5-HE_{12}-DNA strands were mixed with HE_{12}-DNA conjugates in a 25%/75% ratio (Figure 3.12a), followed by thermal annealing (95 °C – 4 °C, over 4 hours) to yield monodisperse spherical dye-labeled nanoparticles with a mean diameter of 28 nm and height of 7 nm (Figure 3.12b). Then, the uptake of Cy5-labeled nanoparticles in NHEK cells was studied by confocal fluorescence microscopy (Figure 3.12c). Interestingly, compared to Cy5-ssDNA, DNA nanoparticle uptake was greatly enhanced in NHEK cells, and showed cytoplasmic localization of nanoparticles.

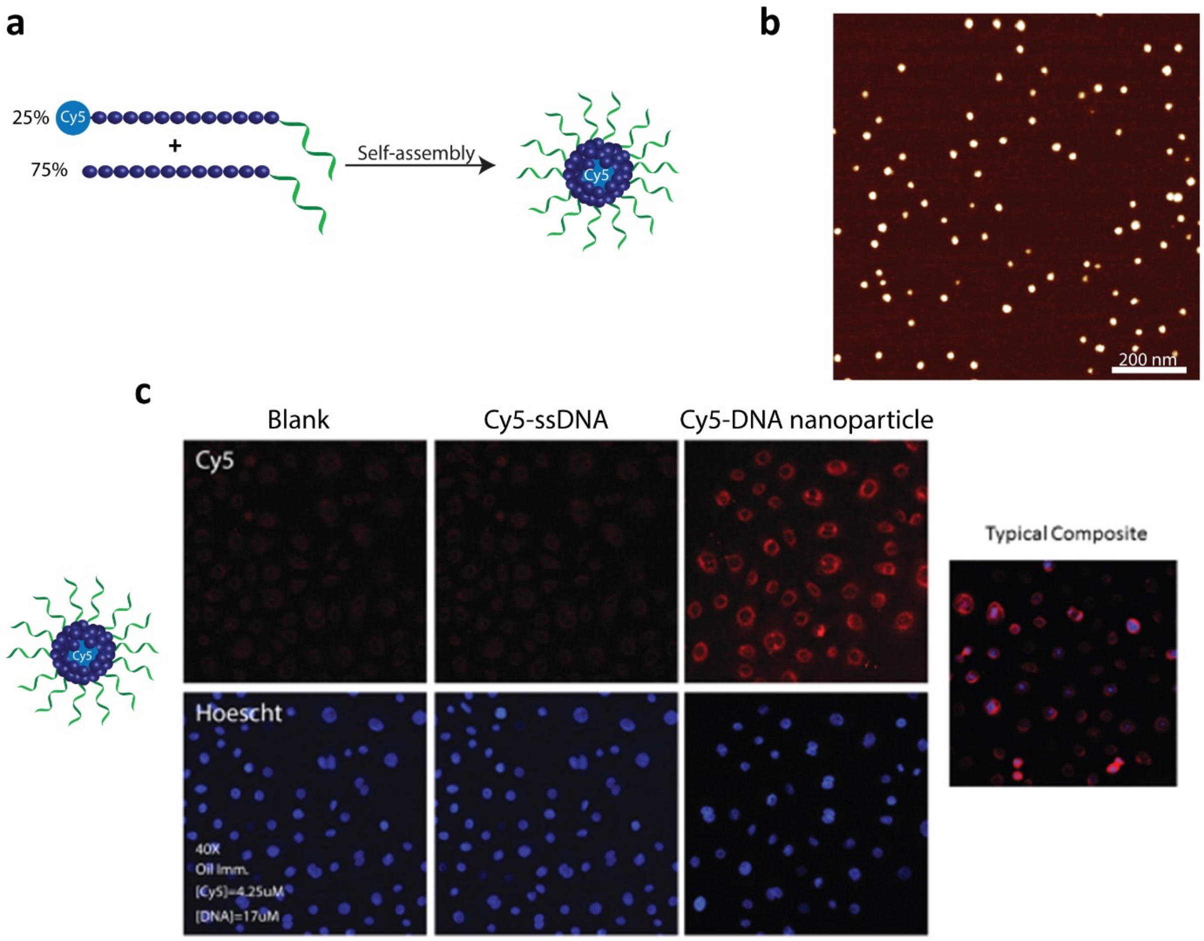

Figure 3.12 – Cellular uptake of Cy5-labeled DNA nanoparticles in NHEK cells. a) Preparation of Cy5-labeled DNA nanoparticles. Structures were prepared by mixing Cy5-HE_{12}-DNA with HE_{12}-DNA strands in a 25%/75% ratio, followed by thermal annealing. b) AFM analysis showing monodisperse spherical Cy5-labeled DNA nanoparticles. c) Fluorescence confocal microscopy showing the high cellular uptake of Cy5-DNA nanoparticles and cytoplasmic localization in NHEK cells. Hoescht was used as a DNA stain to highlight the location of the nucleus.

We then proceeded to confirm the cellular uptake of DNA-nanoparticles using flow cytometry. Cy3, Cy5 and Cy3Cy5-labeled nanoparticles were generated (Figure 3.13). After a 24-hour incubation and several washing steps, flow cytometry data demonstrated that compared to ssDNA, DNA nanoparticles showed greatly enhanced uptake in NHEK cells. For Cy3Cy5-nanoparticles, the uptake profile was similar to nanoparticles containing a single dye type, Cy3 or

Cy5. This suggested that the increased dye content per structure (in Cy3Cy5-particles) had no effect on the cellular uptake profile of DNA nanoparticles.

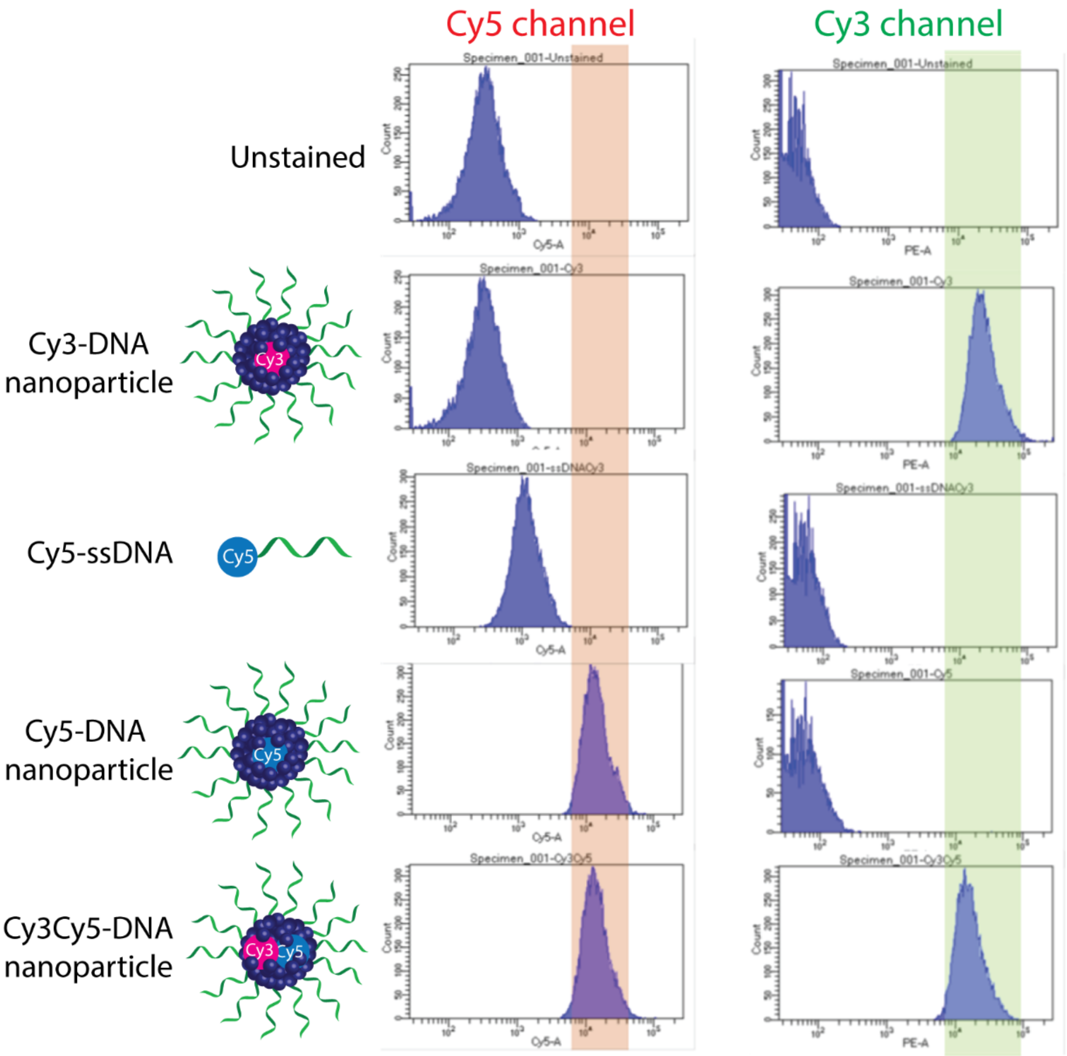

Figure 3.13 – Flow cytometry measurements showing the increased uptake of DNA nanoparticles in NHEK cells. All samples were incubated with NHEK cells for 24 hours, and images were acquired using laser excitation of 514 nm (Cy3-specific) or 635 nm (Cy5-specific).

After confirming the high uptake of DNA-particles in NHEK cells, we conducted a FRET experiment to evaluate their intracellular structural integrity. Cy3Cy5.5-DNA nanoparticles were generated where both dyes were buried in close proximity in the hydrophobic core of the nanoparticle (Figure 3.14a). Following assembly, monodisperse spherical structures with an average diameter of 27 nm where observed by AFM, and further confirmed by DLS and AGE (Figure 3.14b, *see Experimental Figure 3.25*). Cy3Cy5.5-DNA nanoparticles were incubated with NHEK cells for 24 hours and imaged using confocal microscopy. FRET was measured by exciting the Cy3 dye using a 514 nm laser (which minimizes crosstalk between the dyes) and collecting the entire emission spectrum. This methodology was used to evaluate whether donor excitation (Cy3) produced acceptor emission (Cy5.5). A preliminary study is conduced which suggest that the Cy3 dye is present intracellularly but does not transfer its energy through FRET to Cy5.5. Exciting the Cy5.5 dye using a 633 nm laser, revealed the presence of the dye inside the cell suggesting that the DNA-nanoparticles were taken up as intact objects. Due to the lack of a positive control that shows strong intracellular FRET indicative of structural stability, it is difficult to assess whether the absence of FRET is due to particle dissociation or a technicality in the measurements. However, in a case where the nanostructure dissociates, strategies to increase particle stability will involve cross-linking and modifying the DNA for increased nuclease resistance. Additionally, to ensure that particles are available in the cytoplasm for conditional delivery, endosomal escape agents and pH-sensitive polymers (such as poly(propylacrylic acid) can be integrated for endosomal membrane disruption.[55]

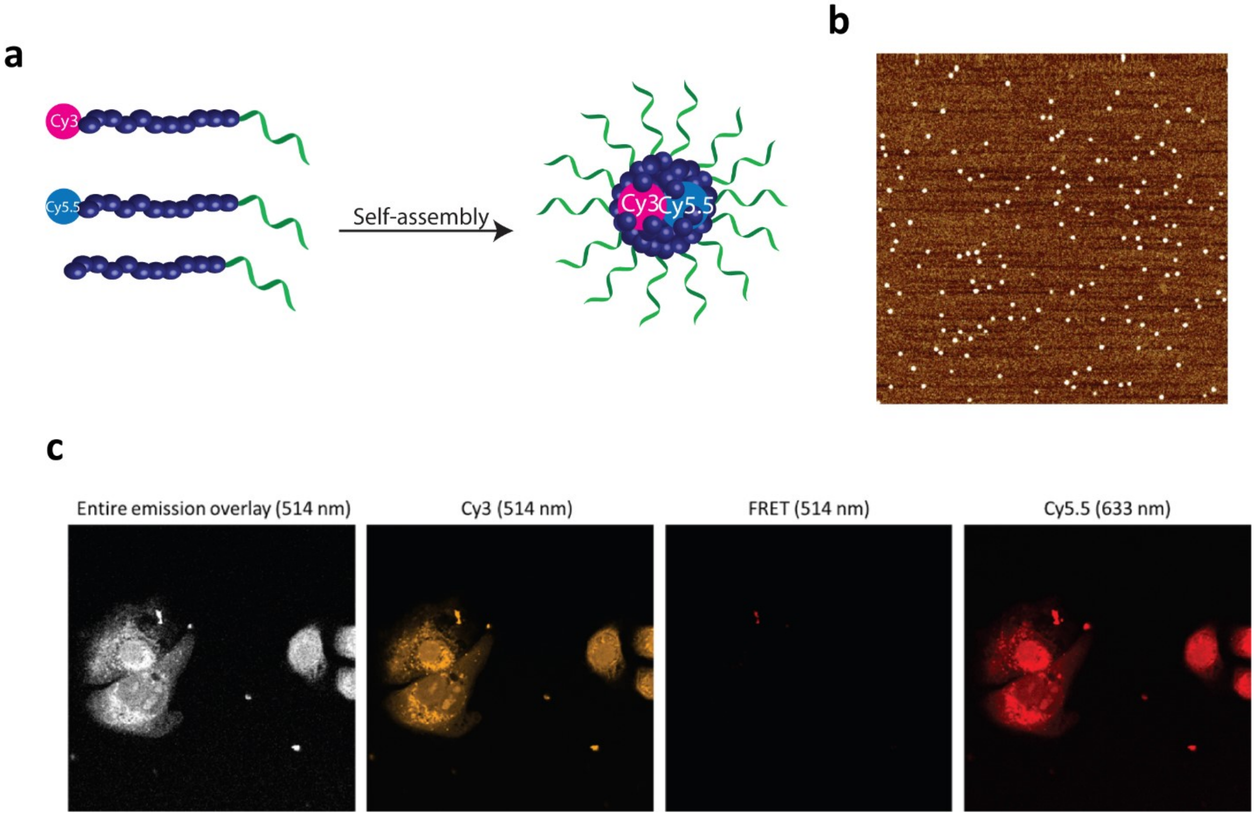

Figure 3.14 – Preliminary study evaluating the intracellular structural integrity of DNA nanoparticles in NHEK cells. a) Preparation of dually-labeled Cy3Cy5.5-DNA nanoparticles. b) AFM analysis showing monodisperse spherical particles with an average diameter of 27 nm. c) Confocal fluorescence microscopy measuring the intracellular FRET signal of Cy3Cy5.5-DNA nanoparticles. The presence of both Cy3-labeled and Cy5.5-labeled strands inside the cells indicates that the structures are likely taken up as intact objects. Preliminary studies show no FRET signal which could suggest intracellular disassembly. A positive control with known intracellular FRET would be required in this study.

In summary, we have demonstrated that DNA nanoparticles show increased uptake not only in cancer cell models, but also in normal epidermal keratinocytes. Our results suggest that DNA nanoparticles enter cells as intact units, however, likely disassemble in the intracellular environment. Additional studies and more controls will be necessary to better characterize the intracellular behaviour of structures. Understanding the fate of nanostructures in complex cellular environments affords great insight into their structure-activity relationships. Efforts underway will focus on the effect of covalent cross-linking of nanoparticles on their intracellular stability. Studies on the specific mechanism of uptake, compartmental localization in cells and intracellular trafficking will also be the focus of our future studies. Our future efforts will also be directed toward developing strategies to enhance the availability of nanostructures in the cytoplasm.

3.3.4 Increasing DNA nanostructure resistance to nuclease degradation

Rapid nuclease degradation presents a major challenge for oligonucleotides when subjected to *in vitro* or *in vivo* environments.[26] Previous studies conducted by our group and others, have shown that the dense packing of DNA in 3D nanostructures affords increased nuclease resistance.[49, 52, 56-57] Still, the increase of "self-protection" afforded by densely packed DNA is yet insufficient; it would be necessary to find more efficient strategies that greatly limit oligonucleotide degradation by nucleases. In our previous work, we demonstrated that DNA-nanoparticles exhibited a blood serum half-life that was 4.6-fold higher than ssDNA of the same length. In this section, we applied a simple modification to the DNA strands where the nonbridging oxygen in the phosphate backbone of the DNA strand was replaced with a sulfur, creating phosphorothioated DNA nanoparticles (Figure 3.15a). We describe preliminary results of the nuclease stability of phosphorothioated DNA nanoparticles using polyacrylamide gel electrophoresis (PAGE). Phosphorothioated DNA nanoparticles, phosphorothioated ssDNA strands, and an unmodified ssDNA were compared after incubation with fetal bovine serum (FBS) for different time intervals. Qualitative PAGE results indicated that this simple modification resulted in substantial nuclease resistance for over 72 hours (Figure 3.15b). Due to the high stability of phosphorothioated DNA over the course of our measurements (72 hours), calculations of the degradation half-life were not applicable. Important to note that degradation of unmodified DNA started at time = 0, where nucleases were added and immediately denatured, showing ssDNA's susceptibility to nucleases (Figure 3.15b). This simple modification could be implemented in any DNA-based polymeric system as a facile strategy for enhanced stability.

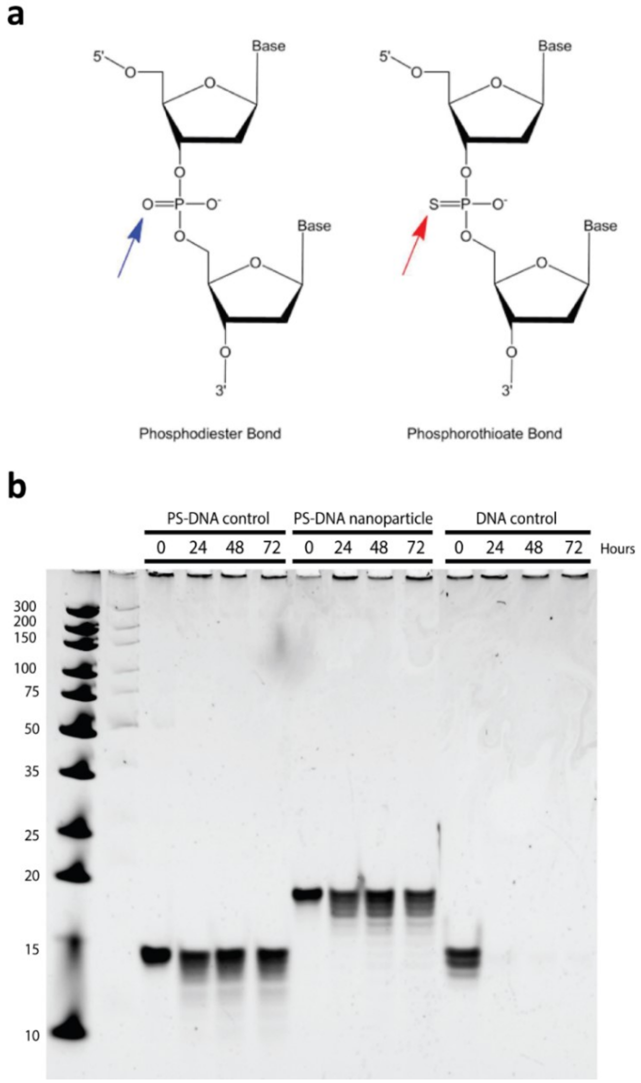

Figure 3.15 – Increasing the nuclease stability of DNA nanoparticles. a) Chemical structure of a phosphorothioated DNA backbone. b) Denaturing PAGE analysis of the FBS degradation products of phosphorothioated DNA nanoparticles. PS-DNA control: phosphorothioated DNA strand, PS-DNA nanoparticle: spherical nanoparticle with phosphorothioated DNA, DNA control: unmodified DNA strand.

3.3.5 Nanoparticle interaction with serum proteins

Previous reports have demonstrated that inert polymers such as hydrophilic polyethylene glycol chains improve the efficacy of nanocarrier-based drugs by reducing *in vivo* opsonisation with serum proteins.[32] This not only prevents the rapid recognition of structures by the reticuloendothelial system (RES), but also provides prolonged blood circulation of nanostructures and higher accumulation at targeted sites.[58-59] The most abundant serum protein is human serum albumin (HSA).[60] In our case, we hypothesized that the dense hydrophilic DNA outer shell would provide a surface unfavorable for binding HSA protein. DNA-HE_{12} nanoparticles were preassembled then incubated with a 5x molar excess of HSA for 2 hours at room temperature and analyzed by agarose gel electrophoresis (AGE) (Figure 3.16). Since HSA exhibits lower mobility on gel compared to DNA nanoparticles, an association with the protein should results in a gel mobility shift of the structures. As illustrated in Figure 3.16, following incubation, no interaction was observed between the DNA particles and HSA protein (GelRed channel). It appears that the outer DNA shell dictates the interaction between HSA and the DNA structures.

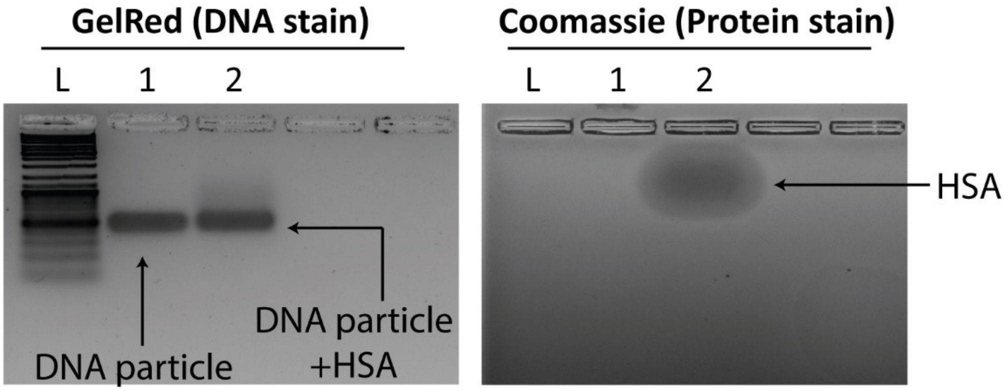

Figure 3.16 – Evaluating the interaction of DNA-HE$_{12}$ nanoparticles with human serum albumin (HSA). Agarose gel electrophoresis of DNA nanoparticles prior (Lane 1) and post incubation (Lane 2) with HSA. The gels were visualized under Gel Red DNA stain channel (left panel), Commassie Blue protein stain channel (right panel). GelRed panel shows the absence of a gel mobility shift of DNA nanoparticles after HSA incubation. Coomassie panel displays the lower mobility shift of HSA protein compared to DNA nanoparticles.

In a control experiment, the micellar DNA structures were denatured by the addition of a solution of urea and depletion of magnesium cations prior to HSA addition, exposing their long aliphatic chains (Figure 13.7, *see Experimental Figure 3.26*). In this case, even at low protein concentrations, HSA was observed to strongly bind to the DNA-polymer conjugates. These findings suggest that the outer hydrophilic ssDNA corona limits albumin adsorption and indicates that the DNA structures remain stable upon exposure to the protein. In addition, we used Nile Red-loaded particles as a visual tool along with gel electrophoresis to further confirm the lack of interaction between DNA nanoparticles and HSA (*see Experimental Figures 3.27, 3.28*).

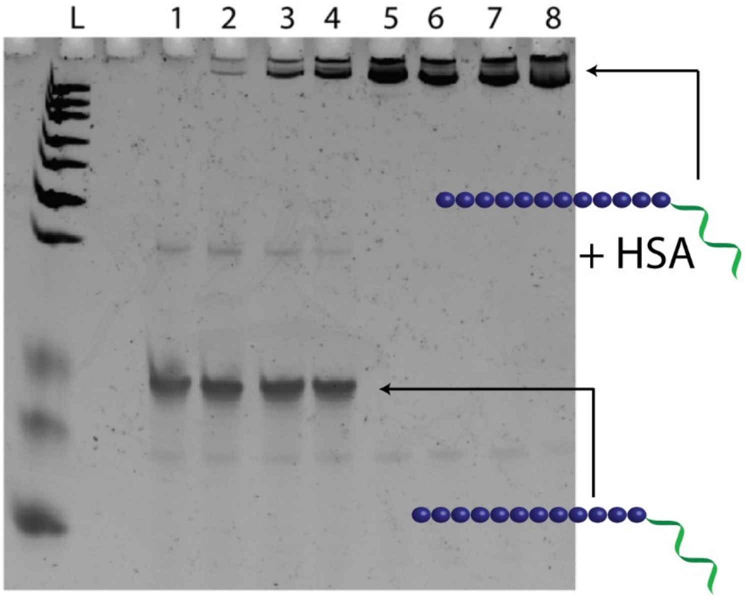

Figure 3.17 - Evaluating the interaction of monomeric ssDNA-HE$_{12}$ strands with human serum albumin (HSA). Denaturing PAGE analysis of disassembled HE$_{12}$-DNA conjugate strands titrated

with different HSA concentrations. Lane 1: HE_{12}-DNA strand control, Lanes 2-8, HSA dilutions of 1/1000, 1/100, 1/50, 1/10, 1/5, 1/2 and undiluted HSA (526 μM stock). Under denaturing conditions, disassembly of the DNA particle exposes the lipophilic HE_{12} segments, which in turn results in strong binding to HSA protein.

The study above focused on the interaction of DNA-nanoparticles with HSA and showed that the intact structures are shielded from protein binding. While HSA is the most abundant protein in serum and could be assumed as a general representative of serum protein make-up, it accounts for 50% of serum proteins.[60] A wide range of other lipoproteins and apolipoproteins are present in blood serum, however investigating their possible interaction with DNA nanoparticles is beyond the scope of this work. Nonetheless, binding of DNA nanoparticles with other serum proteins could be problematic, causing structural destabilization. Additionally, the recognition of nanostructures by the RES system and activation of macrophages as an immune defense mechanism would hinder their success for biomedical applications. One strategy to further limit protein binding and shield nanoparticles from RES recognition is to add an additional layer of protection, namely poly(ethylene glycol) which has been shown to act as a nanoparticle "shield" in blood circulation.[61] Even more desirable, is the capability of adding PEG-moieties that would shed in response to slightly acidic conditions, typical of tumor microenvironments.[62] Toward this end, we sought to investigate the ability of modifying nanoparticle surfaces with cleavable PEG moieties to provide an extra layer of protection to the DNA during blood circulation.

In this study, PEG chains (average M_n = 5000 Da) functionalized with a terminal azide were chosen to be attached to DNA-polymer conjugates containing strained alkyne functionalities through "click" chemistry. The structures of the strained alkyne (DBCO) phosphoramidite and PEG derivaties used are highlighted in Figure 3.18a,b. DNA-polymer conjugates were synthesized using solid-phase chemistry by first coupling a thymine-containing DBCO (dT-DBCO), followed by synthesis of a 19-mer DNA sequence and finally the addition of 12 dodecane (hexaethylene, HE) units (Figure 3.18c). This method yields DBCO-functionalized DNA-polymer conjugates in high yields. Subsequently, DBCO-DNA-HE_{12} conjugates were mixed with assembly buffer and subjected to thermal annealing (95 ° C – 4 °C, over 4 hours) to yield spherical DNA nanoparticles with a DBCO-decorated corona. To that, PEG-azide or PEG-acetal-azide were added and incubated overnight to yield PEG-functionalized DNA nanoparticles.

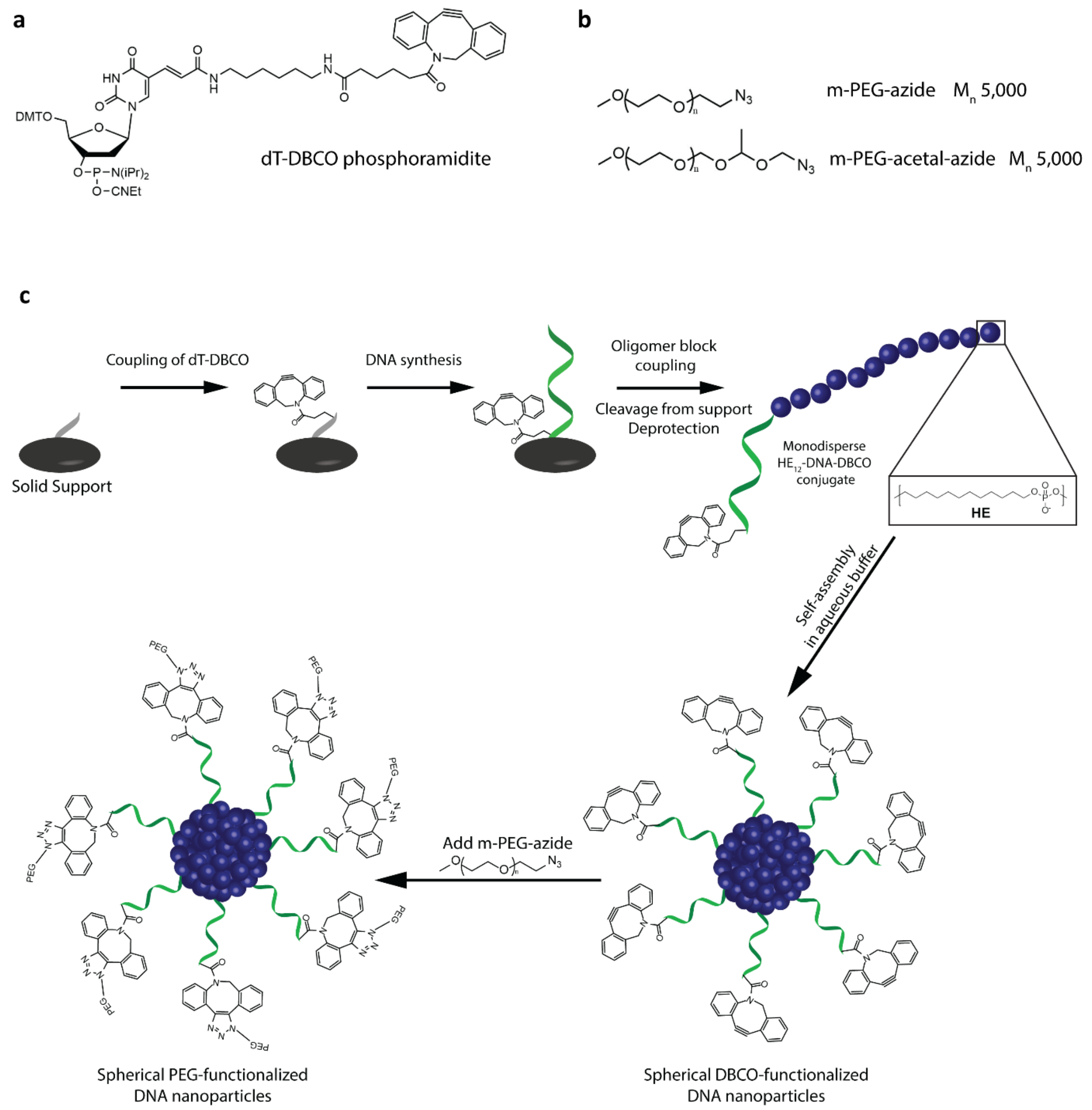

Figure 3.18 – Synthesis of PEG-functionalized DNA nanoparticles. a) Structure of the dT-DBCO phosphoramidite used. b) Structures of the PEG-azide and PEG-acetal-azide functionalities. c) Schematic representation of the synthesis of PEG-functionalized DNA nanoparticles. Phosphoramidite monomers were attached to the controlled pore glass (CPG) in a step-wise fashion. dT DBCO was first attached to the solid-support, followed by a 19-mer DNA strand, and finally 12 dodecane monomer additions (HE_{12}) yielding monodisperse DBCO-DNA-HE_{12} conjugates. Self-assembly of these conjugates results in the formation of monodisperse spherical DNA nanoparticles. The click reaction

between added PEG-azide moieties and DBCO-functionalized nanoparticles yields PEG-decorated DNA nanoparticles.

As a first step, we tested the conjugation of PEG-azide and PEG-acetal-azide groups to DBCO-DNA-HE$_{12}$ monomers in water in their non-aggregated molecular state (Figure 3.19). We first asked whether the incubation time influenced the coupling efficiency. 4x molar excess of PEG-azide was added to the DBCO-functionalized strands and subjected to 3 different incubation times: 2 hours, 24 hours and 48 hours (Figure 3.19b-d). The success and efficiency of conjugation were assessed by denaturing PAGE.

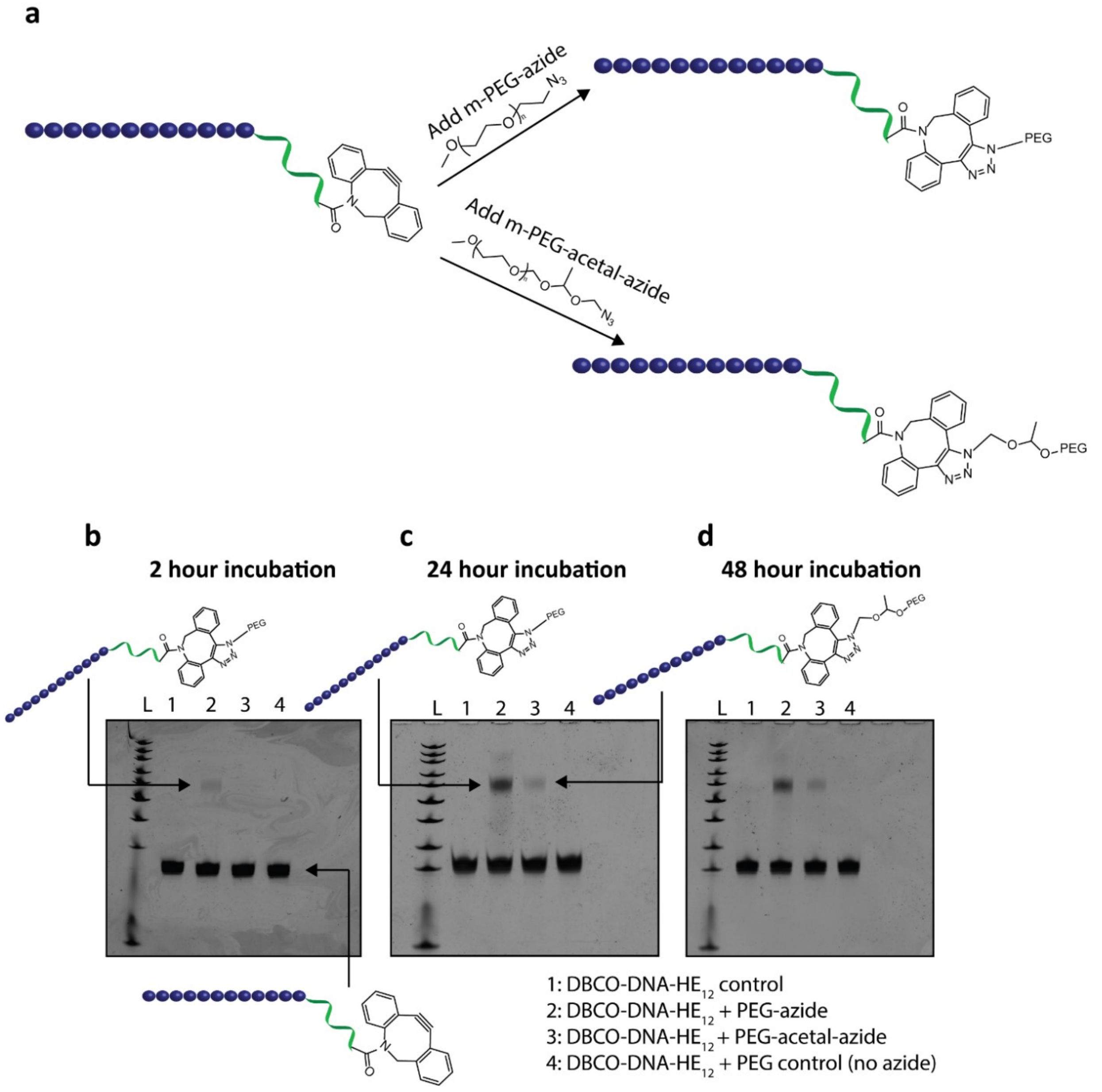

Figure 3.19 – Conjugation of PEG-azide groups to DBCO-DNA-HE$_{12}$ strands. a) Schematic illustration of the conjugation of PEG-azide and PEG-acetal-azide groups to DBCO-DNA-HE$_{12}$ strands. b-d) Denaturing PAGE analysis of PEG-functionalization after b) 2 hours c) 24 hours d) 48 hours of incubation with the DBCO-containing strands.

From PAGE analysis, low efficiency of coupling was obtained with a 2-hour incubation, as observed by a very faint product band for PEG-azide conjugation (Figure 3.19b, Lane 2) and the absence of a product band for PEG-acetal azide (Figure 3.19b, Lane 3). Increasing the incubation period to 24 and 48 hours, resulted in a higher product yield of ~ 40 % for the PEG-azide (Figure 3.19c-d, Lane 2) and the appearance of a faint-band for PEG-acetal (Figure 3.19c-d, Lane 3). No difference in product yield was observed between 24 and 48-hour incubation periods. Additionally, we observed that the conjugation yield of PEG-acetal-azide was significantly lower than PEG-azide. This could be due to the slightly acidic conditions (the measured pH of water used was ~6.5-6.8) causing slow hydrolysis to the acetal moiety of the PEG-acetal-azide group during incubation.

We were then interested in testing whether increasing the amount of PEG functional groups added to DBCO-functionalized strands would increase the reaction yield. Additionally, if the low conjugation yield of PEG-acetal-azide is due to slow hydrolysis, then significantly increasing the amount of this molecule added would likely increase the reaction yield. Toward this end, the added PEG groups were increased from 4x to 100x and 1000x molar equivalents compared to DBCO-DNA-HE$_{12}$. The products were analyzed by denaturing PAGE, which showed no change in yield for PEG-azide with either 100 or 1000x excess (Figure 3.20b-c, Lane 2). A significant increase in the conjugation yield, however, was observed with increasing amounts of added PEG-acetal-azide (Figure 3.20b-c, Lane 3). At such high molar equivalents added, the yields of PEG-acetal-azide coupling were similar to those of PEG-azide. This indicates that strand hydrolysis of PEG-acetal-azide groups is the likely mechanism behind its lower coupling efficiency. With such high excess of PEG-acetal-azide derivatives, the ratio of hydrolyzed monomer becomes negligible, resulting in yields similar to PEG-azide functional groups.

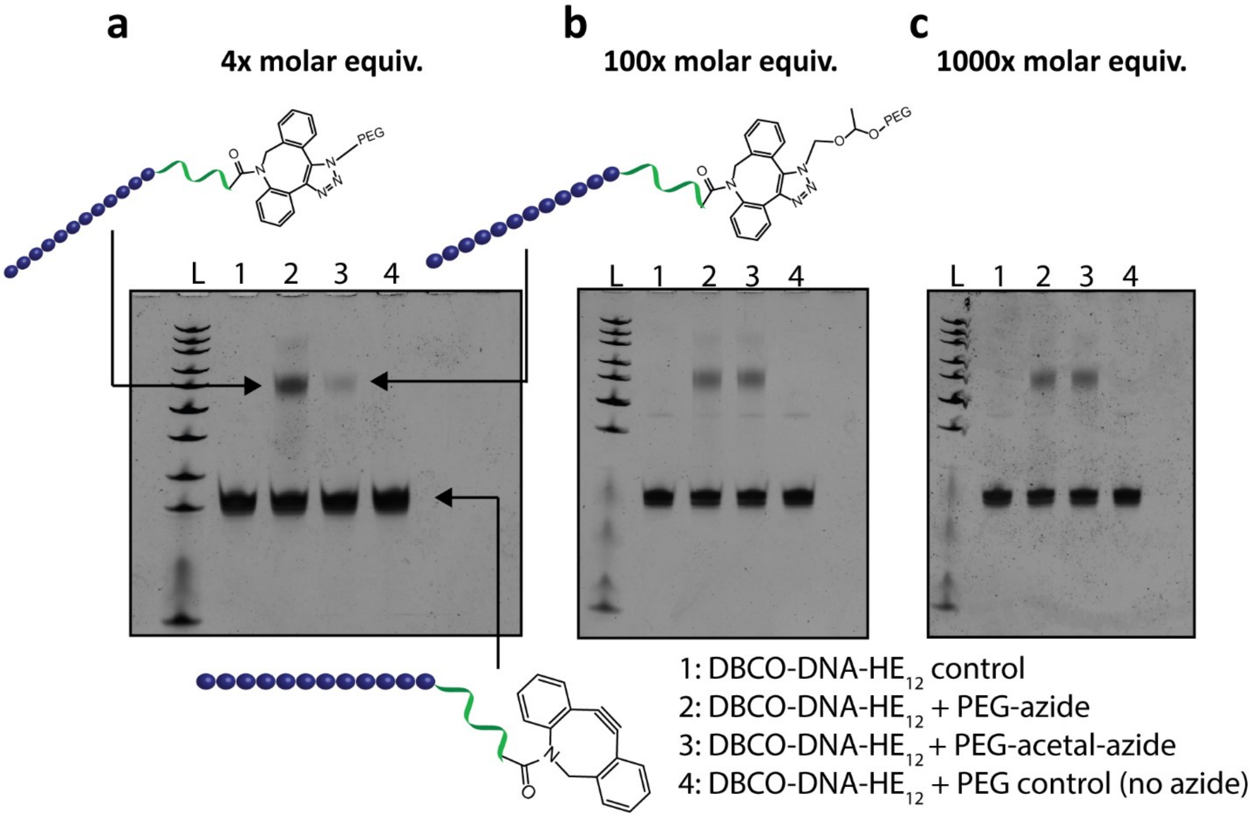

Figure 3.20 – Evaluating the effect of increasing the amount of added PEG-functionality on the coupling yield. Denaturing PAGE analysis measuring the yields of coupling DBCO-DNA-HE$_{12}$ to a) 4x molar equivalent, b) 100x molar equivalent and c) 1000x molar equivalent PEG-functional groups.

After studying the effect of incubation time and added functional groups to strands in water, we then investigated the coupling of active PEG groups to DBCO-DNA nanoparticles under basic conditions. DNA nanoparticles were assembled in a Tris-based buffer containing magnesium ions after a thermal anneal cycle (95 °C – 4 °C). As a representative example, we show the results of DNA nanoparticles mixed with 1000x equivalents of PEG functional groups. Analysis by AGE showed the successful conjugation of PEG-azide and PEG-acetal-azide on preformed DNA nanoparticles (Figure 3.21b, Lanes 2 and 3). This was shown as a clear gel shift to a lower mobility band of the DNA nanoparticles, indicating structures of larger surface area. As expected, functionalized structures were observed as a less defined band due to the inherent molecular weight distribution of PEG polymers. PEG-functionalized nanoparticles were then characterized by atomic force microscopy (AFM), which showed spherical particles surrounded by a mesh cover (Figure 3.21c). These particles had a diameter of 60 nm and showed a core with an increased height of 9.5 nm (compared to 7-8 nm for spherical ssDNA nanoparticles) and a shell height of 1.5 nm, likely resembling a higher nanoparticle core with a PEG corona on surface.

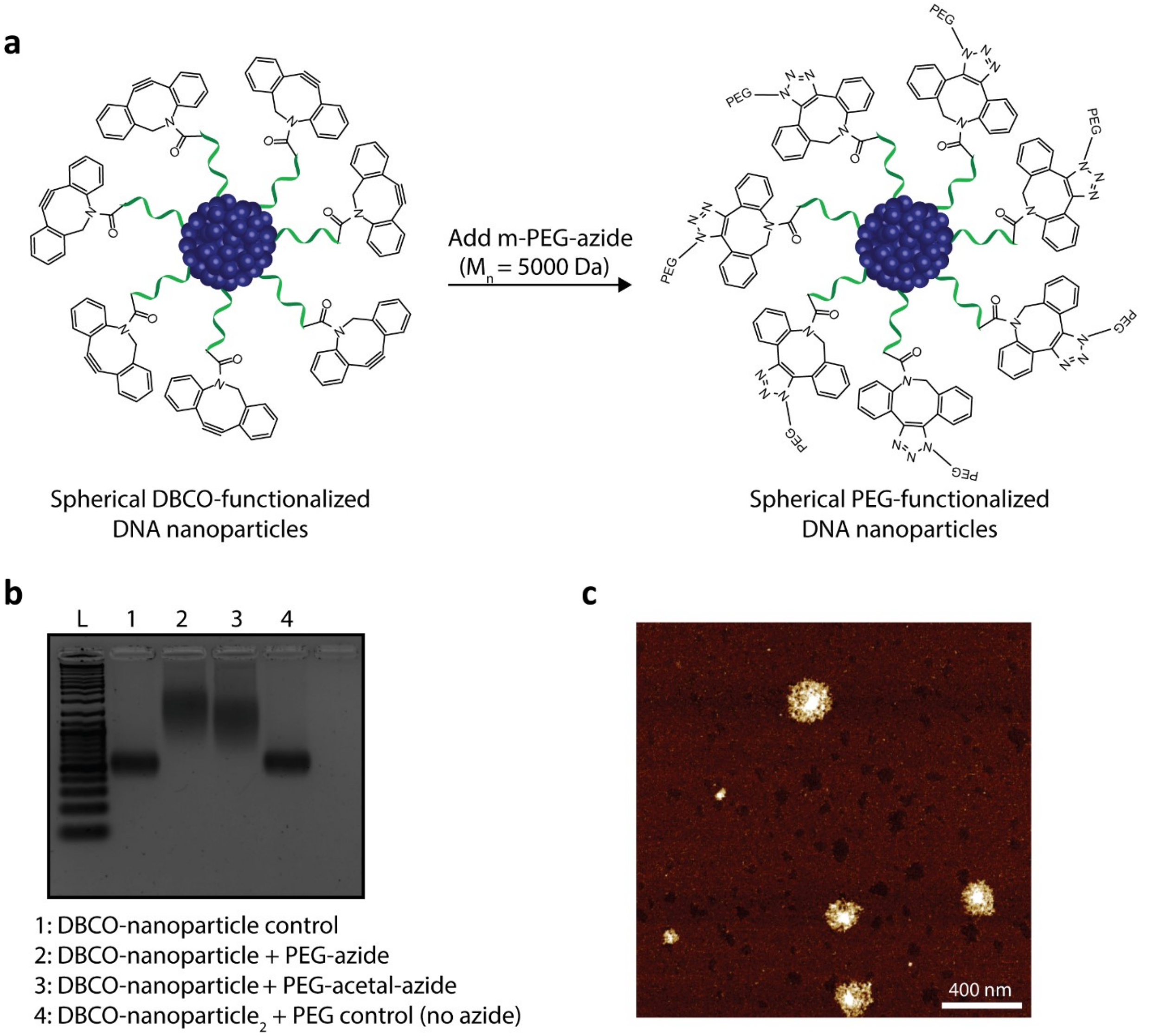

Figure 3.21 – Preparation of PEG-functionalized DNA nanoparticles. a) Schematic representation of the functionalized of DNA nanoparticles with PEG-azide moieties. b) Agarose gel electrophoresis analysis showing the decoration of DNA nanoparticles with PEG-functionalities. The shift of the DNA nanoparticle band to lower mobility upon the addition of PEG-functional groups indicates successful conjugation. c) Representative AFM image of PEG-functionalized DNA nanoparticles.

In summary, we have shown the successful conjugation of PEG-azide and PEG-acetal-azide to DBCO-functionalized DNA-HE_{12} conjugates and DNA nanoparticles. Though the coupling yields could be further improved, our results demonstrate a method of generating DNA-nanoparticles bearing an extra layer of protection to shield oligonucleotides from possible proteins, nucleases and phagocytic uptake in blood circulation. The next set of experiments will focus on increasing the yields of coupling, as well as testing the selective hydrolysis of PEG-acetal-nanoparticles in mildly acidic conditions. We will also test the effect of shielding imposed by the extra layer of conjugated PEG by evaluating blood serum stability and nanoparticle interaction with major serum proteins. The selective release of PEG-acetal moieties in acidic conditions will be evaluated in the context of cellular uptake studies to assess its effect on the nanoparticle uptake profile. We envisage this protocol as a general strategy for increased nanoparticle stability in biological media with potential applications for selective drug delivery in tumor microenvironments.

3.3.6 Cross-linking strategies of DNA nanoparticles

Different approaches have been investigated to stabilize nanoparticles by using covalent[63-66] or reducible linkages.[67-69] Recently, the Mirkin group,[70] Rouge group[71] and Tan group[72] reported cross-linking methods for stabilizing spherical nucleic acid particles, but their approaches require extended reaction times, addition of cross-linkers or are limited to DNA-polymer interface cross-linking. Thus, the challenge of developing a simple versatile methodology which would allow compartment-specific and different degrees of cross-linking still remains. In this section, we propose a facile strategy for DNA nanoparticle cross-linking using disulfide chemistry and highlight preliminary results towards that goal.

In our approach, a disulfide serinol phosphoramidite (DS) was used as the cross-linker (Figure 3.22a). Using solid-phase synthesis, a 19-mer DNA strand was synthesized, followed by the addition of 3 units of DS, and 12 hexaethylene (HE) additions to yield DNA-DS-DS-DS-HE_{12} conjugates. The advantage of this approach is: 1) the cross-linker can be easily incorporated as part of DNA-polymer conjugate providing a simple direct cross-linking method without the need of additional cross-linking agents, 2) by using the solid-phase approach, control over the position and number of cross-linkers in the DNA-polymer conjugate could be achieved, allowing compartment-specific cross-linking (different parts of the hydrophobic core, DNA-polymer interface, DNA segment could be cross-linked) in the self-assembled structure. In this strategy, spherical DNA nanoparticles were formed by the self-assembly of DNA-DS-DS-DS-HE_{12} in aqueous solution, which brings the disulfide serinol groups of different strands in close proximity. Following assembly, a catalytic amount of dithiothreitol (DTT) was added to initiate cross-linking and S-S bond formation between cyclic disulfide groups of neighboring strands (Figure 3.22b). The free thiol groups of DTT would attack the strained 5-membered disulfide ring causing ring opening. Opening of the 5-membered ring frees a thiol group ready to attack a neighbouring cyclic disulfide and the process carries, allowing polymerization.

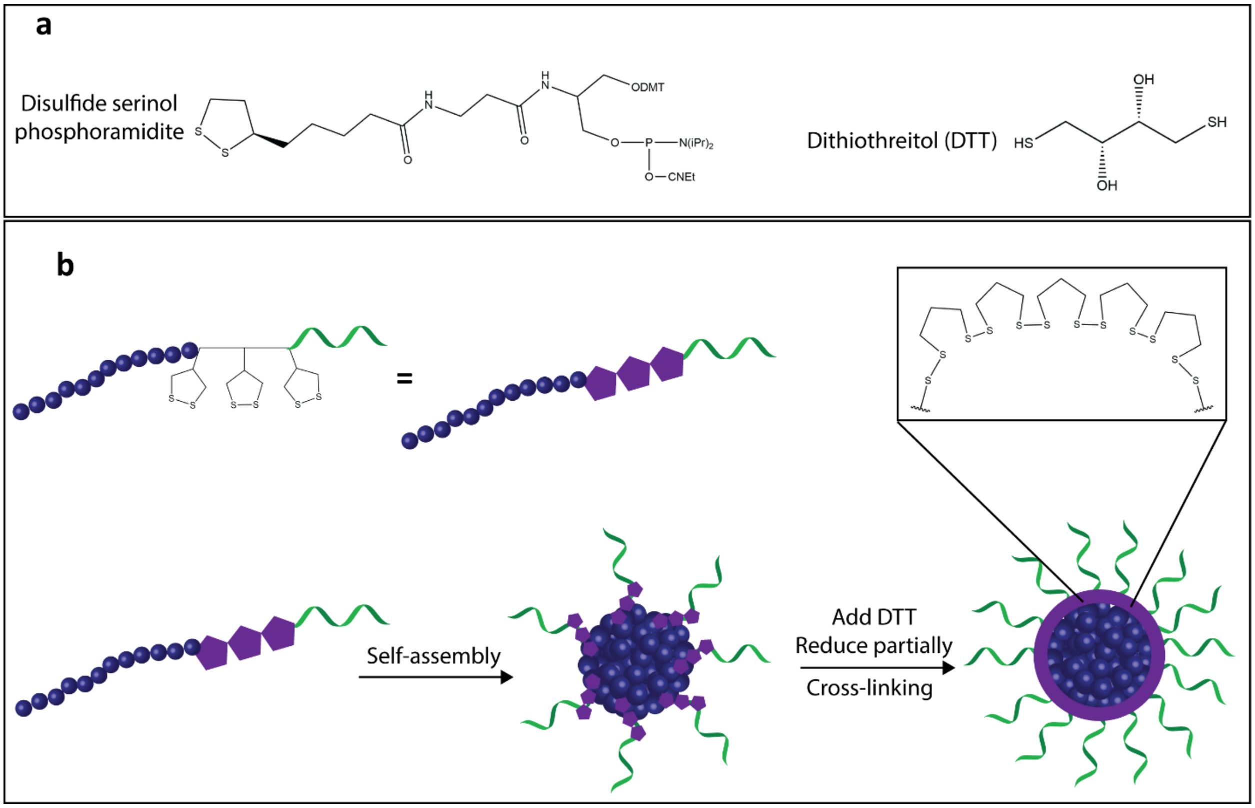

Figure 3.22 – Cross-linking of DNA nanoparticles using disulfide chemistry. a) Structures of the disulfide serinol (DS) phosphoramidite and dithiothreitol (DTT). b) Schematic representation of the cross-linking strategy. DNA-DS-DS-DS-HE_{12} conjugates were synthesized by solid-phase synthesis. Self-assembly of these strands in aqueous solution resulted in spherical DNA nanoparticles, bringing cyclic disulfide serinol groups in close proximity. The addition of a catalytic amount of DTT as an initiator results in cross-linked spherical nanoparticles.

To test our strategy, following nanoparticle assembly, the structures were titrated with different amounts of DTT to allow cross-linking, then disassembled and analyzed by denaturing PAGE (Figure 3.23). As expected, PAGE analysis shows the formation of a mixture of cross-linked products (Lanes 1-5). Despite successful cross-linking and the presence of higher order structures, the reaction yields were low with a 21% yield of the dimer and 15% of the trimer products. While placing 3 adjacent disulfide serinol units would increase their effective concentration, it is also possible that the neighbouring groups undergo an intra-strand instead of an inter-strand disulfide bond formation (Figure 3.23b-d). Such case would hamper reaction yields but could be potentially resolved by spacing out the disulfide moieties in the strand.

As for DTT titration, surprisingly, the addition of varying amounts of DTT had no effect on the degree of cross-linking, as compared to Lane 1 where no DTT was added. However, considering the reaction conditions (thermal annealing at 95 ° C – 4 °C over 4 hours), it is possible that at such high temperature conditions a small fraction of the disulfide linkages is broken to the dithiol species. Such case would result in nanoparticle cross-linking prior to the addition of DTT. Here, the addition of catalytic DTT amounts would not be expected to change the degree of cross-linking. Nevertheless, with an excess amount of DTT added (Lane 5), preformed disulfide linkages are expected to be fully reduced back to thiol functionalities (Figure 3.23d), and effectively, resulting in monomeric DNA-thiol-polymer conjugates on denaturing PAGE. This effect is observed in Lane 5, with the absence of higher order products (trimers, tetramers, pentamers) and significantly lower yields of dimers. Nevertheless, further studies would be required to further characterize the effect of DTT, test other reducing agents and assess the effect of varying the distance between disulfide serinol groups on the reaction efficiency to provide a better control of the cross-linking process.

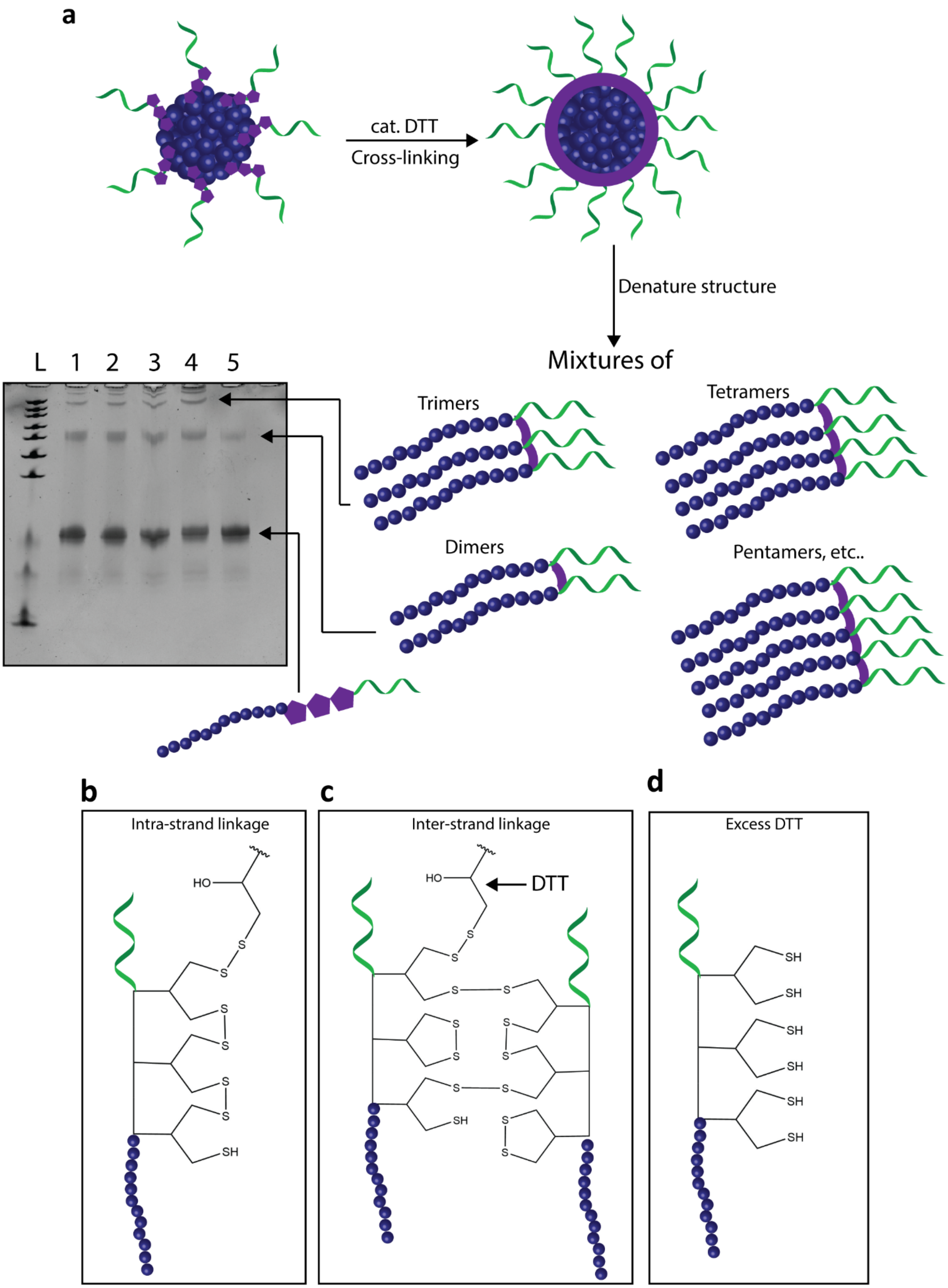
a
cat. DTT
Cross-linking
Denature structure
Mixtures of
L
1
2
3
4
5
Trimers
Tetramers
Dimers
Pentamers, etc..
b
Intra-strand linkage
HO
S
S
S
S
S
S
SH
c
Inter-strand linkage
HO
DTT
S
S
S
S
S
S
S
S
S
S
S
S
SH
S
S
d
Excess DTT
SH
SH
SH
SH
SH
SH

Figure 3.23 – Characterization of disulfide (DS)-functionalized DNA nanoparticle cross-linking by PAGE. DS-DNA nanoparticles were assembled in aqueous buffer through a thermal anneal cycle (95 °C – 4 °C). a) Structures were titrated with different amounts of DTT, then denatured using urea and EDTA prior to analysis with denaturing PAGE. Lane 1: DS-DNA nanoparticle control, lane 2: DS-DNA nanoparticle + 0.1 equiv. DTT (compared to total DS-DNA concentration), lane 3: DS-DNA nanoparticle + 1 equiv. DTT, lane 4: DS-DNA nanoparticle + 10 equiv. DTT, lane 5: DS-DNA nanoparticle + 100 equiv. DTT. b) Schematic illustration of possible intra-strand disulfide bond formation, c) inter-strand bond formation. d) full reduction of disulfides to thiols with excess DTT.

In general, we describe a simple strategy for DNA nanoparticle cross-linking. Preliminary results show the formation of covalently cross-linked strands with this approach. Optimization of the reaction conditions such as the amount and type of reducing agent added, temperature conditions, concentration of functionalized DNA-polymer strands would be required to increase the cross-linking efficiency. It will also be necessary to evaluate the effect of number, position of the disulfide functional groups in the strand, and their relative spacing on cross-linking efficiency en route to developing a facile effective strategy for increasing the stability of DNA-polymer based nanoparticles. A few proposed design strategies are highlighted in Figure 3.24.

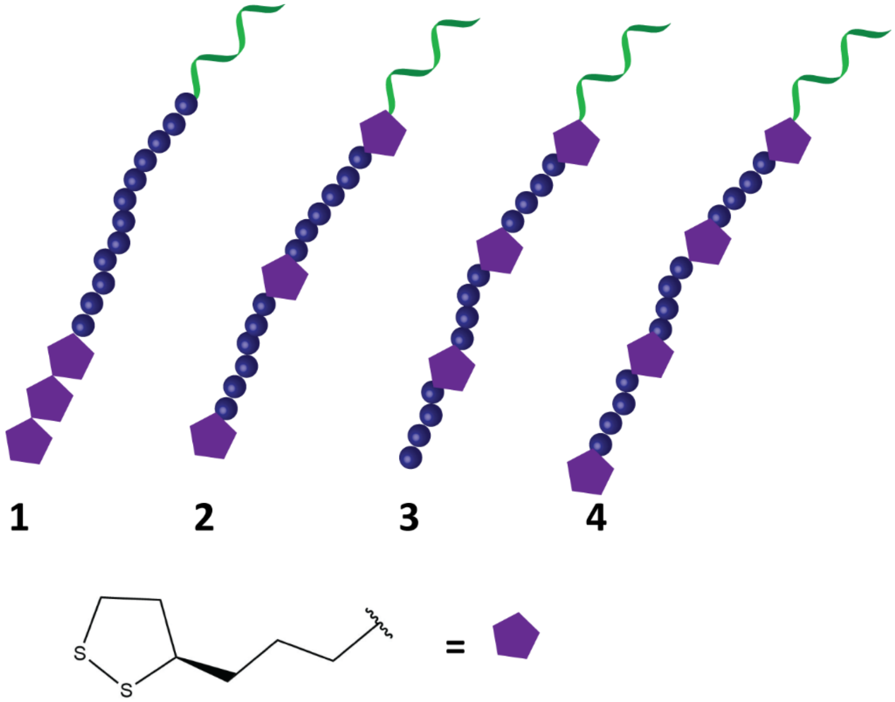

Figure 3.24 – Proposed design strategies for DNA nanoparticle disulfide cross-linking.

3.4 Conclusion

In this chapter, we tackled some of the limitations hampering the success of drug delivery systems. We highlighted a number of important strategies toward constructing an optimized delivery vehicle demonstrating higher stability, targeting capabilities and selective cargo release. We showed that the addition of targeting ligands increased the cellular uptake of structures in cells overexpressing target receptors. We further demonstrated an example of a stimuli-responsive delivery vehicle, capable of selectively shedding cargo upon binding to a genetic marker. In the same context, we investigated the uptake profile of DNA nanoparticles not only in diseased cells, but also in normal epidermis keratinocytes and showed their increased uptake. We further conducted a preliminary intracellular FRET study to assess the integrity of structures inside complex cellular environments – a study often overlooked, but of great importance for any delivery system designed to induce intracellular activity. Additionally, we showed a simple strategy to increase DNA nanoparticle resistance toward nuclease degradation in blood serum. Next, we characterized the interaction of DNA nanoparticles with serum proteins, namely human serum albumin (HSA), and showed that DNA nanoparticles, when intact, show no interaction with HSA. We then show the decoration of DNA nanoparticles with acid cleavable PEG-moieties as a 2nd line of defense against serum proteins, nucleases and the macrophage system. Finally, we highlight preliminary results on our efforts towards further increasing nanoparticle stability by cross-linking through covalent disulfide linkages. Upon structural internalization into reducing intracellular environments, breakage of disulfide bonds would cause structural destabilization and release of therapeutic agents.

The power of our approach lies in the ease of synthesis and modification of sequence-defined DNA-polymers. The sequence of DNA can be chosen at will, along with the sequence and length of the hydrophobic block. Our synthesis method is also compatible with RNA, allowing the incorporation of siRNA-based therapeutics within our platform. Additionally, our self-assembly method allows for mixing varying ratios of DNA-polymer strands with different functionalities offering versatile hybrid structures. This offers the ability to combine all the strategies described in this chapter into one highly sophisticated and "smart" functional device with great potential for nanomedicine. Certainly, there is still much chemistry and biology to be understood, but we could be headed in the right direction.

3.5 Experimental Section

3.5.1 General

The list of reagents is detailed in *Experimental Section 2.5.1* with the following additions. Cyanine 5 (cat# 10-5915-xx) was purchased from Glen Research. mPEG (M_n = 5000 Da) was purchased from Sigma Aldrich (CAS #: 9004-74-4). DBCO-dT-CE phosphoramidite was purchased from Glen Research (cat. #: 10-1539-xx). Disulfide serinol phosphoramidite was purchased from Glen Research (cat. #: 10-1991-xx). Human serum albumin (HSA) was purchased from Sigma Aldrich (CAS #: 70024-90-7).

3.5.2 Instrumentation

Instrumentation used is detailed in *Experimental Section 2.5.2* with the following additions. Confocal imaging was done on a Zeiss LSM 780 confocal laser scanning microscope equipped with a 63X/1.4 NA oil immersion objective lens, an argon ion laser (514/635 nm, 25 mW) and a Quasar 32 PMT array detector. Flow cytometry data was analyzed using a FACS Calibur flow cytometer.

3.5.3 Solid-phase synthesis and purification

DNA synthesis is detailed in *Experimental Section 2.5.3* in Chapter 2. For the coupling of Cy5 phosphoramidite (0.1 M, anhydrous acetonitrile) and dT-DBCO (0.1 M, anhydrous acetonitrile) amidite extended coupling times of 10 minutes were followed using 0.25M 5-(ethylthio)tetrazole in anhydrous acetonitrile. For Cy5-labeled strands, detection was carried out using a diode-array detector, monitoring absorbance at 260 nm (DNA-specific), 646 nm (Cy5-specific).

3.5.4 Sequences of DNA-polymer conjugates

The sequences of the DNA-polymer conjugates and DNA controls are presented in Supporting Table 3.1.

Table 3.1 – Sequences of strands and DNA-polymer conjugates.

D: dodecane phosphoramidite (hexaethylene, HE). Cy3: Cyanine 3, Cy5: Cyanine 5, Cy5.5: Cyanine 5.5. DBCO: DBCO-dT-CE phosphoramidite. DS: Disulfide serinol phosphoramidite

Strand	**Sequence (5'-xx-3')**
ssDNA-HE$_{12}$	**DDDDDDDDDDDD**TTTTTCAGTTGACCATATA
sHB5-HE$_{12}$	**DDDDDDDDDDDD**TTTTTCTAAAAGGATTCTTCCCAAGGGGATCCAATTCAAACAGC
sHB5-extension	TATATGGTCAACTGTTTTTCTAAAAGGATTCTTCCCAAGGGGATCCAATTCAAACAGC
DNA-HE$_{12}$-Cy3	**Cy3DDDDDDDDDDDD**TTTTTCAGTTGACCATATA
DNA-HE$_{12}$-Cy5	**Cy5DDDDDDDDDDDD**TTTTTCAGTTGACCATATA
DNA-HE$_{12}$-Cy5.5	**Cy5.5DDDDDDDDDDDD**TTTTTCAGTTGACCATATA
ssDNA	TTTTTCAGTTGACCATATA
Cy5.5-ssDNA	**Cy5.5**TTTTTCAGTTGACCATATA
Cy3-ssDNA	**Cy3**TTTTTCAGTTGACCATATA
antiMIR134-Cy3-HE$_{12}$	**DDDDDDDDDDDDCy3**TTTTCCCCTCTGGTCAACCAGTCACA
Cy5-cargo strand	GTTGACCAGAGGGGAAAA**Cy5**
miR134	UGUGACUGGUUGACCAGAGGGGAAAA
PS-DNA	TTTTTCAGTTGACCATATA
PS-DNA-HE$_{12}$	**DDDDDDDDDDDD**TTTTTCAGTTGACCATATA
DBCO-DNA-HE$_{12}$	**DDDDDDDDDDDD**TTTTTCAGTTGACCATATA-**DBCO**
DNA-DS-DS-DS-HE$_{12}$	**DDDDDDDDDDDD-DSDSDS**-TTTTTCAGTTGACCATATA

3.5.5 Targeted delivery to HER2-positive breast cancer cells

3.5.5.1 Preparation of first generation aptamer-DNA nanoparticles

Aptamer-DNA particles were prepared by mixing sHB5-HE_{12} and DNA-HE_{12} monomers dispersed in water with the assembly buffer. Final volume: 50 µL, DNA concentration: 10 µM in TAMg buffer $[Mg^{2+}]_{final}$ = 12.5 mM (10x TAMg buffer contains 125 mM Mg^{2+}, 1x TAMg contains 12.5 mM Mg^{2+}), followed by a heat/cool cycle (95 °C to 4 °C over 4 hours). For samples containing 25% aptamer, 12.5 µL of 10 µM sHB5-HE_{12} were mixed with 37.5 µL of 10 µM DNA-HE_{12}. For labeled structures used in flow cytometry studies, 25% aptamer-Cy5-DNA nanoparticles were prepared by mixing 12.5 µL of 15 µM sHB5-HE_{12} with 12.5 µL of 15 µM sHB5-HE_{12}-Cy5 and 25 µL of 15 µM DNA-HE_{12} followed by thermal annealing.

3.5.5.2 Preparation of second generation aptamer-DNA nanoparticles

Second generation aptamer-DNA particles were prepared by mixing DNA-HE_{12} monomers dispersed in water with the assembly buffer. Final volume: 50 µL, DNA concentration: 10 µM in TAMg buffer $[Mg^{2+}]_{final}$ = 12.5 mM (10x TAMg buffer contains 125 mM Mg^{2+}, 1x TAMg contains 12.5 mM Mg^{2+}), followed by a heat/cool cycle (95 °C to 4 °C over 4 hours). Following annealing, to 50 µL of the assembly structure, 25 µL sHB5-extension (10 µM dispersed in 1x TAMg) was added and incubated for 2 hours at room temperature. Alternatively, for one-pot assembly, 50 µL of 10 µM DNA-HE_{12} dispersed in water, was mixed with 25 µL of 10 µM sHB5-extension in water, followed by the addition of TAMg (final [TAMg] contains 12.5 mM Mg^{2+}) and thermal annealing (95 °C to 4 °C over 4 hours). For structures used in flow cytometry studies, Cy3-labeled DNA nanoparticles were prepared from 25% DNA-HE_{12}-Cy3 and 75% DNA-HE_{12}. To achieve that, 25 µL of 15 µM DNA-HE_{12}-Cy3 was mixed with 75 µL of 15 µM DNA-HE_{12} in 1xTAMg and annealed. For room temperature aptamer addition, following annealing, 50 µL of 15 µM sHB5-extension was added and incubated at room temperature.

3.5.5.3 Characterization of aptamer-DNA nanoparticles

Agarose Gel electrophoresis

In each case, 2.5% AGE was carried out at 4 °C for 2.5 hours at a constant voltage of 80V. Typical sample loading is 30 picomoles with respect to the DNA, per lane (3 µL of 10 µM DNA, mixed with 7µL 1x TAMg and 2.5 µL glycerin).

Atomic Force Microscopy

Dry AFM was carried out using a MultiMode8™ SPM connected to a Nanoscope™ V controller (Bruker, Santa Barbara, CA). All images were obtained using ScanAsyst mode in air with AC160TS cantilevers (Nominal values: Tip radius – 2 nm, Resonant frequency – 300 kHz, Spring constant – 42 N/m) from Bruker. 5 µL of each sample prepared at 5 µM in TAMg buffer was deposited on a freshly cleaved mica surface (ca. 7 x 7 mm) and allowed to adsorb for 2-5 seconds. Then 50 µL of 0.22 µm filtered Millipore water was dropped on the surface and instantly removed with filter paper. The surface was then washed with a further 100 µL of water (2 x 50 µL), wicked with a filter paper, and the excess removed with a flow of nitrogen (or air). Samples were dried under vacuum for at least 3 hours prior to imaging.

Dynamic Light Scattering

Dynamic light scattering (DLS) experiments were carried out using a DynaPro™ Instrument from Wyatt Technology. A cumulants fit model was used to confirm the presence and determine the size the Cy3 and Cy3Cy3-DNA nanofibers. Sterile water and 1xTAMg buffer were filtered using a 0.45 µm nylon syringe filter before use in DLS sample preparation. 20 µL of sample (concentration: 5 µM) was used in each measurement. All measurements were carried out in triplicate at 25 °C.

3.5.5.4 Flow cytometry studies of sHB5 aptamer-nanoparticles

SKBR3, MD4 and HeLa cells were seeded at a density of 5 x 10^5 in a 6-well plate. After 24 hours, the cells were incubated with aptamer nanoparticles (100 µL of 15µM DNA in sample added in a total media volume of 1 mL). The final concentration of total DNA was 1.5 µM in both samples. After 4 hours of incubation, cells were detached, washed and resuspended in 1x PBS, followed by fixing with 2% paraformaldehyde. Samples were then processed using FACS FORTESSA. All measurements were performed in triplicates for error analysis.

3.5.6 Stimuli-responsive DNA nanoparticles

3.5.6.1 Preparation of stimuli-responsive DNA nanoparticles

2.5 μL of 10 μM antiMIR-Cy3-HE$_{12}$ was mixed with 97.5 μL of 10 μM DNA-HE$_{12}$. The mixture was suspended in TAMg buffer (final [TAMg] contains 12.5 mM Mg^{2+}) and annealed with a heat/cool cycle (95 °C to 4 °C over 4 hours) to form antiMIR-Cy3-DNA nanoparticles. To that, 50 μL of 20 μM Cy5-cargo strand was added and incubated overnight at room temperature. The following day, a 2x molar excess of miR134 compared to nanoparticle DNA was added and incubated from 37 °C for 2 hours then room temperature overnight allowing cargo strand displacement.

3.5.6.2 Fluorescence spectroscopy

Fluorescence scans were performed on a Cary Eclipse fluorescence spectrophotometer from Agilent technologies. For fluorescence measurements, structures (60 μL at 10 μM DNA concentration) were analyzed prior to and post addition of miR134.

3.5.6.3 Agarose gel electrophoresis

Same gel conditions were used as **Section 3.5.5.3**

3.5.7 Characterizing the uptake and intracellular fate of DNA nanostructures in normal skin cells

3.5.7.1 Preparation of dye-labeled structures

Cy3-labeled, Cy5-labeled or Cy3Cy5.5-labeled DNA nanoparticles were prepared by mixing dye-labeled HE$_{12}$-DNA with unlabelled HE$_{12}$-DNA strands at a 25:75 percent ration (DNA concentration 17 µM) followed by an annealing cycle 95 °C – 4 °C over 4 hours. This percentage of labeled/unlabeled strands was observed to give the cleanest assemblies along with high fluorescence intensity for cellular uptake studies. For Cy3Cy5.5-labeled nanoparticles, Cy3-labeled HE$_{12}$-DNA, Cy5.5-labeled HE$_{12}$-DNA with unlabelled HE$_{12}$-DNA strands were mixed a 25:25:50 percent ratio (DNA concentration 17 µM) followed by an annealing cycle 95 °C – 4 °C over 4 hours.

3.5.7.2 Characterization of Cy3Cy5.5-labeled structures

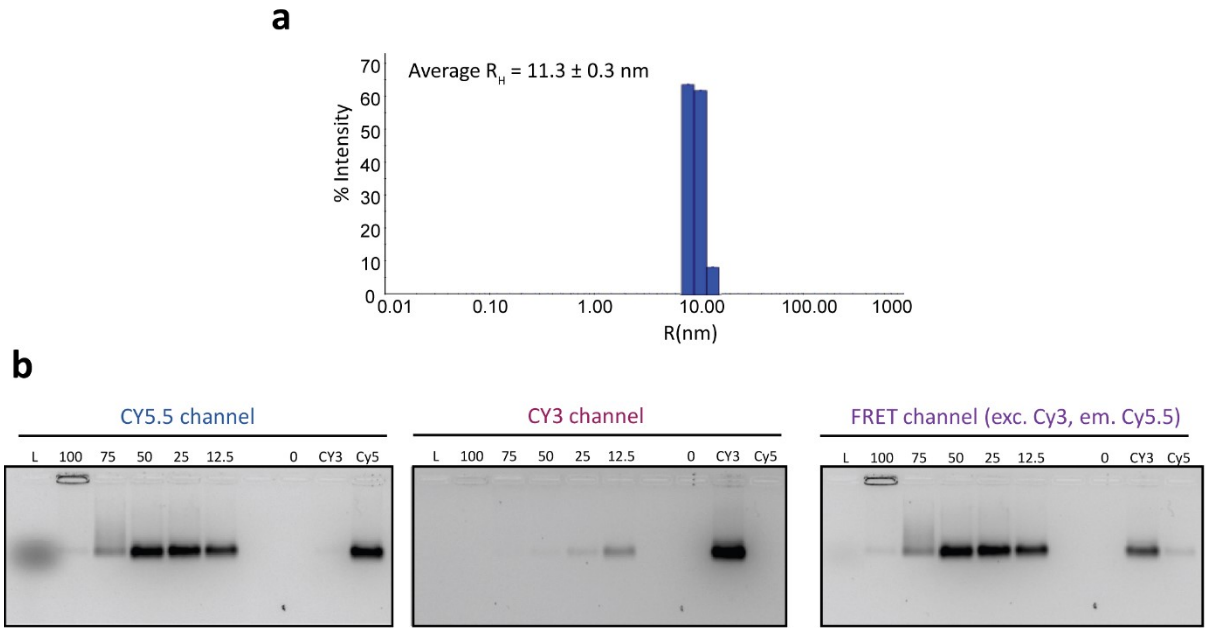

Figure 3.25 – Characterization of Cy3Cy5.5-DNA nanoparticles. a) DLS histogram showing a narrow size distribution of particles in solution. b) AGE analysis of assemblies of different ratios of Cy3-HE$_{12}$-DNA, Cy5.5-HE$_{12}$-DNA and HE$_{12}$-DNA. 100% indicates (100% labeled-structures)

meaning a mixture of 50% Cy3 and 50% Cy5.5-HE$_{12}$-DNA. 50: indicates 50% labeled; meaning 25% Cy3-HE$_{12}$-DNA, 25%-Cy5.5-HE$_{12}$-DNA and 50% unlabeled HE$_{12}$-DNA. Gels were imaged under a Cy5.5, Cy3 and FRET channel. 100% labeled structures show a non-penetrating band, however as the percent of dye decreases in the mixture, a uniform well-defined penetrating band appears (ex. 50%, 25% and 12.5%).

3.5.7.3 Confocal microscopy in NHEK cells

Cells were seeded in 8-slide chamber 50 % confluence (1E+4 cells) in keratinocyte medium. The next day (28 hours after initial seeding. 70 % confluence kept), media was removed, and fresh media was added. Samples was then added at a final concentration of 1.4 µM (total DNA) and cells were allowed to incubate 24 hours. Subsequently, cells were washed with 1X PBS and fixed with 4% paraformaldehyde at room temperature for 15 minutes. Then, cells were washed with 1X PBS and mounted with ProLong Gold. Slides were cured overnight at 4 °C and visualized the next day. Images were recorded using a Zeiss AxioImager and images were analyzed using the Zen software (Zeiss, USA).

3.5.7.4 Flow cytometry studies

Cells were seeded (5E+5 cells) in 6-well plates in keratinocyte medium. Samples were then added 1.5 µM total DNA and incubated with the cells for 24 hours. Cells were then fixed with 4% PFA and washed with 1X PBS. Subsequently, cells were resuspended in 1X PBS + 0.1% sodium azide prior to imaging. Samples were then processed using FACS FORTESSA. All measurements were performed in triplicates for error analysis.

3.5.8 Increasing the serum stability of DNA nanoparticles

3.5.8.1 FBS assay

Same conditions were used as **Chapter 2, Experimental Section 2.5.10**.

3.5.9 Nanoparticle interaction with serum proteins

3.5.9.1 HSA binding studies

DNA nanoparticles (composed of DNA-HE$_{12}$ conjugates) were prepared as a 10 µM solution by thermal annealing 95 °C – 4 °C over 4 hours. For binding studies, 1 µL of HSA stock (526 µM) was added to 10 µL of DNA nanoparticles and incubated for 2 hours prior to analysis by agarose gel electrophoresis. For control experiments, 10 µL of HE$_{12}$-DNA micellar structures were denatured by the addition of denaturing solution of urea (10 µL of each of 8 M urea) and depletion of magnesium cations prior to HSA addition in an EDTA containing TBE buffer, exposing their long aliphatic chains. Titrations of human serum albumin (HSA) prepared at 526 µM were added to the denatured DNA nanoparticle solution to yield final HSA dilutions of 1/1000, 1/100, 1/50, 1/10, 1/5, 1/2 and undiluted excess HSA (526µM stock). The samples were analyzed under denaturing 20% PAGE.

As another control, DNA nanoparticles were incubated with 10% FBS for different time points, and subsequently denatured with 2x formamide (without the addition of proteinase K enzyme). The structures were then run under 20% denaturing PAGE (*Experimental Figure 3.26*).

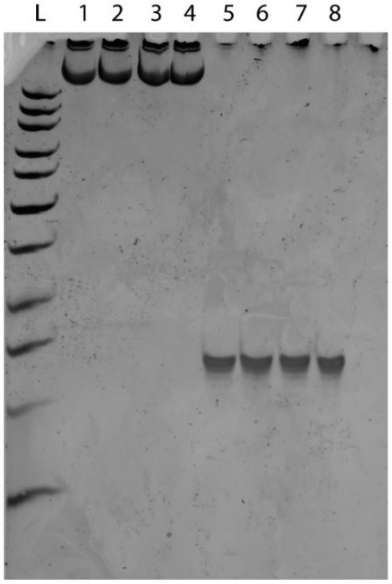

Figure 3.26 – PAGE analysis of denatured HE$_{12}$-DNA conjugate strands incubated with 10% FBS. Incubation times: 0 mins, 1 hour, 2 hours, 4 hours. Lanes 1-4 are in the presence of 10% FBS, lanes 5-8 in the absence of FBS.

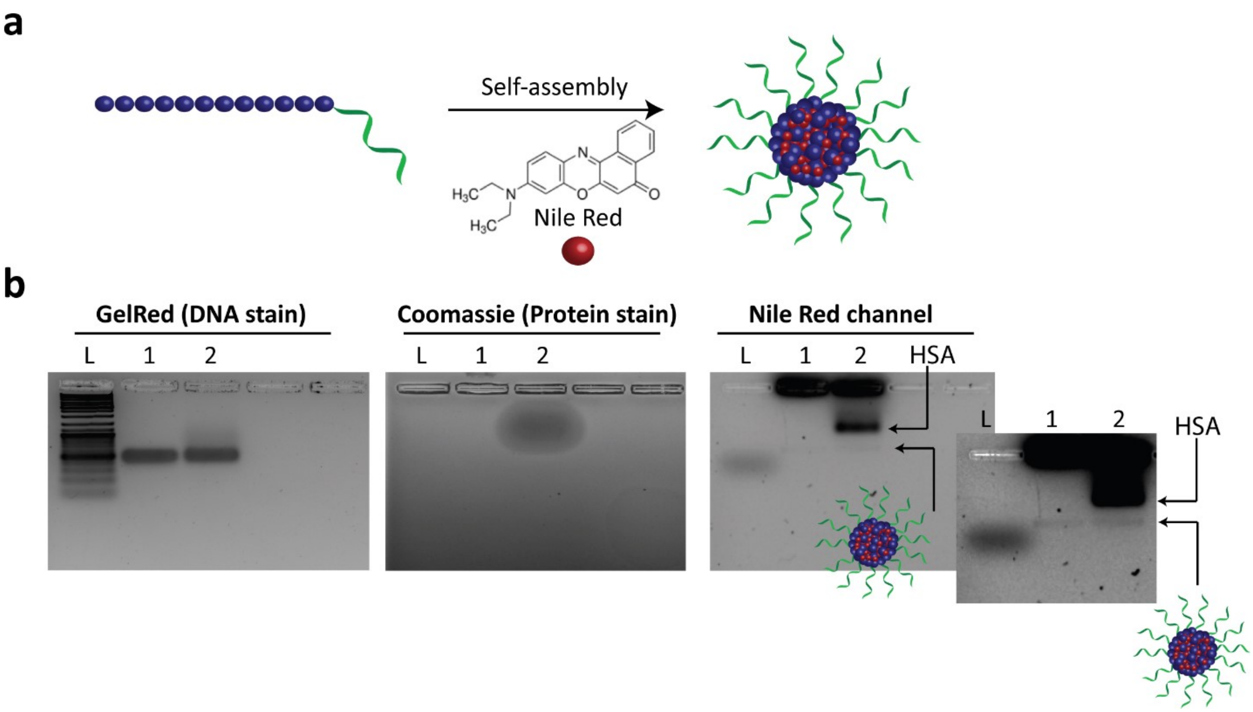

Figure 3.27 – DNA nanoparticle binding studies with human serum albumin (HSA). a) Preparation of Nile Red-loaded nanoparticles. b) Agarose gel electrophoresis of DNA nanoparticles prior to (Lane 1) and post incubation (Lane 2) with HSA. The gels were visualized under Gel Red DNA stain channel (left panel), Commassie Blue protein stain (middle panel) and Nile Red channel (right panel).

The effect of HSA on the release of encapsulated drug was investigated. This would provide some indication as to how our drug-loaded structures would behave *in vivo*. Our studies were conducted by initially preparing Nile Red-loaded DNA nanoparticles (*Experimental Figure 3.27*). These structures would allow to study both: the release of Nile Red upon HSA addition, and the direct interaction of DNA nanoparticles with HSA. Following HSA addition (5x molar excess) and incubation for 2 hours, the products were analyzed by agarose gel electrophoresis AGE. As illustrated in *Experimental Figure 3.27*, upon incubation, no interaction is observed between the DNA nanoparticles and HSA protein. These results are further confirmed in the Nile Red channel, where two distinct populations of DNA particles and HSA are observed. The analysis of AGE data was complicated because under the gel electrophoretic conditions, the dye molecules diffused out of the DNA particles, and remained in the gel wells. Thus, it was difficult to use AGE data to determine Nile Red release. If we assume that the non-penetrating band that is not associated with HSA represents Nile Red originally encapsulated in the nanoparticle, then the data would suggest that only a small fraction of Nile Red is released upon HSA addition, and was bound to protein, possibly to the HSA hydrophobic binding pockets.

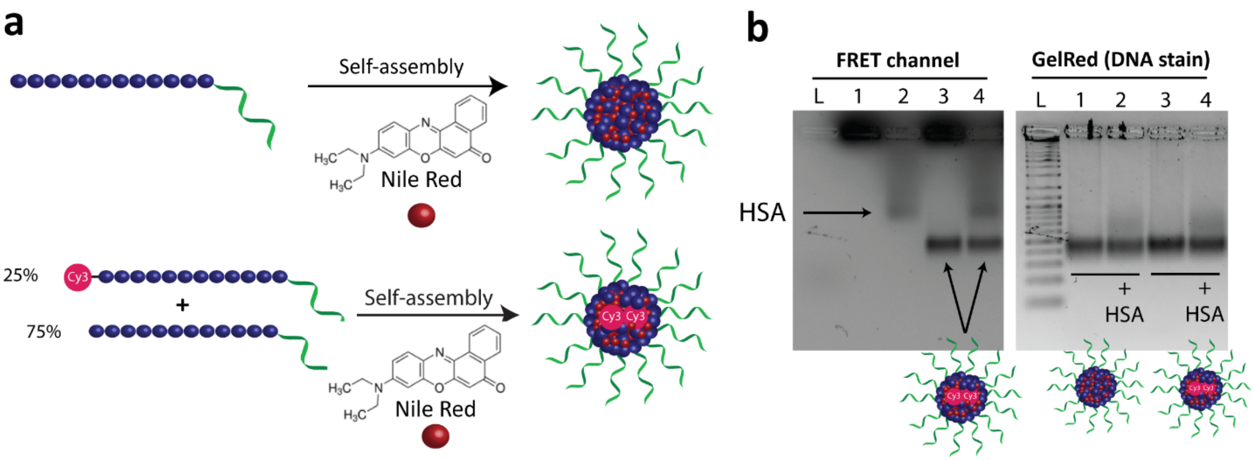

Figure 3.28 – HSA binding studies of DNA nanoparticles and the effect on encapsulated cargo. a) Generation of Nile Red-loaded unlabeled and Cy3-labeled DNA nanoparticles. b) AGE of Nile Red-loaded cyanine-labeled nanoparticles incubated with HSA protein visualized under FRET channel (excitation 546 nm, emission 650 nm) and GelRed DNA stain. Lanes 1 &2: unlabeled DNA nanoparticles, Lanes 3&4: Cy3-labeled nanoparticles, pre-and post HSA incubation.

To further investigate the interaction with HSA, we designed a Nile Red-loaded Cy3-DNA nanoparticle system (*Experimental Figure 3.28*). Due to the spectral overlap between Cy3 and Nile Red, simultaneous observation of released Nile Red molecules bound to HSA and the labeled DNA nanoparticles is possible under one fluorescence channel. In other experiments, we found that under gel electrophoretic conditions Nile Red molecules diffused out of the nanoparticle core, and a small portion of the dye molecules was found associated with HSA (*Experimental Figure 3.27*). These findings would hence allow us to track the mobility shift of the HSA protein by monitoring Nile Red fluorescence. Thus, the spectral overlap between Nile Red and Cy3 would then allow direct observation of HSA and Cy3 nanoparticles under a detection channel common for both Nile Red and Cy3. As illustrated in *Experimental Figure 3.28*, the lack of interaction between labeled DNA particles and HSA is demonstrated through the presence of two populations with different mobility shifts. Additionally, the amount of DNA was observed to remain mostly unchanged after HSA incubation (GelRed channel).

3.5.9.2 Preparation of PEGylated-DNA nanoparticles

100 µL of 10 µM DBCO-DNA-HE_{12} conjugates in water were suspended in TAMg buffer and assembled through a heat/cool cycle (95 °C – 4 °C, over 4 hours). PEG-azide or PEG-acetal-azide were prepared as a 2.4 mM stock solution in water. For 4x molar excess, 1.67 µL of 2.4 mM PEG stock solutions was added to 100 µL of nanoparticles containing 10 µM DBCO-DNA-HE_{12} and incubated for 24 hours at room temperature. The structures were then analyzed by AGE and AFM as described in *Experimental Section 3.5.5.3*. For denaturing PAGE analysis of DBCO-DNA-HE_{12} PEGylation in water, the mixtures were loaded to an 18% polyacrylamide/urea gel. The gel was run at 250 V for 30 minutes followed by 500 V for 60 minutes with 1x TBE as the running buffer.

3.5.10 Cross-linking of DNA nanoparticles

3.5.10.1 Preparation of cross-linked DNA nanoparticles

DNA-DS-DS-DS-HE_{21} conjugates were generated by solid-phase synthesis. Disulfide-modified DNA nanoparticles were prepared by mixing 100 µL of 10 µM DNA-DS-DS-DS-HE_{12} strands in 1xTAMg buffer (final) followed by thermal annealing (95 °C – 4 °C over 4 hours). DTT was prepared as a 100 mM stock in water. Different dilutions of DTT in water were prepared for titration experiments. After the addition of DTT, the structures were incubated overnight at room temperature and analyzed by denaturing PAGE (conditions of denaturing PAGE are mentioned in *Experimental section 3.5.9.2*).

3.6 References

1. Rosenblum, D.; Joshi, N.; Tao, W.; Karp, J. M.; Peer, D., *Nature Communications* **2018,** *9* (1), 1410.
2. Wang, M.; Thanou, M., *Pharmacol. Res.* **2010,** *62* (2), 90-99.
3. Schnitzler, T.; Herrmann, A., *Acc. Chem. Res.* **2012,** *45* (9), 1419-1430.
4. Wu, Y.; Sefah, K.; Liu, H.; Wang, R.; Tan, W., *Proc. Natl. Acad. Sci. U. S. A.* **2010,** *107* (1), 5-10.
5. Du, J.; Lane, L. A.; Nie, S., *J. Control. Release* **2015,** *219*, 205-214.
6. Lu, C. H.; Willner, I., *Angew. Chem. Int. Ed. Engl.* **2015,** *54* (42), 12212-35.
7. Tan, X.; Li, B. B.; Lu, X.; Jia, F.; Santori, C.; Menon, P.; Li, H.; Zhang, B.; Zhao, J. J.; Zhang, K., *J. Am. Chem. Soc.* **2015,** *137* (19), 6112-6115.
8. Wu, X. A.; Choi, C. H. J.; Zhang, C.; Hao, L.; Mirkin, C. A., *J. Am. Chem. Soc.* **2014,** *136* (21), 7726-7733.
9. Cartiera, M. S.; Johnson, K. M.; Rajendran, V.; Caplan, M. J.; Saltzman, W. M., *Biomaterials* **2009,** *30* (14), 2790-8.
10. Sahay, G.; Querbes, W.; Alabi, C.; Eltoukhy, A.; Sarkar, S.; Zurenko, C.; Karagiannis, E.; Love, K.; Chen, D.; Zoncu, R.; Buganim, Y.; Schroeder, A.; Langer, R.; Anderson, D. G., *Nat. Biotechnol.* **2013,** *31* (7), 653-8.
11. Nam, H. Y.; Kwon, S. M.; Chung, H.; Lee, S. Y.; Kwon, S. H.; Jeon, H.; Kim, Y.; Park, J. H.; Kim, J.; Her, S.; Oh, Y. K.; Kwon, I. C.; Kim, K.; Jeong, S. Y., *J. Control. Release* **2009,** *135* (3), 259-67.
12. Bartczak, D.; Nitti, S.; Millar, T. M.; Kanaras, A. G., *Nanoscale* **2012,** *4* (15), 4470-2.
13. Reddy, J. A.; Allagadda, V. M.; Leamon, C. P., *Curr. Pharm. Biotechnol.* **2005,** *6* (2), 131-50.
14. Jayasena, S. D., *Clin. Chem.* **1999,** *45* (9), 1628.
15. Irvine, D.; Tuerk, C.; Gold, L., *J. Mol. Biol.* **1991,** *222* (3), 739-761.
16. Liu, J.; Lu, Y., *Angew. Chem. Int. Ed.* **2005,** *45* (1), 90-94.
17. Yang, H.; Liu, H.; Kang, H.; Tan, W., *J. Am. Chem. Soc.* **2008,** *130* (20), 6320-6321.
18. Mallikaratchy, P. R.; Ruggiero, A.; Gardner, J. R.; Kuryavyi, V.; Maguire, W. F.; Heaney, M. L.; McDevitt, M. R.; Patel, D. J.; Scheinberg, D. A., *Nucleic Acids Res.* **2011,** *39* (6), 2458-2469.
19. Vorobyeva, M.; Vorobjev, P.; Venyaminova, A., *Molecules* **2016,** *21* (12).
20. Cibiel, A.; Pestourie, C.; Ducongé, F., *Biochimie* **2012,** *94* (7), 1595-1606.
21. Farokhzad, O. C.; Cheng, J.; Teply, B. A.; Sherifi, I.; Jon, S.; Kantoff, P. W.; Richie, J. P.; Langer, R., *Proceedings of the National Academy of Sciences* **2006,** *103* (16), 6315.
22. Mahlknecht, G.; Maron, R.; Mancini, M.; Schechter, B.; Sela, M.; Yarden, Y., *Proc. Natl. Acad. Sci. U. S. A.* **2013,** *110* (20), 8170-5.
23. Gijs, M.; Penner, G.; Blackler, G. B.; Impens, N. R.; Baatout, S.; Luxen, A.; Aerts, A. M., *Pharmaceuticals (Basel)* **2016,** *9* (2).
24. Liu, Z.; Duan, J. H.; Song, Y. M.; Ma, J.; Wang, F. D.; Lu, X.; Yang, X. D., *J. Transl. Med.* **2012,** *10*, 148.
25. Kim, S.; Shi, Y.; Kim, J. Y.; Park, K.; Cheng, J. X., *Expert Opin Drug Deliv* **2010,** *7* (1), 49-62.
26. Hahn, J.; Wickham, S. F.; Shih, W. M.; Perrault, S. D., *ACS Nano* **2014,** *8* (9), 8765-75.
27. Guo, S.; Huang, L., *Journal of Nanomaterials* **2011,** *2011*, 12.

28. Lynch, I.; Dawson, K. A., *Nano Today* **2008,** *3* (1), 40-47.

29. Crooke, S. T., *Annu. Rev. Med.* **2004,** *55* (1), 61-95.

30. Wahlestedt, C.; Salmi, P.; Good, L.; Kela, J.; Johnsson, T.; Hökfelt, T.; Broberger, C.; Porreca, F.; Lai, J.; Ren, K.; Ossipov, M.; Koshkin, A.; Jakobsen, N.; Skouv, J.; Oerum, H.; Jacobsen, M. H.; Wengel, J., *Proceedings of the National Academy of Sciences* **2000,** *97* (10), 5633.

31. Ponnuswamy, N.; Bastings, M. M. C.; Nathwani, B.; Ryu, J. H.; Chou, L. Y. T.; Vinther, M.; Li, W. A.; Anastassacos, F. M.; Mooney, D. J.; Shih, W. M., *Nature Communications* **2017,** *8*, 15654.

32. Li, S. D.; Huang, L., *J. Control. Release* **2010,** *145* (3), 178-81.

33. Talelli, M.; Barz, M.; Rijcken, C. J. F.; Kiessling, F.; Hennink, W. E.; Lammers, T., *Nano Today* **2015,** *10* (1), 93-117.

34. Kim, Y.; Pourgholami, M. H.; Morris, D. L.; Stenzel, M. H., *Biomacromolecules* **2012,** *13* (3), 814-825.

35. Duraiyan, J.; Govindarajan, R.; Kaliyappan, K.; Palanisamy, M., *J. Pharm. Bioallied Sci.* **2012,** *4* (Suppl 2), S307-S309.

36. Sharma, S., *Indian Journal of Medical and Paediatric Oncology : Official Journal of Indian Society of Medical & Paediatric Oncology* **2009,** *30* (1), 1-8.

37. Vranic, S.; Gatalica, Z.; Wang, Z.-Y., *Oncol. Lett.* **2011,** *2* (6), 1131-1137.

38. Subik, K.; Lee, J.-F.; Baxter, L.; Strzepek, T.; Costello, D.; Crowley, P.; Xing, L.; Hung, M.-C.; Bonfiglio, T.; Hicks, D. G.; Tang, P., *Breast Cancer : Basic and Clinical Research* **2010,** *4*, 35-41.

39. Theato, P.; Sumerlin, B. S.; O'Reilly, R. K.; Epps, I. I. I. T. H., *Chem. Soc. Rev.* **2013,** *42* (17), 7055-7056.

40. Kahn, J. S.; Hu, Y.; Willner, I., *Acc. Chem. Res.* **2017,** *50* (4), 680-690.

41. Tay, Y. M.; Tam, W. L.; Ang, Y. S.; Gaughwin, P. M.; Yang, H.; Wang, W.; Liu, R.; George, J.; Ng, H. H.; Perera, R. J.; Lufkin, T.; Rigoutsos, I.; Thomson, A. M.; Lim, B., *Stem Cells* **2008,** *26* (1), 17-29.

42. Muther, C.; Jobeili, L.; Garion, M.; Heraud, S.; Thepot, A.; Damour, O.; Lamartine, J., *Aging (Albany NY)* **2017,** *9* (11), 2376-2396.

43. Yurke, B.; Turberfield, A. J.; Mills, A. P., Jr.; Simmel, F. C.; Neumann, J. L., *Nature* **2000,** *406* (6796), 605-8.

44. Grant, B. D.; Donaldson, J. G., *Nature reviews. Molecular cell biology* **2009,** *10* (9), 597-608.

45. Lv, H.; Zhang, S.; Wang, B.; Cui, S.; Yan, J., *J. Controlled Release* **2006,** *114* (1), 100-109.

46. Zintchenko, A.; Philipp, A.; Dehshahri, A.; Wagner, E., *Bioconjugate Chem.* **2008,** *19* (7), 1448-1455.

47. Choi, J. S.; Lee, E. J.; Jang, H. S.; Park, J. S., *Bioconjugate Chem.* **2001,** *12* (1), 108-113.

48. Rush, A. M.; Nelles, D. A.; Blum, A. P.; Barnhill, S. A.; Tatro, E. T.; Yeo, G. W.; Gianneschi, N. C., *J. Am. Chem. Soc.* **2014,** *136* (21), 7615-7618.

49. Rosi, N. L.; Giljohann, D. A.; Thaxton, C. S.; Lytton-Jean, A. K.; Han, M. S.; Mirkin, C. A., *Science* **2006,** *312* (5776), 1027-30.

50. Chen, T.; Wu Cuichen, S.; Jimenez, E.; Zhu, Z.; Dajac Joshua, G.; You, M.; Han, D.; Zhang, X.; Tan, W., *Angew. Chem. Int. Ed.* **2013,** *52* (7), 2012-2016.

51. Zhang, C.; Hao, L.; Calabrese Colin, M.; Zhou, Y.; Choi Chung Hang, J.; Xing, H.; Mirkin Chad, A., *Small* **2015,** *11* (40), 5360-5368.
52. Bousmail, D.; Amrein, L.; Fakhoury, J. J.; Fakih, H. H.; Hsu, J. C. C.; Panasci, L.; Sleiman, H. F., *Chemical Science* **2017,** *8* (9), 6218-6229.
53. Coman, D. R.; Anderson, T. F., *Cancer Res.* **1955,** *15* (8), 541.
54. Zalba, S.; ten Hagen, T. L. M., *Cancer Treat. Rev.* **2017,** *52*, 48-57.
55. Gu, Z.; Biswas, A.; Zhao, M.; Tang, Y., *Chem. Soc. Rev.* **2011,** *40* (7), 3638-3655.
56. Rush, A. M.; Thompson, M. P.; Tatro, E. T.; Gianneschi, N. C., *ACS Nano* **2013,** *7* (2), 1379-1387.
57. Conway, J. W.; McLaughlin, C. K.; Castor, K. J.; Sleiman, H., *Chem. Commun. (Camb.)* **2013,** *49* (12), 1172-4.
58. Allen, T. M., *Trends Pharmacol. Sci.* **1994,** *15* (7), 215-220.
59. Owens Iii, D. E.; Peppas, N. A., *Int. J. Pharm.* **2006,** *307* (1), 93-102.
60. Gotto, A. M.; Pownall, H. J.; Havel, R. J., [1] Introduction to the plasma lipoproteins. In *Methods Enzymol.*, Academic Press: 1986; Vol. 128, pp 3-41.
61. Li, S.-D.; Huang, L., *J. Controlled Release* **2010,** *145* (3), 178-181.
62. Kato, Y.; Ozawa, S.; Miyamoto, C.; Maehata, Y.; Suzuki, A.; Maeda, T.; Baba, Y., *Cancer Cell Int.* **2013,** *13* (1), 89.
63. Sun, X.; Rossin, R.; Turner, J. L.; Becker, M. L.; Joralemon, M. J.; Welch, M. J.; Wooley, K. L., *Biomacromolecules* **2005,** *6* (5), 2541-2554.
64. McHale, R.; Patterson, J. P.; Zetterlund, P. B.; O'Reilly, R. K., *Nat. Chem.* **2012,** *4*, 491.
65. Joralemon, M. J.; O'Reilly, R. K.; Hawker, C. J.; Wooley, K. L., *J. Am. Chem. Soc.* **2005,** *127* (48), 16892-16899.
66. Kwak, M.; Musser, A. J.; Lee, J.; Herrmann, A., *Chem. Commun.* **2010,** *46* (27), 4935-4937.
67. Li, Y.; Xiao, K.; Luo, J.; Xiao, W.; Lee, J. S.; Gonik, A. M.; Kato, J.; Dong, T. A.; Lam, K. S., *Biomaterials* **2011,** *32* (27), 6633-6645.
68. Lee, S.-Y.; Tyler, J. Y.; Kim, S.; Park, K.; Cheng, J.-X., *Mol. Pharm.* **2013,** *10* (9), 3497-3506.
69. Bapat, A. P.; Ray, J. G.; Savin, D. A.; Sumerlin, B. S., *Macromolecules* **2013,** *46* (6), 2188-2198.
70. Banga, R. J.; Meckes, B.; Narayan, S. P.; Sprangers, A. J.; Nguyen, S. T.; Mirkin, C. A., *J. Am. Chem. Soc.* **2017,** *139* (12), 4278-4281.
71. Awino, J. K.; Gudipati, S.; Hartmann, A. K.; Santiana, J. J.; Cairns-Gibson, D. F.; Gomez, N.; Rouge, J. L., *J. Am. Chem. Soc.* **2017,** *139* (18), 6278-6281.
72. Li, X.; Figg, C. A.; Wang, R.; Jiang, Y.; Lyu, Y.; Sun, H.; Liu, Y.; Wang, Y.; Teng, I. T.; Hou, W.; Cai, R.; Cui, C.; Li, L.; Pan, X.; Sumerlin, B. S.; Tan, W., *Angew. Chem.* **2018,** *0* (0).

Preface

In Chapters 2 and 3, sequence-defined DNA polymers were examined in the context of drug delivery. Chapter 4 presents a new application in materials science and describes their importance in giving rise to new supramolecular self-assembled structures with interesting properties and function. A discovery is reported wherein the site-specific introduction of a single Cyanine dye (Cy3) molecule to DNA-polymer conjugates causes a drastic morphological shift in their self-assembly from spheres to one-dimensional rods. A strategy to generate rods with controlled length is presented. Additionally, an unprecedented supramolecular growth mechanism of DNA fibers with controlled dimensionality is discovered. Due to their change in optical properties upon assembly/disassembly, these structures could be used as fluorescent bioanalytical tools. Finally, examples are described for the templation of nanomaterials on DNA fibers and the site-specific alignment of fibers along DNA origami en route toward complex hybrid architectures with sophisticated function.

From Cheeky to Geeky….

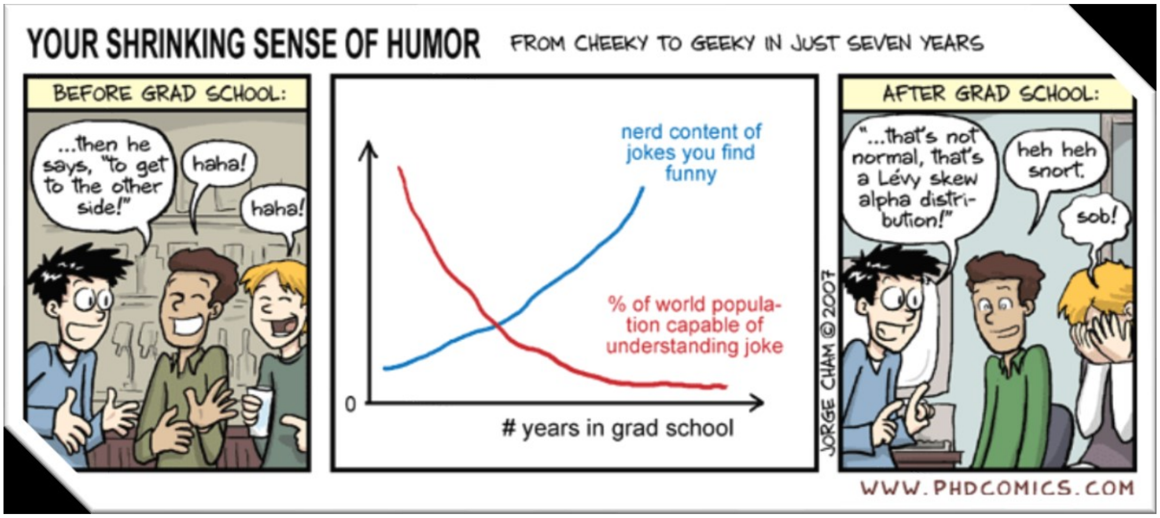

4

Cyanine-mediated DNA Nanofiber Growth with Controlled Dimensionality

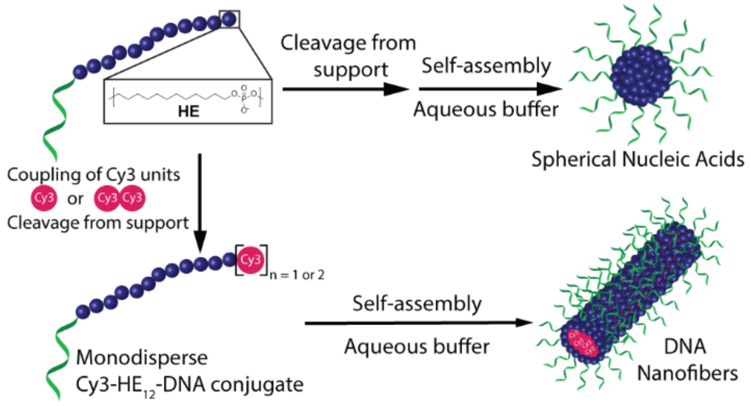

This chapter is composed mainly of work published as "Cyanine-mediated DNA Nanofiber Growth with Controlled Dimensionality" by Danny Bousmail, Pongphak Chidchob and Hanadi F. Sleiman. *Journal of the American Chemical Society*, **2018**, *140* (30), 9518-9530.

Contribution of authors

Danny Bousmail helped design the experiments and primarily contributed to the production of experimental data. **Pongphak Chidchob** helped with TEM analysis, conducted confocal fluorescence microscopy of fiber networks and prepared the DNA origami. **Hanadi F. Sleiman** designed the project, guided interpretation of data and discussion of results. **Danny Bousmail** and **Hanadi F. Sleiman** co-wrote the manuscript.

We thank Xin Luo for providing DNA-AuNP samples.

4.1 Abstract

Supramolecular one-dimensional (1D) architectures are of high interest in drug delivery and templation of complex linear arrays due to their high aspect ratio and rigidity. A particular desire is the access of 1D nanostructures with high functionality and biorelevance, which opens the door to their applications in materials science and nanomedicine. In this chapter, we report the discovery that the site-specific introduction of a cyanine (Cy3) dye unit in sequence-defined DNA amphiphiles causes a complete shift of the overall structure from spheres to 1D DNA nanofibers in aqueous media. We show that the generation of DNA nanofibers is dependent on the presence of cyanine units and their position within the DNA polymer hybrid. We further demonstrate an example of stimuli-responsive shape-shifting DNA nanofibers to highlight the role of the dye in the overall assembly. Notably, we show the preparation of fibers with controlled length by seeded-growth mechanism. Additionally, the DNA nanofibers exhibit a change in Cy3 dye optical properties upon assembly, typical of cyanine dye aggregation, which can be used to monitor the fiber growth process. To demonstrate the functionality of these structures, we show the templation of gold nanoparticles (AuNP) along the fiber length and demonstrate the directional templation of DNA nanofibers on rectangular DNA origami. Our findings provide a method for generating functional nanomaterials and hierarchical complex architectures and show promise as a platform for biosensing and targeted drug delivery.

4.2 Introduction

Supramolecular assembly of nanomaterials into functional one-dimensional (1D) architectures has drawn considerable interest from both applied and fundamental viewpoints.[1,2] Over the past few decades, several molecular building blocks for supramolecular polymers have been utilized which include block copolymers containing poly(ferrocenyl dimethylsilane) units,[3] platinum(II) complexes,[4] polythiophenes,[5] proteins,[6] peptides,[7] and hexabenzocoronenes.[8,9] Particular interest has been directed toward block copolymer self-assembly, which has offered a powerful and versatile bottom-up synthetic route for the realization of various 1D and 2D morphologies with well-defined shape and functionalities.[10–12]

Under thermodynamic equilibrium, supramolecular polymerization most commonly occurs *via* two mechanisms: noncooperative isodesmic or cooperative nucleation-elongation chain growth.[13] The latter requires a thermodynamically unfavorable initial nucleation step, followed by favorable chain elongation, bearing resemblance to chain-growth covalent polymerization defined by initiation and propagation steps.[14] In the case where the monomer continuously attaches to the reactive ends of the growing chain without termination or transfer steps, it presents the possibility of achieving a kinetically controlled polymerization displaying "living" character.[15] A defining feature of this growth is that the length of chain depends linearly on the amount of monomer added, a property resembling the behavior of living covalent polymerization. Kinetic control in supramolecular polymerization has allowed the generation of a range of out-of-equilibrium nanoscale structures with different morphologies and functions.[16–21] In the context of living polymerization, a process termed living "crystallization-driven self-assembly" has recently been reported as a method to readily prepare 1D and 2D structures with controlled lengths in organic media.[22–24] Several other examples of living supramolecular polymerization have also been reported and have allowed ready access to polymers and complex architectures with narrow size distributions.[25–31] These elegant reports have greatly broadened our capability for preparing various 1D, 2D, and 3D hierarchical architectures from block copolymers. Of high interest are 1D supramolecular polymers in aqueous media. While less abundant than assemblies in organic solvents, a few examples have been reported and could see applications in biomedicine.[7,32–36] A particularly attractive goal would be to extend this capability to functional architectures with biological relevance.

DNA has emerged as a highly controllable material for nanotechnology.[37] The self-assembly of DNA can be tailored with great precision, offering well-defined nanostructures with unique programmability.[38,39] However, while highly programmable, the four-letter code assembly language of DNA gives rise to structures with relatively short-range order.[40] On the other hand, block copolymer self-assembly has resulted in predictable morphologies with long-range order using a large number of interactions such as hydrophobic, electrostatic, and π–π interactions.[41] Combining the assembly language of block copolymers with DNA, as in DNA block copolymers, can result in long-range organization and give rise to a new class of DNA-based nanostructures through a number of different orthogonal interactions, expanding the library of self-assembled DNA nanomaterials.[42–51]

DNA block copolymers have been used to shift between various long-range morphologies (spherical to rod-shaped) with externally added DNA strands or enzymes.[52,53] A controllable strategy using amphiphilic DNA conjugates has also been utilized to prepare 2D and 3D assemblies in aqueous solution.[54−56] Reversible switching between spherical micelles and rods has also been reported with DNA−dendron hybrids.[57] Additionally, DNA rods have been obtained through kinetic micellization of nucleic acid−polymer amphiphiles and have been used as drug delivery vehicles.[58,59] These approaches have added valuable tools to the field of DNA nanotechnology with respect to programmed structure manipulation and drug delivery. More recently, an efficient and versatile method to generate DNA block copolymers via solid-phase synthesis has been reported by our group and others.[60−65] This method, unlike conventional synthetic polymer conjugation, yields DNA−polymer conjugates that are fully monodisperse and sequence-defined. These polymers have been used to decorate 3D DNA nanostructures to allow their hierarchical self-assembly, as well as create hydrophobic pockets in DNA cubes for potential drug delivery applications.[43,44] Self-assembly of sequence-defined DNA block copolymers has also been used to produce spherical micellar systems in which the DNA block forms a corona in aqueous media, while hydrophobic sections form bulk-like nonpolar phases.[66−68] These spherical DNA micellar systems have seen applications in materials chemistry and drug delivery,[42,43,62,63,69−76] due to the unique programmability, ease of functionalization, and specific recognition properties of DNA. Despite the recent advances, controlling the dimensionality of DNA block copolymers is still limited.[77,78] Particularly, to our knowledge, no examples of DNA amphiphile-based supramolecular polymerization with a seeded growth mechanism and controlled length have been reported. This type of growth is very desirable, as it allows access to structures with controlled length and narrow size dispersity and also complex assemblies such as block co-micelles.[22,79] Moreover, the DNA component of these structures allows ready functionalization with a variety of biomolecules and materials. Thus, there is a compelling need to expand the library of functional supramolecular 1D DNA architectures.

In this chapter, we report the discovery that the site-specific introduction of a single cyanine dye molecule into sequence-controlled DNA amphiphiles results in a complete morphological switch from spheres to 1D fibers. Fiber formation displays dependence on the position of cyanine dye, where the dye location in the DNA−polymer conjugate is critical for the overall morphology. We further show an example of stimuli-response shape-shifting fibers to highlight the role of the dye in the resulting morphological change. Moreover, we show seeded growth of DNA fibers and size control of the grown fiber by varying the concentration of monomer added. The use of cyanine dyes allows monitoring fiber growth through the change in optical properties and can be used as a bioanalytical tool to diagnose fiber structural integrity. Finally, we show that the presence of DNA as the fiber corona allows hierarchical organization of polyvalent gold nanoparticles (AuNPs) and site-specific directional binding to DNA origami tiles through base pairing. This finding significantly expands the range of supramolecular 1D polymers and, to our knowledge, is the first example of seeded supramolecular polymerization of DNA block copolymers with controlled dimensionality. The ready access to DNA nanofibers in biologically relevant solvents could enable applications as analytical tools in biosensing, stimuli-responsive vehicles for drug delivery and in guided fiber growth using DNA nanostructures, to create optoelectronic wires with arbitrary geometries.

4.3 Results and Discussion

4.3.1 Synthesis and characterization of DNA nanofibers

The original goal of our approach was to generate dye-labeled spherical DNA nanoparticles for cellular uptake studies. As commonly used in biological studies, Cyanine 3 (Cy3) was selected as the dye of choice. Toward this end, a novel Cy3–modified DNA−polymer conjugate was synthesized, which consisted of a 19-mer DNA segment at one end, attached to 12 hexaethylene (HE) units, to which one or two units of Cy3 dye were appended at the opposite end (Cy3−HE_{12}−DNA conjugate for one Cy3 dye addition, Cy3Cy3−HE_{12}−DNA for two Cy3 dye additions, Figure 4.1). The strands were synthesized by solid-phase synthesis using phosphoramidite chemistry, which offers monodisperse DNA amphiphiles in high yields and provides control over the length and the sequence of the monomer in the final structure. The HE units added at the 5′ end of the DNA segment are each spaced by phosphodiesters, as is the case for the Cy3 molecules. The self-assembly of DNA−polymer conjugates into nanostructures was achieved in buffers containing magnesium cations, which can stabilize the unfavorable repulsion of negatively charged phosphodiesters in the overall assembly. In previous studies, we have shown that HE_{12}–DNA conjugates self-assemble into highly monodisperse spherical nucleic acid particles in aqueous media containing divalent cations (Figure 4.1). Based on these observations, we predicted that the Cy3-labeled monomers would display similar assembly behavior, generating spherical DNA nanoparticles with the dye molecules embedded in their core. However, surprisingly, the introduction of a single cyanine dye molecule at the end of the sequence-controlled DNA amphiphile resulted in a complete morphological switch from spheres to 1D DNA nanofibers.

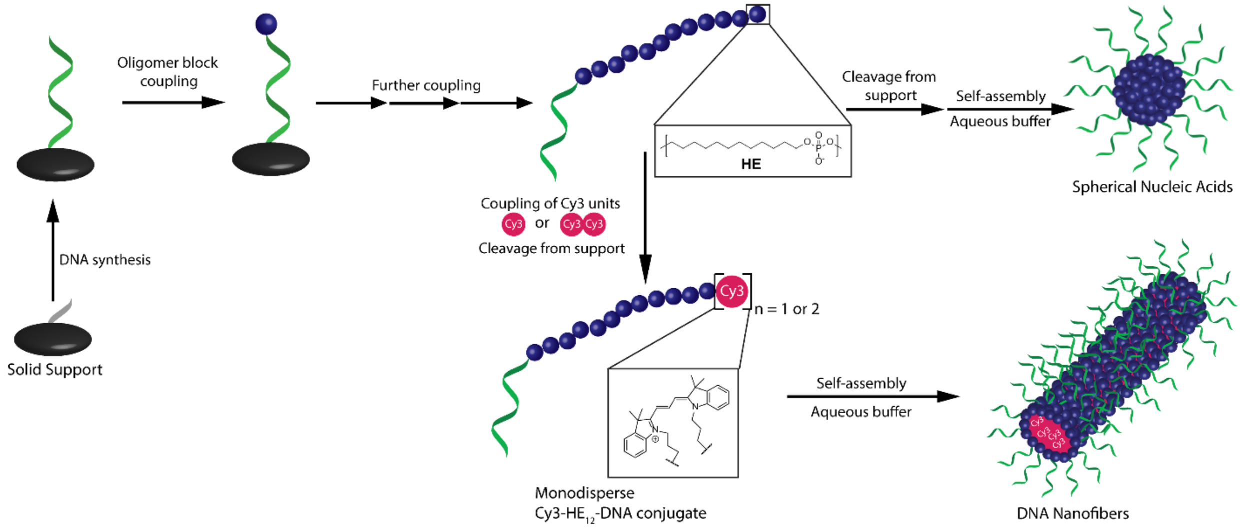

Figure 4.1 – Synthesis of sequence-controlled Cy3-HE_{12}-DNA or Cy3Cy3-HE_{12}-DNA conjugates and their self-assembly behaviour. Phosphoramidite monomers were attached at the 5′-end of a growing DNA strand on controlled pore glass (CPG) in a stepwise and sequence-controlled manner. The 19-mer DNA was first built from the support, followed by 12 hexaethylene monomer additions (HE_{12}). Self-assembly of HE_{12}–DNA conjugates generates spherical DNA nanoparticles. However, the site-specific introduction of one or two units of Cy3 phosphoramidite as a final coupling step, followed by self-assembly in aqueous media, results in a complete change of morphology into 1D DNA nanofibers.

For our assembly process, Cy3-labeled structures were generated by mixing Cy3–HE_{12}–DNA or Cy3Cy3–HE_{12}–DNA monomers in aqueous buffer containing divalent cations, followed by thermal annealing (95 °C to 22 °C) and aging overnight at room temperature.

In this report, we will highlight one system containing Cy3Cy3−HE_{12}−DNA monomers with two Cy3 units. Similar results were obtained for the system with a single Cy3 unit and are found in the *Experimental Sections 4.5.7 and 4.5.12*.

As an initial test, different ratios of Cy3Cy3−HE_{12}−DNA were mixed with unlabeled HE_{12}−DNA followed by annealing and overnight aging at room temperature. The resulting mixtures were analyzed by agarose gel electrophoresis (AGE), atomic force microscopy (AFM), and transmission electron microscopy (TEM) (Figure 4.2, *Experimental Figures 4.22-4.25*). Notably, at 100% Cy3Cy3−HE_{12}−DNA in the assembly mixture, a nonpenetrating band with AGE was observed (Figure 4.2b). Structural analysis of this population by AFM and TEM under dry conditions revealed the formation of extended DNA nanofibers of average length L_n = 200 nm, L_w = 209 nm, L_w/L_n = 1.05 (σ/L_n = 0.17), width = 36 nm and height = 10 nm by AFM analysis, and L_n = 262 nm, L_w = 291 nm, L_w/L_n = 1.11 (σ/L_n = 0.31) and width = 32 nm by TEM measurements (L_n is the number-average contour length, L_w is the weight-average contour length, and σ is the standard deviation) (Figure 4.2d,e, *Experimental Figures 4.22-4.25*). The structures exhibited narrow-size distribution and a predominant stiff linear architecture. As the concentration of unlabeled HE_{12}−DNA was increased in the mixture, thus disrupting dye−dye interactions, the structures reverted to spherical nanoparticles, which was observed as a tight penetrating band with AGE and nearly monodisperse spherical nanoparticles on the surface by AFM analysis (Figure 4.2b, *Experimental Figures 4.26-4.28*). Interestingly, when an excess amount of Cy3Cy3−HE_{12}−DNA was added to spherical populations and reannealed, the structures switched back from spheres to 1D nanofibers, likely due to restored dye−dye interactions (Figure 4.2c). The assembly of the DNA nanofibers in liquid environments was then investigated using fluid AFM and dynamic light scattering (DLS). Fluid AFM analysis showed the presence of long extended structures on the surface under liquid conditions (*Experimental Figure 4.29*), and DLS revealed the presence of structures with much larger hydrodynamic radii in solution as compared to their spherical counterparts (*Experimental Figure 4.30*).

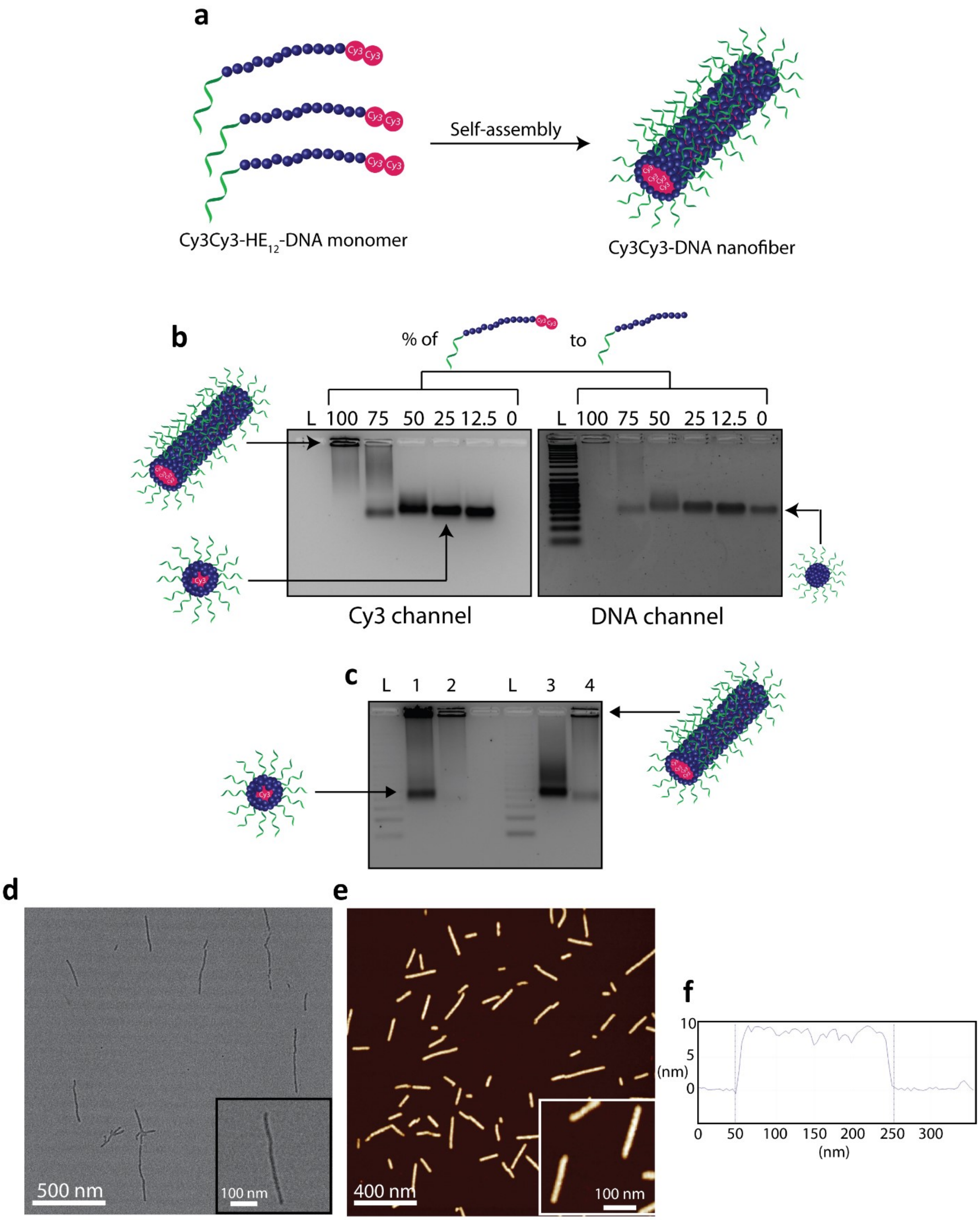
a
Cy3
Cy3
Cy3Cy3-HE$_{12}$-DNA monomer
Self-assembly
Cy3Cy3-DNA nanofiber
b
% of
to
L 100 75 50 25 12.5 0
L 100 75 50 25 12.5 0
Cy3 channel
DNA channel
c
L 1 2 L 3 4
d
500 nm
100 nm
e
400 nm
100 nm
f
10
5
0
(nm)
0 50 100 150 200 250 300
(nm)

Figure 4.2 – Structural characterization of Cy3Cy3−DNA nanofibers. (a) Schematic representation of the assembly of Cy3Cy3−HE_{12}−DNA monomers into DNA nanofibers in aqueous conditions. (b) Agarose gel electrophoresis (AGE) analysis describing the morphological shift of structures made from mixing varying ratios of Cy3Cy3−HE_{12}−DNA with unlabeled HE_{12}−DNA strands followed by thermal annealing. L: Ladder, lane 100: 100% Cy3Cy3−HE_{12}−DNA in the mixture, lane 75: 75% Cy3Cy3−HE_{12}−DNA/25% HE_{12}−DNA, lane 50: 50% Cy3Cy3−HE_{12}−DNA/50% HE_{12}−DNA, lane 25: 25% Cy3Cy3−HE_{12}−DNA/75% HE_{12}−DNA, lane 0: 100% HE_{12}−DNA. The gel was imaged under a Cy3-selective channel (left panel) and a DNA-selective channel (right panel). (c) AGE analysis of structures pre- and post addition of excess Cy3Cy3−HE_{12}− DNA monomer (Cy3-selective channel). Lane 1: Structures assembled at 75% Cy3Cy3-HE_{12}-DNA/25% HE_{12}-DNA, lane 2: structures from lane 1 after the addition of excess Cy3Cy3-HE_{12}-DNA monomer, lane 3: structures assembled at 50% Cy3Cy3-HE_{12}-DNA/50% HE12-DNA, lane 4: structures from lane 3 after the addition of excess labeled monomer. (d) Transmission electron microscopy (TEM) of DNA nanofibers. (e) Atomic force microscopy images of DNA nanofibers on the surface under dry conditions. (f) Height and length analysis of Cy3Cy3−DNA fibers from AFM measurements.

Cy3Cy3−DNA fibers were also stable at room temperature for over 1 week and could also be prepared by simply mixing monomer strands in assembly buffer followed by overnight room temperature incubation. The resulting fibers, however, exhibit wider length dispersity as well as lower height when compared to ones by thermal annealing (Figure 4.3). These observations demonstrate the role of the dye in dictating the resulting morphology and highlight a route for controlling the overall architecture by varying the ratio of dye-labeled to unlabeled monomers in the assembly.

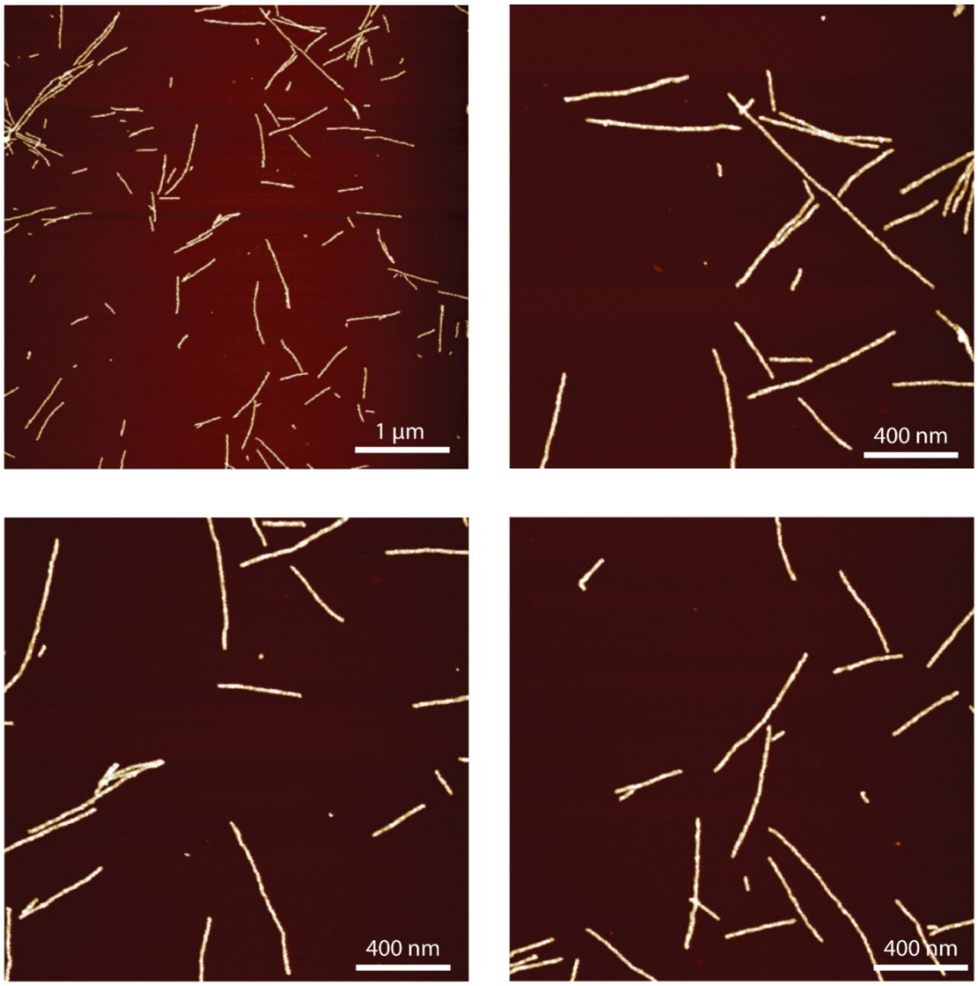

Figure 4.3 – AFM images of Cy3Cy3-DNA fibers generated at room temperature. Cy3Cy3-HE_{12}-DNA monomers were mixed with assembly buffer followed by room temperature overnight incubation.

With the Cy3Cy3−DNA fibers characterized, the packing mode of the hydrophobic core in DNA fibers was investigated (Figure 4.4). TEM data of single-stranded and fully double-stranded DNA fibers showed similar average radii of 16 nm, which suggested that the DNA in the corona was extended. This obtained width is consistent with the tight packing of the dyes and HE chains in the core surrounded by a charged corona made up of DNA. Assuming the linear DNA geometry (6.1 nm) and the cross-section of the dye (~1.7 nm), this suggests that the HE_{12} chain (1.9 nm per HE unit if stretched) is folded on itself multiple times and potentially adopts a “concertina” structure analogous to that of phospholipid bilayers (Figure 4.4a-b).

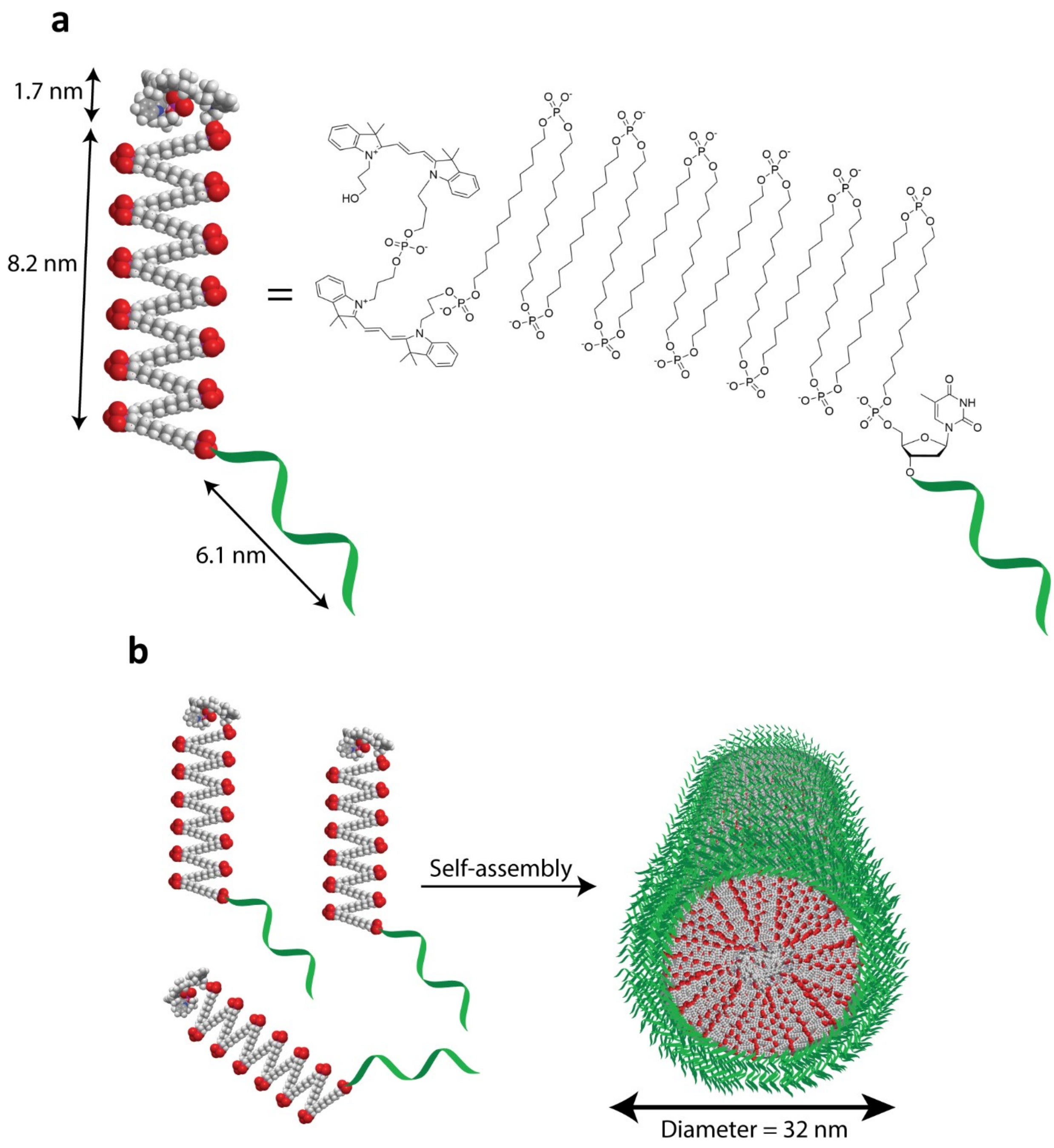

Figure 4.4 – Proposed packing mode of DNA nanofibers. Molecular model (left) and chemical structure (right) of Cy3Cy3−HE$_{12}$−DNA highlighting the three key structural features and their relative dimensions. (h) Proposed model of self-assembly of Cy3Cy3−HE$_{12}$−DNA into DNA fibers. The HE$_{12}$ chain folds on itself multiple times, potentially adopting a “concertina” structure.

As for fibers made from Cy3−HE_{12}−DNA, similar results to Cy3Cy3−DNA fibers were obtained where the introduction of a single Cy3 unit caused the formation of Cy3−DNA nanofibers. The presence of long extended fibers by AGE, AFM, and TEM was observed upon the introduction of a single Cy3 unit at the end of HE_{12}−DNA conjugates followed by assembly and is highlighted in *Experimental Figures 4.31-4.35*. For Cy3−DNA fibers, unlike Cy3Cy3−DNA fibers, after 2 days of aging, the formation of dense interconnected networks of fibers was observed by surface measurements (*Experimental Figure 4.35*).

With these promising results, we then proceeded to investigate if fiber formation is sequence-dependent on the Cy3Cy3 units, i.e. if the position of the Cy3Cy3 units on the polymer chain influences the overall morphology. Taking advantage of the ease of sequence manipulation using our solid-phase synthetic approach, four sets of Cy3-labeled monomers were generated, each bearing the Cy3 units at a different position with respect to the DNA−polymer hybrid (Figure 4.5). Structures were assembled by the addition of assembly buffer containing divalent cations, followed by thermal annealing and overnight incubation at room temperature. AFM analysis was used to test the effect of dye position on the resulting architecture. When the dye was flanked by two hydrophobic units, or positioned at the DNA−polymer interface, spherical nanoparticles were predominantly observed (Figure 4.5b,c). This could be due to steric hindrance of the surrounding chains hampering efficient dye−dye interactions. Interestingly, positioning the dye units at the 5′ end of the DNA−polymer conjugate, resulted in the formation of DNA fibers. (Figure 4.5d). We then studied the sensitivity of fiber formation by varying the number of hydrophobic units surrounding the dye. The self-assembly of HE−Cy3Cy3−HE_{11}−DNA strands (where the dye position was shifted by one HE unit from the terminus) was characterized by AFM. Interestingly, DNA fibers were solely observed on the surface, which suggested that dye−dye interactions could withstand the induced steric of a neighboring 12 carbon chain (Figure 4.5e).

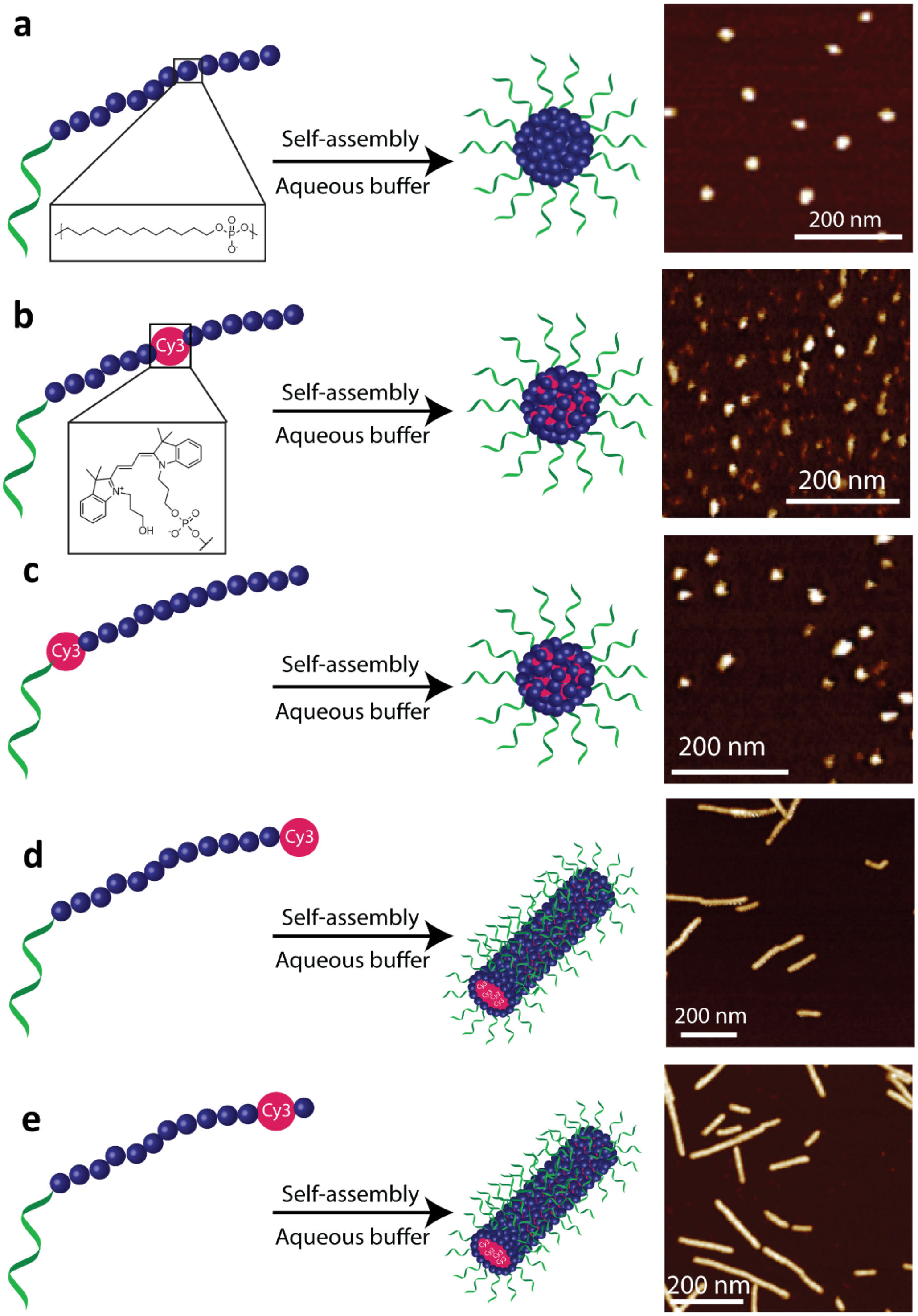

Figure 4.5 – AFM analysis showing the sequence-dependence of DNA nanofibers on Cy3 units. The position of Cy3 was varied at the monomer level to study the effect of dye position on the overall morphology. Spherical nanoparticles were observed (a) in the absence of Cy3 units, (b) when the dye was flanked between the hydrophobic chains, or (c) when the dye was positioned at the DNA−polymer

interface. (d) DNA nanofibers were observed when the dye unit was added at the 5′ end of the DNA−polymer conjugate. (e) The structures maintained the fiber architecture when the dye unit was shifted by one HE unit from the terminus.

The effect of the length of ssDNA and hydrophobic chain on the overall morphology was then studied (Figure 4.6, *Experimental Figure 4.36*). Long DNA strands (19-mer) and short hydrophobic chains (6 units of HE) resulted in spherical nanoparticles. Increasing the length of the hydrophobic chain to 12 HE units gave DNA fibers both for 19- and 38-mer DNA (the width of the 38-mer fibers was larger than that of the 19-mer) (Figure 4.6, *Experimental Figure 4.36*). Interestingly, with short DNA (8-mer) and long hydrophobic chain (12 HE units), DNA nanosheets were observed. These results indicate that the dye position and assembly conditions are critical for the obtained morphology and could provide another way of dictating the overall structure by merely changing the position of the dye units in the monomer strands or manipulating the length of DNA/ hydrophobic units.

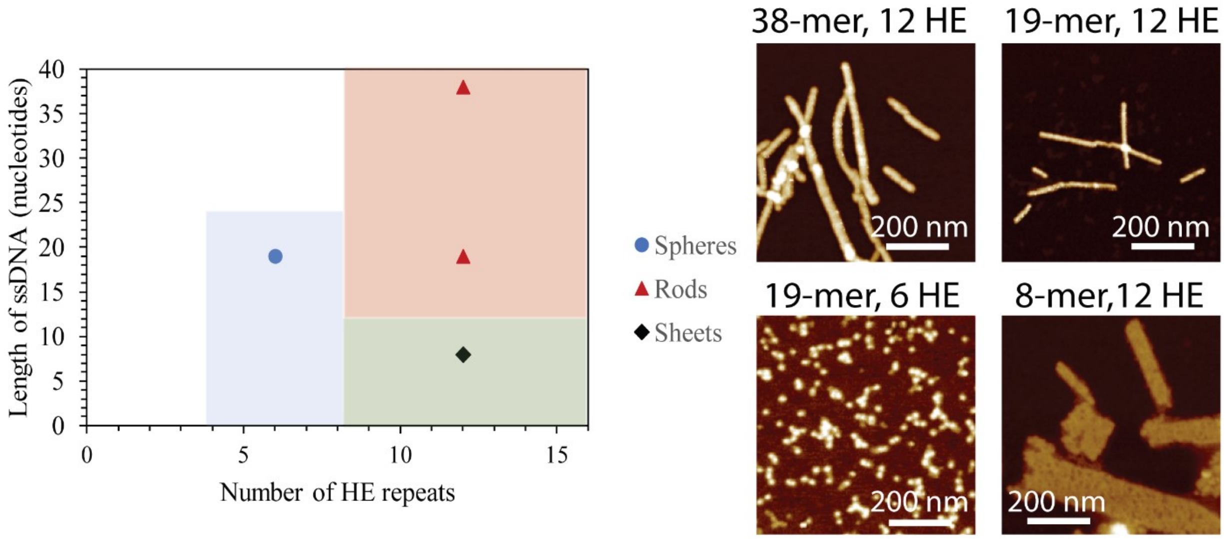

Figure 4.6 – Diagram and AFM images showing the different self-assembly modes of Cy3Cy3−polymer−DNA conjugates with varying length of DNA and polymer chain.

4.3.2 Shape-shifting Cy3Cy3-DNA nanofibers

Nanoparticles that undergo defined changes in morphology in response to stimuli are desirable for a wide range of applications, including targeted drug delivery and detection.[80] In our case, we were interested in introducing selective user-defined morphological transformations in the DNA nanofiber system. Additionally, bearing in mind that Cy3Cy3 association was the likely factor dictating fiber morphology, we hypothesized that selective cleavage of the dye unit from the structure should cause a shift in morphology back into spherical DNA nanoparticles. Toward this end, a photocleavable linker unit (PCL unit) was introduced between the HE_{12} and Cy3Cy3 units during synthesis yielding Cy3Cy3−PCL−HE_{12}−DNA monomers (Figure 4.7a). The assembly process was monitored by AGE and AFM analysis. Prior to photoirradiation, Cy3Cy3−DNA nanofibers containing photocleavable units were generated and characterized (Figure 4.7b,c). Upon irradiation for 1 h and subsequent incubation at room temperature for 12 h, a complete morphological shift was observed from 1D rods to nearly monodisperse spherical structures. The cleavage process, though 95% efficient (*Experimental Figure 4.37*), was sufficient to cause a morphological shift, likely producing dye-labeled spherical structures (faint band observed in the Cy3 channel in Figure 4.2b). These results corroborate AGE data in Figure 4.2b which revealed spherical architectures at a low ratio of Cy3Cy3-monomers.

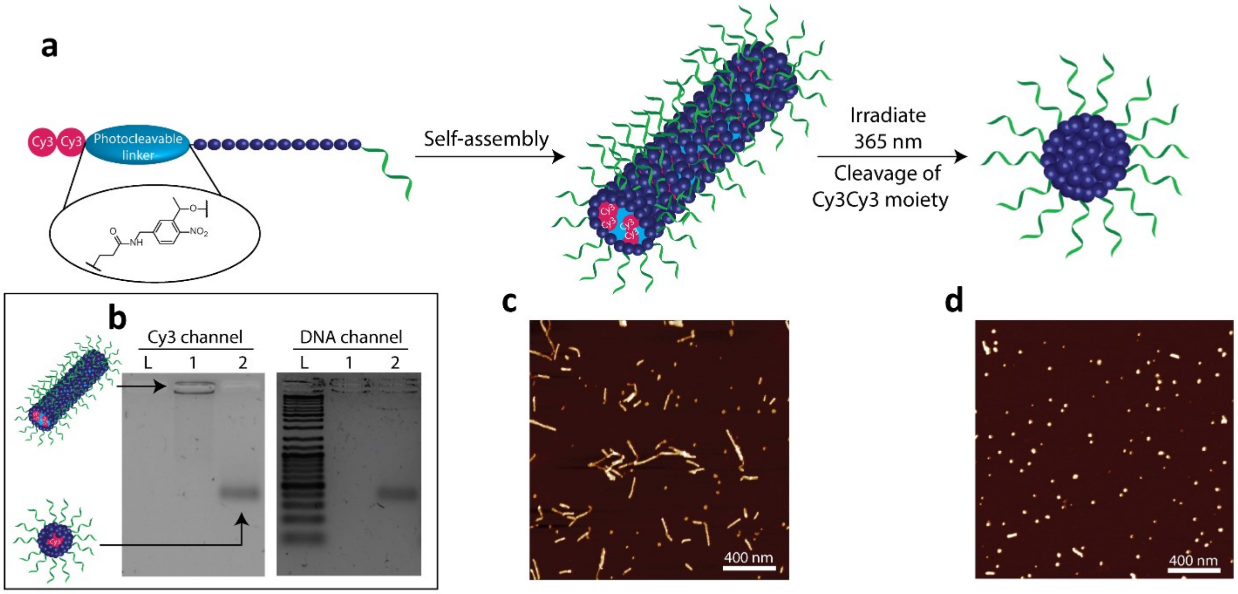

Figure 4.7 – Stimuli-responsive shape-shifting of photocleavable Cy3Cy3−DNA nanofibers. (a) A photocleavable linker (PCL) was introduced between the HE_{12} and Cy3Cy3 units during the synthesis of the monomer strand. Cy3Cy3-fibers containing PCL units were generated upon self-assembly in aqueous buffer. Upon irradiation with a 365 nm light, the Cy3Cy3 units were cleaved from the structure resulting in a morphological shift to spherical nanoparticles. (b) Agarose gel electrophoresis analysis of the structures prior to and post irradiation. L: ladder, lane 1: photocleavable Cy3Cy3−DNA fibers prior to irradiation, lane 2: fibers post irradiation. (c, d) AFM images of photocleavable Cy3Cy3−DNA fibers prior to and post irradiation

As a control, Cy3Cy3−DNA fibers (lacking a photocleavable unit) were subjected to the same stimulus, and their cylindrical morphology remained unchanged (Figure 4.8).

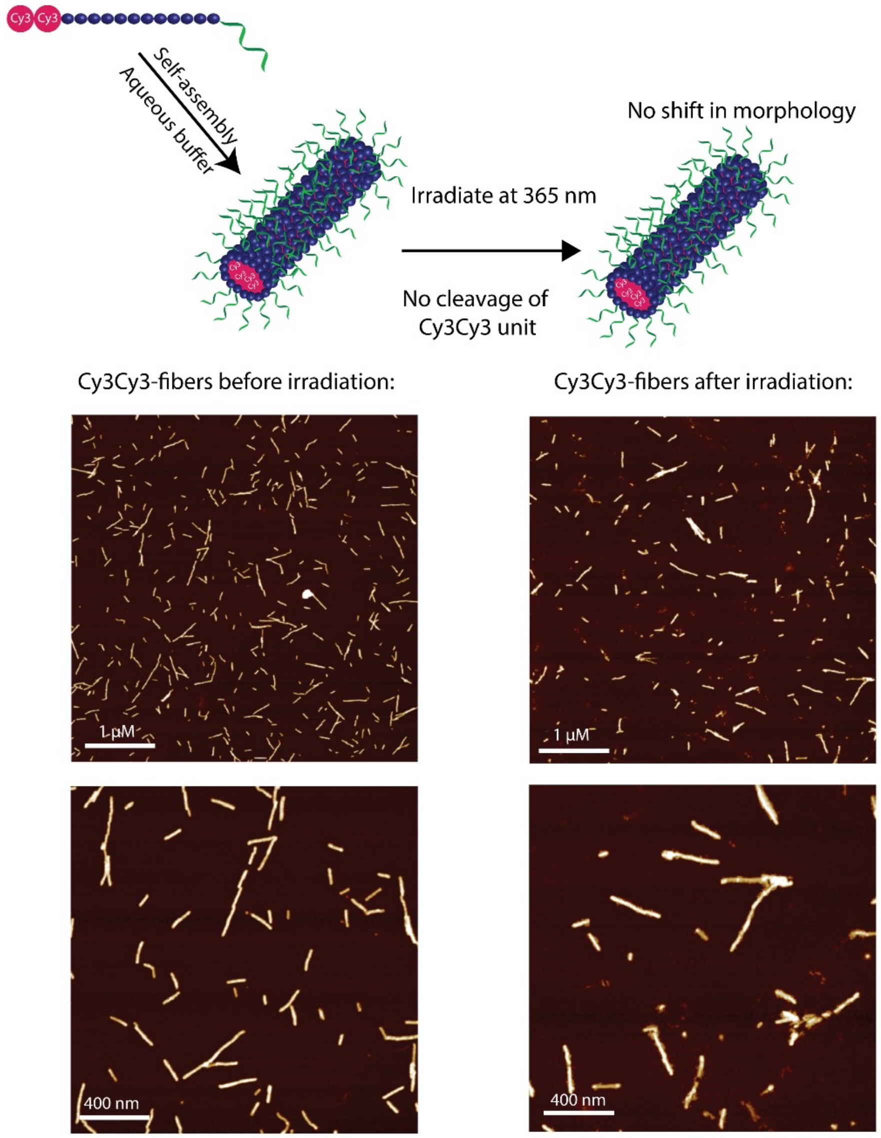

Figure 4.8 – AFM images of Cy3Cy3-DNA nanofibers (lacking a photocleavable unit) before and after irradiation with a 365 nm light source.

Additionally, when Cy3Cy3−PCL−HE_{12}−DNA monomers were first subjected to photoirradiation, followed by assembly in aqueous buffer, spherical nanoparticles were observed, exclusively (*Experimental Figure 4.37*). This was a further indication that the shape-shift behavior was likely due to the loss of Cy3Cy3 units. The controlled aggregation behavior of amphiphilic cyanine dyes has been previously investigated. These molecules are some of the most studied self-aggregating dyes and can form H and J-aggregates that exist as 1D assemblies in solution.[81,82] For example, amphiphilic cyanine dyes have been shown to self-assemble into chiral double-walled nanotubes and rod-like assemblies in solution.[83−85] Our findings suggest that the driving force of the rod-like structures is likely due to dye stacking, transferring the well-studied modes of molecular assembly of amphiphilic cyanine dyes into the overall supramolecular architecture.

4.3.3 Growth mechanism of DNA nanofibers

DNA amphiphile-based fibers have been reported previously;[52,53] however, no length control or investigation of fiber growth mechanism has been described. As a first step to study the growth mechanism of DNA nanofibers, the average contour length of the assemblies was measured as a function of different monomer concentrations by atomic force microscopy (Figure 4.9, *Experimental Figures 4.38, 4.39*). Different concentrations of monomers dispersed in water in their molecular non-aggregated state were mixed with assembly buffer containing magnesium ions and followed by a heat/cool cycle (95 °C to 22 °C) to yield DNA fibers. Notably, fiber length increased with increasing monomer concentration and showed linear dependence of contour length on the concentration of monomer, suggesting a chain-growth rather than step-growth mechanism. Additionally, the interaction between dye molecules appeared to withstand significant variations in monomer concentration, ranging from nanomolar to micromolar concentrations. This property is useful for applications that require maintained structural integrity upon sudden dilution and changes in assembly concentrations. This feature also provides a simple approach for controlling dimensions of DNA nanofibers through simply predefining the monomer concentration prior to assembly.

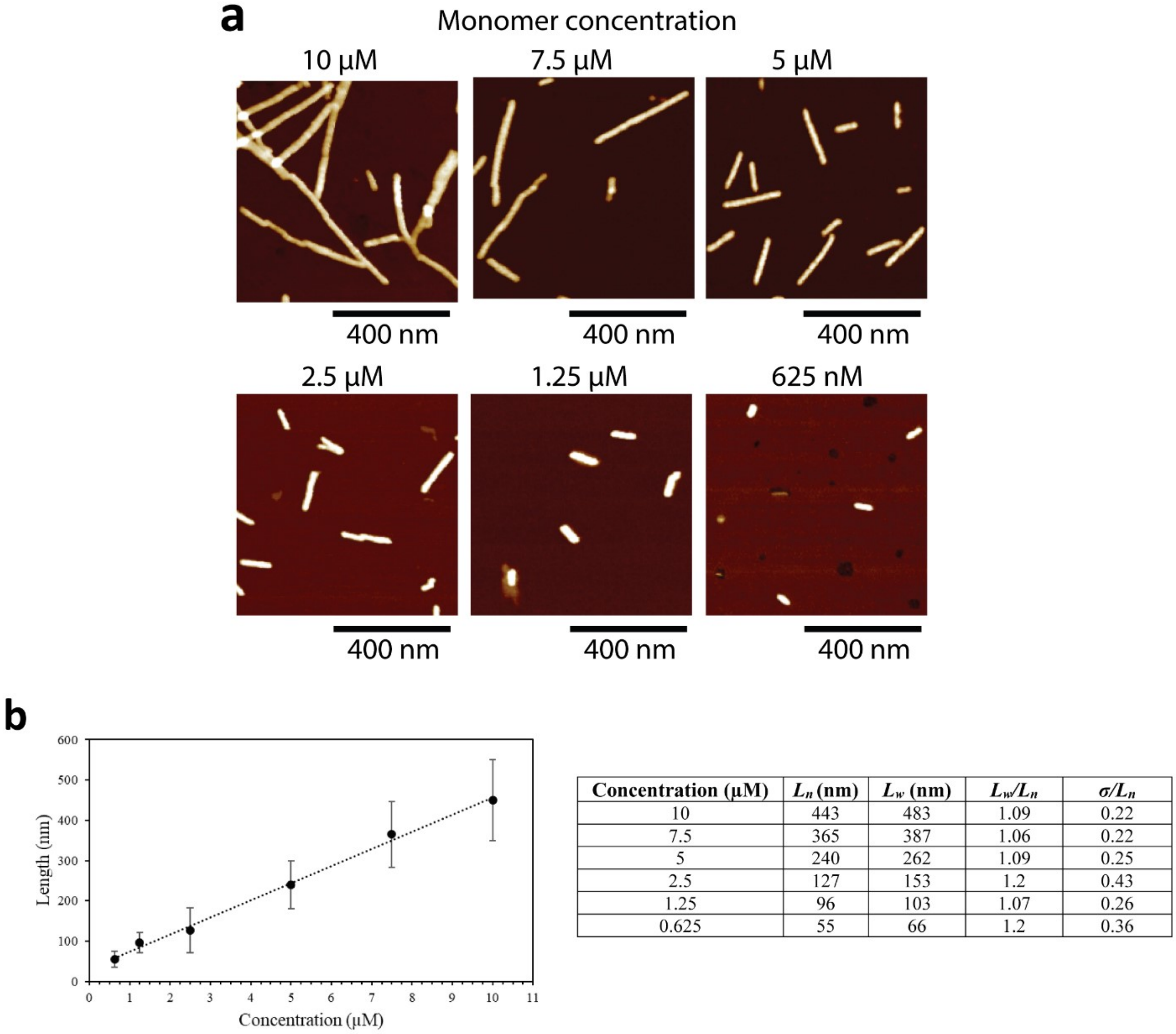

Concentration (μM)	L_n (nm)	L_w (nm)	L_w/L_n	σ/L_n
10	443	483	1.09	0.22
7.5	365	387	1.06	0.22
5	240	262	1.09	0.25
2.5	127	153	1.2	0.43
1.25	96	103	1.07	0.26
0.625	55	66	1.2	0.36

Figure 4.9 – Investigating the effect of monomer concentration on fiber length. (a) AFM analysis of Cy3Cy3−DNA fibers grown from different monomer concentrations. (b) Plot showing the linear dependence of DNA nanofiber length on monomer concentration. Table: Data of average contour length of DNA fibers vs monomer concentration. Error bars represent mean standard deviation.

Earlier reports on controlled supramolecular polymerization have been described by Manners, Winnick, and co-workers.[3] In these studies, seeded growth of cylindrical micelles was demonstrated where the addition of fresh monomer to nanosized cylindrical micelles in tetrahydrofuran resulted in their growth to micrometer long fibers. Inspired by these earlier reports, we sought to investigate the growth mechanism of DNA fibers and test whether the addition of monomer units would extend the growth of DNA nanofibers. To do this, we examined whether we could generate short DNA seed assemblies that could act as nuclei for fiber growth. Given that the monomer strands are punctuated by negatively charged phosphate groups, we studied the effect of varying the amount of magnesium in solution on the overall assembly. Initial studies on the effect of magnesium concentration on fiber assemblies showed that the fibers shortened as a result of decreased magnesium ions in solution (Figure 4.10a). Interestingly, keeping the monomer concentration constant, at low magnesium (3.125 mM Mg^{2+}), monodisperse short assemblies were observed on the surface (Figure 4.10a, *Experimental Figure 4.40*). These structures could then be used as seeds to nucleate the growth process with the addition of monomer (Figure 4.10b). Following the assembly at 3.125 mM Mg^{2+}, different ratios of monomer in water were added to the preformed seeds, followed by incremental increase in magnesium concentration in solution to 12.5 mM throughout an overnight incubation period at room temperature (Figure 4.10b,c, *Experimental Figures 4.41-4.45*). Interestingly, through AFM analysis, we observed that the preformed seeds exhibited a difference in height compared to the growing chain, which allowed direct tracking of the growth process (Figure 4.10c, *Experimental Figure 4.44*). As illustrated in Figure 4.10c, fibers of different lengths were prepared through seeded growth from short fiber seeds by varying the amount of added monomer. The length of grown fibers was linearly correlated to the ratio of monomer added to preformed seeds (*Experimental Figure 4.45*). Additionally, we observed that fiber growth from the seeds propagated at an angle, forming structures resembling “hockey sticks”. The molecular mechanism behind this interesting observation is currently under investigation; however, it could be due to a different mode of packing exhibited by the fiber seeds under such low magnesium conditions.

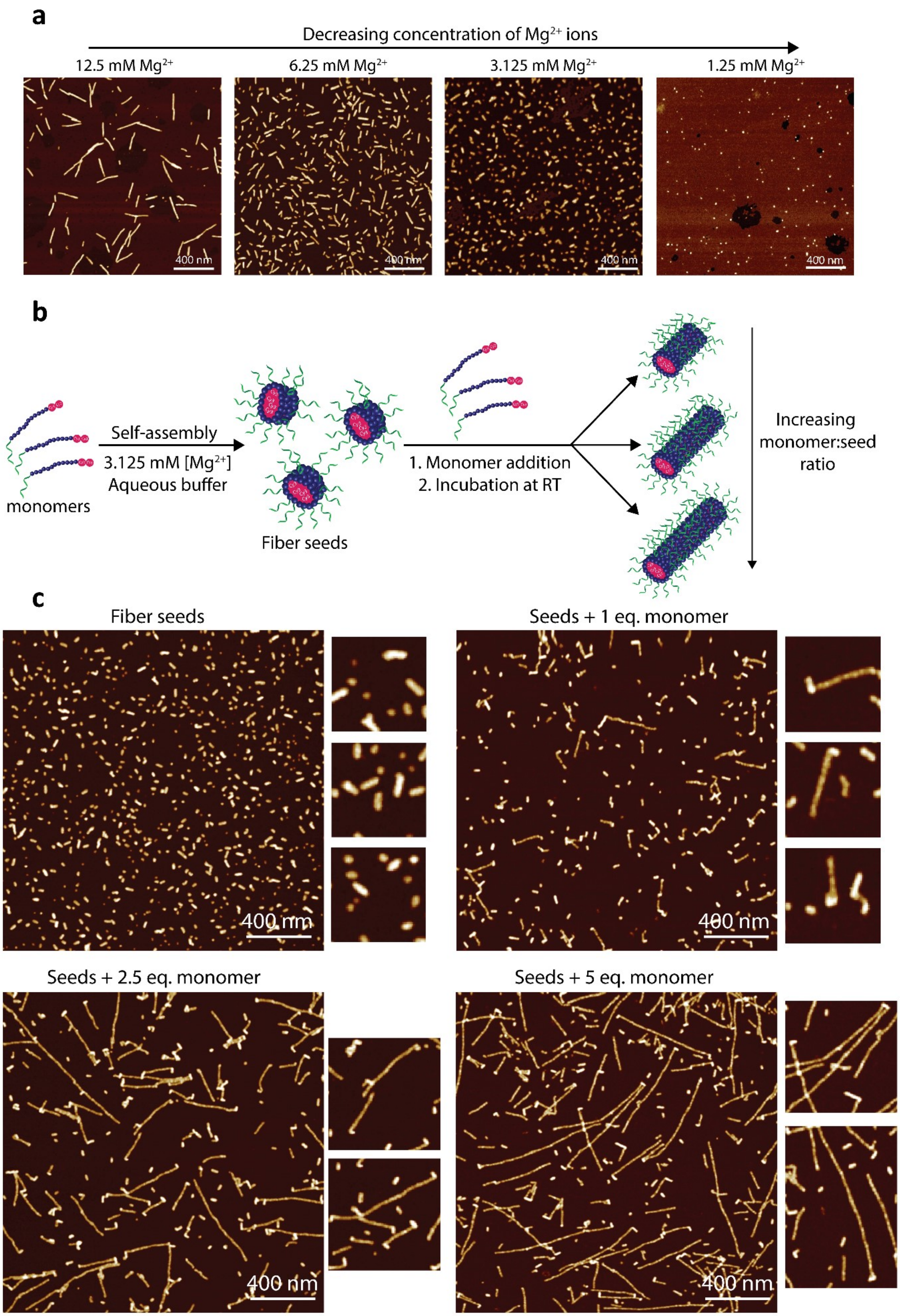
a
Decreasing concentration of Mg2+ ions
12.5 mM Mg2+
6.25 mM Mg2+
3.125 mM Mg2+
1.25 mM Mg2+
400 nm
400 nm
400 nm
400 nm
b
monomers
Self-assembly
3.125 mM [Mg2+]
Aqueous buffer
Fiber seeds
1. Monomer addition
2. Incubation at RT
Increasing
monomer:seed
ratio
c
Fiber seeds
400 nm
Seeds + 1 eq. monomer
400 nm
Seeds + 2.5 eq. monomer
400 nm
Seeds + 5 eq. monomer
400 nm

Figure 4.10 – Seeded growth of DNA nanofibers. (a) AFM analysis studying the effect of magnesium concentration on DNA nanofiber length. Fiber length narrows with a decreasing concentration of magnesium ions in solution. (b) Schematic representation of DNA nanofibers grown from monodisperse seeds in aqueous media. (c) AFM analysis showing DNA nanofiber growth from fiber seeds and the effect of monomer:seed ratio on fiber length. Seeded growth of DNA nanofibers was achieved by the addition of different equivalents of monomer to DNA fiber seeds. The average length of grown DNA nanofibers increased linearly with an increasing ratio of monomer:seed. DNA nanofibers were observed to grow from fiber seeds at an angle, resembling DNA "hockey sticks".

4.3.4 Optical Properties of Cy3Cy3-DNA Nanofibers

The presence of Cy3 units as part of the structure allows monitoring of fiber formation as a result of changes in dye optical properties. Accordingly, the UV−vis absorption of Cy3Cy3−DNA nanofibers was monitored, which showed a red-shift of the maximum absorption from 551 to 561 nm upon fiber formation (Figure 4.11a). The fluorescence intensity of Cy3Cy3-fibers was then measured and showed a 90% decrease upon fiber assembly (Figure 4.11b). These phenomena are typical characteristics of self-aggregation of cyanine dyes, which results in energy transfer between the dye molecules and quenching.[86] Notably, full fluorescence recovery was achieved by denaturation of the structures to monomer units, indicating that the decrease in fluorescence was a direct result of the self-assembly process, and the structural and electronic properties of the dyes remained unaltered (Figure 4.11c). The change in Cy3 optical properties also allowed for studying the kinetics of fiber assembly by monitoring the decrease of Cy3 fluorescence over time (Figure 4.11d, *Experimental Figure 4.46*). Rapid assembly behavior was observed with a calculated fiber formation half-life of ∼100 min. The predicted change in Cy3 fluorescence properties upon fiber formation/disassembly could also be useful for biological applications, as fluorescence enhancement can report on the fate of these structures in the cellular environment.

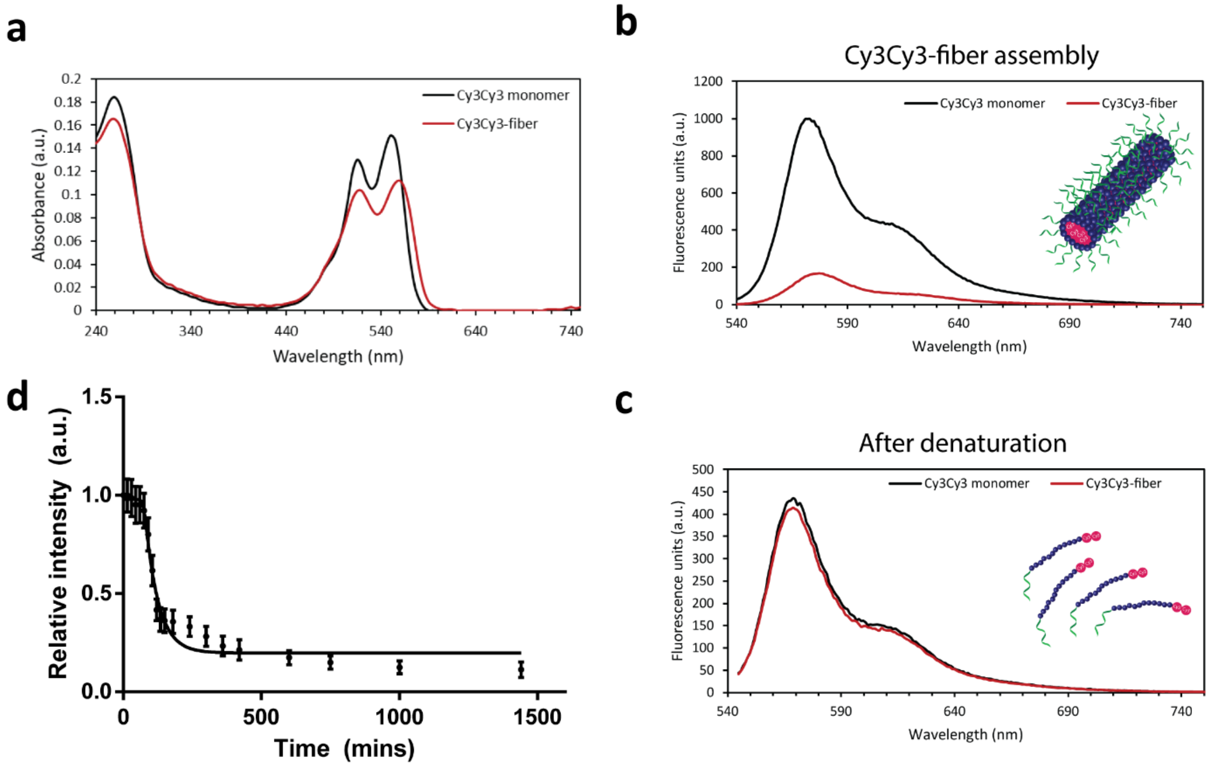

Figure 4.11 – Optical properties of Cy3Cy3−DNA fibers. (a) Absorption spectra and (b) fluorescence spectra of Cy3Cy3-fibers measured at room temperature and (c) following fiber denaturation into monomer units. (d) Monitoring the kinetics of fiber assembly as a result of Cy3 fluorescence decrease over time.

Supramolecular nanostructures can display dynamic behavior. This feature has been recently used to control protein templation.[87,88] With this in mind, we sought to investigate whether the DNA nanofibers exhibit a dynamic character. Two separate populations of DNA nanofibers were generated: Cy3Cy3 and Cy5Cy5 fibers (Figure 4.12, *Experimental Figures 4.47, 4.48*). The dynamic character of such assemblies could then be evaluated by mixing preformed fibers in solution and monitoring strand exchange through Forster resonance energy transfer (FRET) between Cy3 and Cy5 donor−acceptor pairs. An exponential increase of FRET intensity was observed over time with a calculated half-life of ~200 min (Figure 4.12b, *Experimental Figure 4.49*). The rate and efficiency of the exchange process was evaluated by following the decrease in

Cy3 fluorescence over time, which showed a maximum decrease of ~50% after 2 days, suggesting slow and incomplete exchange between the two populations.

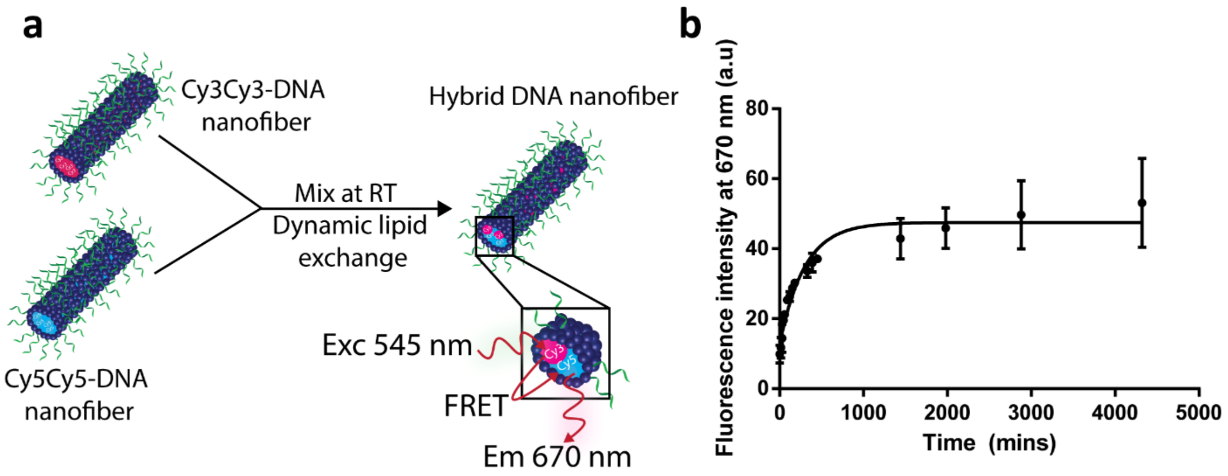

Figure 4.12 – Studying the dynamic properties of DNA nanofibers. a) Schematic representation of dynamic strand mixing between Cy3Cy3 and Cy5Cy5 fibers forming supramolecular hybrid DNA fibers that undergo FRET. (f) Kinetics of strand mixing as a result of FRET signal increase over time. Error bars represent mean standard deviation.

As a control, equal concentrations of Cy3Cy3 and Cy5Cy5−HE_{12}−DNA monomers dispersed in deionized water were mixed and incubated at room temperature for 24 h. No FRET signal was observed, which indicated the lack of interaction of the negatively charged strands in the absence of divalent cations (Figure 4.13a,b). To the same mixture, assembly buffer was added, and followed by a 24-h room temperature incubation to generate completely hybrid fibers. For these structures, fluorescence data showed near complete loss of Cy3 signal and the presence of a strong FRET signal, suggesting close association between Cy3Cy3 and Cy5Cy5− HE_{12}−DNA monomers and high overlap between the FRET pair (Figure 4.13c).

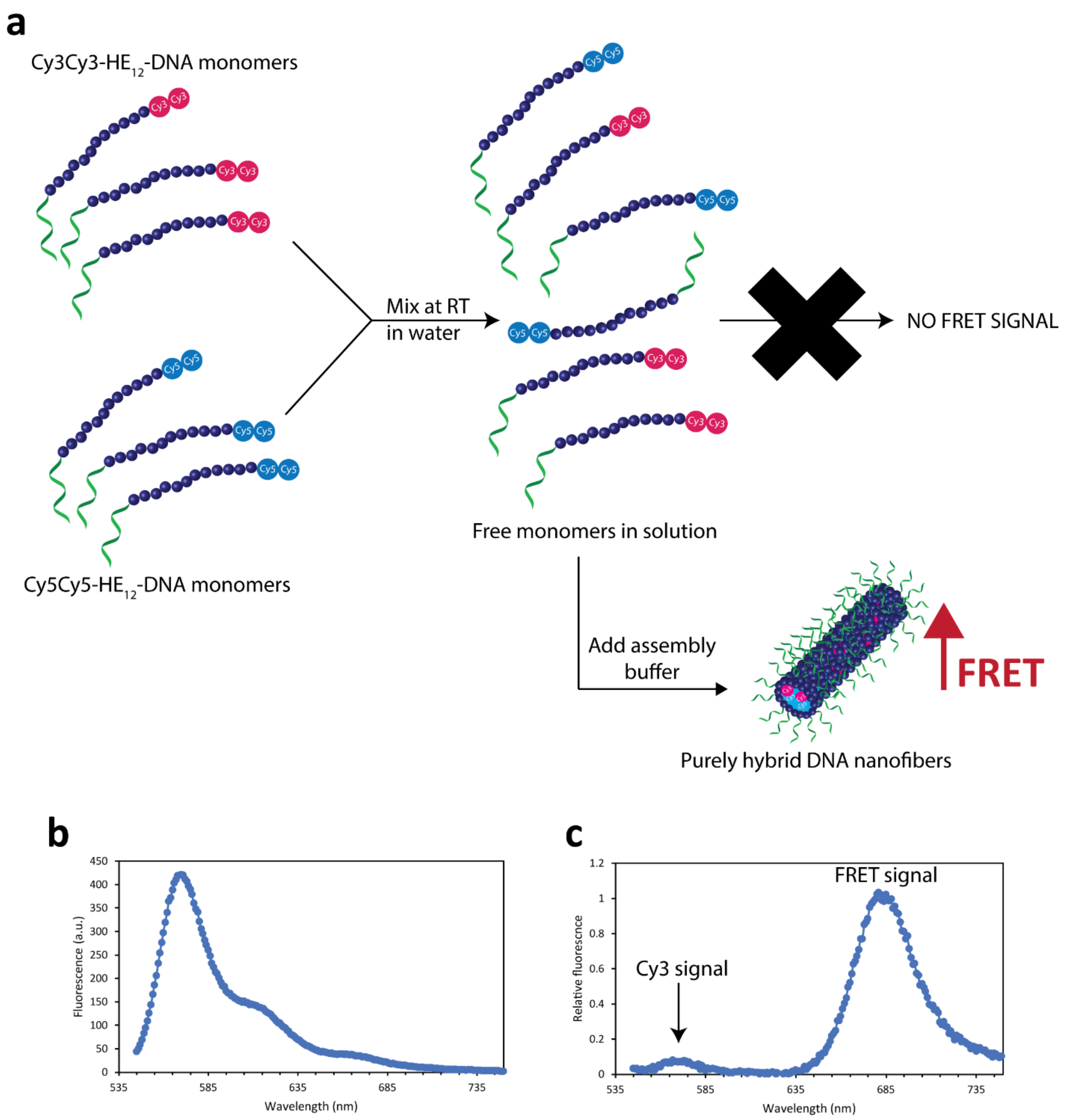

Figure 4.13 – Cy3Cy3 and Cy5Cy5-DNA fiber mixing. a) Schematic illustration and b) fluorescence data showing the absence of FRET when Cy3Cy3-HE$_{12}$-DNA and Cy5Cy5-HE$_{12}$-DNA monomers are mixed in de-ionized water and incubated for 24 hours. c) Fluorescence data showing near complete loss of Cy3 signal and the presence of a strong FRET signal when assembly buffer is added to the mixture of Cy3Cy3 and Cy5Cy5-HE$_{12}$-DNA strands dispersed in water causing the formation of completely hybrid structures.

These results suggest that slow strand exchange between preformed fibers could be due to the presence of a negatively charged DNA corona surrounding the fiber assemblies and creating repulsive forces during strand exchange. In reference to seeded growth experiments (Figure 4.10), the time frame of the experiment (overnight at room temperature) can allow for strand exchange between different fibers, which would be expected to affect the length of the fibers. Exchange kinetics could potentially be further slowed by introducing additional supramolecular interactions such as H-bonding and π−π stacking interactions.

4.3.5 Templation of nanomaterials on Cy3Cy3-DNA nanofibers

With the self-assembly properties of DNA nanofibers characterized, we then investigated the ability of the DNA corona to template the positioning of nanomaterials. Linear and chiral assemblies of gold nanoparticles (AuNPs) exhibit interesting optical and electronic properties useful for a wide variety of applications.[89,90] 1D AuNP assemblies with precise AuNP patterning have been reported using complex DNA nanostructures.[91−93] On the other hand, block copolymers could be utilized for 1D AuNP templation; however, control over the length of template and degree of AuNP functionalization is often limited. Taking advantage of the high aspect ratio of DNA nanofibers, we sought to investigate the templation of 10 nm AuNPs on Cy3Cy3−DNA fibers. To achieve this, DNA nanofibers were prepared in aqueous media and incubated with DNA-polyfunctionalized AuNPs bearing a sequence complementary to the DNA sequence in the nanofiber. The products were characterized by AFM and TEM, which showed successful DNA-mediated templation of AuNPs on DNA fibers (Figure 4.14, *Experimental Figures 4.51-4.55*). Notably, the degree of AuNP templation could be controlled by varying the concentrations of AuNP and DNA fibers in the assembly mixture. At low ratios of AuNPs to DNA fibers, a low number of particles per fiber (2−6 AuNPs/fiber) could be achieved (Figure 4.14a,c, *Experimental Figures 4.51-4.53*). Likely, because the AuNPs can bind any complementary DNA strand protruding from the fiber surface without preference, some nonlinear arrangements of AuNPs are expected to be templated on the fiber surface. Increasing the ratio of AuNP compared to DNA fiber (by decreasing DNA fiber concentration) resulted in almost total decoration of fibers with AuNPs (Figure 4.14b,d, *Experimental Figures 4.54, 4.55*). Bearing in mind that the DNA fiber diameter is ~32 nm, multiple AuNPs could be accommodated along the width of the fiber.

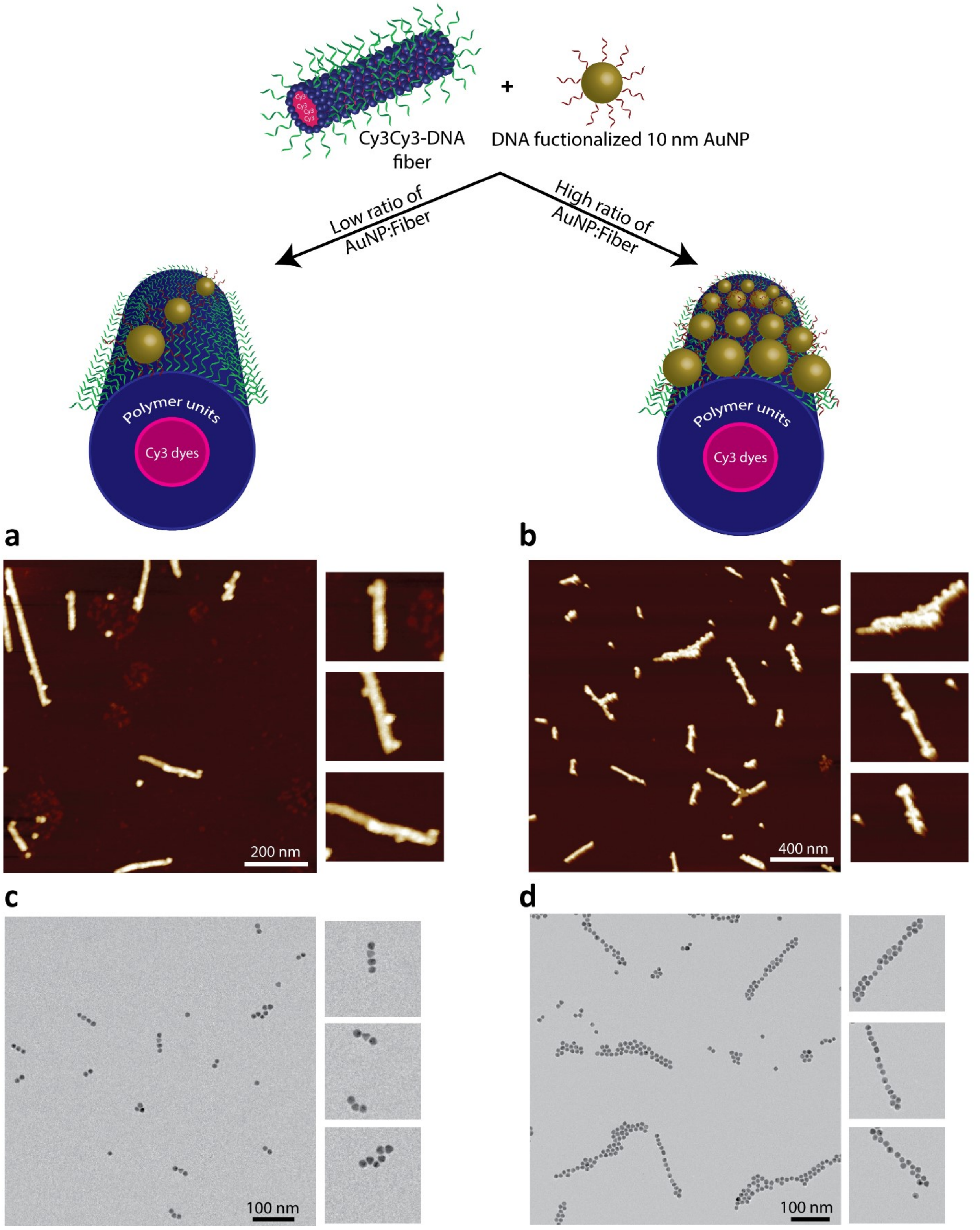

Figure 4.14 – Templation of 10 nm gold nanoparticles (AuNPs) on Cy3Cy3−DNA nanofibers. DNA nanofibers were incubated with 10 nm AuNPs functionalized with a complementary DNA

sequence to the nanofiber DNA strands. (a, b) AFM and (c, d) TEM images of AuNP-decorated Cy3Cy3−DNA nanofibers under low AuNP:DNA fiber ratio (left panel) and higher ratio of AuNP:DNA fiber (right panel).

Upon increasing both the AuNP and fiber concentrations, the formation of AuNP-mediated higher order networks of DNA nanofibers was observed (*Experimental Figure 4.56*). The specificity of AuNP−fiber interaction was investigated by using AuNPs containing a scrambled noncomplementary sequence to the fiber DNA. Upon mixing, no binding was observed, highlighting the specific DNA-mediated templation of the AuNPs (Figure 4.15).

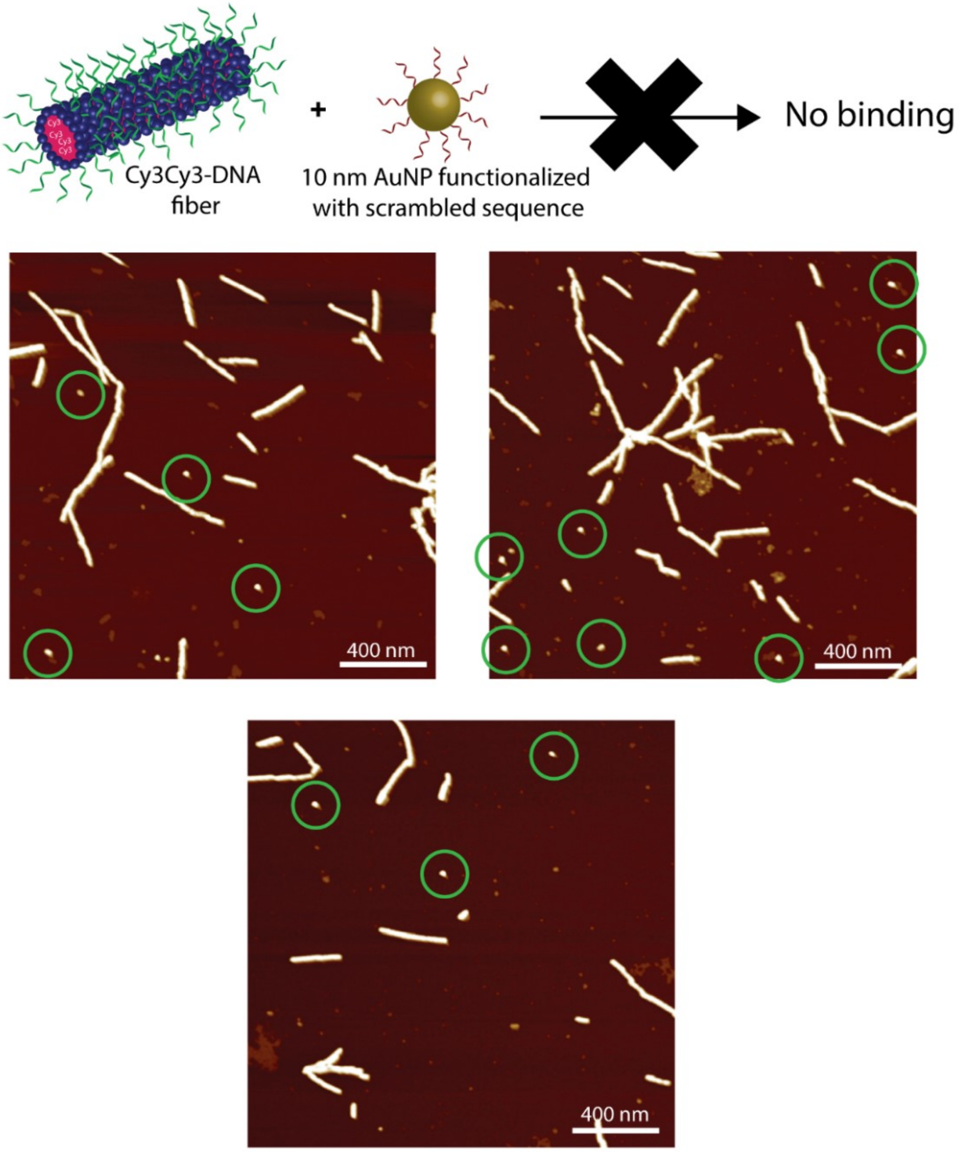

Figure 4.15 – DNA nanofibers mixed with 10 nm AuNP containing a non-complementary scrambled DNA sequence. AFM analysis demonstrated the absence of binding of the AuNPs to DNA nanofibers. 10 nm AuNPs on the surface were circled in green.

These results demonstrate a method of utilizing DNA fibers for the hierarchical assembly of inorganic AuNPs and patterning of nanomaterials; notably, this could yield an efficient route to functional materials through seeded supramolecular polymerization and afford control over the length of the hybrid material.

In the context of hierarchical DNA assemblies, DNA origami has dramatically improved the complexity and scalability of DNA nanostructures.[94] Due to its high degree of customization and spatial addressability, it has provided a versatile platform with which to engineer nanoscale structures and functional devices. One particularly interesting application has been the use of DNA origami for predesigned routings to guide polymer chain positioning through DNA base-pair interactions.[95] This method has allowed ready access to conjugated polymer assemblies with arbitrary geometries. Drawing inspiration from this work, we first tested whether the DNA nanofibers could be templated along the edges of rectangular DNA origami tiles (Figure 4.16a, *Experimental Figures 4.57-4.59*). This would serve as a starting point for guided polymer growth and would also demonstrate the ability to further generate more complex architectures.

In our design, the binding of previously grown Cy3Cy3−DNA nanofibers and origami tiles was achieved through a 14 base-pair homology between the fiber DNA and two extension strands from the origami rectangle. As an initial step, DNA origami binding was characterized by AGE (Figure 4.16b). Strong binding was observed through a mobility shift of the DNA origami band (lane 4) to a nonpenetrating band (lanes 1−3) indicating association with the Cy3Cy3−DNA fibers.

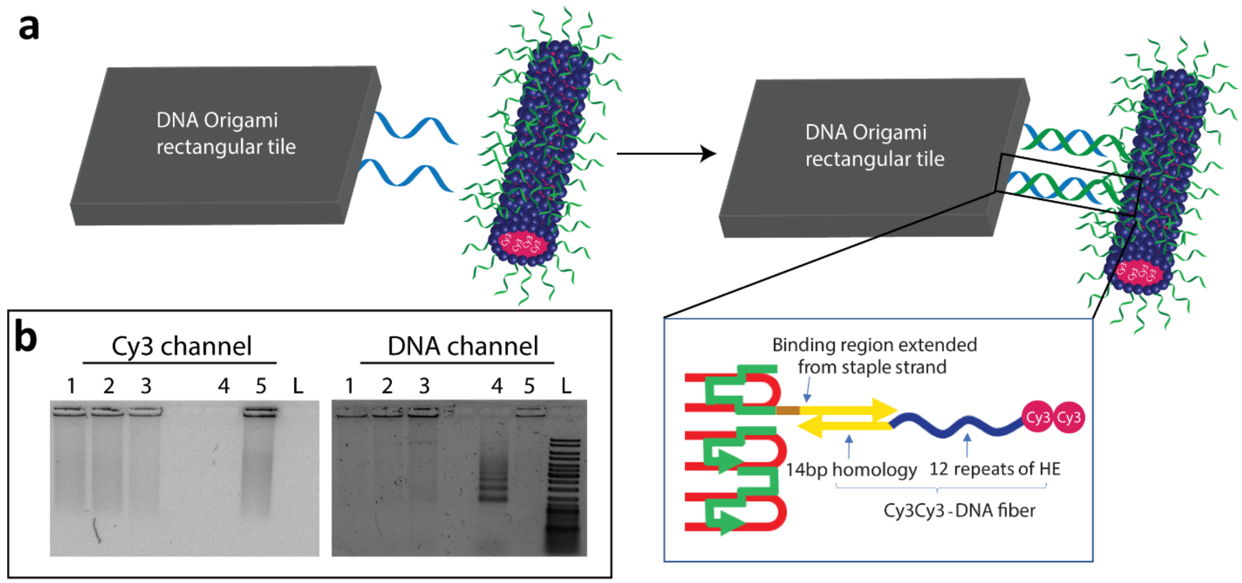

Figure 4.16 – Template of Cy3Cy3−DNA fibers on rectangular DNA origami tiles. (a) Cy3Cy3−DNA fibers were incubated with rectangular DNA origami tiles functionalized on one or two sides with two DNA strands complementary to the fiber DNA strands. (b) Agarose gel electrophoresis analysis of the binding of Cy3Cy3−DNA fibers to DNA origami tiles. L: ladder, lanes 1−3: Different molar ratios of Cy3Cy3-fibers mixed with DNA origami tiles. Lane 1: 1000× excess Cy3Cy3−HE_{12}−DNA monomer to DNA origami tile, lane 2: 800× excess, lane 3: 500× excess, lane 4: DNA origami tile control, lane 5: Cy3Cy3−DNA nanofiber control

The hybrid structures were then characterized by AFM, which showed linear positioning of DNA fibers along the shorter rectangular origami edge as per design (Figure 4.17a-f, *Experimental Figure 4.57*). Interestingly, the fibers displayed perfect alignment along the rectangular origami edge. Large height difference was also observed between DNA fibers and DNA origami (fiber ~9 nm vs DNA origami ~2 nm), as predicted, from AFM analysis of both structures (Figure 4.17c-f), and earlier reported heights of DNA origami tiles.[39]

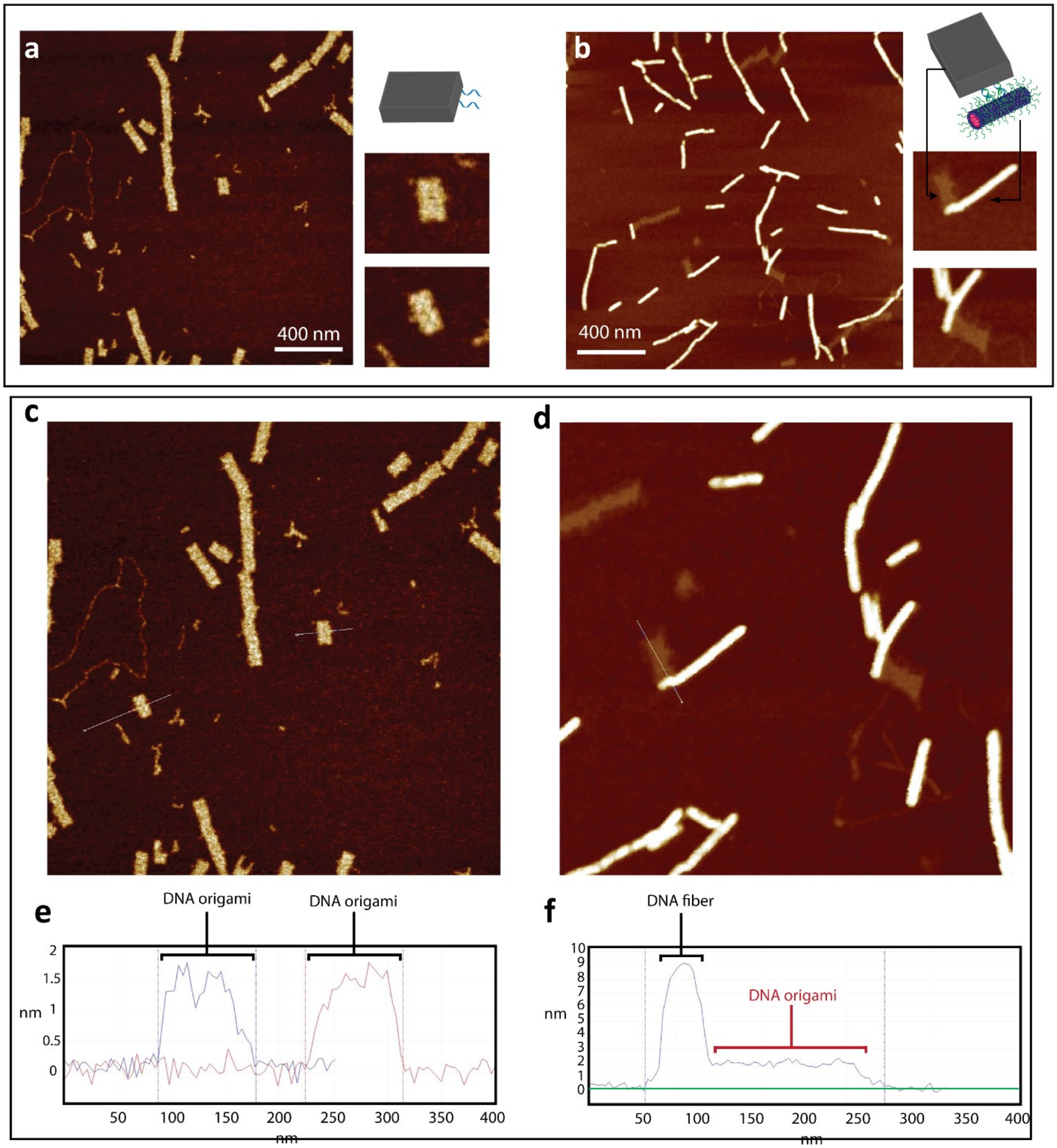

Figure 4.17 – Templation of DNA nanofibers on rectangular origami tiles. a,b) AFM images of the (a) origami tile control, (b) one-sided templation of Cy3Cy3-fibers on DNA origami tiles. c–d) Representative AFM images of DNA origami control and one-sided templated fibers showing the cross-sections used for height analysis. e,f) Height analysis showing the large height difference between DNA fibers and DNA origami tiles (9 nm for fiber vs. 2 nm for DNA origami)

We then tested the possibility to generate a two-way track along the origami tile by placing complementary DNA strands to the fiber on opposite edges of the rectangular tile. As a demonstration, we generated a two-way track of Cy3Cy3−DNA fibers sandwiching DNA origami rectangles (Figure 4.18a,b, *Experimental Figures 4.58, 4.59*). These results serve as an initial proof-of-concept toward building complex hierarchical DNA architectures. The high directional fidelity of polymer binding along DNA origami edges demonstrated through this approach is an important requirement for future efforts toward guiding the growth of our polymer system en route to creating molecular-scale optical wires with arbitrary geometries.

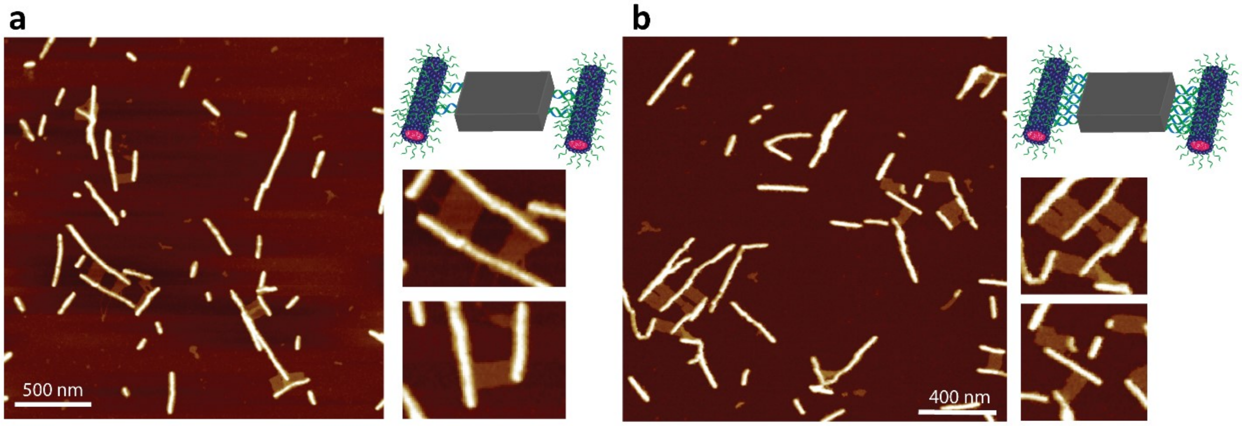

Figure 4.18 – Templation of DNA nanofibers on rectangular origami tiles. a) Two-sided templation using two binding arms/edge, and (b) five binding arms/edge

4.4 Conclusion

In summary, we report the discovery of Cy3-mediated shape-shifting of DNA nanostructures to create functional 1D architectures in aqueous media. The structures were made from sequence-defined monomers that are completely monodisperse. We have shown that the position of the cyanine units and the length of DNA/polymer chain are critical for the formation of 1D assemblies. Furthermore, we demonstrated an example of stimuli-responsive fibers further highlighting the role of cyanine dyes in fiber formation. The linear dependence of DNA fiber length on monomer concentration provides an easy handle to predefine fiber length. Additionally, seeded growth of DNA fibers was demonstrated and provides an approach for controlled fiber length. The mechanism behind the angled directionality in the seeded growth of fibers is the focus of studies underway. Additionally, the change in the optical properties of the cyanine units upon assembly and disassembly of the fiber could allow these structures to be used as biosensors and tools for monitoring the fate and integrity of structures in biological systems. As a demonstration of the functionality of our system, we showed the hierarchical assembly of 10 nm AuNPs on DNA nanofibers, and nanofiber templation on DNA origami structures. This opens the door for generation of complex functional architectures by combining the inherent information contained in each system. From a DNA nanotechnology standpoint, this work represents an interesting avenue toward a facile and inexpensive method for the fabrication of functional DNA hybrid materials and provides an approach to extend the library of "smart" DNA nanostructures. From a drug delivery standpoint, structures with high aspect ratio have been shown to exhibit longer blood circulation times and higher cellular uptake compared to spherical particles.[96,97] Additionally, taking advantage of the DNA shell surrounding the fibers, our method is compatible with DNA/RNA aptamers and oligonucleotide therapeutics, whose properties can be exploited for targeted cellular delivery and diagnostics. The ability to obtain large populations of aptamers per structure has been shown to be important for polyvalent aptamer recognition.[98] The ability to readily synthesize DNA/RNA with therapeutic capability as part of the oligonucleotide− polymer hybrid and the overall nanostructure is also an exciting prospect for nanomedicine and a focus of our future work. Finally, more in-depth photophysical studies will be conducted on the electronic coupling of cyanine dyes, and how its influenced by the local environment for designing potential efficient exciton platforms resembling natural photosynthetic systems.

4.5 Experimental Section

4.5.1 General

The reagents and buffers used are listed in *Experimental Section 2.5.1* in Chapter 2 with the following additions. The DNA origami ssDNA viral scaffold (M13mp18) was purchased from Guild Bioscience. The DNA staple strands were purchased from Bioneer and Integrated DNA Technologies (IDT). Gold(III) chloride trihydrate, magnesium chloride, sodium chloride, Bis(p-sulfonatophenyl)phenylphosphine dihydrate dipotassium salt (BSPP) and other chemicals were purchased from Sigma-Aldrich and used as received.

4.5.2 Instrumentation

Instrumentation used is detailed in *Experimental Section 2.5.2* in Chapter 2 with a few additions. Confocal fluorescence microscopy was conducted using Zeiss LSM710 CLSM with 63x (NA=1.4, oil, DIC).

4.5.3 Solid-phase synthesis and purification

DNA synthesis was performed as outlined in *Experimental Section 2.5.3* in Chapter 2. For Cy3 phosphoramidite (0.1 M, anhydrous acetonitrile) amidites, extended coupling times of 10 minutes were used using 0.25M 5-(ethylthio)tetrazole in anhydrous acetonitrile. Following gel purification, the samples were analyzed by HPLC. Detection was carried out using a diode-array detector, monitoring absorbance at 260 nm and 556 nm. Retention times and for the products are shown in Figure 4.20.

4.5.4 Sequences of Cy3-labeled-polymer conjugates and characterization

The sequences of the Cy3-polymer-DNA conjugates are presented in Table 4.1.

Table 4.1 – Sequences used for DNA amphiphiles and DNA controls. (**D** = DMT-dodecane-diol), (**Cy3** = Cyanine 3 phosphoramidite), (**P** = photocleavable linker).

Strand	Sequence (5'-xx-3')
HE$_{12}$-DNA	**DDDDDDDDDDDD**TTTTTCAGTTGACCATATA
Cy3-HE$_{12}$-DNA	**Cy3DDDDDDDDDDDD**TTTTTCAGTTGACCATATA
Cy3Cy3-HE$_{12}$-DNA	**Cy3Cy3DDDDDDDDDDDD**TTTTTCAGTTGACCATATA
Cy3Cy3-PCL-HE$_{12}$-DNA	**Cy3Cy3PDDDDDDDDDDDD**TTTTTCAGTTGACCATATA
8-mer DNA, 6 HE	**Cy3Cy3DDDDDD**TTTTTCAGT

38-mer DNA, 12 HE	**Cy3Cy3DDDDDDDDDDDD**TTTTTCAGTTGACCATATAT TTTTCAGTTGACCATATA

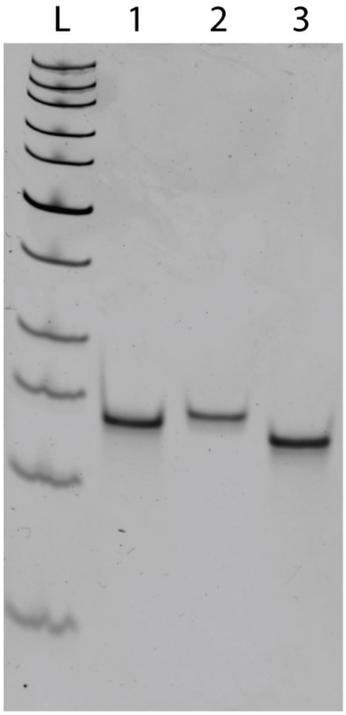

Figure 4.19 – Denaturing gel electrophoresis of the Cy3-polymer-DNA conjugates. (18% denaturing PAGE). L: ladder, lane 1: Cy3-HE_{12}-DNA, Lane 2: Cy3Cy3-HE_{12}-DNA, Lane 3: HE_{12}-DNA.

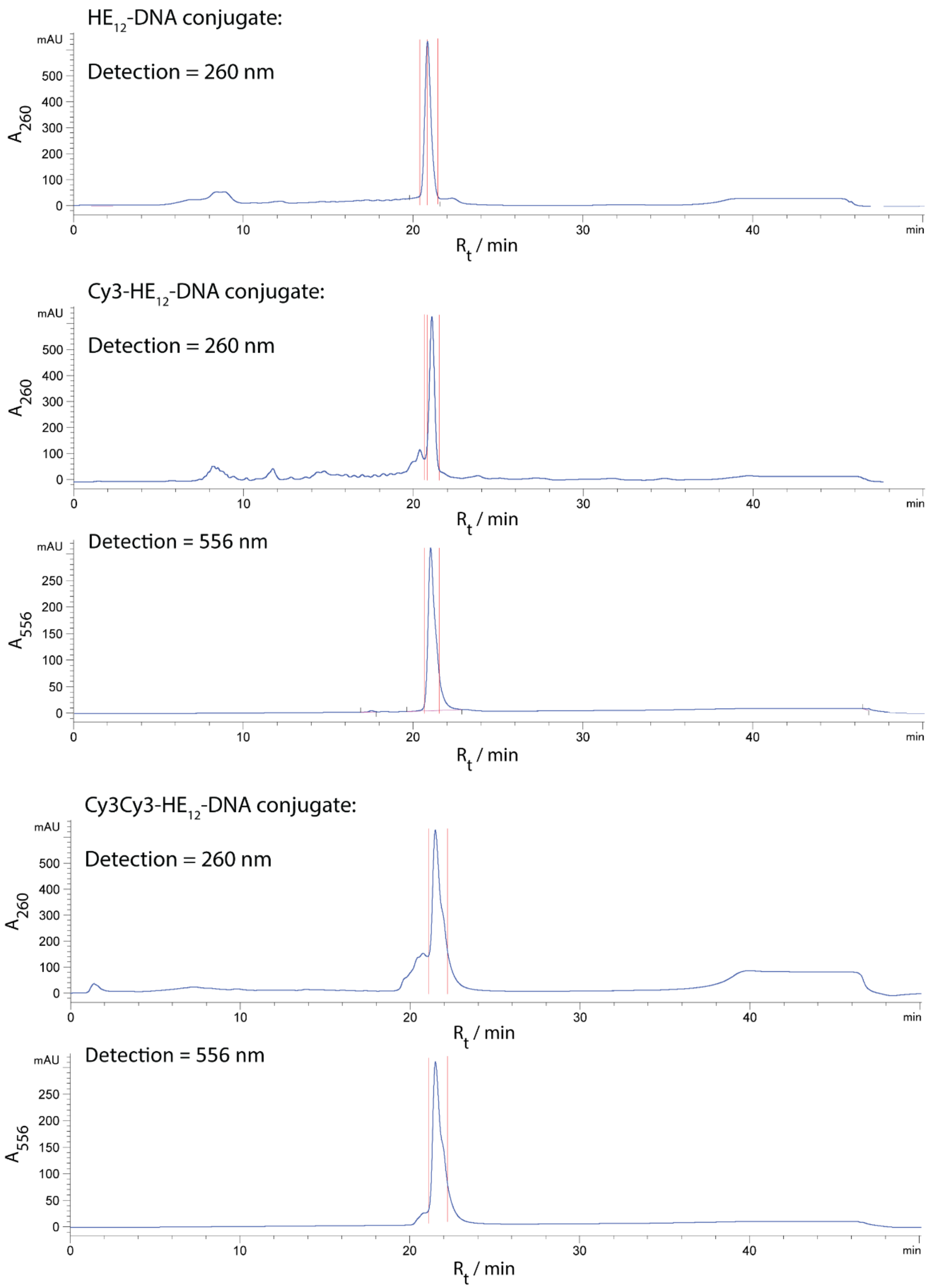

Figure 4.20 – HPLC chromatograms of the crude Cy3-polymer-DNA products. HPLC signals were measured at 260 nm and 556 nm (Cy3-specific channel). Elution gradient: 3-70% acetonitrile over 30 minutes at 60 ºC.

Table 4.2 – LC-ESI-MS data. Calculated and experimental m/z values for synthesized DNA amphiphiles including the unmodified oligonucleotide controls.

Molecule	Calculated m/z	Found m/z
HE_{12}-DNA	8933.77	8934.3750
Cy3-HE_{12}-DNA	9442.02	9445.0886
Cy3Cy3-HE_{12}-DNA	9949.26	9951.6272
Cy3Cy3-PCL-HE_{12}-DNA	10293.34	10295.47

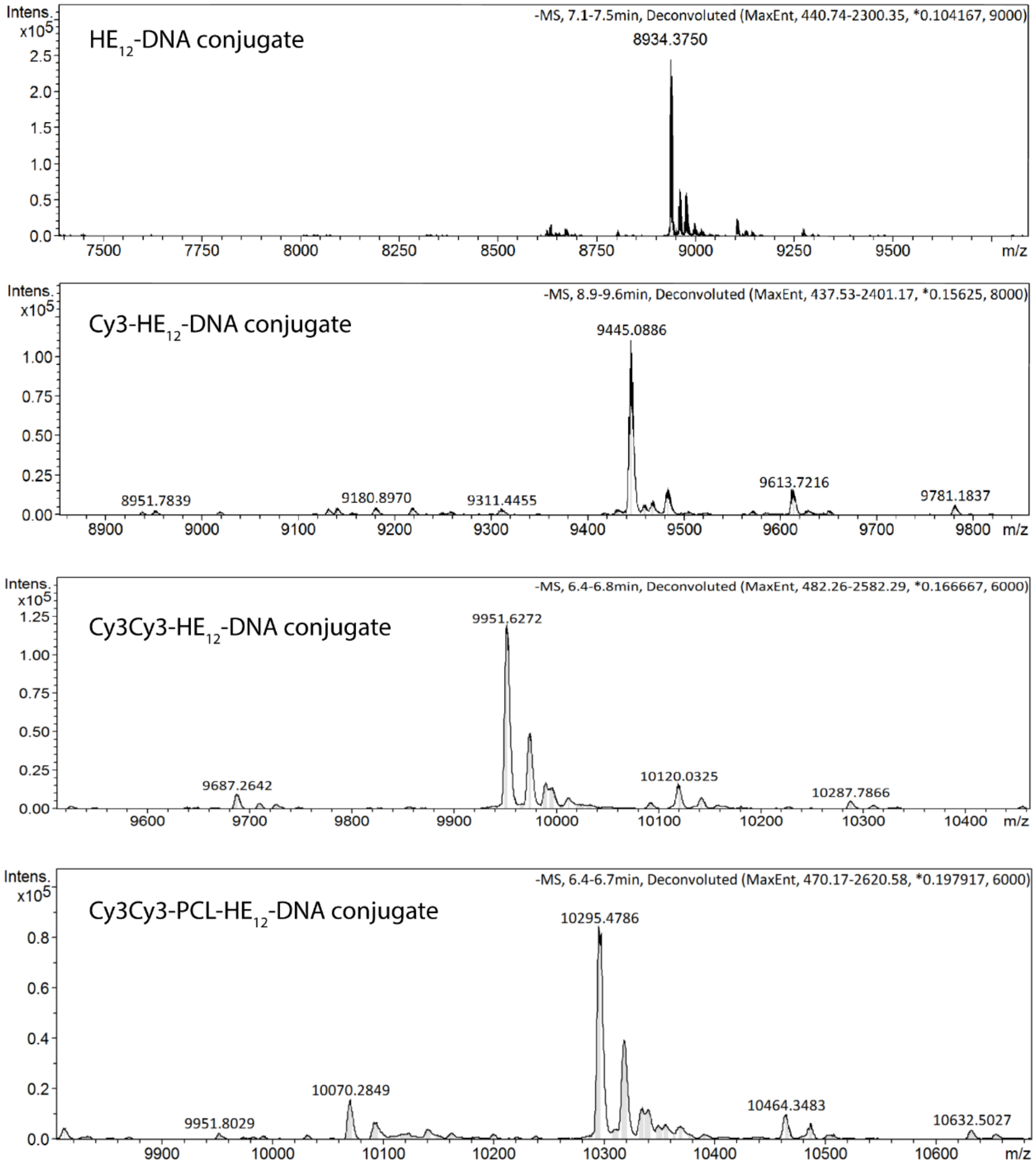

Figure 4.21 – MS characterization of Cy3-labeled DNA-polymer conjugates.

4.5.5 Preparation of Cy3 and Cy3Cy3 DNA nanofibers

Cy3 or Cy3Cy3-DNA nanofibers were prepared by mixing Cy3-HE_{12}-DNA or Cy3Cy3-HE_{12}-DNA monomer dispersed in water with the assembly buffer. Final volume: 50 µL, concentration: 5 µM in TAMg buffer $[Mg^{2+}]_{final}$ = 12.5 mM (10x TAMg buffer contains 125 mM Mg^{2+}, 1x TAMg contains 12.5 mM Mg^{2+}), followed by a heat/cool cycle (95 °C to 22 °C over 1.5 hours). Following the annealing step, the samples were aged at room temperature for 1 day to yield DNA nanofibers.

4.5.6 Characterization of Cy3 and Cy3Cy3-DNA nanofibers

4.5.6.1 Gel mobility Shift Assays

Agarose gel electrophoresis was used to characterize Cy3 and Cy3Cy3-DNA nanofibers. In each case, 2.5% AGE was carried out at 4 °C for 2.5 hours at a constant voltage of 80 V. Typical sample loading is 30 picomoles with respect to the DNA per lane (3 µL of 10 µM DNA). The gel was initially imaged under a Cy3-selective channel, then stained with GelRed DNA stain and imaged under a DNA-selective channel.

4.5.6.2 Dry and Fluid Atomic Force Microscopy (AFM) measurements

Dry AFM was carried out using a MultiMode8™ SPM connected to a Nanoscope™ V controller (Bruker, Santa Barbara, CA). All images were obtained using ScanAsyst mode in air with AC160TS cantilevers (Nominal values: Tip radius – 2 nm, Resonant frequency – 300 kHz, Spring constant – 42 N/m) from Bruker. 5 µL of each sample prepared at 5 µM in TAMg buffer was deposited on a freshly cleaved mica surface (ca. 7 x 7 mm) and allowed to adsorb for 2-5 seconds. Then 50 µL of 0.22 µm filtered Millipore water was dropped on the surface and instantly removed with filter paper. The surface was then washed with a further 100 µL of water (2 x 50 µL), wicked with a filter paper, and the excess removed with a flow of nitrogen (or air). Samples were dried under vacuum for at least 3 hours prior to imaging. For statistical length analysis, a minimum of 120 fibers were carefully picked to determine the contour length, and histograms of the length distribution of fibers were constructed. The standard deviation of the length distribution "sigma" (σ) and the number and weight-average contour length L_n and L_w of each sample were calculated according to the equations below (L = length of fiber, N = number).

$$L_n = \frac{\sum_{i=1}^{n} N_i L_i}{\sum_{i=1}^{n} N_i}$$

$$L_w = \frac{\sum_{i=1}^{n} N_i L_i^2}{\sum_{i=1}^{n} N_i L_i}$$

Fluid AFM was carried out with the same instrumentation used for dry conditions. For sample preparation, 5 µL of sample at 5 µM was deposited directly on freshly cleaved mica surface, followed by injection of 60 µL of 1x TAMg buffer into the cell chamber prior to imaging.

4.5.6.3 Confocal fluorescence microscopy

10 µL of the sample and 2 µL glycerol mix (7:1 glycerol/H_2O) were deposited on a microscope slide (Fisher Scientific, cat.# 125442). A 25x25 mm cover glass (Fisher Scientific, cat.# 12542C) was then lowered over the sample. The images were acquired using Zeiss LSM710 CLSM with 63x (NA=1.4, oil, DIC) plan apochromatic objective. For an acquisition of the cross-sectional image of the fibers, Cy3 dye was excited using 514-nm Argon ion laser (3% laser intensity). The emission range of 538-680 nm was collected. The image resolution was either 1024x1024 or 2048x2048 pixels with the pixel dwell time of 0.39-0.79 µs. The pinhole was 36 µm.

4.5.6.4 Transmission Electron Microscopy

Samples (2 µL at 5 µM with respect to total DNA) were deposited on carbon film coated copper EM grids for one minute, followed by blotting off the excess liquid with the edge of a filter paper, and washing three times with 20 µL of water, before drying under vacuum for at least 2 hours. The samples were imaged using a Tecnai 12 microscope (FEI electron optics) equipped with a Lab 6 filament at 120 kV. Images were acquired using a Gatan 792 Bioscan 1k x 1k Wide Angle Multiscan CCD Camera (Gatan Inc.). Contrast was adjusted automatically. Images were analyzed using ImageJ, which required manually setting threshold levels and measuring the length and width and of features to ensure correct particle picking.

4.5.6.5 Dynamic Light Scattering

Dynamic light scattering (DLS) experiments were carried out using a DynaPro™ Instrument from Wyatt Technology. A cumulants fit model was used to confirm the presence and determine the size the Cy3 and Cy3Cy3-DNA nanofibers. Sterile water and 1xTAMg buffer were filtered using a 0.45 µm nylon syringe filter before use in DLS sample preparation. 20 µL of sample (concentration: 5 µM) was used in each measurement. All measurements were carried out in triplicate at 25 °C.

4.5.6.6 Additional AFM of Cy3Cy3-fibers with size analysis

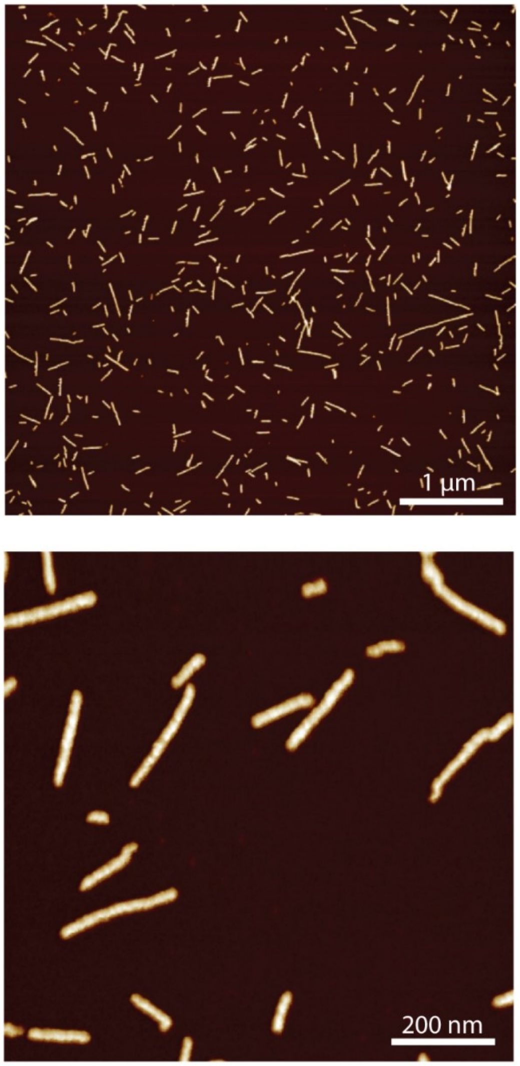

Figure 4.22 – Additional AFM images of Cy3Cy3-DNA nanofibers imaged under dry conditions.

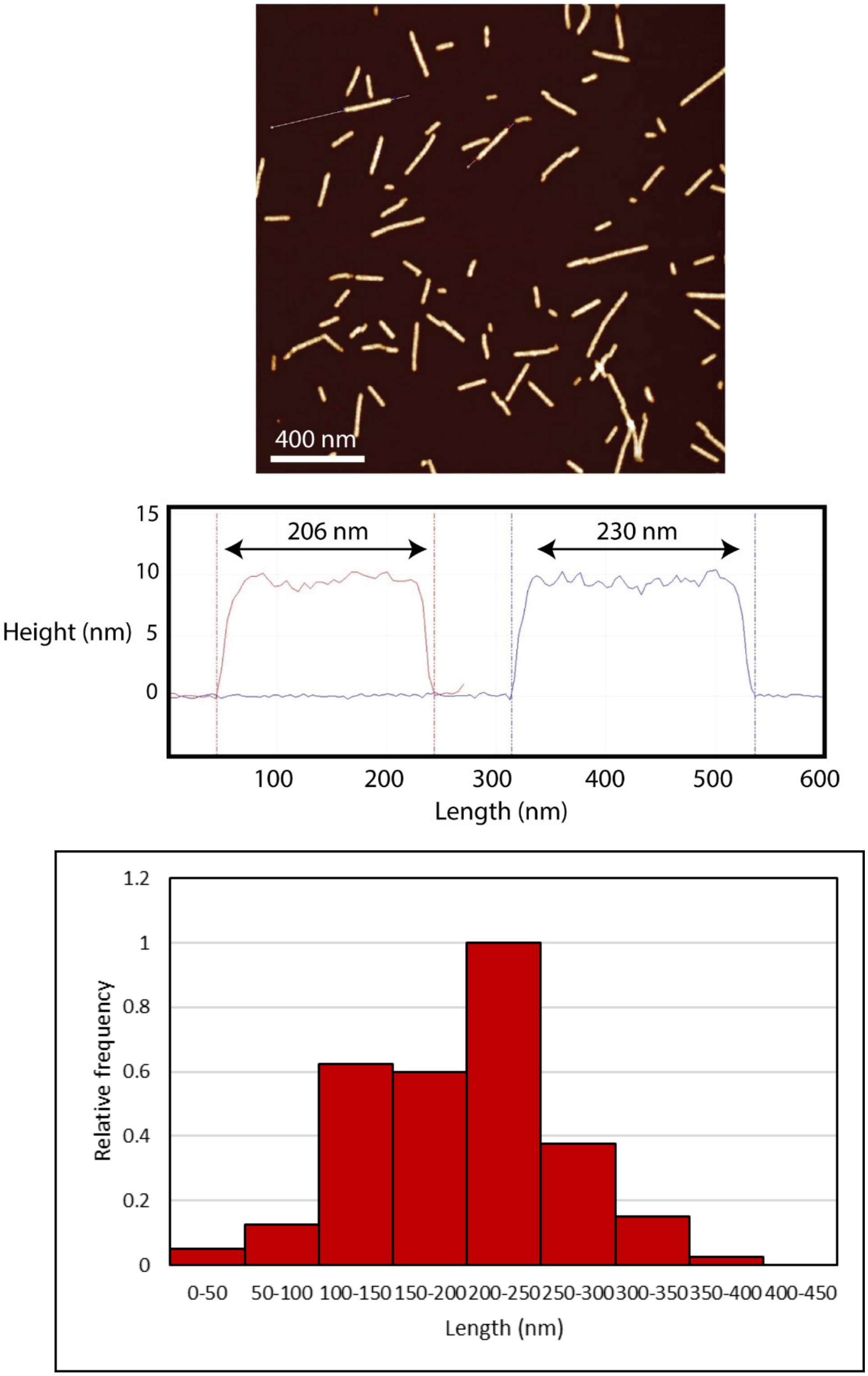

Figure 4.23 – Representative AFM image of Cy3Cy3-nanofibers with length, height and particle distribution analysis. Average contour length: 200 ± 35 nm. Height: 10.3 ± 0.8 nm. Structures counted: 124 fibers.

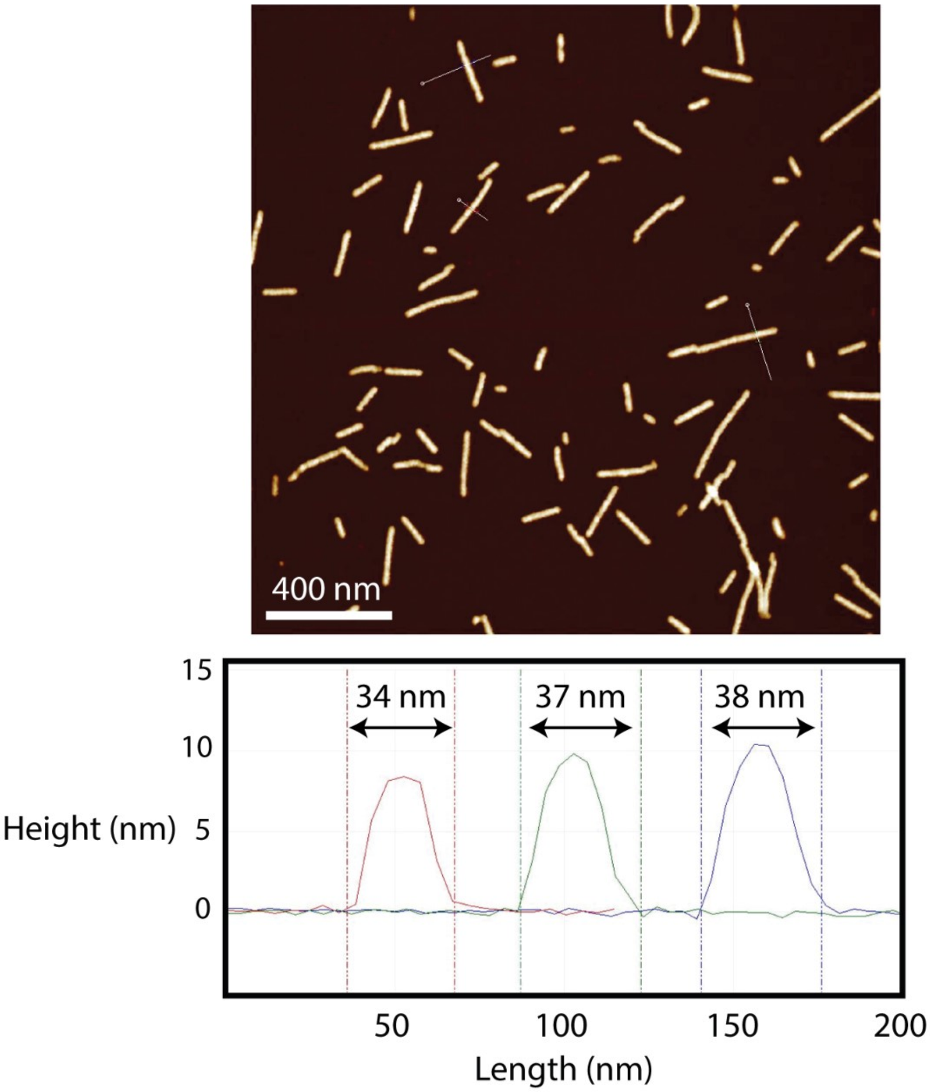

Figure 4.24 – Representative AFM image of Cy3Cy3-DNA nanofibers with width analysis. Average width: 36 nm ± 3 nm.

4.5.6.7 Additional TEM images of CyCy3-fibers

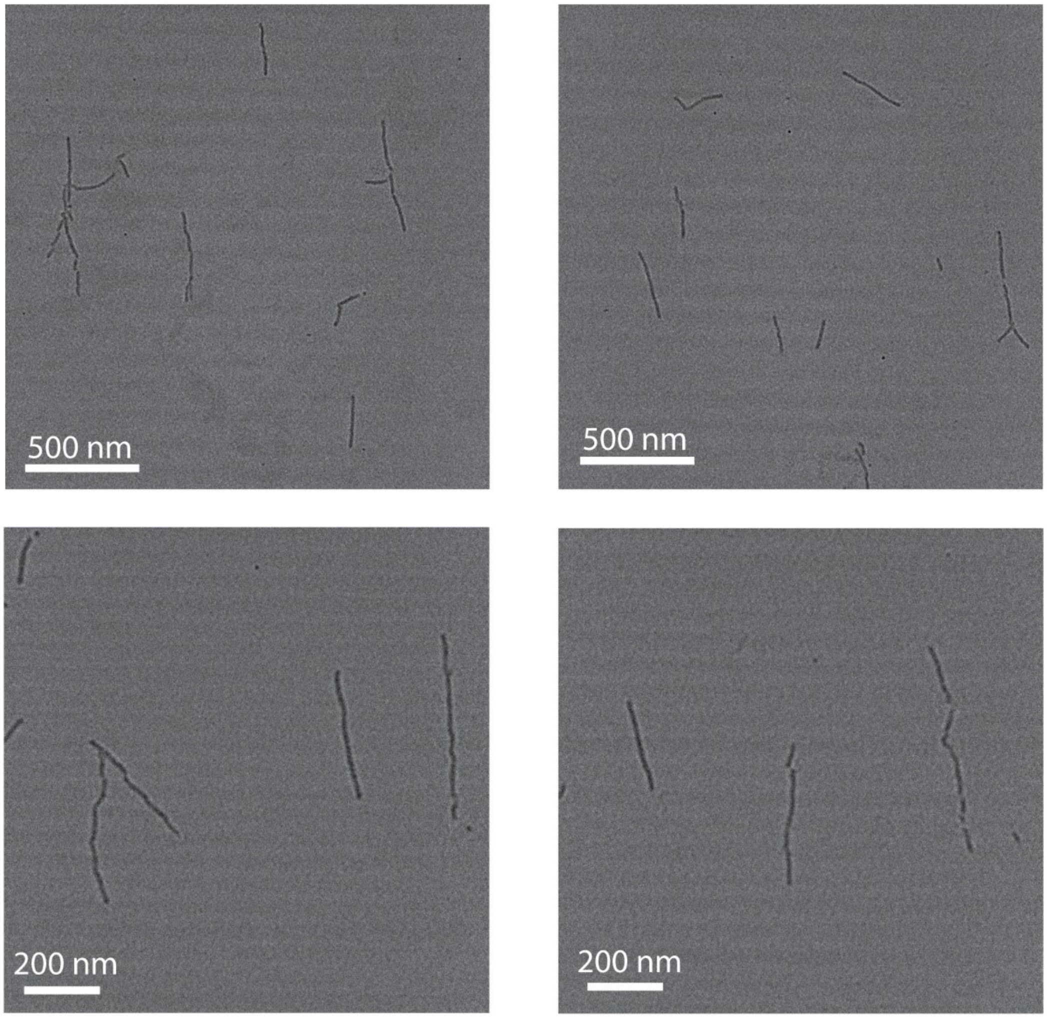

Figure 4.25 – Additional TEM images of Cy3Cy3-DNA nanofibers.

4.5.6.8 Atomic Force Microscopy analysis of spherical Cy3Cy3-DNA nanoparticles

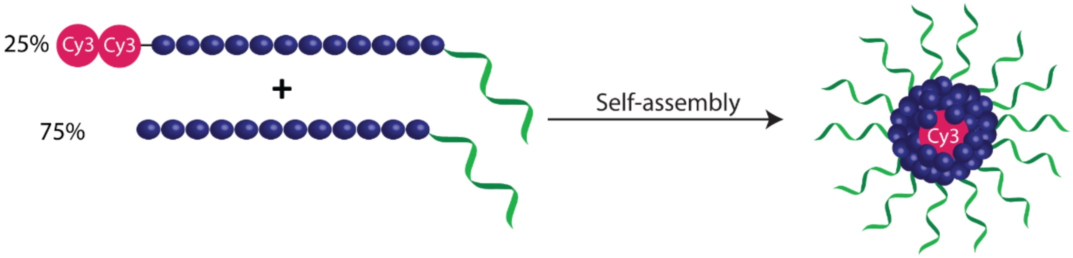

Figure 4.26 – Schematic representation of the formation of Cy3Cy3 spherical DNA nanoparticles. Structures were assembled by mixing ratios of 25% Cy3Cy3-HE$_{12}$-DNA monomer with 75% unlabeled HE$_{12}$-DNA followed by thermal annealing.

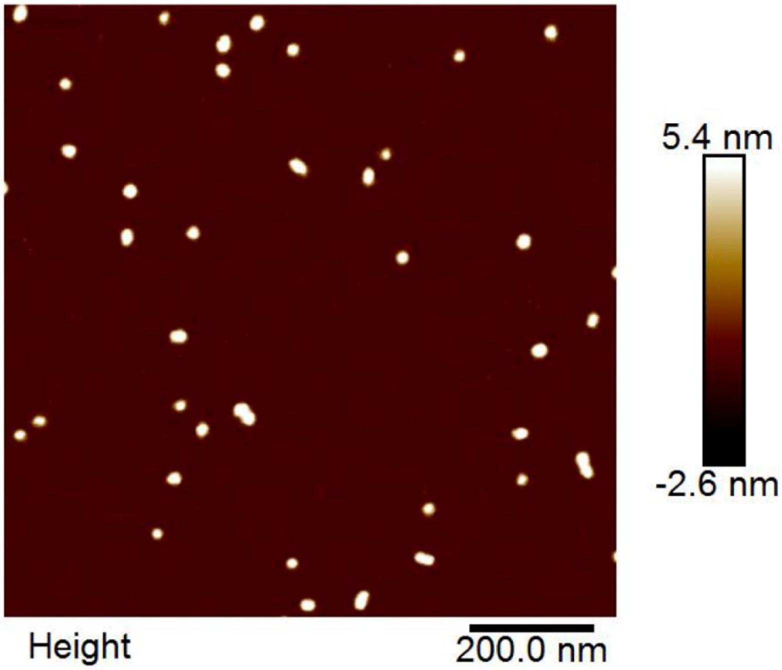

Figure 4.27 – AFM image of the assemblies obtained from a ratio of 25%/75% of Cy3Cy3-HE$_{12}$-DNA/HE$_{12}$-DNA strands. Highly monodisperse spherical particles were observed on surface with an average diameter of 28 nm and height of 8 nm.

4.5.6.9 Atomic force microscopy analysis of spherical nucleic acids

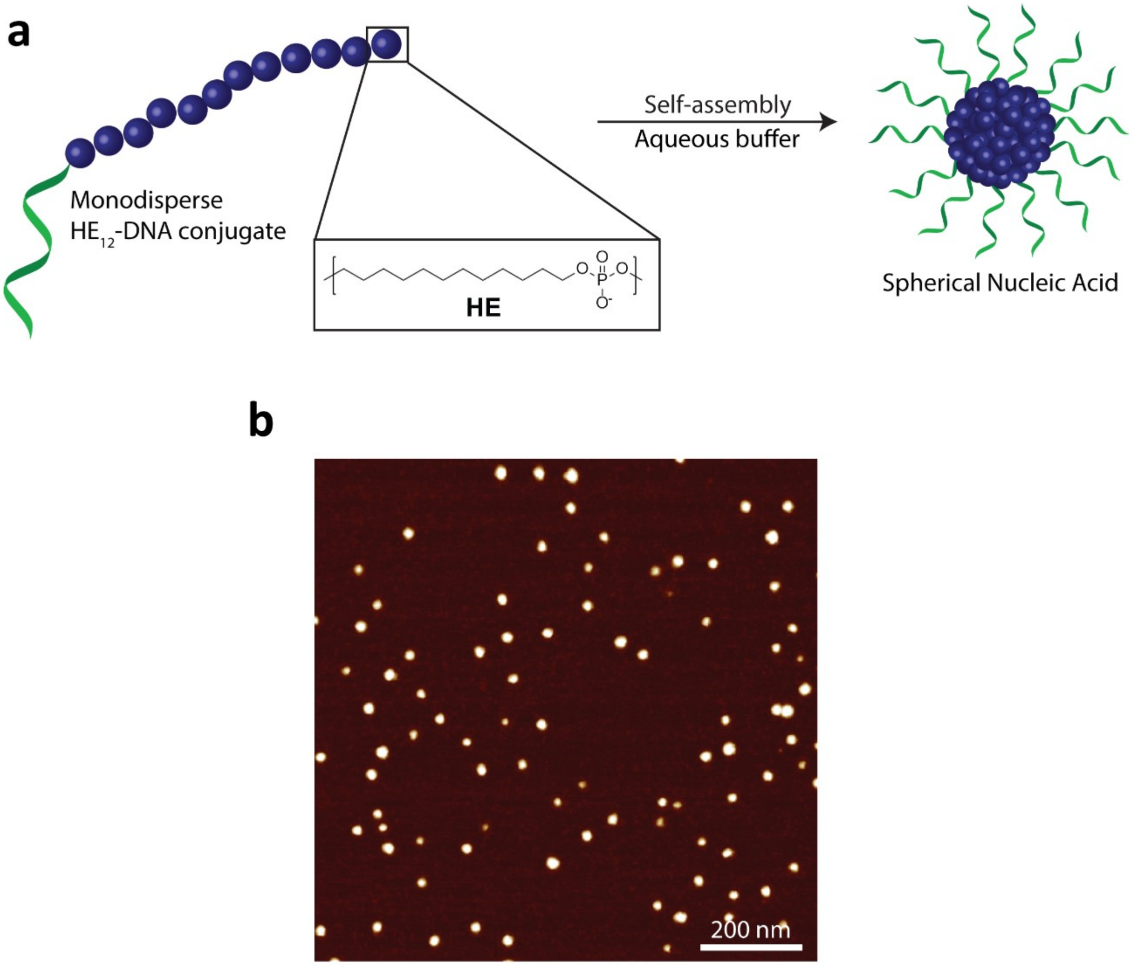

Figure 4.28 – Characterization of spherical nucleic acids. a) Schematic representation of the self-assembly of unlabelled HE_{12}-DNA conjugates into spherical nucleic acids. b) AFM analysis of spherical nucleic acids generated from HE_{12}-DNA monomer units. Nearly monodisperse spherical particles were observed on surface with an average diameter of 26 nm and height of 8 nm.

4.5.6.10 Fluid AFM studies on Cy3Cy3-DNA nanofibers

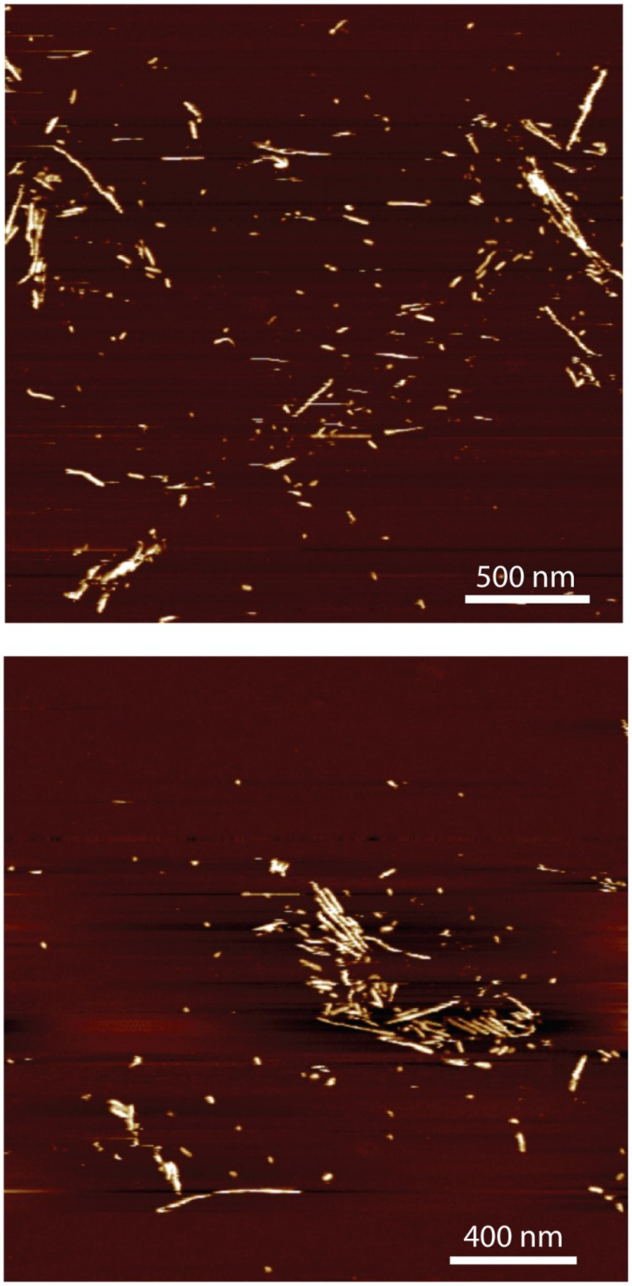

Figure 4.29 – Fluid AFM analysis of Cy3Cy3 DNA fibers showing the presence of extended 1D rods under liquid conditions.

4.5.6.11 Dynamic Light Scattering measurements of Cy3Cy3-DNA nanofibers

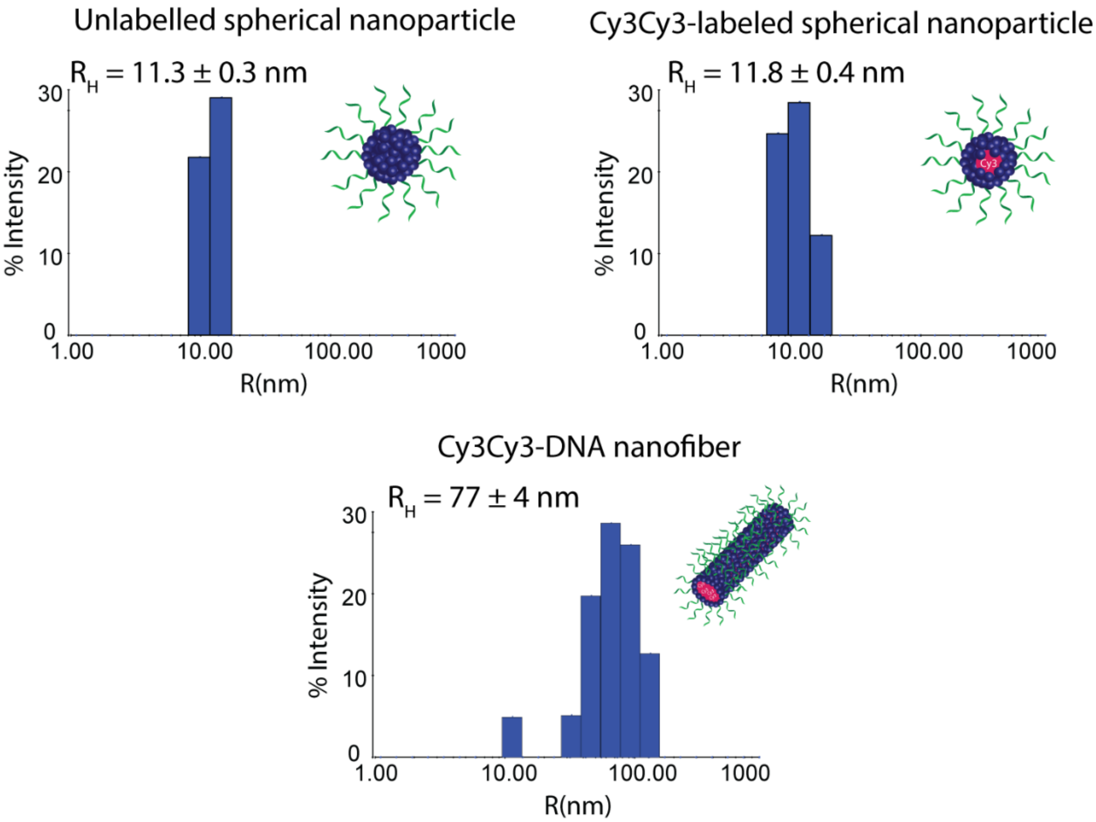

Figure 4.30 – Representative DLS histogram of Cy3Cy3-DNA nanofibers compared with unlabelled and Cy3Cy3-labeled spherical nanoparticles. The hydrodynamic radius of Cy3Cy3-DNA nanofibers was 77 ± 4 nm. The measurements were performed in triplicates.

4.5.7 Characterization of Cy3-DNA nanofibers

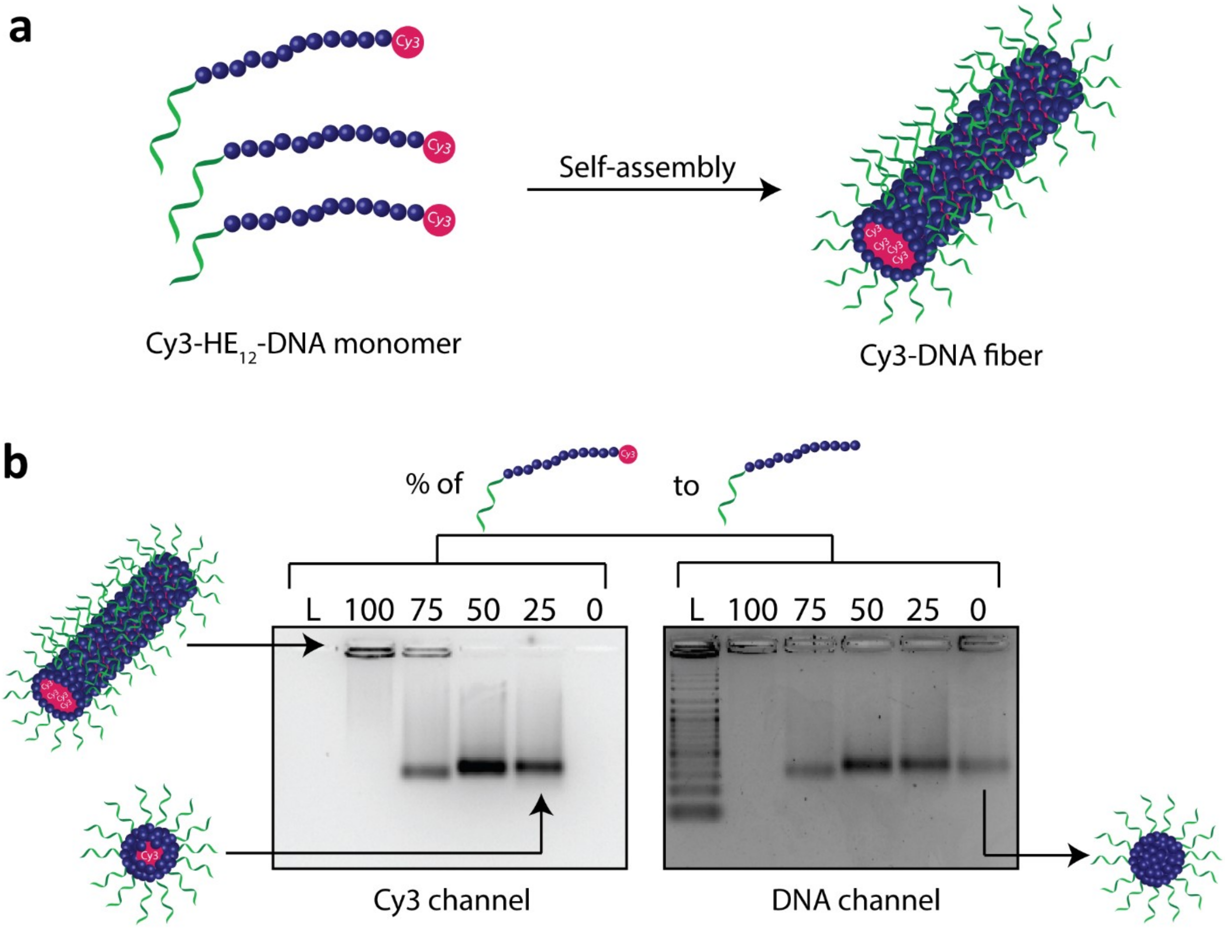

Figure 4.31 – AGE analysis of Cy3-DNA fibers. a) Schematic representation of the formation of Cy3-DNA fibers upon the self-assembly of Cy3-HE_{12}-DNA in aqueous media. b) Agarose gel electrophoresis analysis describing the morphological shift of structures made from mixing varying ratios of Cy3-HE_{12}-DNA with unlabelled HE_{12}-DNA strands followed by thermal annealing. L: Ladder, Lane 100: 100% Cy3-HE_{12}-DNA in the mixture, Lane 75: 75% Cy3-HE_{12}-DNA/25% HE_{12}-DNA, Lane 50: 50% Cy3-HE_{12}-DNA/50% HE_{12}-DNA, Lane 25: 25% Cy3-HE_{12}-DNA/75% HE_{12}-DNA, Lane 0: 100% HE_{12}-DNA. The gel was imaged under Cy3-selective channel (left panel), and a DNA-selective channel (right panel).

AFM analysis showed fiber-like structures with lengths ranging from 100-300 nm, and an average length of 230 nm, average width of 30 nm and height of 8 nm (Figure 4.32a). By TEM, Cy3-DNA nanofibers were observed on surface with an average contour length of 210 nm and width of 24 nm (Figure 4.32c). In solution, DNA fibers were observed by fluid AFM (Figure 4.32b) and DLS, which showed a population of assemblies with an average apparent hydrodynamic radius (R_h) of 176 nm (Figure 4.32d).

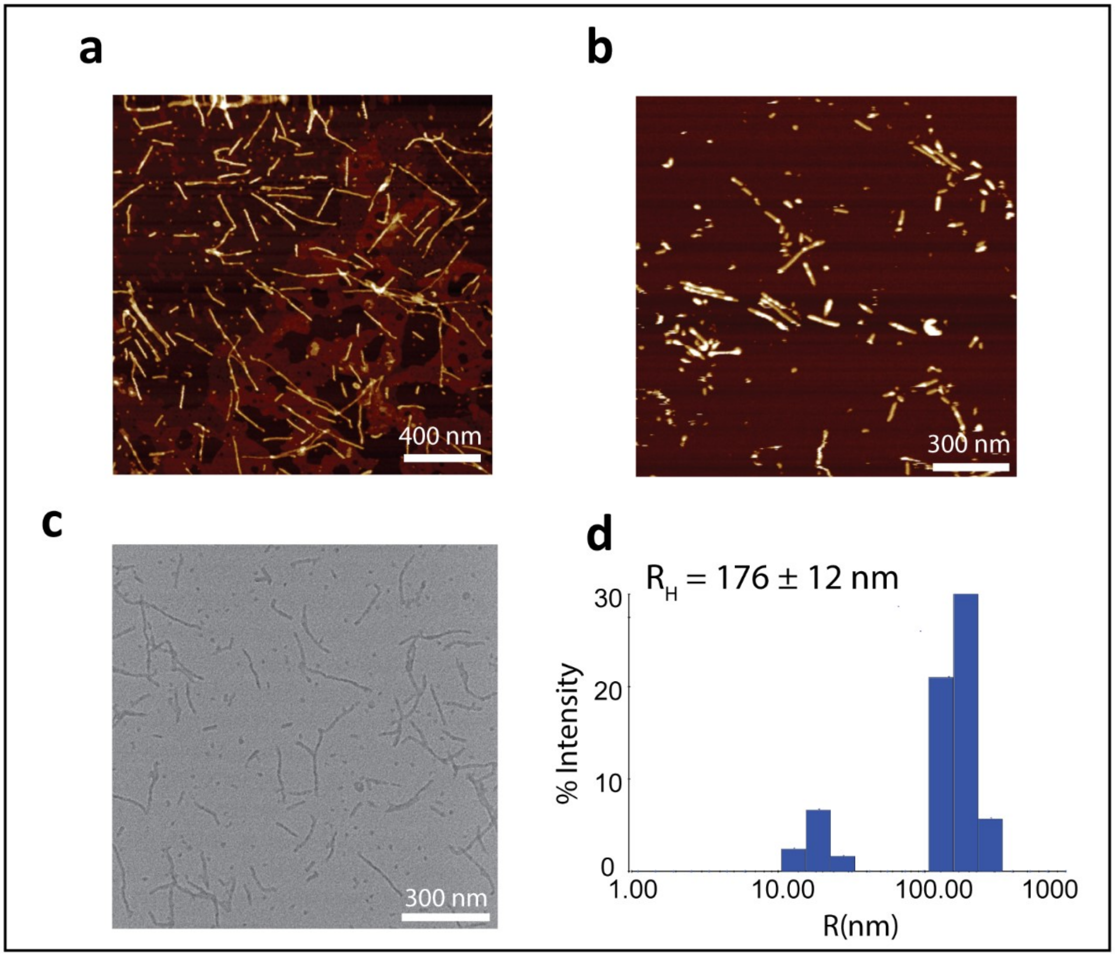

Figure 4.32 – Characterization of Cy3-DNA nanofibers. Atomic force microscopy images of DNA nanofibers on surface under a) dry and b) fluid conditions. c) Transmission electron microscopy (TEM) micrograph of DNA nanofibers. d) DLS histogram of Cy3-DNA nanofibers.

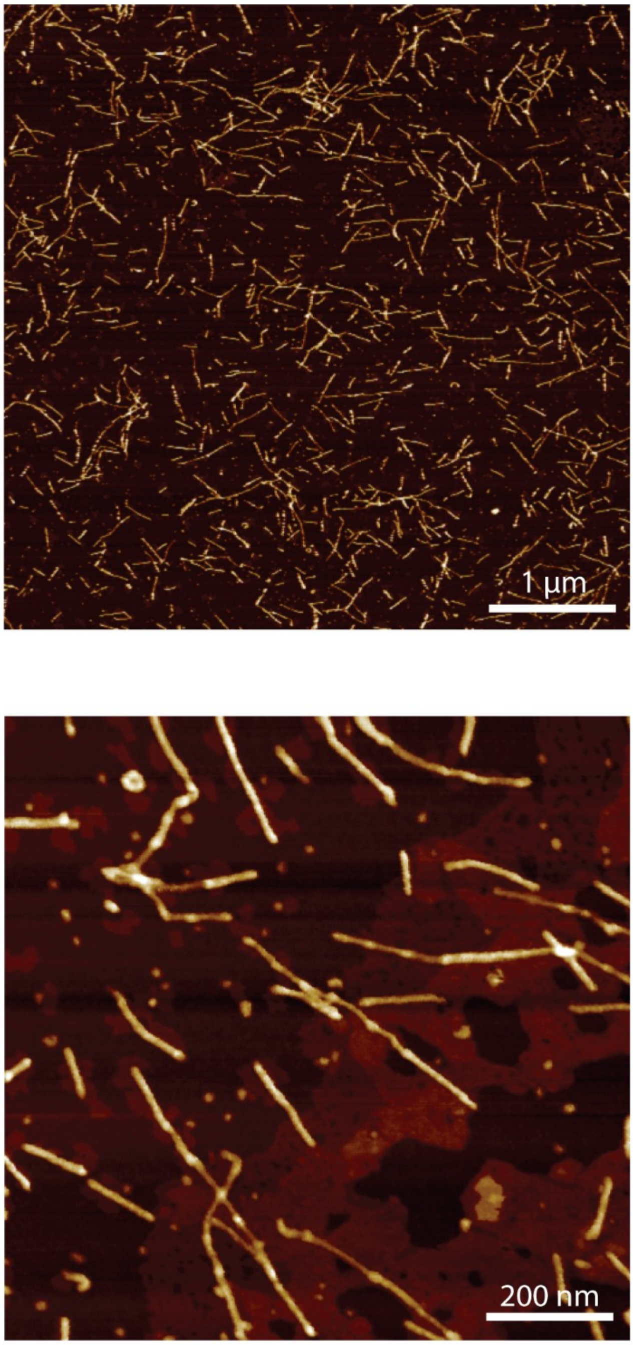

Figure 4.33 – Additional AFM images of Cy3-DNA nanofibers.

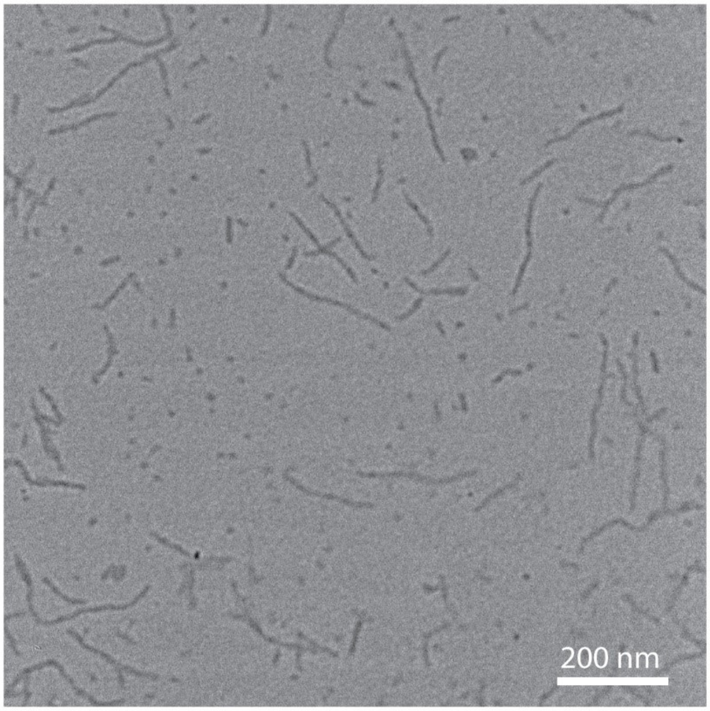

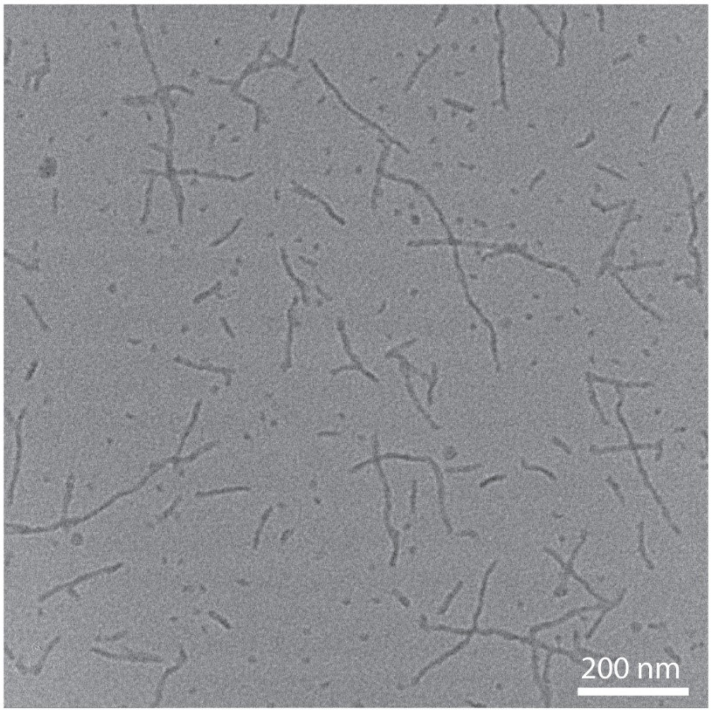

Figure 4.34 – Additional TEM micrographs of Cy3-DNA fibers.

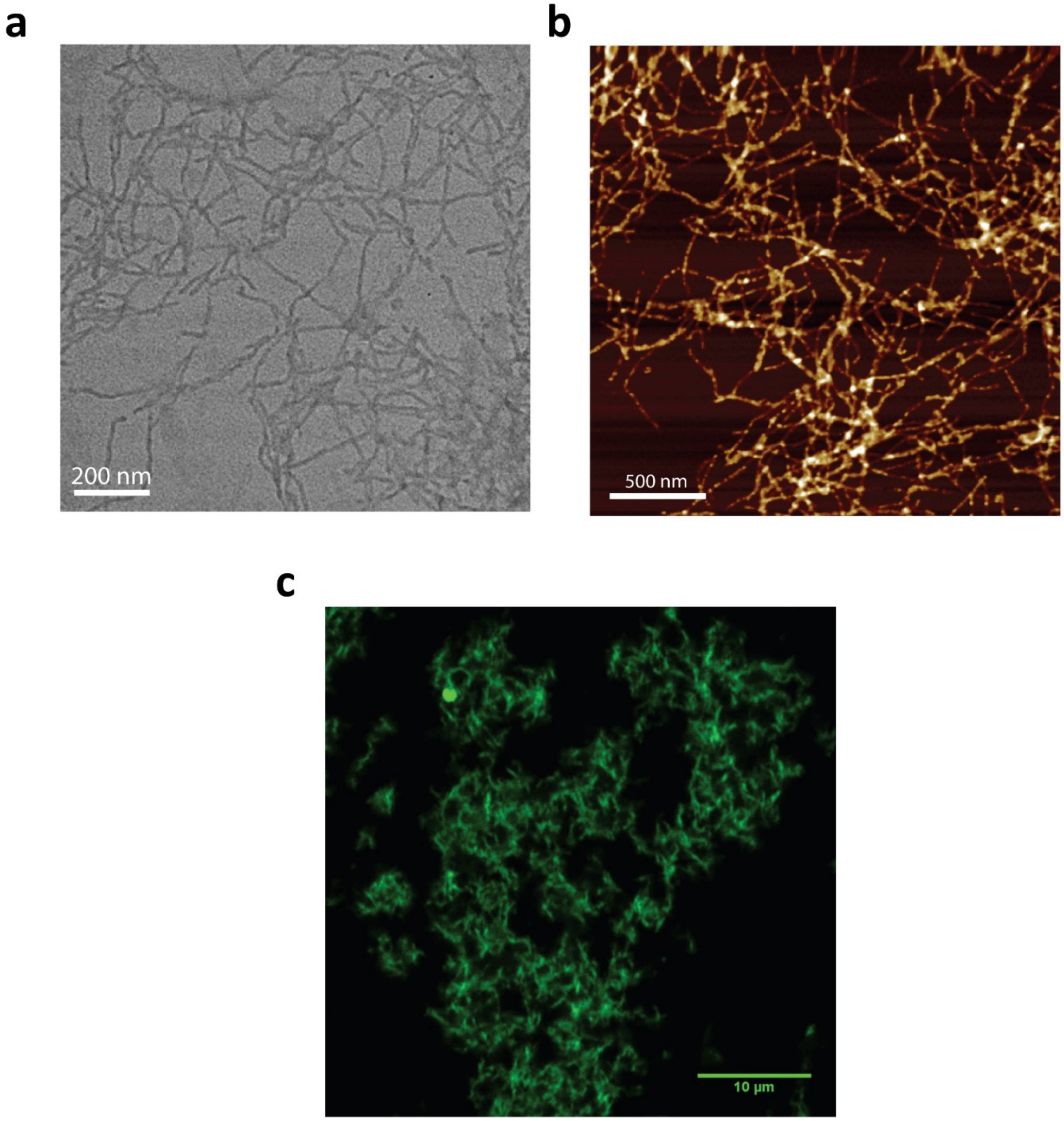

Figure 4.35 – Structural characterization of Cy3-DNA fiber networks generated from aging of Cy3 DNA nanofibers at room temperature for 2-3 days. a) TEM b) AFM and c) Confocal laser scanning microscopy (CLSM) images of Cy3-DNA fiber networks.

4.5.8 Assembly modes with different lengths of DNA and polymer

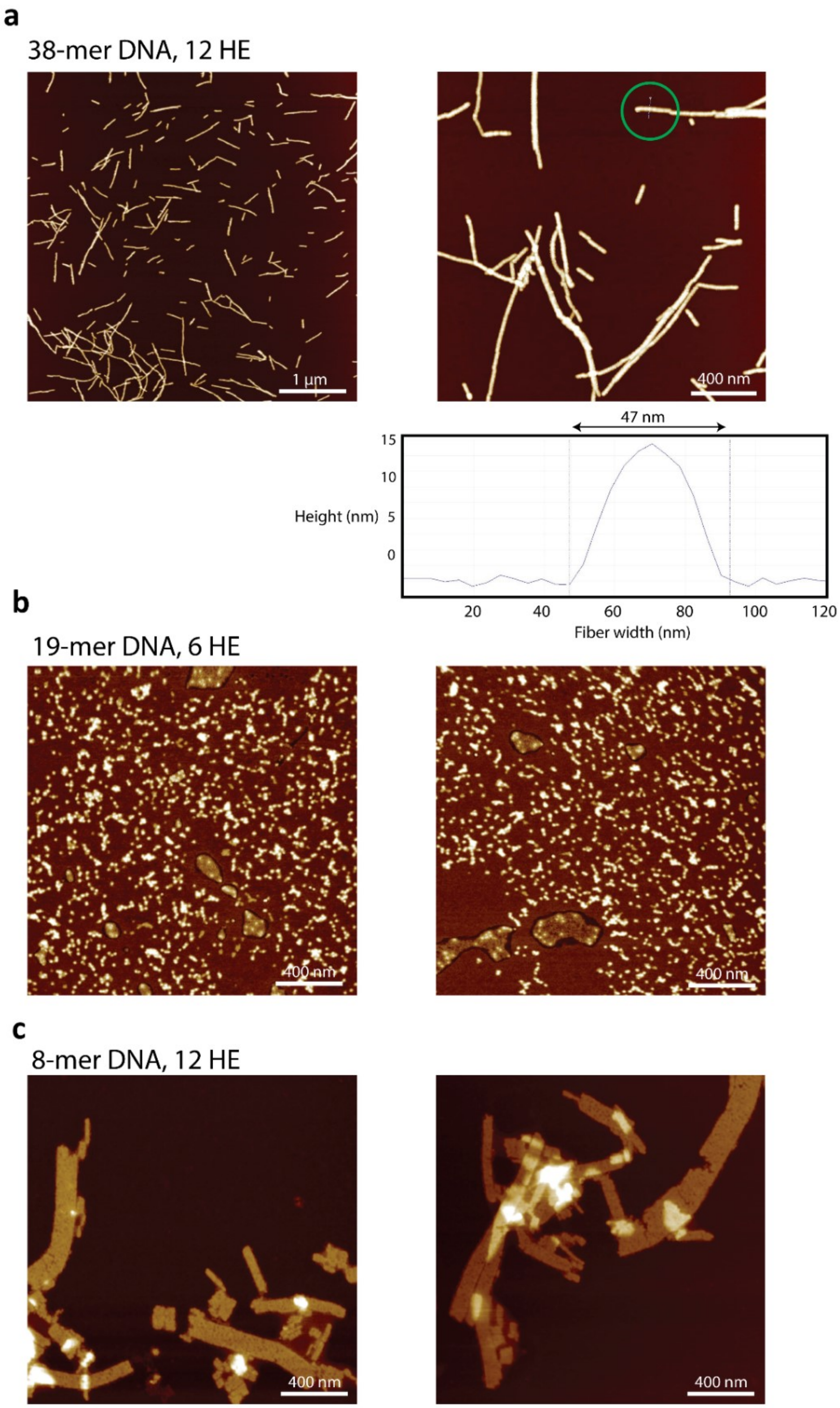

Figure 4.36 – Additional AFM images of the different self-assembly modes of Cy3Cy3-polymer-DNA conjugates with varying length of DNA and HE chains.

4.5.9 Shape-shifting of Cy3Cy3-DNA nanofibers

Photocleavable DNA nanofibers were generated from Cy3Cy3-PCL-HE$_{12}$-DNA monomers (PCL = photocleavable linker). In general, Cy3Cy3-PCL-HE$_{12}$-DNA strands (volume = 100 µL, concentration = 5 µM) were dispersed in TAMg buffer (final [Mg^{2+}] = 12.5 mM) under dark conditions and subjected to a heat/cool cycle (95 °C – 22 °C over 1.5 hours). The resulting products were then aged overnight in dark conditions to yield photocleavable DNA nanofibers. Following overnight aging, photocleavable DNA nanofibers were then photo-irradiated in a 365 nm oven at room temperature for 1 hour prior to AFM and AGE analysis according to previously mentioned protocols. Controls of Cy3Cy3-DNA nanofibers (made from Cy3Cy3-HE$_{12}$-DNA strands lacking a photocleavable linker) were assembled and analyzed in a similar fashion.

As a control experiment, Cy3Cy3-PCL-HE$_{12}$-DNA monomer strands dispersed in water were kept under dark conditions then subjected to irradiation at 365 nm for 1 hour. An aliquot of the resulting products was then analyzed by denaturing polyacrylamide gel electrophoresis (18% polyacrylamide/urea gel). The gel was run at 250 V for 30 minutes followed by 500 V for 60 minutes with 1x TBE as the running buffer. Products of photoirradiation were then suspended in TAMg buffer (final [Mg^{2+}] = 12.5 mM), followed by a heat/cool cycle ((95 °C – 22 °C over 1.5 hours) and incubation overnight at room temperature in dark conditions. Following incubation, the resulting structures were analyzed by AFM under dry conditions.

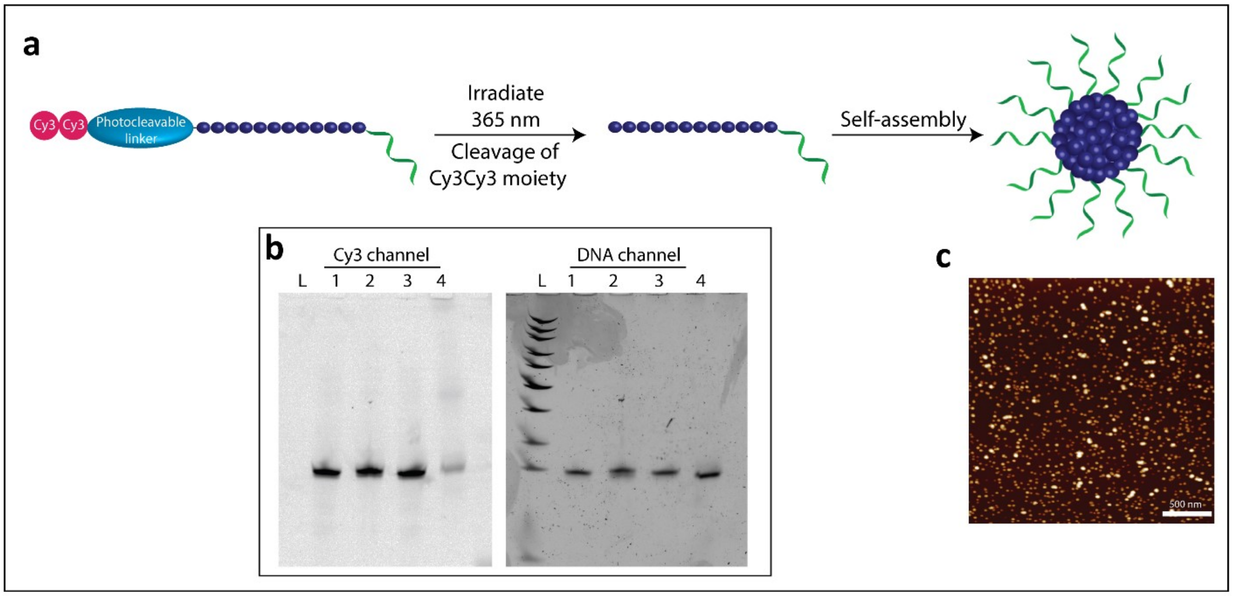

Figure 4.37 – Irradiation of Cy3Cy3-PCL-HE$_{12}$-DNA strands with 365 nm light followed by assembly. a) Schematic representation of the experimental procedure. Cy3Cy3-PCL-HE$_{12}$-DNA monomers in water were first irradiated with 365 nm light causing cleavage of the Cy3Cy3 units, followed by assembly to generate spherical DNA micelles as a result of loss of Cy3Cy3 units. b) Denaturing PAGE gel showing the cleavage process. Lanes 1&2: Cy3Cy3-HE$_{12}$-DNA control prior to and post irradiation, Lane 3-4: Cy3Cy3-PCL-HE$_{12}$-DNA strand prior to and post irradiation. Cy3 channel: Near total loss of the Cy3Cy3 unit is observed after irradiation of the Cy3Cy3-PCL-HE$_{12}$-DNA strands (Lane 4). The efficiency of cleavage was calculated ~ 95%, based on the band intensity of Lanes 3 and 4. This is also confirmed by the appearance of a slightly higher mobility band in the DNA channel (Lane 4). c) AFM image of the assembly products of Cy3Cy3-PCL-HE$_{12}$-DNA post irradiation. Spherical DNA particles were observed on surface.

4.5.10 Growth mechanism of DNA nanofibers

4.5.10.1 *Effect of monomer concentration on fiber length*

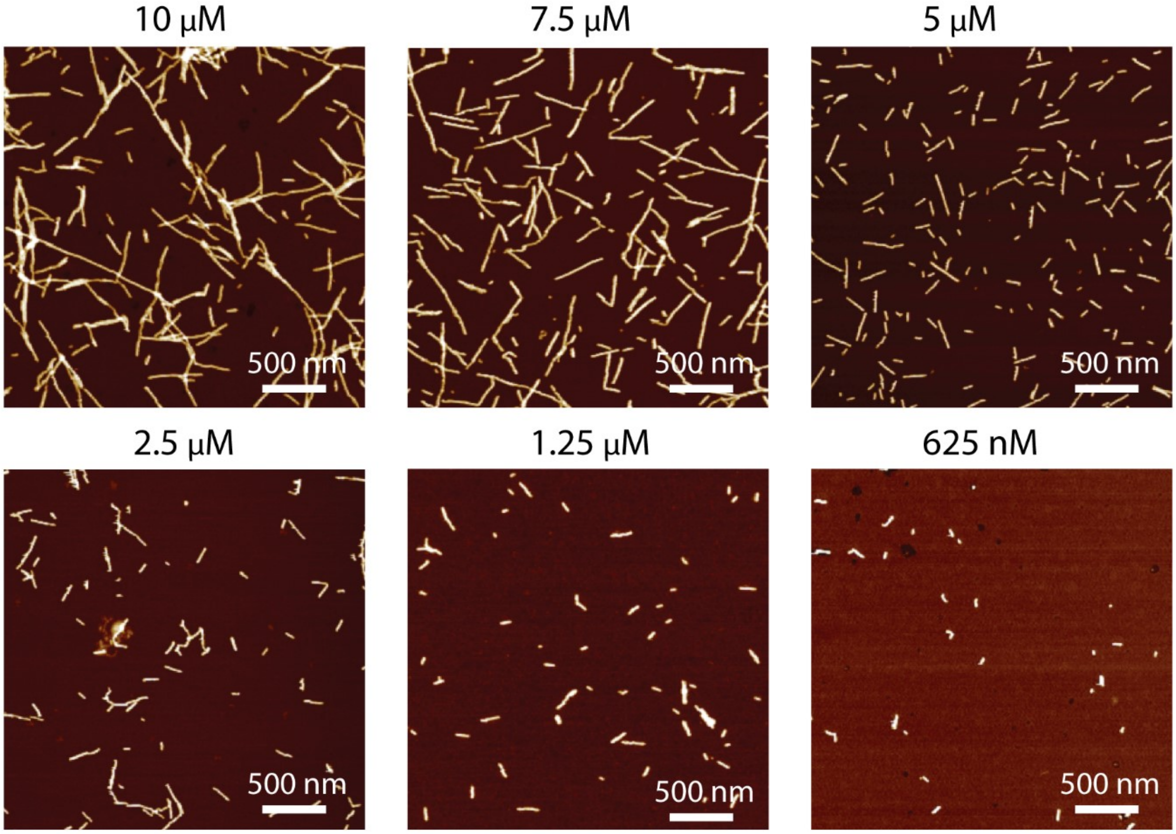

Figure 4.38 – Additional AFM analysis of DNA nanofiber length vs. monomer concentration.

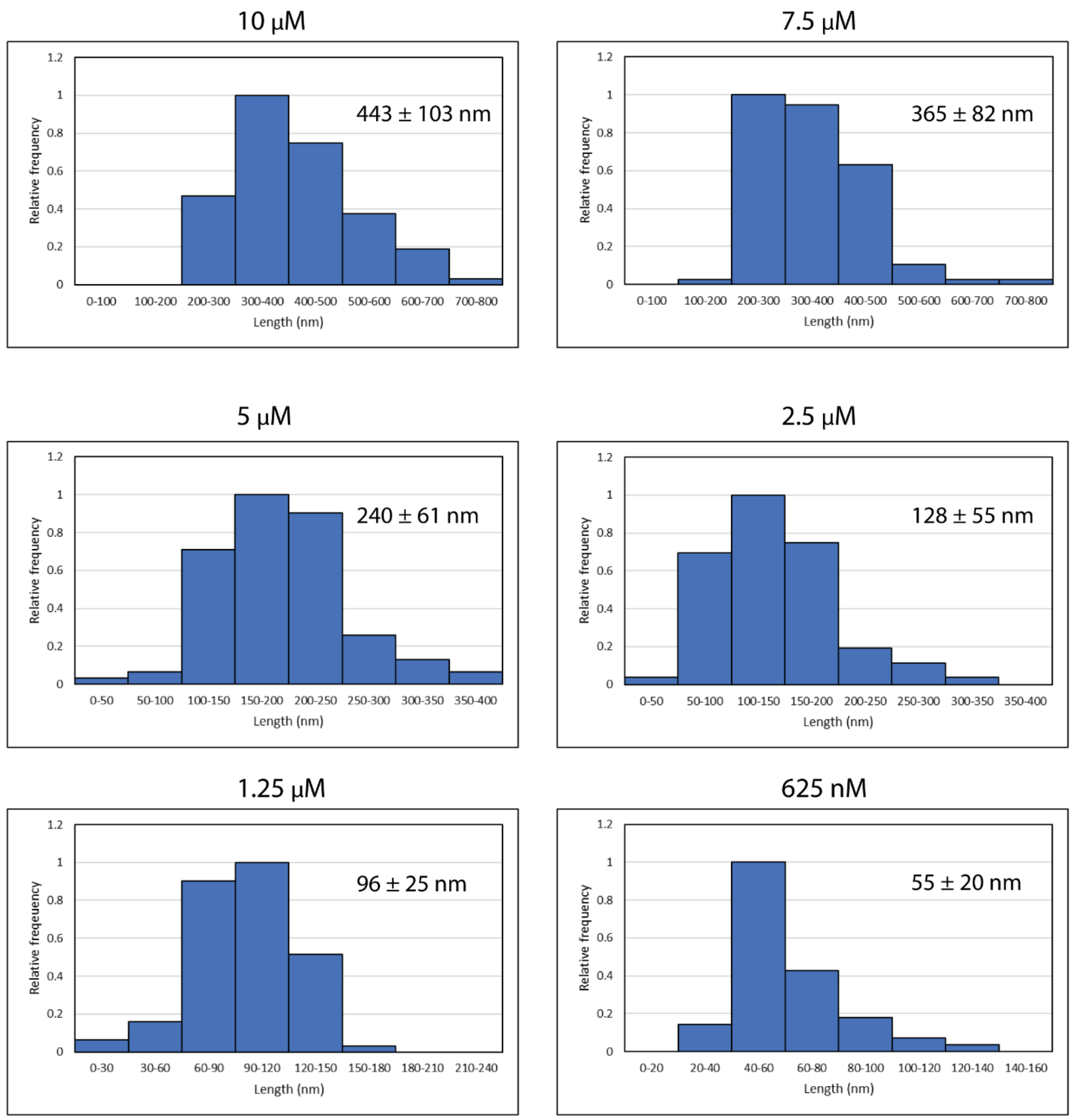

Figure 4.39 – Length histogram describing the structural distribution of Cy3Cy3-DNA fibers assembled at different monomer concentrations.

4.5.10.2 Seeded growth experiments

DNA fibers (2.5 µM with respect to total DNA) were assembled at 0.25x TAMg (final [Mg^{2+}] = 3.125 mM) under a heat/cool cycle (95 °C – 22 °C over 1.5 hours) and aged overnight at room temperature. The next day, different equivalents of the monomer stock in water (1x, 2.5x and 5x mass equivalents) were added to the preformed fiber seeds, followed by incremental injection of 10x TAMg buffer (containing 125 mM [Mg^{2+}]) and incubation at room temperature to increase the magnesium concentration in solution to 12.5 mM (4 injections total over 1 day, 6 hour wait between each buffer injection). The structures were then analyzed by AFM.

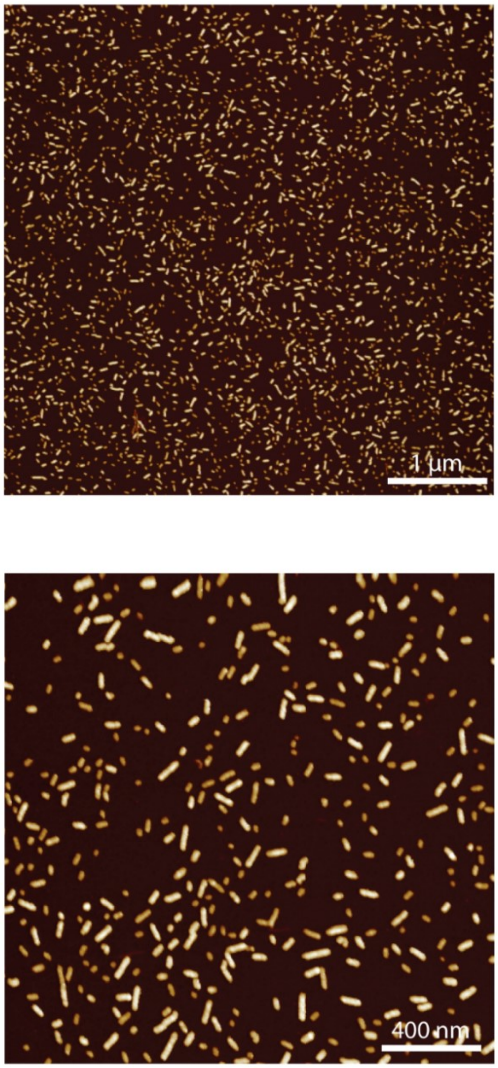

Figure 4.40 – Additional AFM images of Cy3Cy3-DNA fiber seeds generated at a concentration of 3.125 mM Mg^{2+}.

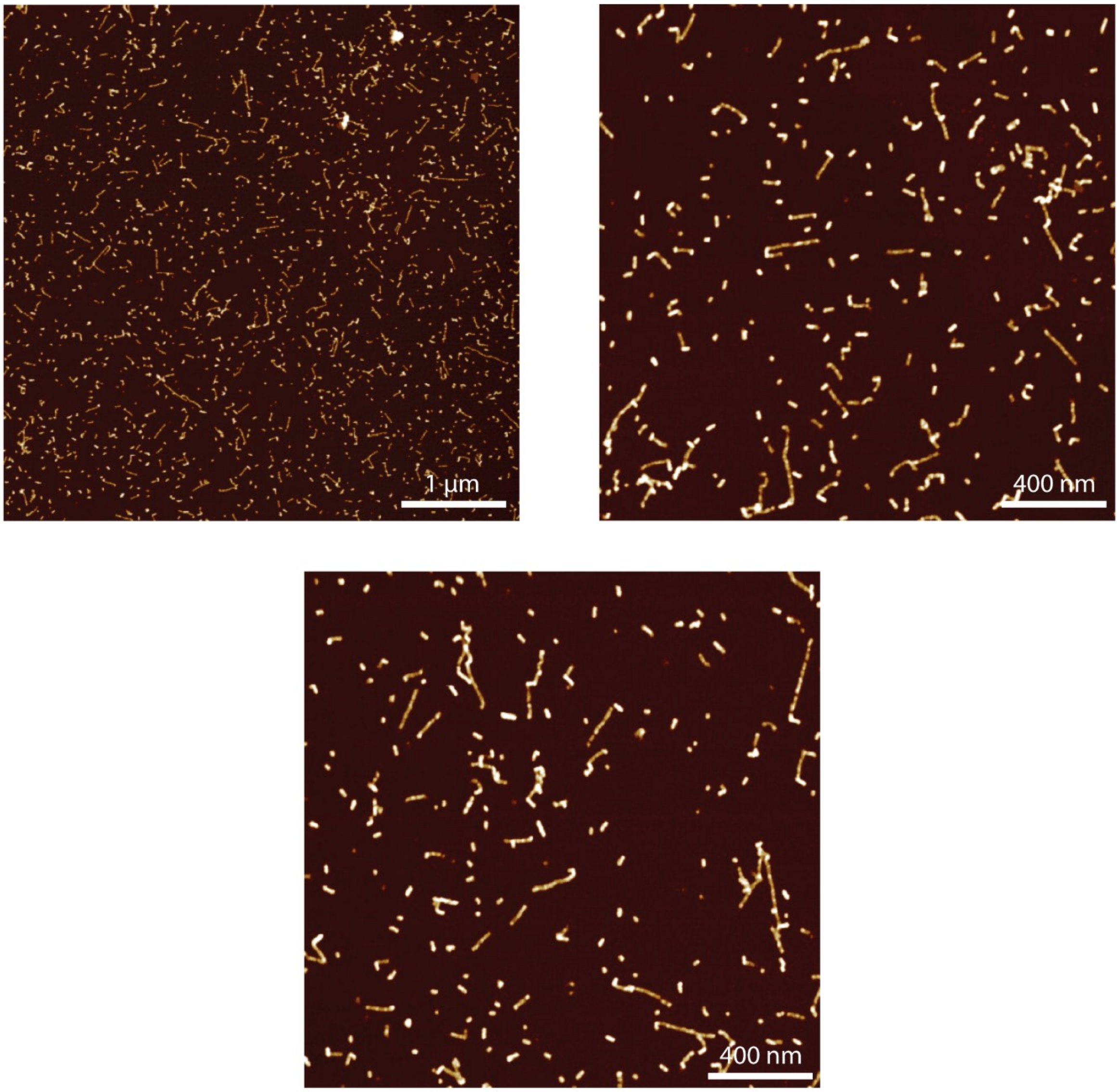

Figure 4.41 – Additional AFM images of Cy3Cy3-DNA fibers grown from the addition of 1x equivalent of monomer to fiber seeds.

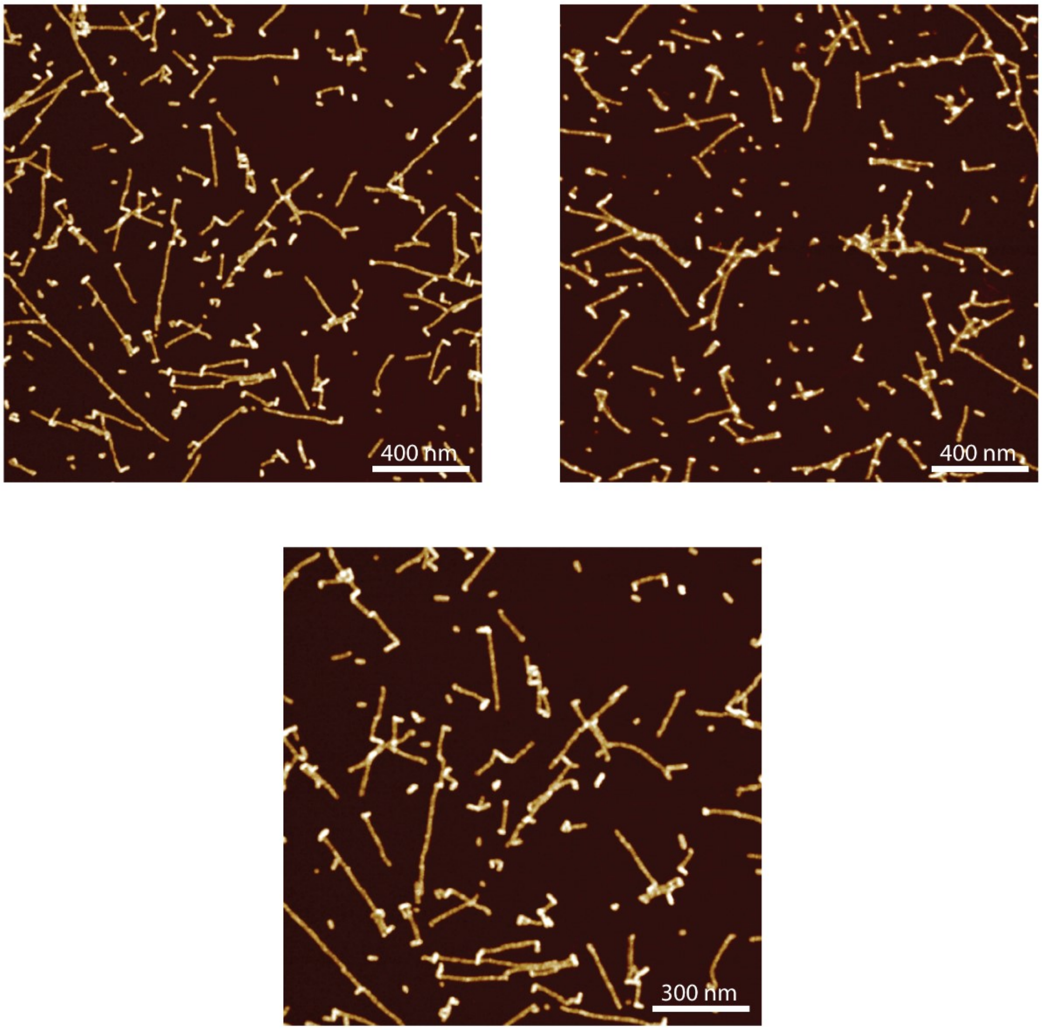

Figure 4.42 – Additional AFM images of Cy3Cy3-DNA fibers grown from the addition of 2.5x equivalents of monomer to fiber seeds.

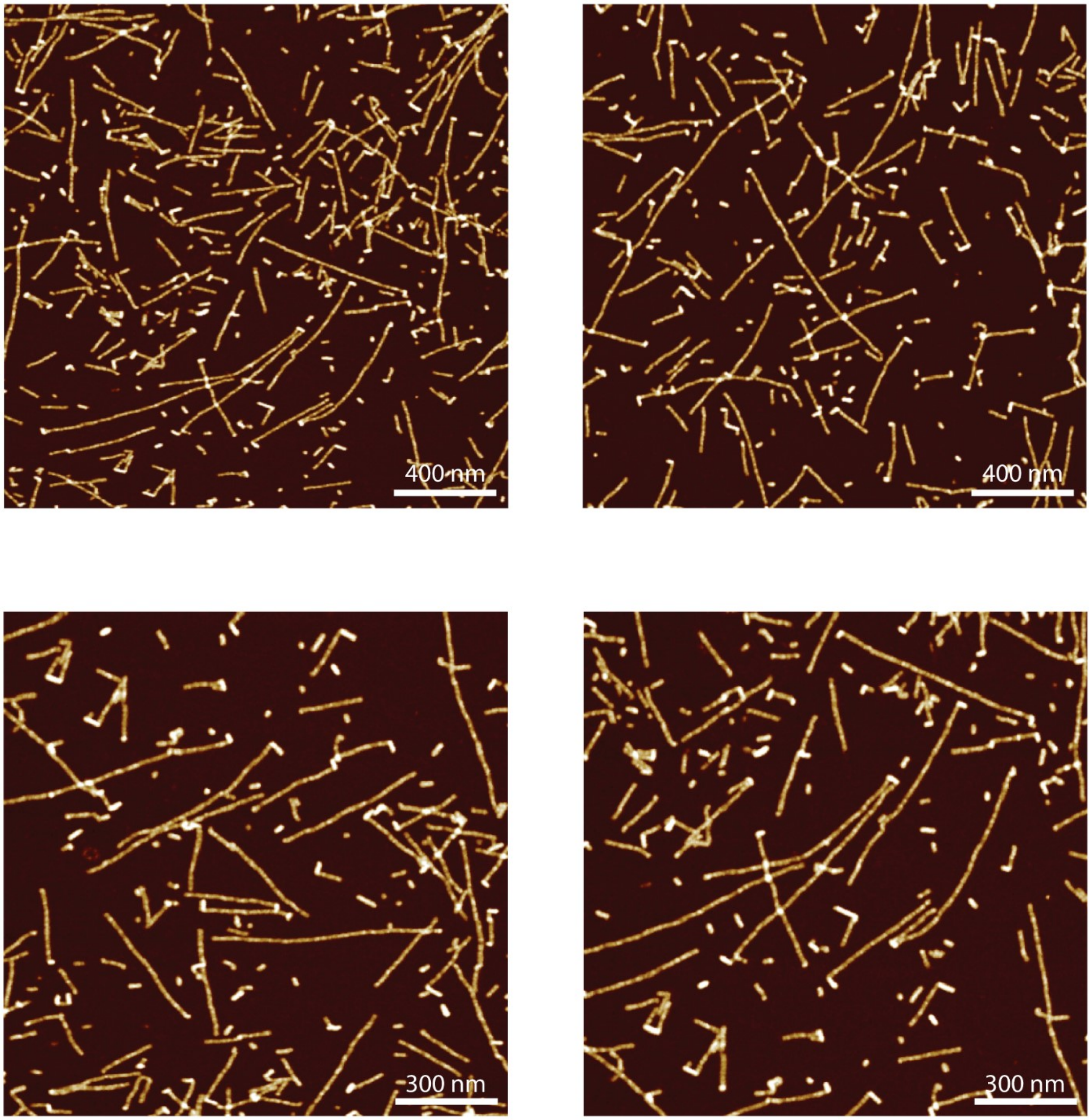

Figure 4.43 – Additional AFM images of Cy3Cy3-DNA fibers grown from the addition of 5x equivalents of monomer to fiber seeds.

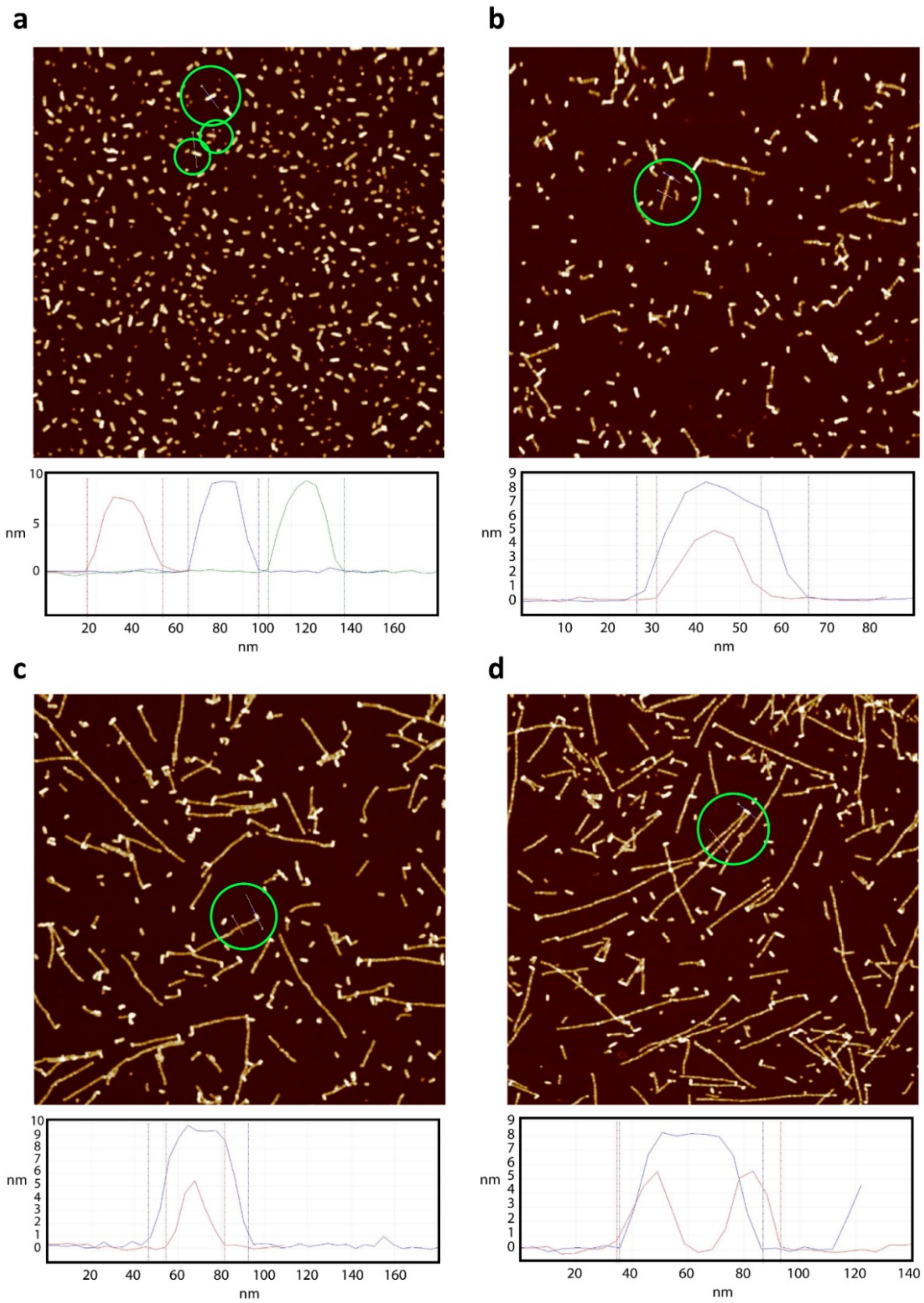

Figure 4.44 – AFM analysis showing the difference in height between fiber seeds and the growing chain. a) Fiber seeds, b) seeds + 1x monomer equivalent c) seeds + 2.5x monomer equivalent and d) seeds + 5x monomer equivalent. Green circles: Representative cross-sections of fiber seeds and growing polymer chains for height analysis. The average height of fiber seeds in all cases is ~ 9 nm, the average height of the growing chain is ~ 6 nm.

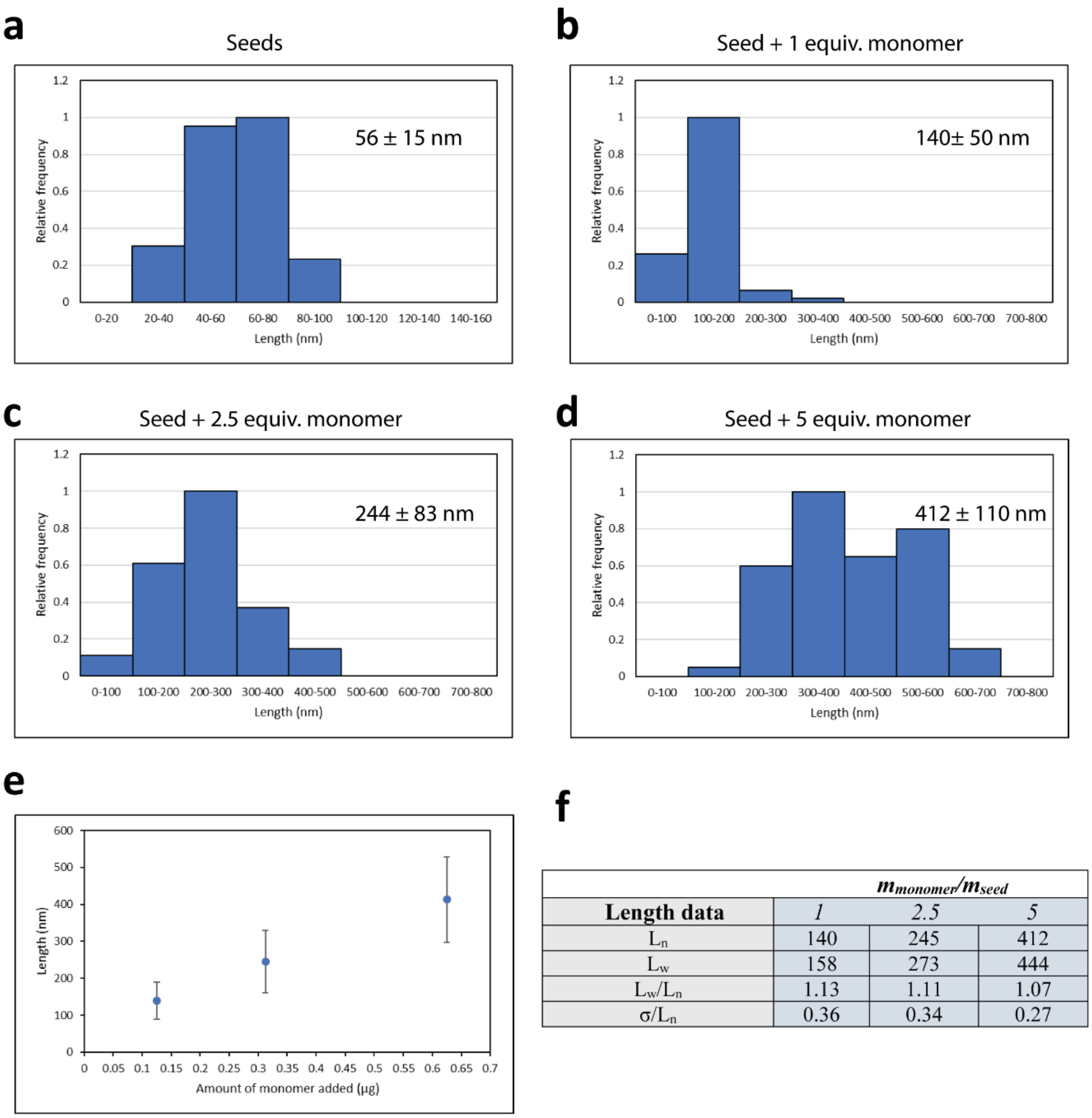

	$m_{monomer}/m_{seed}$		
Length data	*1*	*2.5*	*5*
L_n	140	245	412
L_w	158	273	444
L_w/L_n	1.13	1.11	1.07
σ/L_n	0.36	0.34	0.27

Figure 4.45 – Particle distribution analysis of seeded-growth experiments. Histograms showing particle analysis of a) fiber seeds b) seeds + 1 mass equivalent of monomer c) seeds + 2.5 equivalents of monomer and d) seeds + 5 equivalents of monomer. e) Graph showing the linear dependence of grown fiber length on the ratio of monomer added to preformed seeds. f) Table showing the length dispersity of grown fibers at different monomer:seed ratios.

4.5.11 Optical properties of DNA nanofibers

4.5.11.1 UV-vis spectroscopy

UV-vis measurements were conducted to characterize the optical properties of the Cy3 and Cy3Cy3-DNA fibers. For each measurement, DNA fibers (100 µL and 5 µM w.r.t. total DNA) were dropped on a 96-well plate reader and measured through a BioTek Synergy H4 Hybrid Multi-Mode Microplate Reader. Data from UV-vis spectroscopy was used to confirm fiber assembly by comparing spectra of DNA fibers with Cy3Cy3-HE_{12}-DNA monomers in water.

4.5.11.2 Fluorescence spectroscopy

Fluorescence scans were performed on a Cary Eclipse fluorescence spectrophotometer from Agilent technologies. For fluorescence measurements, DNA fibers (60 µL at 5 µM DNA concentration) were assembled in TAMg buffer, aged overnight and subsequently imaged. The structures were compared to monomer strands dispersed in water.

For denaturation studies, each of DNA nanofibers and DNA monomer strands (60 µL at 10 µM) were mixed with 5 µL of EDTA solution (125 mM EDTA, pH adjusted to 8.0 using Tris) to chelate Mg^{2+} ions in the buffer solution and 60 µL of 8 M Urea solution. The mixture was incubated for 1 hour at room temperature prior to fluorescence studies.

To study the kinetics of fiber formation, Cy3Cy3-HE_{12}-DNA monomers were mixed with TAMg assembly buffer (final [DNA] = 5 µM, V_{total} = 60 µL, final [Mg^{2+}] = 12.5 mM) and immediately analyzed by fluorescence spectroscopy. The sample was left in the dark at room temperature between different measurement time points. The graph was analyzed using a one-phase exponential decay model for calculation of assembly half-life.

For studies on the dynamics of fiber strand exchange, two populations of Cy3Cy3 and Cy5Cy5 fibers were assembled separately ([DNA] = 5 µM, V_{total} = 50 µL). Following 1 day of aging of fibers, preformed Cy3Cy3 and Cy5Cy5 fibers were mixed at room temperature in equal volumes, and immediately analyzed by fluorescence spectroscopy (excitation = 535 nm, emission scan 545-750 nm). Measurements were performed over several time points and incubated at room temperature in dark conditions in between time points.

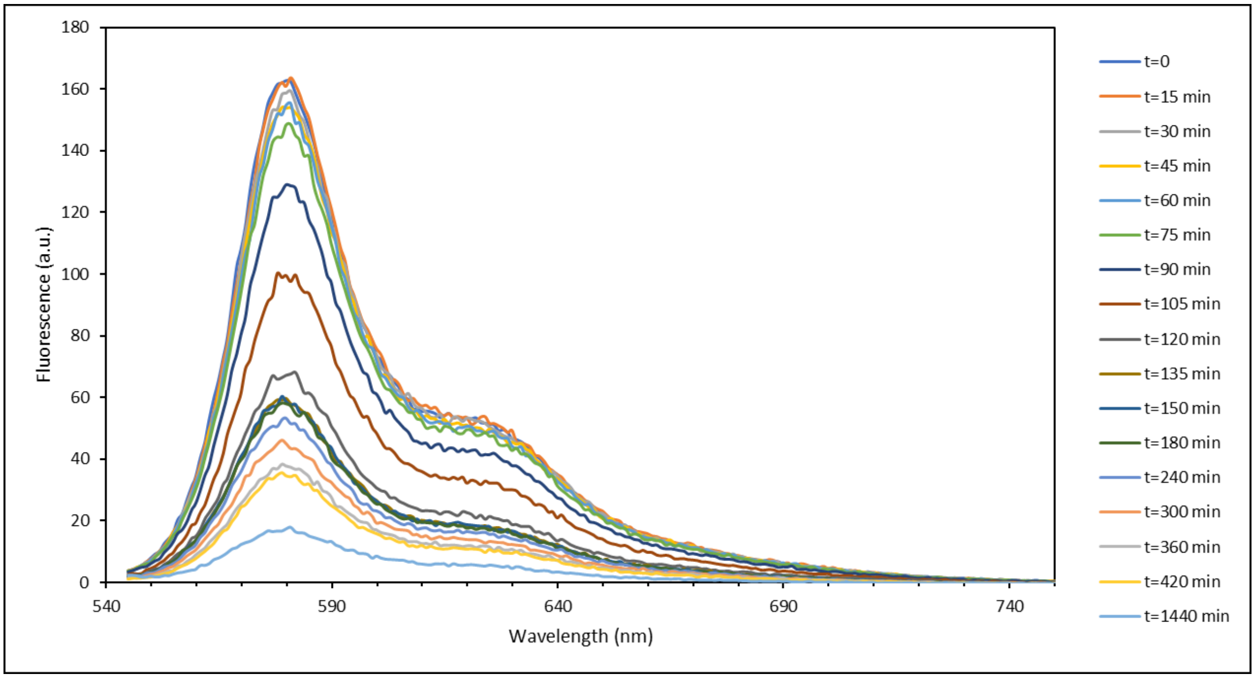

Figure 4.46 – Fluorescence spectra of Cy3Cy3 fiber formation over time. Fluorescence spectra were obtained following the addition of TAMg assembly buffer to Cy3Cy3-HE$_{12}$-DNA conjugates and measured over time intervals.

4.5.11.3 Characterization of Cy5Cy5-DNA fibers

Similar to Cy3 and Cy3Cy3-DNA fibers, at 100% Cy5Cy5-HE$_{12}$-DNA in the assembly mixture, a non-penetrating band on AGE was observed (Experimental Figure 4.47a). DLS revealed the presence of structures with larger hydrodynamic radius (R_H = 37.1) in solution as compared to spherical particles (R_H = 11 nm) (Experimental Figure 4.47b). DNA nanofibers were also imaged by AFM, however, appeared less rigid than Cy3Cy3-DNA fibers, observed as coiled structures on surface (Figure 4.47c).

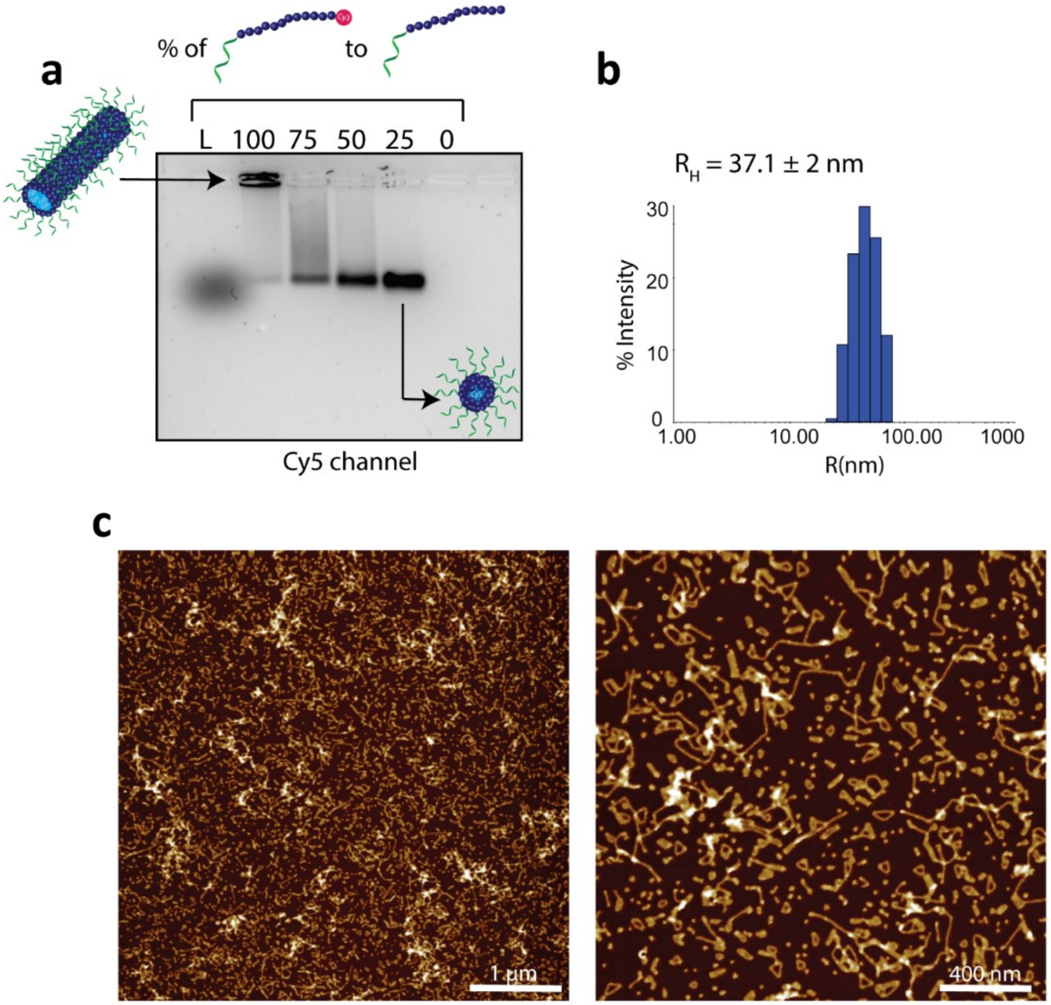

Figure 4.47 – Characterization of Cy5Cy5-DNA fibers. a) Agarose gel electrophoresis analysis describing the morphological shift of structures made from mixing varying ratios of Cy5Cy5-HE$_{12}$-DNA with unlabelled HE$_{12}$-DNA strands followed by thermal annealing. L: Ladder, lane 100: 100% Cy5Cy5-HE$_{12}$-DNA in the mixture, lane 75: 75% Cy5Cy5-HE$_{12}$-DNA/25% HE$_{12}$-DNA, lane 50: 50% Cy5Cy5-HE$_{12}$-DNA/50% HE$_{12}$-DNA, lane 25: 25% Cy5Cy5-HE$_{12}$-DNA/75% HE$_{12}$-DNA, lane 0: 100% HE$_{12}$-DNA. The gel was imaged under a Cy5-selective channel. b) DLS histogram of Cy5Cy5-DNA nanofibers. c) Atomic force microscopy images of DNA nanofibers on mica surface under dry conditions.

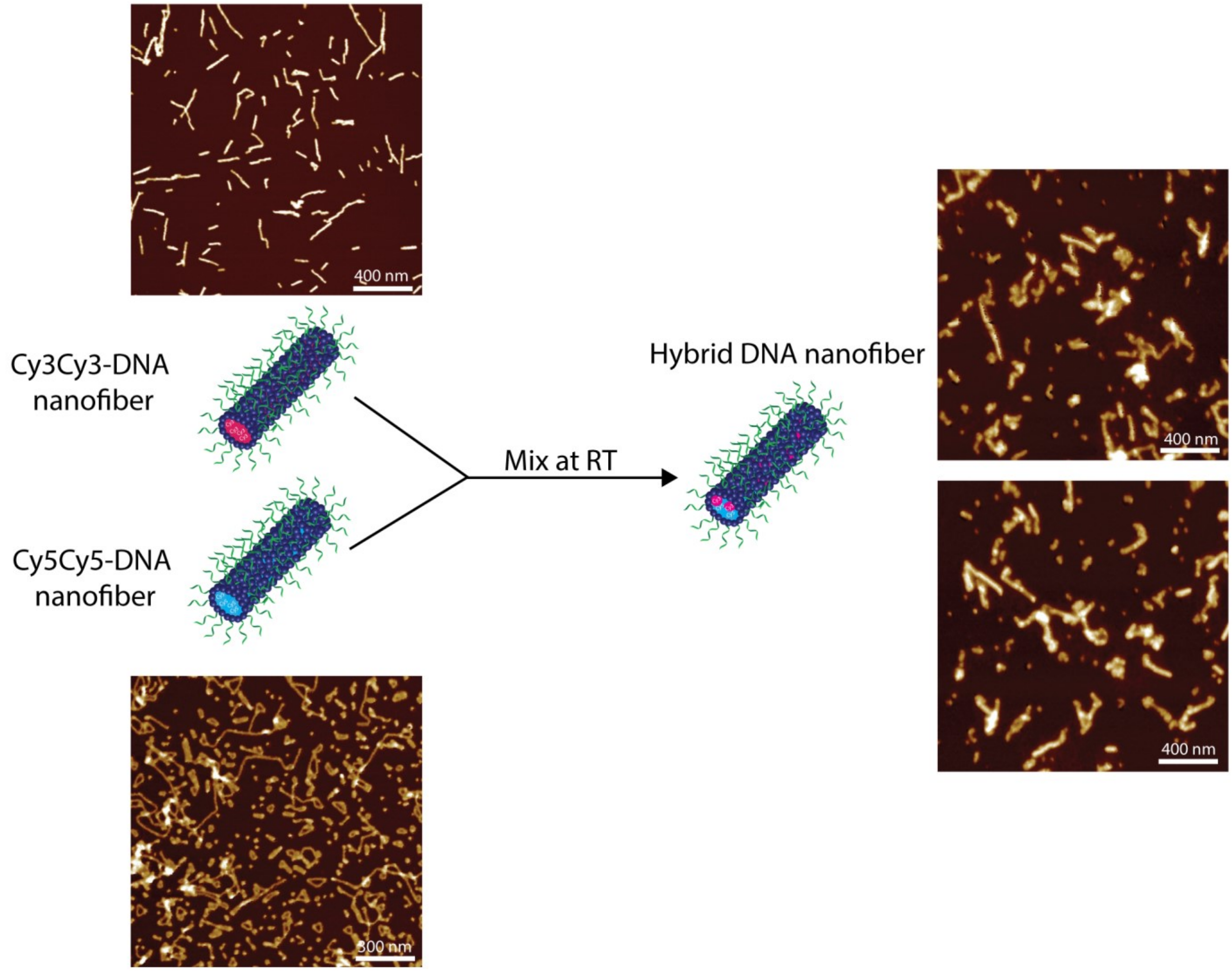

Figure 4.48 – AFM images of hybrid DNA nanofibers generated by mixing Cy3Cy3 and Cy5Cy5-DNA fibers.

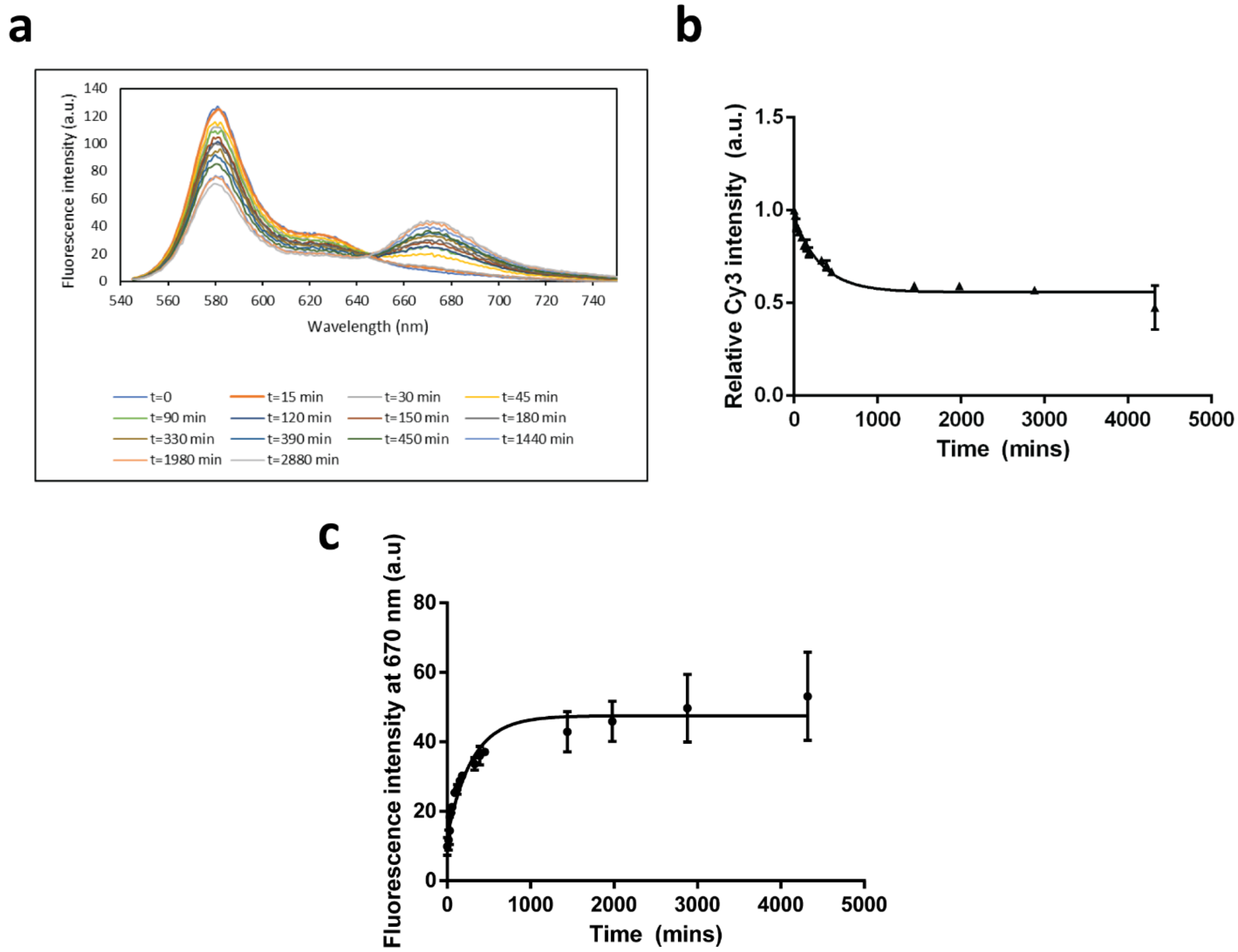

Figure 4.49 – Fluorescence data of Cy3Cy3 and Cy5Cy5 fibers after mixing. a) Fluorescence spectroscopy data measured over time intervals after mixing preformed Cy3Cy3 and Cy5Cy5 DNA nanofibers. b) Graph showing the decrease of Cy3 signal as a result of FRET from strand mixing over time. A decrease of ~ 50% of the Cy3 signal was observed after 48 hours. c) FRET signal increase over time as a results of fiber mixing. Error bars represent mean standard deviation.

4.5.12 Optical properties of Cy3-DNA nanofibers

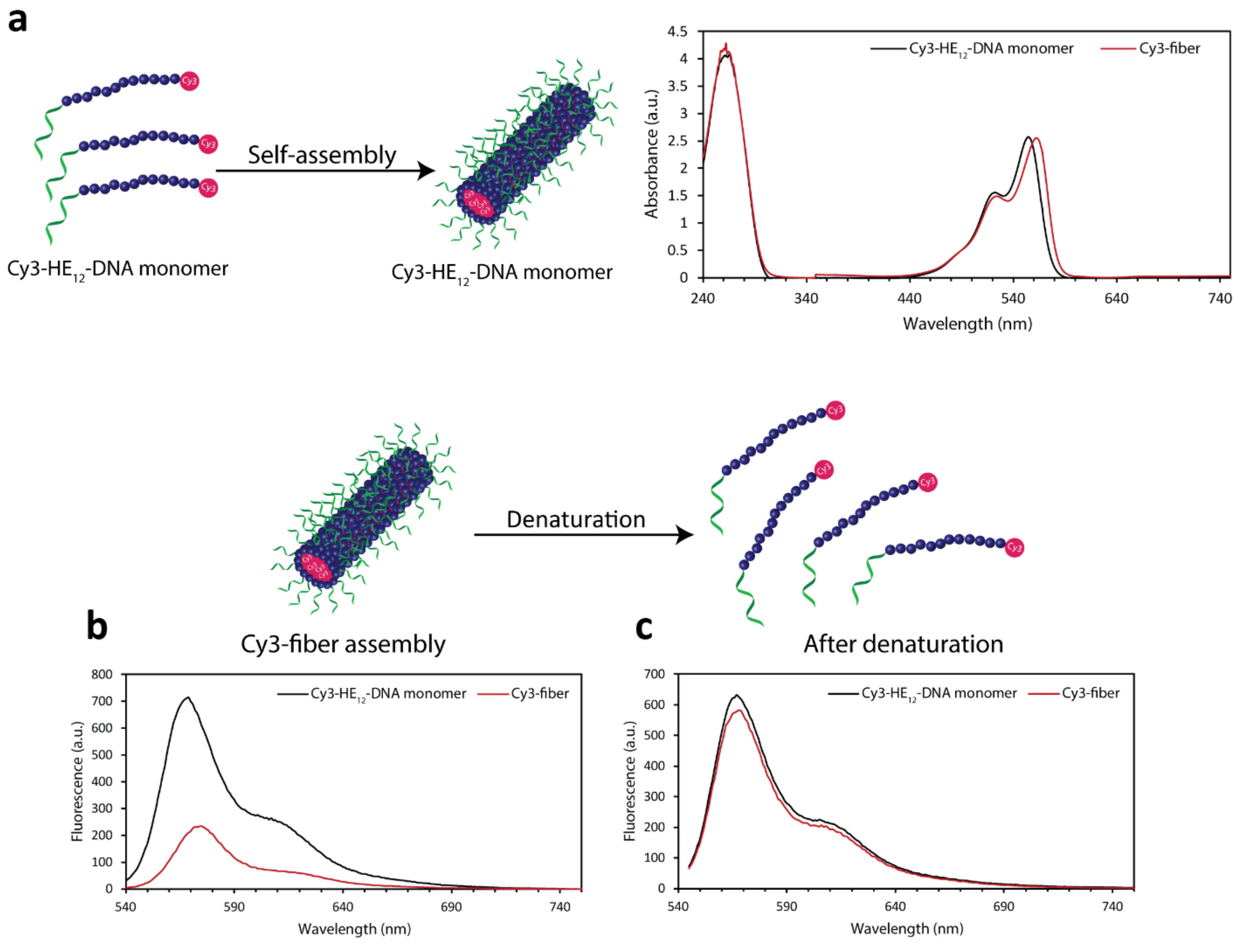

Figure 4.50 – Optical properties of Cy3-DNA fibers. a) Absorption spectra and b) Fluorescence spectra of Cy3-DNA fibers measured at room temperature. c) Fluoresce spectra of Cy3-fibers after denaturation to the monomer units. Cy3-DNA fibers showed a red-shift of the maximum absorption from 553 nm to 562 nm, and a decrease in fluorescence intensity by 70% upon fiber formation.

4.5.13 Gold nanoparticle (AuNP) templation on Cy3Cy3-DNA fibers

All AuNPs used in this manuscript were prepared via standard Turkevich-Frens synthesis, with subsequent passivation by bis(p-sulfonatophenyl)phenylphosphine (BSPP) as described in previous work.[100] AuNPs with poly-conjugated scrambled DNA sequences and sequences complementary to Cy3Cy3-fiber DNA, were synthesized according to a previously reported protocol.[101] For AuNP templation experiments, DNA-functionalized 10 nm AuNP stocks were prepared at 0.2 µM or 1.06 µM. For low ratio of AuNP:DNA fiber conditions, DNA fibers (total DNA concentration = 5 µM) were mixed with 0.2 µM DNA-functionalized AuNP at an 8:2 v/v ratio and incubated at room temperature overnight. To achieve higher AuNP ratios/fiber, DNA fibers (total DNA concentration = 2.5 µM) were mixed with 0.2 µM DNA-functionalized AuNPs at an 8:2 v/v ratio and incubated at room temperature overnight. Alternatively, when DNA fibers (total DNA concentration = 10 µM) were mixed with 1.06 µM DNA-functionalized AuNP at an 8:2 v/v ratio and incubated at room temperature overnight, networks of AuNP-mediated fibers were observed.

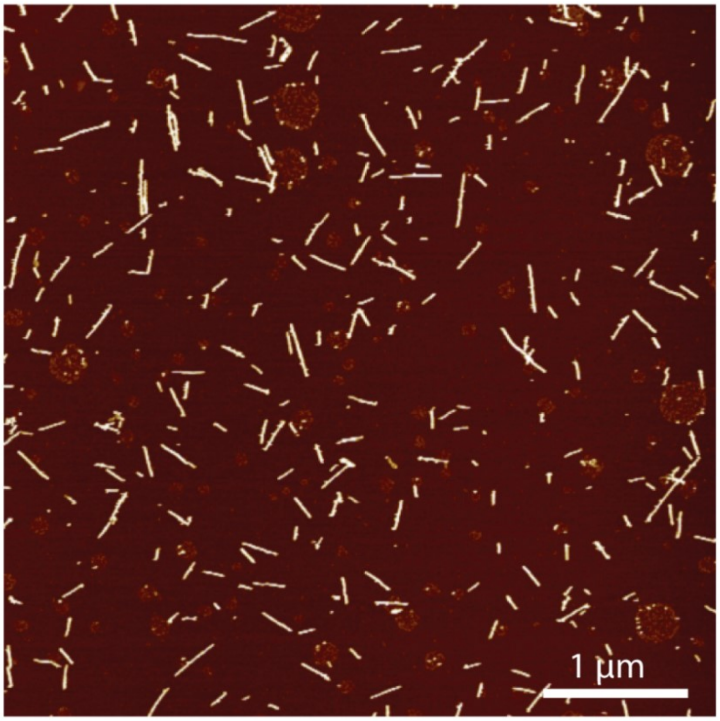

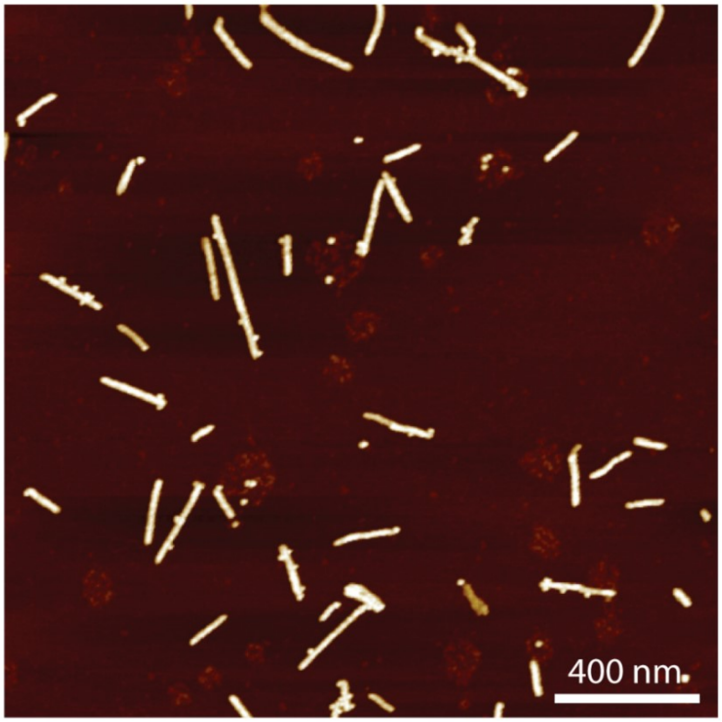

Figure 4.51 – Additional AFM images of AuNP templation on Cy3Cy3-DNA fibers at low AuNP ratio. In this case, 2-6 AuNPs were templated/fiber of length ~ 200 nm.

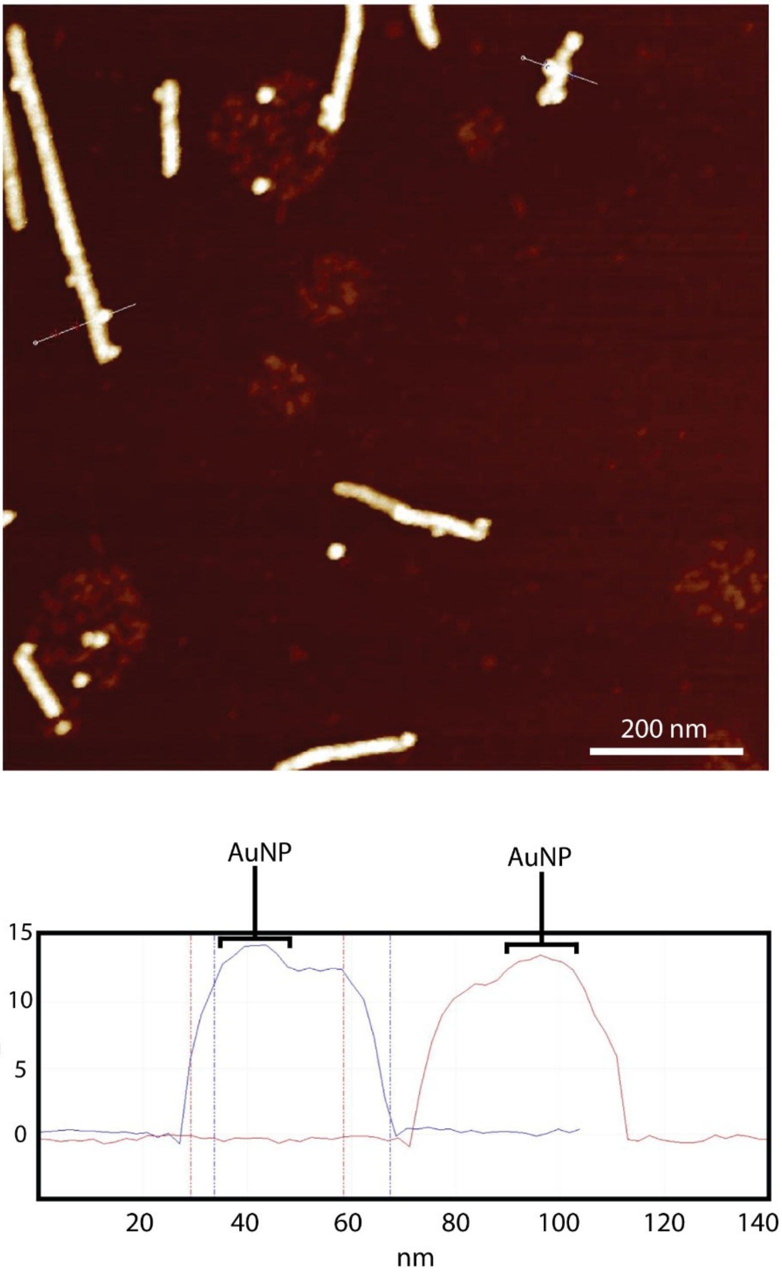

Figure 4.52 – Representative AFM image with height analysis of AuNP templation on Cy3Cy3-DNA fibers. Templated AuNPs displayed an increase in height on fiber surface with measured heights of ~ 15 nm, compared to ~ 10 nm for Cy3Cy3-DNA fibers.

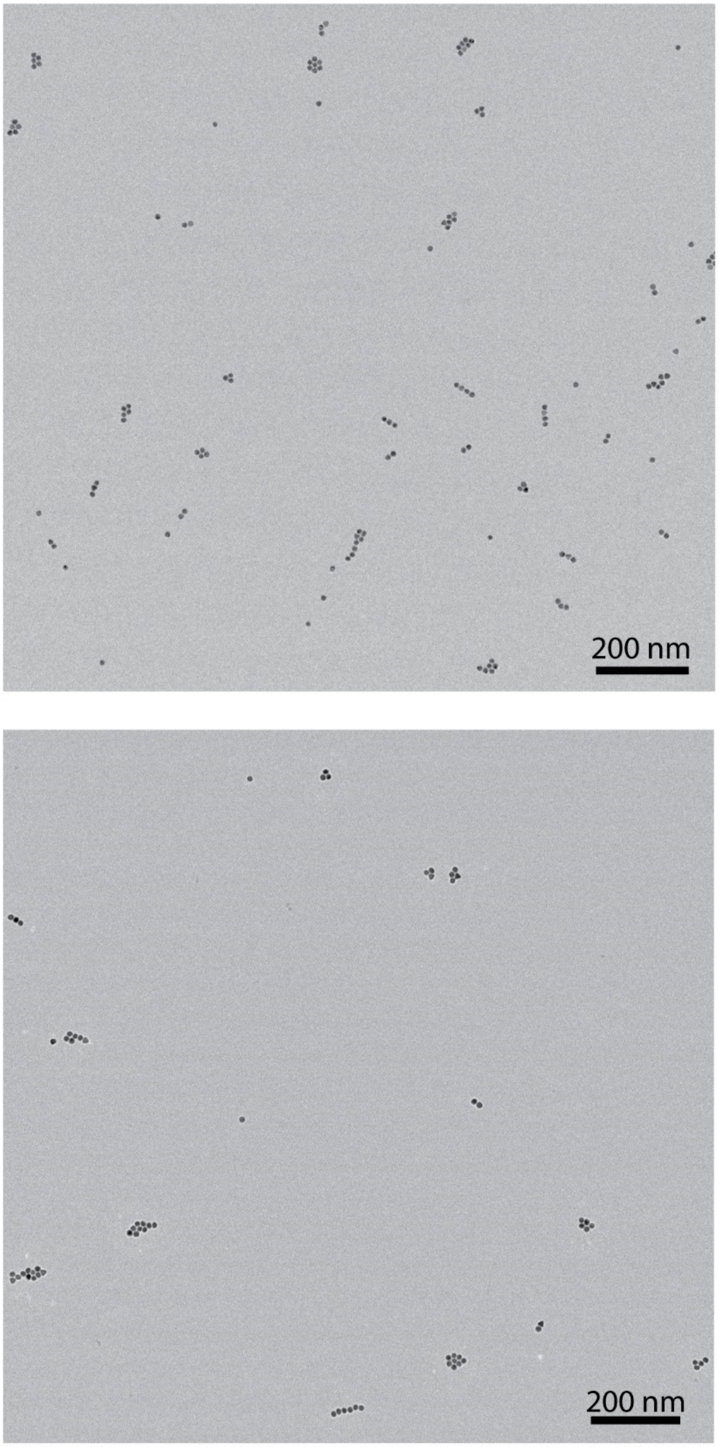

Figure 4.53 – Additional TEM images of AuNP templation on Cy3Cy3-DNA fibers at low AuNP:fiber ratio.

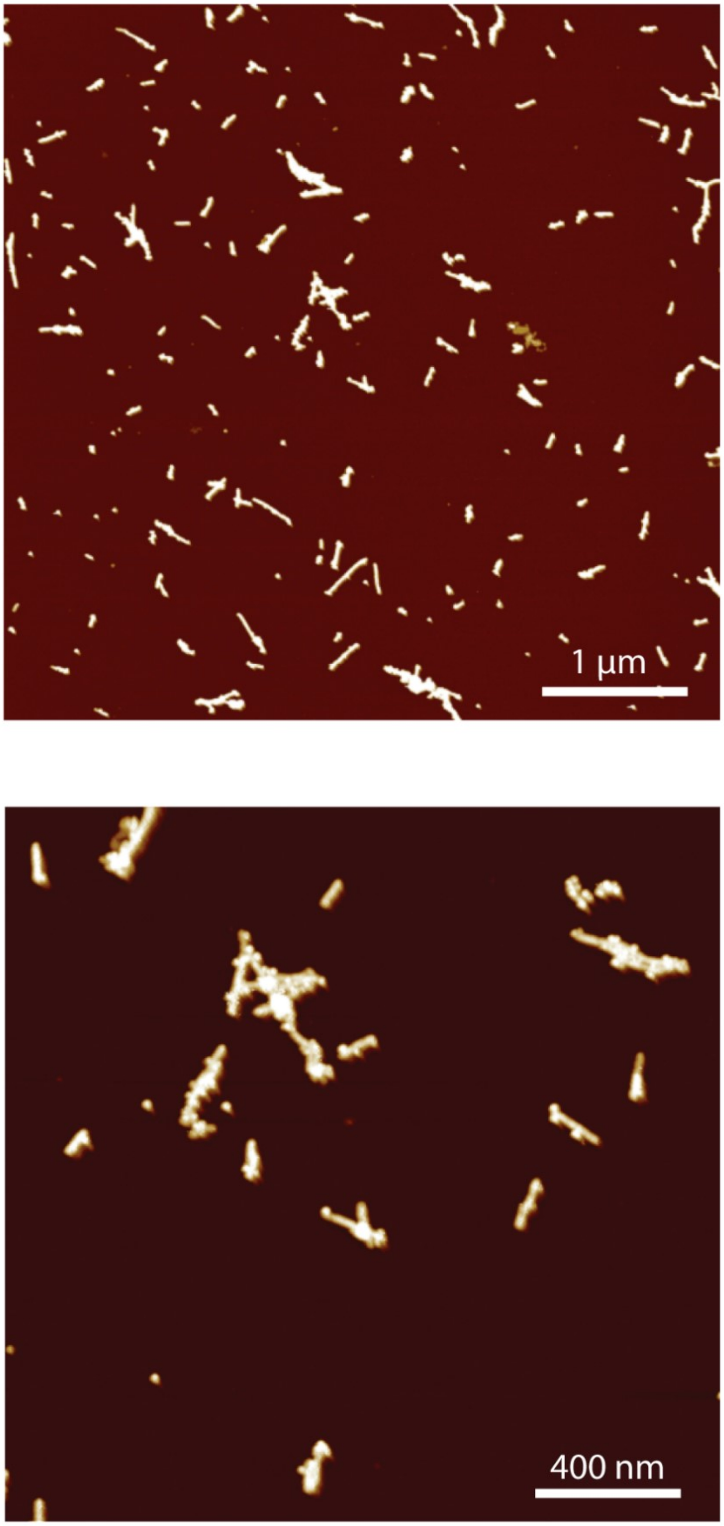

Figure 4.54 – Additional AFM images of AuNP templation on Cy3Cy3-DNA fibers at higher AuNP ratio. By increasing the ratio of AuNP to fiber, the number of templated AuNPs/fiber was further increased.

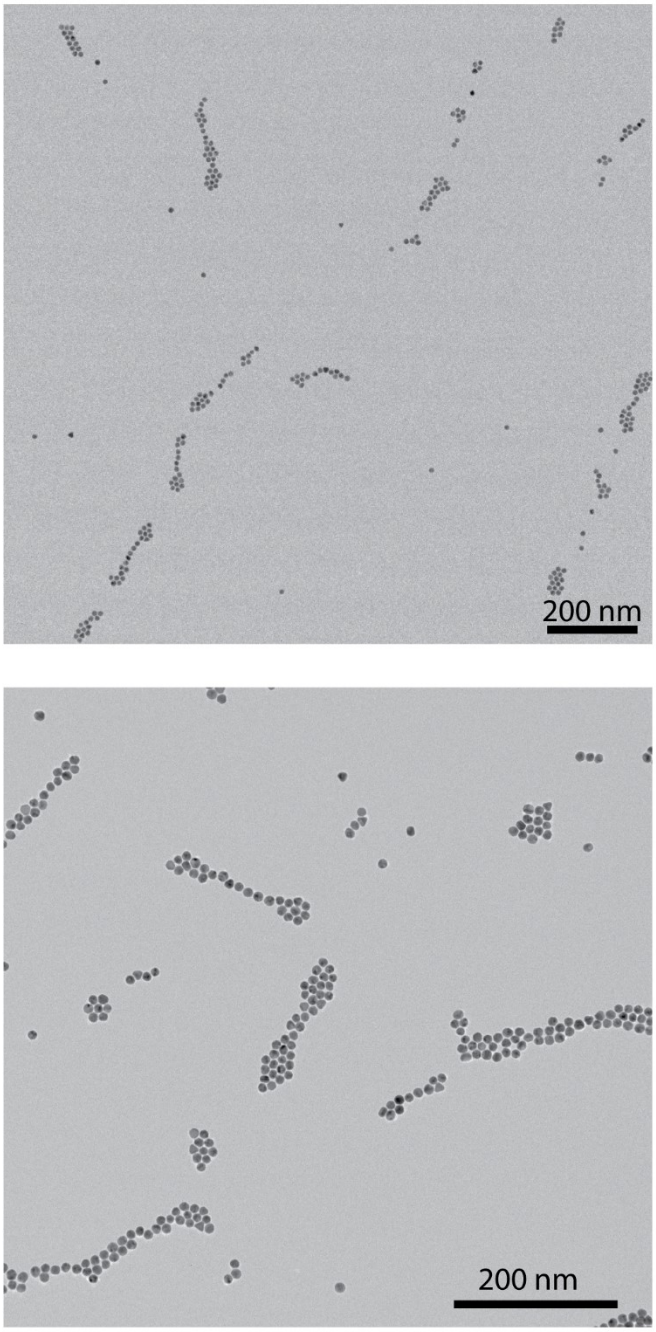

Figure 4.55 – Additional TEM images of AuNP templation on Cy3Cy3-DNA fibers at high AuNP:fiber ratio.

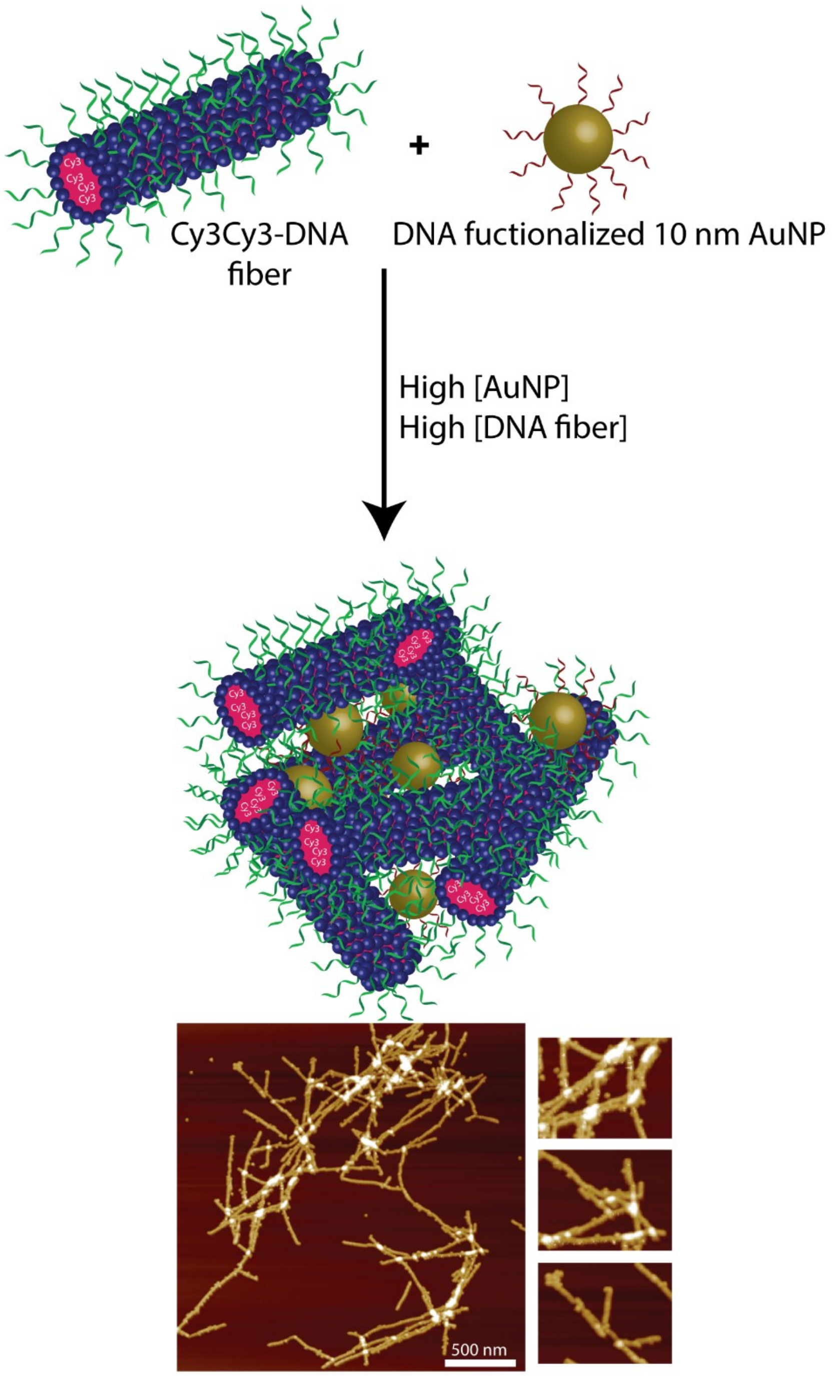

Figure 4.56 – AuNP templation on Cy3Cy3-DNA fibers at high concentrations of both AuNP and DNA fiber. By increasing the concentration of both AuNP and DNA fibers, gold nanoparticle-mediated networks of Cy3Cy3-DNA fibers were observed.

4.5.14 Templation of Cy3Cy3-DNA fibers on DNA origami tiles

4.5.14.1 Strand component of DNA tile

Single-stranded M13mp18 scaffold (100 nM) was purchased from Guild BioSciences. Staple strands with Bio-RP purification were obtained and used without further purification from Bioneer, Inc. Staple strands 1-216 were used in the assembly of all rectangle designs. The modifications of staple strands required for DNA rectangles with polymer-DNA binding sites are listed in Table 1. The modified strands were used in place of unmodified strands of the same number for the assembly of functionalized rectangles.

Table 4.3 – Staple strands for DNA tiles

Tile	Staple strand modifications
T2	A’101, A’110
	S102, S111
T2,2	A’101, A’110, A’206, A215
	S102, S111, S207, S216
T5,5	A’102, A’104, A’106, A’108, A’110, A’206, A’208, A’210, A’212, A’214
	S103, S105, S107, S109, S111, S207, S209, S211, S213, S215

4.5.14.2 Tile assembly and purification

The assembly of DNA tiles was based on the method reported by Rothemund.[39] The tiles were assembled in one-pot annealing at 3.5 nM of M13mp18 scaffold and 52.5 nM of individual staple strands in 1xTAMg buffer. The mixtures were then heated to and held at 95 ºC for 5 minutes and slowly annealed to 20 ºC with a gradient of 1 ºC per minute. To remove excess staple strands, the samples were purified with 100 kDa Amicon centrifugal filters (Millipore). First, 500 µL samples were centrifuged at 6000 rpm at 4 °C for 5 mins. Then, 400 µL 1xTAMg was added and the samples were centrifuged at 5000 rpm at 4 °C for 5 mins. This filtration step was repeated two more times. Approximately 50-100 µL samples were recovered, which can be stored at 4 °C up to a week before use. To determine the accurate concentration of purified DNA tiles, the absorbance at 260 nm was measured. The extinction coefficient of different tile designs can be approximated by equation (1), adapted from the report by Hung *et al.*[102]

$$\varepsilon = 6700\mathrm{ds} + 10000\mathrm{ss} \qquad (1)$$

where ds is the number of double-stranded bases and ss is the number of single-stranded bases. The rectangle concentrations were then calculated by Beer-Lambert's law ($A_{260\ \mathrm{nm}} = \varepsilon bc$, b=1cm).

Unmodified staple strands

1 CAAGCCCAATAGGAACCCATGTACAAACAGTT
2 AATGCCCCGTAACAGTGCCCGTATCTCCCTCA
3 TGCCTTGACTGCCTATTTCGGAACAGGGATAG
4 GAGCCGCCCCACCACCGGAACCGCGACGGAAA
5 AACCAGAGACCCTCAGAACCGCCAGGGGTCAG
6 TTATTCATAGGGAAGGTAAATATTCATTCAGT
7 CATAACCCGAGGCATAGTAAGAGCTTTTTAAG
8 ATTGAGGGTAAAGGTGAATTATCAATCACCGG
9 AAAAGTAATATCTTACCGAAGCCCTTCCAGAG
10 GCAATAGCGCAGATAGCCGAACAATTCAACCG
11 CCTAATTTACGCTAACGAGCGTCTAATCAATA
12 TCTTACCAGCCAGTTACAAAATAAATGAAATA
13 ATCGGCTGCGAGCATGTAGAAACCTATCATAT
14 CTAATTTATCTTTCCTTATCATTCATCCTGAA
15 GCGTTATAGAAAAAGCCTGTTTAGAAGGCCGG
16 GCTCATTTTCGCATTAAATTTTTGAGCTTAGA
17 AATTACTACAAATTCTTACCAGTAATCCCATC
18 TTAAGACGTTGAAAACATAGCGATAACAGTAC
19 TAGAATCCCTGAGAAGAGTCAATAGGAATCAT
20 CTTTTACACAGATGAATATACAGTAAACAATT
21 TTTAACGTTCGGGAGAAACAATAATTTTCCCT
22 CGACAACTAAGTATTAGACTTTACAATACCGA
23 GGATTTAGCGTATTAAATCCTTTGTTTTCAGG
24 ACGAACCAAAACATCGCCATTAAATGGTGGTT
25 GAACGTGGCGAGAAAGGAAGGGAACAAACTAT
26 TAGCCCTACCAGCAGAAGATAAAAACATTTGA
27 CGGCCTTGCTGGTAATATCCAGAACGAACTGA
28 CTCAGAGCCACCACCCTCATTTTCCTATTATT
29 CTGAAACAGGTAATAAGTTTTAACCCCTCAGA
30 AGTGTACTTGAAAGTATTAAGAGGCCGCCACC
31 GCCACCACTCTTTTCATAATCAAACCGTCACC
32 GTTTGCCACCTCAGAGCCGCCACCGATACAGG
33 GACTTGAGAGACAAAAGGGCGACAAGTTACCA
34 AGCGCCAACCATTTGGGAATTAGATTATTAGC

35	GAAGGAAAATAAGAGCAAGAAACAACAGCCAT
36	GCCCAATACCGAGGAAACGCAATAGGTTTACC
37	ATTATTTAACCCAGCTACAATTTTCAAGAACG
38	TATTTTGCTCCCAATCCAAATAAGTGAGTTAA
39	GGTATTAAGAACAAGAAAAATAATTAAAGCCA
40	TAAGTCCTACCAAGTACCGCACTCTTAGTTGC
41	ACGCTCAAAATAAGAATAAACACCGTGAATTT
42	AGGCGTTACAGTAGGGCTTAATTGACAATAGA
43	ATCAAAATCGTCGCTATTAATTAACGGATTCG
44	CTGTAAATCATAGGTCTGAGAGACGATAAATA
45	CCTGATTGAAAGAAATTGCGTAGACCCGAACG
46	ACAGAAATCTTTGAATACCAAGTTCCTTGCTT
47	TTATTAATGCCGTCAATAGATAATCAGAGGTG
48	AGATTAGATTTAAAAGTTTGAGTACACGTAAA
49	AGGCGGTCATTAGTCTTTAATGCGCAATATTA
50	GAATGGCTAGTATTAACACCGCCTCAACTAAT
51	CCGCCAGCCATTGCAACAGGAAAAATATTTTT
52	CCCTCAGAACCGCCACCCTCAGAACTGAGACT
53	CCTCAAGAATACATGGCTTTTGATAGAACCAC
54	TAAGCGTCGAAGGATTAGGATTAGTACCGCCA
55	CACCAGAGTTCGGTCATAGCCCCCGCCAGCAA
56	TCGGCATTCCGCCGCCAGCATTGACGTTCCAG
57	AATCACCAAATAGAAAATTCATATATAACGGA
58	TCACAATCGTAGCACCATTACCATCGTTTTCA
59	ATACCCAAGATAACCCACAAGAATAAACGATT
60	ATCAGAGAAAGAACTGGCATGATTTTATTTTG
61	TTTTGTTTAAGCCTTAAATCAAGAATCGAGAA
62	AGGTTTTGAACGTCAAAAATGAAAGCGCTAAT
63	CAAGCAAGACGCGCCTGTTTATCAAGAATCGC
64	AATGCAGACCGTTTTTATTTTCATCTTGCGGG
65	CATATTTAGAAATACCGACCGTGTTACCTTTT
66	AATGGTTTACAACGCCAACATGTAGTTCAGCT
67	TAACCTCCATATGTGAGTGAATAAACAAAATC
68	AAATCAATGGCTTAGGTTGGGTTACTAAATTT
69	GCGCAGAGATATCAAAATTATTTGACATTATC
70	AACCTACCGCGAATTATTCATTTCCAGTACAT
71	ATTTTGCGTCTTTAGGAGCACTAAGCAACAGT
72	CTAAAATAGAACAAAGAAACCACCAGGGTTAG
73	GCCACGCTATACGTGGCACAGACAACGCTCAT
74	GCGTAAGAGAGAGCCAGCAGCAAAAAGGTTAT
75	GGAAATACCTACATTTTGACGCTCACCTGAAA
76	TATCACCGTACTCAGGAGGTTTAGCGGGGTTT
77	TGCTCAGTCAGTCTCTGAATTTACCAGGAGGT
78	GGAAAGCGACCAGGCGGATAAGTGAATAGGTG
79	TGAGGCAGGCGTCAGACTGTAGCGTAGCAAGG
80	TGCCTTTAGTCAGACGATTGGCCTGCCAGAAT
81	CCGGAAACACACCACGGAATAAGTAAGACTCC
82	ACGCAAAGGTCACCAATGAAACCAATCAAGTT
83	TTATTACGGTCAGAGGGTAATTGAATAGCAGC

84	TGAACAAACAGTATGTTAGCAAACTAAAAGAA
85	CTTTACAGTTAGCGAACCTCCCGACGTAGGAA
86	GAGGCGTTAGAGAATAACATAAAAGAACACCC
87	TCATTACCCGACAATAAACAACATATTTAGGC
88	CCAGACGAGCGCCCAATAGCAAGCAAGAACGC
89	AGAGGCATAATTTCATCTTCTGACTATAACTA
90	TTTTAGTTTTTCGAGCCAGTAATAAATTCTGT
91	TATGTAAACCTTTTTTAATGGAAAAATTACCT
92	TTGAATTATGCTGATGCAAATCCACAAATATA
93	GAGCAAAAACTTCTGAATAATGGAAGAAGGAG
94	TGGATTATGAAGATGATGAAACAAAATTTCAT
95	CGGAATTATTGAAAGGAATTGAGGTGAAAAAT
96	ATCAACAGTCATCATATTCCTGATTGATTGTT
97	CTAAAGCAAGATAGAACCCTTCTGAATCGTCT
98	GCCAACAGTCACCTTGCTGAACCTGTTGGCAA
99	GAAATGGATTATTTACATTGGCAGACATTCTG
100	TTTTTATAAGTATAGCCCGGCCGTCGAG
101	AGGGTTGATTTTATAAATCCTCATTAAATGATATTC
102	ACAAACAATTTTAATCAGTAGCGACAGATCGATAGC
103	AGCACCGTTTTTTAAAGGTGGCAACATAGTAGAAAA
104	TACATACATTTTGACGGGAGAATTAACTACAGGGAA
105	GCGCATTATTTTGCTTATCCGGTATTCTAAATCAGA
106	TATAGAAGTTTTCGACAAAAGGTAAAGTAGAGAATA
107	TAAAGTACTTTTCGCGAGAAAACTTTTTATCGCAAG
108	ACAAAGAATTTTATTAATTACATTTAACACATCAAG
109	AAAACAAATTTTTTCATCAATATAATCCTATCAGAT
110	GATGGCAATTTTAATCAATATCTGGTCACAAATATC
111	AAACCCTCTTTTACCAGTAATAAAAGGGATTCACCAGTCACACGTTTT
112	CCGAAATCCGAAAATCCTGTTTGAAGCCGGAA
113	CCAGCAGGGGCAAAATCCCTTATAAAGCCGGC
114	GCATAAAGTTCCACACAACATACGAAGCGCCA
115	GCTCACAATGTAAAGCCTGGGGTGGGTTTGCC
116	TTCGCCATTGCCGGAAACCAGGCATTAAATCA
117	GCTTCTGGTCAGGCTGCGCAACTGTGTTATCC
118	GTTAAAATTTAACCAATAGGAACCCGGCACC
119	AGACAGTCATTCAAAAGGGTGAGAAGCTATAT
120	AGGTAAAGAAATCACCATCAATATAATATTTT
121	TTTCATTTGGTCAATAACCTGTTTATATCGCG
122	TCGCAAATGGGGCGCGAGCTGAAATAATGTGT
123	TTTTAATTGCCCGAAAGACTTCAAAACACTAT
124	AAGAGGAACGAGCTTCAAAGCGAAGATACATT
125	GGAATTACTCGTTTACCAGACGACAAAAGATT
126	GAATAAGGACGTAACAAAGCTGCTCTAAAACA
127	CCAAATCACTTGCCCTGACGAGAACGCCAAAA
128	CTCATCTTGAGGCAAAAGAATACAGTGAATTT
129	AAACGAAATGACCCCCAGCGATTATTCATTAC
130	CTTAAACATCAGCTTGCTTTCGAGCGTAACAC
131	TCGGTTTAGCTTGATACCGATAGTCCAACCTA
132	TGAGTTTCGTCACCAGTACAAACTTAATTGTA

133	CCCCGATTTAGAGCTTGACGGGGAAATCAAAA
134	GAATAGCCGCAAGCGGTCCACGCTCCTAATGA
135	GAGTTGCACGAGATAGGGTTGAGTAAGGGAGC
136	GTGAGCTAGTTTCCTGTGTGAAATTTGGGAAG
137	TCATAGCTACTCACATTAATTGCGCCCTGAGA
138	GGCGATCGCACTCCAGCCAGCTTTGCCATCAA
139	GAAGATCGGTGCGGGCCTCTTCGCAATCATGG
140	AAATAATTTTAAATTGTAAACGTTGATATTCA
141	GCAAATATCGCGTCTGGCCTTCCTGGCCTCAG
142	ACCGTTCTAAATGCAATGCCTGAGAGGTGGCA
143	TATATTTTAGCTGATAAATTAATGTTGTATAA
144	TCAATTCTTTTAGTTTGACCATTACCAGACCG
145	CGAGTAGAACTAATAGTAGTAGCAAACCCTCA
146	GAAGCAAAAAAGCGGATTGCATCAGATAAAAA
147	TCAGAAGCCTCCAACAGGTCAGGATCTGCGAA
148	CCAAAATATAATGCAGATACATAAACACCAGA
149	CATTCAACGCGAGAGGCTTTTGCATATTATAG
150	ACGAGTAGTGACAAGAACCGGATATACCAAGC
151	AGTAATCTTAAATTGGGCTTGAGAGAATACCA
152	GCGAAACATGCCACTACGAAGGCATGCGCCGA
153	ATACGTAAAAGTACAACGGAGATTTCATCAAG
154	CAATGACACTCCAAAAGGAGCCTTACAACGCC
155	AAAAAAGGACAACCATCGCCCACGCGGGTAAA
156	TGTAGCATTCCACAGACAGCCCTCATCTCCAA
157	GTAAAGCACTAAATCGGAACCCTAGTTGTTCC
158	AGTTTGGAGCCCTTCACCGCCTGGTTGCGCTC
159	AGCTGATTACAAGAGTCCACTATTGAGGTGCC
160	ACTGCCCGCCGAGCTCGAATTCGTTATTACGC
161	CCCGGGTACTTTCCAGTCGGGAAACGGGCAAC
162	CAGCTGGCGGACGACGACAGTATCGTAGCCAG
163	GTTTGAGGGAAAGGGGGATGTGCTAGAGGATC
164	CTTTCATCCCCAAAAACAGGAAGACCGGAGAG
165	AGAAAAGCAACATTAAATGTGAGCATCTGCCA
166	GGTAGCTAGGATAAAAATTTTTAGTTAACATC
167	CAACGCAATTTTTGAGAGATCTACTGATAATC
168	CAATAAATACAGTTGATTCCCAATTTAGAGAG
169	TCCATATACATACAGGCAAGGCAACTTTATTT
170	TACCTTTAAGGTCTTTACCCTGACAAAGAAGT
171	CAAAAATCATTGCTCCTTTTGATAAGTTTCAT
172	TTTGCCAGATCAGTTGAGATTTAGTGGTTTAA
173	AAAGATTCAGGGGGTAATAGTAAACCATAAAT
174	TTTCAACTATAGGCTGGCTGACCTTGTATCAT
175	CCAGGCGCTTAATCATTGTGAATTACAGGTAG
176	CGCCTGATGGAAGTTTCCATTAAACATAACCG
177	TTTCATGAAAATTGTGTCGAAATCTGTACAGA
178	ATATATTCTTTTTTCACGTTGAAAATAGTTAG
179	AATAATAAGGTCGCTGAGGCTTGCAAAGACTT
180	CGTAACGATCTAAAGTTTTGTCGTGAATTGCG
181	ACCCAAATCAAGTTTTTTGGGGTCAAAGAACG

182 TGGACTCCCTTTTCACCAGTGAGACCTGTCGT
183 TGGTTTTTAACGTCAAAGGGCGAAGAACCATC
184 GCCAGCTGCCTGCAGGTCGACTCTGCAAGGCG
185 CTTGCATGCATTAATGAATCGGCCCGCCAGGG
186 ATTAAGTTCGCATCGTAACCGTGCGAGTAACA
187 TAGATGGGGGGTAACGCCAGGGTTGTGCCAAG
188 ACCCGTCGTCATATGTACCCCGGTAAAGGCTA
189 CATGTCAAGATTCTCCGTGGGAACCGTTGGTG
190 TCAGGTCACTTTTGCGGGAGAAGCAGAATTAG
191 CTGTAATATTGCCTGAGAGTCTGGAAAACTAG
192 CAAAATTAAAGTACGGTGTCTGGAAGAGGTCA
193 TGCAACTAAGCAATAAAGCCTCAGTTATGACC
194 TTTTTGCGCAGAAAACGAGAATGAATGTTTAG
195 AAACAGTTGATGGCTTAGAGCTTATTTAAATA
196 ACTGGATAACGGAACAACATTATTACCTTATG
197 ACGAACTAGCGTCCAATACTGCGGAATGCTTT
198 CGATTTAGAGGACAGATGAACGGCGCGACCT
199 CTTTGAAAAGAACTGGCTCATTATTTAATAAA
200 GCTCCATGAGAGGCTTTGAGGACTAGGGAGTT
201 ACGGCTACTTACTTAGCCGGAACGCTGACCAA
202 AAAGGCCGAAAGGAACAACTAAAGCTTTCCAG
203 GAGAATAGCTTTTGCGGGATCGTCGGGTAGCA
204 ACGTTAGTAAATGAATTTTCTGTAAGCGGAGT
205 TTTTCGATGGCCCACTACGTAAACCGTC
206 TATCAGGGTTTTCGGTTTGCGTATTGGGAACGCGCG
207 GGGAGAGGTTTTTGTAAAACGACGGCCATTCCCAGT
208 CACGACGTTTTTGTAATGGGATAGGTCAAAACGGCG
209 GATTGACCTTTTGATGAACGGTAATCGTAGCAAACA
210 AGAGAATCTTTTGGTTGTACCAAAAACAAGCATAAA
211 GCTAAATCTTTTCTGTAGCTCAACATGTATTGCTGA
212 ATATAATGTTTTCATTGAATCCCCCTCAAATCGTCA
213 TAAATATTTTTTGGAAGAAAAATCTACGACCAGTCA
214 GGACGTTGTTTTCATAAGGGAACCGAAAGGCGCAG
215 ACGGTCAATTTTGACAGCATCGGAACGAACCCTCAG
216 CAGCGAAATTTTAACTTTCAACAGTTTCTGGGATTTTGCTAAACTTTT

Modified staple strands

A'101
AGGGTTGATTTTATAAATCCTCATTAAATGATATTCACAAACAATTTTTTATATGGTCAACTG
A'110
GATGGCAATTTTAATCAATATCTGGTCACAAATATCAAACCCTCTTTTTTATATGGTCAACTG
A'206 TATCAGGGTTTTCGGTTTGCGTATTGGGAACGCGCG GGGAGAGG TTTTT TATATGGTCAACTG
A'215 ACGGTCAATTTTGACAGCATCGGAACGAACCCTCAG CAGCGAAA TTTTT TATATGGTCAACTG
A'102 AATCAGTAGCGACAGATCGATAGCAGCACCGTTTTTTTATATGGTCAACTG

A'104	GACGGGAGAATTAACTACAGGGAAGCGCATTATTTTTATATGGTCAACTG
A'106	CGACAAAAGGTAAAGTAGAGAATATAAAGTACTTTTTATATGGTCAACTG
A'108	ATTAATTACATTTAACACATCAAGAAAACAAATTTTTATATGGTCAACTG
A'110	AATCAATATCTGGTCACAAATATCAAACCCTCTTTTTATATGGTCAACTG
A'214	TCATAAGGGAACCGAAAGGCGCAGACGGTCAATTTTTATATGGTCAACTG
A'212	CATTGAATCCCCCTCAAATCGTCATAAATATTTTTTTATATGGTCAACTG
A'210	GGTTGTACCAAAAACAAGCATAAAGCTAAATCTTTTTATATGGTCAACTG
A'208	GTAATGGGATAGGTCAAAACGGCGGATTGACCTTTTTATATGGTCAACTG
A'206	CGGTTTGCGTATTGGGAACGCGCGGGGAGAGGTTTTTATATGGTCAACTG

S102	AATCAGTAGCGACAGATCGATAGC
S103	TAAAGGTGGCAACATAGTAGAAAA
S105	GCTTATCCGGTATTCTAAATCAGA
S107	CGCGAGAAAACTTTTTATCGCAAG
S109	TTCATCAATATAATCCTATCAGAT
S111	ACCAGTAATAAAAGGGATTCACCAGTCACACG
S207	TGTAAAACGACGGCCATTCCCAGT
S209	GATGAACGGTAATCGTAGCAAACA
S211	CTGTAGCTCAACATGTATTGCTGA
S213	GGAAGAAAAATCTACGACCAGTCA
S215	GACAGCATCGGAACGAACCCTCAG
S216	AACTTTCAACAGTTTCTGGGATTTTGCTAAACTTTT

4.5.14.3 Templation experiment

DNA nanofibers were prepared following a previously reported protocol (see preparation of DNA fibers in *Experimental Section 4.5.5*). 8 µL of preformed DNA fibers prepared at 2.5 or 5 µM (total DNA) were mixed with 2 µL assembled DNA origami tiles (initial stock concentration of tile = 4-7.92 nM) and incubated at room temperature overnight. The samples were then analyzed by AFM under dry conditions. For AGE studies, DNA origami samples prepared at 5 nM were mixed with DNA nanofibers prepared at 5 µM (with respect to total DNA) and incubated overnight at room temperature. As an example, for 1000 x excess, 2.5 µL of 5 µM solution (total DNA) of DNA fibers was mixed with 2.5 µL of 5 nM DNA origami tiles. For 800 x and 500 x molar excess conditions, the volume ratio of each sample was adjusted, accordingly.

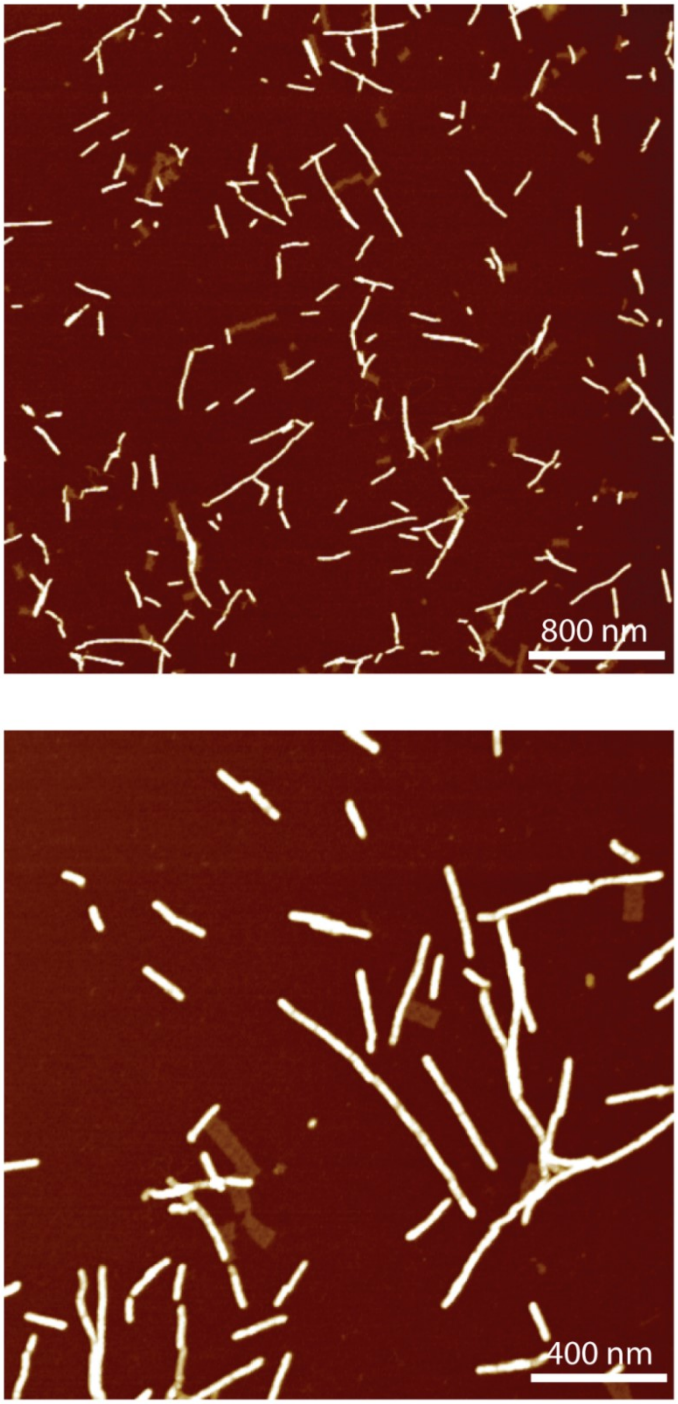

Figure 4.57 – Additional AFM images of one-sided templation of Cy3Cy3-DNA fibers on rectangular DNA origami tiles.

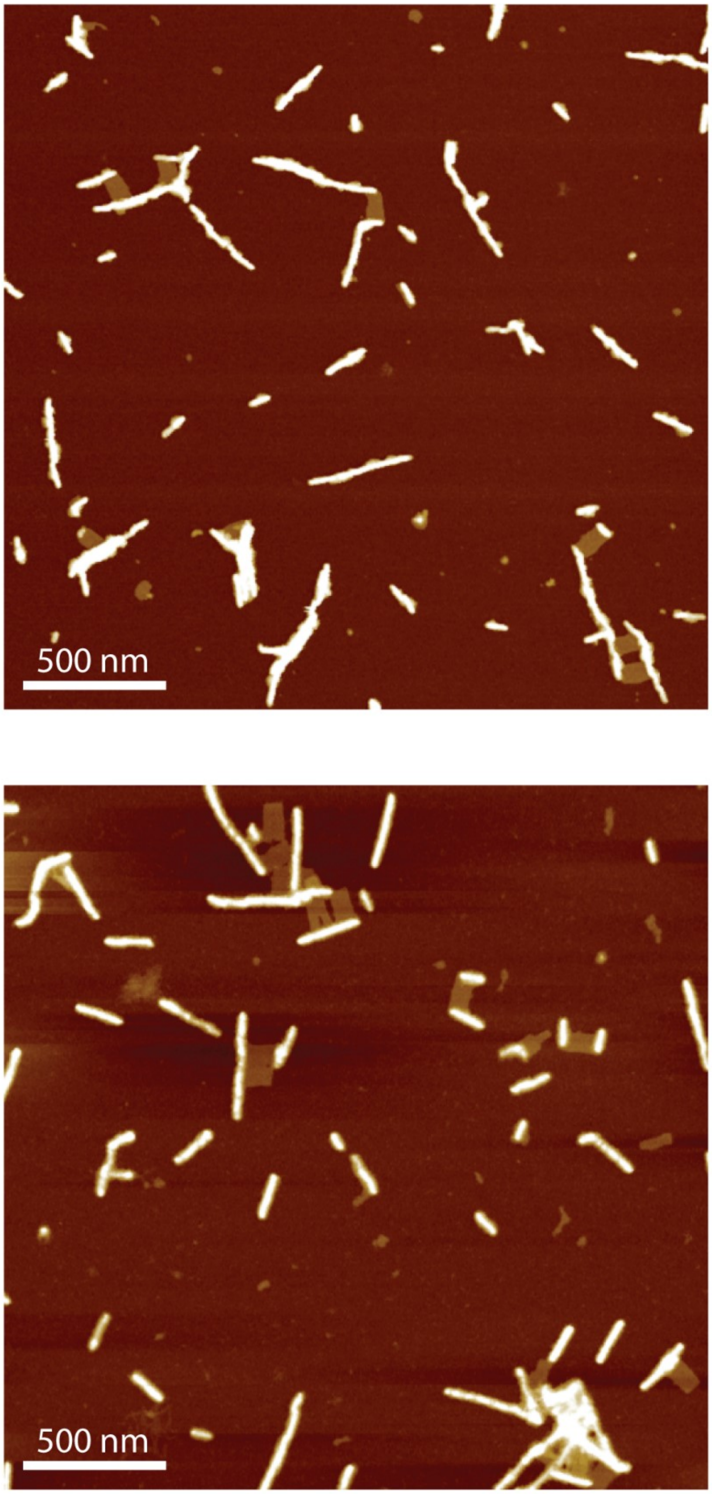

Figure 4.58 – Additional AFM images of two-sided templation of Cy3Cy3-DNA fibers on rectangular DNA origami tiles with 2 binding arms/edge forming a "railroad track".

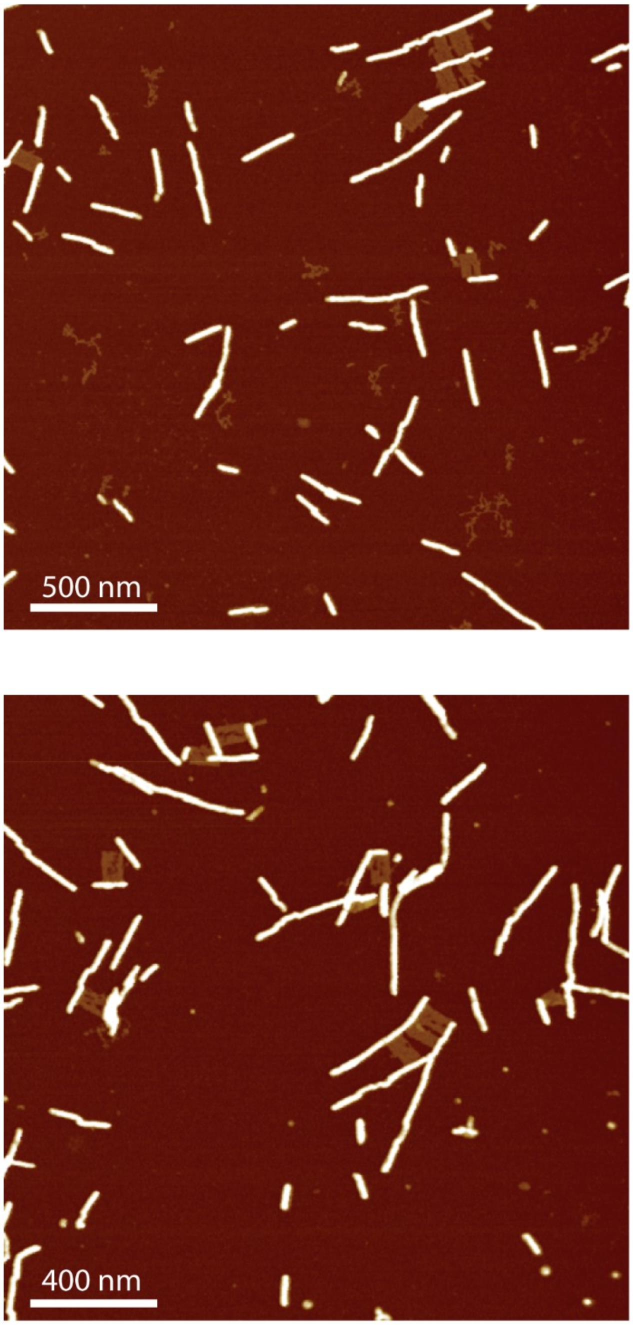

Figure 4.59 – Additional AFM images of two-sided templation of Cy3Cy3-DNA fibers on rectangular DNA origami with 5 binding arms/edge.

4.6 References

1. Lehn, J.-M., *Angew. Chem. Int. Ed. Engl.* **1990,** *29* (11), 1304-1319.

2. Claessens, C. G.; Stoddart, J. F., *J. Phys. Org. Chem.* **1997,** *10* (5), 254-272.

3. Wang, X.; Guerin, G.; Wang, H.; Wang, Y.; Manners, I.; Winnik, M. A., *Science* **2007,** *317* (5838), 644-647.

4. Strassert, C. A.; Chien, C.-H.; Galvez Lopez, M. D.; Kourkoulos, D.; Hertel, D.; Meerholz, K.; De Cola, L., *Angew. Chem. Int. Ed.* **2011,** *50* (4), 946-950.

5. Sirringhaus, H.; Brown, P. J.; Friend, R. H.; Nielsen, M. M.; Bechgaard, K.; Langeveld-Voss, B. M. W.; Spiering, A. J. H.; Janssen, R. A. J.; Meijer, E. W.; Herwig, P.; de Leeuw, D. M., *Nature* **1999,** *401*, 685.

6. Kashiwagi, D.; Sim, S.; Niwa, T.; Taguchi, H.; Aida, T., *J. Am. Chem. Soc.* **2018,** *140* (1), 26-29.

7. Hartgerink, J. D.; Beniash, E.; Stupp, S. I., *Science* **2001,** *294* (5547), 1684-1688.

8. Kastler, M.; Pisula, W.; Wasserfallen, D.; Pakula, T.; Müllen, K., *J. Am. Chem. Soc.* **2005,** *127* (12), 4286-4296.

9. Hill, J. P.; Jin, W.; Kosaka, A.; Fukushima, T.; Ichihara, H.; Shimomura, T.; Ito, K.; Hashizume, T.; Ishii, N.; Aida, T., *Science* **2004,** *304* (5676), 1481-1483.

10. Zhang, L.; Eisenberg, A., *Science* **1995,** *268* (5218), 1728-31.

11. Groschel, A. H.; Walther, A.; Lobling, T. I.; Schacher, F. H.; Schmalz, H.; Muller, A. H. E., *Nature* **2013,** *503* (7475), 247-251.

12. Schacher, F. H.; Rupar, P. A.; Manners, I., *Angew. Chem. Int. Ed.* **2012,** *51* (32), 7898-7921.

13. De Greef, T. F.; Smulders, M. M.; Wolffs, M.; Schenning, A. P.; Sijbesma, R. P.; Meijer, E. W., *Chem. Rev.* **2009,** *109* (11), 5687-754.

14. Smulders, M. M.; Nieuwenhuizen, M. M.; de Greef, T. F.; van der Schoot, P.; Schenning, A. P.; Meijer, E. W., *Chem. Eur J.* **2010,** *16* (1), 362-7.

15. O'Shaughnessy, B.; Vavylonis, D., *Phys. Rev. Lett.* **2003,** *90* (11), 118301.

16. Cui, H.; Chen, Z.; Zhong, S.; Wooley, K. L.; Pochan, D. J., *Science* **2007,** *317* (5838), 647.

17. Korevaar, P. A.; Newcomb, C. J.; Meijer, E. W.; Stupp, S. I., *J. Am. Chem. Soc.* **2014,** *136* (24), 8540-8543.

18. Lohr, A.; Lysetska, M.; Würthner, F., *Angew. Chem. Int. Ed.* **2005,** *44* (32), 5071-5074.

19. Korevaar, P. A.; George, S. J.; Markvoort, A. J.; Smulders, M. M. J.; Hilbers, P. A. J.; Schenning, A. P. H. J.; De Greef, T. F. A.; Meijer, E. W., *Nature* **2012,** *481*, 492.

20. Aliprandi, A.; Mauro, M.; De Cola, L., *Nat. Chem.* **2015,** *8*, 10.

21. Hao, C.; Zehuan, H.; Han, W.; Jiang-Fei, X.; Xi, Z., *Angew. Chem. Int. Ed.* **2017,** *56* (52), 16575-16578.

22. Gilroy, J. B.; Gädt, T.; Whittell, G. R.; Chabanne, L.; Mitchels, J. M.; Richardson, R. M.; Winnik, M. A.; Manners, I., *Nat. Chem.* **2010,** *2* (7), 566-570.

23. Hudson, Z. M.; Boott, C. E.; Robinson, M. E.; Rupar, P. A.; Winnik, M. A.; Manners, I., *Nat. Chem.* **2014,** *6* (10), 893-898.

24. Qiu, H.; Hudson, Z. M.; Winnik, M. A.; Manners, I., *Science* **2015,** *347* (6228), 1329-1332.

25. Mukhopadhyay, R. D.; Ajayaghosh, A., *Science* **2015,** *349* (6245), 241-242.

26. Kang, J.; Miyajima, D.; Mori, T.; Inoue, Y.; Itoh, Y.; Aida, T., *Science* **2015,** *347* (6222), 646-651.

27. Van der Zwaag, D.; de Greef, T. F. A.; Meijer, E. W., *Angew. Chem. Int. Ed.* **2015,** *54* (29), 8334-8336.

28. Huang, Z.; Yang, L.; Liu, Y.; Wang, Z.; Scherman, O. A.; Zhang, X., *Angew. Chem.* **2014,** *126* (21), 5455-5459.

29. Ogi, S.; Sugiyasu, K.; Manna, S.; Samitsu, S.; Takeuchi, M., *Nat. Chem.* **2014,** *6* (3), 188-95.

30. Ogi, S.; Stepanenko, V.; Sugiyasu, K.; Takeuchi, M.; Würthner, F., *J. Am. Chem. Soc.* **2015,** *137* (9), 3300-3307.

31. Zhang, K.; Yeung, M. C.; Leung, S. Y.; Yam, V. W., *Proc. Natl. Acad. Sci. U. S. A.* **2017,** *114* (45), 11844-11849.

32. Krieg, E.; Bastings, M. M. C.; Besenius, P.; Rybtchinski, B., *Chem. Rev.* **2016,** *116* (4), 2414-2477.

33. Dankers Patricia, Y. W.; Hermans Thomas, M.; Baughman Travis, W.; Kamikawa, Y.; Kieltyka Roxanne, E.; Bastings Maartje, M. C.; Janssen Henk, M.; Sommerdijk Nico, A. J. M.; Larsen, A.; van Luyn Marja, J. A.; Bosman Anton, W.; Popa Eliane, R.; Fytas, G.; Meijer, E. W., *Adv. Mater.* **2012,** *24* (20), 2703-2709.

34. Hule, R. A.; Nagarkar, R. P.; Hammouda, B.; Schneider, J. P.; Pochan, D. J., *Macromolecules* **2009,** *42* (18), 7137-7145.

35. Nazemi, A.; Boott, C. E.; Lunn, D. J.; Gwyther, J.; Hayward, D. W.; Richardson, R. M.; Winnik, M. A.; Manners, I., *J. Am. Chem. Soc.* **2016,** *138* (13), 4484-4493.

36. Arno, M. C.; Inam, M.; Coe, Z.; Cambridge, G.; Macdougall, L. J.; Keogh, R.; Dove, A. P.; O'Reilly, R. K., *J. Am. Chem. Soc.* **2017,** *139* (46), 16980-16985.

37. Seeman, N. C., *Annu. Rev. Biochem* **2010,** *79*, 65-87.

38. Aldaye, F. A.; Palmer, A. L.; Sleiman, H. F., *Science* **2008,** *321* (5897), 1795-9.

39. Rothemund, P. W. K., *Nature* **2006,** *440* (7082), 297-302.

40. Seeman, N. C.; Sleiman, H. F., *Nat. Rev. Mater.* **2017,** *3*, 17068.

41. Mai, Y.; Eisenberg, A., *Chem. Soc. Rev.* **2012,** *41* (18), 5969-85.

42. Serpell, C. J.; Edwardson, T. G. W.; Chidchob, P.; Carneiro, K. M. M.; Sleiman, H. F., *J. Am. Chem. Soc.* **2014,** *136* (44), 15767-15774.

43. Chidchob, P.; Edwardson, T. G. W.; Serpell, C. J.; Sleiman, H. F., *J. Am. Chem. Soc.* **2016,** *138* (13), 4416-4425.

44. Edwardson, T. G. W.; Carneiro, K. M. M.; McLaughlin, C. K.; Serpell, C. J.; Sleiman, H. F., *Nat. Chem.* **2013,** *5*, 868.

45. Vyborna, Y.; Vybornyi, M.; Rudnev, A. V.; Häner, R., *Angew. Chem. Int. Ed.* **2015,** *54* (27), 7934-7938.

46. Alemdaroglu, F. E.; Alemdaroglu, N. C.; Langguth, P.; Herrmann, A., *Macromol. Rapid Commun.* **2008,** *29* (4), 326-329.

47. Banga, R. J.; Meckes, B.; Narayan, S. P.; Sprangers, A. J.; Nguyen, S. T.; Mirkin, C. A., *J. Am. Chem. Soc.* **2017,** *139* (12), 4278-4281.

48. Cottenye, N.; Syga, M.-I.; Nosov, S.; Muller, A. H. E.; Ploux, L.; Vebert-Nardin, C., *Chem. Commun.* **2012,** *48* (20), 2615-2617.

49. Kim, C.-J.; Hu, X.; Park, S.-J., *J. Am. Chem. Soc.* **2016,** *138* (45), 14941-14947.

50. Wilks, T. R.; Bath, J.; de Vries, J. W.; Raymond, J. E.; Herrmann, A.; Turberfield, A. J.; O'Reilly, R. K., *ACS Nano* **2013,** *7* (10), 8561-8572.

51. List, J.; Weber, M.; Simmel, F. C., *Angew. Chem. Int. Ed. Engl.* **2014,** *53* (16), 4236-9.

52. Ding, K.; Alemdaroglu, F. E.; Börsch, M.; Berger, R.; Herrmann, A., *Angew. Chem. Int. Ed.* **2007,** *46* (7), 1172-1175.

53. Chien, M.-P.; Rush, A. M.; Thompson, M. P.; Gianneschi, N. C., *Angew. Chem. Int. Ed.* **2010,** *49* (30), 5076-5080.

54. Chao, Z.; Yiyang, Z.; Yuanchen, D.; Fen, W.; Dianming, W.; Ling, X.; Dongsheng, L., *Adv. Mater.* **2016,** *28* (44), 9819-9823.

55. Zhiyong, Z.; Chun, C.; Yuanchen, D.; Zhongqiang, Y.; Qing-Hua, F.; Dongsheng, L., *Angew. Chem. Int. Ed.* **2014,** *53* (49), 13468-13470.

56. Yuanchen, D.; Yawei, S.; Liying, W.; Dianming, W.; Tao, Z.; Zhongqiang, Y.; Zhong, C.; Qiangbin, W.; Qinghua, F.; Dongsheng, L., *Angew. Chem. Int. Ed.* **2014,** *53* (10), 2607-2610.

57. Wang, L.; Feng, Y.; Yang, Z.; He, Y.-M.; Fan, Q.-H.; Liu, D., *Chem. Commun.* **2012,** *48* (31), 3715-3717.

58. Jia, F.; Lu, X.; Tan, X.; Zhang, K., *Chem. Commun.* **2015,** *51* (37), 7843-7846.

59. Tan, X.; Li, B. B.; Lu, X.; Jia, F.; Santori, C.; Menon, P.; Li, H.; Zhang, B.; Zhao, J. J.; Zhang, K., *J. Am. Chem. Soc.* **2015,** *137* (19), 6112-6115.

60. Edwardson, T. G.; Carneiro, K. M.; Serpell, C. J.; Sleiman, H. F., *Angew. Chem. Int. Ed. Engl.* **2014,** *53* (18), 4567-71.

61. Lutz, J.-F.; Ouchi, M.; Liu, D. R.; Sawamoto, M., *Science* **2013,** *341* (6146), 1238149.

62. Li, Z.; Zhang, Y.; Fullhart, P.; Mirkin, C. A., *Nano Lett.* **2004,** *4* (6), 1055-1058.

63. Alemdaroglu, F. E.; Ding, K.; Berger, R.; Herrmann, A., *Angew. Chem. Int. Ed. Engl.* **2006,** *45* (25), 4206-10.

64. Immoos, C. E.; Lee, S. J.; Grinstaff, M. W., *J. Am. Chem. Soc.* **2004,** *126* (35), 10814-10815.

65. de Lambert, B.; Chaix, C.; Charreyrex, M.-T.; Laurent, A.; Aigoui, A.; Perrin-Rubens, A.; Pichot, C., *Bioconjugate Chem.* **2005,** *16* (2), 265-274.

66. Schnitzler, T.; Herrmann, A., *Acc. Chem. Res.* **2012,** *45* (9), 1419-1430.

67. Hong, B. J.; Eryazici, I.; Bleher, R.; Thaner, R. V.; Mirkin, C. A.; Nguyen, S. T., *J. Am. Chem. Soc.* **2015,** *137* (25), 8184-8191.

68. Mirkin, C. A.; Letsinger, R. L.; Mucic, R. C.; Storhoff, J. J., *Nature* **1996,** *382* (6592), 607-9.

69. Alemdaroglu, F. E.; Alemdaroglu, N. C.; Langguth, P.; Herrmann, A., *Adv. Mater.* **2008,** *20* (5), 899-902.

70. Kedracki, D.; Maroni, P.; Schlaad, H.; Vebert-Nardin, C., *Adv. Funct. Mater.* **2014,** *24* (8), 1133-1139.

71. Fakhoury, J. J.; Edwardson, T. G.; Conway, J. W.; Trinh, T.; Khan, F.; Barlog, M.; Bazzi, H. S.; Sleiman, H. F., *Nanoscale* **2015,** *7* (48), 20625-34.

72. Jeong, J. H.; Park, T. G., *Bioconjugate Chem.* **2001,** *12* (6), 917-923.

73. Rush, A. M.; Nelles, D. A.; Blum, A. P.; Barnhill, S. A.; Tatro, E. T.; Yeo, G. W.; Gianneschi, N. C., *J. Am. Chem. Soc.* **2014,** *136* (21), 7615-7618.

74. Trinh, T.; Chidchob, P.; Bazzi, H. S.; Sleiman, H. F., *Chem. Commun.* **2016,** *52* (72), 10914-10917.

75. Bousmail, D.; Amrein, L.; Fakhoury, J. J.; Fakih, H. H.; Hsu, J. C. C.; Panasci, L.; Sleiman, H. F., *Chemical Science* **2017,** *8* (9), 6218-6229.

76. Cutler, J. I.; Auyeung, E.; Mirkin, C. A., *J. Am. Chem. Soc.* **2012,** *134* (3), 1376-1391.

77. Kwak, M.; Herrmann, A., *Chem. Soc. Rev.* **2011,** *40* (12), 5745-5755.

78. Pan, G.; Jin, X.; Mou, Q.; Zhang, C., *Chin. Chem. Lett.* **2017,** *28* (9), 1822-1828.

79. Wang, H.; Lin, W.; Fritz, K. P.; Scholes, G. D.; Winnik, M. A.; Manners, I., *J. Am. Chem. Soc.* **2007,** *129* (43), 12924-12925.

80. Du, J.; Lane, L. A.; Nie, S., *J. Control. Release* **2015,** *219*, 205-214.

81. Jelly, E. E., *Nature* **1936,** *138*, 1009.

82. Scheibe, G., *Angew. Chem.* **1937,** *50* (11), 212-219.

83. Eisele, D. M.; Knoester, J.; Kirstein, S.; Rabe, J. P.; Vanden Bout, D. A., *Nat. Nanotechnol.* **2009,** *4* (10), 658-63.

84. Von Berlepsch, H.; Böttcher, C.; Ouart, A.; Burger, C.; Dähne, S.; Kirstein, S., *J. Phys. Chem. B.* **2000,** *104* (22), 5255-5262.

85. Von Berlepsch, H.; Kirstein, S.; Böttcher, C., *J. Phys. Chem. B.* **2003,** *107* (36), 9646-9654.

86. Markova, L. I.; Malinovskii, V. L.; Patsenker, L. D.; Haner, R., *Chem. Commun.* **2013,** *49* (46), 5298-5300.

87. Wijnands, S. P. W.; Engelen, W.; Lafleur, R. P. M.; Meijer, E. W.; Merkx, M., *Nat. Commun.* **2018,** *9* (1), 65.

88. Lee, S. S.; Fyrner, T.; Chen, F.; Álvarez, Z.; Sleep, E.; Chun, D. S.; Weiner, J. A.; Cook, R. W.; Freshman, R. D.; Schallmo, M. S.; Katchko, K. M.; Schneider, A. D.; Smith, J. T.; Yun, C.; Singh, G.; Hashmi, S. Z.; McClendon, M. T.; Yu, Z.; Stock, S. R.; Hsu, W. K.; Hsu, E. L.; Stupp, S. I., *Nat. Nanotechnol.* **2017,** *12*, 821.

89. Daniel, M. C.; Astruc, D., *Chem. Rev.* **2004,** *104* (1), 293-346.

90. El-Sayed, M. A., *Acc. Chem. Res.* **2001,** *34* (4), 257-264.

91. Kuzyk, A.; Schreiber, R.; Fan, Z.; Pardatscher, G.; Roller, E.-M.; Högele, A.; Simmel, F. C.; Govorov, A. O.; Liedl, T., *Nature* **2012,** *483*, 311.

92. Lau Kai, L.; Hamblin Graham, D.; Sleiman Hanadi, F., *Small* **2014,** *10* (4), 660-666.

93. Gür, F. N.; Schwarz, F. W.; Ye, J.; Diez, S.; Schmidt, T. L., *ACS Nano* **2016,** *10* (5), 5374-5382.

94. Hong, F.; Zhang, F.; Liu, Y.; Yan, H., *Chem. Rev.* **2017,** *117* (20), 12584-12640.

95. Knudsen, J. B.; Liu, L.; Bank Kodal, A. L.; Madsen, M.; Li, Q.; Song, J.; Woehrstein, J. B.; Wickham, S. F.; Strauss, M. T.; Schueder, F.; Vinther, J.; Krissanaprasit, A.; Gudnason, D.; Smith, A. A.; Ogaki, R.; Zelikin, A. N.; Besenbacher, F.; Birkedal, V.; Yin, P.; Shih, W. M.; Jungmann, R.; Dong, M.; Gothelf, K. V., *Nat. Nanotechnol.* **2015,** *10* (10), 892-8.

96. Zhang, K.; Fang, H.; Chen, Z.; Taylor, J.-S. A.; Wooley, K. L., *Bioconjugate Chem.* **2008,** *19* (9), 1880-1887.

97. Geng, Y.; Dalhaimer, P.; Cai, S.; Tsai, R.; Tewari, M.; Minko, T.; Discher, D. E., *Nat. Nanotechnol.* **2007,** *2* (4), 249-55.

98. Mallikaratchy, P. R.; Ruggiero, A.; Gardner, J. R.; Kuryavyi, V.; Maguire, W. F.; Heaney, M. L.; McDevitt, M. R.; Patel, D. J.; Scheinberg, D. A., *Nucleic Acids Res.* **2011,** *39* (6), 2458-2469.

99. S. L. Beaucage, R. P. Iyer. Tetrahedron 1992, 48, 2223

100. Wen, Y.; McLaughlin, C. K.; Lo, P. K.; Yang, H.; Sleiman, H. F., *Bioconjugate Chem.* **2010,** *21* (8), 1413-1416

101. Luo, X.; Chidchob, P.; Rahbani Janane, F.; Sleiman Hanadi, F., *Small* **2017,** *14* (5), 1702660

102. A. M. Hung, C. M. Micheel, L. D. Bozano, L. W. Osterbur, G. M. Wallraff, J. N. Cha, *Nat. Nanotechnol.* **2010**, *5*, 121-126.

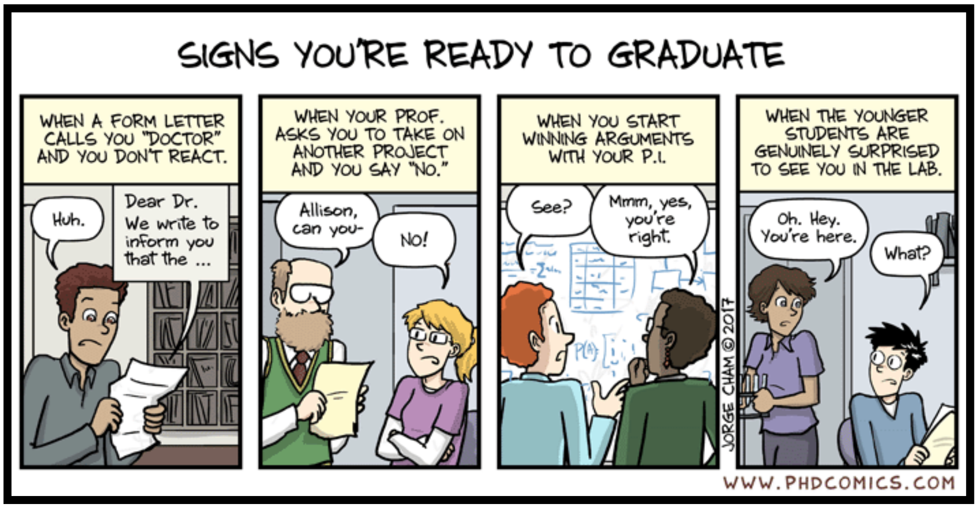

5

Conclusion and Future Work

5.1 Conclusions and contributions to original knowledge

The central theme of the work described in this thesis is the design, self-assembly and evaluation of amphiphilic DNA polymers as functional materials in drug delivery and materials science. Strategies to tackle many of the limitations hindering the success of nanoparticle-based drug delivery systems are demonstrated, and implemented in a DNA-nanoparticle platform, towards developing optimized delivery systems. A key concept is that control of length and sequence at the monomer level translates to highly uniform self-assembled drug delivery vehicles and supramolecular assemblies. Overall, the methods presented in this thesis provide access to new functional DNA-polymer systems with predefined morphologies and optimized properties adapted for applications in drug delivery and materials science.

The research presented in Chapter 2, describes the examination of sequence-defined DNA polymers as drug delivery vehicles for anticancer drugs, namely BKM120, a drug used for the treatment of Chronic Lymphocytic Leukemia (CLL). The use of phosphoramidite solid-phase chemistry as a synthetic method allows for control over the sequence and length of the DNA polymer. Using this system, BKM120-loaded DNA particles are generated with monodispersity superior to other DNA-polymer based drug delivery systems. A thorough study on the stability of the system showed that the structures are stable for over 1 month – a highly desirable property in drug formulation. Additionally, these DNA nanoparticles are one of few examples of oligonucleotide-based nanostructures showing high cellular uptake without transfection. The *in vitro* activity of BKM120-loaded DNA nanoparticles shows their success to act as sensitizers when combined with other anticancer drugs, and their ability to induce programmed cellular death in primary CLL patient cells. Furthermore, we present the first *in vivo* study of a DNA-polymer system. Our results show full-body distribution and long circulation times of DNA nanoparticles in mice, with minimal accumulation in the brain. Since BKM120 exhibits many of its neurological side-effects by crossing the blood-brain barrier, this finding could potentially limit the side-effects of this drug, or any drug exhibiting effects in the central nervous system. Additionally, DNA nanoparticles show high accumulation in tumors, a highly desirable property for cancer-targeted drug delivery. Overall, this chapter highlights the potential of sequence-defined DNA nanoparticles as a general platform for chemotherapeutic drug delivery.

Chapter 3 builds on the findings of Chapter 2 and presents several strategies to address challenges standing in the face of general polymeric nanocarriers, with particular emphasis on DNA nanoparticle-based systems. Optimization studies to our first-generation DNA polymer vehicles start with the introduction of targeting ligands that show enhanced structural uptake in cells expressing specific receptors. This is mediated through DNA hybridization, where DNA aptamers specific to breast cancer cells are bound to the nanoparticle corona. Targeting diseased cells that display specific-cellular markers, while leaving normal cells unaffected, is very important for the success of any potential drug delivery system. A stimuli-responsive system is then presented which releases an oligonucleotide cargo upon binding to a genetic marker. This system can be adapted to respond to any intracellular trigger, to deliver a combination of oligonucleotide therapeutics, or small molecule prodrugs attached to a therapeutic oligonucleotide through a hydrolysable linker allowing dual therapy. We then build on our previous work that evaluated the uptake of nanostructures in cancer cell lines. Here, studies on the cellular uptake of DNA nanoparticles in normal human epidermis keratinocytes show that these structures are readily internalized in cells displaying different plasma membrane make up from cancer cells. This property allows them to be used not only for anticancer drug delivery but also for delivery of cosmetic actives into skin cells. We then show that a simple modification to the DNA greatly enhances nanoparticle resistance to nucleases. Furthermore, we evaluate the interaction of DNA nanoparticles with a major serum protein and show a strategy to further protect structures during circulation and selectively release the "shield" in tumor microenvironments. Finally, we show strategies of enhancing nanoparticle stability through covalent cross-linking using disulfide chemistry. Overall, this chapter presents different strategies that are now made compatible with DNA nanoparticle assemblies towards an optimized drug delivery system. Compared to other systems, which are usually designed to address a single task due to an inherent synthetic limitation or incompatibility of different modifications, our versatile synthetic approach offers an advantage of the added effect of several modifications in a single molecule affording sophisticated smart materials for increasing function.

The work in Chapter 4 presents a method of generating new functional materials that show promise in biosensing and drug delivery applications. The introduction of a single or two cyanine dyes to DNA polymers causes a drastic morphological shift from spheres to length-controlled one-dimensional (1D) DNA nanofibers. Due to their high aspect ratio and rigidity, one-dimensional structures are particularly interesting for applications in creating complex linear arrays and drug delivery where they show increased uptake compared to spheres. The power of this approach is in the creation of 1D architectures with controlled dimensionality, where the length of fiber can be predefined prior to formation. Notably, the preparation DNA nanofibers with controlled length is demonstrated through seeded-growth mechanism, which to our knowledge has not been reported for DNA polymer systems. The potential application of DNA nanofibers as bioanalytical tools is highlighted through changes of dye optical properties upon assembly/disassembly. Templation of gold nanoparticles along fiber lengths with control over the ratio of bound particles, and selective directional templation of fibers on DNA origami, provide a method for generating functional nanomaterials and hierarchical complex architectures. This system will be valuable for creation of extended plasmonic architectures and as a platform for dual drug delivery and biosensing.

Overall, this work reflects our efforts towards developing functional self-assembled structures based on this new class of DNA polymers in relation to drug delivery and supramolecular chemistry. This technology is envisaged to see many more applications in various fields of study and inspire researchers to pursue more exciting functionalities hidden in its potential.

5.2 Suggestions for Future Work

The DNA nanoparticle platform described in Chapters 2 and 3 has great potential to be used in biological applications. As such, future work will be focused on optimizing the system’s scope of anticancer drug encapsulation, which is already underway in our group. Our current efforts have shown the encapsulation of paclitaxel, yet, the generality of this approach with different small molecule drugs would be an important aspect to explore. In previous work, we have shown the incorporation of antisense oligonucleotide therapeutics within this platform which cause gene silencing to a greater extent than antisense therapeutics delivered alone. The potential of DNA nanoparticles for combination small molecule and oligonucleotide therapeutics can be explored by modifying the DNA portion and testing nanoparticle activity *in vitro* and *in vivo*.

As a starting point, cross-linking studies should be optimized for the DNA nanoparticle system. Different positions of disulfide linkages can be evaluated to arrive at an optimal combination of the number and spacing between groups for high reaction yields. A range of different reducing agents can be tested, including hydrophilic and hydrophobic molecules depending on the desired location of cross-linking. In relevance to drug encapsulation, the amount of drug leakage will be compared between cross-linked and unmodified DNA nanoparticles. Small molecule drugs can also be attached to DNA-polymers via cleavable linkages to minimize leakage. Additionally, the critical micellar concentration (CMC) of cross-linked DNA nanoparticles can be evaluated to measure nanoparticle stability under high dilution factors. Cross-linked nanoparticles can also be evaluated for *in vivo* biodistribution and their profile compared to our findings for unmodified nanoparticles. Eventually, *in vivo* studies on the pharmacokinetics, toxicity and efficacy of drug-loaded particles can be evaluated in tumor models to study the nanoparticle therapeutic effect. In parallel, phosphorothioated DNA which shows enhanced resistance towards nuclease can be incorporated as the DNA part during nanoparticle synthesis. Furthermore, PEG and acid-labile PEG-acetal molecules can be evaluated for increased particle stability. First, particle nuclease stability can be tested, then particle interaction with serum proteins can be evaluated. Additionally, for PEG-acetal linkers, DNA functionalization and selective cleavage of the PEG-moiety in acidic buffer conditions can be evaluated in analogy to acidic tumor microenvironments. Cleavable PEG molecules can be ultimately used as a protective “stealth shield” for nanoparticles in circulation that are shed in tumor microenvironments, exposing the active particles.

For targeting studies, we have shown the increased uptake of structures expressing specific receptors. Competition studies can be performed wherein the receptors are saturated with ligands prior to aptamer-nanoparticle addition. This will provide additional characterization on the mechanism of internalization. The uptake of aptamer-DNA nanoparticles can also be evaluated in live cells, and if high uptake is observed then *in vivo* studies can be underway. It will also be necessary to evaluate the effect of targeting ligand density and steric hindrance on receptor binding. Additionally, since cross-linking doesn't involve any DNA manipulation, cross-linked aptamer-DNA micelles could be generated to compare their uptake with unmodified structures and test whether any structural destabilization occurs upon receptor binding. Given that different DNA-polymers can be mixed to generate hybrid structures, particles consisting of targeting ligands and oligonucleotide therapeutics can be generated to test if aptamer-particles exhibit a higher therapeutic activity compared to structures lacking an aptamer in cell types over-expressing specific receptors.

Stimuli-responsive particles show great potential for delivery to live cells since they strictly recognize oligonucleotide sequences present intracellularly. MicroRNA134 was used as a model stimulus for target differentiating skin cells, but the strategy can be modified for different genetic markers overexpressed in specific cell-types. Currently, in most stimuli-responsive systems, a recognition event leads to the release of a single therapeutic molecule. This stoichiometric delivery of therapeutics is limiting but can be addressed by the release of multiple drug molecules from a single binding event. For example, oligomers of small-molecule drugs (joined through labile linkers) can be attached to DNA through enzyme (or redox-sensitive) cleavable linkers to form prodrugs. Upon recognition, the DNA-oligo(drug) conjugate (prodrug) is released and subsequently cleaved releasing the now active drug molecules. The DNA strand can also be chosen as an antisense therapeutic oligonucleotide adding another layer of conditional therapy.

For all the aforementioned studies, understanding the intracellular fate of structures will be valuable for assessing the success of these strategies and for troubleshooting. It will hence be necessary to understand the mechanism of uptake of structures, their intracellular trafficking and translocation. To tackle the limitation of endosomal trapping and recycling, agents that aid compartmental escape can be incorporated into the DNA-nanoparticle platform. Cell-penetrating peptides or pH-sensitive polymers can be conjugated to ensure endosomal disruption and nanoparticle availability in the cytoplasm.

Ultimately, all the described approaches will be merged into one "smart" DNA nanoparticle system equipped with small-molecule drugs and oligonucleotide therapeutics, and that shows increased stability, enhanced blood circulation and high targeting capabilities.

The work in Chapter 4 reports the discovery of a different mode of self-assembly upon the introduction of a cyanine dye unit in DNA polymers, shifting them from spheres to length-defined nanofibers. Given that elongated one-dimensional morphologies show desirable behaviour both *in vitro* and *in vivo*, DNA fibers can be explored for drug delivery applications. Seeded growth of DNA fibers was demonstrated and hierarchical architectures were obtained through directional templation of fibers along DNA origami. Using seeded growth, guided-growth on DNA origami pre-defined tracks can be investigated. The ability to precisely control the orientation of material at the nanoscale is a main objective of nanotechnology. By utilizing the interesting electronic properties of cyanine, this paves the way toward the development of electronic circuitry and optical wires with arbitrary geometries. The assembly of cyanine dyes in close packed structures can generate robust excitons between dye molecules. Additionally, other chromophores such a pyrene can be conjugated to DNA polymers to study their self-assembly and electronic and optical properties. Investigating the electronic coupling between dyes and understanding how nanoparticle core rigidity and the local dye environment can influence electronic coupling will be important towards designing exciton networks. These designs will allow the construction of efficient light-harvesting devices mimicking natural systems, from soft supramolecular materials.

5.3 List of Publications

1. **Bousmail, D.**; Chidchob, P.; Sleiman, H. F. *J. Am. Chem. Soc.* **2018**, *140* (30), 9518-9530.

2. **Bousmail, D**.; Amrein, L.; Fakhoury, J. J.; Fakih, H. H.; Hsu, C. C.; Panasci, L.; Sleiman, H. F. *Chem. Sci.* **2017,** *8* (9), 18-29.

3. Edwardson, T. G. W.; Lau, K. L.; **Bousmail, D.;** Serpell, C. J.; Sleiman, H. F. *Nat. Chem.* **2016**, *8*, 162.